

BULGARIAN CHEMICAL COMMUNICATIONS

2017 Volume 49 / Special Issue D

Dedicated to Academician Ivan Juchnovski on the occasion of his
80th birthday

*Journal of the Chemical Institutes
of the Bulgarian Academy of Sciences
and of the Union of Chemists in Bulgaria*

Scientific biography of Academician Ivan Juchnovski



Ivan Nikolov Juchnovski was born on 12 August 1937 in Sofia. In 1945 his family was exiled in the town of Sevlievo where he finished secondary school in 1955. In 1961 he graduated from the Higher Institute of Chemical Technology which is currently named University of Chemical Technology and Metallurgy (UCTM) in Sofia, as a chemical engineer with a major in Organic synthesis, pharmaceutical drugs and high-molecular compounds. From 1961 to 1963 Juchnovski worked in UCTM as an assistant professor in the Department of Organic Chemistry.

In 1963 Ivan Juchnovski began his work as a Junior scientist at the Institute of Organic Chemistry with Centre of Phytochemistry (IOCP) at the Bulgarian Academy of Sciences (BAS), Sofia where he defended his PhD in 1968. There Juchnovski acquired the academic rank associate professor in 1972. In 1982 he defended his doctor of sciences dissertation and became full professor in physical methods in organic chemistry in 1984. In 1989 Professor Juchnovski was elected a Corresponding Member of the Bulgarian Academy of Sciences, and in 1997 he became an Academician (Full Member).

In 1979 Professor Juchnovski established the Laboratory for Structural Organic Chemistry at IOCP and in 1989 he was elected Director of IOCP. From 1990 to 1996 he served as a Vice President of BAS. Between 1996 and 2008 Academician Ivan Juchnovski was elected three times President of the Bulgarian Academy of Sciences.

The scientific activity of Ivan Juchnovski began at a time when Bulgarian science was isolated from the free world: communication between scientists was limited, and publications of science papers needed permission from a special public institution. In a situation like this and despite the fact that throughout his career Prof. Juchnovski has never been on a specialization abroad, his ability to assign himself research tasks and find subject fields of high scientific significance was remarkable. Even during the time of his student's studies in the UCTM Juchnovski developed and issued research articles, and his PhD thesis was worked out without a scientific advisor. The scientific activity of Academician Ivan Juchnovski is extensively devoted to the study of electronic structure of conjugated organic compounds and the genetically related negative ions, which are intermediates in important organic reactions, by means of the combined application of infrared spectroscopy, quantum chemical methods, the correlation analysis and isotop labelled compounds.

There were established fundamental patterns in the transmission of polar effects of substituents through the systems of conjugated bonds on the characteristic frequencies and intensities, and particularly the exponential decrease of the polar effect of the substituents with the increase of the number of the double bonds in the polyen system. Later these patterns were approved by other authors. Juchnovski and co-workers proved that a number of considerable deviations of the correlations of characteristic frequencies are due to specific electronic effects of substituents (metha effect), incorrect assignment of frequencies, or vibrational interaction in molecules.

A new approach in modelling the derivative of the molecular dipol moment in nitrile group vibration was applied. By means of these model calculations on the basis of empiric and semi-empiric quantum chemical methods all fundamental relations of infrared band intensity in the spectra of the main types of conjugated compounds were explained. It was found that the integral intensity of the nitrile group band depends considerably on the topology of the conjugated system. The application of these model calculations enables the determination of the angles of deviation of aryl substituents in big conjugated molecules on the basis of infrared spectral data.

A considerable part of Prof. Juchnovski and co-workers' research activity has been devoted to studying the electronic structure and reactions of a wide range of negative ions of conjugated organic compounds: carbanions, azanions, anion-radicals, and dianions by means of their infrared spectra and quantum chemical calculations. The interest of these negative ions is due both to their high reactivity and instability, and to the fact that they are intermediates in important chemical reactions. For the most part the research was innovative.

In the course of studying carbanions which contain characteristic groups were established the major electronic interactions, determining the character of vibrational spectra of carbanion systems: i) strong interaction between carbanionic centre and characteristic groups, leading to a considerable lowering of infrared frequencies and force constants; ii) competition for conjugation with carbanionic centre, leading to strong vibrational coupling between the groups connected to this centre.

In a dispute emerged in the society of chemistry about the presence of prototropic and metalotropic forms of metalated acetonitrile Juchnovski and co-authors demonstrated that this concept is wrong. Studying the infrared spectra of isotopically labelled acetonitrile they determined unconditionally that the observed infrared bands served as proof for by-products of chemical reactions, and not for the corresponding carbanion.

Spectral data for the carbanionic centre of saturated nitriles were obtained by means of infrared spectra: deviation from the planar structure was ascertained only for the anion of cyclopropylcyanide; it was determined that the bond of studied carbanions with the corresponding counterions (Li^+ , Na^+ , K^+) has an ion character.

On the basis of studying a large number of carbanionic systems fundamental patterns in the influence of conjugation and polar effects of the substituents over characteristic group frequencies and some skeletal vibrations of the carbanions were found and explained. It was established that the carbanion centre enhances the polar effects of substituents to a greater extent compared to all other groups with positive bridge effect. By means of the correlations of infrared frequencies and intensities σ^+ constants of series of carbanions and other anions with N- and O- substituents were determined. The latter were successfully applied for prediction of frequencies and intensities in series of various conjugated compounds.

The developed potential of infrared spectroscopy for studying instable and inseparable anion-radicals and carbanions and their transformations was demonstrated through the establishment of the convertability of dimerization of a number of anion-radicals to dimeric dianions and isomerisation of methoxide adducts of cyanobutadienes. In the course of this study there was proposed a new mechanism of disproportionation in Michler additions, whose general significance was later presented by other scientists.

Based on the infrared spectral study of representative groups of aromatic nitrile compound anion-radicals a number of important relations between the frequencies and intensities of nitrile groups were established. It was demonstrated that the particularly high sensitivity of the characteristic infrared frequencies is due to the intense mobility of the antibonding molecular orbital. An abnormal increase of nitrile group band intensity in the anion-radicals was found, which was explained by the electron charge mobility in the conjugated systems of these anion-radicals. It was demonstrated for the first time that this peculiarity of the antibonding orbital caused the strong vibroelectronic interaction in these systems.

A new infrared cell for electrochemical generation and spectral investigation of electron transfer products was invented, which helped the creation and study of infrared spectra of a variety of electrochemically generated anion-radicals and carbanions. The infrared spectra of anion-radicals of aromatic ketones (kethyles) were interpreted correctly for the first time by means of isotopically labelled compounds, which led to the correction of a number of mistakes in band assignment and some corresponding findings concerning the influence of the structure over infrared spectra of these anion-radicals. It was shown that infrared spectroscopy could give information about the form of the orbital of the unpaired electron, as well as about the presence of separate, weak interactions between molecular fragments, which are due to the peculiar symmetry of this orbital.

Following the example of aromatic nitriles, infrared band spectral characteristics of extremely reactive dianions of aromatic nitriles were generated and studied for the first time. The observed experimental strong decrease of characteristic frequencies of dianions in comparison with that of anion-radicals was theoretically explained. A number of significant capabilities of infrared spectroscopy for studying the electronic transfer between anion-radicals and dimeric

dianions were indicated. These capabilities of infrared spectroscopy were applied for studying the mechanism of the initiation and polymerization of several important monomers. Moreover, it was established that the initiation passes mainly from anion-radicals or dianions onto the monomer by means of electronic transfer, and the initiation ability depends on the electronic structure of the initiating agent.

During his career Prof. Juchnovski has published over 150 scientific papers, including (in co-authorship with Ivan Binev) the chapter *IR Spectra of Cyano and Isocyano Group*, I. Juchnovski, I. Binev in *The Chemistry of Functional Group, Suppl. C*, S. Patai and Z. Rappoport (Eds), John Wiley, New York, 1983, *Chapt. 4*, pp. 107-135. *Supplement C 1983*, Hohn Wiley Ed. Z. Rappoport.

Ivan Juchnovski started his teaching activity as an assistant professor at the UCTM. In 1963, together with Prof. A. Trifonov he began the first lecture course in Bulgaria in physical methods in organic chemistry, where he himself taught molecular spectroscopy to four-year students in the Faculty of Chemistry at Sofia University. He kept on delivering this lecture course for more than 20 years. In 1970 Juchnovski and Trifonov published the first textbook in Bulgaria on the discipline physical methods in organic chemistry.

Academician I. Juchnovski was the supervisor of 14 successful PhD students and a considerable number of Master's degree students. Some of his former associates from IOC in BAS have successful careers as researchers and teachers. Five of them became full professors, including two in Plovdiv University, and four became associate professors, one of whom acquired this academic rank at the University of Mining and Geology of Sofia.

For his teaching and scientific activity Academician I. Juchnovski was awarded the Honorary Sign with a Blue Band of Sofia University "St. Kliment Ohridski" (1997), Doctor Honoris Causa honorary degree of Plovdiv University "Paisii Hilendarski" (2001), Varna Free University "Chernorizets Hrabar" (2004), University of Chemical Technology and Metallurgy of Sofia (2005), University of Kharkov, Republic of Ukraine (2006). I. Juchnovski is a regular member of the European Academy of Sciences and Arts, Paris (2003) and member of the Leibnitz Society, Berlin. He is also an honorary citizen of the town of Sevlievo.

Academician I. Juchnovski is not only a distinguished specialist in the field of physical organic chemistry and a charismatic university

lecturer. He has made many efforts and spent a lot of time in the applied science since the end of 1960s. This activity is connected mainly with the creation of many highly efficient and ecological technologies for the general and special galvanics, microelectronics, as well as with methods of preparing metal surfaces. These achievements were accomplished by the combined application of physical methods of analysis together with his fundamental study of organic synthesis, and electrochemical and other functional studies. In these explorative studies Prof. Juchnovski has been either the leader or one of the leaders in creating the fundamentals of galvanic additives production industry in Bulgaria. He is the author of 18 inventions (one patent recognized in the former USSR), in 14 of which he was the leading author; 15 of these inventions were introduced in tenths of plants in Bulgaria and in the former USSR, DDR and Czechoslovakia. These developments were introduced to the production of semi-products used in the additives BC-1, BC-2, in the production technology of the galvanic additives B7211 in Bulgaria, and in the automobile industry in the former USSR.

Another important contribution of Prof. Juchnovski and his team was the introduction in over 30 Bulgarian plants, and also in one plant abroad, of environmental technologies for bright acidic zinc electroplating with sulphate and chloride electrolytes. These technologies have replaced the usage of non-ecological and highly dangerous cyanide electrolytes for zinc coating in Bulgaria forever.

In 1974, for the invention of the technology of bright acidic copper electroplating, Prof. Juchnovski, together with two other scientists, was awarded the 'Dimitrov' prize - the most prestigious for the time prize for technical achievements. In 1980 Juchnovski was awarded the title "Honorary Inventor" for his activity in applied science, and in 1970 and 1972 he was awarded twice the prize "For contribution to technological progress". His name entered the „Golden Book" of inventors in Bulgaria in 1998. Academician I. Juchnovski received Prof. Asen Zlatarov Honorary Medal of the Union of Chemists in Bulgaria in 2001, the Honorary Sign of the Union of Bulgarian Scientists in 2004, and the Order of Stara Planina - first grade of the Republic of Bulgaria in 2004.

Prof. G. Andreev,
Plovdiv University "Paisii Hilendarski"

Hydrogen bonding reactivities of atomic sites in the nucleobases

V. Nikolova, D. Cheshmedzhieva, S. Ilieva, B. Galabov*

Department of Chemistry and Pharmacy, University of Sofia, James Bourchier Avenue, Sofia 1164, Bulgaria

Received March 27, 2017; Revised April 10, 2017

Dedicated to Acad. Ivan Juchnovski on the occasion of his 80th birthday

Theoretical parameters characterizing the electrostatic forces at individual atoms were applied in quantifying the hydrogen bonding reactivities of atomic sites in the five primary nucleobases. To avoid ambiguities associated with the usual formation of bidentate hydrogen bonds in the nucleobases, DFT M06-2X/6-311+G(2d,2p) computations were employed in deriving electrostatic potentials at nuclei (EPN), NBO, and Hirshfeld atomic charges for a set of 64 model molecules. For comparison, proton affinities for the proton-accepting sites and deprotonation energies for proton-donating sites also were evaluated. The functional groups in the selected model molecules are able to form single hydrogen bonds. The obtained correlation equations linking computed interaction energies and electrostatics-related parameters were applied in deriving reactivity descriptors for individual atomic sites in the nucleobases. Among the tested theoretical parameters, the EPN values provide the best correlations with hydrogen bonding energies. The derived relationships were employed in defining a hydrogen bond reactivity descriptor for the atomic sites in the nucleobases. The effects of base pairing on site reactivities also were assessed.

Key words: hydrogen bonding, nucleic acid bases, electrostatic potential, atomic charges, reactivity descriptors.

INTRODUCTION

The ability of different atomic sites in the purine and pyrimidine nucleic acid bases to form hydrogen bonds determines a number of key properties of DNA and RNA. These include the formation of double helix structure, the replication mechanisms, and the interactions with proteins and biologically active ligands [1-10]. In the present research we present an efficient computational method for evaluating hydrogen bonding reactivities of individual atomic sites in the nucleobases. The effects of base pairing on hydrogen bonding abilities are also considered.

Numerous theoretical studies have focused on quantifying the proton-accepting and proton-donating abilities of the purine and pyrimidine nucleobases [11-20]. Zeegers-Huiskens et al. [17-20] analysed using DFT computations the effectiveness of intrinsic basicities and acidities of the hydrogen bonding sites in the nucleobases in describing the interactions with a single water molecule. In a computational study Medhi et al. [21] characterized the reactivities of nucleobases by determining proton and metal ion affinities of the nucleobases accepting sites. In several theoretical studies Wetmore et al. [11-14] examined the hydrogen bonding abilities of the nucleobases in

their interactions with small hydrogen bond forming molecules: HF, H₂O and NH₃. A barrier in quantifying the hydrogen bonding abilities of individual atomic sites arises from the particular structure of nucleobases. The interactions of molecules with proton accepting or donating sites in the bases involve in most cases the formation of cooperative bidentate hydrogen bonds with participation of neighbouring atoms. Thus, energy differentiations between these two simultaneous interactions cannot be evaluated from suitable experiments or from theoretical modelling. Information on site reactivities is particularly useful for QSAR and docking studies as well as in understanding fine mechanisms of interactions involving nucleic acid fragments.

Electrostatic forces have been shown to play a major role in defining the structure and properties of biopolymers [1-10,25,26]. Electrostatic interactions are also among the key factor in hydrogen bonding in general [1,8,9,27,28]. It was of interest to follow how quantities, reflecting the electrostatics at different sites in the nucleobases, would be linked with their hydrogen bonding reactivities. In the present research, we evaluate three types of molecular parameters that are intrinsically related to site electrostatics: NBO atomic charges [29], Hirshfeld charges [30], and electrostatic potentials at nuclei (EPN) [22]. In addition, following the already established

* To whom all correspondence should be sent:
E-mail: *e-mail: galabov@chem.uni-sofia.bg*

methodology [17-20], we also determined the proton affinities (PAs) and deprotonation energies (DEs) for the proton accepting and donating sites in the primary nucleobases at the level of theory employed in the present investigation. It thus became possible to assess how well all five theoretical parameters considered correlate with hydrogen bonding energies.

Earlier studies from this laboratory [31-36] revealed the accuracy of electrostatic potential at nuclei (EPN) in characterizing the site reactivities in hydrogen bonding. In a recent investigation [37] on substituted benzenes, we showed that molecular electrostatic potential (MEP) values, evaluated for points in molecular space in close proximity to the ring carbon nuclei, describe quantitatively site reactivities of the respective positions. Using Morokuma energy decomposition analysis [38,39] for selected series of hydrogen bonded molecules we also showed [35] that the different terms contributing to interaction energies (polarization interaction, exchange repulsion, charge transfer) are *linearly correlated* with the electrostatic energy term. These results emphasize the importance of molecular parameters characterizing site electrostatics in quantifying hydrogen bonding reactivities.

To avoid the difficulty of multiple hydrogen bonding of model proton donor and acceptor molecules (such as HF, H₂O and NH₃) with neighbouring atoms in the nucleobases, we conducted computations for series of molecules containing functional groups in environments that resemble the structural arrangements in the nucleobases. The functional groups in the selected model molecules are able to form single hydrogen bonds. The established correlations between reactivity descriptors and interaction energies were than employed in characterizing quantitatively the reactivity of individual proton-accepting and proton-donating centers in the nucleic acid bases.

COMPUTATIONAL METHODS

DFT computations employing the MO6-2X functional [40] combined with the 6-311+G(2d,2p) basis set [41] were applied in evaluating hydrogen bonding energies and a set of molecular parameters characterizing local properties of atomic sites in the investigated systems. Both DFT method and basis set employed have been shown to provide reliable results for the energies of hydrogen bonding [42]. Harmonic vibrational frequency computations showed that the optimized structures are true minima in the potential energy surfaces. Zero point

vibrational energies (ZPE) and bases set superposition error (BSSE) corrections [43] were applied in evaluating the energies of complex formation. The Gaussian09 program [44] was employed for all computations. Site electrostatics at the proton accepting and donating centers in the nucleobases was characterized by EPN values, NBO and Hirshfeld charges. The electrostatic potential at nuclei was first introduced by Wilson [45]. Politzer and Thruhlar [22] defined the electrostatic potential at nuclei Y (V_Y) by eqn (1):

$$V_Y \equiv V(R_Y) = \sum_{A \neq Y} \frac{Z_A}{|R_A - R_Y|} - \int \frac{\rho(r)}{|r - R_Y|} \quad (1)$$

In this relationship, the singular term for nucleus Y is excluded. Z_A is the charge of nucleus A at position R_A , and $\rho(r)$ is the electron density function. As mentioned, following the original findings [31-34] that EPN values define quantitatively the ability of molecules to form hydrogen bonds, the EPN index was extensively applied in describing both hydrogen bonding and chemical reactivity of various molecular systems [35,36,44-51]. In contrast to other theoretical parameters that characterize site properties, the electrostatic potential at nuclei is a rigorously defined quantum mechanical quantity. The $1/r$ dependence of EPN (Eqn 1) determines considerably greater contributions to V_Y of negative and positive charges in close vicinity of nucleus Y.

To have a clearer physical interpretation of the variations of EPN (V_Y), we employed the shifts of EPN in the studied derivatives (X) with respect the values in selected small molecules, containing the same atoms in the respective hybridization state. For this purpose, we selected ammonia (sp³-nitrogen), methanimine (sp²-nitrogen), formaldehyde (sp²-oxygen), and hydrogen molecule (for H atoms). The following relations were employed:

$$\text{For N(sp}^3\text{): } \Delta V_N = V_N(X) - V_N(\text{NH}_3) \quad (2)$$

$$\text{For N(sp}^2\text{): } \Delta V_N = V_N(X) - V_N(\text{H}_2\text{C}=\text{NH}) \quad (3)$$

$$\text{For O(sp}^2\text{): } \Delta V_O = V_O(X) - V_O(\text{H}_2\text{C}=\text{O}) \quad (4)$$

$$\text{For H: } \Delta V_H = V_H(X) - V_H(\text{H}_2) \quad (5)$$

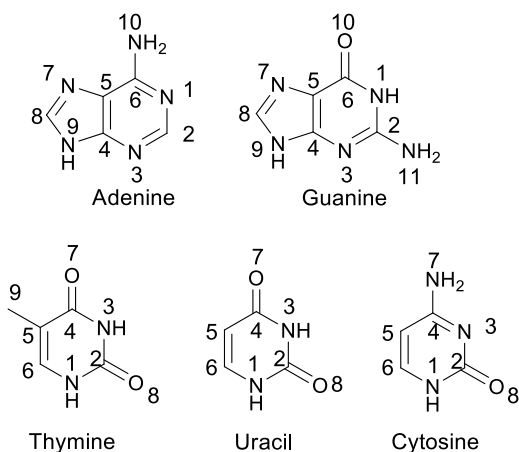
In the tables, we present the shifts of EPN values as defined in Eqns. (2-5). The proton affinities (PA) of all nitrogen and oxygen atomic centers for the series of model nitrogen and oxygen containing compounds as well as for the nucleobases were evaluated as the difference of the ZPE corrected energies of protonated and neutral

molecules. Deprotonation energies were also determined for the proton donating N-H sites.

METHODOLOGICAL APPROACH

Nitrogen and oxygen atomic centers are the principal proton accepting centers in the nucleobases able to form hydrogen bonds, while the N-H bonds may act as proton donors. As emphasized, it is not possible to evaluate theoretically the hydrogen bonding reactivities of individual atomic centers in the nucleobases by analyzing simply the energies of complex formation with model molecules. In most cases, proton donating or accepting molecules interact cooperatively with two atoms in the nucleobases [11-20]. These processes are illustrated in Fig. 1 for the interaction of thymine with HF, H₂O and C₂H₂. It is seen that two cooperative H-bonds are simultaneously formed. Even if a weaker proton donor such as C₂H₂ is employed in modeling the hydrogen bonding with a basic center, the neighboring proton donating groups contribute to the overall complexation energy by forming a π -hydrogen bond (Fig. 1C). Our approach involves four steps:

(1) The basic assumption is that correlations between hydrogen bonding energies and molecular parameters established for model systems may be also applied for the respective functionalities in the nucleobases, following a verification. In general, similarities of the molecular environment of proton accepting and donating groups in the model compounds and in the nucleobases suggest that this is a well-based hypothesis. Nonetheless, to verify further its validity we analyzed the relationships between the employed molecular parameters (atomic charges, EPN values) with computed chemical properties of the respective atomic sites: proton affinities and deprotonation energies.



Scheme 1. Structure and numbering of atomic positions in the primary nucleobases.

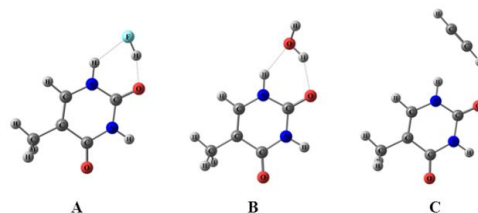


Fig. 1. Bidentate hydrogen bonding in thymine complexes with HF, H₂O and C₂H₂ from M06-2X/6-311+G(2d,2p) computations.

These correlations include both the model compounds and the nucleobases. Based on the obtained results, the most appropriate molecular parameter for the further analyses was selected. The criterion employed was how accurately the respective quantity (NBO and Hirshfeld charges, EPN) describes the local chemical reactivity of atomic sites.

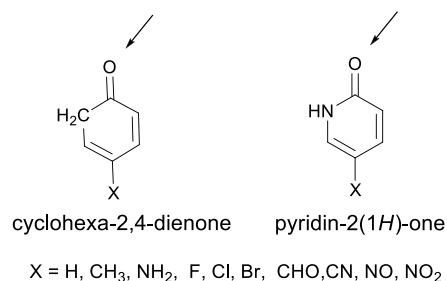
(2) In the second step, we studied in detail the relationships between energies of hydrogen bonding and molecular parameters for the sets of model compounds, containing the same functional groups as the nucleobases. We considered correlations of interaction energies with the already selected site-related parameter as well as with proton affinities and deprotonation energies. Series of substituted pyridine, pyrimidine, purine, aniline, pyridine-2(1H)-one, and imide derivatives (Scheme 2) were investigated computationally to characterize the hydrogen bonding abilities of nitrogen atoms in varying molecular environment.

Scheme 2. Structures of model sets of molecules containing nitrogen atoms in varying molecular environment.

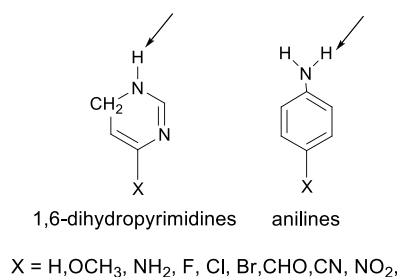
Computations for unsaturated cyclic amides and cyclodienones (Scheme 3) were conducted in

characterizing the reactivities of carbonyl oxygen atoms. The proton affinities for the C=O oxygens were also evaluated. Finally, a suitable set of derivatives (Scheme 4) was selected for analogous computations, aimed at characterizing the proton-donating properties of N-H groups in hydrogen bonding. The arrows also indicate the chosen direction of hydrogen bond formation. We employed hydrogen fluoride as a model proton donor/proton acceptor in these computations. The established relationships between molecular quantities and interaction energies were then employed in characterizing the ability of individual atomic sites in the nucleic acid bases to form hydrogen bonds. The accuracy of theoretical predictions of hydrogen bonding energies by the different theoretical parameters was assessed.

(3) In the third step of our approach, we applied scaling procedures, aimed at generalizing the relationships between theoretical parameters and hydrogen bonding reactivities. The scaling was necessary because of different slopes and segments in the plots of interaction energies vs. theoretical parameters for the different types of functional groups considered in the present research. The generalized plots between hydrogen bonding energies and scaled parameters revealed the accuracy of the adopted approach.



Scheme 3. Series of model compounds containing oxygen proton accepting centers. The arrows point the atoms, for which electrostatic potential at nuclei (V_O), atomic charges (q_{NBO} , q_{Hirsh}), and proton affinities were calculated. The arrows also indicate the chosen direction of hydrogen bond formation.



Scheme 4. Model compounds containing nitrogen proton-donating centers. The arrows point the atoms, for which electrostatic potential at nuclei (V_H), atomic

charges (q_{NBO} , q_{Hirsh}), and deprotonation energies were calculated. The arrows also indicate the chosen direction of hydrogen bond formation.

(4) In the fourth step, we define a suitable hydrogen bonding reactivity descriptor, based on the derived relationships between interactions energies and scaled molecular parameters.

RESULTS AND DISCUSSION

Correlations between site electrostatic parameters and proton affinities

Proton affinity (PA) and deprotonation energies (E_{dep}) are quantities that reflect well local properties of atomic sites in molecules. It was of special interest to examine how well molecular parameters associated with site electrostatics would correlate with quantities (PA, E_{dep}) reflecting purely chemical properties. Subsequent analyses of relationships between hydrogen bonding energies and molecular parameters may provide a clue for selecting the quantity describing *most accurately* the hydrogen bonding interactions. We evaluated by theoretical computations the proton affinities and electrostatics-related parameters (EPNs, NBO and Hirshfeld atomic charges), for sets of molecules containing nitrogen and oxygen proton accepting sites.

Tables S1 and S2 present these theoretically estimated quantities for the nitrogen and oxygen atomic sites in the selected model molecules and the five primary nucleobases. The last rows in Tables S1 and S2 show the correlation coefficients for the relationships between proton affinities and the three local parameters. A very good correlation between PAs and EPN (V_N) values for all considered 54 nitrogen proton accepting sites is established (correlation coefficient $r = 0.986$, $n = 54$). The plot is illustrated in Fig. S1. The correlation covers the model compounds (Scheme 2) and the respective nitrogen centers in the nucleobases. In contrast, the results reveal that the evaluated NBO and Hirshfeld charges for the nitrogen atoms do not correlate well with proton affinities (Table S1).

Table S2 presents the theoretically evaluated shifts of EPN values (ΔV_O) and atomic charges for the oxygen proton accepting centers for the series of model compounds (Scheme 3). A good correlation between PAs and EPN values (V_O) ($r = 0.985$, $n = 24$) characterizes the relationship between these two molecular quantities (Fig. S2). Again, the NBO and Hirshfeld charges for the

oxygen atoms do not correlate satisfactorily with proton affinities.

Table 1. Hydrogen bonding energies and reactivity descriptors for nitrogen proton accepting centers in model molecules (Scheme 2) from M06-2X/6-311+G(2d,2p) computations.

Molecule	ΔE_{corr} [kcal/mol l]	$\Delta V_{\text{N}}^{\text{a}}$ [kcal/mol l]	PA [kcal/mol l]
<i>sp</i> ²			
<i>Pyridine</i>	-9.43	2.64	219.0
<i>Pyrimidines</i>			
<i>H</i>	-8.27	10.47	208.6
<i>4-CH</i> ₃	-8.78	6.14	214.6
<i>4-NH</i> ₂	-9.66	-2.18	224.0
<i>4-F</i>	-7.82	15.71	204.2
<i>4-CHO</i>	-7.33	20.17	203.4
<i>4-CN</i>	-6.91	27.08	197.1
<i>4-NO</i> ₂	-6.57	30.09	193.9
<i>Purines</i>			
<i>H</i>	-8.31	10.31	210.9
<i>2-CH</i> ₃	-8.57	7.71	214.3
<i>2-NH</i> ₂	-8.99	4.16	219.2
<i>2-F</i>	-7.83	15.44	206.5
<i>2-CHO</i>	-7.52	17.42	206.0
<i>2-CN</i>	-7.14	22.69	201.1
<i>2-NO</i> ₂	-7.16	24.78	199.1
Correlation coefficients^b		0.991	0.985
<i>sp</i> ³			
<i>Anilines</i>			
<i>H</i>	-6.83	24.20	207.3
<i>4-CH</i> ₃	-6.90	18.96	210.0
<i>4-OCH</i> ₃	-7.92	17.61	212.0
<i>4-NH</i> ₂	-7.47	15.30	214.9
<i>4-F</i>	-6.77	23.90	204.6
<i>4-Cl</i>	-6.19	26.98	203.3
<i>4-Br</i>	-6.06	27.72	203.1
<i>4-CHO</i>	-4.93	34.54	199.0
<i>4-CN</i>	-4.84	37.74	195.0
<i>5-Amino-pyrimidines</i>			
<i>H</i>	-5.15	35.71	193.1
<i>2-CH</i> ₃	-5.36	32.50	197.3
<i>2-NH</i> ₂	-6.31	26.90	204.7
<i>2-F</i>	-4.90	39.23	189.9
<i>2-CHO</i>	-3.92	46.42	186.8
<i>2-CN</i>	-3.32	51.23	
<i>2-NO</i> ₂	-3.16	53.60	
Correlation coefficients^b		0.987	0.958

Table S3 present the theoretically evaluated deprotonation energies and molecular parameters for N-H proton donating sites in series of model compounds (Scheme 4) and in the nucleobases. The shifts in EPN values for the N-H hydrogen correlates with E_{dep} , though the correlation coefficients ($r = 0.956$) is lower compared to the plots between proton affinities and ΔV_{Y} values

discussed so far. Still, the correlation between ΔV_{H} and E_{dep} is superior than the correlations of E_{dep} with $q_{\text{H}}(\text{NBO})$ and $q_{\text{H}}(\text{Hirsh})$ (Table S3).

Table 2. Hydrogen bonding energies and reactivity descriptors for oxygen proton accepting centers in model molecules (Scheme 3) from M06-2X/6-311+G(2d,2p) computations.

Molecule	ΔE_{corr} [kcal/mol]	$\Delta V_{\text{O}}^{\text{b}}$ [kcal/mol.]	PA [kcal/mol]
<i>Cyclohexa-2,4-dienones</i>			
<i>H</i>	-9.72	-22.41	209.0
<i>4-CH</i> ₃	-10.11	-23.54	211.1
<i>4-NH</i> ₂	-10.00	-23.10	211.8
<i>4-F</i>	-9.14	-15.26	202.5
<i>4-Cl</i>	-8.91	-14.69	203.6
<i>4-Br</i>	-9.21	-14.88	203.3
<i>4-CHO</i>	-8.48	-13.63	202.0
<i>4-CN</i>	-8.56	-8.36	196.8
<i>4-NO</i>	-8.81	-11.87	200.2
<i>4-NO</i> ₂	-8.34	-6.91	195.6
<i>Benzoquinone</i>			
<i>H</i>	-6.92	1.31	188.6
<i>Pyridin-2(1H)-ones</i>			
<i>H</i>	-11.38	-36.91	217.4
<i>5-CH</i> ₃	-11.61	-39.42	220.9
<i>5-NH</i> ₂	-12.18	-41.99	224.7
<i>5-F</i>	-10.80	-30.38	213.3
<i>5-Cl</i>	-11.15	-32.83	213.5
<i>5-CN</i>	-9.53	-18.46	203.9
<i>5-NO</i> ₂	-9.22	-15.01	201.8
Correlation coefficients^a		0.991	0.979

^aCorrelation coefficients for the relationships between ΔE_{corr} and molecular parameters. ^b ΔV_{O} is defined in eqn 4.

The relationships discussed above reveal good correspondence between chemical properties (proton affinities, deprotonation energies) and a theoretical parameter (EPN) describing the electrostatic forces acting at individual atomic sites. In the following discussion of hydrogen bonding interactions we will focus on the relationships employing EPN, PAs, and E_{dep} values. The computations showed that NBO and Hirshfeld atomic charges are less successful in describing small variations in site reactivities for the considered extended series of molecules. The results obtained also revealed the presence of outliers in the PA/EPN and E_{dep} /EPN relationships. Most critical for the purposes of the present investigation is the assessment of how well these molecular quantities would describe the abilities of atomic centers to form hydrogen bonds.

Zeegers et al. [17-20] have applied PAs and E_{dep} in characterizing the hydrogen bonding reactivities of the nucleobases. The derived by these authors relationships are based on analyzing the interaction energies of nucleobase functionalities with water

molecule. As discussed, bidentate hydrogen bonds with neighboring polar groups in the bases form in almost all cases.

Table 3. Hydrogen bonding energies, electrostatic potential at nuclei, and deprotonation energies for N-H hydrogen in 1,6-dihydropyrimidine and aniline derivatives from M06-2X/6-311+G(2d,2p).

Derivative	ΔE_{corr} [kcal/mol]	$\Delta V_{\text{H}}^{\text{b}}$ [kcal/mol]	E_{dep} [kcal/mol]
<i>1,6-Dihydro-pyrimidines</i>			
H	-4.57	31.89	-363.50
4-OCH ₃	-4.69	33.33	-361.05
4-NH ₂	-4.72	31.32	-363.05
4-F	-5.25	41.67	-354.94
4-Cl	-5.33	41.99	-352.15
4-Br	-5.41	41.67	-350.29
4-CHO	-5.42	41.24	-353.23
4-CN	-5.77	41.57	-347.53
4-NO ₂	-5.85	50.27	-345.29
<i>Anilines</i>			
H	-3.64	17.14	-374.40
4-OCH ₃	-3.54	13.31	-377.40
4-NH ₂	-3.38	11.05	-377.89
4-F	-3.94	19.77	-372.49
4-Cl	-4.05	22.91	-367.67
4-Br	-4.04	27.37	-366.35
4-CHO	-4.49	30.57	-355.47
4-CN	-4.84	33.77	-354.91
4-NO ₂	-5.18	36.91	-348.79
Correlation coefficient^a		0.979	0.964

^aCorrelation coefficients for the relationships between ΔE_{corr} and ΔV_{H} . ^b ΔV_{H} is defined in eqn (5).

The specific structure of H₂O, however, may be a factor influencing the nature of such cooperative bonding. In the present work, we aim at establishing relations that are free of such effects

Relationships between hydrogen bonding energies and molecular parameters

Based on the above results it is possible to explore dependences between hydrogen bonding energies and molecular parameters for the sets of model molecules. As discussed, the selected model molecules (Schemes 2-4) possess atomic centers that are able to form single hydrogen bonds, without the complications of cooperative bonding. Our study focuses at analyzing how well proton affinities, deprotonation energies, and electrostatic potentials at atomic sites correlate (and predict) the hydrogen bonding energies for the sets of model molecules.

Interaction energies are, certainly, the most accurate descriptor of the ability of individual atomic centers to form hydrogen bonds. For the

model derivatives, hydrogen bonding energies, associated with individual atomic sites, were theoretically evaluated. As mentioned, hydrogen fluoride was employed as a model proton donor or acceptor molecule. The established good correlations for the PA/EPN and E_{dep} /EPN relationships show that a molecular parameter, representing the electrostatic forces acting at particular atomic sites, may well predict site chemical properties for *both model systems and the nucleobases* (Table S1-S3). We explored the relationships between interaction energies and EPN values and proton affinities for the molecules shown in Schemes 2 and 3. Deprotonation energies were evaluated for proton-donating N-H bonds (Schemes 4). These model systems possess hydrogen bonding functional groups with sp² and sp³ nitrogens, sp² oxygen, and N-H bonds in structural environments similar to those in the nucleobases. As shown, NBO and Hirshfeld charges were found to be less successful in describing site reactivities in the selected model systems. Nonetheless, in the Supporting Information we provide comparative tables (Tables S4-S6) that contain data for these two types of atomic charges.

Table 1 shows the computed hydrogen bonding energies (ΔE_{corr}) for the nitrogen centers (proton acceptors) for the series of model pyrimidine, purine, and aniline derivatives (Scheme 2). These values are juxtaposed to theoretically derived molecular parameters: ΔV_{N} and proton affinities. The results obtained reveal that no *common* relationship between ΔE_{corr} and any of these molecular parameters is found when molecules containing both sp² and sp³ nitrogens are simultaneously considered. The data obtained demonstrate that the pyridine type nitrogens form distinctly stronger hydrogen bonds than the aniline type nitrogen atoms (Table 1). It was thus necessary to investigate separately these two sets of complexes. An excellent correlation between interaction energies and ΔV_{N} (sp² N) ($r = 0.991$, $n = 15$) for the entire set of substituted pyrimidines and purines was found (Table 1). A good correlation, though with *lower correlation coefficient* ($r = 0.985$, $n = 15$), was established between *proton affinities* and ΔE_{corr} (Table 1).

The correlation between ΔE_{corr} and V_{N} values for the series of aniline derivatives is also quite satisfactory with correlation coefficient $r = 0.987$. Again, this correlation is superior to the correlation between ΔE_{cor} and proton affinities for molecules containing sp³ nitrogen centers ($r = 0.958$).

The equations reflecting the above relationships are as follows:

$$\Delta E_{\text{corr}} = 0.097\Delta V_{\text{N}}(\text{sp}^2\text{N}) - 9.390 \quad (6)$$

$n=15, r = 0.991$

$$\Delta E_{\text{corr}} = 0.121\Delta V_{\text{N}}(\text{sp}^3\text{N}) - 9.511 \quad (7)$$

$n= 16, r = 0.987$

The differences in slopes and intercepts in Eqns. 6 and 7 reflect the lower hydrogen bonding ability for the sp^3 nitrogen atoms in amino group environment. An appropriate scaling of $V_{\text{N}}(\text{sp}^3\text{N})$ to reflect these difference results in the relation:

$$\Delta V_{\text{N}}(\text{sp}^3\text{N})_{\text{scaled}} = 1.24 \Delta V_{\text{N}}(\text{sp}^3\text{N}) \quad (8)$$

The segments in eqns. (6) and (7) are very close in value and, thus, the simplified relation 8 holds to a good approximation. Using the $\Delta V_{\text{N}}(\text{sp}^3\text{N})_{\text{scaled}}$ the following relation covering all nitrogen proton accepting sites is derived:

$$\Delta E_{\text{corr}} = 0.096\Delta V_{\text{N}}^{\text{scaled}} - 9.40 \quad (9)$$

$r = 0.994, n = 31$

$\Delta V_{\text{N}}^{\text{scaled}}$ comprises ΔV_{N} for the sp^2 nitrogens (scaling factor = 1) and $\Delta V_{\text{N}}(\text{sp}^3\text{N})_{\text{scaled}}$ obtained from eqn (8). Using eqn (9) it becomes possible to prepare a reactivity scale for all nitrogen proton accepting centers in the model molecules.

To derive analogous relationships between structural variation in carbonyl compounds and molecular parameters (EPN, PAs), associated with oxygen proton accepting sites, a series of 18 carbonyl containing derivatives of cyclohexa-2,4-dienone and pyridin-2(1H)-one (Scheme 3) were considered.

To avoid cooperative bidentate hydrogen bonding of the model proton donor in the case of the aza heterocyclic molecules the hydrogen bond at the carbonyl oxygen was modeled at the side of the C=C double bond adjacent to the carbonyl moiety (Scheme 3). The computed corrected energies of hydrogen bonding (ΔE_{corr}), electrostatic potentials at nuclei (V_{O}), and proton affinities (PA) for the carbonyl oxygen sites are given in Table 2. The excellent correlation coefficient ($r = 0.991$) between the computed EPN values and energies of hydrogen bonding (ZPE and BSSE corrected) shows the near linear relationship between these quantities. A good correlation coefficient ($r=0.979$) characterizes the dependence between ΔE_{corr} and proton affinities. As in the case of nitrogen proton-accepting centers (Table 1), the electrostatic potential at nuclei values provide superior correlations with interaction energies compared to proton affinities for the series of carbonyl

derivatives. This result reflects the strong dependence of hydrogen bonding on the electrostatic interaction between proton donor and acceptor molecules. The relationship between ΔV_{O} values and ΔE_{corr} results in the following expression:

$$\Delta E_{\text{corr}}(\text{C=O}) = 0.112\Delta V_{\text{O}} - 7.382 \quad (10)$$

$n = 18, r = 0.991$

Equation 10 holds for two different series of cyclic compounds containing C=O functionality. This result shows that in spite of different molecular environment (ketone C=O group in the first set and amide C=O group in the second set) the same relationship between interaction energies and EPN values holds. Successful applications of EPN in quantifying hydrogen bonding reactivities of carbonyl derivatives belonging to different classes²⁵⁻²⁷ are in harmony with the present results.

Considerations of the slopes and segments of eqns. (9) and (10) results in the following expression for the scaling of ΔV_{O} :

$$\Delta V_{\text{O}}(\text{sp}^2\text{O})_{\text{scaled}} = 1.167\Delta V_{\text{O}}(\text{sp}^2\text{O}) - 18.01 \quad (11)$$

Considering eqns (9-11) we arrive at a general relation quantifying the hydrogen bonding reactivities of all proton-accepting sites. Scaling of ΔV_{O} eqn. (11) is necessary to obtain such an equation. The derived general relation is:

$$\Delta E_{\text{corr}} = -0.106 \Delta V_{\text{Y}}^{\text{scaled}} - 9.22 \quad (\text{Y}=\text{N},\text{O}) \quad (12)$$

$n = 49, r = 0.995$

Eqn (12) provides a general scale for the hydrogen bonding abilities of all proton accepting site. It is based on the scaled values of the respective ΔV_{Y} values. $\Delta V_{\text{Y}}^{\text{scaled}}$ are presented in Table 6. The plot between hydrogen bonding energies and $\Delta V_{\text{Y}}^{\text{scaled}}$ is shown in Fig. 2.

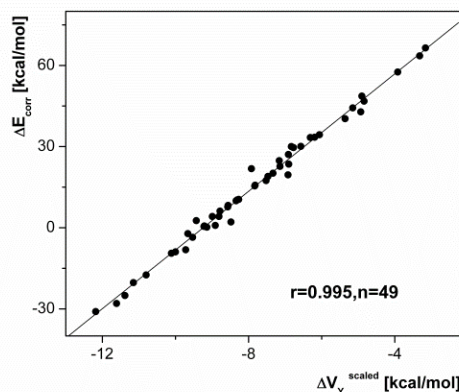


Fig. 2. Plot of hydrogen bonding energies vs. scaled electrostatic potentials at nuclei ($V_{\text{Y}}^{\text{scaled}}$) in model pyrimidines, purines and carbonyl derivatives

Following the same approach we derived relationships between interaction energies and molecular parameters for the N-H proton-donating groups in the series of model 1,6-dihydropyrimidines and anilines shown in Scheme 4. Table 3 presents the computed energies of hydrogen bonding and molecular parameters. A good correlation ($r = 0.979$) is established between ΔV_H and interactions energies (Fig. 3), while the respective relationship with E_{dep} is characterized with lower correlation coefficient ($r = 0.964$). These results confirm that the shifts of EPN provide *superior correlations* with the hydrogen bonding energies compared to proton affinities/deprotonation energies. No scaling of EPN values is necessary in this case since the correlation involves only N-H group hydrogens. Eqn (13) shows that more negative ΔV_H values correspond to higher interaction energies.

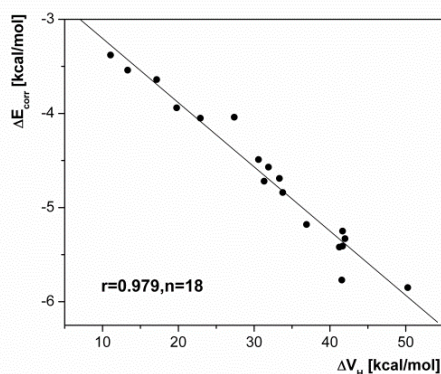


Fig. 3. Energies of hydrogen bonding (ΔE_{cor}) vs. shifts of electrostatic potentials at of proton-donating groups (ΔV_H) in substituted aniline and 1,6-dihydropyrimidine derivatives.

Thus, ΔV_H can directly be employed in deriving suitable hydrogen bonding reactivity descriptor for N-H proton-donating groups. The following equation applies:

$$\Delta E_{corr} = -0.068\Delta V_H - 2.52 \quad (13)$$

$n = 18, r = 0.979$

Hydrogen bonding reactivity descriptors for nucleobases

ΔV_y may be employed in characterizing the hydrogen bonding reactivities in the nucleobases and their polymeric derivatives. It is only necessary to compute the respective scaled electrostatic potential values for the proton accepting centers (ΔV_y^{scaled}). Even easier assessment of bonding abilities comes by comparing the predicted hydrogen bonding energies using Eqn. 12.

It is appropriate to introduce a special hydrogen bond descriptor (HB_{descr}) for reactivities of atomic sites in nucleobases. We define this descriptor as the absolute values of the predicted energies of hydrogen bonding for particular sites in the bases using Eqns (12) and (13):

$$HB_{descr} = |\Delta E^{predicted}| \quad (14)$$

The HB_{descr} values are given in the last columns of Tables 4 and 5. Table 4 shows the order of reactivities of all proton-accepting sites in the nucleobases. Inspection shows that the most reactive center for hydrogen bonding is the N3 nitrogen in uracil ($HB_{descr} = 18.17$).

Table 4. Scaled EPN values, predicted energies of hydrogen bonding ($\Delta E^{predicted}$, in kcal/mol), and hydrogen bond descriptor (HB_{descr}) values for proton-accepting centers in the primary nucleobases.

Nucleo-bases	ΔV_Y	$\Delta V_Y^{scaled, a}$	$\Delta E^{pr, b}$	HB_{descr}
Adenine				
N1(sp ²)	-1.84	-1.84	-9.02	9.02
N3(sp ²)	1.86	1.86	-9.42	9.42
N7(sp ²)	6.88	6.88	-9.95	9.95
N9(sp ³)	61.81	76.64	-17.34	17.34
N10(sp ³)	33.9	42.0	-13.68	13.68
Guanine				
N1(sp ³)	56.85	70.49	-16.69	16.69
N3(sp ²)	9.76	9.76	-10.25	10.25
N7(sp ²)	0.81	0.81	-9.31	9.31
N9(sp ³)	60.94	75.56	-17.23	17.23
N11(sp ³)	45.07	55.89	-15.14	15.14
O10	-29.58	-34.52	-5.56	5.56
Thymine				
N1(sp ³)	54.49	67.57	-16.58	16.58
N3(sp ³)	64.47	79.95	-17.69	17.69
O7	-20.16	-23.53	-6.73	6.73
O8	-19.94	-23.27	-6.75	6.75
Uracil				
N1(sp ³)	55.98	69.41	-16.58	16.58
N3(sp ³)	68.12	84.47	-18.17	18.17
O7	-19.75	-23.04	-6.78	6.78
O8	-16.69	-19.48	-7.16	7.16
Cytosine				
N1(sp ³)	53.87	66.81	-16.30	16.30
N3(sp ²)	-6.74	-6.74	-8.51	8.51
N7(sp ³)	38.77	48.07	-14.32	14.32
O8	-41.87	-48.86	-4.04	4.04

^a Obtained from eqn (8) and eqn (11) ^b Predicted values using eqn (12).

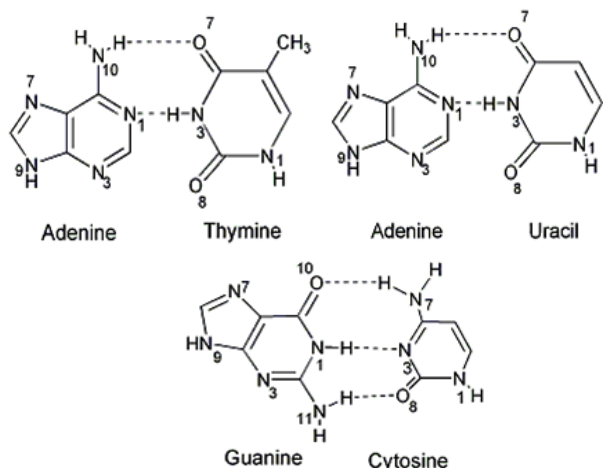
Among the oxygen atomic sites, the O8 atom in uracil ($HB_{descr} = 7.16$) is predicted to possess highest reactivity. Table 5 compares the relative reactivities of proton-donating atomic sites in the nucleobases. The values of reactivity descriptors are obtained using relation 14. The effects of base pairing on hydrogen bond reactivities are illustrated in Table 6. The last column contains HB_{descr} values for the atomic sites in base pairs. The numbering of atomic

sites is shown in Scheme 5. Comparison of Tables 4 and 6 reveals the effects of pairing on hydrogen bonding reactivities.

Table 5. Shifts of EPN values, predicted energies of hydrogen bonding ($\Delta E^{\text{predicted}}$, in kcal/mol), and hydrogen bond descriptor (HB_{descr}) values for proton-donating centers in the primary nucleobases.

Nucleo-bases	$\Delta V_{\text{H}}^{\text{a}}$	$\Delta E^{\text{pr., b}}$	HB_{descr}
Adenine			
N9-H	57.56	-6.44	6.44
N10-H	31.44	-4.66	4.66
Guanine			
N1-H	50.95	-5.99	5.99
N9-H	56.85	-6.39	6.39
N11-H	40.91	-5.30	5.30
Thymine			
N1-H	56.43	-6.36	6.36
N3-H	47.82	-5.77	5.77
Uracil			
N1-H	59.86	-6.59	6.59
N3-H	49.32	-5.88	5.88
Cytosine			
N1-H	44.93	-5.58	5.58
N7-H	39.22	-5.19	5.19

^a ΔV_{H} is defined in eqn (5). ^b Predicted values for interaction energies using eqn (13).



Scheme 5. Structure and numbering of atom position in base pairs Adenine-Thymine, Adenine-Uracil and Guanine-Cytosine.

In the A-U base pair, the HB_{descr} for the N1 atom in adenine shifts from 9.02 to 9.59. For the N10 atom, the shift is from 13.68 to 12.90. Similar HB_{descr} shifts are also found for the A-T base pair. The HB_{descr} for the N1 atom in adenine changes from 9.02 to 9.54, while for the N10 from 13.68 to 12.86. The respective HB_{descr} values for guanine in the G-C pair change also upon base-pairing. The HB_{descr} value for the N1 atom in guanine shifts from 16.69 to 15.08, for the N11 atom from 15.14 to 12.91, and for O7 from 5.56 to

5.74. Distinct shifts are also found for the other base pairs (Tables 3 and 6).

Table 6. Scaled EPN values, predicted values of hydrogen bonding energies ($\Delta E^{\text{predicted}}$, in kcal/mol), and hydrogen bond descriptor (HB_{descr}) for proton-accepting centers in Adenine-Thymine, Adenine-Uracil, and Guanine-Cytosine base pairs.

Base pair	ΔV_{Y}	$\Delta V_{\text{Y}}^{\text{scaled}}$	ΔE^{pr}	$\text{HB}_{\text{descr.}}$
Adenine (A-U)				
N1(sp ²)	3.53	3.53	-9.59	9.59
N10(sp ³)	28.02	34.75	-12.90	12.90
Adenine (A-T)				
N1(sp ²)	2.98	2.98	-9.54	9.54
N10(sp ³)	27.73	34.38	-12.86	12.86
Guanine (G-C)				
N1(sp ³)	44.56	55.26	-15.08	15.08
N11(sp ³)	28.11	34.85	-12.91	12.91
O10	-28.16	-32.86	-5.74	5.74
Thymine (A-T)				
N3(sp ³)	39.19	48.60	-14.37	14.37
O7	-21.99	-25.66	-6.50	6.5
Uracil (A-U)				
N3(sp ³)	40.31	49.99	-14.52	14.52
O7	-21.88	-25.53	-6.51	6.51
Cytosine (G-C)				
N3(sp ²)	36.15	36.15	-13.05	13.05
N7(sp ³)	45.46	56.37	-15.20	15.20
O8	-13.14	-15.33	-7.59	7.59

^a Obtained from eqns (8) and (11). ^b Predicted values using eqn (12).

The shifts in HB_{descr} resulting from base pairing may be distinct, though not large. This is in harmony with the relatively small perturbations caused by hydrogen bonding between the nucleobases.

CONCLUSION

Hydrogen bonding reactivities of individual atomic sites in the primary nucleobases were characterized by applying theoretically derived electrostatic-related theoretical parameters. Several alternative quantities – electrostatic potentials at nuclei (EPN), NBO and Hirshfeld atomic charges as well as proton affinities and deprotonation energies – were employed in the analysis. For all studied systems, the EPN values provided the best correlations with interaction energies. A new reactivity descriptors (HB_{descr}) for the hydrogen bonding reactivities of atomic sites in the nucleobases is introduced based on predicted interaction energies. Using the derived equations, site reactivities for the primary nucleobases were evaluated. The effect of base pairing was also analyzed.

Acknowledgements: This research was supported by the National Science Fund (Bulgaria), Grant DN 09/4.

Electronic Supplementary Data available here.

REFERENCES

- G. C. Pimental, A. L. McClellan, *The Hydrogen Bond*; Freeman: San Francisco, 1960.
- G. A. Jeffrey, W. Saenger, *Hydrogen Bonding in Biological Structures*; Springer: Berlin, 1991.
- J. T. Stivers, Y. L. Jiang, *Chem. Rev.*, **103**, 2729 (2003).
- S. S. David, S. D. Williams, *Chem. Rev.*, **98**, 1221 (1998).
- A. K. McCullough, M. L. Dodson, R. S. Lloyd, *Annu. Rev. Bioche.*, **68**, 255 (1999).
- K. Muller-Dethlefs, P. Hobza, *Chem. Rev.*, **100**, 143 (2000).
- J. D. Watson, F. H. C. Crick, *Nature*, **171**, 737 (1953).
- E. Martin, W. Saenger, *Principles of Nucleic Acid Structure*; Springer: New York, 1984.
- D. Voet, J. G. Voet, *Biochemistry*, 3rd ed.; Hoboken, NJ: Wiley, New York, 2004.
- L. Chan, M. Pineda, J. Heeres, P. Hergenrother, B. Cunningham, *ACS Chem. Biol.*, **3**, 437 (2008).
- M. Di Laudo, S. R. Whittleton, S. D. Wetmore, *J. Phys. Chem. A*, **107**, 10406 (2003).
- S. R. Whittleton, K. C. Hunter, S. D. Wetmore, *J. Phys. Chem. A*, **108**, 7709 (2004).
- K. C. Hunter, L. R. Rutledge, S. D. Wetmore, *J. Phys. Chem. A*, **109**, 9554 (2005).
- T. L. McConnell, C. A. Wheaton, K. C. Hunter, S. D. Wetmore, *J. Phys. Chem. A*, **109**, 6351 (2005).
- T. van Mourik, S. L. Price, D. C. Clary, *J. Phys. Chem. A*, **103**, 1611 (1999).
- S. M. LaPointe, S. D. Wetmore, *Chem. Phys. Lett.*, **408**, 322 (2005).
- J. Chandra, M. Nguyen, T. Uchimar, Th. Zeegers-Huyskens, *J. Phys. Chem. A*, **103**, 8853 (1999).
- J. Chandra, M. Nguyen, T. Uchimar, Th. Zeegers-Huyskens, *J. Phys. Chem. A*, **102**, 6010 (1998).
- J. Chandra, D. Michalska, R. Wysokinski, Th. Zeegers-Huyskens, *J. Chem. Phys. A*, **108**, 9593 (2004).
- R. Wysokinski, D. Bienko, D. Michalska, Th. Zeegers-Huyskens, *Chem. Phys.*, **315**, 17 (2005).
- D. Talukdar, R. Parajuli, R. Kalita, C. Medhi, *Ind. J. Chem.*, **45**, 1804 (2006).
- P. Politzer, D. G. Truhlar, *Chemical Applications of Atomic, Molecular Electrostatic Potentials*; Eds.; Plenum: New York, 1981.
- J. S. Murray, K. Sen, *Molecular Electrostatic Potentials: Concepts, Applications*; Eds.; Elsevier Science: Amsterdam, The Netherlands, 1996.
- G. Naray-Szabo, G. G. Ferenczy, *Chem. Rev.*, **95**, 829 (1995).
- F. B. Sheinerman, B. Honig, *J. Mol. Biol.*, **318**, 161 (2002).
- H. Zheng, K. Comeforo, J. Gao, *J. Am. Chem. Soc.*, **131**, 18 (2009).
- G. A. Jeffrey, *Introduction to Hydrogen Bonding*; Oxford University Press: New York, 1997.
- S. J. Grabowski, *Hydrogen Bonding: New Insights*; Springer: New York, 2006.
- (a) A. Reed, R. Weinstock, F. Weinhold, *J. Chem. Phys.*, **83**, 735 (1985); (b) A. E. Reed, L. A. Curtiss, F. Weinhold, *Chem. Rev.*, **88**, 899 (1988).
- (a) F. L. Hirshfeld, *Theor. Chem. Acc.*, **44**, 129 (1977); (b) J. P. Ritchie, *J. Am. Chem. Soc.*, **107**, 1829 (1985); (c) J. P. Ritchie, S. M. Bachrach, *J. Comp. Chem.*, **8**, 499 (1987).
- P. Bobadova-Parvanova, B. Galabov, *J. Phys. Chem. A*, **102**, 1815 (1998).
- B. Galabov, P. Bobadova-Parvanova, *J. Phys. Chem. A*, **103**, 6793 (1999).
- B. Galabov, P. Bobadova-Parvanova, *J. Mol. Struct.*, **550-551**, 93 (2000).
- V. Dimitrova, S. Ilieva, B. Galabov, *J. Phys. Chem. A*, **106**, 11801 (2002).
- B. Galabov, P. Bobadova-Parvanova, S. Ilieva, V. Dimitrova, *J. Mol. Struct. Theochem*, **630**, 101 (2003).
- B. Galabov, S. Ilieva, G. Koleva, W. D. Allen, H. F. Schaefer, P. v. R. Schleyer, *WIREs Comput. Mol. Sci.*, **3**, 37 (2013).
- B. Galabov, V. Nikolova, S. Ilieva, *Chem.-Eur. J.*, **19**, 5149 (2013).
- K. Morokuma, *J. Chem. Phys.*, **55**, 1236 (1971).
- K. Kitaura, K. Morokuma, *Int. J. Quantum Chem.*, **10**, 325 (1976).
- Y. Zhao, D. G. Truhlar, *Theor. Chem. Acc.*, **120**, 215 (2008).
- a) A. D. McLean, G. S. Chandler, *J. Chem. Phys.*, **72**, 5639 (1980); b) A. Krishnan, J. S. Binkley, R. Seeger, J. A. Pople, *J. Chem. Phys.*, **72**, 650 (1980); c) T. Clark, J. Chandrasekhar, G. W. Spitznagel, P. v. R. Schleyer, *J. Comp. Chem.*, **4**, 294 (1983).
- A. R. Neves, P. A. Fernandes, M. Ramos, *J. Chem. Theor. Comp.*, **7**, 2059 (2011).
- S. F. Boys, F. Bernardi, *Mol. Phys.*, **19**, 553 (1970).
- M. J. Frisch, et al. *Gaussian 09 (Revision-A.02)*; Gaussian, Inc., Wallingford CT, 2009.
- E. B. Wilson, *J. Chem. Phys.*, 2232 (1962).
- B. Galabov, S. Ilieva, H. F. Schaefer, *J. Org. Chem.*, **71**, 6382 (2006).
- B. Galabov, S. Ilieva, B. Hadjieva, Y. Atanasov, H. F. Schaefer, *J. Phys. Chem. A*, **112**, 6700 (2008).
- B. Galabov, V. Nikolova, J. J. Wilke, H. F. Schaefer, W. D. Allen, *J. Am. Chem. Soc.*, **130**, 9887 (2008).

49. N. Mohan, C. H. Suresh, *J. Phys. Chem. A*, **118**, 1697 (2014).
50. K. S. Sandya, C. H. Suresh, *Dalt. Trans.*, **43**, 12279 (2014).
51. F. B. Sayyed, C. H. Suresh, *J. Phys. Chem. A*, **116**, 5723 (2011).

РЕАКТИВОСПОСОБНОСТ КЪМ ВОДОРОДНО СВЪРЗВАНЕ НА АТОМНИТЕ ЦЕНТРОВЕ В
АЗОТНИТЕ БАЗИ НА НУКЛЕИНОВИТЕ КИСЕЛИНИ

В. Николова, Д. Чешмеджиева, С. Илиева, Б. Гълъбов*

*Факултет по химия и фармация, Софийски университет „Св. Климент Охридски”, бул. Дж. Баучер 1,
1164 София, България*

Постъпила на 27 март 2017 г.; Коригирана на 10 април 2017 г

(Резюме)

Приложени са теоретични параметри, характеризиращи електростатичните сили при отделните атоми, за количествено описание на реакционна способност към водородно свързване на атомните центрове в петте основни бази на нуклеиновите киселини. С цел да се избегнат неяснотите, свързани с формирането на бидентатни водородни връзки в нуклеиновите бази, бяха проведени DFT M06-2X/6-311+G(2d,2p) изчисления на атомния електростатичен потенциал (electrostatic potential at nuclei, EPN), NBO и Хиршфелд атомни заряди за серия от 64 моделни системи. За сравнение бяха определени протонните афинитети на протон-акцепторните групи и енергиите на депротониране на протон-донорните групи в базите. Моделните системи са така подбрани, че да могат да формират единични водородни връзки. Получените корелационни уравнения, свързващи изчислените енергии на взаимодействие с параметри, характеризиращи електростатичните сили при атомите, са приложени за извеждането на дескриптори на реактивоспособността за отделните атомни позиции в нуклеиновите бази. Сред изследваните теоретични параметри EPN дава най-добра корелация с енергиите на водородно свързване. Изведените зависимости бяха използвани за дефинирането на дескриптор на реакционната способност към водородно свързване за отделните атомни позиции в нуклеиновите бази. Ефектите на формиране на двойки бази върху реактивоспособността бяха също оценени количествено.

Identification of mixture components by multiple linear regression and subtraction of reference spectra: searching infrared and raman libraries

S. H. Tsoneva, S. R. Nachkova, G. N. Andreev, P. N. Penchev*

Department of Analytical Chemistry and Computer Chemistry, "Paisii Hilendarski" University of Plovdiv, 24 Tzar Asen Str., 4000 Plovdiv, Bulgaria

Received April 13, 2017; Revised April 20, 2017

Dedicated to Acad. Ivan Juchnovski on the occasion of his 80th birthday

A procedure for mixture analysis by searching in infrared and Raman spectral libraries is proposed and tested with more than 60 binary mixtures of organic compounds. The procedure uses a combination of spectra subtraction and multiple linear regression. The infrared spectra appeared to be more informative and suited for that purpose than Raman spectra. The procedure is implemented into a Windows-based program developed earlier for a library search of vibrational spectra.

Key words: Raman spectra; infrared spectra; library search; mixture analysis

INTRODUCTION

Separation of mixture components and their identification and quantification is the main task of various chromatographic techniques [1] by using reference standards or by hyphenated techniques (usually GC-MS and LC-MS) that provide spectra of the separated components. Nevertheless, the number of reference standards in a lab is limited to several hundreds and smaller than a typical number of several thousands of library spectra. Furthermore, the hyphenated techniques instrumentation is much expensive and missing in most organic labs. On the other hand, the infrared (IR) and Raman spectra are well suited for the identification of organic compounds via library search [2-4]. As the mixture spectrum can be approximated by a linear combination of components spectra, it can be resolved if the reference spectra of the components are available [5]. An extensive review of the application of IR and Raman spectroscopy to mixture analysis is given in [3, 6]. No matter how the mixture analysis is applied, its math is based on multiple linear regression that evaluates the coefficients of the linear combination [6]. Even the successive subtraction (so called *spectrum stripping*) of the reference spectra—multiplied by appropriate concentration factors—from that of the mixture [5-6] is a kind of regression procedure. The last is controlled by the user who monitors and sets (or minimizes) the residuals between both spectra.

All proposed procedures are plagued by one or both of two main shortcomings: (1) the component spectra do not appear among the first hits (if the hit list but not the whole library is processed), and (2) some of the calculated regression coefficients are not statistically significant—both happen usually for the component with a low concentration. That is why, in the present paper the combination of spectra subtraction and regression is studied and the obtained results are evaluated with two objectives in mind: first, proposing a robust routine procedure and second, comparison of the performance of IR and Raman spectra. Moreover, the application of Raman spectroscopy for mixture analysis is still underdeveloped and scanty described in papers dealing with library search in general [7-8].

EXPERIMENTAL

The IR spectra were registered on a Perkin-Elmer 1750 FT-IR Spectrometer from 4000 cm^{-1} to 450 cm^{-1} at resolution 4 cm^{-1} with 16 scans and on a VERTEX 70 Spectrometer (Bruker, Germany) from 4000 cm^{-1} to 400 cm^{-1} at resolution 2 cm^{-1} with 25 scans. The Raman spectra were measured on RAM II (Bruker, Germany) with a focused laser beam of Nd:YAG laser (1064 nm). All spectra were subjected to curvilinear baseline correction by the instrument software (CDS-2 or OPUS v. 6.5). When loaded in our software IRIS, the original spectral data were converted by a smoothing procedure based on weights from a normal distribution. In the present work the library and mixture spectra of organic compounds were solely

* To whom all correspondence should be sent:
E-mail: plamen@uni-plovdiv.net

used. Six IR libraries were composed of 911 entries altogether and Raman one of 330 entries with most of the spectra measured in our lab [6].

The Windows-based program, IRSS, for searching in libraries of IR and Raman spectra was programmed in Delphi 1 by one of the authors (P.N.P.) and described elsewhere [6,9]. Seven different measures for comparison of IR spectra were implemented: three for peak matching and four for comparing full spectral curves. IRSS uses the spectral range from 3700 to 500 cm^{-1} , with a sampling interval of 4 cm^{-1} . All IR and Raman spectra, when loaded into IRSS, are normalized in the 0.0-1.0 interval in ordinate; here has to be mentioned that the ordinate of Raman spectra is not in absorbance units but in normalized intensity of the scattered light and future references to the ordinate will be given as dimensionless values. Furthermore, IRSS provides software tools for the import of IR spectra in JCAMP-DX format, for peak picking, and for an analysis of IR spectra of mixtures with a graphical user interface.

Methods

Peak search algorithms described in the literature [2, 6] can be generally divided into two types: (1) *forward* one used for identification of pure compounds, and (2) *reverse* one applied for identification of the components of organic mixtures. The corresponding spectra similarity measures (hit quality indices, HQIs) were implemented in IRSS and described in details in our previous paper [10].

The main requirement for the application of the mixture analysis is that all mixture components have spectra in the used libraries and there are no strong intermolecular interactions between mixture components [5]. Thus, the mixture spectrum (row vector $\mathbf{M}_{1,K}$) can be represented as a linear combination of all hit list spectra (matrix $\mathbf{S}_{N,K}$) by Eqn. 1.

$$\mathbf{M}_{1,K} = \mathbf{C}_{1,N} \mathbf{S}_{N,K}, \quad (1)$$

where the subscripts show the matrix dimensions, i.e. K is the number of used wavenumbers, N is the number of used hits, and the \mathbf{M} 's and \mathbf{S} 's elements represent the corresponding absorbance values. In reality, only the component spectra participate in this linear combination but Eqn. 1 includes all hits as the user does not know in advance which hits are the components.

The mixture analysis procedure is the following. At the beginning, the mixture spectrum is searched

in the libraries by reverse peak search algorithm. A multiple linear regression is performed [11] with the mixture spectrum and hit list spectra by Eqn. 2.

$$\mathbf{C}_{1,N} = \mathbf{M}_{1,K} \mathbf{S}_{K,N}^T (\mathbf{S}_{N,K} \mathbf{S}_{K,N}^T)^{-1} \quad (2)$$

where the superscripts T and -1 designate a transposed and inverse matrix, respectively.

The calculated row vector $\mathbf{C}_{1,N}$ (obviously dimensionless) does not represent concentration of hit list compounds in the mixture because all spectra in IRSS are normalized in ordinate in the 0.0-1.0 range and there is no quantitative sample information recorded in the spectral libraries. That is why, $\mathbf{C}_{1,N}$ represent coefficients of linear combination of hit list spectra and are called *pseudo-concentration* by us. The statistically significant values of $\mathbf{C}_{1,N}$ can be used as a decision criterion, revealing which hits are plausible components. In our software IRSS the 95% and 99% confidence limits of the pseudo-concentrations are estimated according to the cited above Massart *et al.* book [11].

The first of these hits (with number F) with a statistically significant pseudo-concentration is assumed as one of the mixture components and its spectrum is subtracted from the mixture spectrum as designated by Eqn. 3.

$$\mathbf{R}_{1,K} = \mathbf{M}_{1,K} - f \mathbf{S}_{F,K}, \quad (3)$$

where $\mathbf{S}_{F,K}$ is the F row of matrix $\mathbf{S}_{N,K}$, f is a real number such that ' $f \mathbf{S}_{F,K}$ ' removes the spectral bands of this component from the mixture spectrum giving the remainder spectrum $\mathbf{R}_{1,K}$. The coefficient f can be set to 1.0 as it is done in [5] because the spectral bands of the component with a higher concentration prevail over the other components' spectral bands and usually the main component is at the foremost beginning of the hit list. The coefficient f can also be obtained by the user when he/she is monitoring the remainder spectrum acquired by subtraction procedure and decides that the component spectral bands no longer appear in the remainder spectrum. The results with this scheme were published earlier by us [10] and the obtained f 's had values close to 1.0. The software IRSS has a user-friendly interface that facilitates the spectra subtraction. Another option is to set f to a value of $c_{1,F}$ obtained from the multiple linear regression performed initially. These three options are thoroughly studied in the present paper.

Further, the negative values of the remainder spectrum are truncated, the spectrum is normalized and then its peaks are searched in the libraries. A multiple regression is again performed with the

remainder spectrum and the newly obtained hits. The first hit with a statistically significant values of $c_{1,S}$ is chosen as the second component. The cycle can be repeated for the third component and so on but our experience shows that more than three components are hard to be identified.

Described in this way, the mixture analysis looks pretty straightforward, but even for a mixture of components with quite different spectra it could fail and give erroneous results. Recommendations are not given in the literature to what extent the subtraction is performed, except that one or more selected spectral bands of the mixture spectrum have to be nullified. Another complication can arise if the mixture components have similar spectra with nearly all bands overlapping (because of their similar structures) thus leading to an over-subtraction—and as a result of it—the second component might not be among the first hits that are obtained from the second library search.

Our experience shows that to propose a procedure for mixture analysis means not only to give its steps (an algorithm) and the optimal values of its various parameters but also to elucidate all creative ways of solving the problem. Without doubt, the educated user would use a kind of versatile library search beyond any prescriptions. He/she would select various spectral intervals, probably starting with finger print region. He/she would monitor that the plausible components' spectral bands are subset of those of the mixture. He/she would vary both search tolerances (in wavenumber and absorbance) as well as would set various threshold values used by peak-picking (probably he/she would select different ones for the mixture, remainder and library spectra). The spectral match algorithms and the number of hits to be processed is also a variable that most influences the results. All these options cannot be systematically studied in the proposed procedure as it is usually done in analytical chemistry when one performs a consecutive optimization upon two or three parameters. That is why, the following parameters are set rigid to the recommended values derived by our previous experience with the library search.

(1) The threshold for peak-picking of library spectra was set to 0.03. Threshold for peak-picking of mixture spectra was set to 0.01 with the idea in mind that there could be a component with a way

lower concentration. Some IR mixture spectra showed water vapor rotational bands and some Raman spectra were very noisy so a higher threshold (0.02-0.04) was used.

(2) The remainder spectrum is with a lower signal to noise ratio that is why a higher threshold (0.02-0.09) was used. Raman spectra are in principle with a poor signal to noise ratio thus the threshold value is quite higher than that used with IR spectra.

(3) Our experience showed that the optimal wavenumber tolerance for mixture peak search, $\Delta\nu$, is higher than that used for single compound identification, that is why a values of $\Delta\nu = 12 \text{ cm}^{-1}$ was selected.

(4) The search tolerance in ordinate, ΔA , was set to 1.0 (maximum value, i.e. the band intensity was not accounted by peak match). Such was done in our previous studies so that all component spectra were in the hit list what is not a requirement for the present study. Despite that difference, the optimal values of ΔA was not searched upon.

(5) Only the first 40 hits were used for regression calculations but the user is advised to review the hit list entries and use lesser or bigger number.

(6) Despite that the search uses peaks in the whole spectral interval ($3700 - 500 \text{ cm}^{-1}$), the starting regression interval was set to $1300 - 600 \text{ cm}^{-1}$. If no component identification was achieved, the other intervals recommended by us (and tried in this order) were $1800 - 600 \text{ cm}^{-1}$, $1800 - 500 \text{ cm}^{-1}$ and $3700 - 500 \text{ cm}^{-1}$.

(7) The reverse peak search is specially designed for mixture analysis [10] but if the remainder spectrum is with a low signal to noise ratio (this is the case for most Raman spectra), the user can apply one of the four full-spectrum search algorithms [9,13]: for binary mixtures the remainder, that is properly calculated, is a spectrum of one component.

RESULTS AND DISCUSSION

The test of the proposed mixture analysis procedure was performed with 35 IR and 60 Raman spectra of mixtures of organic compounds: all spectra were measured by two of the authors – P.N.P and S.H.T. The spectral files were ordered randomly with a separate numbering for the IR and Raman spectra. Three series of search results were produced. First, the used subtraction procedure was governed only by the first three heuristics derived earlier [10], i.e. without setting the coefficient f in Eqn. 3 close to 1.0. The random IR and Raman

spectra were searched and analyzed by one of the authors (S.R.N.) who knew neither the components nor the composition of the mixtures, i.e. the mixture analysis was performed as close as possible to the so called *blind experiment*. Second, the mixture analysis using all four heuristics [10] (i.e. with additionally $f = 1.00$) was applied, and third, f equal to the corresponding regression coefficient from Eqn. 2 was used for spectra subtraction. The last two series of mixture analysis were performed also on the randomly numbered spectra but setting *a priori* f to 1.00 or to the regression coefficient did not necessitate a kind of blind experiment. Only 20 of the mixtures, Table 1, were used to evaluate the results: the remaining spectra were some sort of ‘padding’ (ballast) in the present study in order to complicate the blind experiment. Those were IR

and Raman spectra of the mixtures of hexane and cyclohexane, benzene and pyridine, and the Raman spectra of the mixtures of 1-octanol and 1-decanol, 1-nonanol and 1-decanol, 2-methyl-1-phenylpropan-1-one and 4'-methylpropiophenone, benzylacetone and butyrophenone, 2-ethylhexane-1-ol and 2-ethylhexane-1,3-diol, cyclopentanone and benzylacetone.

The first and third series produced comparable results that were substantially better than those produced in the second series. It appeared that the f value set by a spectroscopist, Eqn. 3, (i.e. first series of mixture analysis) had been less than the corresponding regression coefficient and the bands of the first-found component retained in the remainder spectrum.

Table 1. The identification of mixture components. The mixture concentration (in volume ratio) is given in the first column and the regression coefficients are designated with f_1 and f_2 ; (error) another compound was found as a component of the mixture

(a) 2'-methylacetophenone (A) and 3'-methylacetophenone (B)

A:B v / v	IR				Raman			
	1 st found	2 nd found	f_1	f_2	1 st found	2 nd found	f_1	f_2
1:1	B	A	0.50	1.07	A	B	0.50	0.94
1:4	B	A	0.81	0.77	B	A	0.91	0.81
1:9	B	A	0.88	0.48	B	A	0.85	0.35
4:1	A	B	0.71	0.66	A	B	0.78	0.86
9:1	A	B	0.83	0.77	A	B	0.84	0.47

(b) 1,4-dioxane (A) and tetrahydrofuran (B)

A:B v / v	IR				Raman			
	1 st found	2 nd found	f_1	f_2	1 st found	2 nd found	f_1	f_2
1:1	A	B	1.05	0.73	A	B	0.65	0.97
1:4	A	B	0.92	1.02	B	A	0.77	0.91
1:9	B	A	1.00	0.84	B	A	0.40	0.58
4:1	A	B ¹⁾	1.08	0.74	A	B	0.85	0.37
9:1	A	- ²⁾	0.99	–	A	B	0.90	0.46

(c) 3-heptanone (A) and 4-heptanone (B)

A:B v / v	IR				Raman			
	1 st found	2 nd found	f_1	f_2	1 st found	2 nd found	f_1	f_2
1:1	B	A	0.35	0.40	B	A	0.38	0.93
1:4	B	A	0.59	0.31	B	A	0.77	1.44
1:9	B	A	0.71	0.38	B	A ¹⁾	0.98	4.04
4:1	A	B	0.49	0.36	A	B ¹⁾	0.95	1.67
9:1	A	error	0.63	1.61	A	B ¹⁾	0.92	1.30

(d) 1-nonanol (A) and 5-nonanol (B)

A:B v / v	IR				Raman			
	1 st found	2 nd found	f_1	f_2	1 st found	2 nd found	f_1	f_2
1:1	A	B	0.16	0.36	- ¹⁾	–	–	–
1:4	B	error ¹⁾	0.47	0.74	B	error ¹⁾	0.43	–
1:9	B	error ¹⁾	0.57	0.72	B ¹⁾	error ¹⁾	0.44	1.12
4:1	A	B	0.23	0.09	B ¹⁾	–	0.15	–
9:1	A	error ¹⁾	0.22	0.60	error ¹⁾	error ¹⁾	0.62	0.48

¹⁾ The original spectral interval for regression calculations was widened (see text).

²⁾ The component was not found, i.e. its regression coefficient is not statistically significant.

Despite that, the correct identification of the second component took place in most cases: the usage of reverse search of the remainder spectrum assisted the appearance of the second component in the second hit list. On the other side, the analysis of the failures in the second series showed that when both components have common spectral bands with high intensity, these bands sum together and the normalized mixture spectrum is a linear combination of the component spectra with coefficients quite less than 1.0.

In Table 1 are given the third series results, i.e. f is set to the regression coefficient. As can be seen, even the very structurally similar components as 3-heptanone and 4-heptanone can be identified from their mixture spectra. As expected, problems appear with some of the 1:9 or 9:1 v/v mixtures. On the other side, the worst results are for the mixtures of 1-nonanol and 5-nonanol and they could be explained with the presence of 1-decanol spectrum in the IR and Raman libraries: there is a very subtle difference between 1-nonanol and 1-decanol IR as well as Raman spectra. Also several other primary alcohols appeared in the hit list and their spectra are very similar to that of 1-nonanol.

Here has to be mentioned that O-H stretching band is completely missing in Raman spectra of saturated alcohols and these spectra are very close to those of the compounds with nearly the same aliphatic part. The C=O stretching band in Raman spectra is of very low intensity, and these both spectral peculiarities are the reason for several of

the errors when the spectral interval used by regression is widened. The other mixtures (not presented in Table 1) showed similar results. As a whole the IR spectra gave better results than the corresponding Raman spectra.

Several particularities can be illustrated with the analysis of the mixture (1:1 v/v) of structurally similar compounds as 1-nonanol and 5-nonanol are. Peak search of the IR mixture spectrum resulted in 1-nonanol as a sixth hit and 5-nonanol as a tenth hit; first five hits are 1-hexanol, 1-decanol twice (a repetition in these libraries), dodecane and octacosane. The remainder spectrum is calculated with the coefficient in Eqn. 3 taken from the performed regression, $f = 0.16$. Fig. 1 shows the mixture and component spectra in the 1500 - 600 cm^{-1} interval, as well as the remainder spectrum. As can be seen, (1) the concentration ratio of 1:1 v/v does not mean equal pseudo-concentrations, (2) in the 1300-600 cm^{-1} interval the components spectra are most different, (3) the components have overlapped bands at 1465 and 1380 cm^{-1} as consequence of their common substructures, CH_3 and CH_2 groups, (4) the main difference between the component spectra is in C-OH stretching bands (primary and secondary alcohol, respectively) and $\rho(\text{CH}_2)$, 724 and 732 cm^{-1} , and (5) the spectral bands of 1-nonanol, $\nu(\text{C-OH}) = 1058 \text{ cm}^{-1}$ and $\rho(\text{CH}_2) = 724 \text{ cm}^{-1}$, were vastly removed by subtraction, i.e. they are not present in the remainder spectrum.

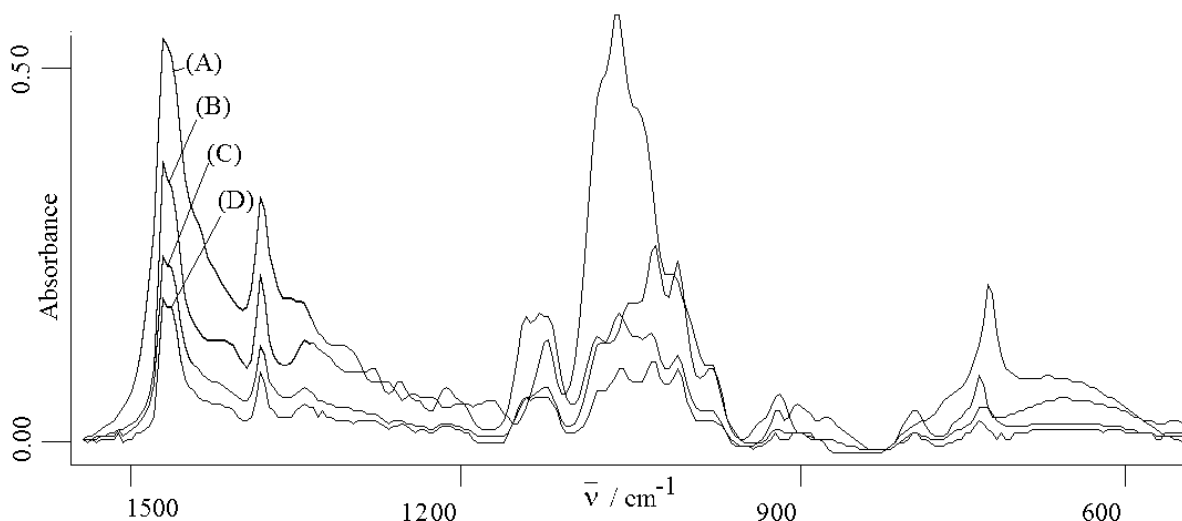


Fig. 1. Spectra of (A) the mixture (1:1 v/v) of 1-nonanol and 5-nonanol, (B) the remainder spectrum (see text), (C) 1-nonanol, (D) 5-nonanol.

CONCLUSION

The procedure for mixture analysis by searching in IR and Raman spectral libraries is implemented and tested. The components are identified by their statistically significant coefficients obtained by multiple linear regression. The user is advised to use the corresponding regression coefficient for subtraction of the spectrum of first-found component from that of the mixture. Another option is for the user to monitor that the certain spectral bands are disappearing in the remainder spectrum in the process of subtraction.

REFERENCES

1. V. Oliveri, G. Vecchio, *EJMECH.*, **120**, 252 (2016).
2. R. Freitag (ed.), *Modern Advances in Chromatography*. Springer-Verlag, Berlin, 2002.
3. J. T. Clerc, E. Pretsch, M. Zuercher, *Microchim. Acta*, **II**, 217 (1986).
4. H. J. Luinge, *Vib. Spectrosc.*, **1**, 3 (1990).
5. W. A. Warr, *Anal. Chem.*, **65**, A1087 (1993).
6. H. Somberg, Qualitative mixture analysis by use of an infrared library search system. Brucker Reports, 1988.
7. P. N. Penchev, Dr. Sc. Dissertation, University of Plovdiv, 2016.
8. M. B. Denton, R. P. Sperline, J. H. Giles, D. A. Gilmore, C. J. S. Pommier, R. T. Downs, *Australian J. Chem.*, **56**, 117 (2003).
9. P. Vandenabeele, *Spectrochim. Acta, Part A*, **80**, 27 (2011).
10. K. Varmuza, P. Penchev, H. Scsibrany, *J. Chem. Inf. Comput. Sci.*, **38**, 420 (1998).
11. P. N. Penchev, V. L. Miteva, A. N. Sohoun, N. T. Kochev, G. N. Andreev, *Bulg. Chem. Commun.*, **40**, 556 (2008).
12. D. L. Massart, B. G. M. Vandeginste, S. N. Deming, Y. Michotte, L. Kaufman, *Chemometrics: A Textbook*, Elsevier, Amsterdam, 1988.
13. P. N. Penchev, A. N. Sohoun, G. N. Andreev. *Spectrosc. Lett.*, **29**, 1513 (1996).
14. P. N. Penchev, N. T. Kochev and G. N. Andreev, *Compt. Rend. Acad. Bulg. Sci.*, **51**, 67 (1998).

ИДЕНТИФИКАЦИЯ НА КОМПОНЕНТИТЕ НА СМЕСИ С МНОГОПРОМЕНЛИВА ЛИНЕЙНА РЕГРЕСИЯ И ИЗВАЖДАНЕ НА СПЕКТРИ: ТЪРСЕНЕ В ИНФРАЧЕРВЕНИ И РАМАН СПЕКТРАЛНИ БИБЛИОТЕКИ

С. Х. Цонева, С. Р. Начкова, Г. Н. Андреев, П. Н. Пенчев *

*Катедра „Аналитична химия и компютърна химия“, Пловдивски Университет „Паисий Хилендарски“, ул. Цар
Асен № 24, 4000 Пловдив*

Постъпила на 13 април 2017 г.; Коригирана на 20 април 2017 г.

(Резюме)

Предложена е процедура за анализ на смеси чрез търсене в библиотеки от инфрачервени и Раман спектри. Процедурата е тествана с повече от 60 смеси от две органични съединения. За анализа се прилага комбинация от многопроменлива регресия и изваждане на спектри. Използването на инфрачервени спектри дава по-добри резултати от тези, получени с Раман спектри. Процедурата е реализирана в програмата, работеща в среда на Windows.

Organic components in leachates from some Bulgarian lignites

A. D. Kosateva^{1*}, M. Stefanova¹, S.P. Marinov¹, L. Gonsalvesh²

¹ Institute of Organic Chemistry with Centre of Phytochemistry, Bulgarian Academy of Science, Sofia 1113, Bulgaria,

²Burgas University "Prof. Dr. Assen Zlatarov", Burgas 8010, Bulgaria

Received March 21, 2017; Revised April 14, 2017

Dedicated to Acad. Ivan Juchnovski on the occasion of his 80th birthday

The information on composition of lignite water-soluble fractions, the so-called leachates, formed during coal mining, storage and exploration is scarce. The aim of the present study is to characterize by wet chemical and spectral methods leachates from some Bulgarian lignites and to estimate their role as potential organic pollutants in groundwaters. In this study, lignites from Thrace- and Sofia- coal basins, i.e. Maritza-East and Stanjanci mines, were subjected to water sequential extraction by distilled water at 25 °C for 10 weeks. The freeze-dried extracts (leachates) were characterized by yields (1.4% for Stanjanci lignites and 1.7% for Maritza-East lignites), technical and elemental analysis. Soluble in dichloromethane portions of leachates, 330 mg/kg Maritza East (ME) lignites and 75 mg/kg Stanjanci (Stan) lignites, were analyzed by GC-MS. Two groups of components were identified: ketophenols, 12 mg/kg ME lignite and 1.2 mg/kg Stan lignite, were 5,6-dehydroferruginol, hinokione, 7-ketototarol and sugiol were the main extracted polar diterpenoids. Oxygenated polar diterpenes of abietane-type are widely distributed in the plant realm. They are not harmful for the environment. Keto- and unsaturated steranes were the other group of compounds in leachates. They are not harmful to human health as well. The study will continue with application of instrumental technique capable to analyze at molecular level essential portion of leachates organic matter. Data from the various approaches will be compared and their joint interpretation will allow making reasonable conclusions for potentially harmful/harmless components in coal leachates.

Key words: lignites, leachate, organic matter, ketophenols, ketosteranes

INTRODUCTION

Currently there is a little information about harmful to human health persistent organic compounds that are leached from coals in the environment. The amounts of leached inorganic substances are under regulation and some organic impurities in surface waters, i.e. industrial pollutants like phthalates, chlorinated products, PAHs, etc., are under control [1]. In order to assess the potential impact of interactions between coal and water that might occur in the environment it is necessary to have more information on the composition of lignite water-soluble fractions, the so-called leachates. They could be formed during coal washing processes, dump storage piles exposed to rain and/or water spray, transport in coal water slurry, disposal of coal, and deposition of waste materials from energy production in thermal power plants, etc. [2-4]. It is proved that during secondary transformations of organic matter proceeding in dumps, mainly oxidation, the content of polar constituent increases, and susceptibility to water run-off arises [5]. It is of utmost importance

to know the type and amount of leachates infiltrated in the environment during coal storage and maintenance.

Coals themselves are not mutagenic, but water-soluble organic matter from lignite produced an appreciable mutagenicity [6-8]. Some studies have reported that groundwater can leach organic matter from Pliocene lignite and they can be hazardous to human health (e.g., urinary tract cancer, tubulointerstitial nephropathies). Long-term exposure to low concentrations of organic compounds leached from Pliocene lignite is probably one of factors in the etiology of the disease so-called Balkan endemic nephropathy (BEN) [9].

In order to appreciate the potential impact of interactions between coal and water that might occur in the environment it is necessary to have information on the composition of lignite water-soluble fractions. The aim of the present study is comparative characterization of organic soluble portions in dichloromethane of leachates from two Bulgarian lignites in view to depict presence/absence of harmful components.

* To whom all correspondence should be sent:
E-mail: ani_popova@orgchm.bas.bg

EXPERIMENTAL

Lignite samples from Thrace- and Sofia-coal basins, i.e. “Maritsa-East” (ME) and “Stanjanci” (Stan) mines were subjected to water sequential extraction at 25 °C for 10 weeks. The protocol at certain extent was adopted from Doskočil *et al.* [10]. Briefly, 10 g of grounded lignite samples at < 0.2 mm and 150 ml of distilled water were placed into a 200 ml Erlenmeyer flask. The slurry was regularly agitated by magnetic stirrer. Each 7 days, the leachate was separated from lignite by centrifugation for 10 min at 4000 rpm at 25^o C. Experiments were performed in duplicate. Subsequently the supernatant was filtered to remove the finest particles eventually penetrated during manipulations. Leachates were freeze-dried and subjected to characterization by chemical and instrumental methods [11].

For isolation of material soluble in organic solvents, freeze-dried leachates were refluxed 3x50 ml for half an hour with dichloromethane (DCM). Soluble portions were combined, dried over CaSO₄, filtrated, concentrated at reduced pressure and studied by GC-MS. Scheme of isolation is illustrated in Fig. 1.

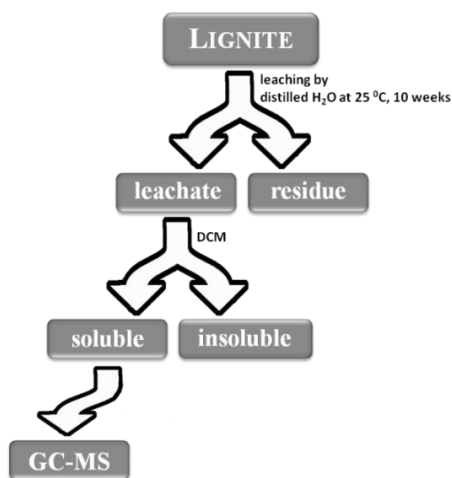


Fig.1. Scheme of extraction and leachate analyses

GC-MS analyses was carried out on a Hewlett-Packard 6890 GC system plus HP 5973 MSD equipped with a HP-5 MS column (0.25mm×30m×0.25μ film thickness) with flame ionization detector (300°C). A split/splitless capillary injector (300°C) is used in the splitless mode (valve reopened 1 min after injection). After 0.5 min isothermal period at 85°C the oven temperature was increased to 200°C at 20°/min and then to 320°C at 5°/min. The MSD was operated in the electron impact (EI) mode with energy of 70 eV and scan range from 50 to 650 Daltons. The data were acquired and processed with the HP software.

Individual compounds were determined by comparison of mass spectra (MS) with literature and library data, comparison of MS and GC retention times with those of authentic standards or interpretation of mass spectra. For MS spectra tracking Xcalibur software was used. MS were quantitatively interpreted by internal standard application, deuterated *n*C₂₄. Amounts were normalized in mg/kg..

RESULTS AND DISCUSSION

Leachates conductivity (2000-4000 μS) demonstrated that extracts from the first two weeks were characterized by high amount of salts, 60-70% ash [11]. Data are in accordance with results for leaching of South Moravian lignites where leachates conductivity from the first weeks was very high [10]. Later on conductivity gradually decreased from 60 to 15 μS and measured total organic carbons, (TOCs 316-380 g/kg) were comparable. Therefore, based on conductivity in our experiment [11] and literature data [10], only leachates enriched in TOCs were further studied by GC-MS. Respectively, leachates from 3 to 10 weeks were combined, freeze-dried and analyzed. Relatively lower residue amounts, 33-36 % (comparing to the first two leachates with ashes 63-70 %,) and high oxygen content, 31-43 %, were determined for the combined leachates.

In Table 1 are shown yields of leachates, in %. Data were recalculated on “dry, ash free basis” and amounts of organic matter in leachates, in % daf, were obtained. Extractability of leachates in DCM were 330 mg/kg for ME lignites and 75 mg/kg for Stan lignites.

Table 1. Yields of leachates and amounts of organic matter, in %

Lignite	Leachate yield	W ^a	Residue	LOM (% ^{daf})
Maritsa-East	1.7	15.93	35.9	0.82
Stanjanci	1.4	11.45	32.8	0.78

LOM= Leachate organic matter

In Figure 2 is illustrated GC-MS separation of DCM extractable organic matter in ME leachate. Identified structures are given in Table 2. In both extracts GC-MS study of DCM extracts has depicted two groups of organic compounds: (i) polar diterpenoids, (ii) and, ketosteranes. Structures of identified compounds are illustrated in Appendix (Fig.3). GC-MS data for polar diterpenoids were quantitatively interpreted and their amounts are given in Table 2.

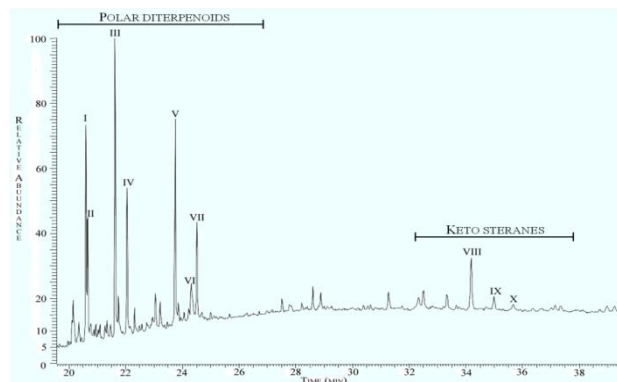


Fig. 2. GC-MS separation of DCM soluble portion of Maritsa East lignite leachate (Structures in Table 2 and Appendix)

Both DCM extracts compositions were comparable. There were differences only in compounds proportions: (i) tenfold higher amount of polar diterpenoids (Polar-Di) for ME lignites, 12 mg/kg, comparing to 1.2 mg/kg for Stan lignites; (ii) and, higher amount of ketosteranes for Stan lignite, 2.6 mg/kg coal, comparing to 1.5 mg/kg coal for ME lignite (Table 2).

A specific flora was growing on our territory during the Tertiary, in a subtropical, warm and humid climate, as proved our studies on biomarker compositions [12-14]. Marshland vegetation including water grass and species of plants and trees (*Taxodium*, *Sequoia*, *Glyptostrobus*, etc.) were presented at the edges of shallow lakes and lagoons. The dead vegetation was buried by sediment and decayed mainly under anaerobic conditions. A systematic study of Pliocene aged lignites in Balkan Peninsula as a reason for the kidney disease abundant only in the territories of Serbia, Romania, Bulgaria, Croatia, has been performed [6-9]. Leachates from the endemic area lignites include aliphatic (mainly cycloalkanes/alkenes and steranic structures) and aromatic (mono- and polyaromatic terpanes, polycyclic aromatic hydrocarbons) structures. By spectral methods, i.e. ^{13}C NMR, GC-MS, was proven that many of these compounds have attached O- functional groups, i.e. phenolic OH, keto groups, OCH_3 , etc., and some of them contain heterocyclic N or NH_2 groups, structural features that could make them nephrotoxic and carcinogenic.

The preservation potential of terpenoids as phenols or ketones is appreciable. In particular diterpenoids were used as (palaeo)chemosystematic indicators for the systematics and phylogeny of conifers. Polar diterpenoids, i.e. ferruginol and its

dehydrogenated analogue, are common constituents of modern species of *Cupressaceae/Taxodiaceae* and *Podocarpaceae*. Their chemotaxonomic value has already been discussed in studies of Bulgarian Neogene lignites where the vegetation in the palaeoswamps was dominated by such conifers [12-15].

Oxygenated polar diterpenes of abietane-type are widely distributed in the plant realm. Potential cytotoxic, antifungal, and antibacterial activities for them have been reported by Kusumoto *et al.* [16,17]. In a suite of studies the authors have enhanced the pharmacological prospects of the natural abietane-type diterpenoids extracted from conifer cones. According to these finding polar diterpenoids of abietane type were not harmful for the environment and possess pharmacological properties with well expressed antioxidant activity, anti-fungal, anti-termitic, anti-ulcerogenic properties, etc.

Among the steroid ketones (ketosteranes) the most abundant are stigmastan-3,5-diene-7-one (VIII) 24-ethylcholest-4-en-3-one (stigmast-4-en-3-one) (IX), with lower contributions of 24-methylcholest-4-en-3-one (ergost-4-en-3-one), 24-methylcholestan-3-one (ergostanone), and 24-ethylcholestan-3,5-dien-7-one (not indicated in Fig.2 and not quantified in Table 2). One diketo sterane, stigmastan-3,6-dione (X), was identified as well. There were some negligible amounts of di- and tri- unsaturated steranes, i.e. stigmastan-3,5-diene, M^+396 , m/z 147 (100%) and stigmastan-3,5,22-triene, M^+394 , m/z 255 (100%). All keto- and unsaturated steranes are typical for coal extractable matter and denote terrigenous input [12]. They are not harmful to human health as well.

CONCLUSION

This study was inspired by the necessity of information on the organic matter composition of coal leachates. Two Bulgarian lignites were leached by distilled water at 25°C for 10 weeks. GC-MS study of organic extractable matter in leachates has revealed the presence of two groups of polar organic compounds: (i) polar diterpenoids, 1.2-12 mg/kg coal, i.e. 5,6-dehydroferruginol, hinokione, 7-ketototarol, sugiol; (ii) and, ketosteranes of terrigenous origin, 1.5-2.6 mg/kg coal. Both groups of compounds are not harmful for human health. The study will continue with application of other instrumental technique capable to analyse leachates essential portions at molecular level.

Compound	Formula	M ⁺	m/z (100%)	Leachate	
				ME	Stan
Polar diterpenoids*, i.e.					
6,7-Dehydroferruginol (I)	C ₂₀ H ₂₈ O	284	202	2.3	0.3
Ferruginol (II)	C ₂₀ H ₃₀ O	286	271	1.3	0.2
Hinokione (III)	C ₂₀ H ₃₀ O ₂	300	189	3.0	0.2
7-Ketototarol (IV)	C ₂₀ H ₂₈ O ₂	300	285	1.5	0.2
Sugiol (V)	C ₂₀ H ₂₈ O ₂	300	285	2.3	0.2
Salvinolone (VI)	C ₂₀ H ₂₆ O ₃	314	244	0.6	-
5,6-Dihydrosugiol (VII)	C ₂₀ H ₂₆ O ₂	298	213	1.0	0.1
TOTAL				12.0	1.2
Keto steroids*, i.e.					
Stigmastan-3,5-diene-7-one (VIII)	C ₂₉ H ₄₆ O	410	174		
Stigmastan-4-en-3-one (IX)	C ₂₉ H ₄₈ O	412	124		
Stigmastan-3,6-diene-dione (X)	C ₂₉ H ₄₈ O ₂	428	245		
TOTAL				1.5	2.6

*- structures in Appendix

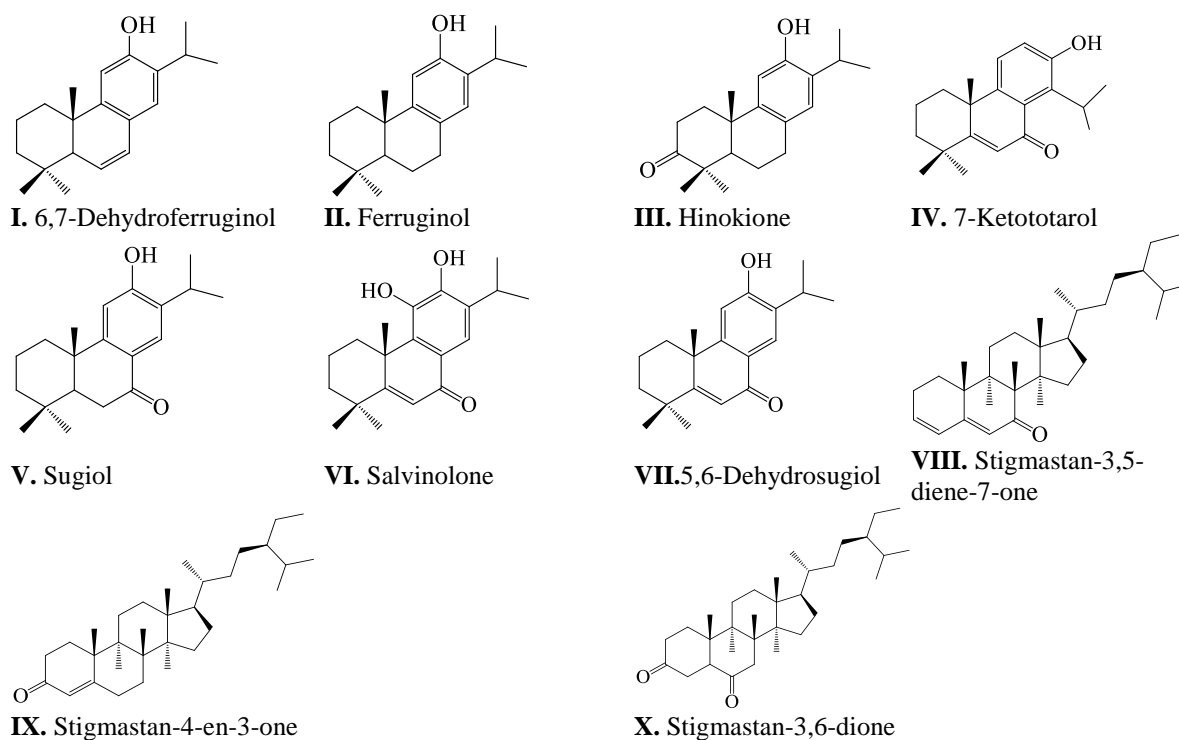


Fig. 3. Appendix: Chemical structures cited in the text

Acknowledgements: The funding in the frame of the National Scientific Fund, Ministry of Education and Science, Bulgaria under Project DN 04/5 is highly acknowledged.

REFERENCES

1. Regulation NoH-4/14.09.2012 of the Bulgarian Ministry of Environment and Water, St. Gazette No22/5.03.2013.
2. C. D. Vassileva, *C. R. Acad. Bulg. Sci.*, **57**, 71 (2004).
3. A. Meawad, D. Bojinova, Y. Pelovski, *Univ. Chem. Tech. Metal. J.*, **45**, 275 (2010).
4. M. Yossifova, D. Dimitrova, T. Iliev, *C.R. Acad. Bulg. Sci.*, **69**, 1611 (2016).
5. K. Markova, M. Stefanova, Z. Milakovska, S.P. Marinov, *Chem. Erde*, **76**, 405 (2016).
6. W.H. Orem, G. L. Feder, R.B. Finkelman, *Int. J. Coal Geol.*, **40**, 237 (1999).

7. R. B. Finkelman, W. H. Orem, V. Castranova, C. A. Tatu, H. E. Belkin, B. Zheng, H. E. Lerch, S. V. Maharaj, A. L. Bates, *Int. J. Coal Geol.*, **50**, 425 (2002).
8. G. L. Feder, C. A. Tatu, W. H. Orem, V. Paunesku, V. Dimitresku, D. N. Szilagyi, R. B. Finkelman, M. Margineanu, F. Schneider, *Facta Univ. Ser. Med. & Biol.*, **9**, 34 (2002).
9. S. V. M. Maharaj, W. H. Orem, C. A. Tatu, H. E. L. III, D. N. Szilagyi, *Envir. Geochem. Health*, **36**, 1 (2014).
10. L. Doskočil, L. Grasset, V. Enev, L. Kalina, M. Pekar, *Environ. Earth Sci.*, Springer (2014).
11. A. D. Popova, S. Marinov, M. Stefanova, I. Goshev, Proc. Sem. Ecol. with Int. Particip. 2016, IBER-BAS, (S. Chankova et al. Eds.), Fargo, 230 (2017).
12. M. Stefanova, D. R. Oros, A. Otto, B. R. T. Simoneit, *Org. Geochem.*, **33**, 1079 (2002).
13. M. Stefanova, B. R. T. Simoneit, *Int. J. Coal Geology*, **75**, 166 (2008).
14. M. Stefanova, B. R. T. Simoneit, S. P. Marinov, A. Zdravkov, J. Kortenski, *Org. Geochem.*, **96**, 1 (2016).
15. A. Bechtel, R. Sachsenhofer, A. Zdravkov, I. Kostova, R. Gratzner, *Org. Geochem.*, **36**, 1498 (2005).
16. N. Kusumoto, PhD Thesis, Iwate Univ., Tsuruoka, Japan, 2011, p. 146.
17. N. Kusumoto, T. Ashitani, Y. Hayasaka, T. Murayama, K. Ogiyama, K. Takahashi, *J. Chem. Ecol.* **35**, 635 (2009).

ОРГАНИЧНИ ВЕЩЕСТВА ОТ ИЗЛУГВАНЕ НА НЯКОИ БЪЛГАРСКИ ЛИГНИТИ

А. Д. Косатева^{1*}, М. Стефанова¹, С. П. Маринов¹, Л. Гонсалвеш²

¹ *Институт по органична химия с Център по фитохимия, Българска академия на науките, ул. Акад. Г. Бончев, бл. 9, 1113 София, България*

² *Бургаски университет "Проф. д-р Асен Златаров", Бургас 8010, България*

Постъпила на 21 май 2017 г.; Коригирана на 14 април 2017 г.

(Резюме)

Понастоящем информацията за състава на лигнитните водоразтворими фракции образувани по време на добив на въглища, съхраняването им и тяхната експлоатация, т. н. инфилтрати, е ограничена. Цел на настоящото изследване е охарактеризирането чрез химически и спектрални методи на инфилтрати от български лигнити и оценката им като потенциални органични замърсители на подпочвени води. Лигнити от Тракийския и Софийския въглищни басейни, в т.ч. мини „Марица Изток” и „Станянци”, бяха подложени на последователна екстракция с дестилирана вода при 25 °С, в продължение на 10 седмици. Лиофилизираните екстракти (инфилтрати) са охарактеризирани с добив 1.4% за Станянски лигнити и 1.7% за лигнити от Марица-Изток, технически и елементни анализи. Разтворимите в дихлорметан порции на инфилтратите, съответно 330 mg/kg за Марица Изток (ME) и 75 mg/kg за Станянци (Stan) бяха анализирани чрез газ хроматография/маспектрометрия (GC-MS). Определени са две групи съединения - кетофеноли, 12 mg/kg за ME лигнити и 1.2 mg/kg за Stan-лигнитни въглища. Основните полярни дитерпеноиди присъстващи в екстрактите са 5,6-дехидроферужинол, хинокион, 7-кетототарол и сужиол. Кислород съдържащите полярни дитерпени от абиетанов тип са широко разпространени в растителния свят и е доказано, че не са вредни за околната среда. Другата група съединения са кето- и ненаситени стерани. Те също са безвредни за човешкото здраве. Изследването ще продължи с търсене и прилагането на инструментални техники, подходящи да се изучи на молекулно ниво представителна част от органичните вещества в изследваните инфилтрати. Данните от различните подходи ще бъдат сравнени, а тяхното съвместно интерпретиране ще позволи да се направят заключения относно присъствието на потенциално вредни/безвредни компоненти в каменовъглените инфилтрати, получени при излугване на лигнитни въглища.

Preparation and comparative photocatalytic study of NiMnO₃/Mn₂O₃ and NiO_{0.8}ZnO_{0.2}/ZnO materials for the removal of Malachite Green dye from aqueous solution

K. L. Zaharieva^{1*}, K. I. Milenova¹, S. V. Vassilev², S. S. Dimova³, I. D. Stambolova⁴, V. N. Blaskov⁴

¹Institute of Catalysis, Bulgarian Academy of Sciences, Acad. G. Bonchev St., bl. 11, 1113 Sofia, Bulgaria

²Institute of Electrochemistry and Energy Systems, Bulgarian Academy of Sciences, Acad. G. Bonchev St., bl. 10, 1113, Sofia, Bulgaria

³Institute of Polymers, Bulgarian Academy of Sciences, "Acad. G. Bonchev" St., Bl.103A, 1113 Sofia, Bulgaria

⁴Institute of General and Inorganic Chemistry, Bulgarian Academy of Sciences, Acad. G. Bonchev St., bl. 11, 1113 Sofia, Bulgaria

Received March 14, 2017; Revised April 16, 2017

Dedicated to Acad. Ivan Juchnovski on the occasion of his 80th birthday

The NiMnO₃/Mn₂O₃ and NiO_{0.8}ZnO_{0.2}/ZnO materials were synthesized by precipitation technique (using different precursors – nitrates or chlorides and sodium hydroxide or sodium bicarbonate as precipitant) followed by calcination at 450°C. The existence of NiMnO₃, Mn₂O₃ and NiO_{0.8}ZnO_{0.2}, ZnO phases were established in the investigated samples by the powder X-ray diffraction analysis and FT-IR spectroscopy. The photocatalytic activity of prepared NiMnO₃/Mn₂O₃ and NiO_{0.8}ZnO_{0.2}/ZnO samples was tested and compared in the degradation of Malachite Green dye (MG) as model contaminant in aqueous solution under UV-irradiation. The photocatalytic tests determined that the degree of degradation of Malachite Green dye after 120 minutes over the NiO_{0.8}ZnO_{0.2}/ZnO and NiMnO₃/Mn₂O₃ samples (99% and 91%) synthesized using nitrates as starting materials is higher compared with that over materials prepared by chlorides (89% and 83%). The results show that synthesized NiO_{0.8}ZnO_{0.2}/ZnO and NiMnO₃/Mn₂O₃ materials in this study are promising photocatalysts for removal of MG dye as model pollutant from aqueous solution under UV illumination.

Key words: preparation, material, photocatalytic efficiency, degradation, Malachite Green, dye.

INTRODUCTION

Synthetic dyes find application in industries such as the leather tanning, textile, food technology, paper production, hair colorings, etc. The wastewaters released from these industries are usually contaminated with dyes. Malachite Green is used for the dyeing of cotton, silk, leather, paper as well as in manufacturing of printing and paints inks. Malachite Green is broadly used in distilleries for coloring purposes [1]. Malachite Green has strong effects on the reproductive and immune systems and possesses potential genotoxic and carcinogenic effects. The use of photocatalysts to degrade organic compounds in polluted water or air or to convert them into harmless substances has been widely investigated to decrease the damage bred by organic dye contamination to the people and environment [2]. For example Zn_xNi_{1-x}O thin films were tested in photodegradation of Methylene

Blue [3]. V. Eskizeybek et al. [4] have studied the photocatalytic properties of PANI homopolymer and PANI/ZnO nanocomposites in the degradation of Methylene Blue and Malachite Green dyes in aqueous medium under natural sunlight and UV light irradiation [4]. L. Saikia et al. [5] have established that the photocatalytic degradation of MG dye by ZnO samples in the form of nanoparticles and flowers were very effective in removal of this dye from aqueous solution [5]. Several research groups have investigated the photocatalytic properties of Mn₂O₃ composites. The photocatalytic activities of Mn₂O₃/TiO₂ material were studied by photooxidation of Rhodamine B, Thymol Blue, Methyl Orange and Bromocresol Green dyes under visible light [6]. R. Talebi [7] tested the photocatalytic ability of Mn₂O₃-TiO₂ nanocomposites about the degradation of Methyl Orange under ultraviolet light irradiation [7]. The photocatalytic activity of α-Mn₂O₃ particles were investigated for photodegradation of the Remazol Red B dye, using a multilamp photo reactor [8]. M.

* To whom all correspondence should be sent:
E-mail: zaharieva@ic.bas.bg

Pudukudy and et al. [9] are shown that the Mn₂O₃ microstructures have a moderate photocatalytic efficiency for the degradation of Methylene Blue dye under UV light irradiation [9]. In [10] the photocatalytic activity of graphene–Mn₂O₃ nanocomposite about photocatalytic degradation of eosin, methylene blue and rhodamine B was tested [10]. G. Panthi et al. [11] determined that the photocatalytic activity of the Mn₂O₃/TiO₂ nanofibers was higher than that of TiO₂ nanofibers for the photodegradation of Methylene Blue dye [11]. D. Mehandjiev et al. [12] were prepared and compared the catalytic activity of the ilmenite-type and spinel-type nickel-manganese oxide materials in the reactions of complete oxidation of hydrocarbons [12].

The present study deals with the synthesis, physicochemical characterization and comparative photocatalytic investigations of NiO_{0.8}ZnO_{0.2}/ZnO and NiMnO₃/Mn₂O₃ materials. For that the investigated samples were prepared by precipitation procedure using different starting materials – nitrates or chlorides and NaOH or NaHCO₃ as precipitating agent. The physicochemical properties of prepared materials were investigated by powder X-ray diffraction analysis (PXRD) and infrared (FT-IR) spectroscopy. The photocatalytic efficiency of synthesized NiO_{0.8}ZnO_{0.2}/ZnO and NiMnO₃/Mn₂O₃ samples was tested and compared in the reaction of degradation of Malachite Green dye in aqueous solution under UV illumination. The aim of this study was to investigate the effect of the type of precursors and precipitant on the photocatalytic activity of prepared NiO_{0.8}ZnO_{0.2}/ZnO and NiMnO₃/Mn₂O₃ materials.

EXPERIMENTAL

Synthesis and physicochemical characterization of the materials

The NiO_{0.8}ZnO_{0.2}/ZnO samples named as Sample 1 and Sample 2 were prepared by precipitation technique. The Sample 1 and Sample 2 was synthesized using aqueous solutions of 0.25M Ni(NO₃)₂•6H₂O (VWR Prolabo BDH chemicals); 0.25M Zn(NO₃)₂•6H₂O (Valerus Co.) (sample 1) and 0.25M NiCl₂•6H₂O (Valerus Co.); 0.25M ZnCl₂ (Valerus Co.), (sample 2) mixed in ratio 1:2. The aqueous solutions of used starting materials (nitrates or chlorides) were prepared separately and then mixed. The mixture was stirred for 15 minutes. After that the precipitant - aqueous solution of 0.75M NaOH (Valerus Co.) was added drop by drop in the mixture until pH reached 12 at

continuous stirring. The NiMnO₃/Mn₂O₃ materials labeled as Sample 3 and Sample 4 were synthesized by the similar precipitation procedure. Sample 3 was prepared from 0.25M Ni(NO₃)₂•6H₂O (VWR Prolabo BDH chemicals); 0.25M Mn(NO₃)₂•4H₂O (Alfa Aesar); 0.75M NaHCO₃ (Valerus Co.), while the sample 4 was prepared using 0.25M NiCl₂•6H₂O (Valerus Co.); 0.25M MnCl₂•4H₂O (Valerus Co.); 0.75M NaOH (Valerus Co.). The precipitants NaHCO₃ and NaOH were added in the mixtures of aqueous solutions of nitrate and chloride precursors until pH became 7 and 12 respectively. After precipitation the suspension was stirred for one hour. The precipitates was filtered and washed with distilled water several times to remove the traces of NaOH or NaHCO₃ respectively. The obtained materials were dried at 35 °C. The precipitates were calcined at 450 °C for 3 hours and 30 minutes in air atmosphere. The Powder X-ray diffraction analysis (PXRD) and FT-IR spectroscopy were used to study the phase composition and structure of the synthesized materials. The PXRD analysis of the samples was performed using Philips PW 1050 with Cu K_α-radiation. The phases were established using the ICDD database. FT-IR spectra of the samples were collected on a Fourier infrared spectrometer Bruker-Vector 22. The prepared materials using KBr tablets were investigated in the 400-4000 cm⁻¹ range.

Photocatalytic tests

The photocatalytic experiment of degradation of Malachite Green (MG) with initial concentration of aqueous solution of the dye - 5 ppm was carried out under UV-A illumination (18 W). The photocatalytic test was performed in semi-batch slurry reactor using 0.15 g photocatalyst and 150 ml of dye solution under constant stirring and air flowing. To reach adsorption-desorption equilibrium state the studied systems were left in the dark for about 30 min before switching on the UV irradiation for 2 hours. The powder was separated from the aliquot solution by centrifugation (4ml of the suspension). After that the change of absorbance during the photocatalytic tests was monitored by UV-Vis absorbance spectrophotometer UV-1600PC in the wavelength range from 200 to 800 nm ($\lambda_{\max} = 615$ nm).

The degree of dye degradation was calculated using the dependence: $(Co-C/Co) \times 100$, where Co and C were initial concentration of the dye solution before turning on the illumination and residual concentration of the dye solution after illumination for the selected time interval.

RESULTS AND DISCUSSION

On the Figures 1 and 2 are illustrated the results of the studied samples recorded by powder X-ray diffraction (PXRD) analysis. The presence of $\text{NiO}_{0.8}\text{ZnO}_{0.2}$ (PDF-750271) and ZnO (PDF 897130) phases are registered in the powder X-ray diffraction spectra of the Sample 1 and Sample 2. The PXRD patterns of the Sample 3 and Sample 4

show the existence of the NiMnO_3 (PDF-653695) and Mn_2O_3 (PDF-721427) phases. Figures 3 and 4 presented FT-IR spectra of synthesized $\text{NiO}_{0.8}\text{ZnO}_{0.2}/\text{ZnO}$ and $\text{NiMnO}_3/\text{Mn}_2\text{O}_3$ materials. The absorption bands at around 3440 and 3444 cm^{-1} can be ascribed to the hydroxyl groups bonded through hydrogen bonds. The peak at wave numbers about 1630 cm^{-1} corresponds to the adsorbed molecular H_2O [8].

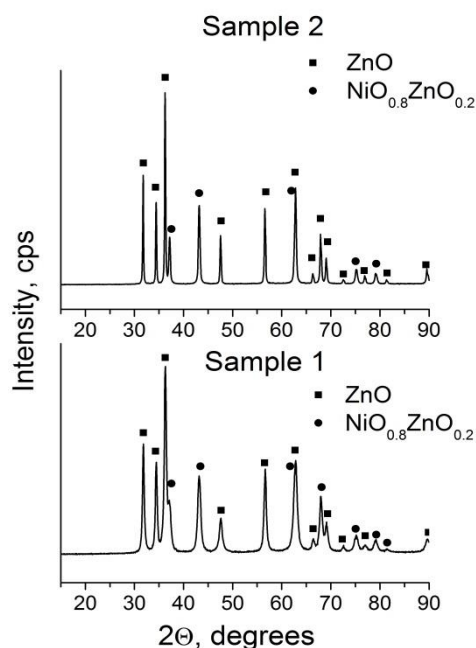


Fig. 1. PXRD patterns of $\text{NiO}_{0.8}\text{ZnO}_{0.2}/\text{ZnO}$ materials.

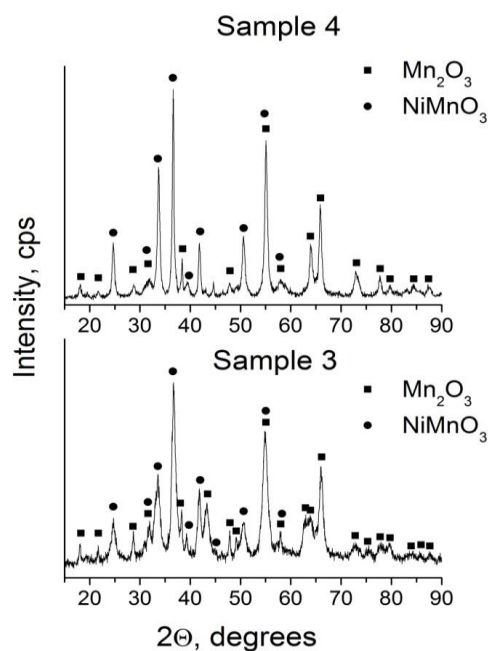


Fig. 2. PXRD patterns of $\text{NiMnO}_3/\text{Mn}_2\text{O}_3$ materials.

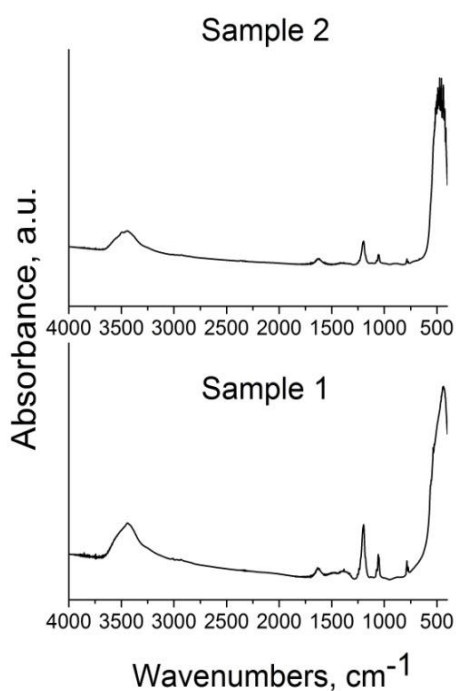


Fig. 3. FT-IR spectra of $\text{NiO}_{0.8}\text{ZnO}_{0.2}/\text{ZnO}$ materials.

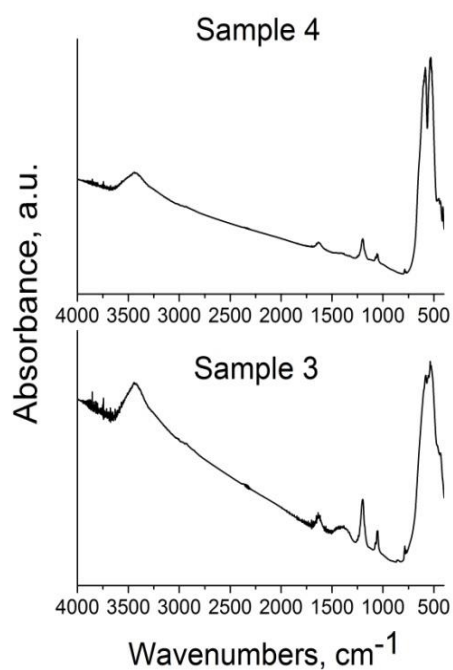


Fig. 4. FT-IR spectra of $\text{NiMnO}_3/\text{Mn}_2\text{O}_3$ materials.

The results indicate that catalysts are hydrated. In the region 400-800 cm⁻¹ are usually the vibration of metallic ion in the crystal lattice. Two main broad M-O bands are seen in the spectra of normal spinels. The highest peak at around 550 cm⁻¹ attributed to the stretching vibration of the metal ion at the tetrahedral site (ν(M-O)) [13]. In the infrared spectra of Sample 3 and 4 are seen the lowest band observed in the range 450-490 cm⁻¹ (NiMnO₃/Mn₂O₃) is octahedral metal ion stretching [13]. The appearance of the two bands in the range of 400-1000 cm⁻¹ shows the presence of mixed oxides. The peaks at about 1191, 1200 and 1051 cm⁻¹ could be assigned to the others admixtures in the studied samples [14-16]. The data obtained by FT-IR spectroscopy are in agreement with the results established by PXRD.

In presented study is discussed the degradation of Malachite Green dye as model pollutant under UV irradiation using synthesized NiO_{0.8}ZnO_{0.2}/ZnO and NiMnO₃/Mn₂O₃ as photocatalysts.

The equation (1) was used to calculate the adsorption capacities of investigated samples:

$$Q = \frac{(C_0 - C) \cdot V}{m} \tag{1}$$

where C₀ and C are the initial and after 30 minutes in the dark concentrations of the dye, V is the volume of the solution and m is the weight of the photocatalyst.

The adsorption capacities give the following order: Sample 4 (0.004 mg/g) < Sample 3 (0.041mg/g) < Sample 2 (0.044mg/g) < Sample 1 (0.051mg/g). As can be seen the NiO_{0.8}ZnO_{0.2}/ZnO material prepared by nitrate precursors shows the highest adsorption capacity in comparison with these of the others samples.

The degradation of Malachite Green dye with time of UV-A illumination is presented on Figure 5.

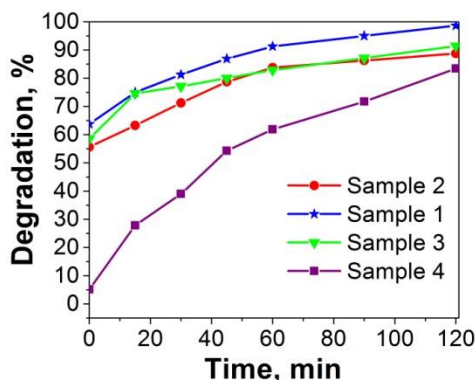


Fig. 5. Degree of degradation of MG dye as a function of the time of UV illumination.

The degree of degradation on Sample 1 (99%) and Sample 2 (89%) was higher in comparison with Sample 3 (91%) and Sample 4 (83%). The catalysts prepared from nitrates possessed better photocatalytic activity than those from chloride precursors. The highest photocatalytic efficiency about degradation of Malachite Green dye is determined for NiO_{0.8}ZnO_{0.2}/ZnO obtained by nitrate precursors.

The apparent rate constants of investigated photocatalysts (Figure 6) were calculated using logarithmic linear dependence $-\ln(C/C_0) = k \cdot t$. They followed the pseudo first-order kinetics. NiMnO₃/Mn₂O₃ samples have demonstrated almost equally rate constants values, no matter of used precursors.

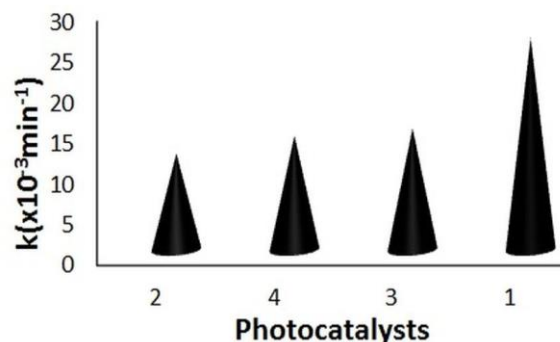


Fig. 6. Comparison data of apparent rate constants of NiO_{0.8}ZnO_{0.2}/ZnO and NiMnO₃/Mn₂O₃ photocatalysts in degradation of MG dye.

Unlike apparent rate constant of NiO_{0.8}ZnO_{0.2}/ZnO prepared by nitrates increased twice in comparison of this of NiO_{0.8}ZnO_{0.2}/ZnO obtained by chlorides.

CONCLUSION

The precipitation technique followed by calcination in air media at 450°C for 3 hours and 30 minutes was successfully used for the synthesis of NiMnO₃/Mn₂O₃ and NiO_{0.8}ZnO_{0.2}/ZnO samples. The NiMnO₃, Mn₂O₃ and NiO_{0.8}ZnO_{0.2}, ZnO phases were determined in the prepared materials using PXRD analysis and FT-IR spectroscopy. The impact of the different precursors on the photocatalytic properties of the prepared samples was found. The photocatalytic activity of NiO_{0.8}ZnO_{0.2}/ZnO and NiMnO₃/Mn₂O₃ materials prepared using nitrates as starting materials is higher than that of the samples synthesized by chlorides. The synthesized NiMnO₃/Mn₂O₃ and NiO_{0.8}ZnO_{0.2}/ZnO powdery materials exhibit high degree of degradation of the MG dye (83%-99%)

and can be potential photocatalysts for removal of MG from contaminated waters under UV irradiation.

Acknowledgements: The financial support of the National Science Fund, Ministry of Education and Sciences of Bulgaria by Contract DFNI- T-02 16 is appreciated.

REFERENCES

1. B. H. Hameed, M. I. El-Khaiary, *J. Hazard. Mater.*, **154**, 237 (2008).
2. E. S. Baeissa, *J. Alloy. Compd.*, **672**, 564 (2016).
3. R. Dridi, M. BenAmor, N. Mahdhi, A. Amlouk, K. Boubaker, M. Amlouk, *J. Non. Cryst. Solids*, **449**, 1 (2016).
4. V. Eskizeybek, F. Sari, H. Gulce, A. Gulce, A. Avci, *Appl. Catal. B*, **119–120**, 197 (2012).
5. L. Saikia, D. Bhuyan, M. Saikia, B. Malakar, D.K. Dutta, P. Sengupta, *Appl. Catal. A*, **490**, 42 (2015).
6. T. K. Ghorai, S. Pramanik, P. Pramanik, *Appl. Surf. Sci.*, **255**, 9026 (2009).
7. R. Talebi, *J. Mater. Sci.: Mater Electron*, **28**, 8316 (2017).
8. S. Gnanam, V. Rajendran, *J. Alloy. Compd.*, **550**, 463 (2013).
9. M. Pudukudy, Z. Yaakob, *J. Nanopart.*, **2016**, 7 pages (2016).
10. S. Chandra, P. Das, S. Bag, R. Bhar, P. Pramanik, *Mat. Sci. Engin. B*, **177**, 855 (2012).
11. G. Panthi, A. Yousef, N.A.M.Barakat, K. A. Khalil, S. Akhter, Y.R.Choi, H.Y.Kim, *Ceram. Internat.*, **39**, 2239 (2013).
12. D. Mehandjiev, E. Zhecheva, G. Ivanov, R. Ioncheva, *Appl. Catal. A*, **167**, 277 (1998).
13. H. Kumar, Manisha and P. Sangwan, *Internat. J. Chem. Chem. Engin.*, **3**, 155 (2013).
14. D. Mehandjiev, A. Naydenov, G. Ivanov, *Appl. Catal. A*, **206**, 13 (2001).
15. F. Kovanda, T. Grygar, V. Dorničák, *Solid State Sci.*, **5**, 1019 (2003).
16. R. Y. Hong, J. H. Li, L.L. Chen, D.Q. Liu, H.Z. Li, Y. Zheng, J. Ding, *Powd. Technol.*, **189**, 426 (2009).

ПОЛУЧАВАНЕ И СРАВНИТЕЛНО ФОТОКАТАЛИТИЧНО ИЗСЛЕДВАНЕ НА NiMnO₃/Mn₂O₃ И NiO_{0.8}ZnO_{0.2}/ZnO МАТЕРИАЛИ ЗА ПРЕМАХВАНЕ НА МАЛАХИТОВО ЗЕЛЕНО БАГРИЛО ОТ ВОДЕН РАЗТВОР

К. Л. Захариева^{1*}, К. И. Миленова¹, С. В. Василев², С. С. Димова³, И. Д. Стамболова⁴, В. Н. Блъсков⁴

¹Институт по катализ, Българска академия на науките, ул. „Акад. Г. Бончев“, бл. 11, 1113 София, България

²Институт по електрохимия и енергийни системи, Българска академия на науките, ул. „Акад. Г. Бончев“, бл. 10, 1113 София, България

³Институт по полимери, Българска академия на науките, ул. „Акад. Г. Бончев“, бл. 103А, 1113 София, България

⁴Институт по обща и неорганична химия, Българска академия на науките, ул. „Акад. Г. Бончев“, бл. 11, 1113 София, България

Постъпила на 14 март 2017 г.; Коририрана на 16 април 2017 г.

(Резюме)

NiMnO₃/Mn₂O₃ и NiO_{0.8}ZnO_{0.2}/ZnO материали бяха синтезирани чрез утаяване (използвайки различни прекурсори – нитрати или хлориди и натриев хидроксид или натриев хидрогенкарбонат като утаител) последвано от наляване при 450°C. Съществуването на NiMnO₃, Mn₂O₃ и NiO_{0.8}ZnO_{0.2}, ZnO фази беше установено в изследваните проби посредством рентгенофазов анализ и инфрачервена спектроскопия с фурие трансформация. Фотокаталитичната активност на получените NiMnO₃/Mn₂O₃ и NiO_{0.8}ZnO_{0.2}/ZnO проби беше тествана и сравнена в разграждането на Малахитово Зелено багрило (МЗ) като моделен замърсител във воден разтвор под действието на УВ облъчване. Фотокаталитичните тестове установиха, че степента на разграждане на Малахитово Зелено багрило след 120 минути с NiO_{0.8}ZnO_{0.2}/ZnO и NiMnO₃/Mn₂O₃ проби (99% и 91%) синтезирани използвайки нитрати като изходни материали е по-висока сравнена с тази при материалите получени от хлориди (89% и 83%). Резултатите показват, че синтезираните NiO_{0.8}ZnO_{0.2}/ZnO и NiMnO₃/Mn₂O₃ материали в това изследване са обещаващи фотокатализатори за премахване на Малахитово Зелено багрило като моделен замърсител във воден разтвор под действието на УВ светлина.

Comparison of photocatalytic behaviour under UV-light of PdO-CeO₂/Al₂O₃ and PdO-CeO₂/ZSM5 for degradation of organic dyes

K. I. Milenova^{1*}, I. A. Avramova², P. M. Nikolov³

¹ Institute of Catalysis, Bulgarian Academy of Sciences, Acad. G. Bonchev St., bl. 11, 1113 Sofia, Bulgaria

² Institute of General and Inorganic Chemistry, Bulgarian Academy of Sciences, Acad. G. Bonchev St., bl. 11, 1113 Sofia, Bulgaria

³ University of Chemical Technology and Metallurgy, 8 Kl. Ohridski, 1756 Sofia, Bulgaria

Received March 14, 2017; Revised April 21, 2017

Dedicated to Acad. Ivan Juchnovski on the occasion of his 80th birthday

PdO-CeO₂/Al₂O₃ and PdO-CeO₂/ZSM5 powder samples were prepared by impregnation and applied for photodegradation of aqueous solution of Malachite Green (MG) and Methyl Orange (MO) dyes under UV light. Physicochemical characterization of the samples was done by the following methods - AAA, BET, XRD, SEM and XPS. The palladium and cerium content in both investigated photocatalysts is found to be around 4.3 and 3 wt. %, the specific surface area for PdO-CeO₂/Al₂O₃ is 133 m²/g while this one for PdO-CeO₂/ZSM5 samples is 188 m²/g. The apparent rate constants of investigated dyes were in the following order: MO, PdO-CeO/Al₂O₃ (21.0 x10⁻³min⁻¹) > MG, PdO-CeO/Al₂O₃ (13.9 x10⁻³min⁻¹) > MO, PdO-CeO/ZSM5 (6.6 x10⁻³min⁻¹) > MG, PdO-CeO/ZSM5 (5.8 x10⁻³min⁻¹).

Key words: CeO₂, PdO, photocatalysis, dyes, waste waters.

INTRODUCTION

In textile industries, dyes are heavily used for coloring. Dye effluents discharged into waters may cause detrimental effects of the environment and as consequence to the human health. Most desired way to reduce pollution of waters is using clean technology such as photocatalytic treatment [1]. Heterogeneous photocatalysis has been considered as an inexpensive and efficient [2] way for the degradation of toxic organic compounds [3]. Recently there is an increase in the interest to semiconductor oxide photocatalysts due to their ability to convert photon energy into chemical energy [4].

It is urgent to create new catalysts, developing synergistic effect between the carrier and supported semiconductor oxides. It is aiming improvement of photocatalytic performance through optimization of processes of charge carrier transfer on semiconductor surfaces [5].

Mesoporous γ -Al₂O₃ support is reported as an electron acceptor with high surface area and ultraviolet-light-response ability [6]. Great attention of researchers have attracted to the supported noble metal catalysts, which may increase catalytic activity by suppressing the recombination of photoinduced carriers [7, 8].

Cerium together with its oxide is the most

intriguing rare earth element and can be photo excited by absorbing photo energy [9]. Band gap of CeO₂ is 3.2 eV. The combinations with other oxides will lower the band gap and increase its reactivity [2]. The use of rare earth oxides has been described as a good opportunity for stabilization of the support and the active phase on it. In that respect, CeO₂ is an excellent choice to stabilize PdO [10].

PdO/CeO₂-Al₂O₃ and Pd/CeO₂/Al₂O₃ catalysts were tested for methane combustion and Water-Gas-Shift Reaction [7, 11]. Yuliati et al. found that cerium oxide supported on SiO₂ or Al₂O₃, promote photocatalytic non-oxidative direct methane coupling [9]. Photocatalysts containing Al₂O₃ modified with rare earth and noble metal oxides have been studied for degradation of pesticides [12].

Cr/ZSM-5 and CeO₂/MCM-48 were investigated for the photocatalytic oxidation of propane and Acid Orange 7 accordingly [13, 14].

Photodegradation of oxalic acids and bisphenol A on Fe₃O₄/SiO₂/CeO₂ and Al₂O₃ - Fe₃O₄ catalysts have been investigated in [15, 16].

In the present work we compare the catalytic behaviour of mixed PdO-CeO₂ oxides supported on Al₂O₃ and ZSM5 carriers. The process of photodegradation under UV-light in aqueous solutions of two different dyes (Malachite Green and Methyl Orange) were also investigated and discussed.

* To whom all correspondence should be sent:
E-mail: kmilenova@ic.bas.bg

EXPERIMENTAL

Sample preparation procedure

Carrier materials of both catalysts – H-ZSM-5 and γ -Al₂O₃ (Rhône Poulenc) were dried overnight at 120 °C, dispersed in water and impregnated for 16 h in prepared aqueous solution containing 5% Ce(IV) obtained from source (NH₄)₂Ce(NO₃)₆ and 1% Pd(II) obtained from source Pd(NH₃)₂Cl₂. The mixture was left until decolorization occurred. Then the zeolite and silica were filtrated, dried and calcined at 600 °C for 6 h [17].

Sample characterization

The X-ray diffraction (XRD) analysis was carried out on a Bruker-AXS, D8 Advance using CuK α radiation within a 2 θ angle of diffraction interval of 10 ÷ 80 degrees.

PYE UNICAM SP 1950 spectrometer was used for determination of palladium content, after extraction with HCl by AAA method. Titrimetrical method was applied for determination of cerium loading.

The specific surface area was established by the BET method using low temperature (77 K) nitrogen adsorption. JSM – 5510 JEOL scanning electron microscope was used for SEM investigations.

XPS investigations were carried out by means of a VG ESCALAB Mk II spectrometer using an Al K α excitation source (1486.6 eV) with a total instrumental resolution of ~1 eV, under base pressure of 1 \times 10⁻⁸ Pa. The C1s, O1s, Pd 3d, Ce3d, Al2p and Si2p photoelectron lines were recorded. The charging effects were corrected by using the C1s peak as reference at 285eV. The atomic concentrations of the constituent elements have been calculated using a peak area and Scofield's photoionization cross-sections.

The photocatalytic activity of PdO-CeO₂/Al₂O₃ and PdO-CeO₂/ZSM5 for the oxidative degradation of 5 ppm aqueous solution of Malachite Green or Methyl Orange dyes was evaluated. The 0.15g photocatalyst samples in 150 ml of dye solution were investigated in a semi-batch reactor under constant stirring, at room temperature. In order to obtain adsorption-desorption characteristics 30 minutes tests were carried out in the dark first, followed by 120 minutes period of UV illumination (power 18 W, λ_{\max} = 365 nm). The separation of the powder from the suspension was carried out by centrifugation before the UV-Vis spectrophotometrical measurements (UV-1600PC

Spectrophotometer). The degree of dye degradation was calculated using the formula:

$$\text{Degradation} = \frac{(C_0 - C)}{C_0} 100\%$$

where C₀ and C were initial concentration before turning on the illumination and residual concentration of the dye solution after illumination for selected time interval. The adsorption capacities of samples after 30 minutes dark period were determined by the equation:

$$Q = \frac{(C_0 - C)V}{m}$$

where C₀ and C are the initial and after half an hour in the dark concentrations of the dye, V is the volume of the solution and m is the weight of the photocatalyst.

RESULTS AND DISCUSSION

The palladium and cerium contents in both investigated samples were evaluated as about 4.3 wt. % and 3.0 wt. %, respectively. The specific surface area of PdO-CeO₂/Al₂O₃ sample is lower (133 m²/g) than this of PdO-CeO₂/ZSM5 sample (188 m²/g) [17]. The obtained XRD patterns of PdO-CeO₂/ZSM5 and PdO-CeO₂/Al₂O₃ photocatalysts are shown in Figure 1a and 1b respectively. In this Figure 1 it is seen that palladium exist mainly as PdO (PDF-75-584) and cerium as CeO₂ (PDF-34-0394). Simultaneously on the diffractograms are present some low temperature form of alumina: γ -Al₂O₃ (PDF-50-0741) and MFI structure [17].

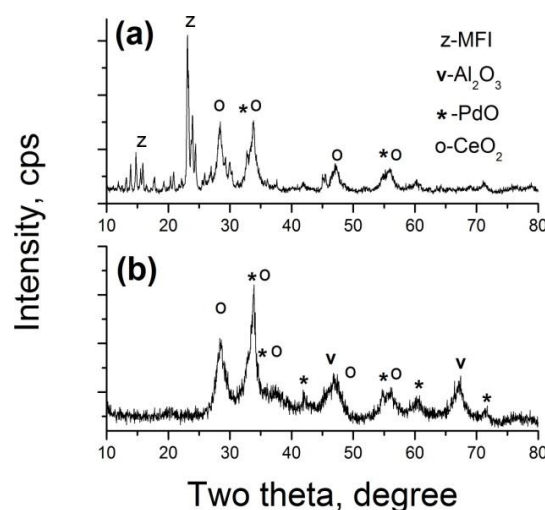


Fig. 1. XRD patterns of: (a) PdO-CeO₂/ZSM5, (b) PdO-CeO₂/Al₂O₃.

The morphology of both catalyst samples was studied by SEM. Figures 2 and 3 represent SEM images of PdO-CeO₂/ZSM5 and PdO-CeO₂/Al₂O₃ samples at magnification x 5,000 μm. The SEM image of PdO-CeO₂/ZSM5 shows porous structure. In the picture are visible round particles of irregular shape with different sizes around (0.3÷1.5 μm), some of them united in aggregates bigger than 5μm. The SEM image of PdO-CeO₂/Al₂O₃ shows big aggregates with cracks on them. Some particles and flakes in the range of 0.1÷2.5μm were alighted on the aggregates. From the SEM pictures of the both samples we can conclude that the sintering processes flow more intense in PdO-CeO₂/Al₂O₃ sample comparing with PdO-CeO₂/ZSM5 one.

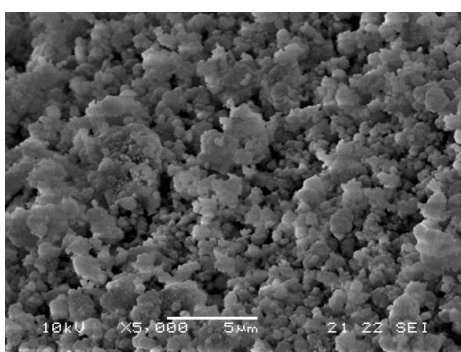


Fig. 2. SEM picture of PdO-CeO₂/ZSM5 sample.

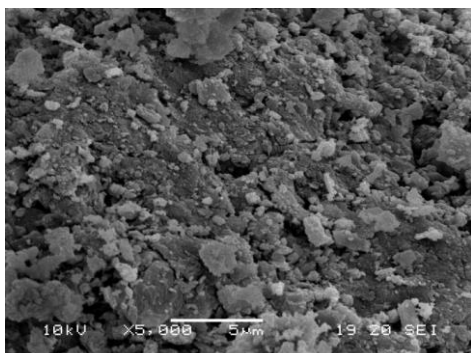


Fig. 3. SEM picture of PdO-CeO₂/Al₂O₃ sample.

The surface composition and the oxidation states of the constituent element in the studied photocatalysts were proved by XPS.

The concentrations of the elements on the surface of the both catalysts are shown in Table 1.

The O1s, Ce3d and Pd3d photoelectron spectra of PdO-CeO₂/Al₂O₃ and PdO-CeO₂/ZSM5 are presented in Fig. 4. In the O1s photoelectron spectrum of PdO-CeO₂/ZSM5 photocatalyst is distinguished, low binding energy wide shoulder with a maximum at around 529.4 eV, a main peak at 532.5 eV and additionally to the main and low binding energy peaks a peak at ~534 eV is observed.

Table 1. Concentrations of the elements (at.%) on the surface of the photocatalysts.

Sample	C	O	Ce	Si	Al	Pd
PdO-CeO ₂ /ZSM5	13.30	56.57	2.27	20.59	1.61	5.65
PdO-CeO ₂ /Al ₂ O ₃	20.67	46.88	0.92	-	29.40	2.13

The first two mentioned peaks are associated to CeO₂ and SiO₂, respectively [18,19,20]. The higher binding energy peak is due to the absorbed water species on the catalyst surface. In region of O1s photoelectron line for the second studied catalyst PdO-CeO₂/Al₂O₃, we detect (only) one peak having binding energy around 531.4 eV, typical for the Al₂O₃. The Pd3d photoelectron spectra are characteristic of presence of PdO on the catalysts surfaces. The visible differences are observed for the recorded Ce3d spectra. It is well known that the Ce3d region has well separated spin-orbit components (Δ=18.6 eV). After deconvolution of the Ce3d complex structure ten peaks are distinguishable that are referenced to the 3d_{3/2} and 3d_{5/2} spin orbital splitting and are signed according the Burroughs et al. [21] to the existence of both Ce³⁺ and Ce⁴⁺ states. The amount of Ce(IV) in the studied catalysts samples could be evaluated as a percentage of the area of the u^{III} peak at 916.8 eV to the total Ce3d area. Thus, the percentage of the u^{III} peak with respect to the total Ce3d peak area varies from 0 to 14%, when the Ce(IV) percentage to total amount of Ce varies from 0 to 100%. The calculated area ratio are 11.57% for PdO-CeO₂/ZSM5 and 5.53% for PdO-CeO₂/Al₂O₃, respectively.

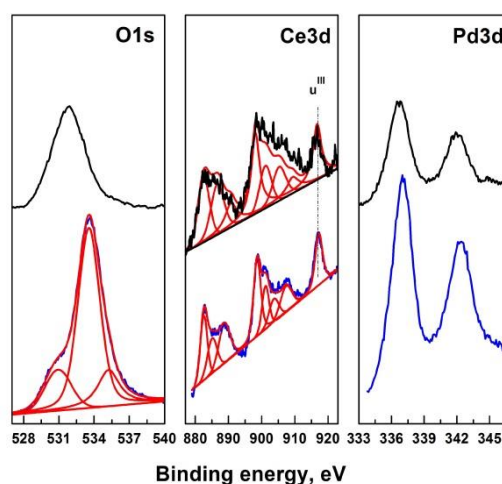


Fig. 4. O1s, Ce3d and Pd3d spectra of PdO-CeO₂/ZSM5 (blue line) and PdO-CeO₂/Al₂O₃ (black line) samples.

The photocatalytic performances of PdO-CeO₂/Al₂O₃ and PdO-CeO₂/ZSM5 samples tested for degradation of two dyes-Malachite Green and Methyl Orange is presented in Fig. 5. The degree of dye degradation of investigated dyes on the two studied photocatalytic systems decrease in the following order: MO, PdO-CeO/Al₂O₃ (97%) > MG, PdO-CeO/Al₂O₃ (90%) > MO, PdO-CeO/ZSM5 (73%) > MG, PdO-CeO/ZSM5 (68%).

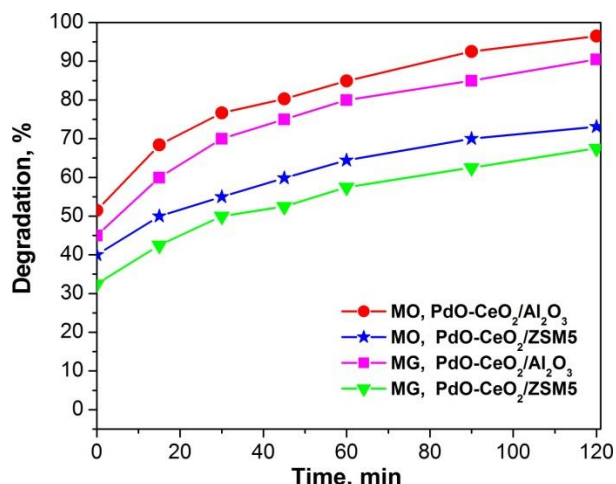


Fig. 5. Photocatalytic degradation of MO ($\lambda_{\max} = 464$ nm) and MG ($\lambda_{\max} = 615$ nm) dyes on investigated catalysts.

In Table 2 are presented the adsorption capacities and apparent rate constants of investigated photocatalytic systems. It is obvious the existed correlation between the adsorption capacities, degree of degradation and apparent rate constants for investigated dye solutions on PdO-CeO₂/Al₂O₃ and PdO-CeO₂/ZSM5 photocatalysts.

Table 2. Calculated adsorption capacities and apparent rate constants of investigated photocatalytic systems.

Sample	Adsorption capacity, mg/g	k (10^{-3} min^{-1})
MG, PdO-CeO/ZSM5	0.065	5.8
MO, PdO-CeO/ZSM5	0.080	6.6
MG, PdO-CeO/Al ₂ O ₃	0.090	13.9
MO, PdO-CeO/Al ₂ O ₃	0.103	21.0

The apparent rate constants (pseudo first order kinetics) have been calculated using logarithmic linear dependence of the concentrations ratio on the time:

$$-\ln\left(\frac{C}{C_0}\right) = k.t$$

and the results are shown on Fig. 6. PdO-CeO₂/Al₂O₃ sample exhibits better photocatalytic

properties in comparison with PdO-CeO₂/ZSM5 one. Existing synergism between supported active phases PdO, CeO₂ and the carrier Al₂O₃ is a possible explanation of registered higher photocatalytic activity. The role of γ -Al₂O₃ support is important, because of its unique surface properties - Brønsted and Lewis acid and base sites [22] which can promote photocatalytic activity of supported materials [23, 24].

The presence of particles of PdO as the photoelectron trapping centers reduces the e⁻/h⁺ pair recombination rate and increases the lifetime of charge carrier [25, 26]. In article [27] was described mechanism of photodegradation of MO on CeO₂ under UV light irradiation. It was discovered that low-coordinate surface cerium cations played important role in the photocatalytic reaction. From the XPS results we can conclude that the more Ce³⁺ states exist on the surface of PdO-CeO₂/Al₂O₃ catalysts which explains its higher photocatalytic activity. We can suppose that during photocatalytic reaction, electrons in the valence band of Ce₂O₃ are excited. At the same time, the transfer of electrons from CeO₂ to Ce₂O₃ occurs, also. Then the electrons react with the adsorbed oxygen molecules to form superoxide radicals, which are responsible for the degradation/oxidation of organic pollutants [28].

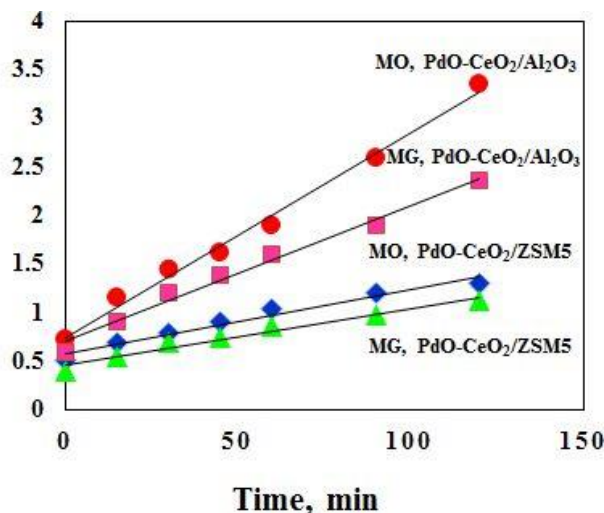


Fig.6. Dependence of $-\ln\left(\frac{C}{C_0}\right)$ versus illumination time on investigated photocatalysts.

CONCLUSION

Impregnation method was used for synthesis of PdO-CeO₂/Al₂O₃ and PdO-CeO₂/ZSM5 powders. Photocatalytic behaviour of the catalysts was

compared for degradation of two organic dyes under UV-light. As model pollutants were used textile dyes: Malachite Green and Methyl Orange.

The XRD and XPS confirmed existence of PdO and CeO₂. It was established correlation between the adsorption capacities, degree of degradation and apparent rate constants of investigated dyes on PdO-CeO₂/Al₂O₃ and PdO-CeO₂/ZSM5 samples. The higher photocatalytic activity was shown by PdO-CeO₂/Al₂O₃ sample in comparison with PdO-CeO₂/ZSM5. The possible reasons were synergism between mixed oxides PdO-CeO₂ and the support Al₂O₃ and existence of higher amount of Ce³⁺ states on the surface of PdO-CeO₂/Al₂O₃ catalysts.

Acknowledgements: The financial support of the National Science Fund, Ministry of Education and Sciences of Bulgaria by Contracts DFNI- T-02 16 is gratefully acknowledged.

REFERENCES

1. R. Saravanan, N. Karthikeyan, S. Govindan, V. Narayanan, A. Stephen, *Adv. Mater. Res.*, **584**, 381 (2012).
2. L. Zou, X. Shen, Q. Wang, Z. Wang, X. Yang, M. Jing, *J. Mater. Res.*, **30**, 2763 (2015).
3. C. Hu, T. Peng, X. Hu, Y. Nie, X. Zhou, J. Qu, H. He, *J. Am. Chem. Soc.*, **132**, 857 (2010).
4. A. Pradhan, S. Martha, S. Mahanta, K.M. Parida, *Int. J. Hydrogen Energ.*, **36**, 12753 (2011).
5. Y. Zhang, N. Zhang, Zi-R. Tang, Yi-J. Xu, *ACS Sustainable Chem. Eng.*, **1**, 1258 (2013).
6. F. Li, S. Liu, Y. Xue, X. Wang, Y. Hao, J. Zhao, R. Liu, D. Zhao, *Chem. Eur. J.*, **21**, 10149 (2015).
7. X. Liu, J. Liu, F. Geng, Z. Li, P. Li, W. Gong, *Front. Chem. Sci. Eng.*, **6**, 34 (2012).
8. X. Fu, W. Tang, L. Ji, S. Chen, *Chem. Eng. J.*, **180**, 170 (2012).
9. L. Yuliati, T. Hamajima, T. Hattori, H. Yoshida, *Chem. Commun.*, **38**, 4824 (2005).
10. L. M. T. Simplicio, S. T. Brandao, D. Domingos, F. Bozon-Verduraz, E. A. Sales, *Appl. Catal. Gen.*, **360**, 2 (2009).
11. N. Wieder, M. Cargnello, K. Bakhmutsky, T. Montini, P. Fornasiero, R. Gorte, *J. Phys. Chem. C*, **115**, 915 (2011).
12. A. Barrera, F. Tzompantzi, J. M. Padilla, J. E. Casillas, G. Jácome-Acatitla, M. E. Cano, R. Gómez, *Appl. Catal. B. Environ.*, **144**, 362 (2014).
13. H. Yamashita, S. Ohshiro, K. Kida, K. Yoshizawa, M. Anpo, *Res. Chem. Intermed.*, **29**, 881 (2003).
14. P. Ji, J. Zhang, F. Chen, M. Anpo, *J. Phys. Chem. C*, **112**, 17809 (2008).
15. D. Channei, B. Inceesungvorn, N. Wetchakun, S. Phanichphant, *Int. Sci. J. Environ. Sci.*, **3**, 22 (2014).
16. F. Li, X. Li, C. Liu, T. Liu, *J. Hazard. Mater.*, **149**, 199 (2007).
17. P. Nikolov, K. Genov, B. Ivanov, K. Milenova, I. Avramova, *C. R. Acad. Bulg. Sci.*, **62**, 1515 (2009).
18. F. Pagliuca, P. Luches, S. Valeri, *Surf. Sci.*, **607**, 164 (2013).
19. B. Hirschauer, M. Göthelid, E. Janin, H. Lu, U.O. Karlsson, *Appl. Surf. Sci.*, **148**, 164 (1999).
20. C. G. Kim, *J. Vac. Sci. Technol. B*, **18**, 2650 (2000).
21. P. Burroughs, A. Hamnett, A. F. Orchard, G. Thornton, *J. Chem. Soc., Dalton Trans.*, **17**, 1686 (1976).
22. W. Leow, W. H. Ng, T. Peng, X. Liu, B. Li, W. Shi, Y. Lum, X. Wang, X. Lang, S. Li, N. Mathews, J. Ager, T. Sum, H. Hirao, X. Chen, *J. Am. Chem. Soc.*, **139**, 269 (2017).
23. F. Tzompantzi, Y. Pina, A. Mantilla, O. Aguilar-Martínez, F. Galindo-Hernández, X. Bokhimi, A. Barrera, *Catal. Today*, **220-222**, 49 (2014).
24. C.-Y. Kuo, *React. Kinet. Catal. Lett.*, **92**, 337 (2007).
25. X. Wang, J. Zhang, W. Sun, W. Yang, J. Cao, Q. Li, Y. Peng, J. K. Shang, *Chem. Eng. J.*, **264**, 437 (2015).
26. A. Barrera, F. Tzompantzi, V. Lara, R. Gómez, *J. Photochem. Photobiol. Chem.*, **227**, 45 (2012).
27. W. Lei, T. Zhang, L. Gu, P. Liu, J. A. Rodriguez, G. Liu, M. Liu, *ACS Catal.*, **5**, 4385 (2015).
28. M. M. Khan, et al., *Ind. Eng. Chem. Res.*, **53**, 9754 (2014).

СРАВНЕНИЕ НА ФОТОКАТАЛИТИЧНОТО ПОВЕДЕНИЕТО ПОД УВ-СВЕТЛИНА НА PdO-CeO₂/Al₂O₃ И PdO-CeO₂/ZSM5 ЗА РАЗГРАЖДАНЕ НА ОРГАНИЧНИ БАГРИЛА

К. И. Миленова^{1*}, И. А. Аврамова², П. М. Николов³

¹ *Институт по катализ, Българска академия на науките, ул. „Акад. Г. Бончев“, бл. 11, 1113 София, България*

² *Институт по обща и неорганична химия, Българска академия на науките, ул. „Акад. Г. Бончев“, бл. 11, 1113 София, България*

³ *Химикотехнологичен и металургичен университет, бул. „Кл. Охридски“ 8, 1756 София, България*

Постъпила на 14 март 2017 г.; Коригирана на 21 април 2017 г.

(Резюме)

Прахообразни образци от PdO-CeO₂/Al₂O₃ и PdO-CeO₂/ZSM5 бяха приготвени чрез метода на импрегниране и приложени за фоторазлагането на водни разтвори на багрила от Малахитово Зелено и Метил Оранжево под УВ светлина. За физикохимичното охарактеризиране на пробите бяха използвани следните методи - ААА, ВЕТ, XRD, SEM и XPS. Установено е, че съдържанието на паладий и церий в двата изследвани фотокатализатора е около 4.3 и 3 тегл. %, специфичната повърхност за PdO-CeO₂/Al₂O₃ е 133 m²/g докато тази при образец PdO-CeO₂/ZSM5 е 188 m²/g. Скоростните константи на изследваните багрила са в следния ред: МО, PdO-CeO/Al₂O₃ (21.0 x10⁻³min⁻¹) > МГ, PdO-CeO/Al₂O₃ (13.9 x10⁻³min⁻¹) > МО, PdO-CeO/ZSM5 (6.6 x10⁻³min⁻¹) > МГ, PdO-CeO/ZSM5 (5.8 x10⁻³min⁻¹).

Activated carbon from waste biomass as host matrix of binary copper and manganese oxide catalysts for methanol decomposition

T. S. Tsoncheva^{1*}, G. S. Issa¹, R. N. Ivanova¹, M. D. Dimitrov¹, I. P. Spassova², D. G. Kovatcheva², B. G. Tsyntsarski¹, N. V. Petrov¹

¹ Institute of Organic Chemistry with Centre of Phytochemistry, Bulgarian Academy of Sciences, 1113 Sofia, Bulgaria,

² Institute of General and Inorganic Chemistry, Bulgarian Academy of Sciences, 1113 Sofia, Bulgaria

Received, 11 April 2017; Revised, 25 April 2017

Dedicated to Acad. Ivan Juchnovski on the occasion of his 80th birthday

Agriculture wastes, such as peach and apricot stones and grape seeds, were used for the preparation of high quality activated carbons. Thus obtained carbon materials were modified by incipient wetness impregnation with methanol solution of copper and manganese nitrates in different proportion, followed by precursor decomposition in nitrogen. The parent and modified materials were characterized by different physicochemical techniques such as XRD, Nitrogen physisorption, FTIR, UV-Vis, TPR with hydrogen and Boehm method. The catalytic properties of the obtained composites were tested in methanol decomposition with a potential as hydrogen carrier. It was demonstrated that the carbon host matrix promoted the formation of complex mixture of copper and manganese species in different oxidative states. The proportion of various components and the related with them catalytic activity could be easily controlled by Cu/Mn ratio as well as by the texture and surface properties of the activated carbon support, the latter being easily tuned by the agriculture waste precursor used.

Key words: activated carbons from biomass; copper-manganese modifications; methanol decomposition

INTRODUCTION

Nowadays, the greenhouse effect and the ozone layer depletion have considered as the main risks from the transport, industrial and human activity and they demand strong monitoring and control of air emissions [1 and refs therein]. Nevertheless the increasing need of energy and the fluctuation in the energy prices provides the development of new generation of energy devices, such as fuel cells, that are efficient and have minimal environmental impact [2]. Methanol is considered as the most attractive source and carrier of hydrogen for fuel cells supply due to its 5-7 times higher energy density than compressed hydrogen, low sulfur content and availability. It can be produced from variety sources including fossil fuels, agriculture and municipal waste as well as by recycling of carbon dioxide [3-6]. Methanol decomposition has been demonstrated as one of the simplest procedures for hydrogen release but the synthesis of low cost and effective catalysts is still a matter of challenge, especially in case of the application for portable and mobile fuel processors [7]. Copper manganese spinel oxides have been found to be superior catalysts for number of catalytic reactions, including methanol steam reforming [8-10 and ref.

therein]. Morales et al. [11] considered that small quantity of copper prevented manganese oxide crystallization, while segregation of CuO was detected in the excess of copper. The high activity of $\text{Cu}_x\text{Mn}_{3-x}\text{O}_4$ phase was generally attributed to the presence of two Jahn-Teller ions, Mn^{3+} and Cu^{2+} . The solid state redox exchange between them provides the existence of copper and manganese ions in different oxidative state [2]. In our previous study we demonstrated that activated carbon could be suitable host matrix for the stabilization of transition metal particles in the nanoscale due to its high surface area and well developed porous structure [12-14]. The most attractive feature of the activated carbons (AC) is related to the decrease of their price using renewable and inexpensive sources such as biomass and industrial wastes [15]. We demonstrated that the active phase in monocomponent copper [16] and manganese [17] AC modifications represents a complex mixture of metal and/or metal oxides due to the reduction activity of carbon support during the preparation procedure. Nevertheless the state of manganese on activated carbon has been a question of intensive debates in the literature [18], and to the best of our knowledge, no data for the effect of AC on the formation of binary copper and manganese oxides has been published yet. This investigation is aimed

* To whom all correspondence should be sent:
E-mail: tsoncheva@orgchm.bas.bg

at the application of AC from different agriculture residues, such as peach and apricot stones and grape seeds, as catalyst support for $\text{Cu}_x\text{Mn}_{3-x}\text{O}_4$ ($x=1$ or 2) binary oxides for methanol decomposition. The effect of AC texture and surface characteristics on the formation of active phase was in the focus of the investigation. KIT-6 mesoporous silica was used as reference support.

EXPERIMENTAL

Materials

Apricot stones and grape seeds based activated carbons, denoted as ACA and ACG, respectively, were produced by hydrolysis at 1023 K for 1 h. This is a one step process involving pyrolysis of the precursor in the presence of steam and activation at the final temperature. Peach stones based activated carbon, denoted as ACP was produced by two-step process, including carbonization at 823 K for 1 h and subsequent activation of the carbonizate with water vapor at 1123 K for 45 min. Mesoporous silica KIT-6 was obtained by procedure described in [19]. The ACs and KIT-6 were modified with copper and manganese (Cu/Mn=1 or 2 mol ratio) by incipient wetness impregnation with methanol solution of the corresponding nitrate precursors. The nitrates decomposition was carried out in a flow of N_2 at 773 K for 2 h (5 K/min). Metal loading in all samples was 8 wt%. The samples were denoted as $x\text{Cu}(3-x)\text{Mn}/\text{S}$, where x was 1 or 2 mol ratio and S was the ACP, ACA, ACG or KIT-6 support.

Methods of characterization

The texture characteristics were determined by N_2 physisorption at 77 K by a Quantachrome NOVA 1200 apparatus. The N_2 adsorption-desorption isotherms were analyzed to evaluate the following parameters: specific surface areas (S_{BET}) was determined on the basis of BET equation; total pore volume (V_t) was estimated in accordance with the Gurvich rule at a relative pressure close to 0.99. The amount of various acidic oxygen-containing functional groups was determined by Boehm's method using aqueous solutions of NaHCO_3 , Na_2CO_3 , NaOH , and $\text{C}_2\text{H}_5\text{ONa}$ [21]. The amount of basic sites was determined with 0.05 N HCl [22]. The pH values were determined after boiling for 5 min in 100 ml H_2O , decantation and cooling of the solution to ambient temperature. Powder X-ray diffraction patterns were collected within the range of 5.3 to 80° on a Bruker D8 Advance

diffractometer with Cu K_α radiation and LynxEye detector. Mean crystallite size were determined by the Topas-4.2 software package using the fundamental parameters peak shape description including appropriate corrections for the instrumental broadening and diffractometer geometry. The UV-Vis spectra were recorded using a Jasco V-650 spectrophotometer, equipped with a diffuse reflectance unit. The FTIR spectra (KBr pellets) were recorded on a Bruker Vector 22 spectrometer with resolution 1 cm^{-1} using 64 scans. The TPR/TG (temperature-programmed reduction/thermo-gravimetric) analysis was performed with a Setaram TG92 instrument in a flow of 50 vol% H_2 in Ar ($100\text{ cm}^3\text{ min}^{-1}$) and heating rate of 5 K min^{-1} .

Catalytic tests

The catalytic tests were carried out in a flow type fixed bed reactor (0.055 g of catalyst). Methanol (1.57 kPa) was introduced into the reactor from a saturator, thermostated at 273 K using argon as a carrier gas ($50\text{ cm}^3\text{ min}^{-1}$). The catalysts were tested under conditions of a temperature-programmed regime within the range of 350–770 K with heating rate of 1 K min^{-1} . Before the catalytic test the samples were treated under Ar flow at 373 K for 1 h and methanol amount was registered using by-pass of the reactor. On-line gas chromatographic analyses were performed on HP apparatus equipped with flame ionization and thermo-conductivity detectors, on a PLOT Q column. Absolute calibration method and a carbon based material balance were used for the calculation of methanol conversion and the yields of various products. The product selectivity at selected temperature was calculated as $Y_i/X \cdot 100$, where Y_i was the yield of the i product (calculated as detected amount of i product/initial amount of methanol, before the introduction in the catalytic reactor) and X was the methanol conversion at this temperature.

RESULTS AND DISCUSSION

The temperature dependencies of methanol decomposition at 550-750 K (Fig. 1a) and the conversion at the final temperature (750 K) for various copper and manganese modifications are presented in Fig. 1. The carbon based materials exhibited catalytic activity just above 650-700 K, while it was registered at about 80-120 K lower temperature for their KIT-6 analogues (Fig. 1a).

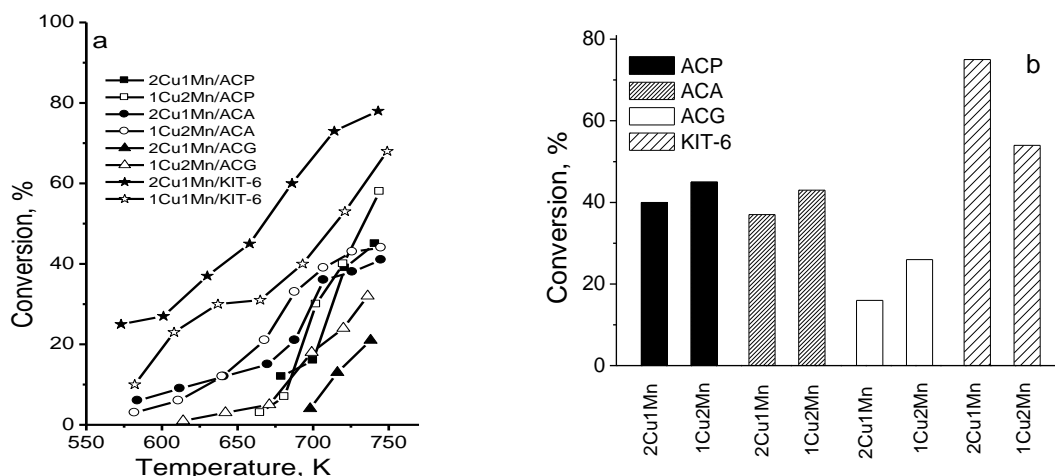


Fig. 1. Temperature dependencies of methanol decomposition (a) and conversion at 750 K (b) for various copper and manganese modifications.

The selectivity to CO, which formation is strongly related to the ability of the samples to release hydrogen from methanol, represented about 80 % at 750 K. Methane and CO₂ were also detected as by-products. On the base of the shift of the conversion curves with the temperature (Fig. 1a) and the conversion achieved at the final temperature (Fig. 1b) the samples with given composition Cu_xMn_(3-x)O₄ (x=1 or 2) could be arranged as follows: xCu(3-x)Mn/KIT-6 > xCu(3-x)Mn/ACP > xCu(3-x)Mn/ACA > xCu(3-x)Mn/ACG. A well defined tendency for a decrease in the catalytic activity with copper content increase was observed for all carbon modifications. Note that this trend was the opposite for the silica based materials. Obviously, a strong effect of the support on the formation of the catalytic active phase could be expected. In order to understand this in detail, complex characterization of the samples by different physicochemical techniques was carried out.

Nitrogen physisorption isotherms (not shown) for the parent and modified activated carbons and KIT-6 were analyzed and the obtained characteristics are listed in Table 1. The parent AC materials characterized with mixed micro-mesoporous texture which ensured significantly high BET surface area. According to the increase in the BET surface area, pore volume and the relative part of mesopores (V_{mes}/V_{mic}) the carbon supports arranged in the following order ACG < ACA < ACP, which is similar to the increase in the catalytic activity of their modifications (see section 3.1). Note that the modification procedure decreased the BET surface area and pore volume and these effects were more pronounced for the

ACP and ACA based samples. This could be attributed to pore blocking due to the deposition of metal containing particles in them. The observed change in the V_{mes}/V_{mic} ratio after the modification suggests predominant location of metal species in the mesopores of ACP, while blocking of micropores in higher extent could be assumed for ACA. The significant increase in the V_{mes}/V_{mic} ratio combined with negligible and even absence of changes in the BET surface area for ACG modifications (Table 1) do not exclude structure collapse with the carbon support during the modification procedure as well as deposition of metal particles on the external surface. KIT-6 represented similar BET surface area and more than twice higher pore volume as compared to ACA due to the presence of high amount of mesopores. The decrease in the BET surface area and pore volume and the slight changes in the V_{mes}/V_{mic} ratio reveal almost random distribution of metal particles into the micro- and mesopores of the silica support. Taking into account the highest activity of KIT-6 modifications (Fig. 1) one could be assumed that the texture characteristics of the support seem to be important, but not the dominant factor for the formation of active phase.

FTIR spectra of parent and modified activated carbons are presented in Fig. 2. The bands at around 3028 cm⁻¹ were attributed to C-H stretching vibrations in CH₃ groups. The band at about 1715 cm⁻¹ corresponded to C=O stretching vibrations in lactonic, carbonyl or anhydride groups. The bands at 1535 and 1036 cm⁻¹ were assigned to ring vibration in aromatic skeleton, typical of carbon materials [23].

Table 1. Nitrogen physisorption data for parent and modified activated carbons and KIT-6 materials: (S_{BET} -BET surface area, S_{mi} - surface area of micropores, V_t -total pore volume, V_{mi} -micropores pore volume, D_{av} -average pore diameter).

Sample	SBET, m ² /g	S _{mi} , m ² /g	V _t , cm ³ /g	V _{mi} cm ³ /g	D _{av} nm	ΔS %	ΔV %	V _{mes} / V _{mic}
ACP	1258	1116	0.61	0.45	1.94			0.35
2Cu1Mn/ACP	1006	956	0.49	0.40	1.97	20	20	0.22
1Cu2Mn/ACP	1080	1024	0.53	0.43	1.97	14	13	0.23
ACA	921	874	0.46	0.37	2.0			0.24
2Cu1Mn/ACA	743	625	0.38	0.28	2.0	19	17	0.36
1Cu2Mn/ACA	794	676	0.39	0.28	1.9	14	15	0.39
ACG	603	577	0.28	0.24	1.9			0.17
2Cu1Mn/ACG	603	522	0.25	0.18	2.0	0	10	0.39
1Cu2Mn/ACG	548	456	0.26	0.17	1.9	9	7	0.53
KIT-6	872	278	1.23	0.14	8.1			7.78
2Cu1Mn/KIT-6	748	220	1.09	0.11	5.8	14	11	8.91
1Cu2Mn/KIT-6	722	189	1.05	0.09	5.8	17	18	10.67

The band at c.a. 1094 cm⁻¹ could be due to vibrations in ether C-O-C groups. The broad band in the 800-600 cm⁻¹ region could be assigned to C=C bending vibrations in aromatic and non-aromatic structures. The change in the intensity and the position of the FTIR bands after the AC modification (Fig.2b) revealed interaction of metal species both with the surface functional groups and carbon basal planes. The additional bands in the 700-400 cm⁻¹ region for the modified materials could be due to Mn-O and Cu-O vibrations in different coordination and oxidative state of the metal ion [24, 25]. More precise characterization of surface functional groups of AC was carried out by Boehm method [21] and titration with HCl [22] and the data are shown in Table 2. Presence of surface hydroxyl and carbonyl acidic groups as well as basic functional groups was detected for all activated carbons. Their amount was lowest for ACP, followed by ACG and ACA. The pH values and the relatively low acidic/basic groups ratio for ACP indicated higher basicity which was provoked by the presence of relatively high amount of surface basic groups.

XRD patterns of parent and modified carbon and silica supports are presented in Fig. 3 and data for the phase composition, unit cell parameters and average crystallite size are listed in Table 3. XRD patterns of activated carbons represented reflections at 2θ= 25-26° and 45° which could be assigned to carbon turbostratic structure [15]. The reflections were narrower for ACP and ACA indicating relatively high carbon crystallinity. Just the

opposite, the broader reflections for ACG evidenced presence of amorphous carbon phase. The additional narrow reflections at 2θ=43.4°, 50.8° and 74.4° which appeared in the XRD patterns of all carbon based modifications could be ascribed to (111), (200) and (220) planes respectively of face centered cubic metallic copper (pdf 85-1326). The average particles size varied in the 20-50 nm range. The reflections became more intensive for the samples with higher copper content (2Cu1Mn/AC) which was in accordance with the data reported in the literature [2]. In addition, slight reflections at 2θ= 29.5°, 36.2°, 42.5°, 61.4° and 73.4° corresponding to (110), (111), (200), (220) and (311) planes of Cu₂O (primitive cubic Pn-3m, pdf 071- 3645) with average particle size of 3-20 nm (Table 3) were observed.

Table 2. Data for the pH and surface acidic and basic groups for the activated carbon supports.

sample	pH	acidic surface functional groups				basic groups
		carb.	lact.	hydr.	carb.	
ACP	9.4	BDL	BDL*	0.29	1.07	1.04
ACA	8.7	BDL	BDL	2.05	3.27	1.34
ACG	8.9	BDL	BDL	1.59	2.98	1.24

*BDL-bellow detection limit

Single manganese phases such as MnO (pdf 075-1090) and Mn₃O₄ (pdf 080-0382) were detected for both ACG based materials and 1Cu2Mn/ACA, respectively. Single manganese phases such as MnO (pdf 075-1090) and Mn₃O₄ (pdf 080-0382) were detected for both ACG based materials and 1Cu2Mn/ACA, respectively.

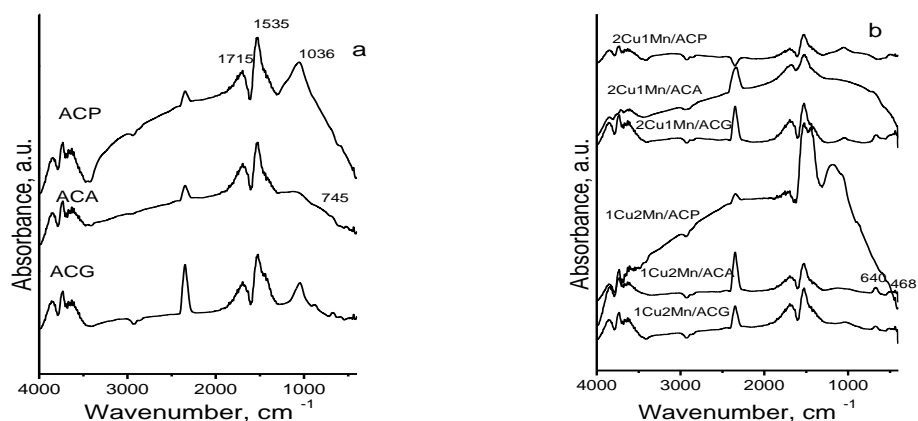


Fig 2. FTIR spectra of parent activated carbons (a) and their copper-manganese modifications (b).

The appearance of well defined, but low intensive reflections at $2\theta=36.6^\circ$, 44° and 58° in the patterns of both ACP modifications and 1Cu2Mn/ACA indicated formation of small amount of finely dispersed face centered cubic Fd-3m non-stoichiometric $\text{Cu}_{1.5}\text{Mn}_{1.5}\text{O}_4$ spinel phase (pdf 070-0262). Thus, carbon support renders difficult the formation of spinel copper-manganese phase. Due to the reduction activity it readily provokes the segregation of reduced copper (Cu , Cu_2O) and manganese (MnO , Mn_3O_4) phases during the metal precursor decomposition. This effect seems to be slightly suppressed for ACP. Taking into account the texture and surface characterization of AC supports (see above) can be concluded that the low concentration of surface functional groups and the better developed mesoporous structure of activated carbon provoke the stabilization and intimate contact between highly dispersed metal oxide entities and facilitate the formation of binary oxides. The assumption for the role of A C support

on the formation of copper-manganese phase was confirmed by the reference KIT-6 based samples (Table3, Fig.3). Here absence (1Cu2Mn/KIT-6) or slight (2Cu1Mn/KIT-6) reflections of face-centered cubic Fd-3m $\text{Cu}_{1.4}\text{Mn}_{1.6}\text{O}_4$ phase (pdf 071-1145) were observed indicating that the inert mesoporous matrix promoted the formation of highly dispersed spinel mixed oxide. UV-Vis spectra of selected carbon materials (ACG) and reference KIT-6 based samples are presented in Fig.4. The intense absorption feature at ca. 325 nm in the spectra of the latter materials could be due to the excitation of surface plasmon in the spinel, in consistence with the XRD data (Fig. 3, Table 3). The additional absorption peak at 688 nm in the spectrum of 2Cu1Mn/KIT6 could be due to the segregation of the excess of CuO in the sample with high Cu/Mn ratio [2]. At the same time, the absorption in the visible region of UV-Vis spectrum of Mn/ACG falls down

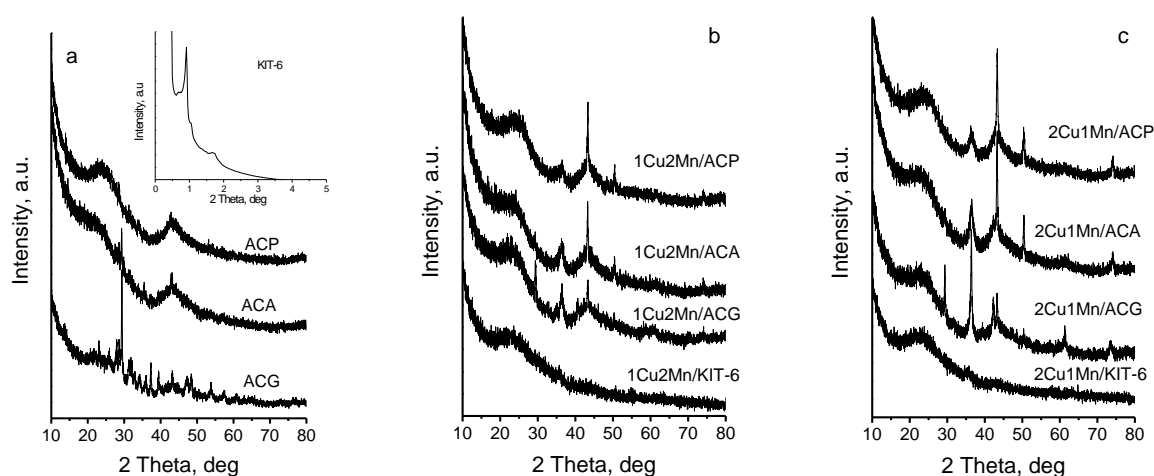


Fig 3. XRD patterns of parent activated carbons (a) and KIT-6 (a, inset) and their 1Cu2Mn/S (b) and 2Cu1Mn/S (c) modifications.

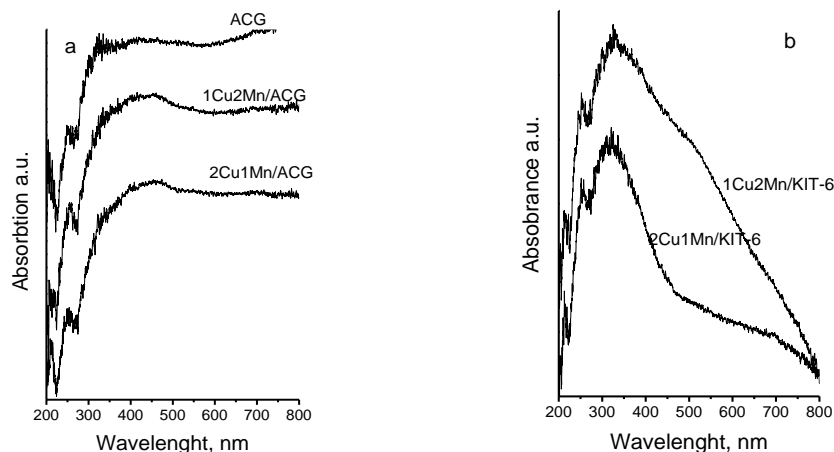


Fig. 4. UV-Vis spectra of ACG (a) and KIT-6 (b) modifications.

This could be due to the non-allowed d-d crystal field transitions of Mn^{2+} ion, which dominated in this sample, in consistence with the XRD analysis [26]. The peaks at 320, 470 and 730 nm could be assigned to $O^{2-} \rightarrow Mn^{3+}$ charge transfer and d-d crystal field transitions in octahedral Mn^{3+} species in hausmannite (Mn_3O_4) phase [26].

In order to characterize the state of copper-manganese active phase more precisely under the conditions that are close to the catalytic experiment, the samples were studied by temperature-programmed reduction with hydrogen. The TPR-TG profiles for carbon and KIT-6 modifications are presented in Fig. 5.

Table 3. Phase composition, unit cell parameters and average crystalline size for various copper-manganese modifications

Sample	Phase composition	Unit cell, Å	Particles size, nm
1Cu2Mn/A CP	Cu^0	.62	50
	Cu_2O	4.28	3
	$Cu_{1.5}Mn_{1.5}O_4$	8.290	
1Cu2Mn/A CA	Cu^0	3.62	27
	Cu_2O	4.28	7
	Mn_3O_4	a=5.765 c=9.442	
1Cu2Mn/A CG	$Cu_{1.5}Mn_{1.5}O_4$	8.290	
	Cu^0	3.62	43
	Cu_2O	4.268	10
	MnO	4.446	
1Cu2Mn/ KIT-6	amorphous		
2Cu1Mn/A CP	Cu^0	3.620(1)	24
	Cu_2O	4.287(3)	6
	$Cu_{1.5}Mn_{1.5}O_4$	8.290	
2Cu1Mn/A CA	Cu^0	3.616(1)	40
	Cu_2O	4.269(2)	8
2Cu1Mn/A CG	Cu^0	3.619(1)	20
	Cu_2O	4.275(1)	25
	MnO	4.446	
2Cu1Mn/ KIT-6	$Cu_{1.4}Mn_{1.6}O_4$	8.30	

The main TPR effects for reference 1Cu2Mn/KIT-6 and 2Cu1Mn/KIT-6 modifications were centered at 535 and 460 K, respectively, which according to the XRD and UV-Vis spectra, could be assigned to the reduction of spinel like $Cu_xMn_{3-x}O_4$ particles. These features are shifted to lower temperatures in comparison with the reported in the literature data for the Mn_xO_y reduction which confirms the facilitated effect of copper addition [2 and refs therein]. The shift of the main TPR effect for the Cu-rich modification to lower temperature (Fig. 5) could be due to the reduction of segregated excess of CuO , which was in consistence with the UV-Vis data (Fig.4). The main reduction effect in the TPR-profiles of AC based binary modifications was broader, less intensive and temperature shifted as compared to their reference analogues. In accordance with the XRD data (Table 3, Fig. 3) it could be due to the superposition of the reduction effects for a mixture of spinel phase and partially reduced copper and manganese oxides (Cu_2O , Mn_3O_4) in different proportion (Table 3). Thus, the extremely low reduction effect for 1Cu2Mn/ACG could be related to domination of metallic Cu and MnO in it (Table 3). In contrast to the silica based samples, strong effect of weight loss above 650 K was also observed for all AC modifications. It overcame the expected weight loss for the reduction of the loaded active phase, which indicates changes with the carbon support under the reduction medium. So, we can expect that under the reduction reaction medium during the methanol decomposition spinel oxides decompose with the formation of metallic Cu and MnO [27]. Although the mechanism of methanol decomposition on copper containing catalysts has been widely studied, the interaction of copper with second metal oxide makes the prediction of its behaviour rather complicated [28].

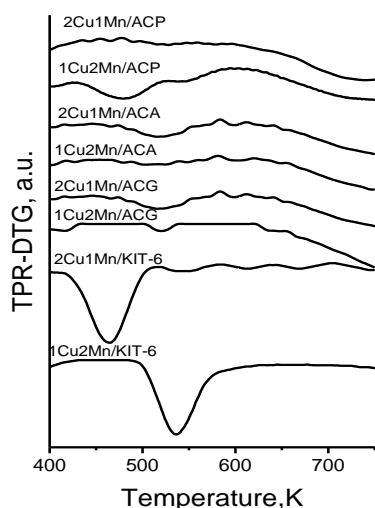


Fig 5. TPR-DTG profiles of AC and KIT-6 modifications

Restoration of OH groups on metal oxide by spillover of hydrogen from copper was proposed for the increase formation of surface intermediate methoxy groups by Bianchi et al. [29], Fisher and Bell [30] assumed reverse spillover of hydrogen from metal oxide to Cu, while Manzoli [31] suggested change in the oxygen vacancy equilibrium between Cu and metal oxide as more appropriate reason for the synergistic effect between them. Nevertheless the type of realized mechanism the dispersion of various metal oxide particles and the close contact between them should be of primary importance for the formation of spinel phase. Obviously the ordered mesoporous structure of silica support facilitates the formation of highly dispersed spinel oxide phase or a mixture of spinel and CuO in the excess of copper (Figs. 3,5, Table 3). Moreover, the stabilization of spinel particles in the ordered mesopores suppresses the aggregation of metallic copper particles, formed during the catalytic process, facilitates the intimate contact with the manganese oxide and maintains the accessibility of the reactant particles to the active sites. This provides high catalytic activity in methanol decomposition which increases with the increase of copper content in the samples (Fig. 1). The XRD, UV-Vis and TPR results clearly demonstrate that this is strongly suppressed on the carbon support. Here, due to the reduction ability of AC, metallic copper aggregates and reduced manganese oxide species are formed even during the modification procedure, which renders difficult the formation of active spinel phase and this is more pronounced with the increase of copper content (Fig. 1). The nitrogen physisorption data

(section 3.2.1) and surface analyses (section 3.2.2) clearly indicate that the texture characteristics and surface functionality of AC regulate the type and proportion between different copper-manganese species. It seems that the relatively small amount of surface acidic groups (Table 2) and higher mesoporosity (Table 1) of ACP promotes the stabilization of more finely dispersed and highly active spinel species. Just the opposite, the relatively high surface functionality (Table 2) and predominantly microporous structure of ACG (Table 1) suppress the formation of spinel phase due to the facile segregation of metallic Cu and MnO phases (Table 3, Figs. 3,5)

CONCLUSION

Activated carbon from different agriculture residues could be suitable support for copper-manganese catalysts for methanol decomposition. It provokes formation of complex mixture of metallic copper, Cu₂O, MnO_x and spinel Cu_xMn_{3-x}O₄ particles in different proportion. The lower surface functionality and higher degree of mesoporosity of activated carbon, which can be readily tuned by the agriculture precursor used, as well as the lower Cu/Mn ratio promote the formation of more active catalysts for methanol decomposition.

Acknowledgements: Financial support project DFNI E02/2/2014 is gratefully acknowledged.

REFERENCES

1. G. A. El-Shobaky, H. G. El-Shobaky, A. A. Badawy, Y. M. Fahmy, *Applied Catalysis A: General*, **409–410**, 234 (2011).
2. J. Papavasiliou, G. Avgouropoulos, T. Ioannides, *J. Catal.*, **251**, 7 (2007).
3. G. Avgouropoulos, T. Ioannides, J. K. Kallitsis, S. Neophytides, *Chem. Eng. J.*, **176–177**, 95 (2011).
4. S. Patel, K. K.Pant, *Appl. Catal. A: General*, **356**, 189 (2009).
5. H. Muroyama, R. Nakase, T. Matsui, K. Eguchi, *Int. J. Hydrogen Energy*, **35**, 1575 (2010).
6. R. M. Navarro, M. A. Pena, J. L. G. Fierro, *Chem. Rev.*, **107**, 395 (2007).
7. J. Papavasiliou, G. Avgouropoulos, T. Ioannides, *Int. J. Hydrogen Energy*, **37**, 16739 (2012).
8. S. Behar, P. Gonzalez, P. Agulhon, F. Quignard, D. Swierczynski, *Catal. Today*, **189**, 35 (2012).
9. V. H. Vu, J. Belkouch, A. Ould-Dris, B. Taouk, *J. Hazardous Mater.*, **169**, 758 (2009).
10. D. A. Aguilera, A. Perez, R. Molina, S. Moreno, *Appl. Catal. B: Environmental*, **104**, 144 (2011).

11. M. R. Morales, B. P. Barbero, L. E. Cadús, *Fuel*, **87**, 1177 (2008).
12. T. Tsoncheva, I. Genova, D. Paneva, M. Dimitrov, B. Tsyntsarski, N. Velinov, R. Ivanova, G. Issa, D. Kovacheva, T. Budinova, I. Mitov, N. Petrov, *Solid State Sci.*, **48**, 286 (2015).
13. B. Tsyntsarski, I. Stoycheva, T. Tsoncheva, I. Genova, M. Dimitrov, B. Petrova, D. Paneva, Z. Cherkezova-Zheleva, T. Budinova, H. Kolev, A. Gomis-Berenguer, C.O. Ania, I. Mitov, N. Petrov, *Fuel Process. Technol.*, **137**, 139 (2015).
14. T. Tsoncheva, A. Mileva, D. Paneva, D. Kovacheva, I. Spassova, D. Nihtianova, P. Markov, N. Petrov, I. Mitov, *Micropor. Mesopor. Mater.*, **229**, 59 (2016).
15. K.-W. Jung, B. H. Choi, M.-J. Hwang, T.-U. Jeong, K.-H. Ahn, *Bioresour. Technol.*, **219**, 185 (2016).
16. T. Tsoncheva, I. Genova, I. Stoycheva, I. Spassova, R. Ivanova, B. Tsyntsarski, G. Issa, D. Kovacheva, N. Petrov, *J. Porous Mater.*, **22**, 1127 (2015).
17. I. Stoycheva, T. Tsoncheva, B. Tsyntsarski, I. Genova, R. Ivanova, B. Petrova, I. Spassova, G. Issa, T. Budinova, N. Petrov, Proc. SGEM 2015 GeoConference of Energy and Clean Technol., 393 (2015).
18. Q. Tang, X. Huang, Y. Chen, T. Liuc, Y. Yang, *J. Mol. Catal. A: Chemical*, **301**, 24 (2009).
19. T. Tsoncheva, I. Genova, M. Stoyanova, M. Pohl, R. Nickolov, M. Dimitrov, E. Priboczki, M. Mihaylov, D. Kovacheva, K. Hadjiivanov, *Appl. Catal. B: Env.*, **147**, 684 (2014).
20. H. P. Boehm, *Adv. Catal. Related Subjects*, **16**, 179 (1966).
21. E. Papier, S. Li, J. B. Donnet, *Carbon*, **25**, 243 (1987).
22. R. C. Sun, J. Tomkinson, *Sep. Purif. Technol.*, **24** 529 (2001).
23. Y. U. Lin, S. U. N. Ming, Y. U. Jian, Y. U. Qian, H.A.O. Zhifeng, L.I. C. Chin, *J. Catal.*, **29**, 1127 (2008).
24. Y. C. Zhang, J. Y. Tang, G. L. Wang, M. Zhang, X. Y. Hu, *J. Cryst. Growth*, **294**, 278 (2006).
25. J. B. Macstre, E. F. Lorez, J. M. Gallardo-Amores, R. R. Casero, V. S. Escribano, E. P. Bernal, *Int. J. Inorg. Chem.*, **3**, 889 (2001).
26. M. R. Morales, B. P. Barbero, L. E. Cadurs, *Fuel*, **87**, 1177 (2008).
27. S.T. Yong, K. Hidajat, S. Kawi, *Catal. Today*, **131**, 188 (2008).
28. D. Bianchi, T. Chafik, M. Khalfallah, S. J. Teichner, *Appl. Catal. A: General*, **123**, 89 (1995).
29. I. A. Fisher, A. T. Bell, *J. Catal.*, **184**, 357 (1999).
30. M. Manzoli, A. Chiorino, F. Boccuzzi, *Appl. Catal. B: Environmental*, **57**, 201 (2005).

АКТИВЕН ВЪГЛЕН, ПОЛУЧЕН ОТ ОТПАДНА БИОМАСА, КАТО НОСИТЕЛ НА СМЕСЕНИ МЕД-МАНГАНОВИ ОКСИДНИ КАТАЛИЗАТОРИ ЗА РАЗЛАГАНЕ НА МЕТАНОЛ

Т. С. Цончева^{1*}, Г. С. Исса¹, Р. Н. Иванова¹, М. Д. Димитров¹, И. П. Спасова², Д. Г. Ковачева², Б. Г. Цинцарски¹, Н. В. Петров¹

¹ Институт по органична химия с Център по фитохимия, Българска академия на науките, 1113 София, България,

² Институт по обща и неорганична химия, Българска академия на науките, 1113 София, България

Постъпила на 11 април 2017 г.; Коригирана на 25 април 2017 г

(Резюме)

Получен е висококачествен активен въглен от различни селскостопански отпадъци, като костилки от праскови и кайсии и семки от грозде. Въглеродните материали бяха модифицирани чрез омокряне с метанолов разтвор на меден и манганов нитрат в различни съотношения и следващо разлагане на прекурсорите в азот. Изходните и модифицирани въглеродни материали бяха характеризирани с различни физикохимични техники като рентгеноструктурен анализ, УВ, ФТИР, ТПР с водород и метод на Бьом. Каталитичните свойства на получените композити бяха изпитани в разлагане на метанол, с потенциално приложение като източник и преносител на водород. Показано е, че въглеродният носител благоприятства формирането на сложна смес от медни и манганови частици в различно окислително състояние. Съотношението между различните компоненти и свързаната с тях каталитична активност може лесно да се контролира чрез отношението Cu/Mn, както и посредством текстурните и повърхностни свойства на активния въглен, като последните могат лесно да се променят чрез използвания селскостопански отпадък.

Silica supported copper and cobalt binary oxides as catalysts for methanol decomposition: Effect of preparation procedure

I. G. Genova*, T. S. Tsoncheva

Institute of Organic Chemistry with Centre of Phytochemistry, Bulgarian Academy of Sciences, 1113 Sofia, Bulgaria,

Received, 12 April 2017; Revised, 26 April 2017

Dedicated to Acad. Ivan Juchnovski on the occasion of his 80th birthday

The present investigation is focused on the effect of preparation procedure on the formation of catalytic active sites on silica supported copper and cobalt binary oxides. Samples with different Cu/Co ratio were obtained by unconventional "chemisorption-hydrolysis" technique consisted of deposition of Cu and Co ammonia complexes, followed by their hydrolysis and thermal decomposition. A conventional wetness impregnation with aqueous solution of the corresponding nitrate precursors was also used for the preparation of similar reference materials. The obtained samples were characterized by a complex of different physicochemical techniques, such as XRD, UV-Vis, FTIR spectroscopy and temperature-programmed reduction with hydrogen. Methanol decomposition to hydrogen and CO was used as a catalytic test in a view of its application as alternative fuel. The preparation techniques strongly affected the dispersion and oxidative state of copper and cobalt species which is easy approach to control their catalytic behaviour.

Key words: copper-cobalt mixed oxide; chemisorption-hydrolyses" technique; methanol decomposition

INTRODUCTION

Transition metal oxides, in particular copper oxides, are known to catalyse many reactions such as Fischer–Tropsch synthesis (FTS), CO₂ hydrogenation, steam reforming of methanol, methane, synthesis of methanol, CO preferential oxidation, and etc. [1 and ref. therein]. It was reported that the activity of such catalysts can be increased by mixing with another oxides [2]. In case of copper-cobalt spinel oxides the increased catalytic activity is usually assigned to the appearance of synergistic and/or cooperative effects between Cu and Co ions. Recently, Subramanian et al. [3] reported that the catalytic performance of mixed Cu and Co nanoparticles is higher than the Co–Cu core–shell nanoparticles. It was also reported that the decomposition of CuCo₂O₄ spinel provides formation of extremely active species for higher alcohols synthesis (HAS) due to the enhanced reduction of Co₃O₄ in the presence of Cu [4]. Obviously, the knowledge for the interaction between different components in binary Cu–Co oxides is a key factor for the optimization of catalytic formula of these materials and could be affected by the preparation method and Cu/Co ratio used. Besides, the catalytic support could be also an important parameter for the design of efficient catalysts by regulation of loaded particles dispersion, location and possibility for the

appearance of strong metal-support interaction. Various supports, such as SiO₂, Al₂O₃, MgO, TiO₂, CeO₂ and ZrO₂, have been used to prepare cobalt and copper based catalysts [4-11]. It was established that the weaker interaction with SiO₂ support favors the reducibility of metal oxide particles, but promotes metal species agglomeration, especially with the increase of metal loading.

The aim of present study is to study the effect of preparation procedure on the formation of catalytic active sites on supported on SiO₂ bi-component copper and cobalt oxides with different Cu/Co ratio. "Chemisorption-hydrolysis" and conventional incipient wetness impregnation techniques were used for the samples preparation. The obtained materials were characterized by different physicochemical techniques, such as XRD, UV-Vis, FTIR and temperature-programmed reduction with hydrogen and tested as catalysts in methanol decomposition to hydrogen and CO as alternative clean and efficient fuel [12 and refs. therein].

EXPERIMENTAL

Materials

Conventional mesoporous SiO₂ (ID 2556, specific surface area of 400 m²/g) was modified with cobalt and/or copper by novel "chemisorption-hydrolyses" technique (CH) as described in [13].

* To whom all correspondence should be sent:
E-mail: izabela_genova@abv.bg

The samples were obtained as follows: (i) impregnation (20 min. at room temperature) of 0.6 g SiO₂ with aqueous solutions (4 ml) containing the corresponding amounts of [Cu(NH₃)₄](OH)₂ (pH=9) and/or [Co(NH₃)₄](OH)₂ (pH=9) for the obtaining of 8 wt. % of metal; (ii) hydrolysis of the obtained product with distilled water (1 L) at 273 K for 30 min; (iii) filtration and drying at 373 K overnight. Similar modifications were prepared by conventional wetness impregnation technique (WI) from aqueous solution of the corresponding nitrate precursors. The obtained CH and WI samples were calcined in air at 623 K and 673 K for 4 h, respectively. All catalysts were denoted as xCoyCu/SiO₂, where x and y represent the weight content of each element.

Methods of characterization

Cobalt content in the samples was determined by Atomic Absorption Spectroscopy on Atomic Absorption Spectrometer 3100–Perkin Elmer; flame: acetylene/air. Powder X-ray diffraction patterns were collected within the range of 5.3 to 80° 2θ on a Bruker D8 Advance diffractometer with Cu Kα radiation and LynxEye detector. The average crystallite size was evaluated according to Scherrer equation. The UV–Vis spectra were recorded on the powder samples using a Jasco V-650 apparatus. The IR spectra (KBr pellets) were recorded on a Bruker Vector 22 FTIR spectrometer at a resolution of 1cm⁻¹, accumulating 64 scans. The TPR/TG analyses were performed in a Setaram TG92 instrument in a flow of 50 vol% H₂ in Ar (100 cm³ min⁻¹) and heating rate of 5 K min⁻¹.

Catalytic tests

Methanol conversion was carried out in a fixed bed flow reactor (0.055 g of catalyst), argon being used as a carrier gas (50 cm³ min⁻¹). The methanol partial pressure was 1.57 kPa. The catalysts were tested under conditions of a temperature-programmed regime within the range of 350–770 K with heating rate of 1 K.min⁻¹. On-line gas chromatographic analyses were performed on HP apparatus equipped with flame ionization and thermo-conductivity detectors, on a PLOT Q column, using an absolute calibration method and a carbon based material balance.

RESULTS AND DISCUSSION

XRD patterns of the samples prepared by different procedures are shown in Fig. 1. The absence of any diffraction peaks in the patterns of all CH samples indicates the formation of finely dispersed metal oxide phase despite the samples composition. Just the opposite, well defined reflections are visible in the patterns of all materials prepared by WI procedure. The reflections (Fig. 1) at 31.2°, 36.8°, 44.8°, 59.4° and 65.3° 2θ in the XRD pattern of Co/SiO₂ could be assigned to centered cubic (fcc) spinel structure (space group Fd3m) of Co₃O₄ [14]. The reflections at 35.5°, 38.7° and 48.6° 2θ in the pattern of Cu/SiO₂ are typical of pure monoclinic CuO (Tenorite, space group C2/c) [15]. The reflections in XRD patterns of bi-component materials are wider and less intensive which indicate formation of more finely dispersed metal oxide phase. The slightly changes in the lattice parameters of Co₃O₄ reveal insertion of metal ions into the spinel structure with the formation of CuCo₂O₄ (Table 1) [16]. Reflections typical of CuO could be detected with the increase of Cu loading in the samples. More information for the state of loaded metal oxide phases was obtained by UV-Vis (Fig. 2a) and FTIR spectroscopy (Fig. 2b).

Table 1. Phase composition, unit cell parameters and average crystallite size for WI samples.

Sample	Space Group	Unit cell, Å	Particles size, nm
Cu/SiO ₂ _WI	CuO - C2/c	4.682(2)	42
		3.424(1)	
		5.128(1)	
		99.49(1)	
Co/SiO ₂ _WI	Co ₃ O ₄	8.086(5)	11
1Cu2Co/SiO ₂ _WI	Co ₃ O ₄	8.124(7)	10
1Cu1Co/SiO ₂ _WI	CuO - C2/c	4.64(1)	38
		3.430(5)	
		5.167(8)	
		99.74(8)	
2Cu1Co/SiO ₂ _WI	Co ₃ O ₄	8.118(8)	9
	CuO - C2/c	4.686(6)	36
3.428(5)			
5.134(4)			
99.57(4)			
	Co ₃ O ₄	8.116(9)	10

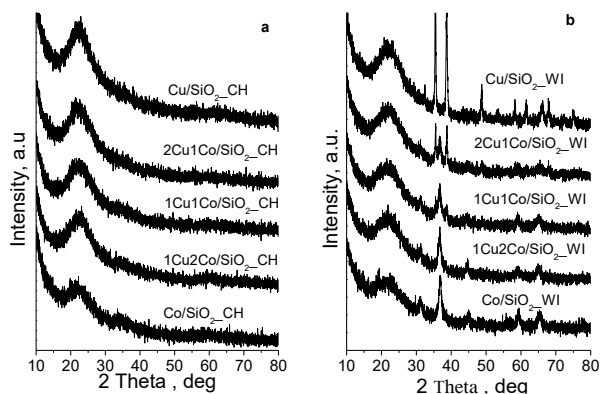


Fig. 1. XRD patterns of CH (a) and WI (b) modifications.

UV-Vis spectra of mono-component copper materials represent absorption band at about 240 nm and a broad band in a 600–800 nm region which could be assigned to the absorption of Cu^{2+} ions in CuO crystallites [11]. The absorption in the 300–400 nm region indicates presence of small Cu-O-Cu oligomeric species. The broad absorption band at 400–550 nm and 650–800 nm in UV-Vis spectra of $\text{Co/SiO}_2\text{-WI}$ are typical of $4T_1(F) \rightarrow 4T_1(P)$ transitions of octahedrally coordinated Co^{3+} and electronic ligand-field $4A_2(F) \rightarrow 4T_1(p)$ transition in tetrahedrally coordinated Co^{2+} , respectively which is in accordance with the XRD data (Fig. 1) for the presence of well crystallized Co_3O_4 phase [13]. The slight absorption at 453, 525, 585 and 650 nm in the spectrum of $\text{Co/SiO}_2\text{-CH}$ could be assigned to the formation of amorphous Co_3O_4 phase, where tetrahedrally coordinated Co^{2+} ions in CoO_4 units are mainly surrounded by oxygen ligands from the silica matrix [17].

Note, the changes in the position and relative part of the main absorption peaks for Co_3O_4 in the UV-Vis spectra of bi-component materials, prepared by WI technique. Taking into account XRD data, this observation could be assigned to the formation of $\text{Co}_x\text{O}_{3-x}\text{O}_4$ spinel phase. The UV-Vis spectra of bi-component CH materials seem to be superposition of the spectra of mono-component $\text{Cu/SiO}_2\text{-CH}$ and $\text{Co/SiO}_2\text{-CH}$ materials, but the observed small changes in the position and intensity of the main peaks do not excluded slight interaction between individual oxides.

Additional information for the state of loaded active phase was obtained by FTIR spectroscopy. The broad band at around 590 cm^{-1} in the FTIR spectrum of $\text{Cu/SiO}_2\text{-WI}$ is due to Cu-O stretching vibrations in the CuO particles, which is in consistence with XRD and UV-Vis data. This band is broader and shifted to lower frequency for the

$\text{Cu/SiO}_2\text{-CH}$ sample, which according to [18] is due to the strong interaction of CuO oligomers species with the silica support. The bands at 570 and 650 cm^{-1} in the FTIR spectra of all cobalt containing WI materials (Fig. 2b) could be assigned to Co-O stretching vibrations of Co^{3+} and Co^{2+} ions in octahedral and tetrahedral coordination, respectively, which is typical of well crystallized spinel Co_3O_4 phase [19]. They are slightly shifted to higher frequency for $\text{Co/SiO}_2\text{-WI}$, indicating formation of cobalt oxide species with higher bond order [20] for this sample. A continuous increase of the absorption in the $600\text{--}500\text{ cm}^{-1}$ region for all CH modified materials (Fig. 2b) is observed. According to [19] and taking into account XRD and UV-Vis data, this could be assigned to the presence of different Co-containing phases (CoO, $\text{CoO}(\text{OH})$, etc.) and absence of well crystallized spinel Co_3O_4 phase.

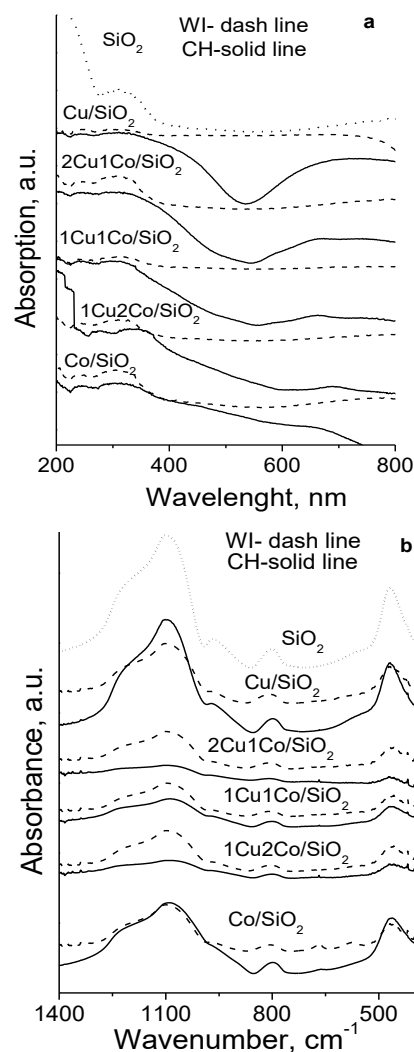


Fig. 2. UV-Vis (a) and FTIR (b) spectra of CH (solid line) and WI (dash line) modifications.

Further information for the metal ions environment in different materials is obtained by the TPR-TG and TPR-DTG profiles of the samples (Fig. 3). For both mono-component copper modifications, TPR-DTG effects in the 410- 530 K region are registered. For Cu/SiO₂_CH, this effect is shifted to about 40 K lower temperature, which could be due to the reduction of more finely dispersed phase in this sample. The observed weight loss (Table 2) corresponds to 80 % reduction of CuO to Cu⁰ for the WI modification and to about 60 % for its CH analogue, respectively. This indicates that CH technique favours the formation of more easily reducible and highly dispersed copper phase than WI method, which is in accordance with our previous data [13, 21].

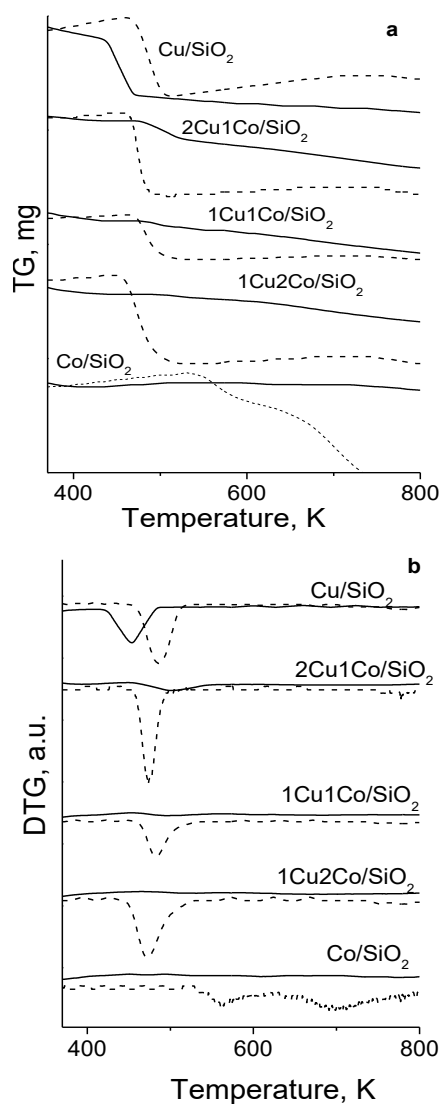


Fig. 3. TPR-TG (a) and TPR-DTG (b) profiles of CH (solid line) and WI (dash line) modifications.

At the same time the observed weight loss for mono-component cobalt materials corresponds to 67 % reduction of Co₃O₄ to metallic Co for the WI modification and below 30 % for its CH analogue. This could be assigned to the reduction of cobalt ions in lower oxidative state and/or strongly interacted with the silica support. Indeed, according to the UV-Vis and FTIR spectra, predominantly presence of Co²⁺ could be assumed for the later material (Fig. 4, Table 2). Taking into account our previous study [13], we could not also fully exclude the formation of finely dispersed cobalt silicate species [22, 23]. Single effect, which is slightly shifted to lower temperature as compared to Cu/SiO₂_WI, is observed for all bi-component WI materials.

Table 2. Samples composition and reduction degree, determined by TPR-TG analyses

Sample	Cu, wt %	Co, wt%	T _{ini} , K	T _{max} , K	Reduction degree, %
Cu/SiO ₂ _CH	8.2		416	454	80
2Cu1Co/SiO ₂ _CH	4.8	2.3	455	502	55
1Cu1Co/SiO ₂ _CH	3.5	3.6	455	500	33
1Cu2Co/SiO ₂ _CH	2.4	4.2	470	520	31
Co/SiO ₂ _CH		10.5	458	472, 612, 760	27
Cu/SiO ₂ _WI	8.2		455	486	60
2Cu1Co/SiO ₂ _WI	4.8	2.3	451	474	91
1Cu1Co/SiO ₂ _WI	3.5	3.6	456	483	42
1Cu2Co/SiO ₂ _WI	2.4	4.2	446	472	85
Co/SiO ₂ _WI		10.5	523	562, 698	67

In accordance with XRD and spectroscopic data this could be assigned to the reduction of Cu_xCo_{3-x}O₄ spinel phase. The variations in the reduction behaviour of all bi-component CH modifications (Fig. 4, Table 2) indicate that the strong interaction of different metal oxide species with the silica matrix renders difficult the interaction between them. In Figure 4 are presented data for the catalytic activity of the samples in methanol decomposition.

Higher catalytic activity is observed for all bi-component materials as compared to mono-component ones, when WI technique was used for their preparation. Here the selectivity to CO was about 90-100%. Relatively lower catalytic activity and selectivity to CO due to formation of CH₄, C₂-C₃ hydrocarbons, DME and CO₂ (up to 20 %) as by-products was observed for their CH analogues. The changes in the specific catalytic activity (SA), calculated per unit metal at selected temperature is presented in Fig. 4 c.

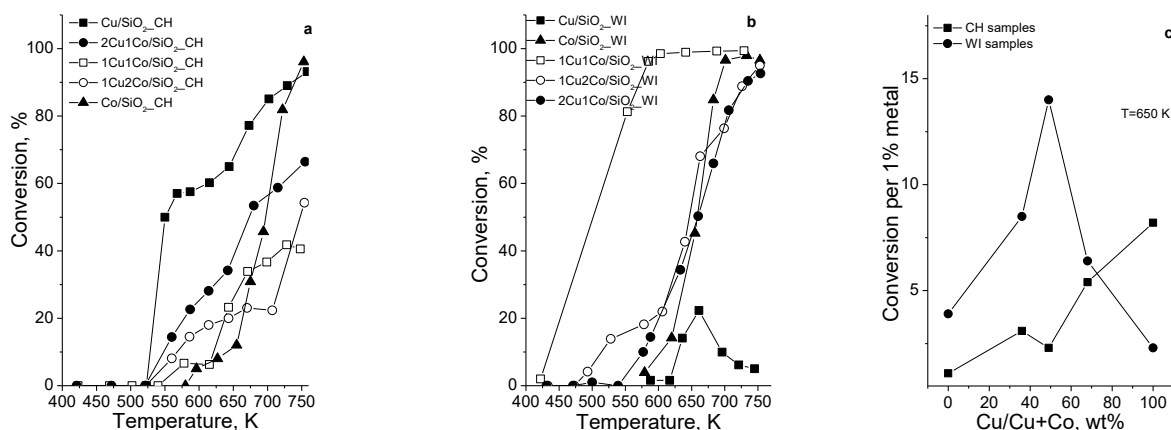


Fig. 4. Methanol conversion vs temperature of CH (a) and WI (b) samples and specific catalytic activity calculated per unit metal (wt. %) at 650 K (c).

With the exception of pure copper materials, the SA values are significantly lower for all cobalt-containing samples, obtained by CH technique. Taking into account the data from the physicochemical analyses (see above) this could be assigned to the facile formation of cobalt species in lower oxidation state and/ or strongly interacted with the silica support. The observed relatively low selectivity to CO on these materials could be due to the formation of additional surface acidic sites. Just the opposite, WI method promotes the formation of finely dispersed, but well crystallized $\text{Cu}_x\text{Co}_{3-x}\text{O}_4$ spinel particles. Obviously, the located on the octahedral sites Cu^{2+} ions share the oxygen with adjacent Co^{2+} , leading to the formation of highly active Cu-O-Co species, in higher for 1Cu1CoSiO₂_WI [13]. This leads to an increase in redox activity and Lewis acidity and facilitates methanol decomposition to CO and hydrogen in synergistic way.

CONCLUSION

The applied preparation techniques allow stabilization of metal oxide particles in different oxidation state and dispersion, which reveals the possibility to fine control of the surface and catalytic properties of Cu and Co bi-component system. “Chemisorption–hydrolysis” technique ensures formation of finely dispersed and strongly bonded to the silica support Co^{2+} containing species. This renders difficult the formation of well crystallized spinel phase and leads to the formation of less active catalysts in comparison with the conventional incipient wetness impregnation technique.

Acknowledgements: Financial support project DFNI E02/2/2014 is gratefully acknowledged.

REFERENCES

1. D. Stoyanova, M. Christova, P. Dimitrova, J. Marinova, N. Kasabova, D. Panayotov, *Appl. Catal. B: Environ.*, **17**, 233 (1998).
2. M. V. Twigg, *Plat. Metals Rev.*, **41**, 2 (1997).
3. N. D. Subramanian, G. Balaji, C. S. S. Kumar, J. J. Spivey, *Catal. Today*, 147 (2009).
4. M. L. Smith, A. Campos, J. J. Spivey, *Catal. Today*, **182**, 60 (2012).
5. R. Reuel, C.H. Bartholomew, *J. Catal.*, **85**, 63 (1984).
6. T. Xiao, S. Ji, H. Wang, K. S. Coleman, M. L. H. Green, *J. Mol. Catal. A: Chemical.*, **175**, 11 (2001).
7. J. Liu, Z. Zhao, J. Wang, C. Xu, A. Duan, G. Jiang, Q. Yang, *Appl. Catal. B: Environ.*, **84**, 185 (2008).
8. F. M. T. Mendes, C. A.C. Perez, F.B. Noronha, M. Schmal, *Catal. Today*, **101**, 45 (2005).
9. Y. Brik, M. Kacimi, M. Ziyad, F. Bozon-Verduraz, *J. Catal.*, **202**, 118 (2001).
10. H. Xiong, Y. Zhang, K. Liew, J. Li, *J. Molec. Catal. A: Chemical.*, **231**, 145 (2005).
11. H. Y. Wang, E. Ruckenstein, *Appl. Catal. A: Gen.*, **209**, 207 (2001).
12. G. Marbán, A. López, I. López, T. Valdés-Solís, *Appl. Catal. B: Environ.*, **99**, 257 (2010).
13. T. Tsoncheva, V. Dal Santo, A. Gallo, N. Scotti, M. Dimitrov, D. Kovacheva, *Appl. Catal. A: Gen.*, **406**, 13 (2011).
14. G. Laugel, J. Arichi, P. Bernhardt, M. Molière, A. Kiennemann, F. Garin, B. Louis, *CR. Chim.*, **12**, 731 (2009).
15. M. Y. Li, W. S. Dong, C. L. Liu, Z. Liu, F. Q. Lin, *J. Cryst. Growth*, **310**, 4628 (2008).
16. N. D. Subramanian, G. Balaji, C. S. S. R. Kumar, J. J. Spivey, *Catal. Today*, **147**, 100 (2009).

17. S. Esposito, M. Turco, G. Ramis, G. Bagnasco, P. Perniced, C. Pagliuca, M. Bevilacqua, A. Aronned, *J. Solid State Chem.*, **12**, 3341 (2007).
18. E. A.-Gheshlaghi, B. Shaabani, A. Khodayari, Y. A. Kalandaragh, R. Rahimi, *Powder Technol.*, **217**, 330 (2012).
19. C. W. Tang, C. B. Wang, S. H. Chien, *Thermochem. Acta*, **473**, 68 (2008).
20. D. R. Brown, C. N. Rhodes, *Catal. Lett.*, **45**, 35 (1997).
21. T. S. Tsoncheva, I. G. Genova, N. Scotti, M. D. Dimitrov, A. Gallo, D. G. Kovacheva, N. Ravasio, *Bulg. Chem. Commun.*, **47**, 1 (2015).
22. A. Marthnez, C. Lypez, F. Mbrquez, I. Dhaz, *J. Catal.*, **220**, 486 (2003).
23. B. Sexton, A. Hughes, T. Turney, *J. Catal.*, **97**, 390 (1986).

БИ-КОМПОНЕНТНИ КАТАЛИЗАТОРИ ЗА РАЗПАДАНЕ НА МЕТАНОЛ НА ОСНОВАТА НА МОДИФИЦИРАН С ОКСИДИ НА МЕДТА И КОБАЛТА СИЛИЦИЕВ ДИОКСИД: ВЛИЯНИЕ НА МЕТОДА НА НАНАСЯНЕ

И. Г. Генова*, Т. С. Цончева

Институт по органична химия с Център по фитохимия, Българска академия на науките, 1113 София, България,

Постъпила на 12 април 2017 г.; Коригирана на 26 април 2017 г.

(Резюме)

Настоящото изследване е насочено към изясняване на влиянието на процедурата на модифициране на SiO_2 върху състоянието на нанесената би-компонентна мед- и кобалт- оксидна фаза. Получени са образци с различно съотношение Cu/Co чрез използване на метода на „хемосорбция-хидролиза“, състоящ се в отлагане на амонячни комплекси на медта и кобалта и следващото им хидролизиране и разлагане. Аналогични референтни образци са получени чрез прилагането на традиционния метод на омокряне с водни разтвори на съответните нитрати. Получените материали са изследвани посредством редица физикохимични методи, като XRD, UV-Vis, FTIR и температурно програмирана редукция с водород. Като каталитичен тест е използван разпадане на метанол до водород и CO с оглед възможността за използването му като алтернативно гориво. Използваните в настоящето изследване техники на модифициране водят до стабилизиране на металооксидни частици в различно окислително състояние и дисперсност, което разкрива възможност за фин контрол на каталитичните свойства на би-компонентните материали.

Copper supported on nanostructured mesoporous ceria-titania composites as catalysts for sustainable environmental protection: Effect of support composition

G. S. Issa^{1*}, T. S. Tsoncheva¹, A. N. Mileva¹, M. D. Dimitrov¹, D. G. Kovacheva², J. Hencych³, V. Štengl³

¹ Institute of Organic Chemistry with Centre of Phytochemistry, BAS, Sofia, 1113, Bulgaria,

² Institute of General and Inorganic Chemistry, BAS, Sofia, Bulgaria

³ Materials Chemistry Department, Institute of Inorganic Chemistry AS CR v.v.i., 25068 Řež, Czech Republic

Received, 13 April 2017; Revised, 25 April 2017

Dedicated to Acad. Ivan Juchnovski on the occasion of his 80th anniversary

Mesoporous ceria-titania binary materials were used as a host matrix of nanosized copper oxide species. The obtained materials were characterized by XRD, nitrogen physisorption, UV-Vis, Raman, FTIR and temperature-programmed reduction with hydrogen. Their catalytic activity was tested in total oxidation of ethyl acetate and methanol decomposition to CO and hydrogen with a potential application in VOCs elimination and alternative fuels, respectively. The variations in the ceria-titania support composition affected the dispersion and the oxidative state of loaded copper species. The facilitated electron transfer between the copper species and ceria-titania support improved the catalytic activity in both catalytic processes and this effect could be successfully controlled by the Ti/Ce ratio in the samples.

Key words: Mesoporous nanostructured ceria-titania doped with copper, template-assisted hydrothermal synthesis, ethyl acetate oxidation, methanol decomposition.

INTRODUCTION

In the last decade methanol has been considered as suitable clean and efficient alternative fuel because it can be synthesized from biomass and other waste products by well-known technologies and easily converted to hydrogen or synthesis gas in case of needs [1]. On the other hand, volatile organic compounds (VOCs) emitted from various industrial processes and transport activities are considered as an important class of air pollutants, and catalytic combustion is one of the most promising strategies for their elimination at relatively low temperatures [2]. An important step in the control of these catalytic processes is the development of highly efficient catalysts with controlled properties. Transition metal oxides are considered as appropriate alternative of noble metals and recently the main efforts are focused on the improvement of their electronic, surface and texture properties by the preparation of nanosized multi-component materials with well developed porous structure. The knowledge of the specific effects within the multi-component nanostructured metal oxides is prerequisite for the optimization of their properties. Recently, titanium oxide has received much attention due to its superior optical,

electrical, mechanical and catalytic properties combined with non-toxicity and cost effectiveness [3]. The introduction of dopant into TiO₂ lattice may significantly affect the electronic band edges or introduce impurity states in the band gap [3]. It has been reported that the addition of ceria to titania decreases its particle size, increases the specific surface area and thermal stability, stabilizes the anatase phase, reduces the bandgap energy and improves the oxygen storage capacity via formation of oxygen vacancies. A lot of data in the literature demonstrates that the modification of TiO₂-CeO₂ mixed oxides with CuO increases the catalytic activity in oxidation processes due to improved dispersion of the supported nanoparticles and the textural characteristics of the composite materials [4-6]. It is known that factors such as the chemical nature of the support, the acid-base functionality, and the location of copper particles in mesoporous oxide matrix significantly affect the catalytic properties of the composite material [5]. CuO/CeO₂-TiO₂ has been reported as an active catalyst for SCR of NO by CO, in which ceria was incorporated into TiO₂ by using the conventional impregnation method [7]. Other authors reported that the catalytic performances of copper based catalysts for NH₃-SCR reaction are closely related to the texture and dispersion of copper oxide

* To whom all correspondence should be sent:
E-mail: issa@abv.bg

species, which are significantly influenced by the supports [8, 9].

The aim of current investigation is to study the effect of copper modification of mesoporous titania-ceria binary oxides. The effect of support composition on their catalytic behaviour in total oxidation of ethyl acetate as a representative VOCs and methanol decomposition as a carrier of hydrogen was studied by complex characterization of the samples with different physicochemical techniques.

EXPERIMENTAL

Materials

The titania-ceria samples were synthesized by template-assisted technique using Hexadecyl-N,N,N-trimethyl ammoniumbromide (CTAB) as a template, hydrothermal treatment at 373 K and calcination at 773 K according to procedure described in [10]. The samples were denoted as xTiyCe, where x:y was the metal mol ratio, which in the bi-component samples was 2:8, 5:5 or 8:2. All initial titania-ceria materials were modified with copper by simple incipient wetness impregnation with aqueous solution of $\text{Cu}(\text{NO}_3)_2 \cdot 9\text{H}_2\text{O}$ in an appropriate amount to obtain 8 wt.% of copper. Then the samples were dried at ambient temperature and calcined with a heating step of 1 °C/min up to 773 K and dwelling time of 2 h.

Methods of characterization

Specific surface area and pore volume data were collected from nitrogen adsorption-desorption isotherms measured at 77 K using a Quantachrome NOVA 1200 apparatus. Powder X-ray diffraction patterns were collected on a Bruker D8 Advance diffractometer with $\text{Cu K}\alpha$ radiation using a LynxEye detector. FTIR spectra in the region of skeletal vibrations were recorded on a Bruker Vector 22 spectrometer at a resolution of 1–2 cm^{-1} , accumulating 64–128 scans and KBr pellets technique. The UV-Vis spectra were recorded on a Jasco V-650 UV-Vis spectrophotometer equipped with a diffuse reflectance unit. Raman spectra were acquired with a DXR Raman microscope using a 780 nm laser.

Catalytic tests

The catalytic oxidation of ethyl acetate was performed in a fixed bed flow reactor (0.030 g of catalyst) with a mixture of ethyl acetate in air (1.21

mol %) and WHSV of 100 h^{-1} . Methanol conversion was carried out in a fixed bed flow reactor (0.055 g of catalyst), argon being used as a carrier gas and methanol partial pressure of 1.57 kPa. On-line gas chromatographic analyses were performed for both reactions using an absolute calibration method and carbon based material balance.

RESULTS AND DISCUSSION

In order to obtain information for the textural characteristics of the studied materials, nitrogen physisorption measurements are done (Table 1). All materials were characterized with well-developed mesoporous structure and high specific surface area and pore volume. The addition of ceria to titania leads to an increase in the specific surface area and pore volume in comparison with the mono-component systems. Note, that the BET surface area of all $\text{CeO}_2\text{-TiO}_2$ samples overcomes that one if the samples were considered as a mechanical mixture of the individual oxides. This suggests for the existence of interaction between the studied metal oxides. The copper addition decreases the surface area and pore volume of titania-ceria supports, probably due to the incorporation of small CuO particles within the support pores.

XRD patterns of all ceria-titania samples are presented in Fig. 1a and the data for phase composition, unit cell parameters and average crystallite size are listed in Table 1. For the pure TiO_2 , only reflections of anatase ($2\theta=25.6^\circ$, 38.3° , 47.8° and 62.5°) were detected [11] (Fig. 1a, Table 1). For pure CeO_2 , the strong reflections are attributed to cubic fluorite-like structure ($2\theta = 28.5^\circ$, 33.1° , 47.5° , 56.3° and 69.4°) with average crystallite sizes of 22 nm. Anatase phase was only registered when titania was doped with small amount of ceria (2Ce8Ti). However, the reflections were broader as compared to pure TiO_2 , which evidences higher dispersion of TiO_2 . With further increase of Ce content the reflections become weaker and wider, which indicates a decrease in the crystal size of TiO_2 (Table 1). For the Ce-rich samples (Fig. 1a) only reflections characteristic of cerianite CeO_2 could be detected. These reflections are slightly shifted to higher Bragg angles, which is due to a slight decrease of ceria unit cell parameter (Table 1). Taking into account that the radius of Ti^{4+} -ion is 0.74 Å, CN=6 and that one for Ce^{4+} -ion is 0.97 Å, CN=6, the latter observation could be assigned to the incorporation of smaller Ti^{4+} -ions into the ceria lattice [12,13]. XRD patterns of copper modified Ce-Ti materials are presented in

Fig. 1b. Typical anatase and fluorite phases were observed on Cu/TiO₂ and Cu/CeO₂ samples, respectively. The diffraction peaks in these samples at 2θ = 35.5°, 38.5° and 48.5° are due to the presence of well crystallized CuO phase with

monoclinic tenorite structure [5], probably located on the outer surface of mesoporous oxide support because of their relatively large crystal size (Table 1).

Table 1. Nitrogen physisorption and XRD data of CeTi and Cu/CeTi materials.

Sample	Space Group	Unit cell	Particles size, nm	BET m ² /g	Total Pore Volume, ml/g
TiO ₂	Anatase, syn	3.786	17.4	85	0.29
	Tetragonal – Body-centered I41/amd	9.493			
Cu/TiO ₂	Anatase, syn	3.786	20.8	40	0.24
	Tetragonal – Body-centered I41/amd	9.488			
5Ce5Ti	Tenorite	4.691	36.4	99	0.45
		3.419			
		5.138			
		99.594			
Cu/5Ce5Ti	Cerium oxide	5.403	12.0	99	0.45
	Cubic - Face center - Fm-3m	5.405			
Cu/5Ce5Ti	Cerium oxide	5.405	12.5	69	0.39
	Cubic - Face center - Fm-3m	5.405			
2Ce8Ti	Tenorite	4.716	45.8	166	0.62
		3.431			
		5.126			
		99.578			
Cu/2Ce8Ti	Anatase, syn	3.784	5	102	0.49
	Tetragonal – Primitive P42/mnm	9.49			
Cu/2Ce8Ti	Anatase, syn	3.793	7	102	0.49
	Tetragonal – Primitive P42/mnm	9.49			
8Ce2Ti	Cerium oxide	5.409	17.0	55	0.30
	Cubic - Face center - Fm-3m	5.409			
Cu/8Ce2Ti	Cerium oxide	5.407	16.8	38	0.28
	Cubic - Face center - Fm-3m	5.407			
Cu/8Ce2Ti	Tenorite	4.688	40.1	46	0.26
		3.432			
		5.127			
		99.323			
CeO ₂	Cerium oxide	5.413	21.8	46	0.26
	Cubic – Face center – Fm-3m	5.413			
Cu/CeO ₂	Cerium oxide	5.413	22.0	24	0.20
	Cubic – Face center – Fm-3m	5.413			
Cu/CeO ₂	Tenorite	4.679	29.3	24	0.20
		3.440			
		5.130			
		99.44			

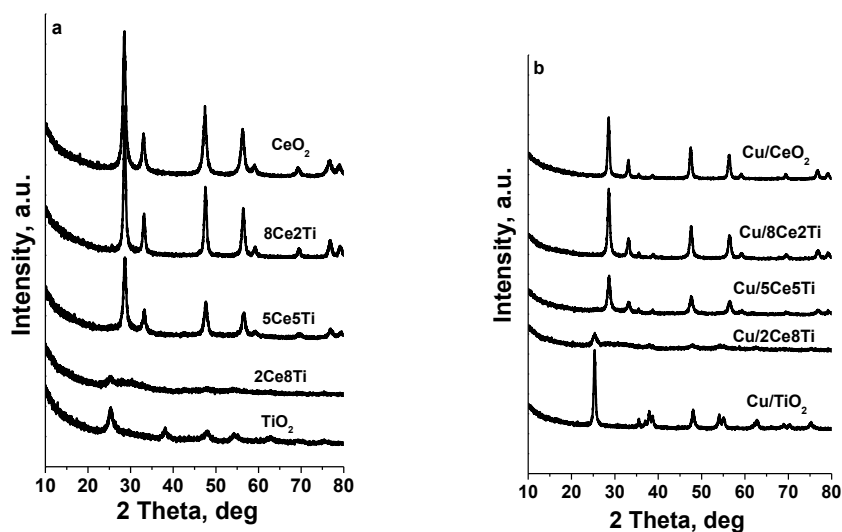


Fig. 1. XRD patterns of CeTi (a) and Cu/CeTi (b) materials.

In the case of Cu/2Ce8Ti, the main reflections belonging to anatase phase appeared with low intensity and no reflections corresponding to CeO₂ and CuO were observed. This observation indicates formation of highly dispersed metal oxide particles. Strong reflections attributable to cubic fluorite-like structure of CuO with average crystallite size of 40 and 45 nm, respectively (Table 1), were detected in the patterns of Cu/8Ce2Ti and Cu/5Ce5Ti. The observed decrease of the unit cell parameter for ceria components in copper containing samples (Table 1) as compared to pure CeO₂ does not exclude partial substitution of Ce⁴⁺ ions by smaller Cu²⁺ ion (0.73 nm). According to [14] it is likely that part of Cu²⁺ ions entered into the CeO₂ lattice to form a solid solution and the rest of Cu²⁺ formed CuO particles on the surface of CeO₂.

FTIR analysis was conducted (not shown) in order to get more information for the studied materials. The spectrum of pure TiO₂ sample consists of peaks at 460, 620 and the shoulder at 910 cm⁻¹, typical of anatase titania [12]. The broad and intensive band below 700 cm⁻¹ observed for the pure CeO₂ sample is related to the Ce–O bond vibrations. The band around 1600 cm⁻¹ is due to adsorbed water molecules. The broad band in the interval 3100–3700 cm⁻¹ is assigned to O–H stretching vibrations. The broad and intensive band below 700 cm⁻¹ observed for the Cu/CeO₂ sample is assigned generally to Ce–O stretching vibrations in defect Ce–O–Cu structures [6]. This feature decreases for the mixed oxide materials, probably due to the creation of new contact between the different metal oxide nanoparticles. The registered

variation in the intensity of the band in the 3100–3700 cm⁻¹ interval in the FTIR spectra of copper CeTi samples implies that the possible interaction between different oxides results in differences in the surface defects, which reflects on the amount of surface hydroxyl groups and adsorbed water (not shown).

UV–vis diffuse reflectance spectra of individual TiO₂ and CeO₂ oxides and their composites are presented in Fig. 2a. Only one adsorption edge which corresponds to the band transition at about 355 and 314 nm was detected in the spectra of TiO₂ and CeO₂, respectively. It is clearly seen, that ceria doping of titania results in shift of the adsorption edge to the visible region. The observed red shift was most pronounced for 2Ce8Ti sample and decreased with the increase of ceria content. In accordance with [15] this could be due to the formation of new energy level within the band gap of TiO₂. The absorption in the range of 240–320 nm and 600–800 nm regions for all copper modification is related to O²⁻→Cu²⁺ CT and d–d transitions, respectively, of crystalline CuO [6] (Fig. 2b). In accordance with the XRD and nitrogen physisorption data, the observed changes in the 350–500 nm region for all copper modifications confirm the assumption done above for the existence of strong interaction between the different metal ions and/or the increase in the metal oxides dispersion.

In order to obtain more information for the type of interaction between metal oxide nanoparticles, Raman spectra were recorded (Fig. 3a).

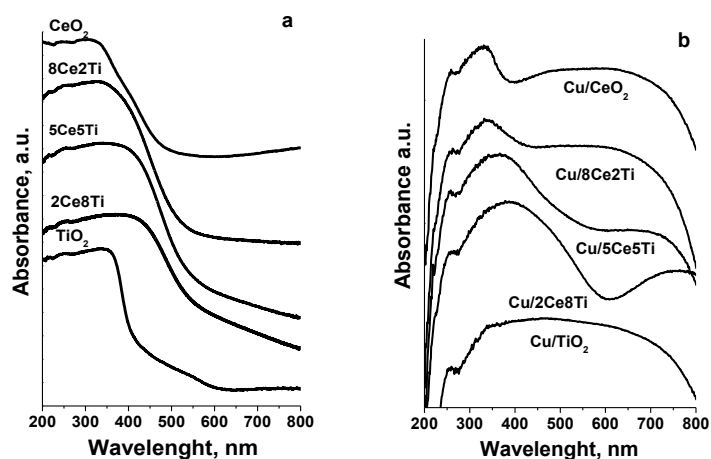


Fig. 2. UV-Vis patterns of CeTi (a) and Cu/CeTi (b) materials

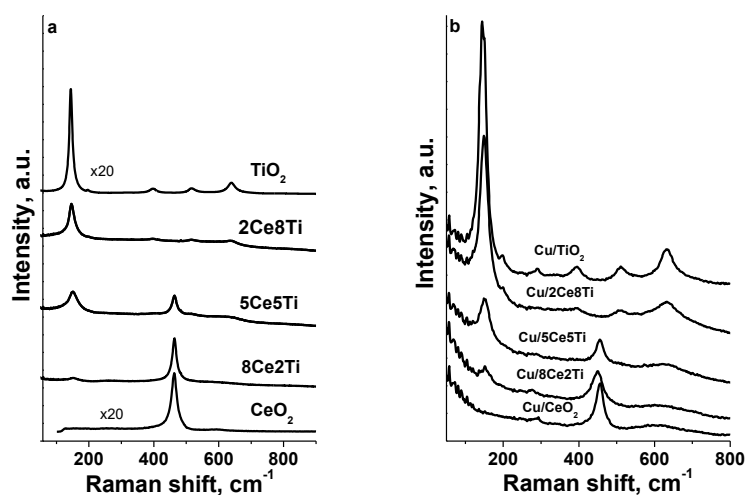


Fig. 3. Raman patterns of CeTi (a) and Cu/CeTi (b) materials

The Raman spectrum of TiO_2 consisted of well defined Raman shifts at 143 cm^{-1} (E1g), 195 cm^{-1} (E2g), 396 cm^{-1} (B1g), 514 cm^{-1} (A1g) and 637 cm^{-1} (E3g), which are typical of pure anatase structure [16]. In case of mixed CeTi samples, the observed decrease in the intensity of the main peak, typical of titanium oxide accompanied with its slight broadening could be due to particle size decrease, which is in accordance with the XRD data (Fig. 1a, Table 1). The spectrum of CeO_2 showed the main Raman shift at 463 cm^{-1} (E2g) typical of CeO_2 [12]. The additional band at 600 cm^{-1} was generally assigned to the presence of oxygen defects in the ceria lattice. For the bi-component CeTi materials, a slight shifting and broadening of the main Raman-active mode accompanied with a decrease in its intensity is detected (Fig. 3a). This could be assigned to partial replacement of Ce ions with Ti ones, resulting in Ce-O bonds shortening and formation of smaller crystallites with defect

structure. In the case of 2Ce8Ti sample, no peaks of CeO_2 are observed. The Raman bands corresponding to CuO was absent for all copper catalysts, indicating that CuO was in highly dispersed state, consistent with the XRD results. The observed slight blue shift of the Raman E1g mode to 150 cm^{-1} for copper modifications could be an indication for the changes in the environment of titanium ions in anatase lattice (Fig. 3b). The appearance of such a non-stoichiometric structure of titania could be due to the formation of distinct atomic defects like Ti^{3+} , interstitial Ti^{4+} , or oxygen vacancies [15]. A slight red shift of the position of the band at 463 cm^{-1} , combined with significant decrease in the intensity and increase of the half-width is observed for all Cu/CeTi materials, suggesting strong interaction between CuO and CeO_2 (Fig. 3b). At the same time the disappearance of the main CuO peaks and a significant increase of the relative intensity of the peak at 600 cm^{-1} is

observed. Generally, the latter feature is assigned to the formation of oxygen vacancies due to the replacement of Ce^{4+} by metal ion with different valence.

In Fig. 4 are presented data from the TPR analyses. The reduction of pure CeO_2 was initiated just above 657 K. The observed weight loss with further temperature increase up to 773 K corresponded to about 10% reduction of Ce^{4+} to Ce^{3+} ions, probably from the surface [12] (Fig. 4a).

The reduction effect for the bi-components samples is larger in comparison with pure CeO_2 and starts at lower temperature. For 5Ce5Ti higher reduction ability as compared to 8Ce2Ti is detected, which could be assigned to the increase of the number of titanium ions, incorporated in ceria lattice. However, the reduction became more difficult with further increase of titania content (2Ce8Ti), but it remains still easier as compared to the pure CeO_2 .

Thus, TPR results clearly demonstrate the existence of interaction between different metal oxide species in bi-component materials, which results in the presence of more readily reducible ceria crystallites, interacting with titania. In Fig. 4b are presented data from the TPR analyses of the copper modifications. Cu/TiO_2 exhibits reduction peak with a maximum at about 470 K, which corresponds to one step reduction of Cu^{2+} to metallic copper [4].

The appearance of two reduction peaks for Cu/CeO_2 centered at 385 and 439K could be assigned to the reduction of Cu^{2+} ions in different environment and/or differently dispersed CuO particles (Fig. 4b). Two reduction effects are observed also for all mixed copper samples, indicating the existence of at least two types of copper species (Fig. 4b). Note that the ratio between them changes with Ce/Ti ratio with a tendency to an increase in the relative part of the low-temperature effect with ceria amount decrease. In accordance with the XRD data, this could be due to the improved dispersion of ceria in the vicinity of titania.

In Fig. 5 are presented temperature dependencies of total oxidation of EA. Beside CO_2 , which is the most important product of EA oxidation, ethanol (EtOH), acetaldehyde (AA), acetic acid (AcAc) and ethene are also registered as by-products. For CeTi samples the ethyl acetate oxidation is initiated above 500 K and 80–100% conversion is achieved at 650 K. Among all materials, pure ceria exhibits the highest catalytic activity. Besides, on this material high selectivity to EtOH (47%) is

observed. The lowest catalytic activity combined with high selectivity to AA (25%), EtOH (22%) and ethene (18%) is registered for TiO_2 sample. The improvement of the selectivity to CO_2 for all binary materials clearly indicates dominant effect of redox over the acid-base properties for these materials [2]. With the exception of Cu/CeO_2 , all copper modifications exhibited improved catalytic activity in total oxidation of ethyl acetate to CO_2 in comparison with the corresponding supports (Fig. 5b).

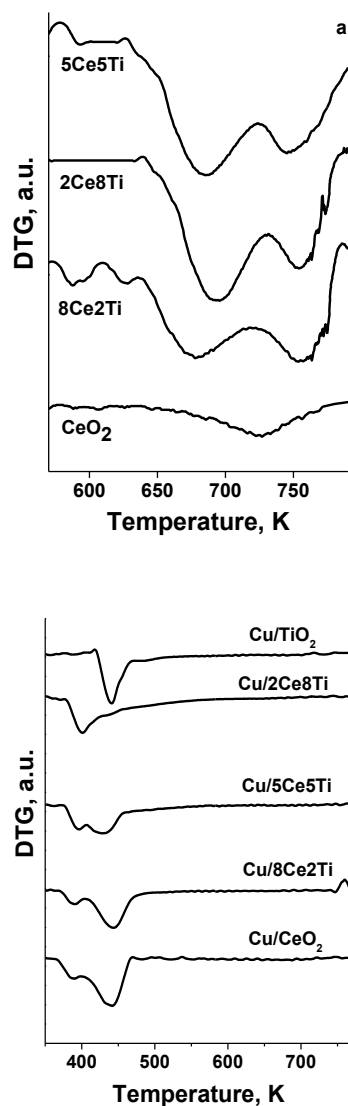


Fig. 4. TPR-DTG patterns of CeTi (a) and Cu/CeTi (b) materials.

XRD, UV-Vis, and Raman analyses demonstrate that the close contact between different metal oxide particles creates an interface layer, where copper ions are penetrated into the support lattice with simultaneous formation of oxygen defects. The formation of this interface seems to facilitate the stabilization of finely dispersed, easily reducible, and highly active CuO nanoparticles.

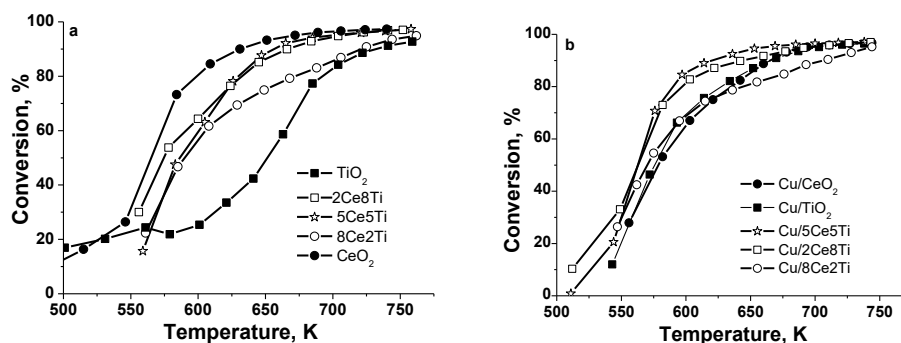


Fig. 5. Ethyl acetate conversion of CeTi (a) and Cu/CeTi (b) materials.

Note the decrease in the catalytic activity with the increase in Ce/Ti ratio in the support. Taking into account the nitrogen physisorption measurements this could be due to a decrease in the BET surface area (Table 1).

The temperature dependencies of methanol conversion and selectivity to CO and hydrogen for titania and ceria samples are presented in Fig. 6a. Besides CO, which formation is directly related to hydrogen production from methanol, CO₂, CH₄, dimethyl ether (DME) and C₂-C₃ hydrocarbons are registered as by-products. All materials exhibit catalytic activity above 500-550 K. The mono-component CeO₂ sample possesses extremely low catalytic activity and about 50% selectivity to CO due to the formation of CH₄ (Fig. 6a).

The main by-products during the methanol decomposition on TiO₂ materials are DME (about 50%) and hydrocarbons (about 17%) which clearly indicates existence of high acidic functionality. Here, well pronounced trend to deactivation with the temperature increase for this material is detected, which could be due to the deposition of non-desorbable products. The binary CeTi

materials demonstrate improved catalytic activity and stability at higher temperatures as compared to the individual oxides (Fig. 6a).

Their relatively low selectivity to CO is due to the contribution of methane (about 30%) and DME (30-40%) as by-products. Copper modifications demonstrated improved catalytic activity in methanol decomposition as compared to ceria-titania supports only in case of relatively low Ce/Ti ratio of the support (Fig. 6b). The complex temperature dependency of their catalytic activity indicates changes in the catalytic active sites under the reaction medium.

CONCLUSION

High surface area mesoporous ceria-titania binary materials can be successfully synthesized using template assisted hydrothermal technique. Binary oxide supports exhibit improved dispersion, high surface area and pore volume combined with excellent oxygen mobility. As a result, a significant increase in the catalytic activity and selectivity in total oxidation of ethyl acetate to CO₂ and methanol decomposition to syngas is achieved.

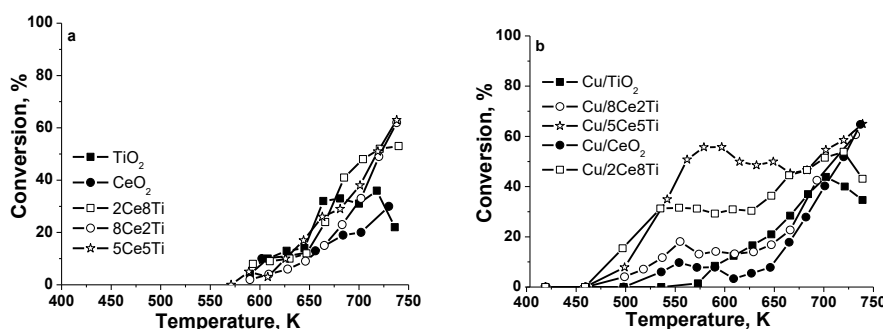


Fig. 6. Methanol conversion of CeTi (a) and Cu/CeTi materials (b).

Small additives of copper to ceria and/or titania oxides promotes their catalytic activity in total oxidation of ethyl acetate and methanol decomposition to syngas, but this effect is strongly influenced by support composition. The lower Ce/Ti ratio promotes the catalytic activity both in ethyl acetate oxidation and methanol decomposition in a higher extent.

Acknowledgements: Financial support from project DM-09/4/2016 and Joint research project between ASCR and BAS is acknowledged.

REFERENCES

1. A. Mahlon, S. Wilson, *Int. J. Hydrogen Energy* **34**, 2955 (2009).
2. C.Y. Lu, M.Y. Wey, L.I. Chen, *Appl. Catal. A: Gen.* **325**, 163 (2007).
3. I.D. González, R.M. Navarro, W. Wen, N. Marinkovic, J.A. Rodríguez, F. Rosa, J.L.G. Fierro, *Catal. Today* **149**, 372 (2010).
4. S. Cao, M. Shi, H. Wang, F. Yu, X. Weng, Y. Liu, Z. Wu, *Chem. Eng. J.* **290**, 147 (2016).
5. M.-S. Kima, D.-W. Lee, S.-Ho Chung, J. Kim, H.-H. Cho, K.-Y. Lee, *J. Molecular Catalysis A: Chem.* **392**, 308 (2014).
6. X. Gao, X. Du, L.W. Cui, Y. Fu, Z.Y. Luo, K. Cen, *Catal. Commun.* **12**, 255 (2010).
7. G. Chi, B. Shen, R. Yu, C. He, X. Zhang, *J. Hazardous Materials* **330**, 83 (2017).
8. K. Zhao, W. Han, G. Lu, J. Lub, Z. Tang, X. Zhen, *Appl. Surface Science* **379**, 316 (2016).
9. J. Liu, X. Li, Q. Zhao, J. Ke, H. Xiao, X. Lv, S. Liu, M. Tadé, S. Wang, *Appl. Catalysis B: Environ.* **200**, 297 (2017).
10. T. Tsoncheva, L. Ivanova, D. Paneva, I. Mitov, C. Minchev, M. Fröba, *Micropor. Mesopor. Mater.* **120**, 389 (2009).
11. M. Altomare, M.V. Dozzi, G.L. Chiarello, A.D. Paola, L. Palmisano, E. Selli, *Catal. Today* **252**, 184 (2015).
12. H. Nur, *Mater. Sci. Eng. B – Sol* **133**, 49 (2006).
13. S. Yuesong, Z. Dahai, Y. Bo, N. Songbo, Z. Shemin, *J. RARE EARTHS*, **30**, No. 5, 431 (2012).
14. T. Tsoncheva, G. Issa, J.M.L. Nieto, T. Blasco, P. Concepcion, M. Dimitrov, G. Atanasova, D. Kovacheva, *Microporous and Mesoporous Materials* **180**, 156 (2013).
15. T. Tsoncheva, A. Mileva, G. Issa, M. Dimitrov, D. Kovacheva, J. Henych, N. Scotti, M. Kormunda, G. Atanasova, V. Stengl, *Appl. Surface Science* **396**, 1289 (2017).
16. T. Kidchob, P. Falcaro, P. Schiavuta, S. Enzo, P. Innocenzi, *J. Am. Ceram. Soc.* **91**, 2112 (2008).

МЕД-МОДИФИЦИРАНИ МЕЗОПОРЕСТИ НАНОСТРУКТУРИРАНИ ЦЕРИЙ-ТИТАН ОКСИДИ КАТО КАТАЛИЗАТОРИ ЗА ЕКОЛОГОСЪОБРАЗНИ ПРОЦЕСИ: ВЛИЯНИЕ НА ФАЗОВИЯ СЪСТАВ

Г. С. Исса¹, Т. С. Цончева¹, А. Н. Милева¹, М. Д. Димитров¹, Д. Н. Ковачева², И. Хених³, В. Щенгъл³

¹ *Институт по органична химия с Център по фитохимия, Българска академия на науките, ул. Акад. Г. Бончев, бл. 9, 1113 София, България*

² *Институт по обща и неорганична химия, Българска академия на науките, ул. Акад. Г. Бончев, бл. 11, 1113 София, България*

³ *Институт по неорганична химия, 25068 Чехия*

Постъпила на 13 април; 2017 г.; Коригирана на 25 април 2017 г.

(Резюме)

Мезопорести церий-титан смесенооксидни материали бяха използвани като матрици за нанасяне на наноразмерни меднооксидни частици. Получените материали бяха характеризирани чрез прахова рентгенова дифракция, физична адсорбция на азот, дифузионно-отражателна ултравиолетова, инфрачервена и Раман спектроскопии, както и температурно-програмирана редукция с водород. Каталитичната им активност беше тествана в реакция на пълно окисление на етилацетат с потенциално приложение съответно за елиминиране на ЛОС съединения и разпадане на метанол до СО и водород като алтернативно гориво. Варирането на състава на церий-титан смесенооксидните носители влияе върху дисперсността и окислителното състояние на нанесените медни частици. Улесненият електронен трансфер между медните частици и церий-титан смесенооксидните носители води до подобряване на каталитичната активност в двата каталитични процеса и този ефект може успешно да се контролира чрез съотношението Ce/Ti в тези образци.

Diamides of squaric acid containing methioninamide fragment – synthesis, spectral and theoretical investigation

E. Cherneva^{1*}, Ts. Kolev²

¹ Department of Chemistry, Faculty of Pharmacy, Medical University - Sofia, 2 Dunav Str., 1000 Sofia, Bulgaria

² Institute of Molecular Biology, Bulgarian Academy of Sciences, 21, G. Bontchev Str., Sofia 1113, Bulgaria

Received May 02, 2017; Revised May 25, 2017

Dedicated to Acad. Ivan Juchnovski on the occasion of his 80th birthday

Four novel diamides of squaric acid were synthesized in high yields using a condensation reaction of methioninamide esteramide of squaric acid with different amides of amino acids. Newly synthesized compounds were investigated by elemental analyses, IR and NMR. The molecular structures of the compounds were elucidated by a DFT method. The theoretical analysis showed that squaric fragment and NH-groups lied in one plane which was almost perpendicularly oriented to the plane of asymmetric C-atom.

Key words: diamide of squaric acid; methioninamide; IR; DFT calculations

INTRODUCTION

Methionine, one of the two sulfur-containing amino acids, is found in all living cells [1] and is critical for the synthesis of many proteins. It plays an important role in many biochemical processes involved in producing substances necessary for normal functioning of the cardiovascular, bone and nervous system [2]. Methionine is a major source of methyl groups in the body.

On the other hand, mono and diamides of squaric acid (H₂Sq) received much attention in the recent years. Their unique structural features: strained ring, two carbonyl groups and a C=C bond, two carbonyl acceptor and two NH donor groups are able to form hydrogen bonds [3] determined their specific reactivity and properties. These derivatives are important from pharmacological point of view due to the broad range of their biological activity. Many amides of H₂Sq are used as phosphates, carboxylate and amino acids isosters due to the similar structure [4-6], metal chelators for the inhibition of matrix metalloprotease enzymes [7,8] and ion receptors [3,9] in medicinal chemistry. Squaramide fragment is used as binding unit in bioconjugate chemistry [10,11]. Also squaramides have application as chiral ligands and catalyst in organometallic chemistry and organocatalysis [12,13]. For this reason, the synthesis of new mono- and diamides of squaric acid and the investigation of their properties are important for several chemistry fields.

Herein is presented the synthesis and spectral investigation of four novel methioninamide containing diamides of squaric acid. In order to get more information about their molecular structure the newly synthesized compounds were studied by theoretical methods.

MATERIALS AND METHODS

Amide of amino acids hydrochlorides were purchased from Bachem AG. Diethyl ester of squaric acid ethanol and triethylamine were purchased from Sigma-Aldrich.

The IR spectra were measured on a Bruker Tensor 27 FTIR spectrometer. In all cases the spectra were recorded at a resolution of 2 cm⁻¹ (64 scans). The NMR spectra were recorded on a Bruker DRX250 spectrometer in solvent DMSO-d₆ using TMS as internal standard. Standard Bruker pulse sequences and software were used to record and process the spectra. The elemental analyses were carried out according to the standard procedures for C and H (as CO₂, and H₂O) and N (by the Dumas method). The molecular structure and vibrational spectra of the compounds were studied by computational method. Thin layer chromatography (TLC) was performed on aluminum sheets pre-coated with Merck Kieselgel 60 F254 0.25 mm (Merck). All density functional theory (DFT) computations were performed with the Gaussian 09 program package [14] employing the B3LYP (Becke's three-parameter non-local exchange) [15,16] correlation functional and 6-311++G** basis set

* To whom all correspondence should be sent:
E-mail: e.d.cherneva@gmail.com

Synthesis of methionine containing diamides of squaric acid (**5a-d**)

Aqueous ethanolic solution (1:4) of corresponding amide of amino acids hydrochlorides (1mmol) was mixed with excess of Et₃N (5mmol) and the mixture was stirred for 10 minutes at room temperature. After that ethanol solution of methioninamide esteramide of H₂Sq (1 mmol) was added. The mixture was stirred at room temperature to complete the reaction. The products were isolated by precipitation and purified by recrystallization.

Spectral data of methionine containing diamides of H₂Sq **5a-d**:

5a: 2-[2-(1-Carbamoyl-3-methylsulfanyl-propylamino)-3,4-dioxo-cyclobut-1-enylamino]-3-methyl-butylamide

M = 342.41; Elemental analysis: C₁₄H₂₂N₄O₄S (Met/Val) (%), Calcd. C 49.1, H 6.4, N 16.3, S 9.3; Found C 49.0, H 6.4, N 16.4, S 9.3;

¹H NMR (DMSO- d₆, 250 MHz), δ (ppm): 8.00 (dd, J=9.0, 14.5 Hz, 2H, 2NH), 7.74 (d, J=5.9, 2H, NH₂), 7.28 (d, J=16.9 Hz, 2H, NH₂), 4.65 (dd, J=7.2, 13.1 Hz, 1H, CH), 4.53 (dd, J=5.1, 9.4 Hz, 1H, CH), 2.43 (m, 2H, CH₂), 2.05 (s, 3H, SCH₃), 1.89 (m, 2H, CH₂), 0.86 (dd, J=6.8, 11.4 Hz, 6H, 2CH₃);

¹³C NMR (DMSO - d₆, 250 MHz), δ (ppm): 182.41, 182.36, 172.06, 167.67, 166.75, 60.67, 55.26, 34.58, 32.08, 28.69, 18.80, 16.78, 14.66

+ MS, m/e (relative intensity): 343.22 (M⁺);

5b: 2-[2-(1-Carbamoyl-3-methylsulfanyl-propylamino)-3,4-dioxo-cyclobut-1-enylamino]-3-methyl-pentanoic acid amide

M = 356.44; Elemental analysis C₁₅H₂₄N₄O₄S (Met/Ile) (%), Calcd. C 50.5, H 6.7, N 15.7, S 9.0; Found C 50.4, H 6.8, N 8.8; S 9.0

¹H NMR (DMSO- d₆, 250 MHz), δ (ppm): 7.98 (dd, J=9.0, 13.0 Hz, 2H, 2NH), 7.73 (d, J=8.7 Hz, 2H, NH₂), 7.28 (d, J=16.8 Hz, 2H, NH₂), 4.65 (dd, J=6.3, 11.2 Hz, 1H, CH), 4.53 (dd, J=5.3, 9.0 Hz, 1H, CH), 2.44 (m, 2H, CH₂), 2.03 (s, 3H, SCH₃), 1.85 (m, 2H, CH₂), 1.04 (m, 2H, CH₂), 0.85 (dd, J=6.8, 11.4 Hz, 6H, 2CH₃)

¹³C NMR (DMSO- d₆, 250 MHz), δ (ppm): 182.40, 182.32, 172.14, 172.06, 167.56, 166.77, 60.47, 55.27, 34.58, 28.70, 23.50, 15.13, 14.67, 11.46

+ MS, m/e (relative intensity): 357.18 (M⁺);

5c: 2-[2-(1-Carbamoyl-2-hydroxy-ethylamino)-3,4-dioxo-cyclobut-1-enylamino]-4-methylsulfanyl-butylamide

M = 330.36; Elemental analyses: C₁₂H₁₈N₄O₅S (Met/Ser) (%), Calcd. C 43.6, H 5.4, N 16.9, S 9.7;

Found C 43.6, H 6.2, N 16.7, S 9.6

¹³C NMR (DMSO- d₆, 250 MHz), δ (ppm): 182.49, 182.30, 172.20, 172.11, 167.30, 166.42, 60.01, 55.80, 55.53, 33.24, 28.72, 14.48

+ MS, m/e (relative intensity): 331.66 (M⁺);

5d: 2-[2-[1-Carbamoyl-2-(4-hydroxy-phenyl)-ethylamino]-3,4-dioxo-cyclobut-1-enylamino]-4-methylsulfanyl-butylamide

M = 406.5; Elemental analyses C₁₈H₂₂N₄O₅S (Met/Tyr) (%), Calcd. C 53.1, H 5.4, N 13.7, S 7.8; Found C 52.7, H 4.9, N 13.5, S 7.9;

¹H NMR (DMSO- d₆, 250 MHz), δ (ppm): 9.20 (s, 1H, OH), 7.95 (m, 2H, NH), 7.70 (s, 2H, NH₂), 7.27 (d, J=12.0 Hz, 2H, NH₂), 6.96 (d, J=8.4, 2H, Ar), 6.63 (d, J=8.4, 2H, Ar), 4.76 (d, J=7.1, 1H, CH), 4.63 (d, J=5.7, 1H, CH), 2.78-2.98 (m, 2H, CH₂), 2.40 (m, 2H, CH₂), 2.02 (s, 3H, SCH₃), 1.86 (m, 2H, CH₂)

¹³C NMR (DMSO- d₆, 250 MHz), δ (ppm): 182.42, 172.02, 167.20, 166.93, 162.38, 156.01, 130.42, 126.65, 114.98, 57.32, 55.24, 35.85, 34.58, 30.83, 28.72, 14.69

+ MS, m/e (relative intensity): 407.46 (M⁺).

RESULTS AND DISCUSSION

Synthesis

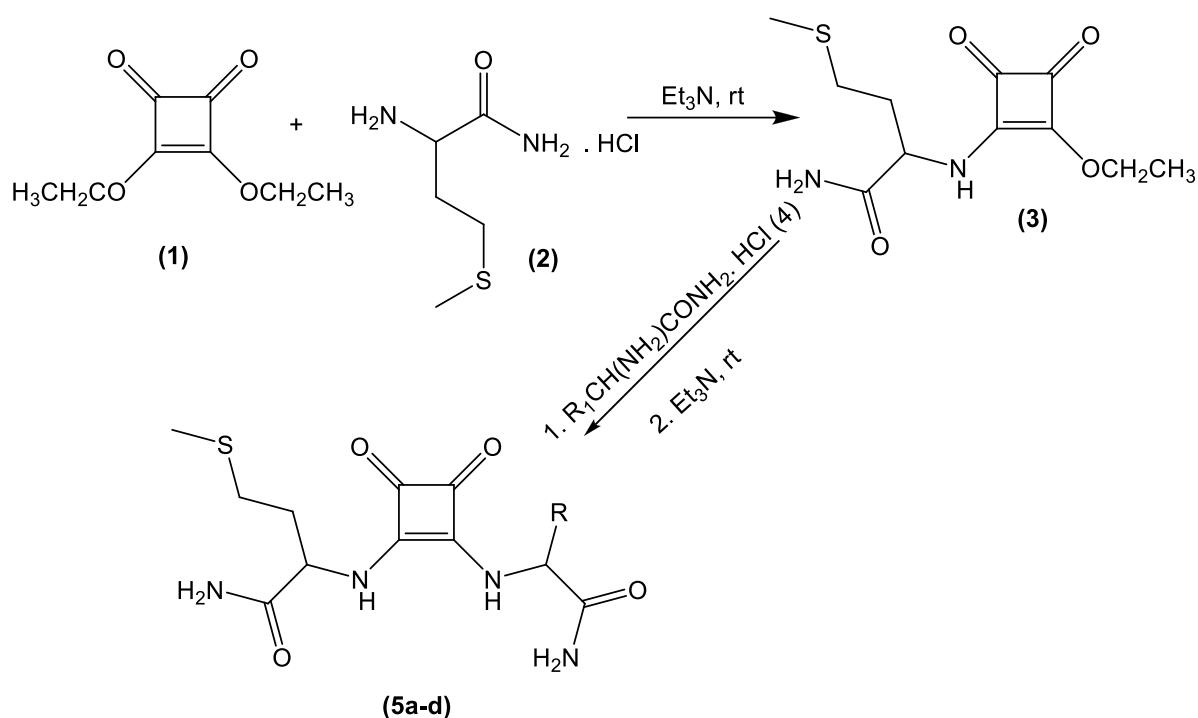
Nonsymmetric diamides of H₂Sq **5a-d** were prepared in two steps *via* condensation of amino acid amides and diethyl squarate (**1**), using as a catalyst Et₃N in ethanol at room temperature to methioninamide esteramide of H₂Sq (**3**) and condensation of monoamide to diamides. Synthetic pathway to obtain the new derivatives is illustrated on the Scheme 1. The synthesis and properties of methioninamide esteramide of squaric acid were described in our previously published work [17].

The products were isolated by precipitation from the corresponding reaction mixture in good to excellent yields and high purity (Table 1).

Vibrational analysis

For the investigated diamides of squaric acid the most important vibrational frequencies were stretching vibrations of amide NH₂ groups, secondary amino groups, ν^{as}_{C=O(Sq)}, ν^s_{C=O(Sq)}, ν_{C=C(Sq)}, Amide I (ν_{C=O}), amide II (δ_{NH₂}) and deformation vibrations of NH groups (δ_{NH}).

The accurate assignment of the main experimental frequencies of compounds **5a-d** to the corresponding normal modes was supported by B3LYP/6-311++G ** calculations.



Scheme 1. Synthesis of methionine containing diamides of squaric acid (**5a-d**).

Table 1. Diamides of squaric acid obtained according to the Scheme 1.

5	R		Reaction conditions*	Yield (%)	M.p. (°C)
a	-CH(CH ₃) ₂	(Val)	r.t., 17 h., EtOH/H ₂ O	75	325-334
b	-CH(CH ₃)CH ₂ CH	(Ile)	r.t., 20 h., EtOH/H ₂ O	86	330-349
c	-CH ₂ OH	(Ser)	r.t., 24 h., EtOH/H ₂ O	80	330-351
d	-CH ₂ C ₆ H ₄ OH	(Tyr)	r.t., 24 h., EtOH/H ₂ O	85	210-266

*Temperature, reaction time, solvent

Selected experimental and calculated vibrations are summarized in Tables 2 and 3. Predicted frequency of the stretching vibrations of the amide groups and secondary amino groups occur at higher frequencies in comparison with the experimental data. This discrepancy is due to the fact that the calculations were performed in the gas phase, where there are no intramolecular hydrogen bonds, while IR spectra were measured in the solid state, where in the formation of hydrogen bonds is possible.

The vibrations of cyclobutene fragment appear as a two bands for the C=O bonds (weak symmetric, strong asymmetric) and a very intensive band for C=C bond. The band for the stretching vibration of double bond in diamides of H₂Sq was shifted to lower frequency, while the bending vibrations of the amino groups were shifted to high

frequency in comparison with esteramides.

As should be expected, in the case of **5c** and **5d** the ν_{OH} vibration was influenced by hydrogen bonding and its assignment to a separate band in the spectrum was difficult. The bands for ν_{OH} and $\nu_{NH_2}^{as}$ were overlapped, the first one appeared as a shoulder of the second one.

NMR analysis

The NMR spectra of compounds showed protons signals for the secondary amino groups around 8.02-7.94 ppm. The protons of primary amino groups were observed as a doublet in the 7.32-7.25 ppm and 7.76-7.72 ppm. In the case of the compound **5d** signals appeared as a singlet at 7.71 ppm and a doublet at 7.27 ppm ($J=12.0$ Hz).

Table 2. Selected theoretical and experimental vibrational frequencies (ν in cm^{-1}) of **5a** and **5b**.

Assignment ^a	5a		5b	
	<i>B3LYP</i> ^b	IR	<i>B3LYP</i> ^b	IR
$\nu^{\text{as}}_{\text{NH}_2}$	3544; 3541	3353, 3333	3544, 3542	3356; 3332
ν_{NH}	3465; 3458	3272, 3248	3466, 3455	3278; 3250
$\nu^{\text{s}}_{\text{NH}_2}$	3397; 3379	3201, 3166	3401, 3378	3170; 3141
$\nu^{\text{s}}_{\text{C=O}}$ (Sq)	1785	1805	1785	1803
$\nu^{\text{as}}_{\text{C=O}}$ (Sq)	1693	1702	1692	1700
$\nu_{\text{C=O}}$ (Amide I)	1711; 1706	1670, 1660	1711; 1706	1670; 1658
δ_{NH_2} (Amide II)	1588; 1587	1647, 1636	1587; 1585	1648sh; 1638
$\nu_{\text{C=C}}$ (Sq)	1597	1590	1596	1595
δ_{NH}	1476	1538, 1527	1475	1538; 1529
$\nu_{\text{C-S(CH}_3)}$	683	721	684	721

^aVibrational modes: ν , stretching; δ , bending^bScaled by 0.9686 [18]**Table 3.** Selected theoretical and experimental vibrational frequencies (ν in cm^{-1}) of **5c** and **5d**.

Assignment ^a	5c		5d	
	<i>B3LYP</i> ^b	IR	<i>B3LYP</i> ^b	IR
ν_{OH}	3701	3471sh	3714	3438sh
$\nu^{\text{as}}_{\text{NH}_2}$	3554; 3543	3374sh; 3340	3549; 3543	3400sh
ν_{NH}	3466; 3450	3273; 3250sh	3466; 3464	3272; 3167
$\nu^{\text{s}}_{\text{NH}_2}$	3419; 3384	3172; 3140	3395; 3381	3370; 3325
$\nu^{\text{s}}_{\text{C=O}}$ (Sq)	1787	1809	1786	1809
$\nu^{\text{as}}_{\text{C=O}}$ (Sq)	1697	1705	1693	1700
$\nu_{\text{C=O}}$ (Amide I)	1717; 1710	1676; 1666	1712; 1705	1673; 1653
δ_{NH_2} (Amide II)	1587; 1586	1646sh; 1623	1588; 1586	1612; 1606
$\nu_{\text{C=C}}$ (Sq)	1598	1593	1598	1597
δ_{NH}	1476	1539; 1520	1475	1533; 1521
$\nu_{\text{C-S(CH}_3)}$	684	721	683	721

^aVibrational modes: ν , stretching; δ , bending^bScaled by 0.9686 [18]

In the experimental ^{13}C NMR spectra the signals of the carbon atoms of the cyclobutene moiety appeared at a slightly higher field (167 ppm and 182 ppm) than that of the methioninamide esteramide of squaric acids (170 ppm and 188 ppm). The amide carbons were detected at 172–173 ppm in the ^{13}C NMR spectra. The carbon atoms from C=C bond in diamides are shifted to higher fields than those of esteramides.

Computational analysis

Due to the difficulties to obtain crystals suitable for X-ray analysis we studied the structure of the diamides of H_2Sq mainly by theoretical methods. All the structures were optimized at the DFT level/*B3LYP* functional and the 6-311++ G^{**} basis set. The calculations were used to obtain important information about the structural characteristics and spectroscopic properties of synthesized compounds (**5a-d**). The optimized structures of the compounds (**5a-d**) are presented in Figure 1.

Since all investigated compounds contain Sq fragment and methioninamide residue, the theoretically found structural parameters for this part of the molecule were compared with the corresponding experimental data from the X-ray analysis for methioninamide and valinamide esteramides of H_2Sq [17,19]. Squaric fragment and NH-groups lied in one plane which was almost perpendicularly oriented to the plane of asymmetric C-atom and amides groups ($76-77^\circ$). By comparing the theoretical data of the studied methioninamide containing diamides of H_2Sq with experimental data of the methioninamide esteramide, it becomes apparent that the theoretical method predicts with particularly good accuracy the lengths of the C=O (theor. 1.21 Å, exp. 1.21 Å) and C=C (theor. 1.40 Å, exp. 1.39 Å) bonds in the cyclobutene ring. In contrast to methioninamide esteramide, due to the presence of two structurally analogous substituents on the cyclobutanedione ring, the lengths of the carbonyl bonds of the diamides H_2Sq were the identical.

CONCLUSION

In summary, an efficient and simple method was used to prepare a novel methioninamide containing diamides of squaric acid. The structures of the synthesized compounds were confirmed by IR, ^1H NMR, ^{13}C NMR spectra and elemental analyses. We determined the frequency range of the most characteristic vibrations - $\nu^{\text{as}}_{\text{C}=\text{O}(\text{Sq})}$, $\nu^{\text{s}}_{\text{C}=\text{O}(\text{Sq})}$, $\nu_{\text{C}=\text{C}(\text{Sq})}$, Amide I ($\nu_{\text{C}=\text{O}}$), Amide II (δ_{NH_2}) and δ_{NH} . The molecular optimization showed that the NH-groups lie in plane of squaric fragment which was almost perpendicularly oriented to the plane of asymmetric C-atom and amides groups.

REFERENCES

1. C. M. Antonio, M. C. Nunes, H. Refsum, A. Abraham, *Biochem. J.* **328**, 165 (1997)
2. A. L. Miller, N. D. Kelly, G. S. Kelly, *Altern. Med. Rev.* **1**, 220 (1996)
3. R. Ian Storer, C. Aciroa, L. H. Jones, *Chem. Soc. Rev.*, **40**, 2330 (2011)
4. K. Sato, K. Seio, M. Sekine, *J. Am. Chem. Soc.* **124**, 12715 (2002)
5. K. Seio, T. Miyashita, K. Sato, M. Sekine, *Eur. J. Org. Chem.* 15163 (2005)
6. M. Ohono, S. Eguchi, *Top Heterocycl. Chem.* **6**, 1 (2006)
7. M. B. Onaran, A. B. Comeau, C. T. Seto, *J. Org. Chem.* **70**, 10792 (2005)
8. S. Hanessian, V. Vinci, L. Auzzas, M. Marzi, G. Giannini, *Bioorg. Med. Chem. Lett.*, **16**, 4784 (2006)
9. P. Manesiotis, A. Riley and B. Bollen, *J. Mater. Chem. C*, **2**, 8990 (2014)
10. L. Titze, *Bioconjug. Chem.* **2**, 148 (1991)
11. H. Yan, A. L. Aguilar, Y. Zhao, *Bioorg. Med. Chem. Lett.*, **17**, 6535 (2007)
12. J. P. Malerich, K. Hagihara, V. H. Rawal, *J. Am. Chem. Soc.*, **130**, 14416 (2008)
13. G. Kardos, T. Soós, *Eur. J. Org. Chem.* 4490 (2013)
14. M.J. Frisch, G.W. Trucks, H.B. Schlegel, G.E. Scuseria, M.A. Robb, J.R. Cheeseman, G. Scalmani, V. Barone, B. Mennucci, G.A. Petersson, H. Nakatsuji, M. Caricato, X. Li, H.P. Hratchian, A.F. Izmaylov, J. Bloino, G. Zheng, J.L. Sonnenberg, M. Hada, M. Ehara, K. Toyota, R. Fukuda, J. Hasegawa, M. Ishida, T. Nakajima, Y. Honda, O. Kitao, H. Nakai, T. Vreven, J.A. Montgomery, J.E. Peralta, F. Ogliaro, M. Bearpark, J.J. Heyd, E. Brothers, K.N. Kudin, V.N. Staroverov, R. Kobayashi, J. Normand, K. Raghavachari, A. Rendell, J.C. Burant, S.S. Iyengar, J. Tomasi, M. Cossi, N. Rega, J.M. Millam, M. Klene, J.E. Knox, J.B. Cross, V. Bakken, C. Adamo, J. Jaramillo, R. Gomperts, R.E. Stratmann, O. Yazyev, A.J. Austin, R. Cammi, C. Pomelli, J.W. Ochterski, R.L. Martin, K. Morokuma, V.G. Zakrzewski, G.A. Voth, P.

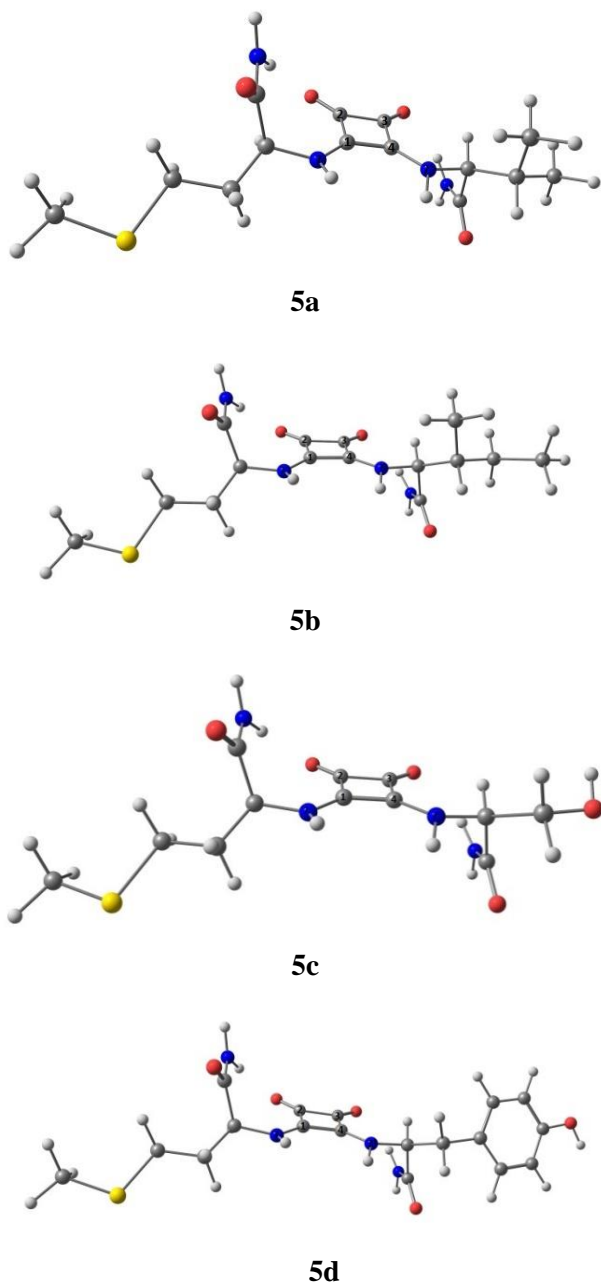


Fig. 1. Optimized structure of methioninamide containing diamides of H_2Sq , performed at DFT/B3LYP/6-311++G** level.

The $\text{C}_1\text{-N}_7$ and $\text{C}_4\text{-N}_7$ bonds that connect the Sq fragment with the amino acid residue were also similar and were in the range of 1.341-1.346 Å, independently of the side chains. In alkyl side chains, as in the experimentally studied squamarides, these bonds were shorter with 0.027-0.021 Å [20].

- Salvador, J. J. Dannenberg, S. Dapprich, A.D. Daniels, O. Farkas, J. B. Foresman, J. V. Ortiz, J. Cioslowski, D. J. Fox, Gaussian 09, Revision A1, Gaussian Inc., Wallingford, CT, 2009
15. P. J Stephens, F. J Devlin, C. F Chabalowski, M. J. Frisch, *J. Phys. Chem.*, **98**, 11623 (1994)
16. C. T Lee, W. T Yang, R. G. Parr, *Phys. Rev. B*, **37**, 785 (1988)
17. T. Kolev, E. Cherneva, M. Spiteller; W. S. Sheldrick, H. Mayer-Figge, *Acta. Cryst. E* **62**, o1390 (2006)
18. J. Merrick, D. Moran, L. Radom, *J. Phys. Chem. A* **111** 11683 (2007)
19. T. Kolev, B. B. Koleva, E. Cherneva, M. Spiteller, W. S. Sheldrick, H. Mayer-Figge, *Struct. Chem.* **17**, 63 (2006)
20. G. Ambrosi, M. Formica, V. Fusi, L. Giorgi, A. Guerri, M. Micheloni, P. Paoli, R. Pontellini, P. Rossi, *Chem. Eur. J.* **13**, 702 (2007)

ДИАМИДИ НА КВАДРАТНАТА КИСЕЛИНА, СЪДЪРЖАЩИ МЕТИОНИНАМИДОВ ОСТАТЪК – СИНТЕЗ, СПЕКТРАЛНО И ТЕОРЕТИЧНО ИЗСЛЕДВАНЕ

Е. Чернева^{1*}, Ц. Колев²

¹ Катедра „Химия“, Фармацевтичен факултет, Медицински университет-София, ул. Дунав № 2, София 1000

² Институт по молекулярна биология "Акад. Румен Цанев", Българска академия на науките,
ул. Акад. Г. Бончев, бл. 21, София 1113, България

Постъпила на 02 май 2017 г.; Коригирана на 25 май 2017 г.

(Резюме)

Синтезирани са четири нови диамида на квадратната киселина с висок добив, кондензирайки метионинамид естерамид на квадратната киселина с различни амиди на аминокиселини. Новосинтезираните съединения са охарактеризирани чрез елементарен анализ, ИЧ и ЯМР спектроскопия. Молекулната структура на съединенията беше изследвана чрез DFT метод. Теоретичният анализ показва, че сквартната част и НН-групите лежат в една равнина, която се пресича от равнините на асиметричните С-атоми.

Phenolic acids content and antioxidant capacity of commercially available *Melissa officinalis* L. teas in Bulgaria

N. Petkova¹, I. Ivanov¹, D. Mihaylova^{2*}, A. Krastanov²

¹ Department of Organic Chemistry and Inorganic Chemistry, University of Food Technologies, 26 Maritza Blvd., Plovdiv, Bulgaria

² Department of Biotechnology, University of Food Technologies, 26 Maritza Blvd., Plovdiv, Bulgaria

Received April 12, 2017; Revised May 10, 2017

Dedicated to Acad. Ivan Juchnovski on the occasion of his 80th birthday

The Lemon balm (*Melissa officinalis* L.) is an important aromatic and medicinal plant from Lamiaceae family. Its leaves and essential oils are used in folk medicine for the treatment of fevers and colds, hyperthyroidism, headaches and toothaches. *Melissa officinalis* is a rich source of volatile oil, flavonoid glycosides and derivatives of caffeic acid (rosmarinic acid). The aim of current study was to evaluate and compare the polyphenol content and antioxidant activity of infusions prepared from commercially available lemon balm brands on Bulgarian market. The total polyphenol content was established to be in range from 18.17 ± 0.04 to 64.17 ± 0.52 mg GAE/g dw, the total derivatives of caffeic acid from 3.80 ± 0.05 to 21.66 ± 0.10 mg CAE/g dw, caffeic acid content from 0.16 ± 0.01 to 0.97 ± 0.03 mg/g dw and rosmarinic acid between 2.4 ± 0.02 and 23.1 ± 0.5 mg/g dw, respectively. *In vitro* radical scavenging activity was evaluated by DPPH method ($106.31 \pm 9.87 - 553.51 \pm 46.04$ mM TE/g dw) and the metal reducing antioxidant potential was established by CUPRAC method ($321.32 \pm 14.39 - 1476.63 \pm 11.32$ mM TE/g dw). As a result the consumption of *M. officinalis* infusions could be recommended as a good preventive and therapeutic source of biologically active substances with potential benefit effects.

Key words: lemon balm, infusion, phenolic compounds, antioxidant activity.

INTRODUCTION

An increasing attention is paid in recent years to the role of diet in human health. Nutraceuticals are widely accepted as an adjunct to conventional therapies for enhancing general well being of human body in addition to the resistance against diseases. Many researchers recognized as "alternative" therapy the use of traditional remedies to help curing diseases [1, 2].

Epidemiological studies have indicated correlation between the high intake of natural products and the reduced risk of various chronic diseases like atherosclerosis and cancer [3-5]. Medicinal plants are the main sources of natural antioxidants and in this respect are widely used in human nutrition. *Melissa officinalis* L. (lemon balm) belongs to the family of *Lamiaceae*. The most commonly known therapeutic properties of lemon balm are sedative, carminative, antispasmodic, antibacterial, antiviral, anti-inflammatory and antioxidative [6-14]. Leaves of *M. officinalis* L. have been frequently used in folk medicine and in the everyday life of the population as well [15]. The plant contains caffeic acid

derivatives (rosmarinic acid), flavonoids (cynaroside, cosmosin, rhamnocitrin, isoquercitrin), phenolic acid (carnosic acid), and triterpene acids (ursolic and oleanolic acid) [16].

Rosmarinic acid is originally identified in rosemary (*Rosmarinus officinalis* L.) and the structure was elucidated as an ester of caffeic acid and 3-(3,4-dihydroxyphenyl)lactic acid [17]. Since rosmarinic acid was identified to be the main compound responsible for the antiviral activity of lemon balm in treating *Herpes simplex* it content has attracted much attention [7, 12, 13]. In addition, caffeic acid has been proposed to act as a multipurpose active polyphenolic compound and its derivatives have also been subjected to considerable study [18]. Furthermore, it is known that the phenolic content in plants contribute to their antioxidant potential [19].

Due to the great variety of commercial available products on the market containing lemon balm, for consumers is difficult to choose a particular product. Therefore, the aim of the present research was to evaluate the polyphenolic compounds content and antioxidant capacity of *M. officinalis* L. infusions in respect to define the most appropriate product to be recommended for daily use.

* To whom all correspondence should be sent:
E-mail: dashamihaylova@yahoo.com

MATERIAL AND METHODS

Samples

Eight commercially available *Melissa officinalis* L. dry leaves tea bags of different Bulgarian brands (A-H) were purchased from the local market in Plovdiv (Bulgaria) and one sample (I) was harvested from a herbal garden (Kostievo village, Plovdiv region) and used in fresh state for analysis (Table 1). Two of the samples consisted mainly of leaves (I and E), two other of leaves and some stems (C and D), while in another four (B, F, G and H) both leaves and stems were presented and one consisted of leaves, stems and fruits (A). Brands A and B had both brown color, while the other samples were green. For each commercial lemon balm sample studied, three randomly chosen bags were used for analysis.

Infusion preparation

The aqueous extracts were obtained according to Pistón *et al.* [20]. In brief, infusions were prepared by adding 100 ml of hot water at 95 °C to 1 g of dried samples. The mixture was left to stand for 20 min and then it was filtered through filter paper.

Total caffeic acid derivatives

The lemon balm extract (1 ml) was added to 2 ml 0.5 M HCl, 2 ml Arnov's reagent, 2 ml NaOH (2.125 M) and 3 ml of water. Each solution was compared with the same mixture without Arnov's reagent. Absorbance was read at 525 nm. Total dihydroxycinnamic acid content (including caffeoyl derivatives) was expressed as mg chlorogenic acid derivatives (CAE) per g dw as previously described by Ivanov *et al.* [22].

Antioxidant activity assays

DPPH radical scavenging activity: Each lemon balm extract (150 µl) was added to 2850 µl freshly

prepared DPPH solution (0.1 mM in methanol). The mixtures were incubated for 15 min at 37 °C in darkness and the reduction of absorbance was measured at 517 nm. A calibration curve was created using Trolox as standard (0.005 - 1.0 mM) and the results were expressed in mM TE per g dw [21].

CUPRAC assay: The assay was performed according to Apak *et al.* [23] with some modifications. In brief, 1.0 ml 10 mM CuCl₂·2H₂O was mixed with 1.0 ml 7.5 mM Neocuproine in methanol, 1.0 ml 0.1 M ammonium acetate buffer (pH 7.0), 0.1 ml of the investigated infusion and 1.0 ml dd H₂O. The reaction was carried out for 20 min at 50 °C in darkness and the sample absorption at 450 nm was recorded against blank. Antioxidant activity was expressed as mM (TE)/g dw by using calibration curve, build in range of 0.05-0.5 mM Trolox.

Rosmarinic and caffeic acids content

The HPLC analyses were performed on HPLC system- Agilent 1220 Infinity LC system in order to establish both the rosmarinic and caffeic acids content. The mobile phase used for separation consisted of methanol : phosphoric acid (83 %) : water = 50 : 0.3 : 49.7 (v/v). UV-VIS detector operating at 327 nm and 26 °C, was used for detection. The flow rate was 1 ml/min and the duration of method was 15 min. The injection volume was 20 µl.

Statistical analysis

All measurements were carried out in triplicates. The results were expressed as mean ± SD and statistically analyzed using MS-Excel software.

Table 1. Commercial available tea products of *Melissa officinalis* L. explored

Brand name	Producer	Content in bags	Samples
Herbal tea Melissa	Bulgarian Herb Ltd., Plovdiv	dark brown leaves, fruits and stalks	A
Melissa Herbal tea	Bulgarian herb 1893, Ltd.	dark brown leaves and stalks	B
Melissa Bioprograma	Bioprograma Ltd, Dobroslavchi	dark green leaves and stem	C
Herbal Melissa	Eko Herb Pirin Ltd.	dark green leaves and stem	D
biVital Melissa	Eurostok Ltd, Sofia	Green leaves	E
Bioselect herbal tea Melissa	Mercuriy P&P, AD, Gabrovo	Green leaves and stem	F
Bioset Melissa	Bioset Ltd	Green leaves and stem	G
Tonika herb tea Melissa	ET Ve Pe Pi –Veso Pipev	Green leaves and stem	H
Plant from herbal garden	Kostievo, Plovdiv region	Green leaves	I

RESULTS AND DISCUSSION

Total phenolic content and total caffeic acid derivatives

In the present work, the total polyphenol content and total caffeic acid derivatives of nine *M. officinalis* samples were analyzed. Eight samples (A-H) were commercially available brands and the last sample (I) was harvested from a herbal garden in order to compare the different manner of harvesting and handling.

The total polyphenol content (TPC) in lemon balm was found to vary from 18.17 ± 0.04 in sample A to 64.17 ± 0.52 mg GAE/g dw in sample I (Table 2). It has to be noted that the highest value was established in the non-commercial sample. The values for brands C, E and F were relatively similar. As seen from the results, the polyphenolic content of the investigated *M. officinalis* samples varied depending on brands and on different content of the tea bags, respectively.

Table 2. Total phenolics and total caffeic acid derivatives content in *Melissa officinalis* infusions

Samples	Total phenolics, mg GAE ¹ /g dw	Total caffeic acid derivatives, mg CAE ² /g dw
A	18.17 ± 0.04	3.80 ± 0.05
B	27.45 ± 0.09	6.75 ± 0.12
C	49.49 ± 0.34	18.92 ± 0.44
D	41.97 ± 0.42	21.66 ± 0.10
E	54.36 ± 1.08	16.04 ± 0.20
F	49.25 ± 0.81	10.31 ± 0.08
G	42.97 ± 0.04	16.12 ± 0.12
H	27.07 ± 0.40	7.86 ± 0.12
I	64.17 ± 0.52	20.27 ± 0.30

¹GAE- gallic acid equivalents; ²CAE- caffeic acid equivalents

Rusaczonok *et al.* [24] reported for lemon balm infusions TPC of 209 ± 36.9 mg GA/g in addition to the established by Kratchanova *et al.* [25] total phenolic content in water and 80 % acetone extracts – 8240 ± 207 and 11885 ± 109 mg GAE/100g, respectively. On the other hand, Popova *et al.* [26] reported for infusion of *M. officinalis* TPC - 27.17 ± 0.51 mg GAE/g dw. Tusevski *et al.* [27] established that the total phenolic content in methanol ultrasound extract of Macedonian lemon balm was 70.86 ± 1.01 mg GAE/g dw.

As shown in Table 2, the total caffeic acid derivatives in *M. officinalis* infusions ranged from 3.80 ± 0.05 to 21.66 ± 0.10 mg CAE/g dw. The highest values

were established in sample D and non commercial sample I, confirming the reported for the total phenolic content. The wide variation of the caffeic acid derivatives content among the investigated samples should be noted. The brown colored herbal materials (A and B samples) were evaluated with the lowest content of both total phenolics and caffeic acids derivatives. Despite of its green color sample H shows relatively low values as well. The differences established could be due to a maturation, drying and type of the predominant plant parts as suggested by Gheisari and Abhari [28].

Caffeic and rosmarinic acids content

The caffeic acid content in the studied samples varied from 0.16 ± 0.01 to 0.97 ± 0.03 mg/g dw (Table 3). The highest values were detected in samples E and D. Regarding the rosmarinic acid content the highest values were established in samples D and I. However, the rosmarinic acid content in the samples varied considerably - from 2.4 ± 0.02 to 23.1 ± 0.5 mg/g dw. The lowest values were established in sample A. Ibragić *et al.* [29] examined lemon balm from Bosnia and Herzegovina and Turkey and established 0.14 and 0.71 mg caffeic acid/g of fresh weight and 5.10 and 0.24 mg rosmarinic acid/g of fresh weight, respectively. Dastmalchi *et al.* [30] identified rosmarinic acid as a major compound in the lemon balm by medium pressure liquid–solid extraction with aqueous ethanol.

Other authors reported dependence between the maximal yield of rosmarinic acid and the maturation stage. The highest results were established in the plant development phase of full flowering (3.91 %) [31]. Comparing the results, a difference among the various research papers had to be noted.

Table 3. Caffeic and rosmarinic acids content in *Melissa officinalis* infusions, mg/g dw

Sample/ Assay	Caffeic acid content	Rosmarinic acid content
A	0.16 ± 0.01	2.40 ± 0.02
B	0.31 ± 0.01	3.70 ± 0.03
C	0.57 ± 0.02	16.30 ± 0.43
D	0.96 ± 0.02	23.10 ± 0.5
E	0.97 ± 0.03	17.00 ± 0.21
F	0.44 ± 0.01	9.30 ± 0.08
G	0.63 ± 0.01	14.90 ± 0.08
H	0.40 ± 0.01	5.30 ± 0.03
I	0.84 ± 0.02	20.90 ± 0.56

This could be explained with the application of different extraction solvents and various plant parts as material for analysis. Several factors, including soil and climatic conditions, plant ontogenesis phases, harvest and plant storage [32-34] could affect the composition and may mislead the consumers. In addition, Rusaczonok *et al.* [24] have previously concluded difficulties for comparing results obtained by different studies due to the different approaches in extraction procedures, analytical methods and mathematical calculations.

Antioxidant activity

The antioxidant activity of *M. officinalis* samples was evaluated using two reliable methods- DPPH and CUPRAC assays. Comparing the results of both methods applied the objective evaluation of the antioxidant potential of the plant was possible. As shown on Table 4 the antioxidant potential toward the synthetic radical DPPH was in range from 106.31 ± 9.87 to 553.51 ± 46.04 mM TE/g dw, as the highest value was determined in sample I. The results regarding the CUPRAC assay showed the same tendency, the highest value was detected in sample I and the results varied from 321.32 ± 14.39 to 1476.63 ± 11.32 mM TE/g dw.

The conducted antioxidant activity assays revealed the higher potential of the harvested from a herbal garden *M. officinalis* - sample I. The same tendency was observed by the total phenolic content assay. This could be due to the more careful handling of the plant material when home grown.

Table 4. Antioxidant activity in *Melissa officinalis* infusions, mM TE/g dw

Sample /Assay	DPPH	CUPRAC
A	106.31 ± 9.87	321.32 ± 14.49
B	196.85 ± 14.98	545.71 ± 31.12
C	422.46 ± 4.19	1137.71 ± 41.55
D	310.87 ± 10.41	906.82 ± 16.2
E	441.75 ± 14.42	1165.05 ± 17.60
F	383.32 ± 9.47	1101.21 ± 11.13
G	337.08 ± 9.47	947.49 ± 5.56
H	176.38 ± 4.37	537.12 ± 8.67
I	553.51 ± 46.04	1476.63 ± 11.32

Popova *et al.* [26] reported for infusion of *M. officinalis* TEAC_{DPPH} - 389.52 ± 3.11 μ M TE/g dw and TEAC_{CUPRAC}- 715.54 ± 4.79 . μ M TE/g dw, respectively. Tusevski *et al.* [27] established for methanol extract of Macedonian lemon balm 542.28 ± 0.54 μ M TE/g dw according to CUPRAC

assay and 406.03 ± 13.57 μ M TE/g dw according to DPPH ones. In another study, Ivanova *et al.* [15] considered Bulgarian *M. officinalis* as plant with high antioxidative potential.

The present research concerned both polyphenolic constituents content and antioxidant properties and is carried out based on the lack of information and uniform methodology for *M. officinalis* infusions in the available literature. Authors used various methods of extraction (temperature, time, solvent) while preparing solutions for research and expressed the final results considering different calculations [15, 35-38]. This makes it difficult to compare results obtained in the present research with previously reported by other authors. In spite of this, great consistency was observed between the results obtained and previously published data. The differences in the antioxidant activity presented in previous studies may be due to implementation of different analytical methods and methods for infusions preparation (infusion concentration, temperature, brewing time). The antioxidant properties of plants and polyphenol content depend on many factors, i.e. soil and climate conditions in which plant was cultivated, harvest seasons, methods of processing and storage [39], parts of plant which the infusion was made of [15, 36, 40] and plant species [15]. Hence, the antioxidant properties of plant can be different in water infusions. That indicates the necessity of controlling and monitoring these parameters for each particular raw material.

CONCLUSION

The present study represents a detailed characteristic of different lemon balm (*Melissa officinalis* L.) brands commercially available on Bulgarian market compared to the harvested from a local herbal garden. The results obtained revealed lemon balm as good source of polyphenolic compounds especially rosmarinic acid resulted in antioxidant activity potential. The investigated samples consist of bioactive compounds in varying amounts, which could be possible due to the influence of different factors such as conditions of storage and drying, plant parts used, as well as the geographic and climatic growing conditions. The reported data provide to the consumer's valuable information for the quality of products as well as their beneficial health effects.

REFERENCES

1. C. Klein, T. Sato, M. M. Meguid, G. Miyata, *J. Gastroenterol.*, **35**, 1 (2000).
2. C. S. Ramaa, A. R. Shirole, A.S. Mundada, V. J. Kadam, *Curr. Pharm. Biotechnol.*, **7**, 15 (2006).
3. K. Hashimoto, S. Kawamata, N. Usui, A. Tanaka, Y. Uda, *Cancer Lett.*, **180**, 1 (2002).
4. J. Gundgaard, J.N. Nielsen, J. Olsen, J. Sorensen, *Public Health Nutr.*, **6**, 25 (2003).
5. A. Gosslau, K. Y. Chen, *Nutrition*, **20**, 95 (2004).
6. H. Wagner, L. Sprinkmeyer, *Dtsch. Apoth. Ztg.*, **113**, 1159 (1973).
7. G. May, G. Willuhn, *Arzneim.-Forsch.*, **28**, 1 (1978).
8. N. S. Masakova, B. S. Tserevatuy, S. L. Trofimenko, G. S. Remmer, *Planta Med.*, **36**, 274 (1979).
9. I. Koch-Heitzmann, W. Schultze, *Dtsch. Apoth. Ztg.*, **124**, 2137 (1984).
10. J. L. Lamaison, C. Petitjean-Freytet, A. Carnat, *Pharm. Acta Helv.*, **66**, 185 (1991).
11. J. L. Lamaison, C. Petitjean-Freytet, F. Duband, A. P. Carnat, *Fitoterapia*, **62**, 166 (1991).
12. H. J. Vogt, I. Tausch, R. H. Wölbling, R. M. Kaiser, *Allgemeinarzt*, **13**, 832 (1991).
13. B. Borkowski, A. Biesiadecka, *Herba Pol.*, **42**, 317 (1996).
14. K. Yamasaki, M. Nakano, T. Kawahata, H. Mori, T. Otake, N. Ueba, I. Oishi, R. Inami, M. Yamane, M. Nakamura, H. Murata, T. Nakanishi, *Biol. Pharm. Bull.*, **21**, 829 (1998).
15. D. Ivanova, D. Gerova, T. Chervenkov, T. Yankova, *J. Ethnopharmacol.*, **69**, 145 (2005).
16. W. Schultze, W. A. Kolnig, A. Hilker, R. Richter, *Dtsch. Apoth. Ztg.*, **135**, 557 (1995).
17. M.L. Scarpati, G. Oriente, *Ric. Sci.*, **28**, 2329 (1958).
18. G. Murtaza, A. Sajjad, Z. Mehmood, S. H. Shah, A. R. Siddiqi, *J. Food Drug. Anal.*, **23**, 11 (2014).
19. H. Chen, Y. Zuo, Y. Deng, *J. Chromatogr. A*, **913**, 387 (2001).
20. M. Pistón, I. Machado, C. S. Branco, V. Cesio, H. Heinzen, D. Ribeiro, E. Fernandes, R. C. Chisté, M. Freitas, *Food Res. Int.*, **64**, 150 (2014).
21. I. Ivanov, R. Vrancheva, A. Marchev, N. Petkova, I. Aneva, P. Denev, V. Georgiev, A. Pavlov, *Int. J. Curr. Microbiol. App. Sci.*, **3**, 296 (2014).
22. I. Ivanov, *Int. J. Pharm. Phytochem. Res.*, **6**, 889 (2014).
23. R. Apac, K. Güçlü, B. Demirata, M. Özyürek, S. E. Çelil, B. Bektaşoğlu, K. I. Berker, D. Özyurt, *Molecules*, **12**, 1496 (2007).
24. A. Rusaczonek, F. Świdorski, B. Waszkiewicz-Robak, *Pol. J. Food Nutr. Sci.*, **60**, 33 (2010).
25. M. Kratchanova, P. Denev, M. Ciz, A. Lojek, A. Mihailov, *Acta Bioch. Pol.*, **57**, 229 (2010).
26. A. Popova, Z. Dalemska, D. Mihaylova, I. Hristova, I. Alexieva, *Int. J. Pharm. Phytochem. Res.*, **8**, 634 (2016).
27. O. Tusevski, A. Kostovska, A. Iloska, L. Trajkovska, S. G. Simic, *Cent. Eur. J. Biol.*, **9**, 888 (2014).
28. H. Gheisari, K. Abhari, *Acta Sci. Pol., Technol. Aliment.*, **13**, 129 (2014).
29. S. Ibragić, M. Salihović, I. Tahirović, J. Toromanović, *Bull. Chem. Technol. Bosnia Herzeg.*, **42**, 47 (2014).
30. K. Dastmalchia, H. Dormana, P. Oiononena, Y. Darwisd, I. Laaksoa, R. Hiltunena, *LWT -Food Sci. Technol.*, **41**, 391 (2008).
31. J. Tóth, M. Mrlianová, D. Tekalova, W. Korenova, *Acta Facult. Pharm. Univ. Comenianae*, **50**, 139 (2003).
32. T. Adzet, R. Ponz, E. Wolf, E. Schulte, *Planta Med.*, **58**, 562 (1992).
33. S. Hose, A. Zänglein, T. Van Den Berg, W. Schultze, K. H. Kubeczka, F. C. Czygan, *Pharmazie*, **52**, 247 (1997).
34. M. Mrlianová, D. Tekel'ová, M. Felklová, V. Reinöhl, J. Tóth, *Planta Med.*, **68**, 178 (2002).
35. V. L. Singleton, R. Orthofer, R. M. Lamuela-Ravento's, *Methods Enzymol.*, **299**, 152 (1999).
36. D. Mantle, F. Eddeb, A. T. Pickering, *J. Ethnopharmacol.*, **72**, 47 (2000).
37. M. Zujko, A. Witkowska, B. Kiernozek, *Brom. Chem. Toksykol.*, **37**, 189 (2005). (in Polish; English abstract).
38. M. S. Cosio, S. Buratti, S. Mannino, S. Benedetti, *Food Chem.*, **97**, 725 (2006).
39. E. Capecka, A. Mareczek, M. Leja, *Food Chem.*, **93**, 223 (2005).
40. A. P. Carnat, A. Carnat, D. Fraisse, J. L. Lamaison, *Pharm. Acta Helv.*, **72**, 301 (1998).

СЪДЪРЖАНИЕ НА ФЕНОЛНИ КИСЕЛИНИ И АНТИОКСИДАНТЕН КАПАЦИТЕТ НА ЧАЙОВЕ
Melissa officinalis L., ДОСТЪПНИ В ТЪРГОВСКАТА МРЕЖА НА БЪЛГАРИЯ

Надежда Петкова¹, Иван Иванов¹, Даша Михайлова², Алберт Кръстанов²

¹ Катедра Органична химия и Неорганична химия, Университет по хранителни технологии, бул. „Марица“ 26, Пловдив, България

² Катедра Биотехнология, Университет по хранителни технологии, бул. „Марица“ 26, Пловдив, България

Постъпила на 12 април 2017 г.; Коригирана на 10 май 2017 г.

(Резюме)

Маточината (*Melissa officinalis* L.) е важно ароматно и лечебно растение от семейство Lamiaceae. Листата и етерични масла от нея се използват в народната медицина за лечение на треска и настинки, хипертироидизъм, главоболие и зъбобол. *Melissa officinalis* е богат източник на летливо масло, флавоноидни гликозиди и производни на кафеена киселина (розмаринова киселина). Целта на настоящото проучване е да се установи и да се сравни съдържанието на полифеноли и антиоксидантна активност на инфузии, приготвени от достъпни на българския пазар марки маточина. Установено е общото съдържание на полифеноли в диапазон от $18,17 \pm 0,04$ до $64,17 \pm 0,52$ mg GAE/g dw, на общите деривати на кафеена киселина от $3,80 \pm 0,05$ до $21,66 \pm 0,10$ mg CAE/g dw, съдържание на кафеена киселина от $0,16 \pm 0,01$ до $0,97 \pm 0,03$ mg/g dw и на розмаринова киселина между $2,4 \pm 0,02$ и $23,1 \pm 0,5$ mg/g dw, съответно. *In vitro* радикал улавящата активност е оценена чрез DPPH метод ($106,31 \pm 9,87$ - $553,51 \pm 46,04$ mM TE/g dw), а метал редуциращия антиоксидантен потенциал е установен чрез CUPRAC метод ($321,32 \pm 14,39$ - $1476,63 \pm 11,32$ mM TE/g dw). В резултат на това консумацията на инфузии от *M. officinalis* може да се препоръча като добър превантивен и терапевтичен източник на биологично активни вещества с потенциалните ползи ефекти.

Production of adsorbents from "End of Life" tyres and characterization of their porous structure

L. Gonsalvesh^{1*}, M. Dimov², S. P. Marinov³

¹Central Scientific Research Laboratory, Assen Zlatarov University, Burgas 8000, Bulgaria

²Department of Physical and Organic Chemistry, Assen Zlatarov University, Burgas 8000, Bulgaria

³Institute of Organic Chemistry with Centre of Phytochemistry, BAS, Sofia 1113, Bulgaria

Received April 11, 2017; Revised May 15, 2017

Dedicated to Acad. Ivan Juchnovski on the occasion of his 80th birthday

The valorisation of waste tyres into adsorbents, i.e. technical and activated carbons, is considered in the current research. The technical carbons (TCs) are prepared through treatments with conc. HNO₃, conc. HNO₃ + conc. H₃PO₄ or conc. HNO₃ + C₂H₄Cl₂ and subsequent Soxhlet extraction with acetone, while activated carbon (AC) is obtained through physical activation of TCs in a stream of water vapour. Using low temperature N₂ adsorption and Surfer apparatus of Thermo Scientific, the adsorption isotherms of samples under consideration are measured and used for assessment of porous structure. It has been revealed that TCs are mesoporous material characterized by "poor" porous structure since calculated S_{BET} and $V_{0.95}$ are rather low, i.e. up to 63 m² g⁻¹ and 0.205 cm³ g⁻¹, respectively. Thus further processing as physical activation is required in order to improve their porous texture characteristics and respectively their adsorption abilities. The obtained AC exhibits much better developed porous structure represented by micro- and the mesopores. The calculated S_{BET} and $V_{0.95}$ are 527 m² g⁻¹ and 0.489 cm³ g⁻¹, respectively. This determines the promising features of prepared AC to be used as an adsorbent.

Key words: „end of life” tyres, technical and activated carbons, N₂ adsorption isotherms, porous structure

INTRODUCTION

The outstanding increase in the number of vehicles worldwide and the lack of adequate processing of the "end of life" (waste tyres), define the last as a serious ecological problem in terms of waste disposal. Consequently, the increased ecological concern has led to environmental legislation norms that limits the landfill of "end of life" tyres [1] and policies that encourage the valorisation of this waste stream and has driven the tyre sector towards recovery and recycling [2]. However, since tyres are complex materials designed to be resistant to severe mechanical stress and different weather conditions their recycling and further processing is not an easy task.

Tyres are a mixture of constituent components such as rubbers (60-65 wt.%, in the form of natural rubber and synthetic rubber, i.e. butyl rubber and styrene-butadiene rubber), carbon black (25-35 wt.%), steel, textiles and some inorganics acting as accelerators and fillers [2-4]. The tyre manufacturing process involves vulcanization during which irreversible reactions between elastomers, sulphur and other reagent take place and creates a three-dimensional chemical network

through formation of crosslinks between the elastomer molecular chains [4]. Thus created cross-linked elastomers are solid, insoluble and infusible thermoset materials that define high strength and elasticity properties to tyres and hinder their decomposition.

Recently, the European tyre industry has been trying to move towards a zero-waste scenario and increased valorisation of "end of life" tyres through their recycling or usage for energy recovery [2]. From recycling point of view, the tyres recovered rubber can be incorporated in asphalt and concrete and thus lighten material with high durability and increased resistance to cracking, deformation, and aggressive reagents can be obtained [2]. The steel elements recovered from tyres can be reused for production of new steel and reinforced concrete. However, the level of contamination of recovered components, i.e. rubber or steel, is a critical factor affecting the quality of the obtained end product.

The energetic valorisation is a valuable use of "end of life" tyres [5]. In this sense, the thermochemical methods as combustion, gasification and pyrolysis have been studied [4-6]. The incineration or combustion are considered as the easiest and cheapest processes for production of energy from tyres [6]. However both are rather not

* To whom all correspondence should be sent:
E-mail: lenia_gonsalvesh@abv.bg

advisable due to the release of serious poisonous emissions as NO_x, CO/CO₂, SO₂, PAH, which are higher even in comparison to combustion of fossil fuels. Gasification and pyrolysis are more attractive approaches to tackle the waste tyres valorisation due to the less environmental impact. Additionally, value added products are produced. Pyrolysis results in high-energy-density volatile gases (condensable and non-condensable) that can be used as a fuel or chemical feedstock and solid carbonaceous fraction, named char or pyrolytic carbon black, that can be used as a fuel, carbon black or adsorbent. However, the use of pyrolytic char as a fuel and carbon black is limited. The combustion of tyre char is rarely applied due to required long residence times at elevated temperature and high rate of unburned particle [4]. The char is not often reused as carbon black as well due to the presence of organic impurities, high ash content, low surface area, large particle size, and due to the fact that it does not seem to have the particle structure desired for rubber compounding [7]. The most proper application of pyrolytic char seems to be as adsorbent after its upgrade at higher temperature by means of physical [8-11] or chemical treatment [12-15] into activated carbon (AC). Thus prepared ACs can be used as cheap adsorbents with broad applications, i.e. environmental protection and recovery of chemicals with added value. However, the specific application of tyre based ACs depends on their characteristics, i.e. porous texture and surface chemistry, determined by the composition and peculiarities of the initial precursor, nature of activating agent and process parameters [3,4,16].

It has been found that immediate reaction of tyre wastes with concentrated nitric acid undergoes through nitration, oxidation and destruction processes that leads to formation of polyfunctional products (PFPs), low-molecular carboxylic acids and carbonaceous solid residue (technical carbon, TC) after subsequent extraction with a suitable organic solvent [17]. PFPs have been reported to be used as a growth stimulators and as an incubation medium for microorganisms, while the TC has been tested as an adsorbent for removal Cu²⁺ ions from aqueous solution [17-19].

The objective of the current research is to characterize the porous structure of carbonaceous solid residues produced by oxidative destruction of waste tyres and an activated carbon obtained on their basis and to assess the possibility of their usage as adsorbents.

MATERIALS AND METHODS

Precursor and applied treatments

"End of life" tyres (with an average particle sizes of 0.2-0.4 mm) supplied by A Factory of Rubber Productivities-LTD, Yambol, Bulgaria were used as a carbon precursor feedstock. The tyre particles (10 g) were gradually added with an average rate of 0.2 g min⁻¹ to 30 ml 65% HNO₃ (p.a., Merck) (treatment A) or its mixture with 20 ml 85% H₃PO₄ (p.a., Merck) (treatment B) or with 20 ml C₂H₄Cl₂ (p.a., Merck) (treatment C) as described in Fig. 1. The treatments were conducted at 60 °C and continuous stirring for 2h. The reaction products were cooled down and subjected to filtration. Low-molecular dicarboxylic acids were leached in the filtrate, while the solid residue is an oxygenated vulcanized rubber, comprising the mixture of PFP and TC [18]. The obtained solid residue was extensively rinsed up to neutral reaction and dried at 60 °C up to constant weight. For separation of PFP and TC, the solid residues were placed in a Soxhlet thimble and extracted by acetone (~300ml), with a reflux process continuing for about 24 h. The concentrated after vacuum distillation acetone extracts were poured into water and PFP precipitates were formed. The TC residues, i.e. TC-A (obtained after treatment A, Fig.1), TC-B (obtained after treatment B, Fig.1) and TC-C (obtained after treatment C, Fig.1), left in the Soxhlet thimble were dried and subjected to porous structure characterization and further processing in the current study.

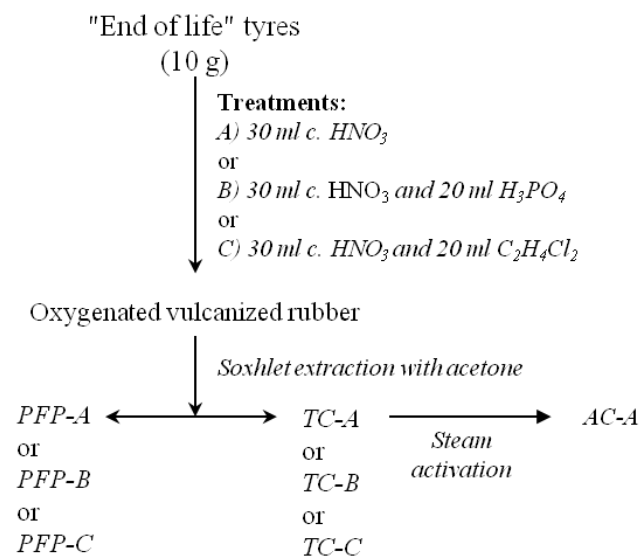


Fig. 1. Experimental strategy

Preparation of activated carbon (AC) through physical activation typically comprises a two-stage pyrolytic process. Carbonization of the precursor is carried out in the first stage, while in the second step the physical activation of the resulting char is performed in the presence of suitable oxidizing gases such as water vapour, CO₂ and others. In the present study a relatively new, one-stage pyrolysis process in the presence of water vapour is applied [20]. The technical carbons (particle size <0.2 mm) were pyrolysed in a stainless steel reactor at the following experimental conditions: heating rate of 10 °C min⁻¹ in an inert atmosphere up to 400 °C, kept isothermal for 15 min, then heating continued up to activation temperature of 800 °C, kept isothermal for 30 min. When the activation temperature was reached, the inert atmosphere was switched to steam with a constant water vapour flow of 2 ml min⁻¹. The process was ended with the cooling of the reactor in an inert atmosphere and drying of the resultant AC at 110 °C.

Characterization of the samples under study

The TC and AC samples were subjected to thermogravimetric analysis (TGA) for obtaining data of proximate analysis (i.e. moisture (*W*), volatile matter (*VM*), fixed carbon (*C_{fix}*) and ash (*A*) contents) using a Netzsch STA 449 F3 Jupiter thermogravimetric analyser as described in Gonsalvesh et. al. [21,22]. A porous textural characterization was carried out by measuring nitrogen adsorption isotherms at -196 °C on an automatic apparatus Surfer sorption analyzer (Thermo Scientific). The surface area of the TCs and AC is determined by the BET method (*S_{BET}*) using data from the adsorption isotherms in the range of relative pressures up to 8.3.10⁻² (for hybrid type isotherms I-IV) or from 0.05 to 0.28 (for isotherms type IV) [23,24]. The total pore volume, known as volume of *Gurvich*, is determined based on the volume of adsorbate *V_{0.95}*, recorded on the desorption branch of the adsorption isotherm at a relative pressure $P_i/P_0 = 0.95$. The micropore volume (*V_{DR,micro}*) is calculated by using the Dubinin-Radushkevich equation up to $P_i/P_0 \leq 0.15$ [25]. The pore size distribution and pore diameters *L₀* are obtained by applying the Non Local Density Functional Theory (NLDFT) on N₂ adsorption data [26].

RESULTS AND DISCUSSION

The proximate analysis and yields of TC samples are gathered in Table 1. Apparently the obtained TCs are carbon-enriched products as *C_{fix}*

Table 1. Proximate analysis and recoveries of samples under consideration in wt.%

Sample	<i>W</i>	Ash ^{db}	VM ^{daf}	<i>C_{fix}</i> ^{daf}	Re
TC-A	3.5	9.2	7.4	83.4	35.6
TC-B	4.3	13.5	11.7	74.8	32.0
TC-C	5.1	3.4	7.1	89.5	31.0
AC-A	12.0	5.5	7.5	87.0	49.0*

^{db}-dry basis; ^{daf}-dry ash free basis; *calculated based on TC-A sample.

content varies in the range of 74.8 to 89.5 wt.%. The highest *C_{fix}* content and lowest VM and Ash contents are registered for TC-C sample, while TC-B sample is characterized by the highest VM and ash contents and lowest *C_{fix}* content. Consequently it can be assumed that applied treatments for production of TC samples somewhat influence their proximate characteristics. The recoveries of obtained TCs are in the range of 31.0 - 35.6 wt.%. It should also be mentioned that both proximate characteristics and recoveries of studied TCs are comparable to that of pyrolytic carbon black [3,4,27,28]. This largely means that TCs obtained by applying our experimental strategy have relevance and applications commensurable with that of pyrolytic carbon black.

The N₂ adsorption isotherms of TC samples are shown on Fig. 2.

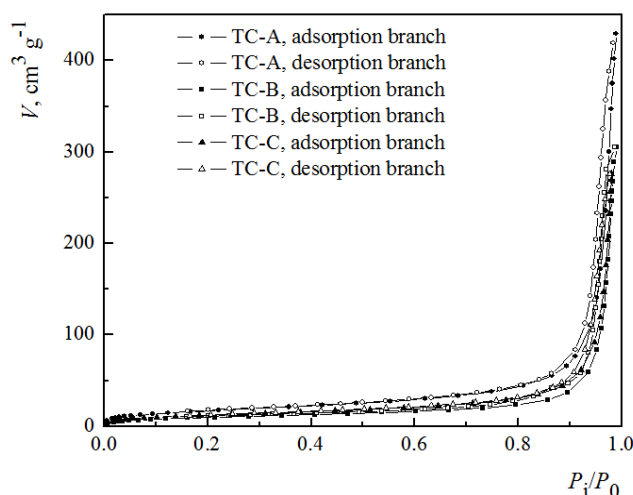


Fig. 2. N₂ adsorption isotherms of TCs obtained from "end of life" tyres

It can be seen that TC samples are characterized by adsorption isotherms of type IV according to

classification of IUPAC, which are typical for mesoporous materials. The existence of discrepancy between the adsorption and desorption branches of the isotherms, i.e. hysteresis loop, is an indication for differences in the mechanisms of pore filling with an adsorbate and its evaporation and the presence of mesoporous structure in which a capillary condensation of the adsorbate occurs. The type of hysteresis loop for various mesoporous materials can be different, depending on the nature of mesoporous material and the shape and size of its pores. In our study hysteresis loops of type H-1 according to classification of IUPAC are observed in the course of all isotherms of TC samples. This can be related to cylindrical geometry of the mesopores and the high degree of uniformity of the pore sizes. Inasmuch as registered hysteresis loops are pulled to the high relative pressures it can be assumed that the size of the mesopores is rather large.

Pore size distribution of investigated TCs is assessed as well by applying NLDFT theory. Inasmuch as cylindrical geometry of mesopores is supposed, the *n2c77_cyl* kernel developed for carbon materials with cylindrical pores is used for NLDFT computation. The theoretical adsorption isotherms described by using this kernel is in best agreement with the registered experimental adsorption isotherms of the TCs. The obtained pore size distribution of TCs is presented in Fig. 3. The maximums in the pore size distribution curve correspond to the prevailing pore sizes of the investigated samples. It can be clearly seen that pore size distribution curves, built according to NLDFT computational procedure exhibit a bimodal distribution of the pore volumes with a predominant L_0 about 32.34 and 43.36 nm.

The monolayer capacities α_m of the TC samples, on the basis of which the specific surface areas and physicochemical constants C are calculated, are determined using the linear form of the BET adsorption isotherm (Fig. 4). The obtained results together with the total pore volume of *Gurvich* and micro- and mesopore volumes of investigated TCs are summarized in Table 2.

Analysis of the obtained data confirms aforementioned peculiarities: i) porous texture characteristics of prepared TCs do not differ considerably; ii) indeed the prepared TCs are mesoporous materials since V_{meso} (about 90%) significantly prevails over $V_{DR,micro}$. However, the calculated S_{BET} and $V_{0.95}$ are rather low, which hinder adsorption abilities of prepared TCs and thus further processing is required in order to improve

their porous characteristics. S_{BET} and $V_{0.95}$ varied in the range of 36 - 63 $m^2 g^{-1}$ and 0.121 - 0.205 $cm^3 g^{-1}$, respectively, as both parameters maximizing in the case of TC-A sample. This is an indication that among applied treatments, i.e. HNO_3 , $HNO_3+H_3PO_4$ and $HNO_3+C_2H_4Cl_2$ (see Fig.1), the one using only HNO_3 leads to better development of mesoporous structure. Therefore exactly TC-A samples is subjected to further processing into AC.

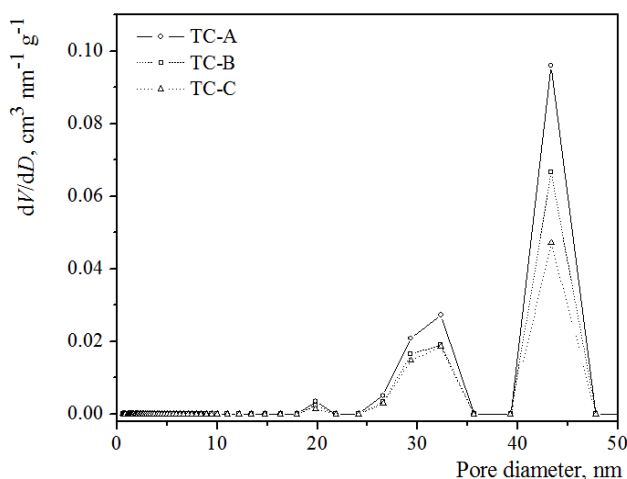


Fig. 3. Pore size distribution of TCs obtained from "end of life" tyres

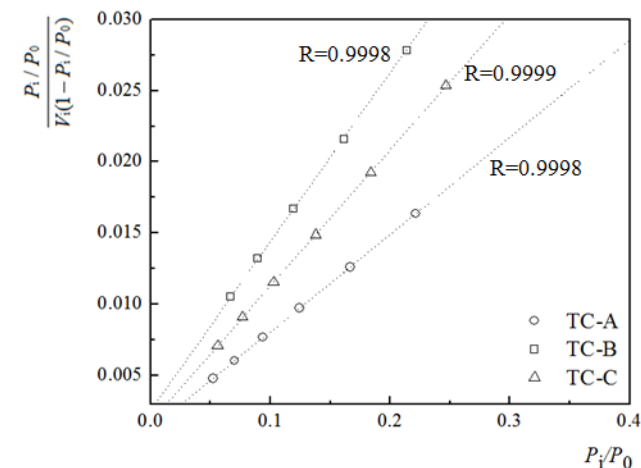


Fig. 4. The linear form of the BET equation for TCs.

The proximate analysis and the yield of AC-A sample are presented in Table 1. Clearly, a good yield of AC (49.0 wt.%) with relatively low ash content (5.5 wt.%) is obtained. However, of outmost importance is the porous structure. The N_2 adsorption isotherms of AC-A sample is visualized on Fig. 5 together with N_2 adsorption isotherms of TC-A sample for better comparison and clearness of presentation.

Table 2. Textural properties of prepared TCs and AC

Sample	$V_{0.95}$ ($\text{cm}^3 \text{g}^{-1}$)	S_{BET} ($\text{m}^2 \text{g}^{-1}$)	C	$V_{\text{DR,micro}}$ ($\text{cm}^3 \text{g}^{-1}$)	V_{meso}^* ($\text{cm}^3 \text{g}^{-1}$)	$V_{\text{mezo}}/V_{0.95}$	L_0 (nm)
TC-A	0.205	63	56.1	0.021	0.184	0.90	32.34
							43.36
TC-B	0.121	36	47.3	0.012	0.109	0.90	32.34
							43.36
TC-C	0.148	48	55.6	0.015	0.133	0.90	32.34
							43.36
AC-A	0.489	527	2240.8	0.207	0.282	0.58	1.68
							2.11
							2.82
							43.36

$$V_{\text{meso}}^* = V_{0.95} - V_{\text{DR,micro}}$$

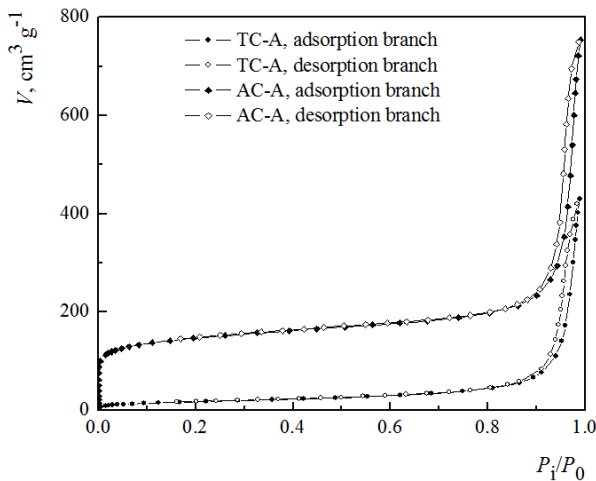


Fig. 5. N_2 adsorption isotherms of AC-A and TC-A samples

According to IUPAC classification N_2 isotherm of AC-A sample represents a hybrid type I-IV. The adsorption isotherm manifest a steep rise at low relative pressures, sharp shoulder/knee in the relative pressure P_i/P_0 about 0.01 and almost parallel to the abscissa course at medium and high relative pressures. In the course of the isotherm a hysteresis loop of the type H-1 is also observed.

This behaviour of the adsorption isotherm reveals that the porous structure of AC-A is represented by both micro- and the mesopores. The isotherm of AC-A sample compared to that of TC-A sample displays an increase of the adsorbed N_2 which is caused by the appearance and development of microporosity, and an increase in mesoporosity with preserved cylindrical geometry

(hysteresis loop of H-1 type is observed in the isotherms of AC-A and TC-A samples). Apparently, physical activation of TC-A sample in a stream of water vapour had gasified some of the carbon, which gave rise to more deeply developed porosity.

The specific surface area S_{BET} of AC-A sample is determined using the linear form of the BET adsorption isotherm. In general, BET equation is applicable for determining the specific surface area of non porous, macro- and mesoporous materials consisting of pores with large diameter, but its application to determine the specific surface area of microporous adsorbents is problematic due to difficulties to distinguish mono- and polylayer adsorption of micropores volumetric filling, which generally ends at relative pressures less than 0.1 [29]. Therefore, the specific surface area of microporous materials obtained by the BET method does not reflect the true internal surface area, and should be regarded only as a reference, or a kind of equivalent BET surface. In this case, it is obligatory to note the range of relative pressures in which linear BET dependence occur. In general, linear BET dependence for microporous materials is shifted to a significantly low relative pressures compared to mesoporous material and can be determined by applying Rouquerol criteria [30]. The linear form of BET equation and criteria of Rouquerol for AC-A sample are shown on Fig. 6. Based on them S_{BET} of $527 \text{ m}^2 \text{g}^{-1}$ is calculated, which is significantly higher compared to TC-A precursor characterized by S_{BET} of about $63 \text{ m}^2 \text{g}^{-1}$.

Total pore volume, $V_{0.95}$, is also higher (double) for the activated carbon, which is mainly due to the development of microporous structure (micropores with diameters L_0 of 1.68, 2.11 and 2.82 nm are registered, Fig. 7) and to a lesser extent due to widening of mesoporous structure (mesopores diameter L_0 is 43.36 nm, Fig. 7).

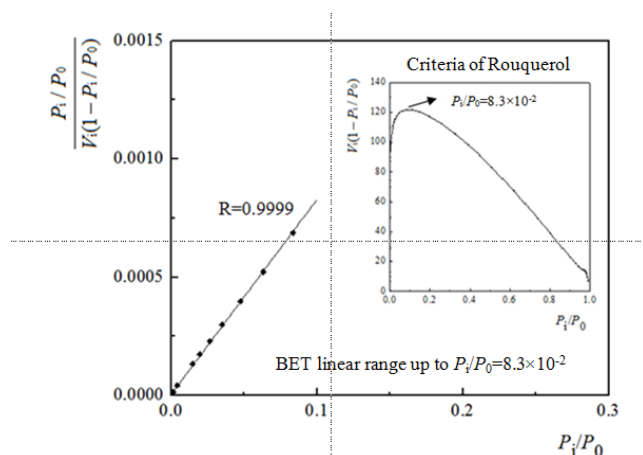


Fig. 6. The linear form of the BET equation for AC-A by applying criteria of Rouquerol.

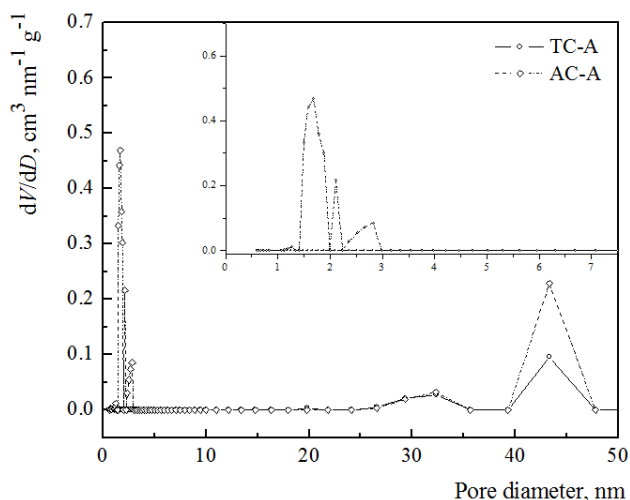


Fig. 7. Pore size distribution of TC-A and AC-A samples.

However, the contribution of the mesopores to $V_{0.95}$ is still prevailing as about 60% of AC-A pores are presented by mesopores. Thus, as a result of the detailed description of porous texture characteristics of prepared AC, it can be concluded that porous structure of AC-A is rather different to that of commercial activated carbons which are mainly microporous, but similar and comparable to that of other activated carbons derived from "end of life" tyre wastes [11,15,16,31].

CONCLUSION

The current study, focusing on valorisation of "end of life" tyres, reveals that these wastes can be successfully used for production of adsorbents. The technical carbons, prepared by treatments tyre wastes with HNO_3 , $\text{HNO}_3+\text{H}_3\text{PO}_4$ or $\text{HNO}_3+\text{C}_2\text{H}_4\text{Cl}_2$ and subsequent Soxhlet extraction with acetone, are mesoporous material characterized by "poor" porous structure since calculated S_{BET} (varying in the range of 36 - 63 $\text{m}^2 \text{g}^{-1}$), and $V_{0.95}$ (varying in the range of 0.121 - 0.205 $\text{cm}^3 \text{g}^{-1}$), are rather low. This hinder their adsorption abilities and thus further processing as physical activation is required in order to improve their porous texture characteristics. The obtained AC through activation of TC-A sample in a stream of water vapour exhibits promising porous texture features and demonstrates promising abilities to be used as an adsorbent. The AC-A sample is characterized by porous structure represented by both micro- and mesopores. The calculated S_{BET} and $V_{0.95}$ are 527 $\text{m}^2 \text{g}^{-1}$ and 0.489 $\text{cm}^3 \text{g}^{-1}$, respectively.

REFERENCES

1. The Council of the European Union, *Official Journal of the European Communities*, **L 182** (1999).
2. ETRMA, End-of-life tyre report (2015).
3. P. T. Williams, *Waste Manage.*, **33**, 1714 (2013).
4. J. D. Martínez, N. Puy, R. Murillo, T. García, M. V. Navarro, A. M. Mastral, *Renew. Sust. Energ. Rev.*, **23**, 179 (2013).
5. E. B. Machin, D. T. Pedrosa, J. A. de Carvalho Jr, *Renew.Sust. Energ. Rev.*, **68, Part 1**, 306 (2017).
6. A. M. Mastral, R. Murillo, M. S. Callén, T. García, *Fuel. Process. Technol.*, **60**, 231 (1999).
7. J. F. González, J. M. Encinar, J. L. Canito, J. J. Rodríguez, *J. Anal Appl. Pyrol.*, **58–59**, 667 (2001).
8. O. S. Chan, W. H. Cheung, G. McKay, *Carbon*, **49**, 4674 (2011).
9. E. L. K. Mui, W. H. Cheung, M. Valix, G. McKay, *Micropor. Mesopor. Mat.*, **130**, 287 (2010).
10. B. Acevedo, C. Barriocanal, *Fuel Process. Technol.*, **134**, 275 (2015).
11. P. Hadi, K. Y. Yeung, J. Guo, H. Wang, G. McKay, *J. Environ. Manage.*, **170**, 1 (2016).
12. A. Nieto-Márquez, A. Pinedo-Flores, G. Picasso, E. Atanes, R. Sun Kou, *J. Environ. Chem. Eng.*, **5**, 1060 (2017).
13. A. S. Al-Rahbi, P. T. Williams, *Waste. Manage.*, **49**, 188 (2016).
14. A. Nieto-Márquez, E. Atanes, J. Morena, F. Fernández-Martínez, J. L. Valverde, *Fuel. Process. Technol.*, **144**, 274 (2016).
15. R. Acosta, V. Fierro, A. Martínez de Yuso, D. Nabarlaz, A. Celzard, *Chemosphere*, **149**, 168 (2016).

16. T. A. Saleh, V. K. Gupta, *Adv. Colloid. Interfac.*, **211**, 93 (2014).
17. M. Dimov, S. Tsaikova, in: 20th Anniversary International Scientific Conference, Stara Zagora, 2010.
18. M. Dimov, S. Stoeva, S. Tsaikova, *Oxid. Commun.*, **4**, 931 (2008).
19. M. Dimov, S. Tsaikova, D. Aleksiev, in: Economic and Society development on the Base of Knowledge Stara Zagora, Bulgaria, 2009.
20. N. Petrov, T. Budinova, M. Razvigorova, J. Parra, P. Galiatsatou, *Biomass. Bioenerg.*, **32**, 1303 (2008).
21. L. Gonsalvesh, J. Yperman, R. Carleer, M. Mench, R. Herzig, J. Vangronsveld, *J. Chem. Technol. Biot.*, **91**, 1585 (2016).
22. L. Gonsalvesh, S. P. Marinov, G. Gryglewicz, R. Carleer, J. Yperman, *Fuel. Process. Technol.*, **149**, 75 (2016).
23. International Organization for Standardization In ISO 9277:2010, 2010; Vol. ISO 9277:2010.
24. S. Brunauer, P. H. Emmett, E. Teller, *J. Am. Chem. Soc.*, **60**, 309 (1938).
25. F. Stoeckli, M. V. López-Ramón, D. Hugli-Cleary, A. Guillot, *Carbon*, **39**, 1115 (2001).
26. [26] A. V. Neimark, Y. Lin, P. I. Ravikovitch, M. Thommes, *Carbon*, **47**, 1617 (2009).
27. J. D. Martínez, R. Murillo, T. García, *Bol. Grupo Español Carbón*, **30**, 10 (2013).
28. J. Pilusa, E. Muzenda, *International Journal of Chemical, Molecular, Nuclear, Materials and Metallurgical Engineering* **7**, 733 (2013)
29. International Organization for Standardization In ISO 9277:2010, 2010.
30. J. Rouquerol, P. Llewellyn, F. Rouquerol, in: Studies in Surface Science and Catalysis, P. L. Llewellyn, Rodriguez-Reinoso, F. J. Rouquerol, N. Seaton (eds.), Elsevier, 2007, Vol. 160.
31. B. Acevedo, C. Barriocanal, I. Lupul, G. Gryglewicz, *Fuel*, **151**, 83 (2015).

ПРОИЗВОДСТВО НА АДСОРБЕНТИ ОТ ОТПАДНИ ГУМИ И ОХАРАКТЕРИЗИРАНЕ НА ТЯХНАТА ПОРИСТА СТРУКТУРА

Л. Гонсалвеш^{1*}, М. Димов², С. Маринов³

¹ Централна научно-изследователска лаборатория, Университет "Проф. д-р Асен Златаров", Бургас 8000, България

² Катедра по физикохимия и органична химия, Университет "Проф. д-р Асен Златаров", Бургас 8000, България

³ Институт по органична химия с Център по фитохимия, Българска академия на науките, София 1113, България

Постъпила на 11 април 2017 г.; Коригирана на 15 май 2017 г

(Резюме)

Фокусът на настоящото изследване е върху оползотворяването на отпадни гуми като адсорбенти, в т.ч. технически и активни въглини. Техническите въглини са получени чрез третиране на отпадни гуми с к. HNO_3 , к. $\text{HNO}_3 + \text{k. H}_3\text{PO}_4$ или к. $\text{HNO}_3 + \text{C}_2\text{H}_4\text{Cl}_2$ и последваща сокслет екстракция с ацетон, докато активният въглен е получен чрез физическа активация на един от техническите въглини в поток на водна пара. Пористата структура на получените материали е охарактеризирана въз основа на N_2 адсорбционни изотерми, снети чрез азотна физисорбция при -196°C на апарат Surfer (Thermo Scientific). Установено бе, че получените технически въглини са мезопорести материали, характеризиращи се със слабо развита пориста структура и сравнително ниски стойности на $S_{\text{ВЕТ}}$ и $V_{0.95}$, т.ч. до $63 \text{ m}^2 \text{ g}^{-1}$ и $0.205 \text{ cm}^3 \text{ g}^{-1}$, съответно. Това налага прилагането на допълнителна обработка на техническите въглини, като физическо активиране с водна пара, с цел подобряване на тяхната пориста структура и техните качества като адсорбенти. Полученият активен въглен се характеризира с много по-добре развита пориста структура, представена от микро- и мезопори. Изчислените стойности на $S_{\text{ВЕТ}}$ и $V_{0.95}$ са $527 \text{ m}^2 \text{ g}^{-1}$ и $0.489 \text{ cm}^3 \text{ g}^{-1}$.

Structural destabilization and enhanced cytotoxicity on murine fibroblasts of *Helix pomatia* β -hemocyanin in presence of four cholinium amino acids

M. Guncheva^{1*}, D. Yancheva¹, V. Uzunova², P. Ossowicz³, K. Idakieva¹, Y. Raynova¹, E. Janus³, R. Tzoneva²

¹ Institute of Organic Chemistry with Centre of Phytochemistry, Bulgarian Academy of Sciences, Sofia, Bulgaria

² Institute of Biophysics and Biomedical Engineering, Bulgarian Academy of Sciences, Sofia, Bulgaria

³ Institute of Organic Chemical Technology, Faculty of Chemical Technology and Engineering, West Pomeranian University of Technology Szczecin, Szczecin, Poland

Received April 21, 2017; Revised May 09, 2017

Dedicated to Acad. Ivan Juchnovski on the occasion of his 80th birthday

Four complexes of β -hemocyanin from *Helix pomatia* (β -HpH) with ionic liquids (ILs) based on cholinium cation and amino acid anion were prepared. Using FTIR spectroscopy we observed that the tested ILs were able to induce conformational changes in the protein molecule. In the presence of cholinium methionate we detected the most significant changes in β -HpH secondary structure, which is expressed in a 2-fold increase of the intensity of the absorption band that is assigned to the side-chain amino acid residues and a complete loss of the α -helical structures at expense of the β -structures. Interestingly, the aggregation in this case seemed to be suppressed. In an experiment in vivo using 3T3 cells (fibroblasts), we found that the destabilization of the protein structure resulted in an enhanced cytotoxicity of the β -HpH-IL complexes in respect to the native β -HpH. The effect is stronger, both concentration- and time-dependent for the complex of β -HpH with cholinium tryptophanate.

Key words: *Helix pomatia* hemocyanin; cholinium amino acids; protein secondary structure; cytotoxicity assay

INTRODUCTION

Hemocyanins (Hcs) are large copper-containing oxygen-transporting proteins that are freely dissolved in the hemolymph of many mollusks and arthropods [1]. The interest of these proteins has increased markedly over the last decades due to their great potential for application in medicine. Many authors reported on immunostimulatory, anti-cancer and antibacterial properties of Hcs isolated from various sources [2–6]. Many studies have been focused on the elucidation of structure and factors that contribute or affect the stability of Hcs [1,7,8].

The hemocyanin isolated from the hemolymph of terrestrial snail *Helix pomatia* (HpH) consists of two alpha components (α_D -HpH and α_N -HpH) and one beta component (β -HpH). Beta-hemocyanin is characterized with subunit homogeneity, and therefore in comparison to α_D -HpH and α_N -HpH, has been more frequently used for structural studies [9, 10]. HpH characterizes with relatively high carbohydrate content (ca 9%), which probably correlates with the protein immunogenicity tested in animal models but did not have an effect on the

protein thermal stability [5,8,11]. The therapeutic effect of β -HpH was shown in murine model of colon carcinoma as well as its adjuvant potential for microbial and viral antigens [5,12]. In addition, β -HpH exhibits a phenoloxidase activity, which can be enhanced by detergent treatment and lyophilisation which results in conformational changes of the protein [13].

Ionic liquids (ILs) are salts that consist of an organic cation and/or organic anion that are characterized with melting temperatures below 100°C, low vapor pressure and tunable physicochemical characteristics [14]. Biodegradable and biocompatible ILs are of great interest in view of their biotechnological application as reaction media for biocatalysis or isolation of proteins or plant metabolites, as additives aiming to enhance thermal or storage stability of proteins [15–18].

The aim of this paper is to follow the changes of the secondary structure of β -HpH induced by four ILs containing cholinium cation and amino acid anion. All anions that are in the focus of the study are non polar amino acids, however their side-chains differ substantially in size and structure; therefore, we suppose that possibly differences in their interactions with proteins can be observed. In addition, we evaluated the cytotoxic effect of the

* To whom all correspondence should be sent:

E-mail: maia@orgchm.bas.bg

modified β -HpH on murine fibroblasts in respect to changes in its structure. Results are discussed in comparison to those obtained for the native β -HpH.

EXPERIMENTAL

Materials

Beta-hemocyanin from *Helix pomatia* (β -HpH) was isolated as described in previous study [10]. Cholinium glycinate [Chol][Gly], cholinium valinate [Chol][Val], cholinium methionate [Chol][Met] and cholinium tryptophanate [Chol][Trp] were synthesized as given in [19]. Murine embryonic fibroblast (3T3) cell line was purchased from American Type Culture Collection (ATCC). Thiazolyl Blue Tetrazolium Bromide (MTT) (98%) was obtained from Sigma. DMEM high glucose media, L-glutamine and sodium bicarbonate were purchased from PAN-Biotech GmbH, Aidenbach, Germany.

Fourier transform infrared spectroscopy (FTIR)

Prior to the measurements, 0.08 mL β -HpH (16.4 mg/mL) were incubated for 60 min at room temperature with 0.02 mL of 1M solution of the corresponding [Chol][AA] dissolved in sodium phosphate buffer (pH 7.2, 5mM). FTIR spectra of the β -HpH-[Chol][AA] complexes were recorded on Bruker Tensor 27 spectrometer, equipped with a detector of deuterated triglycine sulphate (DTGS). The FTIR spectra were collected by direct deposition of the samples on attenuated total reflectance (ATR) element, a diamond crystal, in the frequency region 4000 – 600 cm^{-1} with 128 scanning and at resolution of 1 cm^{-1} . The absorptions of the medium and ILs were taken into account. For each sample, the protein secondary structure content was estimated in few steps: 1) Fourier deconvolution using Opus software version 5.5 at band width of 14 cm^{-1} , 2.9 resolution enhancement factor, and Lorentzian lineshape; 2) obtaining the second derivative spectra by the Savitzky-Golay algorithm based on 25 smoothing points; 3) curve fitting according to the Local Least Squares algorithm as the initial bandwidth of all components was set to 14 cm^{-1} and the components were approximated by mixed Lorentzian/Gaussian functions and setting [20].

Cytotoxicity assay

Murine fibroblasts (3T3) were cultured in DMEM high glucose medium containing L-Glutamine, Penicillin-Streptomycin-Amphotericin

B and 10% fetal bovine serum at humidified atmosphere, 37°C and 5% CO₂. Then, the cells were seeded in a sterile 96-well plate at 1x 10⁴ cells per well and incubated for 24 hrs at 37°C and 5% CO₂ for obtaining adherent cell cultures and good cell spreading. Next, the cells were incubated for additional 24 or 48 hrs with β -HpH or β -HpH - [Chol][AA] complexes, at concentrations ranging from 100–700 $\mu\text{g/mL}$. The β -HpH-[Chol][AA] complexes were obtained as described above. Cytotoxicity assay was performed as described in the literature using tetrazolium dye, (3-[4,5-dimethylthiazol-2-yl]-2,5-diphenyltetrazolium bromide (MTT) [21]. For each well, the conversion of MTT into formazan was monitored spectrophotometrically at 570 nm and was used to be estimated the percentage of the viable cells in respect to control experiment without added β -HpH or β -HpH-IL-complexes. Blank experiments containing only reaction medium were also performed. All experiments were performed in duplicate.

RESULTS AND DISCUSSION

IL-induced structural changes

The effect of the four selected for this study choline amino acids on β -HpH secondary were followed using ATR-FTIR spectroscopy. Analysis of the amide I adsorption band was done in order to be determined the secondary structure content for each sample. The observed peak positions in the spectral region 1700-1600 cm^{-1} are: α -helix (1660-1652 cm^{-1}), unordered structures or random coils (1951-1942 cm^{-1}), β -sheets (1640-1624 cm^{-1}), β -turns (1679-1668 cm^{-1}), anti-parallel β -sheets (1693-1681 cm^{-1}) and side chains of the amino acid residues (1609-16003 cm^{-1}). The band area of each structural element was presented as a percentage of the total area and the changes of the conformation of the native β -HpH in presence of [Chol][AA] can be seen in Fig.1. The most significant changes in the secondary structure were observed in presence of [Chol][Met]. For example, for this β -HpH-IL complex we detected a complete loss of the α -helical structures at expense of the β -structures. The 2-fold increase of the intensity of the absorption band that is assigned to the side-chain amino acid residues implies a denaturation of the protein in presence of the methionate, however, it seems that in this medium the protein aggregation is suppressed. In presence of the glycinate an increase in the α -helices is observed implying that β -HpH occupies more folded conformation in this solution.

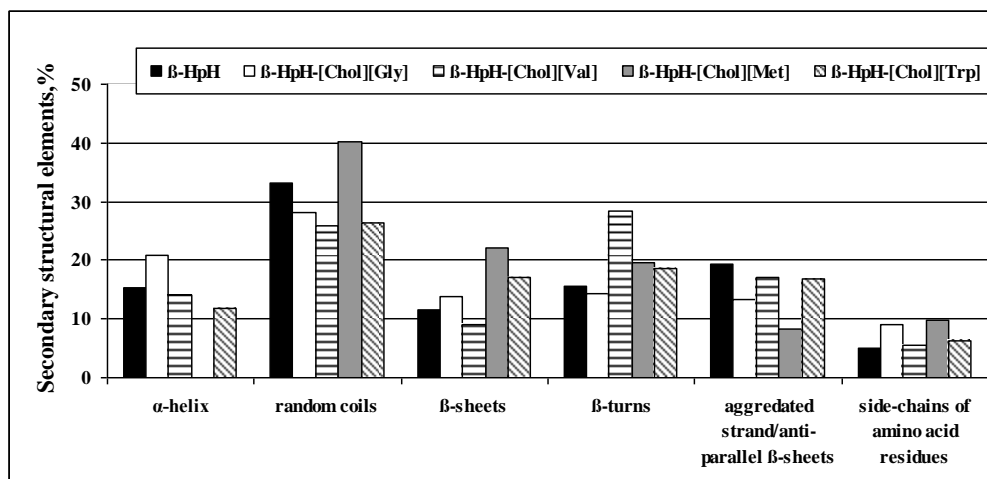


Fig. 1. Elements of the protein secondary structure (%) determined from deconvoluted ATR-FTIR spectra for native β -HpH and its complexes with choline amino acids.

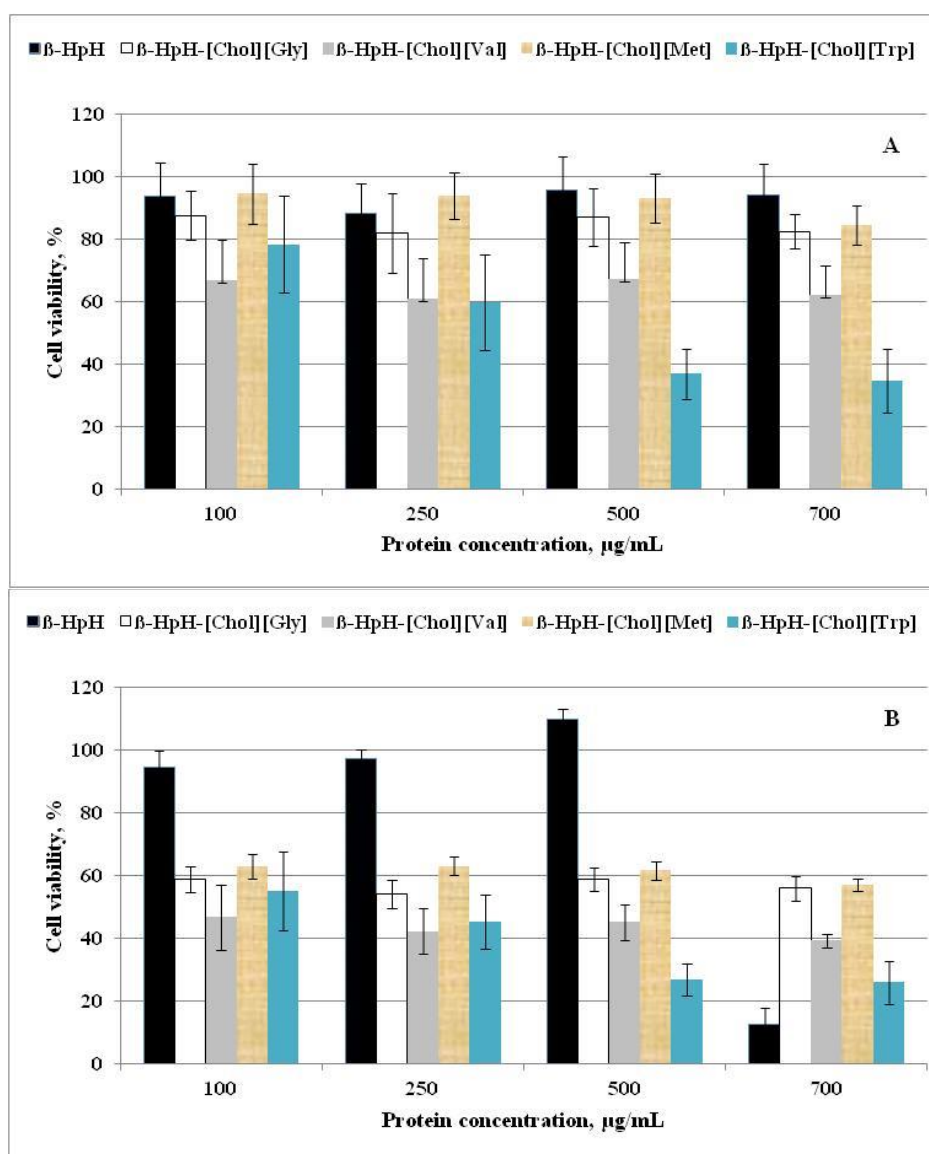


Fig. 2. Percentage of viable fibroblasts after incubation with β -HpH and its complexes for 24 h (A) and 48 h (B).

In comparison to the native protein, β -HpH-[Chol][Val] characterizes with an increase of the coil and unordered structures mostly at expenses of the β -structures. Rearrangement in the protein molecule, but still close to the native conformation, was also observed in presence of the tryptophan-based IL.

3T3 cytotoxicity assay

Murine fibroblasts (3T3 cells) cytotoxicity assay is used as supporting identification or screening of substances with potential acute oral toxicity or skin irritation [22]. Viability of 3T3 cells in presence of β -HpH and β -HpH-IL was assessed at 24 and 48h after incubation. The native protein and its complexes were tested in a concentration range from 100 to 700 μ g/mL. The exposure of 3T3 cells to a high concentration (> 500 μ g/mL) of native β -HpH for 48 h resulted to a moderate cell growth stimulation. However, tested at lower concentrations or after a short-term incubation (24h) β -HpH did not affect the viability of the fibroblasts. As can be seen in Fig. 2, β -HpH became more cytotoxic to 3T3 cells after being modified with the four choline amino acids. The strongest negative effect which is both concentration- and time-dependent was observed for β -HpH-[Chol][Trp]. A 24-hour exposure of fibroblasts to β -HpH-[Chol][Met] do not reduce cell growth. However, longer exposure to this complex resulted in a decrease in cell viability by 40% which was observed for the whole concentration range (Fig. 2B). The effect of β -HpH-[Chol][Gly] was concentration independent. For this complex, we observed a moderate (15-18%) to high (40%) decrease in cell viability after 24 and 48 h incubation, respectively. β -HpH-[Chol][Val] exhibited stronger inhibitory effect on the 3T3 cell growth in comparison to that found for the glycinate complex, however it was also only time dependent.

CONCLUSION

Even added in low concentration to the reaction mixture, the four tested [Chol][AA] induce significant changes in the secondary structure of β -HpH. The structural destabilization of the hemocyanin results in its enhanced cytotoxicity on fibroblasts. The observed effect is time-dependent for the whole series of the tested compounds. However, concentration dependence is found only for β -HpH-[Chol][Trp].

REFERENCES

1. J. Markl, *BBA PROTEINS PROTEOM.*, **1834** (9), 1840 (2013).
2. D. W. McFadden, D. R. Riggs, B. J. Jackson, L. Vona-Davis, *Am. J. Surg.*, **186**, 552 (2003).
3. C. J. Coates, J. Nairn, *Dev. Comp. Immunol.*, **45**, 43 (2014).
4. S. Arancibia, C. Espinoza, F. Salazar, M. Del Campo, R. Tampe, T.-Y. Zhong, P. De Ioannes, B. Moltedo, J. Ferreira, E. C. Lavelle, A. Manubens, A. E. De Ioannes, M. I. Becker, *PLoS ONE*, **9** (1), e87240 (2014).
5. V. Gesheva, S. Chausheva, N. Mihaylova, I. Manoylov, L. Doumanova, K. Idakieva, A. Tchorbanov, *BMC Immunol.*, **15**, 34 (2014).
6. J. Zhuang, C. J. Coates, H. Zhud, P. Zhud, Z. Wua, L. Xie, *Dev. Comp. Immunol.*, **49** (1), 96 (2015).
7. H. Decker, N. Hellmann, E. Jaenicke, B. Lieb, U. Meissner, J. Markl, *Integr. Comp. Biol.*, **47** (4), 631 (2007).
8. J. R. Harris, J. Markl, *Micron*, **30**, 597 (1999).
9. C. Gielens, L. J. Verschueren, G. Pr aux, R. Lontie, *Comp. Biochem. Physiol. Part B: Comp. Biochem.*, **69**, 455 (1981).
10. K. Idakieva, C. Gielens, N. Siddiqui, L. Doumanova, B. Vasseva, G. Kostov, V. L. Shnyrov, *Z. Naturforsch.*, **62a**, 499 (2007).
11. B. T. Yesilyurt, C. Gielens, F. Meersman, *FEBS J.*, **275**, 3625 (2008).
12. V. Gesheva, S. Chausheva, N. Stefanova, N. Mihaylova, L. Doumanova, K. Idakieva, A. Tchorbanov, *Int Immunopharmacol.*, **26**, 162 (2015).
13. K. Idakieva, N. I. Siddiqui, F. Meersman, M. De Maeyer, I. Chakarska, C. Gielens, *Int. J. Biol. Macromol.*, **45**, 181 (2009).
14. G. Liu, R. Zhong, R. Hu, F. Zhang, *Biophys. Rev. Lett.*, **7** (3-4), 121 (2012).
15. F. van Rantwijk, R. Madeira Lau, R.A. Sheldon, *TRENDS Biotechnol.*, **21** (3), 131 (2003).
16. Z. Pietralik, A. Skrzypczak, M. Kozak, Z. Pietralik, A. Skrzypczak, M. Kozak, *Chem. Phys. Chem.*, **17**(15), 2424 (2016).
17. M. M. Pereira, S. N. Pedro, M. V. Quental, A. S. Lima, J. A. P. Coutinho, M. G. Freire, *J. Biotechnol.*, **206**, 17 (2015).
18. R. M. Vrikkis, K. J. Fraser, K. Fujita, D. R. Macfarlane, G.D. Elliott, *J. Biomech. Eng.* **131**, 074514-1 074514-4 (2009).
19. M. Guncheva, K. Paunova, P. Ossowicz, Z. Rozwadowski, E. Janus, K. Idakieva, S. Todinova, Y. Raynova, V. Uzunova, S. Apostolova, R. Tzoneva, D. Yancheva, *RSC Adv.*, **5**, 63345 (2015).
20. A. Barth, C. Zscherp, *Q. Rev. Biophys.*, **35**, 369 (2002).
21. T. Mosmann, *J. Immunol. Meth.*, **65**, 55 (1983).
22. A. V. King, P. A. Jones, *Toxicol. in Vitro*, **17**, 717 (2003).

ДЕСТАБИЛИЗАЦИЯ И ПОВИШЕНА ЦИТОТОКСИЧНОСТ ВЪРХУ ФИБРОБЛАСТИ НА БЕТА-ХЕМОЦИАНИН ОТ *HELIX POMATIA* В ПРИСЪСТВИЕ НА ЧЕТИРИ ОРГАНИЧНИ СОЛИ НА ОСНОВАТА НА ХОЛИН И АМИНОКИСЕЛИНИ

М. Гунчева^{1*}, Д. Янчева¹, В. Узунова², П. Осовиц³, К. Идакиева¹, Ю. Райнова¹, Е. Янус³, Р. Цонева²

¹ *Институт по органична химия с Център по фитохимия, Българска Академия на Науките, София, България*

² *Институт по биофизика и биомедицинско инженерство, Българска Академия на Науките, София, България*

³ *Институт по органична химична технология, Западно Померански технологичен университет на Шчечин, Полша*

Постъпила на 21 април 2017 г.; Коригирана на 09 май 2017 г.

(Резюме)

Получени са четири комплекса на бета хемоцианин от *Helix pomatia* (β -НрН) с йонни течности (ЙТ) на основата на холинов катион и аниони, остатъци от аминокиселини. Промените във вторичната структура на протеина индуцирани от ЙТ са проследени с помощта на ИЧ спектроскопия. Установено е, че холинил метионата оказва най-голям ефект върху структурата на β -НрН. В ИЧ спектрите на този комплекс не се наблюдава абсорбционната ивица характерна за α -спирални структури, а интензивността на ивицата, отнасяща се за страничните вериги на аминокиселинните остатъци на протеина е увеличена до два пъти. Въпреки наблюдаваната значителна денатурация на β -НрН в присъствие на холинил метионат, се вижда, че агрегацията на протеина в този разтвор е подтисната. В допълнение, беше установено, че структурната дестабилизация на β -НрН води до повишаване на цитотоксичността на комплексите на β -НрН-ЙТ спрямо фибробластни клетки. Ефектът е най-значителен за комплекса на β -НрН с холинил триптофанат и зависи от концентрацията на ЙТ и времето за третиране.

Modification with sodium periodate increases the structural stability of molluscan hemocyanins

Y. Raynova¹, S. Todinova², K. Idakieva^{1*}

¹ Institute of Organic Chemistry with Centre of Phytochemistry, Bulgarian Academy of Sciences, Acad. G. Bonchev Str., bl. 9, Sofia 1113, Bulgaria

² Institute of Biophysics and Biomedical Engineering, Bulgarian Academy of Sciences, Acad. G. Bonchev Str., bl. 21, Sofia 1113, Bulgaria

Received, 9 April 2017; Revised, 17 May 2017

Dedicated to Acad. Ivan Juchnovski on the occasion of his 80th anniversary

Hemocyanins (Hcs) are large glycoproteins present in the blood of some mollusks and arthropods. In addition to their biological function, molluscan Hcs have shown promising properties in the development of various medicinal products. In the present study, the carbohydrate moieties of two representatives of Hcs from molluscan species, namely those isolated from the marine snails *Rapana thomasiana* and terrestrial snails *Helix pomatia*, were oxidized with sodium periodate. This chemical modification led to increased structural and thermal stability of oxygen-transport proteins.

Key words: hemocyanin; periodate oxidation; thermal stability

INTRODUCTION

Hemocyanins (Hcs) are large oligomeric proteins present in the blood of some mollusks and arthropods, whose biological function is mainly related with the oxygen transport to the tissues [1]. Hcs are multifunctional proteins. It has been shown that the oxygen-binding function of Hc can be converted to phenoloxidase (PO) activity and furthermore that PO activity can be induced in Hcs by *in vivo* and *in vitro* activation [2, 3]. In addition, molluscan Hcs have indicated promising properties in the development of various medicinal products including antiviral agents, conjugate vaccines and immunotherapy of cancer [4-6]. Thus, it was revealed that the Hcs isolated from marine snail *Rapana thomasiana* (RtH) and from terrestrial snail *Helix pomatia* (HpH) were able to elicit strong antiviral or antibacterial immune response in mouse models when combined with bacterial and viral antigens [7,8]. Moreover, it was demonstrated that these Hcs expressed strong *in vivo* anti-cancer and anti-proliferative effects in murine model of colon carcinoma [9].

Achieving structural stabilization in proteins having therapeutic application is an important task. Chemical modification is one approach to improve the protein's stability. It has been reported that the periodate oxidation of the carbohydrate moieties of

proteins with sodium periodate has induced structural stabilization and enhanced their immunogenicity [10, 11].

Hcs, isolated from various gastropodan organisms, have a carbohydrate content of 2 - 9% w/w, with mannose being the major monosaccharide found in these structures [12]. The aim of the present study is to enhance the structural stability of two representatives of gastropodan Hcs, namely RtH and HpH, by chemical oxidation of their sugar moieties.

EXPERIMENTAL

Reagents

Sodium periodate, ethylene glycol and phenylmethylsulfonyl fluoride (PMSF) were purchased from Merck, Darmstadt, Germany. Trypsin and proteinase K were supplied by Sigma-Aldrich Chemie GmbH. All other chemicals used were of analytical grade.

Isolation and purification of Hcs

RtH was purified from the hemolymph, collected from marine snails *R. thomasiana*, according to the procedure described in [13]. The β -isoform of HpH was isolated from the hemolymph of terrestrial snails *H. pomatia* as described elsewhere [14,15].

* To whom all correspondence should be sent:
E-mail: idakieva@orgchm.bas.bg

Absorption spectroscopy

Absorption spectra of Hcs were recorded using Evolution™ 300 UV-Vis spectrophotometer (Thermo Electron Corporation). The concentration of protein solutions was determined spectrophotometrically using specific absorption coefficient $A_{278}^{0.1\%} = 1.36 \text{ ml}\cdot\text{mg}^{-1}\cdot\text{cm}^{-1}$ for RtH [13] and $A_{278}^{0.1\%} = 1.416 \text{ ml}\cdot\text{mg}^{-1}\cdot\text{cm}^{-1}$ for β -HpH [16], respectively.

Chemical modification of Hcs

The chemical oxidation with sodium periodate method was performed to modify RtH and β -HpH as described in [11]. Briefly, each Hc (protein concentration 2 mg/ml) was dissolved in 0.1 M sodium acetate buffer, pH 5.5, containing 15 mM sodium periodate and incubated for 1 h in the dark at room temperature. Next, 25 μl of a solution of ethylene glycol was added to each 2 ml of protein and incubated overnight at 4 °C. At the last step, the protein samples were concentrated by ultrafiltration, dialyzed against buffer 50 mM Tris-HCl, pH 8.0, and filtered through 0.22- μm membrane filter.

Protease digestion of Hcs

Modified Hcs and their respective native forms were digested with trypsin and proteinase K at a concentration of 0.2 % (w/w). The enzymatic reactions were performed at 37 °C for 30 min in a buffer 50 mM Tris-HCl, pH 8.6, and stopped with an addition of 1 % PMSF.

Differential scanning calorimetry (DSC)

Calorimetric measurements were performed on a high-sensitivity differential scanning microcalorimeter DASM-4 (Biopribor, Pushchino, Russia), with sensitivity greater than 0.017 mJ/K and a noise level less than $\pm 0.05 \mu\text{W}$. A constant pressure of 2 atm was maintained during all experiments to prevent possible degassing of the solution on heating. The protein solution in the calorimetric cell was reheated after the cooling from the first run to estimate the reversibility of the thermally induced transitions. The calorimetric data were evaluated using the ORIGIN (MicroCal Software) program package. Molecular mass of 9 000 000 Da for Hc was used in the calculation of molar quantities.

SDS-PAGE

Hc samples were analyzed by SDS-PAGE on 10% separating gel, as described by Laemmli [17]. Electrophoresis was performed using a Mini Protean electrophoresis system (Bio-Rad). Sensitive silver staining was used to detect the proteins after electrophoretic separation on polyacrylamide gels.

RESULTS AND DISCUSSION

Carbohydrate content of 2.6 % (w/w) has been determined for RtH [12], while β -HpH contains 7 % (w/w) carbohydrates [16]. These Hcs contain, besides the commonly occurring sugars D-mannose, D-galactose, L-fucose, N-acetyl-D-glucosamine and N-acetyl-D-galactosamine also D-xylose and 3-O-methyl-D-galactose, unusual carbohydrates for animal glycoproteins. To stabilize the structure of investigated Hcs, the carbohydrate chains from the surface of molecules were oxidized with sodium periodate to generate Schiff bases between the free amine groups from proteins and the reactive aldehydes, formed by the oxidation procedure (Fig. 1).

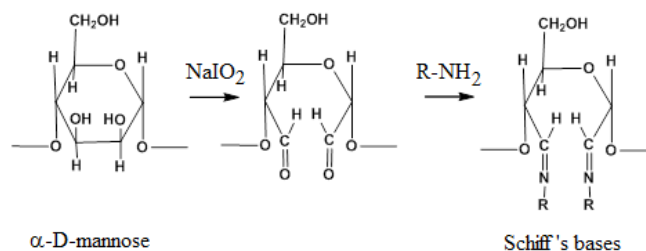


Fig. 1. Chemical strategy for oxidation of carbohydrates with sodium periodate and Schiff's base formation.

SDS-PAGE analysis showed differences in the mobility pattern between the native and modified Hcs. Oxidized Hcs (Ox-Hcs) did not enter the resolving portion of the gel (Fig. 2, lane 4). This effect was attributed to the internal cross-linking within Hc molecules as a result of periodate treatment [11].

Digestion of investigated Hcs with trypsin and proteinase K were used to assess whether Schiff bases were formed in Ox-Hcs. Both proteolytic enzymes possess different specificity.

Trypsin cleaves polypeptide chains mainly at the carboxyl side of the amino acids Lys or Arg. Proteinase K has broad specificity – it preferentially cleaves peptide bonds adjacent to the carboxyl group of aliphatic and aromatic amino acids.

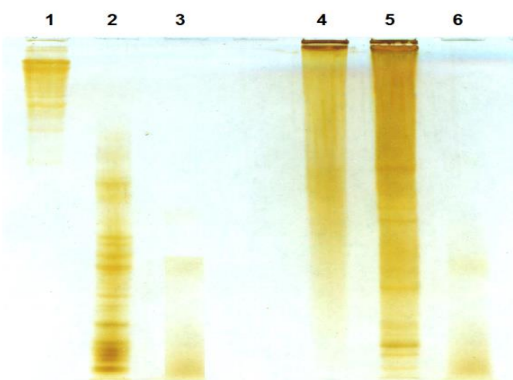


Fig. 2. 10 % SDS-PAGE: lane 1, native RtH; lane 2 and 3, native RtH digested with trypsin (0.2 % w/w) and proteinase K (0.2 % w/w) for 10 min at 37 °C, respectively; lane 4, oxy-RtH; lane 5 and 6, oxy-RtH digested with (0.2 % w/w) and proteinase K (0.2 % w/w) for 10 min at 37 °C, respectively.

We assumed that trypsin would not be able to digest Ox-Hcs because the ϵ -amino groups of Lys were involved in formation of Schiff bases. Indeed, the results showed that the native Hc molecules were rapidly degraded after incubation with trypsin (0.2% w/w) for 30 min (Fig. 2, lane 2). By contrast, Ox-Hcs were only partially degraded and retained in the stacking portion of the gel (Fig. 2, lane 5). Proteinase K (0.2% w/w) equally cleaved native and Ox-Hcs, confirming the conclusion made above (Fig. 2, lane 3 and 6).

Absorption spectra taken for native and Ox-Hcs showed that the intensity of the characteristic copper-dioxygen band at 345 nm slightly decreased as a result of modification with sodium periodate (Fig. 3). Therefore, induced local conformational changes did not affect the integrity of copper active sites in Hc molecules.

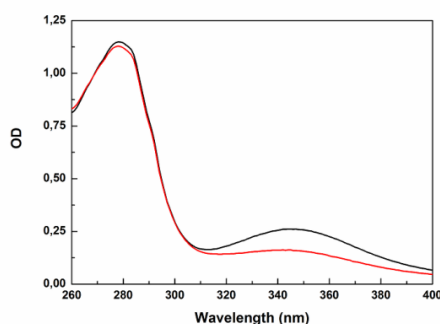


Fig. 3. Absorption spectra of native β -HpH (black line) and Ox- β -HpH (red line) in buffer 50 mM Tris-HCl, pH 8.

Intramolecular cross-linking has shown to increase thermal stability of different proteins [18, 19]. Differential scanning calorimetry (DSC) is the

most useful technique for characterizing thermal stability of proteins in terms of their thermodynamic characteristics [20]. DSC measurements of the native and modified Hcs were performed in buffer 50 mM Tris-HCl, pH 8.0, at a heating rate of 1 °C/min. In all cases the thermal unfolding was found to be calorimetrically irreversible, as no thermal effect was observed in a second heating of the protein solutions. Consistent with our previous study [21], one main transition and a shoulder with apparent transition temperatures (T_m) at 77.49 °C and 88.6 °C, were detected in the thermogram of native RtH (Fig. 4).

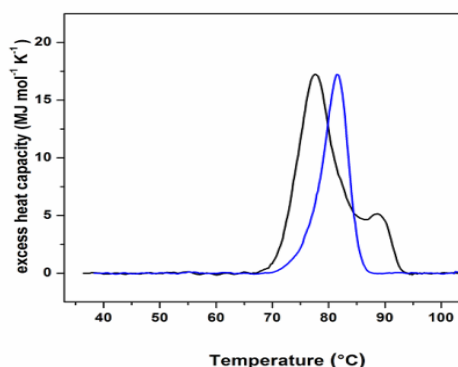


Fig. 4. Experimental C_p transition curves of native RtH (black line) and Ox-RtH (blue line) in buffer 50 mM Tris-HCl, pH 8.0, recorded at a heating rate of 1 °C/min. Protein concentration was 2.8 mg/ml.

The thermal stability of Ox-RtH is higher compared with native Hc. The T_m value for the main transition increased to 81.61 °C. Moreover, the thermogram of Ox-RtH has more cooperative character with $T_{1/2}$ of 5.13 °C (Table 1).

Table 1. Parameters for the thermal denaturation of native and modified Hcs from *R. thomasiensis* and *H. pomatia*, obtained by DSC, at a heating rate of 1 °C/min.

Hemocyanin	ΔH_{cal} [MJmol ⁻¹]	C_p^{ex} [MJ mol ⁻¹ K ⁻¹]	T_m , [°C]	$T_{1/2}$ [°C]
Native RtH	173.1	17.22	77.49*	7.67
Ox-RtH	102.2	17.21	81.61	5.13
Native β -HpH	110.6	20.1	82.4	4.64
Ox- β -HpH	96.3	14.7	84.2	5.46

* Main transition

Integration of the heat capacity (C_p) of the protein sample vs. temperature yields the enthalpy (ΔH) of the unfolding process, which is due to endothermic events such as the breaking of hydrogen bonds, and exothermic processes such as the disruption of hydrophobic interactions [22]. The ΔH_{cal} value for native RtH is 70.9 MJ mol⁻¹ higher than that determined for Ox-RtH. This effect is probably related to the induced cross-linking in the

protein molecule as a result of modification. One transition with T_m value of 82.4 °C was detected in the thermogram of native β -HpH [23]. The T_m value obtained for Ox- β -HpH also was shifted towards the higher temperature of 84.2 °C (Fig. 5).

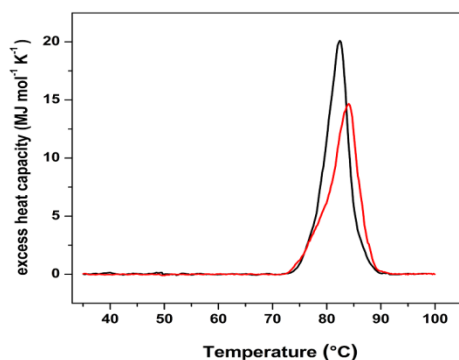


Fig. 5. Experimental C_p transition curves of native β -HpH (black line) and Ox- β -HpH (red line) in buffer 50 mM Tris-HCl, pH 8.0, recorded at a heating rate of 1 °C/min. protein concentration was 2.35 mg/ml.

The ΔH_{cal} value for modified β -HpH decreases with 14.3 MJ mol⁻¹. It seems structural differences between both Hcs in terms of reactive functional groups have determined the effect of modification. Table 1 summarizes DSC data for the process of thermal denaturation of native and modified Hcs.

CONCLUSION

In conclusion, the results of the present investigation reveal that the oxidation of carbohydrate moieties in Hcs with sodium periodate leads to enhance of the structural stability, in particular the resistance to proteolytic cleavage, as well as the thermal stability of these oxygen-transport proteins. Further evaluation the influence of the increased structural stability of modified Hcs on their immunological properties would be of interest.

Acknowledgements: This work was supported by research grant DFNP-152/ 12.05.2016 from Program for career development of young scientists, BAS, Bulgaria.

REFERENCES

1. K. E. van Holde, K. I. Miller, *Adv. Protein. Chem.*, **47**, 1 (1995).
2. H. Decker, E. Jaenicke, *Dev. Comp. Immunol.*, **28**, 673 (2004).
3. K. Idakieva, N. I. Siddiqui, F. Meersman, M. De Maeyer, I. Chakarska, C. Gielens, *Int. J. Biol. Macromol.*, **45**, 181 (2009).
4. J. Markl, B. Lieb, W. Gebauer, B. Altenhein, U. Meissner, J. R. Harris, *J. Cancer Res. Clin. Oncol.*, **127**, R3 (2001).
5. B. Moltedo, F. Faunes, D. Haussmann, P. De Ioannes, A. E. De Ioannes, J. Puente, M. I. Becker, M. I., *J. Urol.*, **176**, 2690 (2006).
6. P. Genova, D. Dundarova, K. Idakieva, A. Mohammed, S. Dundarov, R. Argirova, *Z. Naturforsch.*, **63c**, 429 (2008).
7. A. Tchorbanov, K. Idakieva, N. Mihaylova, L. Doumanova, *Int. Immunopharmacol.*, **8**, 1033 (2008).
8. V. Gesheva, S. Chausheva, N. Stefanova, N. Mihaylova, L. Doumanova, K. Idakieva, A. Tchorbanov, *Int. Immunopharmacol.*, **26**, 162 (2015).
9. V. Gesheva, S. Chausheva, N. Mihaylova, I. Manoylov, Doumanova, K. Idakieva, A. Tchorbanov, *BMC Immunol.*, **15**, 33 (2014).
10. M. E. Allison, D. T. Fearon, *Eur. J. Immunol.*, **30**, 2881 (2000).
11. S. Arancibia, M. Del Campo, E. Nova, F. Salazar, M. I. Becker, *Eur. J. Immunol.*, **42**, 688 (2012).
12. K. Idakieva, S. Stoeva, W. Voelter, C. Gielens, *Comp. Biochem. Physiol.*, **138B**, 221 (2004).
13. K. Idakieva, S. Severov, I. Svendsen, N. Genov, S. Stoeva, M. Beltramini, G. Tognon, P. Di Muro, B. Salvato, *Comp. Biochem. Physiol. Part B: Comp. Biochem.*, **106**, 53 (1993).
14. K. Heirwegh, H. Borginon, R. Lontie, R., *Biochem. Biophys. Acta.* **48**, 517 (1961).
15. C. Gielens, L. J. Verschuere, G. Preraux, R. Lontie, *Comp. Biochem. Physiol.*, **69B**, 455 (1981).
16. E. J. Wood, M. F. Chaplin, C. Gielens, J. De Sadeleer, G. Preaux, R. Lontie, *Comp. Biochem. Physiol.*, **82B**, 179 (1985).
17. U. K. Laemmli, *Nature* **227**, 680 (1970).
18. S. Igarashi, K. Sode, *Mol. Biotechnol.*, **24**, 97 (2003).
19. T. Ueda, K. Masumoto, R. Ishibashi, T. So, T. Imoto, *Protein Eng.*, **13**, 193 (2000).
20. P. L. Privalov, *Adv. Protein Chem.*, **35**, 1 (1982).
21. K. Idakieva, K. Parvanova, S. Todinova, *Biochem. Biophys. Acta.*, **1748**, 50 (2005).
22. G. Bruylants, J. Wouters, C. Michaux, *Curr. Med. Chem.*, **12**, 2011 (2005).
23. K. Idakieva, C. Gielens, N. I. Siddiqui, L. Doumanova, B. Vaseva, G. Kostov, V. L. Shnyrov, *Z. Naturforschung*, **62a**, 499 (2007).

МОДИФИКАЦИЯ С НАТРИЕВ ПЕРИОДАТ УВЕЛИЧАВА СТРУКТУРНАТА СТАБИЛНОСТ НА ХЕМОЦИАНИН ОТ МОЛЮСКОВИ ОРГАНИЗМИ

Ю. Райнова¹, С. Тодинова², К. Идакиева^{1*}

¹ *Институт по органична химия с Център по фитохимия, Българска академия на науките, ул. „Акад. Г. Бончев“, бл. 9, 1113 София, България*

² *Институт по биофизика и биомедицинско инженерство, Българска академия на науките, ул. „Акад. Г. Бончев“, бл. 21, 1113 София, България*

Постъпила на 09 април 2017 г.; Коригирана на 17 май 2017 г.

(Резюме)

Хемоцианините са олигомерни гликопротеини присъстващи в кръвта на някои мекотели и членестоноги. В допълнение към тяхната важна биологична функция, хемоцианините от моллюсковите организми показват обещаващи свойства в разработването на различни лекарствени продукти. В настоящото изследване, въглеводородните вериги на два представителя на моллюсковите хемоцианини, а именно тези, изолирани от морски охлюви *Rapana thomasiana* и градински охлюви *Helix pomatia*, бяха окислени с натриев периодат. Тази химична модификация доведе до повишена структурна и термична стабилност на изследваните кислород-пренасящи протеини.

Copper and/or cobalt modified nanostructured Ce-Zr mixed oxides as efficient catalysts for ethyl acetate total oxidation

R. N. Ivanova^{1*}, M. D. Dimitrov¹, D. G. Kovatcheva², T. S. Tsoncheva¹

¹ Institute of Organic Chemistry with Centre of Phytochemistry, Bulgarian Academy of Sciences, 1113 Sofia, Bulgaria,

² Institute of General and Inorganic Chemistry, Bulgarian Academy of Sciences, 1113 Sofia, Bulgaria

Received, 13 April 2017; Revised, 15 May 2017

Dedicated to Acad. Ivan Juchnovski on the occasion of his 80th birthday

By using an original approach combining the utilization of urea as a precipitator followed by hydrothermal treatment were obtained nanostructured Ce-Zr mixed oxides (Ce/Zr = 3:7 or 5:5). The obtained oxides were modified with copper and/or cobalt via incipient wetness impregnation from the corresponding metal nitrates. The obtained materials were characterized by X-ray diffraction, nitrogen physisorption, UV-Vis spectroscopy, temperature-programmed reduction (TPR) with hydrogen and their catalytic activity and selectivity in ethyl acetate oxidation was studied as well. The introduction of transition metal oxide within the parent Ce-Zr oxides decreases the start of the conversion with up to 50 K, increases substantially of the catalytic activity within the 550-650 K range and facilitates the selectivity to total oxidation of ethyl acetate. The influence of the type of modifying transition metal is better distinguished for the 3Ce7Zr support, especially within 550-600 K range, showing that the addition of copper only is sufficient for achieving the best catalytic results. At the same time, the support with higher ceria amount (5Ce5Zr) favors the catalytic behavior of the cobalt-containing modifications as well due to enhanced Co-Ce interaction.

Key words: CeO₂-ZrO₂ mixed oxides; cobalt and copper oxide modification; ethyl acetate total oxidation

INTRODUCTION

Ceria-zirconia mixed oxides are widely studied due to their excellent redox properties provoked by the formation of Ce_{1-x}Zr_xO₂ solid solution [1-3]. In our previous studies we have shown the potential of ceria-zirconia mixed oxides in ethyl acetate total oxidation [4,5]. The ethyl acetate oxidation is known as two-step process including dehydration to ethanol and acetic acid on acidic sites and their further oxidation with lattice oxygen following Mars-van-Krevelen mechanism [6,7]. Depending on the efficiency of the catalysts, several by-products, such as ethanol, acetaldehyde and acetic acid could be produced. We demonstrated that the selectivity to CO₂ on ceria-zirconia oxides was not satisfactory below 600-650 K, nevertheless the variations in the samples composition and the preparation procedure used [4,5]. The formation of ceria-zirconia solid solution in the nanoscale could provide more active oxygen species and further enhance the overall redox capability [8]. Another important advantage of the nanostructured metal oxides due to their well developed specific surface area is the facilitated introduction within them of another metal/metal oxide component in highly

dispersed state [9]. The introduction of readily reducible transition metal oxide could further improve the catalyst redox function. Copper and cobalt have favorable effect on the redox properties of both ceria and zirconia not only as monocomponent- [10-13] but as bicomponent [14-18] support systems as well. The aim of the present paper is to show the perspective of using nanostructured transition metal oxides in the design of multicomponent nanocomposite materials with potential application as efficient catalytic systems for total oxidation of ethyl acetate as representative of volatile organic compounds. For this purpose, on the basis of previously optimized synthesis procedure in the absence of long-chain organic template [4], Ce-Zr mesoporous oxides with optimal Ce/Zr ratio (Ce/Zr=5:5 or 3:7) were used as supports for the introduction and stabilization of copper and/or cobalt oxides nanoparticles.

EXPERIMENTAL

Materials

Two nanostructured Ce-Zr mixed oxides with various metal ratio (3:7 and 5:5) were synthesized using precipitation technique from the corresponding metal chlorides and in absence of long-chain surfactant followed by hydrothermal

* To whom all correspondence should be sent:
E-mail: radostinaiv@abv.bg

treatment step at 373 K according to a procedure reported previously [4]. The obtained Ce-Zr samples are calcined at 573 K and afterwards were modified with copper and/or cobalt by incipient wetness impregnation technique from the corresponding metal nitrates aqueous solutions. The total amount of copper and/or cobalt in the obtained multicomponent nanocomposites is 8 wt. %. The samples are designated as follows: $x\text{Cu}_y\text{Co}_z/\text{Ce}_w\text{Zr}$ where x and y correspond to the amount of metal in weight percents, while z/w represents the mol ratio between Ce and Zr. For comparison data for the analogous pure ceria-zirconia nanocomposites calcined either at 573 K (samples 3Ce7Zr and 5Ce5Zr) or at 773 K (samples 3Ce7Zr(773) and 5Ce5Zr(773)) are presented as well.

Methods of characterization

Nitrogen sorption measurements were recorded on a Quantachrome NOVA 1200e instrument at 77 K. Before the measurements the samples were evacuated at 423 K overnight under vacuum. The pore size distribution was calculated using a microscopic model, i.e. the non-local density functional theory NLDFT. The crystallinity of the samples was investigated by powder X-ray diffraction (PXRD) measurements performed on Bruker D8 Advance diffractometer equipped with Cu K α radiation and LynxEye detector. The size of the crystalline domains in the samples was determined using Topas 4.2 software with Rietveld quantification refinement. The UV-Vis spectra were recorded on a Jasco V-650 UV-Vis spectrophotometer equipped with a diffuse reflectance unit. The TPR/TG (temperature-programmed reduction/ thermogravimetric) analyses were performed in a Setaram TG92 instrument. Typically, 40 mg of the sample were placed in a microbalance crucible and heated in a

flow of 50 vol. % H₂ in Ar (100 cm³min⁻¹) up to 773 K at 5 Kmin⁻¹ and a final hold-up of 1 h. The catalytic experiments were performed in a flow type reactor (0.030 g of catalyst) with a mixture of ethyl acetate (1.21 mol %) in air with WHSV – 335 h⁻¹. Gas chromatographic (GC) analyses were carried out on HP5850 apparatus using carbon-based calibration. The samples were pretreated in Ar at 423 K for 1 h and then the temperature was raised with a rate of 2 K/min in the range of 423–773 K.

RESULTS AND DISCUSSION

Some physicochemical characteristics of the obtained samples are presented in Table 1. Nitrogen physisorption measurements were conducted in order to elucidate the textural properties of the studied samples (Fig. 1, Table 1). All isotherms are of type IV characteristic of mesoporous materials. Two effects are worth to be mentioned here. First, the modification with copper only leads to a complete loss of microporosity, nevertheless of the support used, which could be a result of preferred copper deposition within the present micropores of the Ce-Zr host leading to its closer contact with the host structure. On the other hand, the extent of microporosity registered within the other modifications is preserved, and even increases in case of 5Ce5Zr host material while in case of 3Ce7Zr support only 6.3 % microporosity is found after its modification within 8Co/Ce3Zr7 sample (Table 1). Besides, almost complete lost of support mesopores with sizes in 2-4 nm range is registered for the bicomponent and pure cobalt modifications (Fig 1, insets). More information about the phase composition and crystallinity of the obtained Ce-Zr hosts and their copper and/or cobalt modifications is found by PXRD technique (Fig. 2).

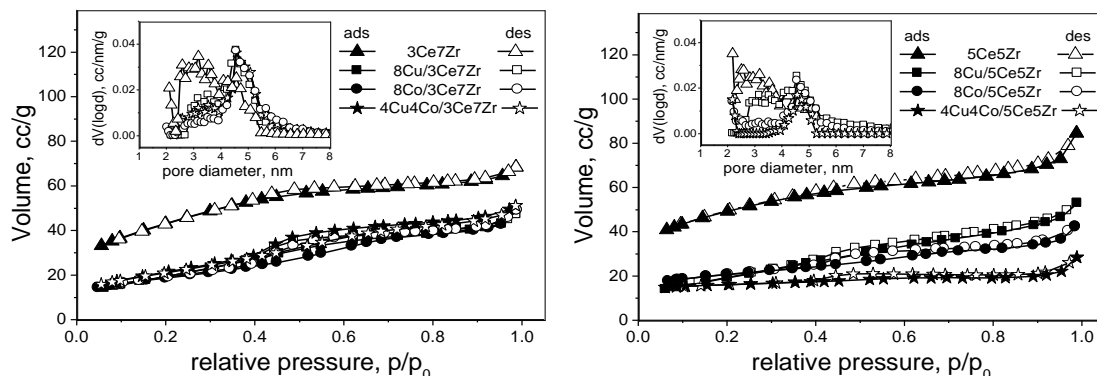


Fig. 1. Nitrogen physisorption isotherms with pore size distributions as insets for the studied pure and mixed metal oxide samples.

Table 1. Some physicochemical characteristics of the studied samples.

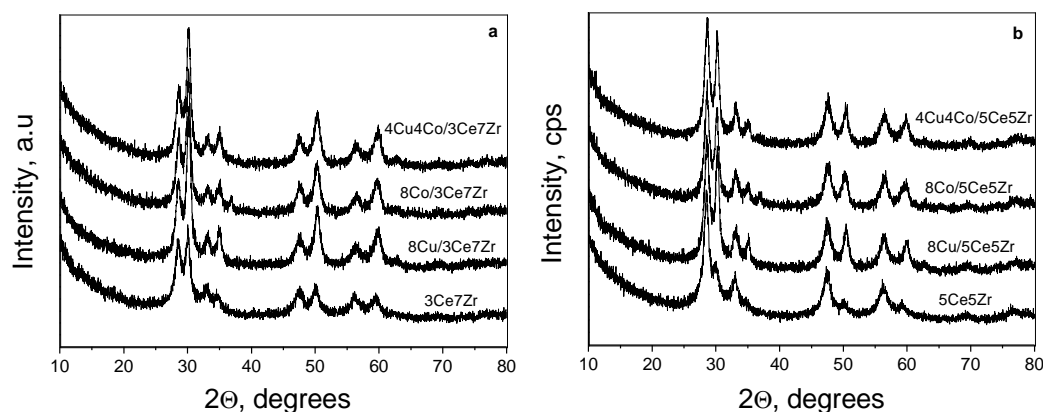
Sample	S_{BET} , m^2/g	V_{total} , cc/g	S_{micro} , m^2/g	V_{micro} , cc/g	Space Group	Unit cell, Å	Crystallite size, nm
3Ce7Zr	154.3	0.11	24.1 (15.6 %)	0.01	Fm-3m	5.424(3)	6
					P4 ₂ /nm	a=3.625(3) c=5.196(6)	9
8Cu/3Ce7Zr	74.0	0.073	-	-	Fm-3m	5.411(2)	8
					P4 ₂ /nm	a=3.615(2) c=5.172(4)	12
4Cu4Co/3Ce7Zr	76.3	0.079	-	-	Fm-3m	5.409(2)	8
					P4 ₂ /nm	a=3.617(2) c=5.185(4)	12
8Co/3Ce7Zr	65.2	0.076 (6.3 %)*	4.1	0.002	Fm-3m	5.407(2)	9
					P4 ₂ /nm	a=3.617(2) c=5.191(4)	13
					Fd-3m	8.088(5)	16
5Ce5Zr	175.9	0.13	72.8 (41.4 %)	0.031	Fm-3m	5.419(2)	7
					P4 ₂ /nm	a=3.603(4) c=5.199(7)	6
8Cu/5Ce5Zr	72.5	0.082	-	-	Fm-3m	5.415(2)	8
					P4 ₂ /nm	a=3.614(1) c=5.157(4)	14
4Cu4Co/5Ce5Zr	59.9	0.044	44.1 (73.6 %)	0.018	Fm-3m	5.409(2)	9
					P4 ₂ /nm	a=3.614(2) c=5.160(4)	15
8Co/5Ce5Zr	75.3	0.066	33.8 (44.9 %)	0.014	Fm-3m	5.402(2)	9
					P4 ₂ /nm	a=3.610(2) c=5.180(4)	14
					Fd-3m	8.073(5)	13

S_{BET} – BET specific surface area; V_{total} – total pore volume; S_{micro} – micropore specific surface area defined by t-plot method; V_{micro} – micropore volume by t-plot method; * in brackets is presented the microporosity of the sample as percentage of S_{BET} .

Both initial supports (5Ce5Zr and 3Ce7Zr) show well-defined reflections of both ceria crystallites with cubic fluorite-like Fm-3m structure and zirconia crystallites with tetragonal P4₂/nm structure and sizes within 6-9 nm range (Fig. 2, Table 1). After the modification, these two phases are preserved, however, the crystallite size increases up to 14-16 nm (Table 1). Besides, only in case of pure cobalt modifications, a new Co₃O₄ spinel phase with cubic Fd-3m structure is

registered as well (Fig. 1) with 13-17 nm crystallite sizes (Table 1). In all other modifications no additional reflections were observed and this is an indication that the copper presence increases the dispersion of the loaded phases nevertheless of the support used.

Uv-Vis analysis has been used to obtain information for the coordination and oxidative state of the present metal ions (Fig. 3).

**Fig. 2.** XRD patterns of the initial and modified Ce-Zr samples.

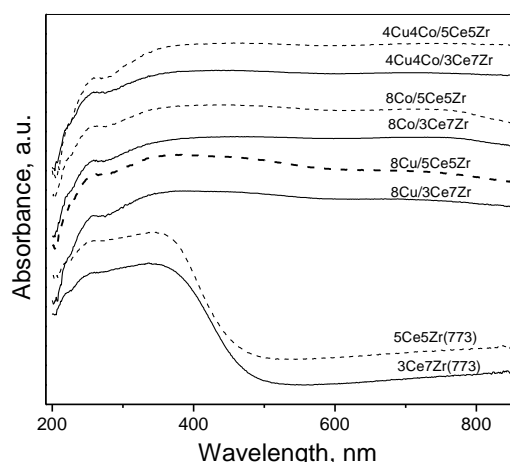


Fig. 3. UV-Vis spectra for the pure ceria-zirconia samples and their modifications

The spectra of both Ce-Zr supports consist of absorption bands characteristic of tetragonal zirconia by the broad feature in their spectra positioned at around 320 nm, while the strong absorption with maximum at about 350–360 nm is ascribed to $O^{2-} \rightarrow Ce^{4+}$ charge transfer (CT) transitions, while that one at about 250 nm – to $O^{2-} \rightarrow Ce^{3+}$ CT transitions (Fig. 3). After the modification these bands are preserved, however, the high absorption registered above 400 nm could be ascribed to the presence of various copper and cobalt oxide species in highly dispersed state. The observed absorption features in the 400–550 and 650–800 nm ranges could be ascribed to either Cu^{2+} ions in finely dispersed CuO crystallites in case of pure copper modifications or to the presence of Co_3O_4 particles within the pure cobalt modifications because of $4T1(F) \rightarrow 4T1(P)$ transitions of octahedrally coordinated Co^{3+} that occur in the former range and the electronic ligand-field $4A2(F) \rightarrow 4T1(P)$ transitions in tetrahedrally coordinated Co^{2+} that occur above 650 nm [19]. This is in agreement with the XRD results where Co_3O_4 spinel phase was found for both 8Co/5Ce5Zr and 8Co/3Ce7Zr samples. In case of the bicomponent modifications, the observed absorption spectra could be interpreted as superposition of the spectra of both pure copper and cobalt modifications, however, the registered very broad bands (Fig. 3) with not well defined maxima do not exclude also the existence of interaction between the individual copper and cobalt oxides.

Additional information for the redox properties of the obtained modifications was obtained by temperature-programmed reduction (TPR) with hydrogen (Fig. 4, Table 2). Here, data for the initial

supports is not presented, however, our previous investigation showed that the increasing of Zr content within Ce-Zr mixed oxides leads to an increase in the reducibility of these materials with reduction starting just above 550 K [4]. In case of both pure copper modifications the main reduction effect starts at very low temperatures (below 400 K) which could be ascribed to the reduction of very finely and narrowly dispersed CuO particles (Fig. 4, Table 2) because they undergo a complete reduction within relatively narrow temperature interval (380 – 450 K).

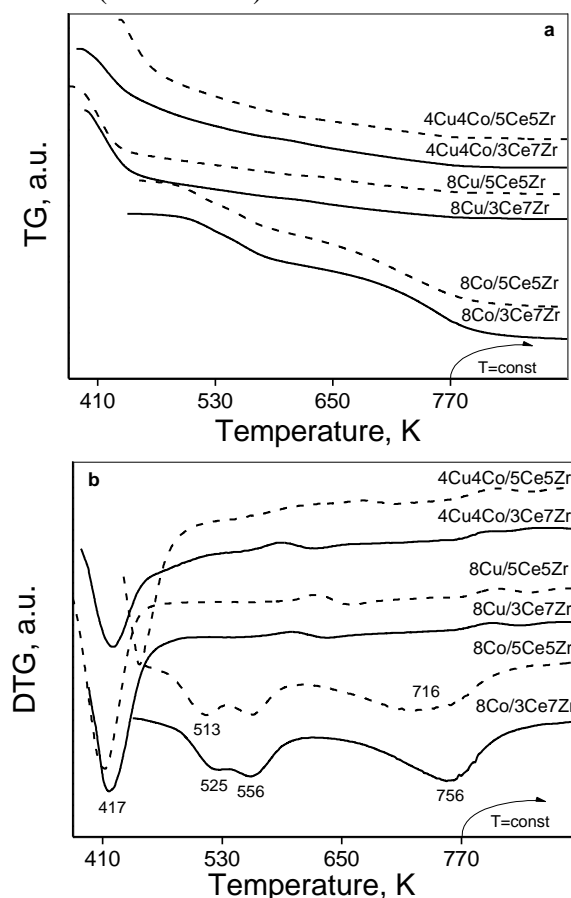


Fig. 4. TG (a) and DTG (b) data for the studied Cu and/or Co modifications.

The observed effects above 450 K could be ascribed to the reduction of Ce-Zr support which is facilitated by the reduced copper phase. In case of pure cobalt modifications, the reduction initiates at 460–470 K and stepwise reduction of Co^{3+} first to $Co^{2.5+}$ then to Co^{2+} and finally to Co^0 occurs (Fig. 4b). The observed overall weight loss corresponds to slightly less than 100 % reduction. In accordance with the XRD and UV-Vis data, this could be due to the reduction of a mixture of Co_2O_3 and Co_3O_4 phase. It should be noted the certain

shift of the reduction effects to lower temperatures in case of 5Ce5Zr cobalt modification, which could be a result of enhanced Co-Ce interactions due to higher cerium amount in this sample.

Table 2. TPR data for the obtained copper and/or cobalt modifications.

Sample	Tini, K	Tmax, K	Total weight loss, mg	Reduction degree, %
8Cu/3Ce7Zr	395	417	1.08	134
8Cu/5Ce5Zr	380	412	1.06	132
4Cu4Co/3Ce7Zr	388	420	1.16	110
4Cu4Co/5Ce5Zr	430	446	1.17	111
8Co/3Ce7Zr	470	525; 557; 756	1.22	94
8Co/5Ce5Zr	462	513; 556; 716	1.24	95

*The reduction degree is calculated on the basis of theoretic calculations for $\text{Cu}^{2+} \rightarrow \text{Cu}^0$ reduction in the case of copper modifications, $\text{Co}^{3+} \rightarrow \text{Co}^0$ reduction for the cobalt modifications and both $\text{Cu}^{2+} \rightarrow \text{Cu}^0$ and $\text{Co}^{3+} \rightarrow \text{Co}^0$ reduction transitions for Cu-Co bicomponent modifications.

According to the literature [20] cobalt cations modify the surface oxygen vacancy of ceria at the atomic level and well defined reactive faces are exposed between the interface of ceria host and the cobalt oxide. The mixed Cu-Co modifications show only one well defined effect at lower temperatures (Fig. 4, Table 2) followed by a broad tail that could be ascribed to the reduction of copper-cobalt spinel phase. The found higher than the theoretical degrees of reduction for both samples (Table 2) are an indication of facilitated reduction of the Ce-Zr supports as in the case of the pure copper modifications. The catalytic properties of the modified samples were studied in temperature-

programmed regime within the range of 423–773 K (Fig. 5). For comparison are presented data for the pure Ce-Zr mixed oxide supports calcined at 773 K as the obtained modifications. The results clearly show that the introduction of copper and/or cobalt (8 wt. % in total) within the parent Ce-Zr nanomaterial could decrease the start of the conversion with up to 50 K, leads to a substantial increase in the catalytic activity within the 550–650 K range and to almost complete selectivity to total oxidation of ethyl acetate in the whole studied temperature interval in comparison with the pure Ce-Zr supports (Figure 5a, and b). We ascribe these findings to the significantly improved redox function of the catalysts, especially at low conversion temperatures. The influence of the type of modifying transition metal is better distinguished for the 3Ce7Zr support, especially within 550–600 K range, and the results show that the presence of copper has a higher beneficial effect on the catalytic activity than cobalt (Fig. 5). At the same time, in case of all 5Ce5Zr modifications the conversion curves are very similar and close to the best results found for 8Cu/3Ce7Zr (Fig. 5a) most probably due to the higher ceria content within them, which in case of cobalt containing modifications is very beneficial as Co-Ce interactions induce the exposure of well-defined reactive faces between ceria and cobalt oxide interface [20]. On the basis of the latter results we could conclude that the presence of copper oxide particles in very highly dispersed state is of primary significance for the studied reaction. Similar findings we have already observed for nanocomposite catalysts containing nanosized Cu-Ce oxides supported on various porous silica materials [21].

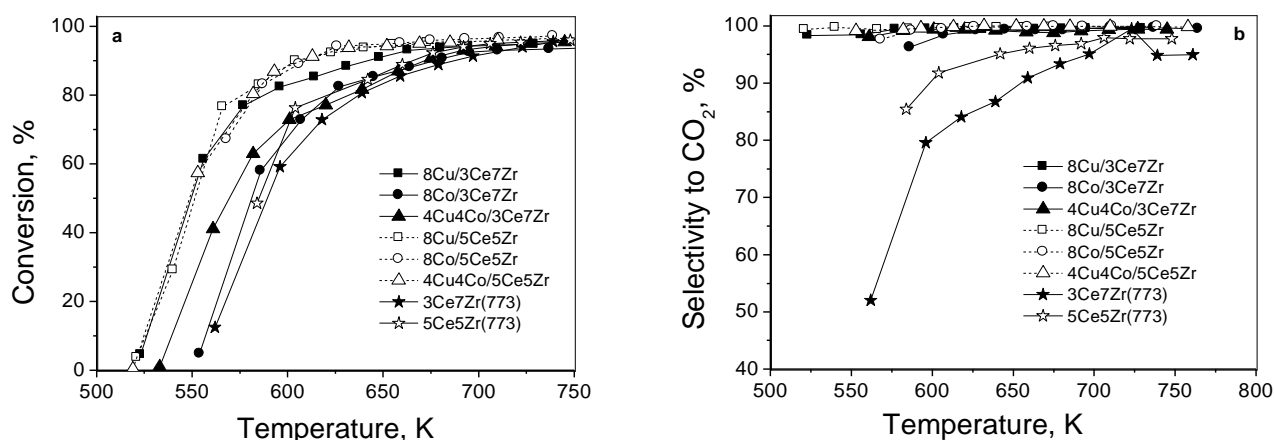


Fig 5. Temperature dependency of ethyl acetate oxidation for the studied samples.

CONCLUSION

By using a simple incipient wetness impregnation technique we could introduce and stabilize very finely dispersed copper oxide particles preferably within the micropores of nanosized mixed Ce-Zr oxides with micro-/mesoporous structure. The close contact of the obtained copper oxide species with the support structure improves substantially the overall redox properties of the obtained nanocomposites, especially at low temperatures (below 550 K), which is of primary importance for their ability to decrease the start of the conversion with about 50 K and to almost completely oxidize ethyl acetate to CO₂ even at low conversion rates and temperatures in comparison with the pure Ce-Zr nanomaterials. On the other hand, the introduction of cobalt- or copper-cobalt oxide phase leads to its deposition preferably within the smaller support mesopores (2-4 nm) and/or on the outer surface (in the case of pure cobalt modifications) which leads to a decrease in the catalytic activity for 4Cu4Co/3Ce7Zr and 8Co/3Ce7Zr modifications in comparison with 8Cu/3Ce7Zr. At the same time all 5Ce5Zr modifications show very close catalytic behavior similar to that of 8Cu/3Ce7Zr, which make these materials very perspective as catalysts for the total oxidation of ethylacetate and also other volatile organic compounds.

Acknowledgements: Financial support by Program for career development of young scientists, BAS (project DFNP 145 /12.05.2016) is gratefully acknowledged

REFERENCES

1. J. R. Salge, B. J. Dreyer, P. J. Dauenhauer, L. D. Schmidt, *Science*, **314**, 801 (2006).
2. W. Ruettinger, X. S. Liu, R. J. Farrauto, *Appl. Catal., B*, **65**, 135 (2006).
3. S. McIntosh, R. J. Gorte, *Chem. Rev.*, **104**, 4845 (2004).
4. R. N. Ivanova, M. D. Dimitrov, D. G. Kovacheva, T. S. Tsoncheva, *Bulg. Chem. Commun.*, **48-G**, 125 (2016).
5. R. N. Ivanova, M. D. Dimitrov, D. G. Kovacheva, T. S. Tsoncheva, *Bulg. Chem. Commun.*, **49-A**, 84 (2017).
6. P.-O. Larsson, A. Andersson, *Appl. Catal., B*, **24**, 175 (2000).
7. A. R. Gandhe, J. S. Rebello, J. L. Figueiredo, J. B. Fernandes, *Appl. Catal., B*, **72**, 129 (2007).
8. P. Fang, J. Lu, X. Xiao, M. Luo, *J. Rare Earth*, **26**, 250 (2008).
9. M. Dimitrov, R. Ivanova, N. Velinov, J. Henych, M. Slušná, V. Štengl, I. Mitov, T. Tsoncheva, *Nano-Structures and Nano-Objects*, **7**, 56 (2016).
10. R. Prasad, G. Rattan, *Bull. Chem. React. Eng. Catal.*, **5**, 7 (2010).
11. H. Zhu, L. Dong, Y. Chen, *J. Coll. Int. Sci.*, **357**, 497 (2011).
12. H. Chen, A. Yin, X. Guo, W.-L. Dai, K.-N. Fan, *Catal. Lett.*, **131**, 632 (2009).
13. T. Tsoncheva, I. Genova, M. Dimitrov, E. Sarcadi-Priboczki, A. M. Venezia, D. Kovacheva, N. Scotti, V. dal Santo, *Appl. Catal., B*, **165**, 599 (2015).
14. M. Manzoli, R. Di Monte, F. Boccuzzi, S. Coluccia, J. Kašpar, *Appl. Catal., B*, **61**, 192 (2005).
15. Z. Zhao, R. Jin, T. Bao, X. Lin, G. Wang, *Appl. Catal., B*, **110**, 154 (2011).
16. X. Weng, J. Zhang, Z. Wu, Y. Liu, *Catal. Today*, **175**, 386 (2011).
17. J. Huang, Y. Kang, L. Wang, T. Yang, Y. Wang, S. Wang, *Catal. Commun.*, **15**, 41 (2011).
18. J. Hao, J. Wang, Q. Wang, Y. Yu, S. Cai, F. Zhao, *Appl. Catal., A*, **368**, 29 (2009).
19. T. S. Tsoncheva, I. G. Genova, N. Scotti, M. D. Dimitrov, A. Gallo, D. G. Kovacheva, N. Ravasio, *Bulg. Chem. Commun.*, **47**, 283 (2015).
20. N. Qiu, J. Zhang, Z. Wu, *Phys. Chem. Chem. Phys.*, **16**, 22659 (2014).
21. T. Tsoncheva, G. Issa, J. M. López Nieto, T. Blasco, P. Concepcion, M. Dimitrov, G. Atanasova, D. Kovacheva, *Micropor. Mesopor. Mater.*, **180**, 156 (2013).

МОДИФИЦИРАНИ С МЕД И/ИЛИ КОБАЛТ НАНОСТРУКТУРИРАНИ Ce-Zr СМЕСЕНИ ОКСИДИ КАТО ЕФЕКТИВНИ КАТАЛИЗАТОРИ ЗА ПЪЛНО ОКИСЛЕНИЕ НА ЕТИЛАЦЕТАТ

Р. Н. Иванова^{1*}, М. Д. Димитров¹, Д. Г. Ковачева², Т. С. Цончева¹

¹ *Институт по органична химия с Център по фитохимия, Българска академия на науките, 1113 София, България,*

² *Институт по обща и неорганична химия, Българска академия на науките, 1113 София, България*

Постъпила на 13 април 2017 г.; Коригирана на 15 май 2017 г

(Резюме)

Чрез използването на оригинален подход, включващ участието на уреа като утайтел и последваща хидротермална обработка, бяха получени два наноструктурирани Ce-Zr смесени оксиди с различно отношение на метала в тях (3:7 и 5:5), които впоследствие бяха модифицирани с мед и/или кобалт посредством метод на омокряне с воден разтвор на съответните метални нитрати. Получените материали бяха характеризирани с помощта на прахова рентгенова дифракция, физична адсорбция на азот, UV-Vis спектроскопия, температурно-програмирана редукция с водород, а тяхната каталитична активност и селективност беше изследвана в реакцията на окисление на етилацетат. Въвеждането на допълнителен преходен метален оксид в изходните Ce-Zr наноматериали води до намаление на началната температура на превръщане на етилацетат с до 50 K, увеличава съществено каталитичната активност в интервала 550-650 K и дава почти пълно окисление на етилацетат в цялата изследвана температурна област. Влиянието на вида на използвания преходен метал може да бъде по-добре разграничена при 3Ce7Zr носителя, особено в интервала 550-600 K, като резултатите показват, че добавянето единствено на мед е достатъчно за постигане на най-добрите каталитични резултати. Същевременно, носителят с по-високо съдържание на церий (5Ce5Zr) благоприятства каталитичното поведение и на Co-съдържащите образци, поради подобро взаимодействие Co-Ce.

Structure and radical scavenging activity of isoxazolo- and thiazolohydrazinylidene-chroman-2,4-diones

B. Stamboliyska^{1*}, A. Jashari², D. Yancheva¹, B. Mikhova¹, D. Batovska¹, E. Popovski³, K. Mladenovska^{4,5}

¹ Institute of Organic Chemistry with Centre of Phytochemistry, Bulgarian Academy of Sciences, Acad. G. Bonchev street, bl. 9, 1113 Sofia, Bulgaria

² Faculty of Natural Sciences and Mathematics, State University of Tetova, 1200 Tetova, Macedonia

³ Research Center for Environment and Materials, Macedonian Academy of Sciences and Arts, Krste Misirkov 2, 1000 Skopje, Republic of Macedonia

⁴ Institute of Chemistry, Faculty of Natural Sciences and Mathematics, University "Ss. Cyril and Methodius", Arhimedova 5, PO Box 162, 1000 Skopje, Macedonia

⁵ Faculty of Pharmacy, University "Ss Cyril and Methodius", Mother Theresa 47, 1000 Skopje, Macedonia

Received April 20, 2017; Revised May 18, 2017

Dedicated to Acad. Ivan Juchnovski on the occasion of his 80th birthday

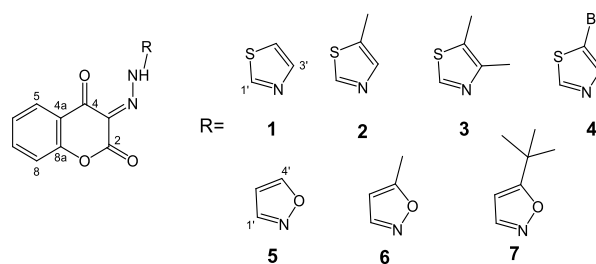
Quantum chemical calculations based on the density functional theory and NMR spectroscopy have been employed to perform structural analysis of four thiazolo- and three isoxazolohydrazinylidene-chroman-2,4-diones and to predict their relevant structural isomers. The scavenging capacities of the studied molecules towards nitric oxide (NO[•]), superoxide anion radical (O₂^{•-}) and DPPH[•] radicals were estimated. The compounds possessing a thiazolidine ring were 10-fold more active in the test with nitric oxide (NO[•]) than the rest of coumarins with isoxazolidine ring. A radical scavenging mechanism in aqueous medium was proposed to explain this activity.

Key words: hydrazinylidene-chroman-2,4-diones, radical scavenging activity, structure, DFT, NMR

INTRODUCTION

Coumarins and related compounds are of remarkable interest to medicinal chemists due to their multiple pharmacological effects based on the antioxidative activity and modification of immune responses, cell proliferation and differentiation [1]. Coumarins and their derivatives are proved precursors in synthesis of a number of medical compounds and the heterocycles obtained from them are examined for their anticoagulant [2,3], anti-inflammatory and analgesic [4-6], antibacterial and antifungal [7-9], antiviral [10], antioxidant [11] and anticancer effect [12-18]. In a previous study [19], isoxazolo- and thiazolohydrazinylidene-chroman-2,4-diones that combine the coumarin core with five membered heterocycles (Scheme 1) have been synthesized and structurally characterized. In addition, their anticancer activity in vitro on different (metastatic) cancer cell lines was evaluated, when administered alone or in synergy with tamoxifen and doxorubicin [19-22]. In general, all synthesized compounds showed dose- and time-dependent effects, highlighting as the

most potent the molecules containing a thiazole entity, with or without additional methyl groups bound to the carbons at positions 5 and/or 4 of the thiazole ring.



Scheme 1. Studied thiazolo- (1-4) and isoxazolo-hydrazinylidene-chroman-2,4-diones (5-7).

In continuation of the studies, here we present the RSA of isoxazolo- and thiazolohydrazinylidene-chroman-2,4-diones. Since the characterization of the most stable geometrical isomers of the studied molecules and the factors that contributed to their relative stability are essential to a complete understanding of their biological properties, we used Density Functional Theory (DFT) to perform structural analysis of the studied molecules and to predict the NMR spectra of their relevant structural isomers. The main goal of the present contribution

* To whom all correspondence should be sent:
E-mail: bs@orgchm.bas.bg

is to evaluate the potential antioxidant activity of the synthesized compounds as well as to determine the preferred mechanism of this activity in polar environment, as a description of the processes taking place in the living organism.

EXPERIMENTAL

Synthesis and NMR spectroscopy

The compounds were prepared by derivatization of the appropriate heterocyclic amines which were used as electrophiles to attack the coumarine ring [19]. The NMR spectra were run on a Bruker-250 DRX Spectrometer in DMSO-d₆, as solvent using standard Bruker Topspin software. The chemical shifts were referenced to the residual solvent signal (2.5 ppm for the ¹H and 39.5 ppm for the ¹³C spectra).

Nitric oxide radical scavenging micro-assay

For nitric oxide radical scavenging assay, the method of Harput *et al.* [23] was employed. Briefly, a strip plate, containing 100 µl of serial diluted compounds and 100 µl of freshly prepared 10 mM sodium nitroprusside in phosphate buffer (0.1 mM, pH 7.4), was irradiated with fluorescent light (36 W) for 15 minutes. Then, 100 µl of fresh Griess reagent were added and the absorption of the resulting mixture was measured at 560 nm.

Superoxide anion radical (O₂^{•-}) scavenging assay

The superoxide anion radical scavenging capacity of the compounds was estimated in a riboflavin-light-NBT system, as described by Leelaprakash *et al.* [24]. The reaction mixture contained 75 µL riboflavin (0.04 mM), 75 µL phenazine methosulphate (1.0 mM) and 75 µL nitroblue tetrazolium (0.1 mM), prior to the addition of 75 µL sample. The reaction was started by illuminating the reaction mixture with the sample using a fluorescent lamp. After 20 min of incubation, the absorbance was measured at 560 nm.

DPPH radical micro-assay

The DPPH assay was performed using the method described by Nenadis and Tsimidou [25]. Briefly, an aliquot (296 µL) of a 0.1 mM ethanolic DPPH[•] solution was mixed with 4 µL of each of the ethanolic sample solutions. The decrease of the absorption at 516 nm of the DPPH[•] solution was measured 30 min after addition of each sample.

DFT calculations

The quantum chemical calculations were performed using the Gaussian 09 package [26]. The geometry optimizations of the structures investigated were done without symmetry restrictions, using DFT. We employed the B3LYP hybrid functional, which combines Becke's three-parameter nonlocal exchange with the correlation functional of Lee *et al.* [27,28], adopting 6-311++G**. The stationary points found on the molecular potential energy hypersurfaces were characterized using standard harmonic vibrational analysis. ¹H and ¹³C-NMR chemical shifts of the studied compounds and of the solvent DMSO-d₆ were calculated by using the GIAO method [29] at the same level of theory (reference compound TMS was calculated at the same level).

The equations used for calculation of dissociation enthalpy (BDE) and ionization potential (IP) of the studied compounds are given below:

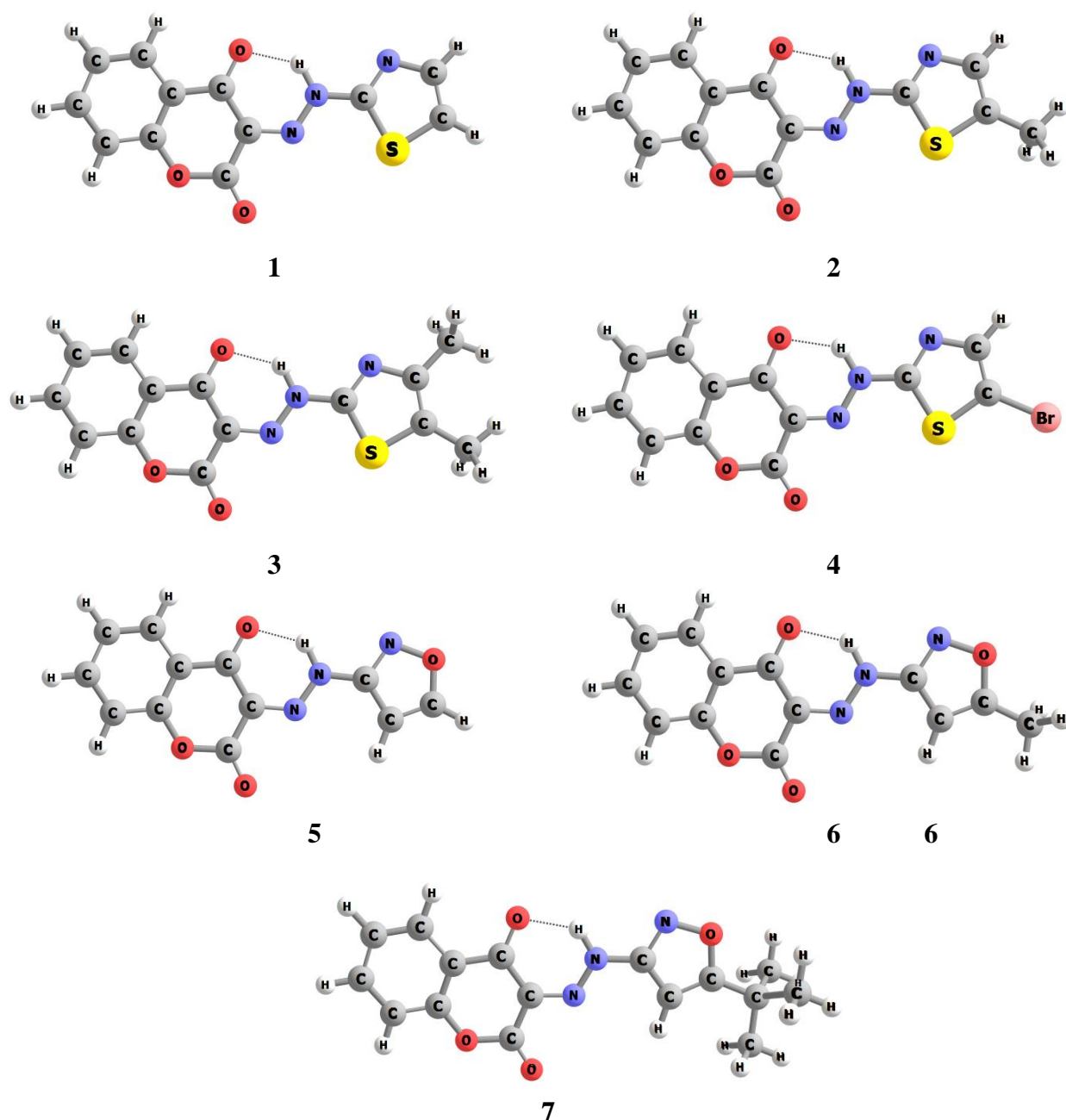
$$\text{BDE} = \text{H}(\text{A}^\bullet) + \text{H}(\text{H}^\bullet) - \text{H}(\text{AH})$$

$$\text{IP} = \text{H}(\text{AH}^{\bullet+}) + \text{H}(\text{e}^-) - \text{H}(\text{AH})$$

The enthalpy of the hydrogen atom, H(H) was obtained by the same method and basis set. All reaction enthalpies were calculated at 298 K. The enthalpies of proton H(H⁺), and electron, H(e⁻), were taken from the literature – 6.197 kJ mol⁻¹ and 3.145 kJ mol⁻¹, respectively [30]. Solvation enthalpies of proton H(H⁺), electron, H(e⁻), in water, determined using IEF-PCM DFT/B3LYP/6-311++G** calculations, were used as reported [31].

RESULTS AND DISCUSSION

All of thiazolo- and isoxazolohydrazinylidene-chroman-2,4-diones studied (**1-7**) can exist in three different tautomeric forms (**A**, **B** and **C**; Scheme 2). The possible tautomeric forms of the thiazolo- and isoxazolohydrazinylidene-chroman-2,4-diones (**1-7**) were studied by quantum chemical calculations (B3LYP/6-311++G**). According to our calculations in gaseous phase the most stable is the diketo form **A**. The hydroxyl imines tautomeric forms **B** and **C** were found to be of no practical interest, because their energies are higher more than 20 kJ mol⁻¹ for **B** and more than 40 kJ mol⁻¹ for **C**. According to Minkin *et al.* [32], prototropic conversions are probable in case when the energy differences between the initial and the final structure do not exceed 20 kJ mol⁻¹ with activation barrier not higher than 105 kJ mol⁻¹.



Scheme 2. Geometry of the most stable forms of compounds **1-7**.

As it could be seen in Table 1, the energy differences are larger in the present case, and convince that only **A** should be expected to exist in real system. Different conformations resulting from internal rotation around the C3-N and N-R bonds are possible and should be taken into account. The energy differences of the respective conformations of tautomer **A** resulting from the rotation around C3-N fall in the interval between 1.0 and 1.5 kJmol⁻¹. The internal rotation around the N-R bond leads to energy differences from 4.5 to 5.4 kJ mol⁻¹

¹. The most stable conformers for each studied compound (**1-7**) are represented in Scheme 2.

The most stable conformer for compound **7** corresponds to the structure which we have established by crystallographic analysis [33]. The calculated ¹³C chemical shifts for the compounds **1-7** are in a good agreement with the experimental NMR data (Table 1). The only substantial difference between the experimental and calculated chemical shifts for C4' in compound **4** may be attributed to relativistic effects [34].

Table 1. Calculated and experimental ^{13}C chemical shifts (DMSO- d_6) for compounds **1–7**.

	1		2		3		4		5		6		7	
	calc.	exp.												
2	155.0	157.3	155.1	157.3	155.2	157.3	154.8	157.2	155.5	157.6	155.5	157.6	159.4	157.6
3	123.5	125.0	123.3	124.6	123.2	124.0	124.0	125.3	124.6	126.0	124.2	125.7	122.7	125.7
4	179.9	177.9	179.8	177.6	179.3	177.2	180.6	177.3	179.7	178.6	179.7	178.4	174.3	178.3
4a	120.5	120.4	120.4	120.4	120.4	120.6	120.2	120.7	120.5	120.4	120.4	120.4	122.1	120.4
5	129.6	126.7	129.5	126.6	129.2	126.7	129.7	126.8	129.6	126.8	129.7	126.8	130.1	126.8
6	123.3	124.7	123.2	124.7	123.0	124.7	123.8	124.7	123.4	124.9	123.3	124.8	124.4	124.9
7	137.3	136.8	137.0	136.7	136.9	136.5	137.6	136.6	137.5	137.0	137.2	136.9	135.5	137.0
8	117.7	117.3	117.6	117.3	117.6	117.3	117.8	117.3	117.7	117.4	117.6	117.7	117.4	117.4
8a	158.7	154.1	158.2	153.9	159.0	153.9	157.5	154.0	159.2	154.1	158.6	154.1	157.0	154.1
1'	170.8	166.3	169.3	164.5	166.7	163.9	169.7	163.1	166.2	162.2	166.6	162.7	166.4	162.4
3'	140.3	140.4	137.8	137.5	147.5	144.5	142.0	142.3						
4'	122.7	117.6	143.0	131.7	135.9	124.0	136.9	105.3	161.3	162.4	175.0	172	187.1	182.0
5'									96.0	97.3	93.1	94.1	89.6	91.2
C4-Me			9.2	11.9	9.5	11.2					8.6	12.3	34.8	32.9
C3-Me					12.8	14.0								
Me													23.7	28.2
Me													25.2	28.2
Me													25.2	28.2

The ^{13}C chemical shift of C4 is characteristic for C=O rather than C-OH and supports the predicted structure. No signals for OH and NH were observed in the ^1H spectrum [19] and this fact is also in accordance with the structure proposed by the quantum chemical calculations. The similarity of ^1H and ^{13}C chemical shifts of the coumarine moiety of compounds **1-7** reveals a similar electronic distribution. The different substituents do not influence it.

Having in mind the good NMR spectral descriptions obtained in this work and the relevance to the X-ray structural data of the compound **7** [33], we consider that the predictions of the structures of all studied compounds are reliable and the molecular structures of the compounds in solution are similar to their crystal structures. The scavenging capacities of the synthesized coumarin derivatives were estimated towards nitric oxide (NO^\bullet), superoxide anion radical ($\text{O}_2^{\bullet-}$) and 1,1-diphenyl-2-picryl-hydrazyl (DPPH) radicals by classical methods adapted for a micro-scale on Elisa strip reader STATFAX 303+. Caffeic acid was used as a positive control. The absorbance of the negative control (A of control) was determined by replacing the sample with methanol. Seven

concentrations of each compound ($n = 3$) were analyzed. The radical scavenging activities of the compounds (RSA) were calculated using the following formula:

$$\text{RSA} (\%) = (A_{\text{of control}} - A_{\text{of sample}}) / A_{\text{of control}} \times 100$$

The SC_{50} values ($\mu\text{g}/\text{mL}$) for each compound were calculated from the $\text{RSA} = f(\text{concentration})$ curves and were used in the structure–activity relationship study.

The seven compounds were less active than the caffeic acid (Table 2). The superoxide anion radical ($\text{O}_2^{\bullet-}$) and DPPH assays showed that the synthesized compounds were inactive in the concentration region between 0.5 and 7.2 mM. Under the same experimental conditions, the positive control caffeic acid was a strong scavenger, with concentration providing 50% inhibition (IC_{50}) of 61.1 μM (DPPH). However, some interesting correlations were observed between the title compounds and their RSA towards nitric oxide. The compounds were divided in two sets. The first one contained the most active compounds (**1-4**) with IC_{50} of 0.5 mM. All of them possess a thiazolidine ring and are 10-fold more active than the rest of coumarins, which form the second group.

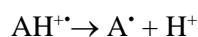
Table 2. Radical scavenging capacities of compounds **1-7** towards nitric oxide (NO[•]) and calculated reaction enthalpies

	IC ₅₀ μM	BDE(Gas), kJ mol ⁻¹	IP(Gas) kJ mol ⁻¹	BDE(H ₂ O) kJ mol ⁻¹	IP(H ₂ O) kJ mol ⁻¹
1	454.4	370.8	773.9	359.6	370.2
2	525.2	367.4	749.0	354.6	353.5
3	492.2	366.6	724.6	350.9	339.3
4	488.6	368.2	764.3	360.2	366.7
5	5489.5	382.0	823.7	373.3	430.6
6	5276.2	381.4	806.1	372.4	422.5
7	3948.3	380.9	799.6	372.0	418.6

One possible mechanism by which the antioxidants can deactivate a free radical is H-atom abstraction (HAT mechanism) [30]:



The efficacy of the antioxidant to react via HAT is characterized by the bond dissociation enthalpy (BDE). Higher stability of A *i.e.* lower BDE values correspond to good antioxidant capacity of A-H. Another possible mechanism is electron transfer (SET mechanism), in which the radical cation is first formed followed by deprotonation [31]:



For evaluation of reactivity via SET, the ionization potential (IP) is used. A lower IP implies an easier extraction of the electron. Based on calculation of the reaction enthalpies for each of the mechanisms, it is possible to suggest the most probable mechanism of action of a particular group of compounds [31].

The calculated reaction enthalpies, involved in the two mechanisms of antiradical activity of **1-7**, are presented in Table 2. We performed calculations of the respective values in nonpolar conditions (gas) and in polar medium (water). In the Table 2, the calculated reaction enthalpies are listed together with the experimentally found scavenging capacities of the coumarin derivatives towards nitric oxide (NO[•]).

As can be seen, in gas phase the BDEs of all studied compounds are almost the same and are considerably lower than the respective IPs, which indicates the HAT mechanism as the most favorable. BDEs are similar in water *i.e.* the energy requirements for HAT do not change much with the environment polarity. On the other hand, as a result

of the greater stabilization in polar environment (water) the corresponding IPs are significantly lower than in gas phase. The calculated IP values in polar medium are substantially reduced compared to gas phase due to the fact that the electron and the radical cations are solvated and stabilized in polar medium. Furthermore, the IPs of the compounds possessing a thiazolidine ring are comparable or lower than their BDE values. The BDE values of the coumarins that do not possess a thiazolidine ring are still higher than the BDE values in all studied media. Therefore, it could be concluded that the SET mechanism would be competitive to the HAT one for compounds **1-4**, possessing a thiazolidine ring, in water. In this way, the superior activity of compounds **1-4** most probably could be explained by their capacity to deactivate free radicals simultaneously by two mechanisms (HAT and SET) in water.

The observed radical scavenging capacity towards nitric oxide (NO[•]) correlates with the results of a previous study about anticancer activity of the reported compounds [19-22]. The derivatives having sulphur in the five membered heterocycle showed a more potent effect on cancer cell viability. Nitric oxide (NO[•]) is a ubiquitous, water soluble, free radical gas, which plays key role in various physiological as well as pathological processes. Over the past decades, NO[•] has emerged as a 'Doubled-Edged Sword' in cancer. It is said to have both tumoracidal as well as tumor promoting effects which depends on its timing, location, and concentration. Interestingly, a statistically significant correlation was found between the measured in this study ability of the synthesized coumarin derivatives to scavenge NO[•] and their previously estimated growth-inhibition activity towards some cancer cell lines [35, 36]. This fact may be interpreted as a probable key role of the NO[•] molecule in the anticancer activity of the studied compounds.

CONCLUSION

The ability of four thiazolo- and three isoxazolohydrazinylidene-chroman-2,4-diones to scavenge superoxide (O₂^{•-}) anion, nitric monoxide (NO[•]) radicals and 2,2-diphenyl-1-picrylhydrazyl free radical (DPPH[•]) was evaluated. The possible tautomeric forms of the thiazolo- and isoxazolo-hydrazinylidene-chroman-2,4-diones (**1-7**) were studied by quantum chemical calculations (B3LYP/6-311++G**) and in gaseous phase the most stable was the enamine structure **A** in

accordance with the crystallographic analysis and the NMR spectra. The compounds possessing a thiazolidine ring were 10-fold more active than the rest of coumarins possessing isoxazolidine ring towards nitric oxide (NO[•]). The observed radical scavenging capacity correlates with the results of a previous study about anticancer activity of the reported compounds. This superior activity could be explained by the ability of the thiazolo-derivatives to deactivate free radicals simultaneously by two mechanisms (HAT and SET) in water. The presented study is a complementation of the thorough investigation on various aspects of biological activities of this perspective class of compounds.

Acknowledgements: The financial support of this work by the National Science Fund of Bulgaria (Contracts BM-2/2007 and RNF01/0110 is gratefully acknowledged.

REFERENCES

- P. K. Jain, H. Joshi, *J. Appl. Pharm. Sci.*, **2**, 236 (2012).
- O. Danis, B. D., Yuce, C. Gunduz, A. Ogan, G. Sener, M. Bulut, *Arzneimittelforsch.*, **60**, 617 (2010).
- L. Lei, Y-B. Xue, Z. Liu, S-S. Peng, Y. He, Y. Zhang, *Sci. Rep.*, **5**, 13544 (2015).
- R. K. Arora, N. Kaur, Y. Bansal, G. Bansal, *Acta Pharm. Sinica*, **B4**, 368 (2014).
- J. D. Hadjipavlou-Litina, E. K., Litinas, C. Kontogiorgis, *Antiinflamm. Antiallergy Agents Med. Chem.*, **6**, 29 (2007).
- S. G. Bolakatti, S. V. Maddi, N. S. Mammedesai, M. P. Ronad, M. B. Palkar, S. Swamy, *Arzneimittelforsch.*, **58**, 515 (2008).
- B. R. Dekić, N. S. Radulović, V. S. Dekić, R. D. Vukićević, R. M. Palić, *Molecules*, **15**, 2246 (2010).
- K. S. Nimavat, K. B. Vyas, G. R. Jani, M. V. Hathi, *Electr. J. Chem.*, **1**, 183 (2009).
- M. R. Zaki, A. Y. Elossaily, M. A. El-Dean, *Bioorg. Khim.*, **38**, 721 (2012).
- R. J. Hwu, R. Singha, C. S. Hong, H. Y. Chang, R. A. Das, I. Vliegen, E. C. De, J. Neyts, *Antivir. Res.*, **77**, 157 (2008).
- R. Torres, F. Faini, B. Modak, F. Urbina, C. Labbé, J. J. Guerrero, *Phytochemistry*, **67**, 984 (2006).
- F. Belluti, G. Fontana, L. B. Dal, N. Carenini, C. Giommarelli, F. Zunino, *Bioorg. Med. Chem.*, **18**, 3543 (2010).
- A. Kamal, F. S. Adil, R. J. Tamboli, B. Siddardha, U. S. N. Murthy, *Lett. Drug Des. Disc.*, **6**, 201 (2009).
- S. Bhattacharyya, S. Paul, S. Mandal, A. Banerjee, N. Boujedaini, A.B. Khuda, *Eur. J. Pharmacol.*, **614**, 128 (2009).
- Z. Chen, J. Bi, W. Su, *Chin. J. Chem.*, **31**, 507 (2013).
- V. Ranganatha, F. Zameer, S. Meghashri, N. D. Rekha, V. Girish, H. D. Gurupadaswamy, S. A. Khanum, *Arch. Pharm. (Weinheim)*, **346**, 901 (2013).
- X-Q. Wu, C. Huang, Y-M. Jia, B-A. Song, L. Li, X-H. Liu, *Eur. J. Med. Chem.*, **74**, 717 (2014).
- M. Musa, J. Cooperwood, M. Khan, *Curr. Med. Chem.*, **15**, 2664 (2008).
- A. Jashari, F. Imeri, L. Ballazhi, A. Shabani, B. Mikhova, G. Dräger, E. Popovski, A. Huwiler, *Bioorg. Med. Chem.*, **22**, 2655 (2014).
- L. Ballazhi, F. Imeri, A. Dimovski, A. Jashari, E. Popovski, P. Breznica-Selmani, B. Mikhova, G. Dräger, E. Alili-Idrizi, K. Mladenovska, *Mac. Pharm. Bull.*, **60**, 35 (2014).
- L. Ballazhi, E. Popovski, A. Jashari, F. Imeri, I. Ibrahim, B. Mikhova, K. Mladenovska, *Acta Pharm.*, **65**, 53 (2015).
- L. Ballazhi, F. Imeri, A. Jashari, E. Popovski, G. Stojković, A. J. Dimovski, B. Mikhova, K. Mladenovska, *Acta Pharm.*, **67**, 35 (2017).
- U. Harput, Y. Genc, N. Khan, *Rec. Nat. Prod.*, **5**, 100 (2011).
- G. Leelaprakash, S. Mohan Dass, V. Sivajothi, *J. Pharm. Res.*, **4**, 617 (2011).
- N. Nenadis, M. Tsimidou, *J. Am. Oil. Chem. Soc.*, **79**, 1191 (2002).
- M. J. Frisch, G. W. Trucks, H. B. Schlegel, G. E. Scuseria, M. A. Robb, J. R. Cheeseman, G. Scalmani, V. Barone, B. Mennucci, G. A. Petersson, H. Nakatsuji, M. Caricato, X. Li, H. P. Hratchian, A. F. Izmaylov, J. Bloino, G. Zheng, J. L. Sonnenberg, M. Hada, M. Ehara, K. Toyota, R. Fukuda, J. Hasegawa, M. Ishida, T. Nakajima, Y. Honda, O. Kitao, H. Nakai, T. Vreven, J. A. Montgomery, Jr., J. E. Peralta, F. Ogliaro, M. Bearpark, J. J. Heyd, E. Brothers, K. N. Kudin, V. N. Staroverov, R. Kobayashi, J. Normand, K. Raghavachari, A. Rendell, J. C. Burant, S. S. Iyengar, J. Tomasi, M. Cossi, N. Rega, J. M. Millam, M. Klene, J. E. Knox, J. B. Cross, V. Bakken, C. Adamo, J. Jaramillo, R. Gomperts, R. E. Stratmann, O. Yazyev, A. J. Austin, R. Cammi, C. Pomelli, J. W. Ochterski, R. L. Martin, K. Morokuma, V. G. Zakrzewski, G. A. Voth, P. Salvador, J. J. Dannenberg, S. Dapprich, A. D. Daniels, O. Farkas, J. B. Foresman, J. V. Ortiz, J. Cioslowski, and D. J. Fox, Gaussian 09, Revision A.1, Gaussian Inc., Wallingford CT, 2009.
- D. J. Becke, *J. Chem. Phys.*, **98**, 5648 (1993).
- C. Lee, W. Yang, G.R. Parr, *Phys. Rev.*, **37B**, 785 (1988).
- R. Ditchfield, *Mol. Phys.*, **27**, 789 (1974).
- E. Klein, V. Lukes, M. Ilcin, *Chem. Phys.*, **336**, 51 (2007).

31. J. Rimarcik, V. Lukes, E. Klein, M. Ilcin, *J. Mol. Struct. (Theochem)*, **952**, 25 (2010).
32. A.I. Minkin, B. Y. Simkin, R. M. Minyaev, Quantum chemistry of organic compounds. Mechanisms of reactions, Springer, Heidelberg, 1990.
33. A. Jashari, E. Popovski, B. Mikhova, R. Nikolova, B. Shivachev, *Acta Cryst.*, **E69**, o258 (2013).
34. T. B. Demissie, M. Repisky, S. Komorovsky, J. Isaksson, J. S. Svendsen, H. Dodziuk, K. Ruud, *J. Phys. Org. Chem.*, **26**, 679 (2013)
35. S. K. Choudhari, M. Chaudhary, S. Bagde, A. R. Gadbaile, V. Joshi, *World J. Surg. Oncol.*, **11**, 118 (2013)
36. W. Xu, L. Z. Liu, M. Loizidou, M. Ahmed, I. G. Charles, *Cell Res.*, **12**, 311 (2002).

СТРУКТУРА И РАДИКАЛ – УЛАВЯЩА АКТИВНОСТ НА ТИАЗОЛО- И ИЗОКСАЗОЛОХИДРАЗЕНИЛИДЕН-ХРОМАН-2,4-ДИОНИ

Б. Стамболийска^{1*}, А. Яшари², Д. Янчева¹, Б. Михова¹, Д. Бътовска¹, Е. Поповски³, К. Младеновска^{4,5}

¹ Институт по органична химия с Център по фитохимия, Българска академия на науките, ул. "Акад. Г. Бончев, бл.9, 1113 София

² Факултет по естествени науки и математика, Държавен университет Тетово, 1200 Тетово, Македония

³ Институт по химия, Факултет по естествени науки и математика, Университет „Св. Св.Кирил и Методий“, Скопие, Македония

⁴ Изследователски център по околна среда и материали, Македонска академия на науките и изкуствата, ул. „Кръсте Мисирков“2, Скопие, Македония

⁵ Факултет по фармация, Университет „Св. Св.Кирил и Методий“, Скопие, Македония

Постъпила на 20 април 2017 г.; Коригирана на 18 май 2017 г.

(Резюме)

Квантово-химични изчисления на базата на теорията на плътностния функционал (DFT/B3LYP/6-311++G**), както и ЯМР спектроскопия бяха приложени за структурен анализ и предсказване на енергетично изгодните изомери на четири тиазоло- и три изоксазоло-хидразинилиден-хроман-2,4-диони. Беше изследвана радикал – улавящата активност спрямо азотен оксид (NO[•]), супероксиден анион радикал (O₂^{•-}) и 1,1,-дифенил-2-пикрил-хидразил радикал (DPPH[•]). Установено беше, че кумарините с тиазолов пръстен са 10 пъти по-активни спрямо азотен оксид (NO[•]) в сравнение с изоксазоловите производни. С цел обяснение на тази активност е предложен механизъм на процеса в полярна среда.

Atropisomeric phosphorus-decorated 1-phenyl-3,4-dihydroquinazolin-1-ium NHC precursors

R. H. Lyapchev¹, M. G. Dangalov², G. G. Gencheva¹, N. G. Vassilev², P. Y. Petrov^{1*}

¹ Department of Organic Chemistry and Pharmacognosy, Faculty of Chemistry and Pharmacy, Sofia University St. Kliment Ohridsky, James Bourchier 1, 1164 Sofia, Bulgaria

² Institute of Organic Chemistry with Centre of Phytochemistry, Bulgarian Academy of Sciences, Acad. G. Bonchev street, bl. 9, 1113 Sofia, Bulgaria

Received May 03, 2017; Revised May 22, 2017

Dedicated to Acad. Ivan Juchnovski on the occasion of his 80th birthday

Bidentate atropisomeric 3-(2-(diphenylphosphorothioyl)phenyl)-1-phenyl 3,4-dihydroquinazolinium salts as N-heterocyclic carbene (NHC) precursors were prepared using *N*-(2-(diphenylphosphorothioyl)phenyl)-2-(*N*-phenylformamido)benzamide as starting material.

Key words: organophosphorous compounds; N-heterocyclic carbenes; homogeneous catalysis; atropisomerism; ligand

INTRODUCTION

N-heterocyclic carbenes (NHCs) in their σ -donor abilities towards transition metals as ligands surpass phosphanes and form more stable complexes which are not prone to ligand dissociation and are excellent catalysts for hydrogenation and cross-coupling reactions [1]. One area in which NHCs still lack (due to the intrinsic distance between the metal center and the substituents on the N-atoms) is asymmetric catalytic transformations, where phosphanes are still indispensable. Only scarce examples of successful asymmetric induction by NHC ligands can be found in the literature [2–6]. Herein we present our first efforts towards an atropisomeric 3,4-dihydroquinazolin concept in which desymmetrization of the quinazoline plane is achieved by an angular 3-2-(diphenylphosphorothioyl)phenyl or 3-2-(diphenylphosphanyl)phenyl substituent at N3 - these bidentate ligand precursors contain two (protected) donor centers - a phosphorus atom and a carbene at C2.

EXPERIMENTAL

Synthesis

All solvents and chemicals were purchased from commercial suppliers. Petroleum ether and methanol were used as received. Raney Ni was obtained immediately before use by treating 0.603

g of nickel-aluminum alloy (NiAl₂) with a twofold excess of degassed 15% aqueous solution of NaOH for 40 min at room temperature and subsequent washing with degassed methanol.

Dichloromethane was dried over anhydrous CaCl₂ and distilled. THF was distilled from sodium/benzophenone. Silica gel 0.035-0.070 mm, 60 A was used for flash chromatography. TLC on silica gel 60 F₂₅₄ on aluminum sheets was used for monitoring of the reactions.

The NMR spectra were recorded on a Bruker Avance II+ 600 (600.13 for ¹H NMR, 150.92 MHz for ¹³C NMR and 242.92 MHz for ³¹P NMR) spectrometer with a reference TMS (85% H₃PO₄ for ³¹P) as internal standard or chemical shifts of residue solvent peaks (δ , ppm). ¹H and ¹³C NMR data are reported as follows: chemical shift, multiplicity (s = singlet, d = doublet, t = triplet, q = quartet, br = broad, m = multiplet), coupling constants J (Hz), integration and identification.

N-(2-(diphenylphosphorothioyl)phenyl)-2-(*N*-phenylformamido)benzamide (**2**): 0.400 g (7.93 x 10⁻⁴ mol) of compound **1** were suspended in 9.5 ml THF. The reaction mixture was cooled in an ice bath, and dropwise for about 10 min were added 16 ml of mixture of equal volumes of formic acid and acetic anhydride, which had been stirred at room temperature for 2 hours. After 24 hours, another 5 ml of Ac₂O/HCOOH mixture were added. 3 hours later the acidic solution was neutralized with K₂CO₃, extracted with ethyl acetate, dried (Na₂CO₃) and purified by column chromatography on silica gel. Yield: 0.330 g (**2**) (78%) of slowly solidifying colorless oil.

* To whom all correspondence should be sent:
E-mail: ppetrov@chem.uni-sofia.bg

¹H NMR (600 MHz, CDCl₃, two conformers in ratio 1:0.7 at 293K) Major δ = 10.03 (s, 1H, **NH**), 8.64 (s, 1H, **CHO**), 7.92 (dd, J = 4.8, 8.0 Hz, 1H, **H6'**), 7.74 (ddd, J = 1.2, 8.4, 13.8 Hz, 4H, **o-Ar-P**), 7.58-7.53 (m, 2H, **p-Ar-P**), 7.51-7.47 (m, 5H, **m-Ar-P**, **H5'**), 7.41 (dt, J = 1.5, 7.7 Hz, 1H, **H6**), 7.34 (dd, J = 7.5, 8.3 Hz, 1H, **p-Ar-N**), 7.24-7.21 (m, 2H, **m-Ar-N**), 7.20-7.19 (m, 3H, **H8** and **o-Ar-N**), 7.16-7.13 (m, 1H, **H7**), 7.07-7.04 (m, 1H, **H4'**), 6.98 (dd, J = 1.3, 7.7 Hz, 1H, **H5**), 6.77-6.72 (m, 1H, **H3'**); Minor δ = 10.29 (s, 1H, **NH**), 8.36 (s, 1H, **CHO**), 7.78 (dd, J = 4.8, 8.0 Hz, 1H, **H6'**), 7.69 (ddd, J = 1.2, 8.4, 13.8 Hz, 4H, **o-Ar-P**), 7.58-7.53 (m, 2H, **p-Ar-P**), 7.51-7.47 (m, 6H, **m-Ar-P**, **H5'** and **H6**), 7.34 (dd, J = 7.5, 8.3 Hz, 1H, **p-Ar-N**), 7.27-7.25 (m, 1H, **H8**), 7.24-7.21 (m, 2H, **m-Ar-N**), 7.22-7.21 (m, 1H, **H7**), 7.20-7.19 (m, 2H, **o-Ar-N**), 7.07-7.04 (m, 1H, **H4'**), 6.91 (dd, J = 1.3, 7.7 Hz, 1H, **H5**), 6.77-6.72 (m, 1H, **H3'**); ¹³C NMR (151 MHz, CDCl₃, two conformers in ratio 1:0.7 at 293K) Major δ = 165.00 (⁴C_{carbonyl}), 162.09 (**CHO**), 141.94 (⁴C-**Ar**), 140.97 (d, J = 4.4 Hz, **CI'**), 133.46 (⁴C-**Ar**), 132.95 (d, J = 2.3 Hz, **C5'**), 132.48-132.29 (**o-Ar-P**, **p-Ar-P**, **C3'**), 131.57 (**C6**), 130.98 (d, J = 86.1 Hz, **ipso-Ar-P**), 129.54 (**p-Ar-N**), 129.13-128.88 (**m-Ar-P**, **C7**), 127.89 (**C8**), 127.71 (**C5**), 126.27 (d, J = 8.0 Hz, **C6'**), 125.59 (**m-Ar-N**), 124.64 (d, J = 12.1 Hz, **C4'**), 124.53 (**o-Ar-N**), 123.14 (d, J = 85.2 Hz, **ipso-Ar-P**); Minor δ = 164.58 (⁴C_{carbonyl}), 161.71 (**CHO**), 140.64 (d, J = 4.4 Hz, **CI'**), 139.88 (⁴C-**Ar**), 139.39 (⁴C-**Ar**), 137.56 (⁴C-**Ar**), 133.73 (⁴C-**Ar**), 133.08 (d, J = 2.2 Hz, **C5'**), 132.48-132.29 (**o-Ar-P**, **p-Ar-P**, **C3'**), 131.78 (**C6**), 130.68 (d, J = 86.1 Hz, **ipso-Ar-P**), 129.54 (**p-Ar-N**), 128.88 (**m-Ar-P**, **C7**), 128.71 (**C5**), 128.03 (**C8**), 125.62 (d, J = 8.0 Hz, **C6'**), 125.59 (**m-Ar-N**), 124.67 (d, J = 12.1 Hz, **C4'**), 124.53 (**o-Ar-N**), 122.35 (d, J = 85.2 Hz, **ipso-Ar-P**); ³¹P{¹H} NMR (243 MHz, CDCl₃, two conformers in ratio 1:0.7 at 293K) Major δ = 40.20 (bs); Minor δ = 40.19 (bs). C₃₂H₂₅N₂O₂PS: calcd. C, 72.17; H, 4.73; N, 5.26; S, 6.02; found: C, 72.34; H, 4.60; N, 5.38; S, 5.89.

3-(2-(diphenylphosphorothioyl)phenyl)-4-oxo-1-phenyl-3,4-dihydroquinazolin-1-ium perchlorate (**3**): 0.089 g (1.67 x 10⁻⁴ mol) of the formamide (**2**) were dissolved in 1 ml of methanol. The resulting solution was heated to reflux and 14.3 μ l of 70% perchloric acid were added. Heating was continued for 3 hours. The reaction mixture was filtered. The white precipitate was washed with methanol and DCM, and then recrystallized from methanol. Crystal suitable for X-ray analysis was obtained from methanol solution by slow evaporation of the solvent. Yield - 24 mg (**3**) (23%).

¹H NMR (600 MHz, DMSO-d₆) δ = 10.48 (s, 1H, **H2**), 8.01 (t, J = 7.9 Hz, 1H, **H6**), 7.96 (t, J = 7.7 Hz, 1H, **H5'**), 7.90 (d, J = 7.7 Hz, 1H, **H5**), 7.88-7.75 (m, 9H, **H6'**(7.84), **H4'**(7.77), **H7**(7.76), **o-Ar-N**, **m-Ar-N**, **m-Ar-P**), 7.69 (m, J = 5.7 Hz, 3H, **m-Ar-P** and **p-Ar-P**), 7.64-7.59 (m, 3H, **o-Ar-P** and **p-Ar-N**), 7.46 (t, J = 7.1 Hz, 1H, **p-Ar-P**), 7.34 (dt, J = 2.7, 7.6 Hz, 2H, **o-Ar-P**), 7.27 (dd, J = 7.9, 13.8 Hz, 1H, **H3'**), 7.15 (d, J = 8.5 Hz, 1H, **H8**); ¹³C NMR (151 MHz, DMSO-d₆) δ = 157.26 (⁴C₄), 156.05 (**C2**), 138.80 (⁴C-**Ar**), 137.84 (**C6**), 137.67 (d, J = 4.1 Hz, ⁴C-**Ar-N**), 136.01 (⁴C-**Ar**), 134.40 (**C5'**), 133.93 (d, J = 8.8 Hz, **C3'**), 133.25 (d, J = 13.2 Hz, **m-Ar-P**), 133.23 (d, J = 13.3 Hz, **p-Ar-P**), 132.64 (d, J = 11.2 Hz, **m-Ar-P**), 132.56 (d, J = 12.2 Hz, **p-Ar-P**), 132.25 (**C7**), 131.82 (d, J = 10.7 Hz, **C4'**), 131.21 (d, J = 24.8 Hz, **C6'**), 130.58 (**m-Ar-N**), 130.23 (d, J = 81.7 Hz, ⁴C-**Ar-P**), 130.09 (d, J = 86.7, ⁴C-**Ar-P**), 129.70 (d, J = 12.5 Hz, **o-Ar-P**), 128.94 (d, J = 84.7 Hz, ⁴C-**Ar-P**), 129.13 (d, J = 12.0 Hz, **o-Ar-P**), 128.70 (**C5**), 127.77 (**o-Ar-N**), 127.25 (**p-Ar-N**), 120.04 (⁴C-**Ar**), 119.53 (**C8**); ³¹P{¹H} NMR (243 MHz, DMSO-d₆) δ = 38.54 (s). C₃₂H₂₄ClN₂O₂PS: calcd. C, 62.49; H, 3.93; N, 4.55; S, 5.21; found: C, 62.62; H, 3.83; N, 4.59; S, 5.01.

3-(2-(diphenylphosphorothioyl)phenyl)-4-oxo-1-phenyl-3,4-dihydroquinazolin-1-ium tetrafluoroborate (**4**): 0.500 g (9.9 x 10⁻⁴ mol) of **1** and 12 ml trimethylorthoformate were heated to 80°C under argon. 0.114 g (1.09 x 10⁻³ mol) NH₄BF₄ were added in four portions for 9 hours. Heating was continued for 52 hours, then another 0.030 g (2.86x10⁻⁴ mol) of NH₄BF₄ were added and the heating was continued for 17 hours. The volatiles were evaporated under reduced pressure. The residue was dissolved in a minimal amount of DCM, filtered and equal volume of Et₂O was added to the solution. One half of the volume of the solution was evaporated and the resulting white crystalline precipitate was filtered, washed with ether and dried. Yield - 0.575 g (96%) white powder which can be recrystallized from acetonitrile or methanol.

¹H NMR (600 MHz, DMSO-d₆) δ = 10.48 (s, 1H, **H2**), 8.01 (tddd, J = 1.4, 7.3, 8.6 Hz, **H6**), 7.96 (t, J = 7.7 Hz, 1H, **H5'**), 7.90 (d, J = 7.7 Hz, 1H, **H5**), 7.88-7.75 (m, 9H, **H6'**(7.84), **H4'**(7.77), **H7**(7.76), **o-Ar-N**, **m-Ar-N**, **m-Ar-P**), 7.69 (m, J = 5.7 Hz, 3H, **m-Ar-P** and **p-Ar-P**), 7.64-7.59 (m, 3H, **o-Ar-P** and **p-Ar-N**), 7.46 (t, J = 7.1 Hz, 1H, **p-Ar-P**), 7.34 (dt, J = 2.7, 7.6 Hz, 2H, **o-Ar-P**), 7.27 (dd, J = 7.9, 13.8 Hz, 1H, **H3'**), 7.15 (d, J = 8.5 Hz, 1H, **H8**); ¹³C NMR (151 MHz, DMSO-d₆) δ = 157.26 (⁴C₄), 156.05 (**C2**), 138.80 (⁴C-**Ar**), 137.84 (**C6**),

137.67 (d, $J = 4.1$ Hz, $^4\text{C-Ar-N}$), 136.01 ($^4\text{C-Ar}$), 134.40 ($\text{C5}'$), 133.93 (d, $J = 8.8$ Hz, $\text{C3}'$), 133.25 (d, $J = 13.2$ Hz, $m\text{-Ar-P}$), 133.23 (d, $J = 13.3$ Hz, $p\text{-Ar-P}$), 132.64 (d, $J = 11.2$ Hz, $m\text{-Ar-P}$), 132.56 (d, $J = 12.2$ Hz, $p\text{-Ar-P}$), 132.25 (C7), 131.82 (d, $J = 10.7$ Hz, $\text{C4}'$), 131.21 (d, $J = 24.8$ Hz, $\text{C6}'$), 130.58 ($m\text{-Ar-N}$), 130.23 (d, $J = 81.7$ Hz, $^4\text{C-Ar-P}$), 130.09 (d, $J = 86.7$, $^4\text{C-Ar-P}$), 129.70 (d, $J = 12.5$ Hz, $o\text{-Ar-P}$), 128.94 (, $J = 84.7$ Hz, $^4\text{C-Ar-P}$), 129.13 (d, $J = 12.0$ Hz, $o\text{-Ar-P}$), 128.70 (C5), 127.77 ($o\text{-Ar-N}$), 127.25 ($p\text{-Ar-N}$), 120.04 ($^4\text{C-Ar}$), 119.53 (C8); $^{31}\text{P}\{^1\text{H}\}$ NMR (243 MHz, DMSO- d_6) $\delta = 38.54$ (s). The spectra completely match with the reported spectra of **3**. $\text{C}_{32}\text{H}_{24}\text{BF}_4\text{N}_2\text{OPS}$: calcd. C, 63.80; H, 4.02; N, 4.65; S, 5.32; found: C, 63.67; H, 4.16; N, 4.56; S, 5.46.

2-(diphenylphosphanyl)-N-(2-(phenylamino)benzyl)aniline (5): 0.650 g (1.29×10^{-3} mol) of **1** and 0.147 g (3.86×10^{-3} mol) LiAlH_4 were flushed with argon in a flask and 19.5 ml dry THF were added. The suspension was stirred at room temperature until hydrogen evolution ceases (about 40 minutes), then was heated for 1 hour at 83°C . 0.65 ml H_2O were added and the aqueous layer was extracted with Et_2O . The combined ether extracts were dried (Na_2SO_4) and the solvent was evaporated under reduced pressure, leaving white crystals (quantitative yield).

^1H NMR (600 MHz, CDCl_3) δ 7.49 (bs, 1H, NH), 7.40-7.27 (m, 13H), 7.21-7.19 (m, 2H), 7.13 (dd, $J = 7.4, 8.4$ Hz, 2H), 6.96 (bs, 1H, NH), 6.87 (dt, $J = 1.1, 7.4$ Hz, 1H), 6.86-6.83 (m, 2H), 6.81 (t, $J = 7.3$ Hz, 1H), 6.59 (d, $J = 8.0$ Hz, 2H), 4.29 (s, 2H, CH_2); ^{13}C NMR (151 MHz, CDCl_3) δ 143.18 (d, $J = 32.5$ Hz), 135.26 (d, $J = 6.9$ Hz), 134.67 (s), 133.82 (d, $J = 19.0$ Hz), 132.23 (d, $J = 10.2$ Hz), 130.95 (s), 130.73 (s), 129.20 (s), 129.13 (s), 128.89 (d, $J = 7.0$ Hz), 126.23 (s), 120.73 (d, $J = 13.7$ Hz), 118.27 (s), 117.20 (s), 53.58 (s); $^{31}\text{P}\{^1\text{H}\}$ NMR (243 MHz, CDCl_3) δ (-23.32). $\text{C}_{31}\text{H}_{27}\text{N}_2\text{P}$: calcd. C, 81.20; H, 5.94; N, 6.11; found: C, 80.99; H, 5.77; N, 6.20.

Diphenyl(2-((2-(phenylamino)benzyl)amino)phenyl)phosphine sulfide (7): 0.591 g (1.29×10^{-3} mol) of **5** were dissolved in 20 ml DCM and 0.050 g (1.55×10^{-3} mol) of finely powdered sulfur were added. The suspension was stirred for 24 hours at room temperature, then the solvent was removed under reduced pressure and the crude product was purified by flash chromatography (hexanes:DCM=2:1). Yield 0.583 g (92%) of white powder.

^1H NMR (600 MHz, DMSO- d_6) δ 7.70-7.64 (m, 6H), 7.60-7.58 (m, 4H), 7.42 (bs, 1H, NH), 7.32-7.29 (m, 1H), 7.18 (dd, $J = 7.5, 8.4$ Hz, 2H), 7.15

(bs, 1H), 7.11 (ddd, $J = 2.0, 6.3, 8.2$ Hz, 1H), 6.84-6.80 (m, 3H), 6.78-6.75 (m, 3H), 6.62-6.59 (m, 2H), 6.57 (dt, $J = 1.8, 7.5$ Hz, 1H), 4.25 (d, $J = 5.5$ Hz, 2H, CH_2); ^{13}C NMR (151 MHz, DMSO- d_6) δ 150.45 (d, $J = 5.6$ Hz), 144.88 (s), 140.69 (s), 133.59 (s), 132.52 (d, $J = 9.4$ Hz), 132.19 (d, $J = 2.2$ Hz), 131.90 (d, $J = 10.7$ Hz), 130.97 (d, $J = 85.1$ Hz), 129.84 (s), 129.12 (s), 128.97 (d, $J = 12.4$ Hz), 127.44 (s), 127.16 (s), 122.04 (s), 120.14 (s), 119.13 (s), 116.20 (s), 116.01 (d, $J = 12.5$ Hz), 112.04 (d, $J = 7.4$ Hz), 42.50 (s); $^{31}\text{P}\{^1\text{H}\}$ NMR (243 MHz, DMSO- d_6) δ (38.61). $\text{C}_{31}\text{H}_{27}\text{N}_2\text{PS}$: calcd. C, 75.89; H, 5.55; N, 5.71; S, 6.53; found: C, 75.97; H, 5.38; N, 5.62; S, 6.71.

3-(2-(diphenylphosphorothioyl)phenyl)-1-phenyl-3,4-dihydroquinazolin-1-ium tetrafluoroborate (8): 0.100 g (2.04×10^{-4} mol) of **7**, 0.024 g (2.24×10^{-4} mol) NH_4BF_4 and 4 ml trimethylorthoformate were heated under argon for 5 hours at 80°C . The volatile components were removed under reduced pressure. The residue was dissolved in a minimal amount of DCM, filtered and precipitated with Et_2O as described for **4**. Yield - 0.113 g (94%) of white powder.

^1H NMR (600 MHz, DMSO- d_6) δ 8.93 (s, 1H), 8.01 (ddd, $J = 1.1, 4.9, 7.9$ Hz, 1H), 87.93 (tt, $J = 1.4, 7.7$ Hz, 1H), 7.87-7.84 (m, 4H), 7.70-7.64 (m, 5H), 7.57 (bs, 1H), 7.50-7.48 (m, 3H), 7.46 (bs, 1H), 7.28-7.24 (m, 2H), 7.19 (ddd, $J = 1.4, 7.9, 14.3$ Hz, 1H), 6.93-6.91 (m, 1H), 6.49-6.46 (m, 1H), 5.30 (d, $J = 14.5$ Hz, 1H), 4.56 (d, $J = 14.5$ Hz, 1H); ^{13}C NMR (151 MHz, DMSO- d_6) δ 155.68 (s), 142.22 (d, $J = 3.6$ Hz), 136.18 (s), 134.43 (s), 133.87 (d, $J = 9.3$ Hz), 132.77 (d, $J = 35.1$ Hz), 131.95 (s), 131.83 (d, $J = 77.1$ Hz), 130.78 (d, $J = 11.0$ Hz), 130.56 (s), 130.46 (s), 130.19 (d, $J = 6.3$ Hz), 129.65 (s), 129.23 (s), 128.24 (s), 127.18 (d, $J = 11.6$ Hz), 118.64 (s), 116.32 (s), 51.11 (s); $^{31}\text{P}\{^1\text{H}\}$ NMR (243 MHz, DMSO- d_6) δ (38.36). $\text{C}_{32}\text{H}_{26}\text{BF}_4\text{N}_2\text{PS}$: calcd. C, 65.32; H, 4.45; N, 4.76; S, 5.45; found: C, 65.55; H, 4.26; N, 4.67; S, 5.59.

3-(2-(diphenylphosphanyl)phenyl)-1-phenyl-3,4-dihydroquinazolin-1-ium tetrafluoroborate (6): 0.200 g (4.36×10^{-4} mol) of **5**, 0.055 g (5.23×10^{-4} mol) NH_4BF_4 and 4 ml trimethylorthoformate were heated at 85°C for 15 hours under argon. The volatile components of the mixture were removed under reduced pressure. The residue was dissolved in 5 ml of DCM, 35 ml of Et_2O were added and after 20 minutes of stirring the resulting white precipitate was filtered and washed with ether. Yield: 0.192 g (79%) white powder.

^1H NMR (600 MHz, DMSO- d_6) δ 9.03 (d, $J = 2.3$ Hz, 1H), 7.84 (ddd, $J = 0.8, 4.2, 8.0$ Hz, 1H),

7.69 (dt, $J = 1.3, 7.7$ Hz, 1H), 7.67-7.64 (m, $J = 2.8$ Hz, 3H), 7.57 (dt, $J = 0.8, 7.6$ Hz, 1H), 7.46-7.27 (m, $J = 7.9$ Hz, 14H), 7.17 (dd, $J = 0.9, 7.5$ Hz, 1H), 6.96 (ddd, $J = 1.2, 3.7, 7.7$ Hz, 1H), 6.51 (dd, $J = 0.7, 8.1$ Hz, 1H), 5.30-4.93 (bs, 2H). ^{13}C NMR (151 MHz, DMSO- d_6) δ 154.56 (s), 143.00 (d, $J = 19.9$ Hz), 136.01 (s), 134.66 (d, $J = 16.8$ Hz), 133.87 (d, $J = 20.8$ Hz), 133.67 (s), 133.46 (d, $J = 8.7$ Hz), 132.20 (s), 131.17 (s), 130.69 (d, $J = 26.4$ Hz), 130.55 (s), 130.02 (s), 129.37 (s), 129.24 (d, $J = 7.5$ Hz), 128.45 (s), 127.35 (s), 127.26 (s), 50.70 (d, $J = 5.6$ Hz). $^{31}\text{P}\{^1\text{H}\}$ NMR (243 MHz, DMSO- d_6) δ (-16.52). $\text{C}_{32}\text{H}_{26}\text{BF}_4\text{N}_2\text{P}$: calcd. C, 69.08; H, 4.71; N, 5.04; found: C, 68.97; H, 4.81; N, 5.11.

Synthesis of 6 from 8: 0.070 g (1.19×10^{-4} mol) of **8**, freshly prepared Raney nickel and 3 ml of methanol were stirred for 24 hours at room temperature. The reaction mixture was diluted with DCM, filtered through celite and the solvents were removed under reduced pressure. The residue is washed with Et_2O and dried. Yield 0.023 g (35%) of white powder.

X-ray crystallography

A colorless plate crystal of **3** with the size 0.07 x 0.22 x 0.45 was selected for geometry and intensity data collection with a Bruker SMART X2S diffractometer using a monochromatic Mo- $K\alpha$ ($\kappa=0.71073$ Å) microfocus source with a Bruker APEX-II CCD detector at 300.15 K. A Bruker SMART APEX II system was applied for data collection, cell refinement and data reduction [7]. The intensities were measured by ω scan mode for θ ranges 2.30 to 22.44°. 2480 reflections were treated as observed ($I > 2\sigma(I)$). Data were corrected for Lorentz, polarisation and absorption factors. The structure was solved by direct method using SHELXS97 [8, 9]. All non-hydrogen atoms of the molecule were located in the best electron-density map. To refine the structure the program SHELXL97, version 2014/7 implemented in program OLEX2 was used [9, 10]. Full-matrix least-squares refinement was carried out until the final refinement cycles converged to an $R = 0.0564$ and $wR(F^2) = 0.0933$ for the observed data. Residual electron densities ranged from $-0.334 < \Delta\rho < 0.439$ $\text{e}\text{Å}^{-3}$. The OLEX software was applied to prepare the materials for publication. The crystallographic data are summarized in Table S1, and the respective bond lengths and angles are shown in Table S2 and S3. ORTEP diagram and crystal packing for compound **3** are shown in Fig. 1

and Fig. 2. CCDC-1403455 contains the supplementary crystallographic data for the compound **3** [11]. The diagrams were prepared using Mercury version 3.3 [12].

RESULTS AND DISCUSSION

It is known that for asymmetric induction in a reaction to occur, there must be an intermediate or a transition state in which a possible creation of a bond (be it on a face, a side or on/in a conformation) must be favored. Most transition metal catalyzed reactions proceed through cis-arranged reactive ligands/species, therefore bidentate cis-binding spectator ligands that are chiral, are desirable in the field of asymmetric homogeneous catalysis. Guided by these fundamental principles we designed a concept bidentate ligand structure that have the potential for atropisomerism, combined with the beneficial properties of both an NHC and a phosphane donors.

Herein we present the synthesis and structures of 3-(2-(diphenylphosphorothioyl)phenyl)-1-phenyl 3,4-dihydroquinazolinium and 3-(2-(diphenylphosphanyl)phenyl)-1-phenyl 3,4-dihydroquinazolinium salts (Fig. 1).

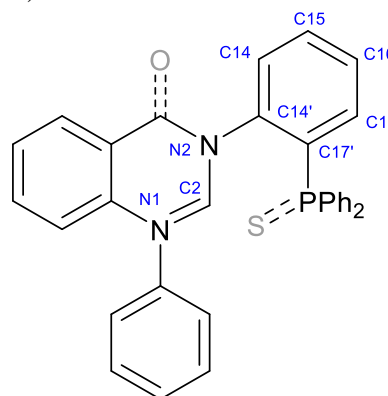


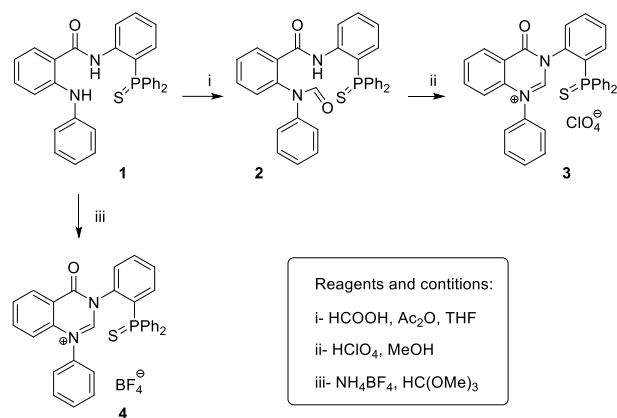
Fig. 1. General structure of target compounds.

These NHC precursors possess atropisomerism due to the chiral $\text{N}2\text{-C}14'$ axis that connects the quinazolinium plane with the C_6H_4 ($\text{C}14'\text{-C}17'$) one. The 4-oxo substituent on the quinazolinium combined with the bulky PPh_2 provide steric hindrance to prevent easy rotation around the chiral axis and therefore - interconversion of the rotamers.

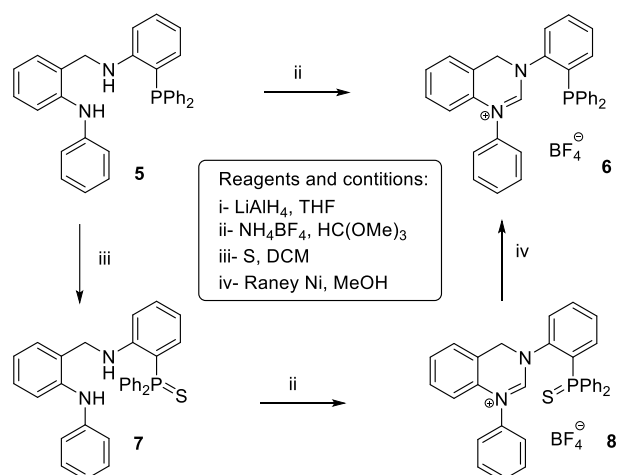
Synthesis

Starting from *N*-(2-(diphenylphosphorothioyl)phenyl)-2-(phenylamino)benzamide **1**, which we have reported in a previous communication [13], two types of 1-phenyl-3,4-dihydroquinazolinium

salts - 4-oxo (**3** and **4** on Scheme 1) and 4-H (**6** and **8** on Scheme 2) were synthesized.



Scheme 1. Synthesis of **3** and **4**.



Scheme 2. Synthesis of **5** - **8**.

Compound **1** was cleanly converted to the respective formamide **2** using HCOOH/Ac₂O mixture [14]. This product was cyclized in boiling methanol in the presence of excess HClO₄ [15] to the desired 3-(2-(diphenylphosphorothioyl)phenyl)-4-oxo-1-phenyl-3,4-dihydroquinazolinium perchlorate (**3**). An alternative simpler approach to 3,4-dihydroquinazolinium salts was also tested, by reacting **1** with trimethyl orthoformate and ammonium tetrafluoroborate [16] in one step, thus eliminating the steps of synthesis and purification of the formamide **2**. This reaction, although time consuming, proved to be more straightforward and high yielding and was adopted as a standard method in the following synthetic steps.

The amido group in **1** opens opportunities for the synthesis of 1-phenyl-3,4-dihydroquinazolinium salts that have different than in **3** and **4** rotation barriers. To remove the oxo-group, **1** was reacted

with LAH to the diamine **5**. This reaction also led to deprotection of the phosphorus atom. The resulting **5** was either directly cyclized to **6** or the phosphorus atom in it was protected, then the resulting phosphorothioate **7** was converted to **8**. Alternatively, **6** could be prepared from **8** by deprotecting the phosphane moiety with the aid of Raney Ni.

X-ray crystallography

Crystal data collection and refinement parameters are presented in Table S1. The crystal structure of the compound **3** consists of a 3-(2-diphenylphosphorothioyl)-4-dihydro-quinazolin-1-ium) cation neutralized with a perchlorate anion. An ORTEP view of the compound with atomic labeling is shown in Fig. 2. The overall molecular geometry of the compound, including bond distances and angles has a normal range [17]. The deviation from the least-squares aromatic plane of the fused rings in the 4-quinazolinone moiety is ~2,3°. The bond lengths C4-N2 (1.433(4) Å), C2-N1 (1.319(4)Å) and N1-C8' (1.425(4)Å) prove the electronic density delocalization in the dihydroquinazolin-1-ium ring and the C-O distance of 1.205(5) Å are consistent with a double bond. In the tertiary phosphine oxide residue, the phosphorus atoms possess distorted tetrahedral arrangement with bond angles range between 105.80(1) – 113.21(1)° and relatively delocalized P=S double bonds (1.955(1)Å). The aromatic rings of this part of the molecule are inclined towards each other with 107.49° and 100.28°.

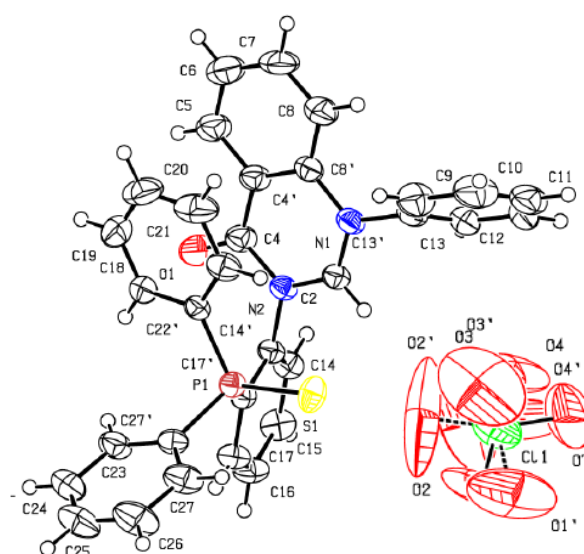


Fig. 2. ORTEP drawing of molecular structure of the compound **3**. The thermal displacement ellipsoids are drawn at the 50% probability.

Some groups in chemical compounds exhibit disorder problems very often and the perchlorate anions are amongst them. In this structure, the all four oxygen atoms in the perchlorate anion are found disordered over two set of sites with occupancy ratio 0.545:0.455.

Packing view of the molecule in the unit cell viewed down the b-axis is shown in Fig. 3. The unit cell consists of two enantiomeric molecules located opposite with parallel 4-quinazolinone moieties.

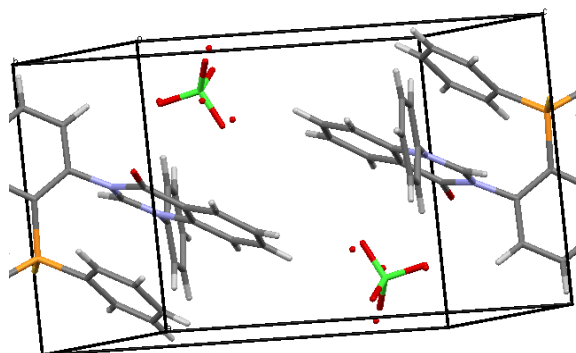


Fig. 3. View of the compound **3** cell packing.

Compound **3** crystallizes in the centrosymmetric triclinic *P*-1 space group. The bond lengths and angles are shown in Tables S2 and S3.

CONCLUSION

Atropisomeric 3-(2-(diphenylphosphorothioyl)phenyl)-1-phenyl 3,4-dihydroquinazolinium (**3**, **4** and **8**) and 3-(2-(diphenylphosphanyl)phenyl)-1-phenyl 3,4-dihydroquinazolinium (**6**) salts were designed and successfully synthesized by means of straightforward synthetic procedures. Structure studies of **3** reveals the existence of two well defined expected axial enantiomers. Fine tuning of the rotational barriers is possible by modifying the fourth position of the dihydroquinazolinium ring system. The synthesized compounds are precursors to chiral NHC and P-NHC ligands. Undergoing studies will reveal the exact interconversion barriers of the newly synthesized compounds and test their properties as ligands for transition metals.

Acknowledgements: The authors acknowledge the support by the Horizon 2020 program of the

European Commission (project Materials Networking, ref. no. 692146) and the Research Fund of Sofia University (project 093/08.05.2014).

Electronic Supplementary Data available here.

REFERENCES

1. M. N. Hopkinson, C. Richter, M. Schedler, F. Glorius, *Nature*, **510**, 485 (2014).
2. L. G. Bonnet, R. E. Douthwaite, *Organometallics*, **22**, 4187 (2003).
3. F. Wang, L.-J. Liu, W. Wang, S. Li, M. Shi, *Coord. Chem. Rev.*, **256**, 804 (2012).
4. M. T. Powell, D.-R. Hou, M. C. Perry, X. Cui, K. Burgess, *J. Am. Chem. Soc.*, **123**, 8878 (2001).
5. A. Schumacher, M. Bernasconi, A. Pfaltz, *Angew. Chem. Int. Ed.*, **52**, 7422 (2013).
6. N. Ortega, S. Urban, B. Beiring, F. Glorius, *Angew. Chem. Int. Ed.* **51**, 1710 (2012).
7. Bruker (2012). SADABS. Bruker AXS Inc., Madison, Wisconsin, USA; Bruker (2013). APEX2 and SAINT. Bruker AXS Inc., Madison, Wisconsin, USA.
8. G. M. Sheldrick, *Acta Cryst. A*, **64**, 112 (2008).
9. G. M. Sheldrick, *Acta Cryst. C*, **71**, 3 (2015).
10. O. V. Dolomanov, L. J. Bourhis, R. J. Gildea, J. A. Howard, H. Puschmann, *J. Appl. Cryst.*, **42**, 339 (2009).
11. The crystallographic data for **3** were deposited at the Cambridge Crystallographic Data Centre and allocated the deposition number CCDC 1403455. Copies of the data can be obtained, free of charge, on application to CCDC, 12 Union Road, Cambridge CB2 1EZ, UK; tel: +441223762910; fax: +441223336033; e-mail: deposit@ccdc.cam.ac.uk; <http://www.ccdc.cam.ac.uk/deposit>.
12. C. F. Macrae, I. J. Bruno, J. A. Chisholm, P. R. Edgington, P. McCabe, E. Pidock, L. Rodriguez-Monge, R. Taylor, J. Van de Streek, P. A. Wood, *J. Appl. Crystallogr.*, **41**, 466 (2008).
13. R. H. Lyapchev, M. G. Dangelov, N. G. Vassilev, P. Y. Petrov, *Bulg. Chem. Commun.*, **49**, Special Edition B, 50 (2017).
14. A. Furstner, M. Alcarazo, V. Cesar, C. W. Lehmann, *Chem. Commun.*, 2176 (2006).
15. N. I. Chernobrovin, Y. V. Kozhevnikov, G. E. Morozova, *Pharm. Chem. J.*, **26**, 245 (1992).
16. J. Zhang, X. Qin, J. Fu, X. Wang, X. Su, F. Hu, J. Jiao, M. Shi; *Organometallics*, **31**, 8275 (2012).
17. P. W. Coddind, K. A. Kerr, *Acta Cryst. B*, **34**, 3785 (1978).

АТРОПИЗОМЕРНИ ФОСФОР ЗАМЕСТЕНИ 1-ФЕНИЛ-3,4-ДИГИДРОХИНАЗОЛИН-1-ИЕВИ ННС ПРЕКУРСОРИ

Р. Хр. Ляпчев¹, М. Г. Дангалов², Г. Г. Генчева¹, Н. Г. Василев², П. Й. Петров^{1*}

¹ Катедра "Органична химия и фармакогнозия", Факултет по химия и фармация, Софийски университет „Св. Климент Охридски“, бул. „Джеймс Баучер“ 1, София 1164, България

² Институт по органична химия с Център по фитохимия, Българска академия на науките, ул. Акад. Г. Бончев, бл. 9, 1113 София, България

Постъпила на 03 май 2017 г.; Коригирана на 22 май 2017 г.

(Резюме)

Бидентатни атропизомерни 3-(2-(дифенилфосфоротиоил)фенил)-1-фенил 3,4-дихидрохиназолиниеви соли като прекурсори на N-хетероциклени карбени са синтезирани с използване на N-(2-(дифенилфосфоротиоил)фенил)-2-(фениламино)бензамид.

The effect of demineralisation on characteristics and adsorption behaviour of activated carbons prepared from swine manure

L. Gonsalvesh^{1*}, A. Popova², S. P. Marinov², M. Stefanova², R. Carleer³, J. Yperman³

¹ Central Scientific Research Laboratory, Assen Zlatarov University, Burgas 8000, Bulgaria

² Institute of Organic Chemistry with Centre of Phytochemistry, BAS, Sofia 1113, Bulgaria

³ Hasselt University, CMK, Research group of Applied and Analytical Chemistry, Agoralaan – gebouw D, B-3590 Diepenbeek, Belgium

Received April 13, 2017; Revised May 19, 2017

Dedicated to Acad. Ivan Juchnovski on the occasion of his 80th birthday

Activated carbons (ACs) from swine manure (SM), i.e. preliminary de-watered SM cake (Mc) and solid digestate (Md) were prepared by pyrolysis and water vapour activation. Demineralisation on obtained chars after carbonization was applied as well. Additionally, the adsorption capacity of demineralised ACs towards chromium in aqueous solutions was investigated and compared to non-demineralised ACs. Demineralisation caused a decrease in mineral matter content with more than 50% and affected characteristics and adsorption behaviour of these ACs. As a result, ACs with better developed porous texture were produced. Prepared ACs with reduced ash content demonstrated higher adsorption capacity toward Cr compared to non-demineralised ACs. The adsorption kinetics were investigated by applying two kinetic models, i.e. Lagergren pseudo-first order and pseudo-second order. The pseudo-second order kinetic model provided a better fit. Better fits are obtained for the Langmuir isotherm model and therefore a monolayer coverage chemisorption of the Cr(VI) on the ACs surface is suggested.

Key words: swine manure; activated carbons; demineralisation; adsorption; chromium ions

INTRODUCTION

Increasing awareness and environmental concern towards manure wastes impact on environmental contamination, reflecting in public health and biosystems life quality, determine the focus of scientific interest on minimization, re-use and recycling of these wastes into value added products. In this regard, thermochemical conversion technologies, i.e. pyrolysis, have been widely applied for successful manure valorisation. Pyrolysis results in high-energy-density volatile gases (condensable and non-condensable) that can be used as a fuel or chemical feedstock and a solid fraction (char) that could be applied as soil amendments [1,2]. Additionally, a profitable method for manure char utilization is the preparation of activated carbons (ACs) after char upgrade at higher temperature by means of physical or chemical treatment. Several studies on ACs preparation from manures and their usage for heavy metals remediation in aqueous solution have been reported. Recently, Lima and Marshall have prepared ACs from turkey manure by steam activation and used them for copper removal from aqueous solution [3]. They found that physical,

chemical and adsorptive properties were all dependent on the activation conditions, i.e. steam flow rate and activation time. Yields, surface area and Cu²⁺ adsorption up to 37 wt.%, 472 m² g⁻¹ and 1.86 mmol g⁻¹, respectively, are achieved. Studied ACs were considered to have substantial potential in Cu²⁺ removal from water. Similar results were obtained for ACs prepared from broiler manure [4]. Poultry manure based ACs have shown excellent adsorption properties towards Cd and Zn as well [5]. Actually, their metal ion sequestering ability greatly exceeded characteristics of carbons made from conventional feedstocks, i.e. coal, coconut shell and wood, and of commercial ACs. Cattle-manure compost has been also efficiently converted to ACs [6,7]. Relatively high yields up to 47.5 wt.% and large surface area up to 2170 m² g⁻¹ were obtained as a result of chemical activation by ZnCl₂. Cattle-manure compost based ACs have been successfully applied for removal of metal ions [8] and organic pollutants [9]. Swine manures have been also tested for activated carbons preparation [10,11]. Swine manure-based carbons demonstrated excellent adsorption abilities and a preference towards ions of copper, followed by zinc and cadmium. It is assumed that negatively charged phosphate groups attached to the carbon skeleton are responsible for their affinity towards positively

* To whom all correspondence should be sent:

E-mail: lenia_gonsalvesh@abv.bg

charged metal ions. In several investigations the effect of mineral matter removal on the characteristics of ACs has been examined. The removal of inorganic matter decreases char reactivity [12,13] and changes the surface area development of the carbons [14]. Similar behaviour has been observed for chars produced from six different lignites [15]. Fernandez-Morales and co-workers concluded that the demineralization process resulted in lowering the char reactivity and in an activation energy increase. For different rank coals, i.e. from lignite to anthracite, the effect of inorganic matter removal on surface area development, respectively adsorption behaviour, has been verified by Mahajan and Walker [16]. They found that inorganic matter removal by acid treatment resulted in random but significant changes in surface areas. It has been assumed that coal inorganic matter removal prior to carbonization affects the subsequent heating process and, hence, the surface area of the resultant material. The author admitted that surface area changes could be related to the inorganic matter removal from the orifice and to the displacement of insoluble inorganic species from the cavities, as well as to acid retention in the coal porous structure.

The aim of the present study is to elucidate the effect of demineralisation on the characteristics and adsorption properties of ACs produced from swine manures. Additionally, the adsorption capacity of prepared demineralised ACs towards chromium in aqueous solutions will be studied and compared to the non-demineralised ACs.

MATERIALS AND METHODS

Samples and treatments

In current research grounded, sieved (< 2 mm) and oven-dried at 110 °C swine manure (SM) samples, preliminary de-watered SM cake (Mc) and solid digestate (Md), are under consideration. For activated carbon preparation, a two-steps process, comprising carbonization and physical activation in a stream of water vapour, is carried out. The carbonization of SM samples is performed in an inert atmosphere in a lab-scale pyrolysis reactor, described in a preliminary study [17]. The treatment has been performed by applying heating at a rate of 10 °C min⁻¹ up to a desired pyrolysis temperature of 500 °C and kept isothermal for 1h. The obtained SM chars (20 g) were treated with 500ml of 5% HCl for 1h at 60°C in order to reduce ash content. Subsequently, the acid-washed char

was extensively washed with hot distilled water till the lack of chloride ions and then dried. The demineralised chars are labelled as dc-Mc and dc-Md, while non-demineralised chars are marked as c-Mc and c-Md. Demineralised (dc-Mc and dc-Md) and non-demineralised (c-Mc and c-Md) chars were further subjected to activation by steam in a horizontal tubular reactor by applying the following experimental conditions: i) ~8g precursor materials; ii) heating rate of 35 °C min⁻¹ in an inert N₂ atmosphere (60 ml min⁻¹) up to activation temperature of 800 °C; iii) isothermal period at 800 °C for 30 min; and iv) when the activation temperature is reached the inert atmosphere is replaced by a constant steam flow of 330 μL min⁻¹. Activated carbons obtained from demineralised chars are labelled as AC-dc-Mc and AC-dc-Md, while those obtained from non-demineralised chars are marked as AC-Mc and AC-Md.

Analyses

Determinations of proximate analysis (i.e moisture (W), volatile matter (VM), fixed carbon (C_{fix}) and ash contents) using DuPont Instrument 951 thermogravimetric analyser and elemental analysis, i.e. C, H, N, S and O by difference using a Thermo Electron Flash EA1113 elemental analyzer are performed as described in Stals et al. [18]. In our study, pH_{pzc} value of ACs is determined following the experimental procedure described by Moreno-Castilla et al. [19]. Porous texture characteristics of ACs are estimated by measuring nitrogen adsorption isotherms at -196 °C on an automatic sorption apparatus Surfer (Thermo Scientific). The surface area S_{BET} is determined by the BET method using data from the adsorption isotherms in the range of relative pressures determined by the criteria of Rouquerol [20-21]. Total pore volume V_{0,95} is determined based on the volume of adsorbate, recorded on the desorption branch of the adsorption isotherm at a relative pressure P_i/P_o = 0,95. The micropore volume (V_{DR,micro}) is calculated by using the Dubinin-Radushkevich equation up to P_i/P_o ≤ 0.15 [22]. The pore size distribution and pore diameters L₀ are obtained by applying the Non Local Density Functional Theory (NLDFT) on N₂ adsorption data [23].

Adsorption experiments and modelling

The chromium adsorption experiments are performed in thermostatic water bath (25 °C) using 100 ml Erlenmeyer flasks containing 0.030 g of ACs and 50ml of Cr(VI) solutions with

concentrations varying in the range of 10 to 200 mg L⁻¹. The initial chromium solutions are prepared by dissolving K₂Cr₂O₇ (oven dried at 105 °C for 1h) in Milli-Q water. The effect of pH of initial solution on Cr adsorption was studied by varying the pH in the range of 1 to 4. The initial pH of solutions is adjusted by adding 0.1N HCl or 0.1N NaOH and is not further altered during the adsorption experimental run. The exact total chromium (Cr_{tot}) concentrations of initial and equilibrium solutions are determined by Perkin Elmer Optima 3000 DV ICP AES device, while Cr(VI) concentrations are determined spectrophotometrically after complexing Cr(VI) with 1,5-diphenylcarbohydrazide according to the standard method ASTM D1687-92, Test Method A. The chromium adsorption capacities are calculated using the following equation:

$$q_e = \frac{(C_0 - C_e)V}{m} \quad 1$$

where q_e is the adsorption capacity at equilibrium (mg g⁻¹), C_0 and C_e are the Cr initial and equilibrium concentrations (mg L⁻¹), respectively, V is the volume of Cr solutions (L) and m is the weight of AC (g).

Two isotherm models, i.e. Freundlich and Langmuir, are applied to equilibrium adsorption data in order to clarify the mechanism of adsorption and to calculate estimates of adsorbent efficiency. The equilibrium data (experimental values) are fitted with linear forms of the Freundlich (Eq. 2) and Langmuir (Eq. 3) equations in order to determine the model parameters:

$$\log q_e = \frac{1}{n} \log C_e + \log K_F \quad 2$$

where K_F and n are indicators of adsorption capacity and adsorption intensity, respectively;

$$\frac{C_e}{q_e} = \frac{1}{q_m} C_e + \frac{1}{K_L q_m} \quad 3$$

where K_L (L mg⁻¹) and q_m (mg g⁻¹) are the Langmuir constants. K_L is the sorption equilibrium constant for distribution of adsorbate, while q_m is the maximum adsorption capacity which represents the mass of adsorbate adsorbed in a complete monolayer having one molecule thickness per mass of adsorbent. The adsorption kinetics are investigated by varying the contact time up to 72 h in the batch adsorption mode. In order to analyze the adsorption kinetics, two different models, i.e. Lagergren pseudo-first order and pseudo-second order are applied to the experimental data.

The pseudo-first order rate equation of Lagergren in its linear form is presented as follows:

$$\log(q_e - q_t) = \log q_e - \frac{k_1}{2.303} t \quad 4$$

where q_e and q_t (mg g⁻¹) are the adsorption capacities at the equilibrium and at time t (min), respectively, and k_1 (min⁻¹) is the rate constant of the pseudo-first order adsorption. The plot of $\log(q_e - q_t)$ vs t should give a linear relationship in which the value of k_1 can be determined from the slope of the plot.

The pseudo-second order kinetic model can be expressed by the following linear equation:

$$\frac{t}{q_t} = \frac{1}{k_2 q_e^2} + \frac{t}{q_e} \quad 5$$

where k_2 (g mg⁻¹ min⁻¹) is the equilibrium rate constant for the pseudo-second order adsorption. The value of k_2 and adsorption capacity, q_e , can be obtained from the intercept and the slope of the plot of t/q_t vs. t , respectively. The initial adsorption rate, h , of pseudo-second order kinetic can be defined as:

$$h = k_2 q_e^2 \quad 6$$

Beside the correlation coefficient, a real measure of the validity of pseudo-first (eq. (4)) and pseudo-second order (eq. (5)) kinetic models is the comparison between the experimentally determined q_e values and those obtained from the plots of $\log(q_e - q_t)$ vs. t and t/q_t vs. t , respectively

RESULTS AND DISCUSSION

The proximate and ultimate analyses as well as the char yields after demineralisation and ACs yields are summarised in Table 1. It is obvious that demineralisation with HCl acid results in a product yield of 66.4 wt.% and 69.6 wt.% for dc-Mc and dc-Md samples, respectively. Both samples are characterised by a high C_{fix} content of ~70 wt.%, and an ash content of ~18 wt. %. In general, the ash in swine manures is associated with the pigs bedding material such as shredded corn stalks, different types of straw, wood chips and(or) shredded paper scattered on the floor which could be even not cemented but sandy. All these materials cannot effectively be separated from swine manures and contribute to the mineral matter content of manures. It is revealed that demineralisation treatment results in char's ash content decrease with about 65.5 wt.% for dc-Mc and 55.7 wt.% for dc-Md in comparison to not demineralised chars, c-Mc and c-Md, respectively. The decrease in ash content is mainly related to the removal of carbonates, sulphates, etc., while the remained ash is attributed to HCl acid insoluble inorganics, mainly silicates.

Table 1. Characteristics of samples under consideration.

Analysis	Samples			
	dc-Mc	AC-dc-Mc	dc-Md	AC-dc-MD
Yield (wt. %)	64.6*	48.0**	69.6*	50.0**
Proximate (wt. %)				
W ^{ad}	1.7	1.0	1.7	0.7
Ash ^{db}	17.7	26.9	17.5	25.1
VM ^{db}	12.6	13.3	12.3	4.2
C _{fix} ^{db}	69.7	59.8	70.2	70.7
Ultimate Analysis wt. %^{db}				
C	66.0	65.2	70.5	62.6
H	2.1	0.3	1.6	0.6
N	3.6	2.0	1.6	0.6
S	0.9	0.8	1.3	1.0
O ^{diff}	9.7	4.8	7.5	10.1
pH _{pzc}	-	8.6	-	8.2
Porous texture characteristics				
S _{BET} (m ² g ⁻¹)	-	362	-	436
V _{0.95} (cm ³ g ⁻¹)	-	0.260	-	0.276
V _{DR,micro} (cm ³ g ⁻¹)	-	0.141	-	0.169
V _{meso} (cm ³ g ⁻¹)	-	0.119	-	0.106
L ₀ (nm)	-	1.58	-	1.68

^{ad}- air dried; ^{db}-dry basis; *-product yield as a result of demineralisation procedure; **-activated carbon yield calculated based on demineralised char counterpart.

As a result of physical activation of demineralised chars with water vapour, ACs with product yield of about 50 wt.% are prepared. Although the yields of demineralised char based ACs are lowered with about 20 wt.% in comparison with the yield of non-demineralised char based ACs, the former possess lower ash content ($\geq 50\%$ decrease) and higher C_{fix} content, hence, improved AC characteristics are expected. The removal of mineral matter is reflected in a change of pH_{pzc} value of AC-dc-Mc and AC-dc-Md samples as well. The pH_{pzc} value of AC-dc-Mc and AC-dc-Md samples are 8.6 and 8.2, respectively, while for non-demineralised char based ACs a pH_{pzc} of about 11 is found. Porous texture characteristics are also affected due to demineralization. N₂ adsorption isotherms of AC-dc-Mc and AC-dc-Md (Fig.1) similar to those of AC-Mc and AC-Md (not shown) represent a type I-IV hybrid shapes, according to the IUPAC classification [26]. This behaviour of the adsorption isotherms reveals that the porous structure of investigated carbons is characterized by both micro- and mesopores. However, the isotherms of AC-dc-Mc and AC-dc-Md compared to AC-Mc and AC-Md, respectively, display an increase in the adsorbed N₂. Consequently, higher S_{BET} and V_{0.95}, especially in the case of AC-dc-Mc, are calculated,

mainly related to the development of microporosity and to a lesser extent of mesoporosity increase.

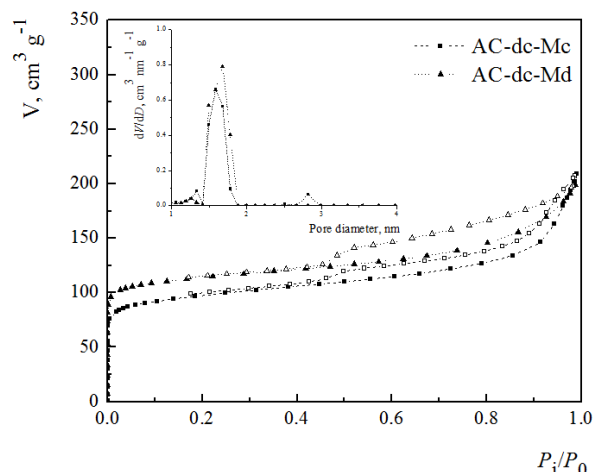


Fig. 1. N₂ adsorption isotherms of AC-dc-Mc and AC-dc-Md samples. Inset: Pore size distribution.

Apparently, physical activation of dc-Mc char by water vapour demonstrates a stronger gasification effect on carbons compared to the physical activation of c-Mc char, evoking a better developed porosity of AC-dc-Mc in comparison to AC-Mc. Nevertheless, from N₂ adsorption-desorption isotherms it can be revealed that dc-Md based AC demonstrates higher N₂ adsorption capacity, respectively larger surface area, than dc-Mc based

AC. This behaviour is again in accordance with ACs produced from not demineralised chars. S_{BET} values calculated for AC-dc-Mc and AC-dc-Md are $362 \text{ m}^2 \text{ g}^{-1}$ and $436 \text{ m}^2 \text{ g}^{-1}$, respectively, while for AC-Mc and AC-Md $267 \text{ m}^2 \text{ g}^{-1}$ and $428 \text{ m}^2 \text{ g}^{-1}$ are noticed, respectively.

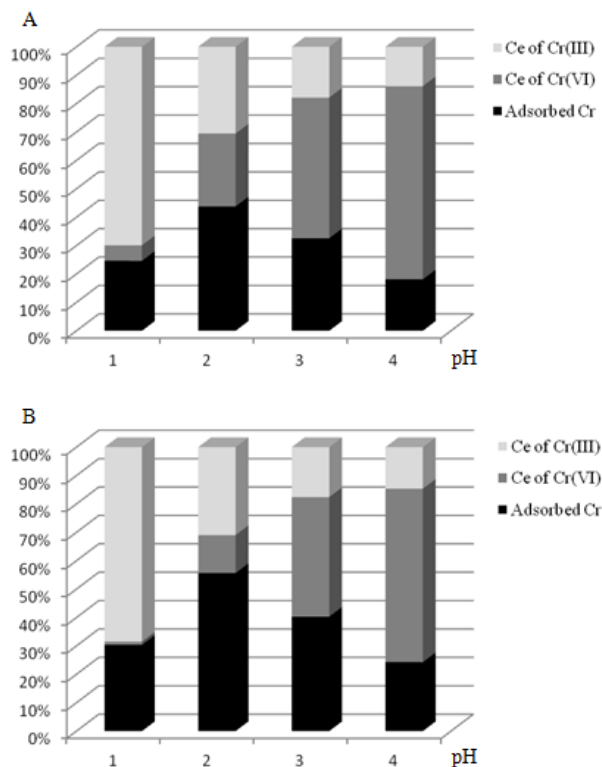


Fig. 2. Chromium distribution as a result of adsorption experiments on AC-dc-Mc (A) and AC-dc-Md (B) at different pH. Different colors of the columns represent adsorbed $C_{r_{tot}}$ (black), C_e of Cr(III) in the solution (light grey) and C_e of Cr(VI) in the solution (dark grey). Experimental conditions: $m = 0.030 \text{ g}$, $V = 50 \text{ ml}$, $C_o = 40 \text{ mg L}^{-1}$, $T = 25 \text{ }^\circ\text{C}$, 48 h

The two oxidation states of chromium present in the environment are Cr(III) and Cr(VI). Trivalent chromium is considered to be less toxic than the hexavalent chromium, which is recognized as a carcinogenic and mutagenic agent. However, due to the possible oxidation of Cr(III) to Cr(VI), environmental legislation limits both, total and hexavalent chromium concentration in water [24]. It is well documented that Cr(VI) adsorption from aqueous solution by AC is favoured at low pH [25,26]. Therefore, the effect of pH on the removal of Cr(VI) by AC-dc-Mc and AC-dc-Md is investigated in a pH range of 1.0 to 4.0. Among existing Cr(VI) species, i.e. H_2CrO_4 , HCrO_4^- , CrO_4^{2-} , HCr_2O_7^- and $\text{Cr}_2\text{O}_7^{2-}$, the dominant form of Cr(VI) in this pH range is HCrO_4^- . Its adsorption by ACs can be explained by the following mechanisms

[24,26]: i) an electrostatic attraction with protonated acidic groups or protonated basic surface sites; and ii) AC oxidation by HCrO_4^- in which Cr(VI) is reduced to Cr(III) and thus eventually adsorbed on AC external surface. The chromium distribution during Cr(VI) adsorption experiments on AC-dc-Mc and AC-dc-Md at different pH is assessed and is shown in Figure 2. It is obvious that beside adsorption, reduction of Cr(VI) to Cr(III) takes place. The following peculiarities in Cr(VI) removal process by AC-dc-Mc and AC-dc-Md is depicted: i) the maximal Cr adsorption occurred at pH 2; and ii) the maximal reduction of Cr(VI) to Cr(III) appeared at pH 1. However, of utmost importance is the extent of total chromium ($C_{r_{tot}}$) removal. As mentioned earlier, Cr(III) is less toxic but in the environment oxidation of Cr(III) to Cr(VI) can occur. Consequently, it is advisable both Cr(VI) and Cr(III) to be removed by ACs. Therefore, the influence of initial solution pH on $C_{r_{tot}}$ adsorption is assessed (Fig. 3). The results demonstrate that the optimal initial solution pH for $C_{r_{tot}}$ adsorption by AC-dc-Mc and AC-dc-Md is pH 2. Similar results are observed for AC-Mc and AC-Md as well.

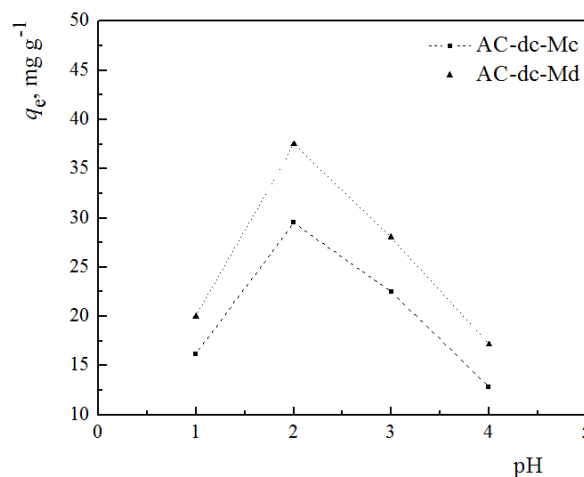


Fig. 3. Influence of initial solution pH on $C_{r_{tot}}$ adsorption. Experimental conditions: $m = 0.030 \text{ g}$, $V = 50 \text{ ml}$, $C_o = 40 \text{ mg L}^{-1}$, $T = 25 \text{ }^\circ\text{C}$, 48 h .

Freundlich and Langmuir isotherm models have been applied to $C_{r_{tot}}$ equilibrium adsorption data obtained for AC-dc-Mc and AC-dc-Md at initial solution pH 2 (Fig. 4). Estimated parameters and correlation coefficients of isotherm modelling are presented in Table 2. In order to distinguish the influence of mineral matter content of studied ACs on Cr adsorption behaviour, data of isotherm modelling for AC-Mc and AC-Md are included as well. For all samples the Langmuir model describes better $C_{r_{tot}}$ adsorption data at the studied

experimental conditions. Consequently, the applicability of a monolayer coverage chemisorption of Cr on the ACs surface could be considered. Calculated Langmuir monolayer adsorption capacity q_m demonstrates that higher Cr_{tot} adsorption is determined for AC-Md and AC-dc-Md. The observation could be explained by the higher surface of these ACs. Apparently applied demineralisation treatment also affects Cr_{tot} adsorption. Demineralised char based ACs reveal higher Cr_{tot} adsorption capacities. This is especially pronounced for AC-dc-Mc characterised by highly developed porous texture comparing to the non-demineralised counterpart.

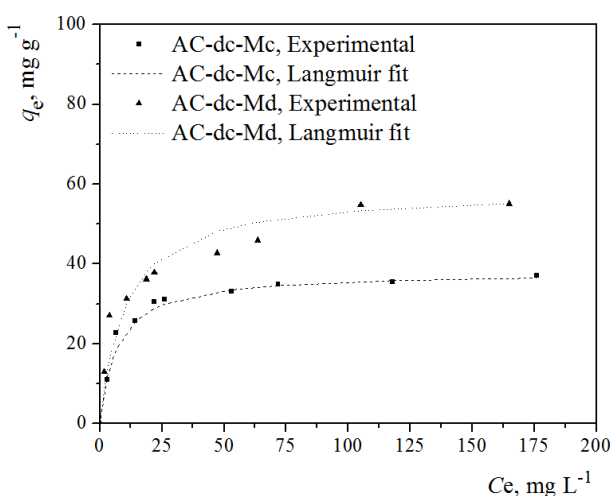


Fig. 4. Equilibrium Cr_{tot} adsorption isotherm for AC-dc-Mc and AC-dc-Md samples, i.e. experimental data and Langmuir fitting. Experimental conditions: initial Cr_{tot} solution pH = 2, $m = 0.030$ g, $V = 50$ ml, $C_0 = 10-200$ mg L⁻¹, $T = 25$ °C, 48 h.

The adsorption of Cr_{tot} by the best ACs for Cr removal, i.e. AC-Md and AC-dc-Md, is studied as a function of contact time at the optimal initial solution pH as well (Fig. 5).

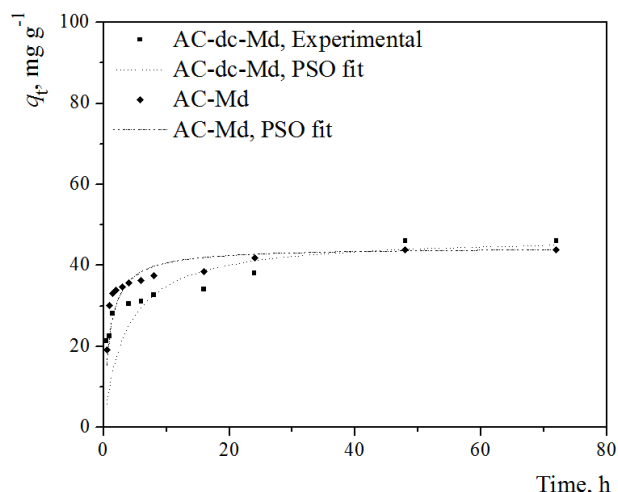


Fig. 5. Effect of contact time on adsorption of Cr_{tot} by AC-dc-Md and AC-Md. Experimental conditions: initial Cr_{tot} solution pH=2, $m=0.030$ g, $C_0=40$ mg L⁻¹, $V=50$ ml, $T=25$ °C.

In the first 3h adsorption for both samples increases rapidly, approaching slowly the equilibrium within 48 hour. Two reaction based kinetic models, i.e. pseudo-first and pseudo-second order (PSO) models, were applied to the experimental adsorption data. Calculated kinetic parameters as well as correlation coefficients of the models are presented in Table 3. Obviously, the PSO kinetic model provided a better fit, approved by the high correlation coefficient and better match for the experimental $q_{e(exp)}$ and the calculated one. This supports the assumption that the overall rate of Cr_{tot} adsorption might be controlled by a chemical process through sharing electrons or by oxidation/reduction reactions through exchanging of electrons between adsorbent and adsorbate. Calculated equilibrium rate constant for the pseudo-second order and the initial adsorption rate, h , are higher for AC-Md.

Table 2. Parameters and correlation coefficients of isotherm modelling

Sample	Langmuir			Freundlich		
	K_L L mg ⁻¹	q_m mg g ⁻¹	R^2	K_F mg g ⁻¹ (mg L ⁻¹) ⁿ	n	R^2
AC-Mc	0.137	23.1	0.980	10.733	6.550	0.596
AC-dc-Mc	0.145	37.9	0.998	12.001	4.070	0.765
AC-Md	0.263	52.1	0.986	18.854	4.352	0.791
AC-dc-Md	0.099	58.5	0.991	14.649	3.510	0.890

Table 3. Parameters and correlation coefficients of kinetic modelling

Parameter		AC-Md	AC-dc-Md	
Pseudo-first order	q_e (exp)	(mg g ⁻¹)	43.9	46.1
	q_e (cal)	(mg g ⁻¹)	13.8	21.0
	k_1	(min ⁻¹)	0.6×10^{-3}	0.7×10^{-3}
	R ²		0.8345	0.8755
Pseudo-second order	q_e (cal)	(mg g ⁻¹)	44.4	47.2
	k_2	(g mg ⁻¹ min ⁻¹)	0.4×10^{-3}	0.1×10^{-3}
	h		0.79	0.22
	R ²		0.9993	0.9933

CONCLUSION

The present study demonstrates that the decrease in mineral matter content of manure based ACs influences their characteristics and adsorption behaviour. The HCl demineralisation of chars prior to physical activation decreases ash content with more than 50 %. The treatment affects the activation mechanism and ACs with better developed porous texture are prepared demonstrating higher adsorption capacity towards Cr compared to that of non-demineralised char based ACs. Among applied isotherm models to experimental adsorption data, better fits are depicted for the Langmuir model. Consequently, a monolayer coverage chemisorption of Cr on the ACs surface is in line with the obtained data

Acknowledgements: The study was financed in the frame of FWO and BAS-IOCh bilateral research project (2015-2017).

REFERENCES

- M. Uchimiya, D. I. Bannon, L. H. Wartelle, I. M. Lima, K. T. Klasson, *J. Agr. Food Chem.*, **60**, 5035 (2012).
- K. B. Cantrell, P. G. Hunt, M. Uchimiya, J. M. Novak, K. S. Ro, *Bioresource Technol.*, **107**, 419 (2012).
- I. Lima, W. E. Marshall, *Waste Manage.*, **25**, 726 (2005).
- I. M. Lima, W. E. Marshall, *Bioresource Technol.*, **96**, 699 (2005).
- I. M. Lima, W. E. Marshall, *J. Chem. Technol. Biot.*, **80**, 1054 (2005).
- Q. Qian, M. Machida, H. Tatsumoto, *Bioresource Technol.*, **98**, 353 (2007).
- Q. Qian, M. Machida, H. Tatsumoto, *Waste Manage.*, **28**, 1064 (2008).
- M. A. A. Zaini, R. Okayama, M. Machida, *J. Hazard. Mater.*, **170**, 1119 (2009).
- Q. Qian, Q. Chen, M. Machida, H. Tatsumoto, K. Mochidzuki, A. Sakoda, *Appl. Surf. Sci.*, **255**, 6107 (2009).
- I. M. Lima, W. E. Marshall, *J. Residuals Sci. Tech.*, **4**, 9 (2007).
- I. M. Lima, W. E. Marshall, K. T. Klasson, *Eleventh International Waste Management and Landfill Symposium*, Sardinia, Italy, (2007).
- L. R. Radovic, P. L. W. Jr., R. G. Jenkins, *Fuel*, **62**, 209 (1983).
- E. Hippo, J. P. L. Walker, *Fuel*, **54**, 245 (1975).
- V.-C. C., T. C. Cano, V. G. Serrano, *Fuel*, **66**, 479 (1987).
- I. Fernandez-Morales, F. J. Lopez-Garzon, A. Lopez-Peinado, C. Moreno-Castilla, J. Rivera-Utrilla, *Fuel*, **64**, 666 (1985).
- M. O. P., W. P. L. Jr., *Fuel*, **58**, 333 (1979).
- L. Gonsalvesh, J. Yperman, R. Carleer, M. Mench, R. Herzig, J. Vangronsveld, *J. Chem. Technol. Biot.*, **91**, 1585 (2016).
- M. Stals, R. Carleer, G. Reggers, S. Schreurs, J. Yperman, *J. Anal. Appl. Pyrol.*, **89**, 22 (2010).
- C. Moreno-Castilla, M. V. López-Ramón, F. Carrasco-Marín, *Carbon*, **38**, 1995 (2000).
- J. Rouquerol, P. Llewellyn, F. Rouquerol, in: *Studies in Surface Science and Catalysis*, Vol. **160**, P. L. Llewellyn, Rodriguez-Reinoso, F. J. Rouquerol, N. Seaton (Eds.), Elsevier, 2007.
- International Organization for Standardization in *ISO 9277:2010*, 2010, Vol. ISO 9277:2010.

22. Stoeckli, M. V. López-Ramón, D. Hugli-Cleary, A. Guillot, *Carbon*, **39**, 1115 (2001).
23. A. V. Neimark, Y. Lin, P. I. Ravikovitch, M. Thommes, *Carbon*, **47**, 1617 (2009).
24. F. Di Natale, A. Lancia, A. Molino, D. Musmarra, *J. Hazard. Mater.*, **145**, 381 (2007).
25. H. Demiral, İ. Demiral, F. Tımsek, B. Karabacakođlu, *Chem. Eng. J.*, **144**, 188 (2008).
26. D. Duranođlu, A. W. Trochimczuk, U. Beker, *Chem. Eng. J.*, **187**, 193 (2012).

ВЛИЯНИЕ НА ДЕМИНЕРАЛИЗАЦИЯТА ВЪРХУ ХАРАКТЕРИСТИКИТЕ И АДСОРБЦИОННОТО ПОВЕДЕНИЕ НА АКТИВНИ ВЪГЛЕНИ, ПОЛУЧЕНИ ОТ СВИНСКИ ТОР

Л. Гонсалвеш^{1*}, А. Попова², С. Маринов², М. Стефанова², Р. Карлеер³, Я. Иперман³

¹Централна научно-изследователска лаборатория, Университет „Асен Златаров“, Бургас 8000, България

²Институт по органична химия с Център по фитохимия, Българска академия на науките, София 1113, България

³Университет на Хаселт, Изследователска група по приложна и аналитична химия, Агора път - сграда Д, В-3590 Дийпенбек, Белгия

Постъпила на 13 април 2017 г.; Коригирана на 19 май 2017 г

(Резюме)

Активни въглини (АВ^{III}) от проби свински тор (СТ) бяха получени чрез пиролиз и активация с водна пара. Приложена също бе и деминерализация на получените след карбонизация въглини. Допълнително бе изследван адсорбционния капацитет на деминерализираните АВ^{III} по отношение на съдържанието на хром във водни разтвори и бе сравнен адсорбционния им капацитет с този на АВ^{III} получени от недеминерализираните въглини. Проведената деминерализационна обработка доведе до намаление съдържанието на минералната маса на АВ^{III} с над 50% и до промяна в техните характеристики и адсорбционно поведение. Получените деминерализирани АВ^{III} се характеризират с по-добре развита пориста текстура и по-висок адсорбционен капацитет по отношение на хрома в сравнение с недеминерализираните АВ^{III}

Metallodendrimers for catalytic epoxidation – theoretical insights into structure of Mo(VI) complexes of poly(propylene imine) dendrimers

V. Trifonova¹, K. Vassilev², A. Ahmedova^{3*}

¹ Department of Analytical and Inorganic Chemistry, University "Prof. Assen Zlatarov", 1, Prof. Yakimov str., 8010 Burgas, Bulgaria

² Department of Biotechnology, University "Prof. Assen Zlatarov", 1, Prof. Yakimov str., 8010 Burgas, Bulgaria

³ Faculty of Chemistry and Pharmacy, University of Sofia, 1, J. Bourchier av., 1164 Sofia, Bulgaria

Received May 01, 2017; Revised May 19, 2017,

Dedicated to Acad. Ivan Juchnovski on the occasion of his 80th birthday

The present theoretical study is focused on detailed structural description of Mo(VI) complex of a second generation poly(propylene imine) dendrimer DAB-G₂-PPI-(NH₂)₈ that has previously been synthesized and evaluated as catalyst for alkenes epoxidation with organic hydroperoxides. In order to verify the suggested geometry with five-coordinate metal centers, which is rare case for Mo(VI), we performed structural description of possible complexes by quantum chemical (DFT) calculations. This was achieved through modeling and geometry optimization of the MoO₂²⁺ complex with the smallest triamine fragment of the dendrimer. Different compositions of model complexes were taken into account and numerous combinations of DFT functionals (B3LYP, B2LYP, O3LYP, M05 and M06) and basis sets were used for optimizations. The M06/6-31G(d,p)-(LanL2DZ; Mo) calculations gave the best agreement with available crystallographic data for similar cis-dioxo Mo(VI) complexes. Therefore, this method was used to optimize the structure of the tetrameric Mo(VI) complex of DAB-G₂-PPI-(NH₂)₈. The results pointed out that M06/6-31G(d,p) optimized structure of the five-coordinate cis-dioxo Mo(VI) complex with the tridentate dendrimer fragments is possible and confirms the feasibility of the experimentally suggested coordination mode of DAB-G₂-PPI-(NH₂)₈. Calculations on a complex with additionally coordinated water molecule indicated that the five-coordinate Mo(VI) complexes of PPI dendrimer preserve the potential to coordinate one O-donor solvent molecule. These structural characteristics can explain the ability of the Mo-centers of the modeled metallodendrimer to coordinate also hydroperoxides, used as oxygen sources for the catalytic epoxidation of alkenes, and thus, ensure the realization of a crucial catalytic step in the olefin epoxidation reactions.

Key words: DFT calculations; cis-dioxo Mo(VI) complexes; PPI dendrimers; alkene epoxidation

INTRODUCTION

The metal-catalyzed, partial and selective oxidation of alkenes has been of practical importance for more than 50 years due to the broad variety of possible transformations of the formed epoxides [1]. The most selective catalytic reactions for epoxidation of alkenes are those that employ alkyl hydroperoxides and metal complexes of d⁰ transition metal ions in their highest oxidation state, e.g. Mo(VI), W(VI), Ti(IV), V(V) [2]. The mechanistic aspects of these catalytic processes have been thoroughly studied and indicated that the cis-dioxomolybdenum(VI) complexes are the catalyst of choice for highly selective epoxidation of cycloalkenes with *tert*-butyl hydroperoxide (TBHP, *t*-BuOOH) [3]. This could be explained with the high Lewis acidity of the Mo(VI) ion and its ability to withdraw electron density from the

peroxide oxygens, which makes them more susceptible to nucleophilic attack by olefins. Despite the significant progress that has been achieved in this field [4-6], there is still intense research attempting to improve the catalyst stability, the rate and yield of substrate conversion under mild conditions preserving the high selectivity, and their implementation as recyclable (heterogeneous) catalysts [7-13]. In our research dedicated to the use of various metal complexes for catalytic applications [14-16] we have demonstrated the high potential of metallodendrimers in this field [13] which was later employed by other authors [17,18]. In view of future implementation of chelating fragments from dendritic macromolecules for formation of polymeric metal complexes as highly efficient catalysts, we focus the current theoretical study on detailed structural description of the Mo(VI) complex of second generation (G₂) dendrimer based on poly(propylene imine), PPI. The complexes of

* To whom all correspondence should be sent:
E-mail: Ahmedova@chem.uni-sofia.bg

second- (G_2) and forth- (G_4) generation poly(propylene imine) dendrimers with various metal ions have previously been synthesized and experimentally tested for their catalytic activity for epoxidation of alkenes with different organic hydroperoxides [13]. The highest activity showed the Mo(VI) complex with the G_4 PPI dendrimer having 32 amino end-groups, DAB- G_4 -PPI-(NH_2)₃₂, and using the TBHP. The structure of the Mo(VI) complexes have been proposed based on FT-IR spectroscopy and titration data only. However, the suggested five-coordinate metal centers is rare case for Mo(VI), especially with N-donor ligands, and needed further confirmation. Therefore, we subjected the structural description on quantum chemical (DFT) calculations of various possible geometries of the metal centers in order to verify the most probable structure of the formed metallodendrimers. For that purpose we modeled the coordination of the MoO_2^{2+} ion with the smallest tridentate fragment of the dendrimer, namely bis(propyleneamine)-methylamine (denoted as **L-N3**, Fig.1), and taking into account different compositions and coordination modes. The best computational method was selected out of numerous combinations of DFT functionals (B3LYP, B2LYP, O3LYP, M05 and M06) with different basis sets (6-31G(d,p), 6-311G, 6-311G(d,p), D95 and D95V for all non-metals and LanL2DZ for Mo) based on the agreement of the calculated results with available crystallographic

data on similar structures. The closest agreement with experimental bond lengths for cis-dioxo Mo(VI) complexes was obtained with the M06/6-31G(d,p)-(LanL2DZ; Mo) method, which was used further on to optimize the structure of various complexes with different compositions as well as the tetrameric cis-dioxo Mo(VI) complex of the second generation poly(propylene imine) dendrimer **DAB- G_2 -PPI-(NH_2)₈**. (Fig. 1). Thereby, we could confirm the feasibility of the five-coordinate cis-dioxo Mo(VI) centers with the tridentate alkylamine ligands and provide additional details on the geometry and electronic structures of the modeled complexes and the corresponding spectroscopic (IR) characteristics.

COMPUTATIONAL DETAILS

All quantum chemical calculations were performed using the Gaussian 09 suite of programs [19]. Various DFT methods were applied for geometry optimizations including hybrid functionals that combine the Becke exchange [20] and LYP correlation functionals [21, 22], such as B3LYP and B2LYP, or the O3LYP functional [23, 24], as well as the pure functionals of Truhlar and Zhao, M06 [25] and M05 [26]. All listed functionals were combined with the split-valence basis set of double-zeta quality including polarization functions 6-31G(d,p) [27,28] for all light elements.

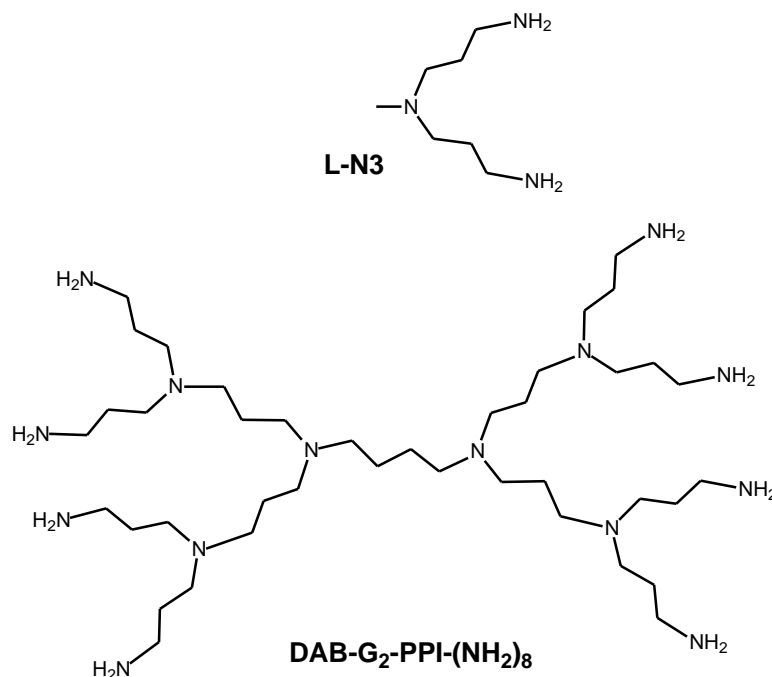


Fig. 1. Chemical formula of the smallest dendrimer fragment **L-N3** and the second generation poly(propylene imine) dendrimer **DAB- G_2 -PPI-(NH_2)₈**.

To test the basis sets performance, the B3LYP functional was combined with the 6-31G(d,p), 6-311G and 6-311G(d,p) basis sets, and the Dunning/Huzinaga full or valence double-zeta basis sets D95 and D95V [29]. In all cases the molybdenum orbitals were calculated using the LanL2DZ basis set including the Los Alamos effective core potentials (ECP) [30]. The geometry optimizations, employing all described DFT methods, were performed on the MoO_2^{2+} unit coordinated to the smallest tridentate fragment of the dendrimer, **L-N3**, with the composition $[\text{MoO}_2(\text{L-N3})]^{2+}$. All geometry optimizations were followed by calculation of the vibrational frequencies and intensities at the same level of theory and proved that local minima have been attained. Based on critical evaluation of the calculated geometrical parameters through comparison with available experimental data, the best performing DFT method has been selected and employed in the additional calculations of complexes with different structure and compositions. The M06/6-31G(d,p)-(LanL2DZ; Mo) method was used to calculate complexes of the following compositions $[\text{MoO}_2(\text{L-N3})]^{2+}$, $[\text{MoO}_2(\text{L-N3})\text{Cl}]^+$, $\text{MoO}_2(\text{L-N3})\text{Cl}_2$ and $[(\text{MoO}_2)_4(\text{DAB-G}_2)]^{8+}$, where DAB-G₂ is a short-hand notation for the **DAB-G₂-PPI-(NH₂)₈** dendrimer. Due to better convergence with the B3LYP functional that was obtained in the case of water coordinated Mo(VI) complexes, it was used to calculate the structures with compositions $[\text{MoO}_2(\text{L-N3})(\text{H}_2\text{O})]^{2+}$, using the 6-31G(d,p) or 6-311G(d,p) basis sets for all non-metals.

RESULTS AND DISCUSSION

Currently, we modeled and optimized all probable structures of cis-dioxo Mo(VI) complexes of a poly(propylene imine) dendrimer using the smallest dendritic fragment **L-N3** to form complexes with different compositions and charge. The aim was to evaluate the feasibility of the spectroscopically suggested five-coordinate Mo(VI) complexes of **DAB-G₂-PPI-(NH₂)₈** and **DAB-G₄-PPI-(NH₂)₃₂** dendrimers, used as catalyst for alkenes epoxidation [13]. Compulsory starting step was to select the most suitable theoretical model for the studied systems. Therefore, we compared the structural parameters calculated by five different DFT functionals (B3LYP, B2LYP, O3LYP, M05 and M06) and five different basis sets (6-31G(d,p), 6-311G, 6-311G(d,p), D95 and D95V for all non-

metals) with available crystallographic data on similar cis-dioxo Mo(VI) complexes. It should be noted that there are no reports on crystal structures of MoO_2^{2+} complexes of dendrimers. That is why we mostly compared our calculated results with reported crystallographic data on cis-dioxo Mo(VI) complexes of three- or tetra- dentate Schiff bases or hydrazones that coordinate by at least one or two N-donor atoms [31-36]. In most of these cases the sixth coordination site of Mo(VI) is occupied by a weakly bound solvent molecule (e.g. alcohol). However, there are also recent data on five-coordinate Mo(VI) complexes that have been isolated and their crystal structures were solved [37]. The basic finding of our calculations suggested that the most suitable method is M06/6-31G(d,p)-(LanL2DZ; Mo) giving acceptable Mo-N distances. Only this method gave lengths of the Mo-N bonds shorter than 2.230 Å (for the terminal amino groups) and Mo-Nm bond (with the tertiary amino group) shorter than 2.270 Å (Table 1 and Fig. 2). Although these bond lengths are longer than 2.180 Å, they are fairly acceptable if compared with the crystallographic data for Mo(VI) complexes with tridentate ligands that coordinate with three [38] or two N-donor atoms [32] in which the longest Mo-N bonds range from 2.31 to 2.42 Å. These data let us conclude that M06/6-31G(d,p) optimized structure of the five-coordinate cis-dioxo Mo(VI) complex with the tridentate dendrite fragment **L-N3** is possible and confirms the feasibility of the experimentally suggested coordination mode of the **DAB-G₂-PPI-(NH₂)₈** and **DAB-G₄-PPI-(NH₂)₃₂** dendrimers [13]. All other functionals, we have tested, predicted Mo-N bonds shorter or equal to 2.310 Å for the five-coordinate cis-dioxo Mo(VI) complexes $[\text{MoO}_2(\text{L-N3})]^{2+}$. However, these values are larger by ca. 1% than the Mo-N bonds calculated with the M06 functional and the same holds for the Mo-O bonds. Therefore, we selected the M06/6-31G(d,p)-(LanL2DZ; Mo) method for geometry optimization of other possible complex structures. The model of a six-coordinate cis-dioxo Mo(VI) complex with one chloride ligand added, $[\text{MoO}_2(\text{L-N3})\text{Cl}]^+$, resulted in strong elongation of the M-Nm bond to 2.592 Å and elongation of the Mo-O bonds by 0.02 Å (Table 1 and Fig. 2). These results indicate that the supposed Cl-bound six-coordinate Mo(VI) complex is less probable.

To further elaborate the expected high possibility for six-coordinate Mo(VI) complexes we made a model with coordinated water molecule

$[\text{MoO}_2(\text{L-N3})(\text{H}_2\text{O})]^{2+}$. In this case successful convergence was achieved using the B3LYP functional, and therefore, it was the method of choice for the water-bound complex. For the sake of comparison the results obtained with the B3LYP/6-31G(d,p) and B3LYP/6-311G(d,p) methods for five- and six-coordinate Mo(VI) complexes are listed in Table 1 and the optimized geometries are depicted in Fig. 3. It can be noted that appreciable elongation resulted only for the Mo-Nm bond (by *ca.* 0.13 Å). Despite the elongation, calculated bond lengths for the water-bound complex remain in the range of experimentally reported ones for cis-dioxo Mo(VI) complexes coordinated with a tridentate ligand and a solvent molecule (with Mo-O distances within the 2.319 – 2.385 Å range) [33-37]. This let us propose

that the optimized five-coordinate Mo(VI) complexes of the studied PPI dendrimer, although probable, preserves the potential to coordinate additional O-donor solvent molecule. Similarly, it can be supposed that the Mo-centers of the modeled metallodendrimer are available for coordination with a hydroperoxide that is used as an oxygen source for the catalytic epoxidation of alkenes. This possibility is yet to be confirmed by our ongoing theoretical studies on the catalytic steps of olefin epoxidation by metallodendrimers and TBPH. Attempts to model a neutral complex of bidentately coordinating L-N3 fragment with MoO_2Cl_2 core, and complex composition $\text{MoO}_2(\text{L-N3})\text{Cl}_2$, proved that such coordination mode of the PPI dendrimer is sterically hindered.

Table 1. Calculated (M06 and B3LYP) bond lengths (in Å) of the cis-dioxo Mo(VI) complexes with the PPI dendrimer **DAB-G₂-PPI-(NH₂)₈**, $[(\text{MoO}_2)_4\text{DAB-G}_2]^{8+}$, or with its smallest tridentate fragment (**L-N3**) and having the following compositions: $[\text{MoO}_2(\text{L-N3})]^{2+}$, $[\text{MoO}_2(\text{L-N3})\text{Cl}]^+$ or $[\text{MoO}_2(\text{L-N3})(\text{H}_2\text{O})]^{2+}$. The ECP basis set LanL2DZ is used for Mo. In the six-coordinate complexes the axial ligand is either water (Ow) or a chloride (Cl). The Nm notation is used for the tertiary amine from the tridentate fragment of the dendrimer.

Comput. method	M06 optimized structures			B3LYP optimized structures			
	6-31G(d,p)			6-31G(d,p)/	6-311G(d,p)/		
Structure	$[\text{MoO}_2(\text{L-N3})]^{2+}$	$[\text{MoO}_2(\text{L-N3})\text{Cl}]^+$	$[(\text{MoO}_2)_4\text{DAB-G}_2]^{8+}$	$[\text{MoO}_2(\text{L-N3})]^{2+}$	$[\text{MoO}_2(\text{L-N3})(\text{H}_2\text{O})]^{2+}$	$[\text{MoO}_2(\text{L-N3})]^{2+}$	$[\text{MoO}_2(\text{L-N3})(\text{H}_2\text{O})]^{2+}$
Bond distances							
Mo-O1	1.686	1.705	1.674 ÷ 1.681	1.694	1.700	1.697	1.703
Mo-O2	1.678	1.691	1.675 ÷ 1.680	1.688	1.689	1.691	1.691
Mo-N	2.229	2.227	2.217 ÷ 2.229	2.244	2.249	2.245	2.248
Mo-Nm	2.267	2.592	2.366 ÷ 2.373	2.293	2.430	2.289	2.416
Mo-Ow					2.396		2.407
Mo-Cl		2.451					

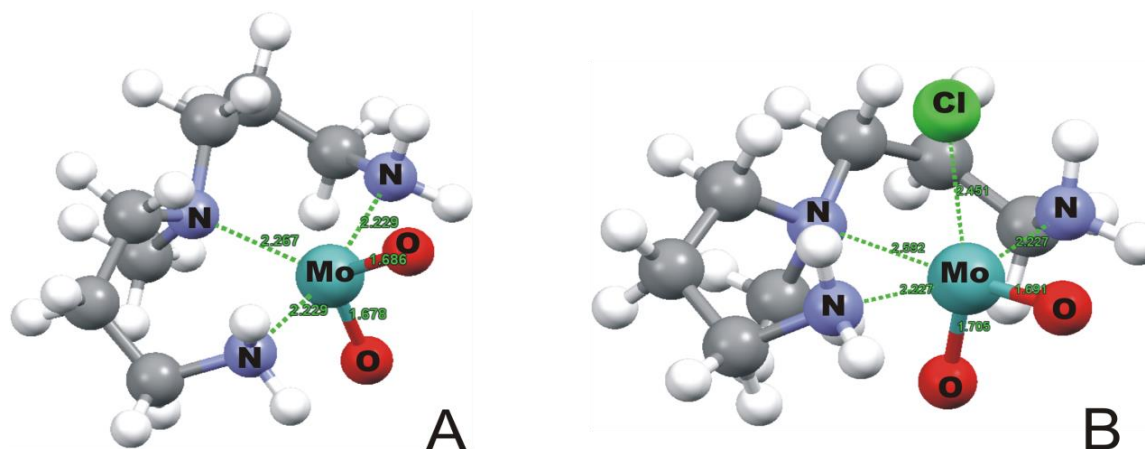


Fig. 2. Optimized (M06/6-31G(d,p)-(LanL2DZ; Mo)) structures of the five- and six-coordinate cis-dioxo Mo(VI) complexes having the compositions: A) $[\text{MoO}_2(\text{L-N3})]^{2+}$ and B) $[\text{MoO}_2(\text{L-N3})\text{Cl}]^+$. The dotted lines represent the coordination bonds Mo-N or Mo-Cl, and the numbers give the corresponding distances, listed also in Table 1.

Using the selected superior method for our system, M06/6-31G(d,p)-(LanL2DZ; Mo), we optimized the structure of the Mo(VI) complex of the **DAB-G₂-PPI-(NH₂)₈** dendrimer, referred to as [(MoO₂)₄DAB-G₂]⁸⁺. Two views of the optimized structure are depicted in Fig. 4 and selected bond lengths are given in Table 1. The four metal centers exhibit virtually the same geometry. The slight variations in the lengths of the molybdenum bonds are indicated with the given range (Table 1). All optimized bond distances are virtually equal to the ones obtained for the similar monomeric complex with the **L-N3** fragment, except for the Mo-Nm (with the tertiary amine) which elongates by *ca.* 0.10 Å in the tetrameric complex. Thus, the longest calculated Mo-N distances approach 2.37 Å but still remain within the range of experimentally reported ones for a complex with sterically crowded tetradentate ligand coordinating with two tertiary

amine groups to cis-dioxo Mo(VI) [32], where the Mo-N bonds are estimated to 2.260 - 2.423 Å.

The calculated vibrational frequencies of the five-coordinate monomeric and tetrameric complexes, [MoO₂(L-N3)]²⁺ and [(MoO₂)₄(DAB-G₂)]⁸⁺, agree with the experimentally reported ones for the stretching modes involving the metal center. The M06/6-31G(d,p) calculated stretching vibrations of Mo-N in [MoO₂(L-N3)]²⁺ are 423 and 431 cm⁻¹, which are very close to the experimental data of 405 to 430 cm⁻¹ [13]. The most intense vibrations of the Mo=O bonds appear at 1016 and 1049 cm⁻¹ in the calculated [MoO₂(L-N3)]²⁺ model structure and at 1013 and 1021 - 1024 cm⁻¹ for [(MoO₂)₄(DAB-G₂)]⁸⁺. These unscaled values would become closer to the experimental data (of 900 - 950 cm⁻¹) if a scaling factor of *ca.* 0.90 is used.

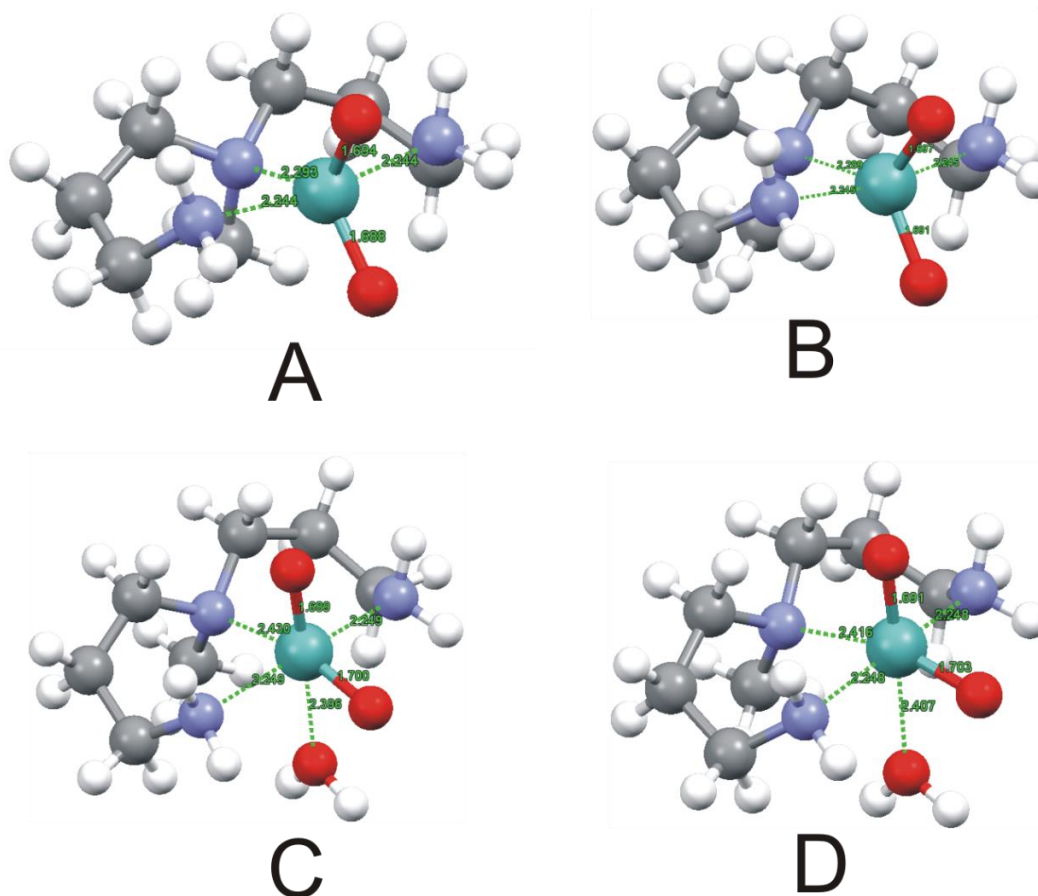


Fig. 3. Comparison of the B3LYP optimized geometries of five- and six-coordinate cis-dioxo Mo(VI) complexes with compositions [MoO₂(L-N3)]²⁺ (in A and B) and [MoO₂(L-N3)(H₂O)]²⁺ (in C and D), and using different basis sets for the light elements - the 6-31G(d,p) in A and C or 6-311G(d,p) in B and D. The dotted lines represent the coordination bonds Mo-N and Mo-OH₂, and the numbers giving the corresponding distances are listed in Table 1. The same color code for all heteroatoms is used as in Fig. 2.

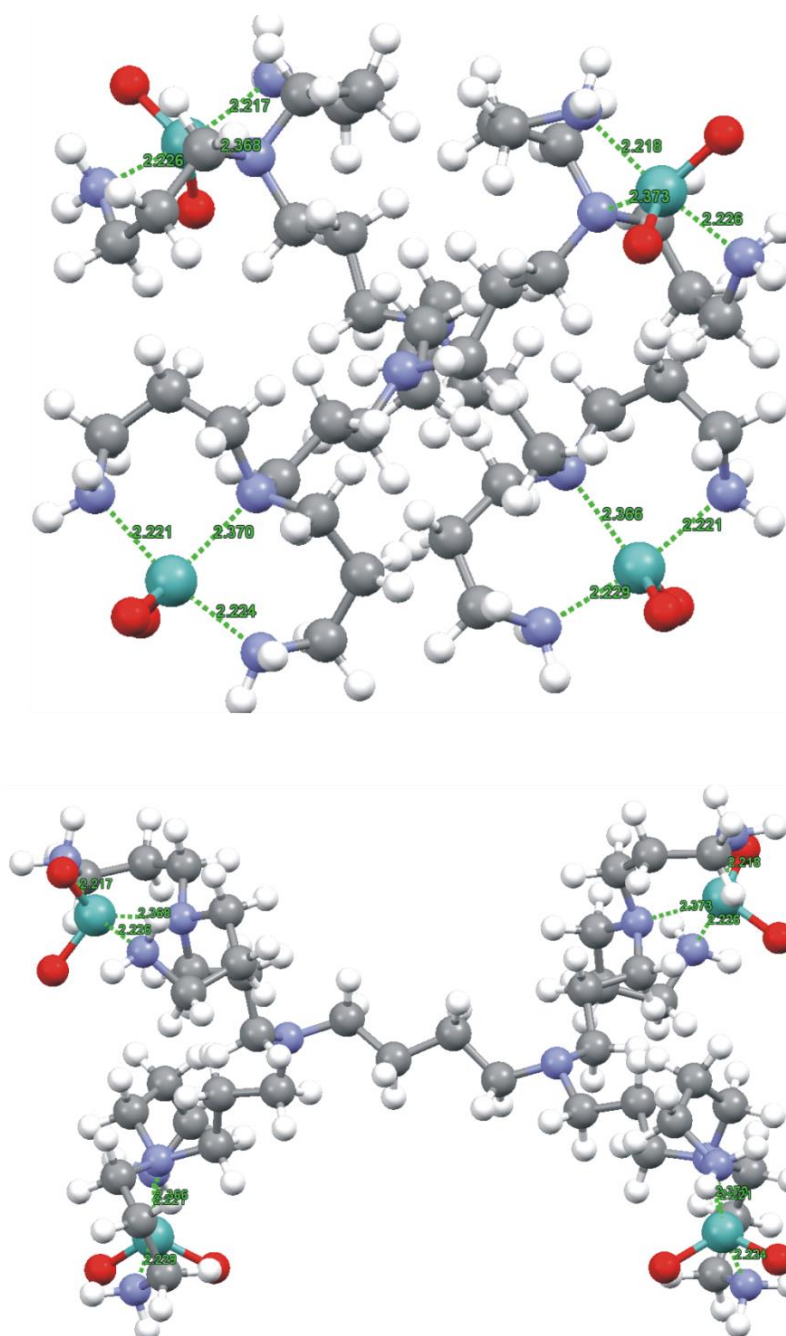


Fig. 4. Two different views of the M06/6-31G(d,p)-(LanL2DZ; Mo) optimized structure of the tetrameric cis-dioxo Mo(VI) complex of the second generation PPI dendrimer **DAB-G₂-PPI-(NH₂)₈** with composition $[(\text{MoO}_2)_4(\text{DAB-G}_2)]^{8+}$. Top view is oriented normal to the core diaminobutane chain and the bottom view depicts the structure along that chain. The dotted lines represent the Mo-N coordination bonds and the corresponding distances are listed in Table 1. The same color code for all heteroatoms is used as in Fig. 2.

In conclusion, the investigated rare case of five-coordinate Mo(VI) complexes appeared as the most plausible structure for the PPI dendrimers, which we confirmed by the current detailed computational study. Moreover, the suggested structure agrees with available crystallographic data on similar system of cis-dioxo Mo(VI) complexes with two- or three- N-donor atoms. The obtained optimized structure of $[(\text{MoO}_2)_4(\text{DAB-G}_2)]^{8+}$ can be further

elaborated to evaluate the catalytic steps of the cyclohexene epoxidation, in which the studied system performed as an excellent catalyst.

Acknowledgements: The authors are grateful for the calculation time, granted on PHYSON computer cluster, operating under the National Science Fund of Bulgaria grants DO-02-90/2008, DO-02-136/2008, DO-02-167/2008, and DDVU-02/42.

REFERENCES

1. K. A. Jørgensen, *Chem. Rev.* **89**, 431 (1989).
2. R. Sheldon, *J. Mol. Catal.*, **7**, 107 (1980).
3. C.-C. Su, J. W. Reed, E. S. Gould, *Inorg. Chem.*, **12**, 337 (1973).
4. S. Turmanova, K. Vassilev, in: *Molybdenum: Characteristics, Production and Applications*, M. Otriz, T. Herrera, (eds.) NOVA Science Publisher, Inc., 2011, p. 77.
5. M. R. Maurya, *Current Org. Chem.*, **16**, 73 (2012).
6. P. Chandra, S. L. Pandhare, S. B. Umbarkar, M. K. Dongare, K. Vanka, *Chemistry - Eur. J.*, **19**, 2030 (2013).
7. C. I. Fernandes, M. S. Saraiva, T. G. Nunes, P. D. Vaz, C. D. Nunes, *J. Catalysis*, **309**, 21 (2014).
8. S. Tangestaninejad, M. H. Habibi, V. Mirkhani, M. Moghadam, G. Grivani, *Inorg. Chem. Comm.*, **9**, 575 (2006).
9. G. Grivani, S. Tangestaninejad, A. Halili, *Inorg. Chem. Comm.*, **10**, 914 (2007).
10. R. Mbeleck, K. Ambroziak, B. Saha, D. C. Sherrington, *Reactive and Funct. Polym.* **67**, 1448 (2007).
11. K. R. Jain, F. E. Kuhn, *Dalton Trans.*, 2221 (2008).
12. S. Turmanova, K. Vassilev, S. Boneva, *Reactive and Funct. Polym.* **68**, 759 (2008).
13. K. Vassilev, S. Turmanova, M. Dimitrova, S. Boneva, *Eur. Polym. J.* **45**, 2269 (2009).
14. K. Vassilev, S. Turmanova, E. Ivanova, V. Trifonova, *J. Biomat. Nanobiotech.* **4**, 28 (2013).
15. K. Vassilev, M. Dimitrova, S. Turmanova, R. Milina, *Synth.React. Inorg., Metal-Org., and Nano-Metal Chem.* **43**, 243 (2013).
16. S. Turmanova, K. Vassilev, *Synth. React. Inorg., Metal-Org., and Nano-Metal Chem.*, **46**, 1395 (2016).
17. M. A. Fardjahromi, M. Moghadam, S. Tangestaninejad, V. Mirkhani, I. Mohammadpoor-Baltork, *RSC Advances*, **6**, 20128 (2016).
18. J.-H. Noh, R. Patala, R. Meijboom, *Applied Catalysis A: General*, **514**, 253 (2016).
19. M. J. Frisch, G. W. Trucks, H. B. Schlegel, G. E. Scuseria, M. A. Robb, J. R. Cheeseman, G. Scalmani, V. Barone, B. Mennucci, G. A. Petersson, H. Nakatsuji, M. Caricato, X. Li, H. P. Hratchian, A. F. Izmaylov, J. Bloino, G. Zheng, J. L. Sonnenberg, M. Hada, M. Ehara, K. Toyota, R. Fukuda, J. Hasegawa, M. Ishida, T. Nakajima, Y. Honda, O. Kitao, H. Nakai, T. Vreven, J. A. Montgomery, Jr., J. E. Peralta, F. Ogliaro, M. Bearpark, J. J. Heyd, E. Brothers, K. N. Kudin, V. N. Staroverov, R. Kobayashi, J. Normand, K. Raghavachari, A. Rendell, J. C. Burant, S. S. Iyengar, J. Tomasi, M. Cossi, N. Rega, J. M. Millam, M. Klene, J. E. Knox, J. B. Cross, V. Bakken, C. Adamo, J. Jaramillo, R. Gomperts, R. E. Stratmann, O. Yazyev, A. J. Austin, R. Cammi, C. Pomelli, J. W. Ochterski, R. L. Martin, K. Morokuma, V. G. Zakrzewski, G. A. Voth, P. Salvador, J. J. Dannenberg, S. Dapprich, A. D. Daniels, O. Farkas, J. B. Foresman, J. V. Ortiz, J. Cioslowski, and D. J. Fox Gaussian 09, Revision A.02, Gaussian, Inc., Wallingford CT (2009).
20. A. D. Becke, *J. Chem. Phys.*, **98**, 5648 (1993).
21. C. Lee, W. Yang, R. G. Parr, *Phys. Rev., B* **37**, 785 (1988).
22. B. Miehlich, A. Savin, H. Stoll, H. Preuss, *Chem. Phys. Lett.*, **157**, 200 (1989).
23. A. J. Cohen, N. C. Handy, *Mol. Phys.*, **99**, 607 (2001).
24. N. C. Handy, A. J. Cohen, *Mol. Phys.*, **99**, 403 (2001).
25. Y. Zhao, D. G. Truhlar, *Theor. Chem. Acc.*, **120**, 215 (2008).
26. Y. Zhao, N. E. Schultz, D. G. Truhlar, *J. Chem. Phys.*, **123**, 161103 (2005).
27. W. J. Hehre, R. Ditchfield, J. A. Pople, *J. Chem. Phys.*, **56**, 2257 (1972).
28. V. A. Rassolov, M. A. Ratner, J. A. Pople, P. C. Redfern, L. A. Curtiss, *J. Comp. Chem.*, **22**, 976 (2001).
29. T. H. Dunning Jr., P. J. Hay, in: *Modern Theoretical Chemistry*, H. F. Schaefer III, (ed.) vol. 3, Plenum, New York, 1977, p. 1.
30. P. J. Hay, W. R. Wadt, *J. Chem. Phys.*, **82**, 270 (1985).
31. Y. Cui, Q. Liu, J. Lin, J. Liu, W. Chen, *Acta Chim. Slovenica*, 279 (2016).
32. R. Mayilmurugan, B.N. Harum, M. Volpe, A.F. Sax, M. Palaniandavar, N.C. Mosch-Zanetti, *Chemistry - Eur. J.*, **17**, 704 (2011).
33. A. Dupé, M. K. Hossain, J. A. Schachner, F. Belaj, A. Lehtonen, E. Nordlander, N. C. Mösche-Zanetti, *Eur. J. Inorg. Chem.*, **2015**, 3572 (2015).
34. V. Vrdoljak, B. Prugovečki, D. Matković-Čalogović, T. Hrenar, R. Dreos, P. Siega, *Crystal Growth & Design*, **13**, 3773 (2013).
35. V. Vrdoljak, J. Pisk, D. Agustin, P. Novak, J. Parlov Vuković, D. Matković-Čalogović, *New J. Chem.*, **38**, 6176 (2014).

36. J. Pisk, B. Prugovečki, D. Matković-Čalogović, T. Jednačak, P. Novak, D. Agustin, V. Vrdoljak, *RSC Advances*, **4**, 39000 (2014).
37. S. Pasayat, S.P. Dash, S. Roy, R. Dinda, S. Dhaka, M. R. Maurya, W. Kaminsky, Y. P. Patil, M. Nethaji, *Polyhedron*, **67**, 1 (2014).
38. L. M. R. Hill, M. K. Taylor, V. W. L. Ng, C. G. Young, *Inorg. Chem.*, **47**, 1044 (2008).

МЕТАЛОДЕНДИМЕРИ ЗА КАТАЛИТИЧНО ЕПОКСИДИРАНЕ - ТЕОРЕТИЧНИ ПОЗНАНИЯ ЗА СТРУКТУРАТА НА Mo (VI) КОМПЛЕКСИ НА ПОЛИ (ПРОПИЛЕН ИМИН) ДЕНДРИМЕРИ

В. Трифонова¹, К. Василев², А. Ахмедова^{3*},

¹ Катедра Аналитична и неорганична химия, Университет "Проф. Асен Златаров", ул. "Проф. Якимов" 1, 8010 Бургас, България

² Катедра "Биотехнология", Университет "Проф. Асен Златаров", ул. "Проф. Якимов" 1, 8010 Бургас, България

³ Факултет по химия и фармация, Софийски университет "Св. Климент Охридски", ул. "Дж. Бучър" 1, 1164 София, България

Постъпила на 1 май 2017 г.; Коригирана на 19 май 2017 г.

(Резюме)

Настоящото теоретично изследване е фокусирано върху подробното структурно описание на комплекс на Mo (VI) с полипропилен-иминов дендример от второ поколение, DAB-G₂-PPI-(NH₂)₈, който по-рано бе синтезиран и оценен като катализатор за епоксидиране на алкени с органични хидропероксиди. За да се провери предложената геометрия с пет координирани метални центрове, което е рядък случай за Mo (VI), ние извършихме структурно описание на възможните комплекси чрез квантово-химични (DFT) изчисления. Това беше постигнато чрез моделиране и геометрична оптимизация на MoO₂²⁺ комплекс с най-малкия триаминов фрагмент на дендримера. Бяха взети под внимание моделни комплекси с различен състав и бяха използвани множество комбинации от DFT функционали (B3LYP, B2LYP, O3LYP, M05 и M06) и базисни функции. Изчисленията с метода M06/6-31G(d,p)-(LanL2DZ; Mo) дадоха най-добро съгласие с наличните кристалографски данни за подобни комплекси на цис-диоксо Mo(VI). Поради това, този метод бе използван за оптимизиране на структурата на тетрамерния Mo(VI) комплекс на DAB-G₂-PPI-(NH₂)₈. Резултатите сочат, че оптимизираната с M06/6-31G (d,p) метода структура на пет-координирания цис-диоксо Mo(VI) комплекс с тридендримерни фрагменти е възможна, потвърждавайки експериментално предложения начин на координация на DAB-G₂-PPI-(NH₂)₈. Изчисленията върху комплекс с допълнително координирана водна молекула показват, че пет-координираните комплекси на Mo(VI) с PPI дендример съхраняват възможността да координират и една молекула разтворител с O-донор. Тези структурни характеристики могат да обяснят способността на молибденовите центрове в моделирания металодендимер да координират и хидропероксидите, използвани като източници на кислород за каталитично епоксидиране на алкени, и по този начин да осигурят осъществяването на решаващ каталитичен етап в реакциите на епоксидиране на олефини.

Aluminium-scandium tungstates solid solutions $\text{Al}_{2-x}\text{Sc}_x(\text{WO}_4)_3$: Al and Sc distribution on a local scale

A. Yordanova¹, S. Simova², I. Koseva¹, R. Nikolova³, V. Nikolov¹, R. Stoyanova^{1*}

¹ Institute of General and Inorganic Chemistry, Bulgarian Academy of Sciences, Acad. G. Bonchev Str., Bldg. 11, Sofia 1113, Bulgaria

² Institute of Organic Chemistry with Centre of Phytochemistry, Bulgarian Academy of Sciences, Acad. G. Bonchev street, bl. 9, 1113 Sofia, Bulgaria

³ Institute of Mineralogy and Crystallography "Acad. Ivan Kostov", Bulgarian Academy of Sciences, Acad. G. Bonchev street, bl. 107, 1113 Sofia, Bulgaria

Received April 27, 2017; Revised May 23, 2017

Dedicated to Acad. Ivan Juchnovski on the occasion of his 80th birthday

Multinuclear and multiple-quantum magic angle spinning (MQMAS) ²⁷Al and ⁴⁵Sc NMR spectroscopy and single crystal X-ray diffraction have been combined to assess and to quantify the distribution of Al and Sc on a local scale in mixed aluminium-scandium tungstates, which are of interest as materials with negative thermal expansion. The specific features of local cationic distribution have been studied by using $\text{Al}_{2-x}\text{Sc}_x(\text{WO}_4)_3$ solid solutions ($0 \leq x \leq 2$) in the form of single crystals and nano-powders. The ²⁷Al MAS and MQMAS NMR spectra indicate that Al atoms have two distinctly different coordination types in $\text{Al}_{2-x}\text{Sc}_x(\text{WO}_4)_3$. On the contrary, ⁴⁵Sc MAS and MQMAS NMR spectra display single coordination for Sc only. The crystal structure of $\text{Al}_{2-x}\text{Sc}_x(\text{WO}_4)_3$ is revised to the orthorhombic space group $P2_12_12_1$, a non-isomorphic subgroup of $Pbcn$. In this structural model, there are two distinct non-equivalent Al/Sc positions: one of them is preferentially occupied by Al ions, while Sc ions reside at both positions. The coordination of Al and Sc in $\text{Al}_{2-x}\text{Sc}_x(\text{WO}_4)_3$ is an intrinsic property, not depending on the form of $\text{Al}_{2-x}\text{Sc}_x(\text{WO}_4)_3$ - single crystal or nano-powder.

Key words: Solid State NMR; Single Crystal X-ray Diffraction; Tungstates

INTRODUCTION

Aluminium and scandium tungstates belong to a class of materials, which have a variety of functional properties that can easily be rationalized on the basis of their crystal structure. All members of the family $\text{Me}_2(\text{WO}_4)_3$ crystallize in an orthorhombic space group [1–8]. The structure is composed of a three dimensional framework of corner-shared MeO_6 octahedra and WO_4 tetrahedra [9]. This type of linkage between cations ensures the structural flexibility, leading to the accommodation of metal ions with different sizes in the octahedral positions: the ionic radii of Al^{3+} and Sc^{3+} are 0.535 Å and 0.745 Å, respectively. The $\text{Me}_2(\text{WO}_4)_3$ undergo a structure phase transition at temperatures, depending on the nature of the metal ion: -6 °C and -263 °C for $\text{Al}_2(\text{WO}_4)_3$ and for $\text{Sc}_2(\text{WO}_4)_3$, respectively [10, 11]. The orthorhombic structure is easily transformed into a more dense monoclinic structure [12].

One approach to design the functional properties of tungstates comprises modelling of the structure by appropriate cationic substitution. This approach

is effective for improvement of the thermal expansion and optical properties of $\text{Al}_{2-x}\text{Sc}_x(\text{WO}_4)_3$ solid solutions [7, 13–15]. Based on diffraction methods, it has been demonstrated that $\text{Al}_2(\text{WO}_4)_3$ reacts with $\text{Sc}_2(\text{WO}_4)_3$ forming solid solutions within the whole concentration range, the crystal structure being orthorhombic [16–18]. The solid solutions of $\text{Al}_{2-x}\text{Sc}_x(\text{WO}_4)_3$ have been prepared in the form of single crystals and powders [16–18]. It is worth mentioning that growing of tungstate single crystals with defined compositions represents a difficult task by the Czochralski and the flux methods due to the volatility of WO_3 , in the case of the first method and low growth rates and anisometric growth in the case of the flux method [16, 18]. Recently we have reported a new and facile method for the preparation of nano-powders $\text{Al}_{2-x}\text{Sc}_x(\text{WO}_4)_3$ with defined composition varying from $x=0$ to $x=2$ [17]. The method consists in co-precipitation, followed by thermal treatment at 600°C using short heating time.

Although the properties of the individual compounds $\text{Al}_2(\text{WO}_4)_3$ and $\text{Al}_{2-x}\text{Sc}_x(\text{WO}_4)_3$ have been validated by many research groups, the properties of $\text{Al}_{2-x}\text{Sc}_x(\text{WO}_4)_3$ solid solutions are still

* To whom all correspondence should be sent:
E-mail: radstoy@svr.igic.bas.bg

under debate [19]. These discrepancies could be explained with structural peculiarities of solid solutions $Al_{2-x}Sc_x(WO_4)_3$ occurring on a local scale level due to the big mismatch between the ionic radii of Al^{3+} and Sc^{3+} (more than 10%). To the best of our knowledge, the cationic substitution on a local scale has not been explored yet, despite the long-range structure of solid solutions has been determined both by single crystal and powder X-ray diffraction techniques [19, 20]. The desired method of choice to probe the local structure of $Al_{2-x}Sc_x(WO_4)_3$ is solid state NMR spectroscopy. The mechanism of ionic conductivity of $Sc_2(WO_4)_3$ and $Sc_2(MoO_4)_3$ and their solid solutions has been examined in terms of ^{45}Sc MAS NMR spectroscopy [21]. The formation of $Al_2(WO_4)_3$ during the co-precipitation reaction is monitored by us using ^{27}Al MAS NMR [22].

This contribution aims to assess the cationic distribution in $Al_{2-x}Sc_x(WO_4)_3$ solid solutions on a local scale by means of solid state ^{27}Al and ^{45}Sc MQMAS NMR spectroscopy and single crystal X-ray diffraction analysis. Tungstates are investigated in form of both single crystals and nano-powders. These series are already characterized as solid solutions $Al_{2-x}Sc_x(WO_4)_3$ by means of powder X-ray diffraction. The single crystal X-ray diffraction is used to refine the crystal structure of $Al_{2-x}Sc_x(WO_4)_3$. The complementary application of both multinuclear solid state NMR and single crystal X-ray diffraction represents a new approach for structural characterization of tungstates $Me_2(WO_4)_3$ on a local scale.

EXPERIMENTAL

The nano-sized powders of $Al_{2-x}Sc_x(WO_4)_3$ ($x = 0.5, 1.0, 1.5$) were obtained using the co-precipitation method. Each of the solid solutions was synthesized using two separate aqueous solutions: sodium tungstate, obtained by dissolving $Na_2WO_4 \cdot 2H_2O$ (p.a.) reagent, and mixed aluminium-scandium solution containing $Al(NO_3)_3 \cdot 9H_2O$ and $Sc(NO_3)_3 \cdot 4H_2O$ (14.4 wt.% Sc). The ratio between the two solutions, as well as the Al-to-Sc ratio, corresponds to the stoichiometric composition. The details of synthesis procedure have been given elsewhere [17]. Well crystallized $Al_{2-x}Sc_x(WO_4)_3$ as solid solutions with particle sizes varying between 10 and 70 nm are obtained by this method [17, 23].

Single crystals of pure tungstates and their solid solutions (used as references) were obtained in the present investigation by the high-temperature

method using top-seeded solution growth and slow cooling down. The solvent used in all experiments was 27.5 Na_2O –72.5 WO_3 mol %. The initial solute concentration and Al-to-Sc ratio were chosen on the basis of our previous investigation on the solubility of the solute into the above-mentioned solvent and in view of the distribution coefficient of Sc and Al [18].

For the sake of simplicity, $Al_{2-x}Sc_x(WO_4)_3$ compositions will be further on denoted as N-ASW and SC-ASW, where N and SC symbols identify nano-powders and single crystals. Fig. 1 shows the images of N-ASW and SC-ASW samples.

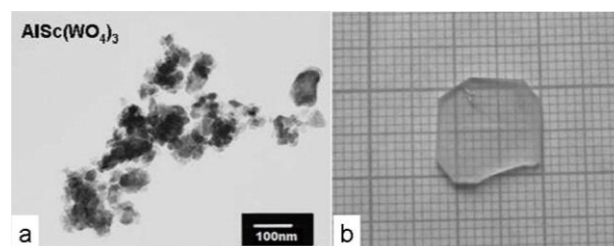


Fig. 1. TEM image of N-ASW (a) and optical image of SC-ASW (b).

Solid-state MAS ^{27}Al and ^{45}Sc NMR spectra were recorded at 156.4 MHz and 145.8 MHz on a Bruker AVII+ 600SB NMR spectrometer (magnetic field of 14.1 T). Single pulse excitation of 1 μ s, 0.2 s recycle delay and total number of scans of 1-2k were used. The samples were loaded into 4 mm zirconia rotors and spun at 9 and 14 kHz. Chemical shifts are quoted in parts per million, from external DSS (sodium 3-(trimethylsilyl)propane-1-sulfonate, Ξ scale).

3Q MQMAS ^{27}Al and ^{45}Sc NMR spectra were recorded at 130.3 MHz and 121.5 MHz on a Bruker HD 500SB NMR spectrometer (magnetic field of 11.7 T), using a 2.5 mm MAS probe. Samples were spun at 5 and 15 kHz using the 3- and 4-pulse z-filter pulse programs and the optimization procedure according to the Solids manual [24]. Experiments were obtained using rf-field strengths of 62.5 kHz for ^{27}Al and 73.5 kHz for ^{45}Sc with excitation and conversion pulses with lengths 4.0 (3.4) μ s and 1.2 (0.9) μ s and selective pulses of 18 (14) μ s at 28 db lower intensity, respectively. Relaxation interval of 4-5 s, F2 spectral width of 105.6 ppm for both nuclei, 64 (80) time increments for F1 set to the rotor period and States-TPPI sign discrimination were used.

Structural characterization of nanopowders was carried out by powder X-ray diffraction using a Bruker D8 Advance powder diffractometer with $Cu K\alpha$ radiation. Data were collected in the 2θ range

from 10 to 80 ° with a step of 0.04° and 1 s/step counting time. Concerning single crystal structure characterization, the intensity data were collected at room temperature by the ω -scan technique on the Agilent Diffraction SuperNova Dual four-circle diffractometer, equipped with Atlas CCD detector, using mirror-monochromatized Mo-K α radiation from micro-focus source ($\lambda=0.7107$ Å). The determination of cell parameters and the data processing procedure were performed by using the CrysAlis Pro program package [25]. The structure was solved by direct methods (SHELXS-97) and refined by full-matrix least-square procedures on F² (SHELXL-97) [26]. The structure visualization was performed by Crystal Maker (version 2.6.2, SN2080) [27]. The occupancies of Al and Sc in the mixed positions were refined simultaneously with the atomic coordinates and the atomic displacement parameters. The same isotropic or anisotropic displacement parameters are used for the atoms occupying the same position. Further details about the structure investigation may be obtained from Fachinformationszentrum (FIZ) Karlsruhe, under the CSD 429327 for *Pbcn* space group and CSD 429328 for *P2₁2₁2* space group.

RESULTS AND DISCUSSION

²⁷Al and ⁴⁵Sc MQMAS NMR of $Al_{2-x}Sc_x(WO_4)_3$ solid solutions

Solid state ²⁷Al NMR spectroscopy was used aiming at the analysis of the structure of both single crystals and nano-powders $Al_{2-x}Sc_x(WO_4)_3$ solid solutions by probing the Al local environment. Fig. 2 compares the ²⁷Al MAS NMR spectra for SC-ASW and N-ASW, where the amount of Al is varied from $x=0$ to $x=1.5$. For the individual aluminium analogue, the ²⁷Al MAS NMR spectrum consists of a single resonance centred at about -4 ppm, the resonance position being the same for $Al_2(WO_4)_3$ both in single crystals and nano-powders. The difference arises from the line width: the resonance of the single crystal is narrower than that of the nano-powder: 224 vs 294 Hz. This feature reveals the lower variation in the local coordination of Al in the case of the single crystal. Upon increasing the Sc content, a new resonance at -1 ppm, which is superimposed on the main resonance, grows up in its intensity. The resonance positions and line widths for the two signals are summarized in Table 1. The resonance positions of the two signals are independent of the Al-to-Sc ratio. The line widths of the intermediate compositions are similar and they are higher in

comparison with that of the individual composition. The only parameter, that is changing systematically with the Al-to-Sc ratio, is the resonance intensity (Table 1). Upon increasing the Sc content there is an increase in intensity of the signal centered at -1 ppm at the expense of the resonance at -4 ppm. This trend is observed for $Al_{2-x}Sc_x(WO_4)_3$ both in the form of single crystals and nano-powders, thus indicating that the Al coordination in solid solutions of $Al_{2-x}Sc_x(WO_4)_3$ is an intrinsic property.

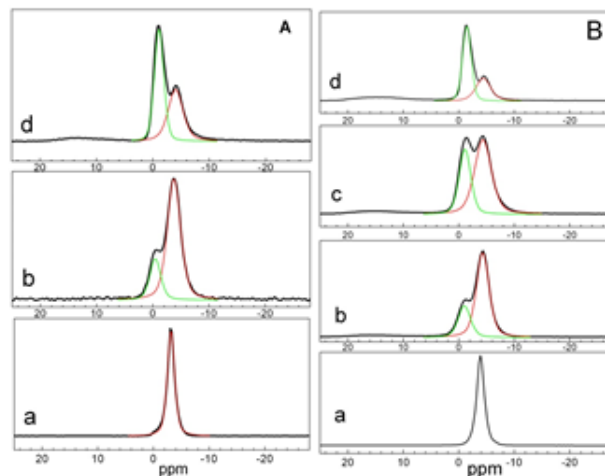


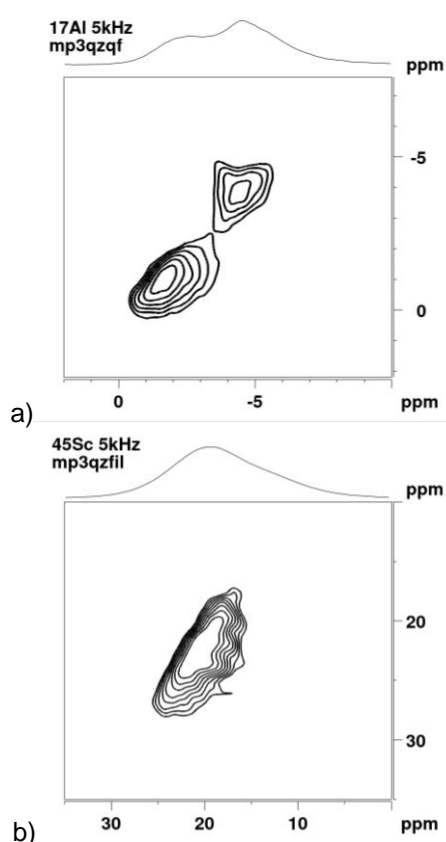
Fig. 2. ²⁷Al MAS NMR spectra of SC- $Al_{2-x}Sc_x(WO_4)_3$ (A) and N- $Al_{2-x}Sc_x(WO_4)_3$ (B): $x=0$ (a); $x=0.5$ (b); $x=1.0$ (c) and $x=1.5$ (d).

Because of the quadruple moment of Al, MQMAS NMR experiments were undertaken in order to increase the resolution of the ²⁷Al spectra. Fig. 3a shows the ²⁷Al MQMAS NMR spectrum. As one can see, there are two well separated signals. This means that MQMAS experiments confirm unambiguously the occurrence of two well defined coordinations of Al in $Al_{2-x}Sc_x(WO_4)_3$ solid solutions.

Due to the larger quadrupole constant, the ⁴⁵Sc NMR spectra are usually broader and less resolved in comparison with that of ²⁷Al. However, the second order perturbation quadrupolar effects on the ⁴⁵Sc resonance line become negligible, when ⁴⁵Sc NMR spectra are registered at a stronger magnetic field (i.e. 11.7 T) [28]. That is why, the MAS NMR spectra are registered at a magnetic field of 14.1 T (Fig. 4). The ⁴⁵Sc NMR spectra of $Al_{2-x}Sc_x(WO_4)_3$ solid solutions show broad resonance lines with centre of gravity at about 20 ppm (Fig. 4), in accordance with literature values for octahedrally coordinated Sc in $Sc_2(WO_4)_3$: 15.6 ppm and 9.3 ppm [21, 28]. The line widths of more than 1400 Hz are higher in comparison with these of ²⁷Al, which vary between 220 and 500 Hz.

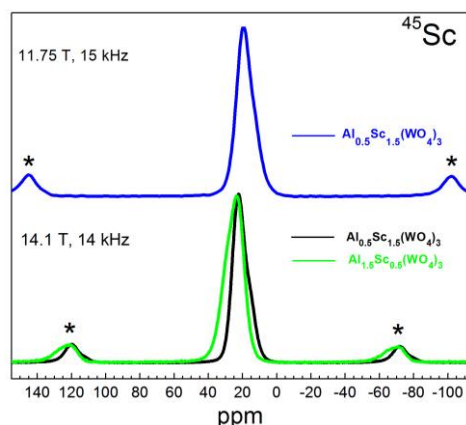
Table 1. Chemical shifts (δ , ppm), line widths ($\Delta\delta$, Hz) and relative intensities of ^{27}Al and ^{45}Sc NMR signals in N-ASW and SC-ASW.

Samples	^{27}Al Si1		^{27}Al Si2		Relative part of ^{27}Al Si1	
	$\delta \pm 0.04$, ppm	Δ , Hz	$\delta \pm 0.04$, ppm	Δ , Hz		
N-ASW, x = 0	-3.92	297				1.00
N-ASW, x = 0.5	-4.02	403	-0.62	389	0.73	
N-ASW, x = 1.0	-4.48	494	-1.27	357	0.63	
N-ASW, x = 1.5	-4.07	446	-1.0	288	0.37	
SC-ASW, x = 0	-3.15	224				1.00
SC-ASW, x = 0.5	-3.77	406	-0.45	333	0.78	
SC-ASW, x = 1.5	-4.02	452	-1.10	317	0.44	

**Fig. 3.** MQMAS spectra of ^{27}Al (a) and ^{45}Sc (b) in $Al_{0.5}Sc_{1.5}(WO_4)_3$.

The relatively weak quadrupolar moment of ^{45}Sc allows acquisition of the spectra also at a magnetic field of 11.71 T, shown on the same figure. A broad line is also visible, which does not permit discrimination of the ^{45}Sc atoms in different coordinations. Moreover, the center of gravity seems not to be dependent on the Sc content. The 4-pulse z-filter ^{45}Sc 3Q MQMAS NMR experiment was acquired for $Al_{0.5}Sc_{1.5}(WO_4)_3$ (Fig. 3b). Contrary to the ^{27}Al case, the ^{45}Sc MQMAS spectrum displays only one signal with a dispersed shape. This

indicates that Sc atoms do not have distinct coordinations in solid solutions of $Al_{2-x}Sc_x(WO_4)_3$. This means that the main factor for the large line width is the distribution of ^{45}Sc chemical shifts.

**Fig. 4.** ^{45}Sc MAS NMR spectra of N-ASW: $Al_{1.5}Sc_{0.5}(WO_4)_3$ (green lines) and $Al_{0.5}Sc_{1.5}(WO_4)_3$ (black lines) registered at 14.1 T; $Al_{0.5}Sc_{1.5}(WO_4)_3$ (blue lines) collected at 11.7 T.

The occurrence of dispersed MQMAS signals and broad MAS NMR signals can be related with smooth changes in the local coordination of Sc when Al is substituted for Sc, which is in agreement with a homogeneous distribution of ^{45}Sc in $Al_{2-x}Sc_x(WO_4)_3$ solid solutions.

The ^{27}Al MAS NMR spectra clearly show that Al atoms have two distinctly different coordinations in $Al_{2-x}Sc_x(WO_4)_3$ solid solutions, which is opposite to that for Sc. Taking into account that Al and Sc occupy only one crystallographic site in the orthorhombic crystal structure, the most obvious explanation is to associate the splitting of Al coordination with the effect of the neighbouring metal ions on the chemical shift. In the orthorhombic structure, every

Al/ScO_6 -octahedron shares common vertices with six WO_4 tetrahedra, which, in their turn, are corner-connected with 18 Al/Sc ions. The small effect of the first W neighbours on the chemical shift of ^{45}Sc has already been demonstrated for solid solutions of $Sc_2(WO_4)_3$ - $Sc_2(MoO_4)_3$, where a shift of about 5 ppm has been found during replacement of W by Mo [21, 28]. For the $Al_{2-x}Sc_x(WO_4)_3$ solid solutions studied by us, we can expect a smaller effect of second Al/Sc neighbours on the chemical shifts of both ^{27}Al and ^{45}Sc . Although the W^{6+} and Mo^{6+} ions have similar ionic radii, the ionic mismatch for Al^{3+} and Sc^{3+} ions will create a more significant local distortion around the central Al/Sc nucleus, as a result of which a high variation in the chemical shift can be expected. On the other hand, Al^{3+} and Sc^{3+} neighbours are separated from the central Al/Sc nucleus at longer distances in comparison with that of W/Mo ions, which would create an opposite effect. Thus, the resonance at -4 ppm is attributed to Al nucleus having only Al^{3+} ions as first neighbours, while the resonance at -1 ppm originates from the Al nucleus surrounded mainly by Sc^{3+} ions. The negative shift of the resonance due to Al in Al^{3+} environment reveals that Al^{3+} neighbours create a stronger crystal field in comparison with that created by the Sc^{3+} ion neighbours. This is in agreement with the mean bond length Al/Sc-O in the two final compositions $Al_2(WO_4)_3$ and $Sc_2(WO_4)_3$: 1.88 Å and 2.08 Å for Al-O and Sc-O, respectively [8]. Contrary to Al, the one ^{45}Sc resonance can be attributed to Sc nucleus, whose metal surrounding is smoothly changed during progressive replacement of Al by Sc.

The next important feature is related with the type of Al/Sc distribution in $Al_{2-x}Sc_x(WO_4)_3$ solid solutions. In accordance with our previous studies [17], all $Al_{2-x}Sc_x(WO_4)_3$ crystallized in an orthorhombic space group, the lattice parameters being increased linearly with the Sc content. The Vegard dependence is also obeyed for tungstates $Al_{2-x}Sc_x(WO_4)_3$ in the form of the single crystals [17]. The detection of two distinctly different coordinations of Al and only one coordination for Sc in the orthorhombic structure of $Al_{2-x}Sc_x(WO_4)_3$, ensuring only one crystallographic metal ion site, means that Al ions are not homogeneously distributed on a local scale in respect of Sc ions. On the other hand, the distances between Al/Sc nucleus and the Al^{3+}/Sc^{3+} neighbours are large (varying between 5.165 and 6.705 Å), which implies that non-homogeneous Al/Sc distribution is not a local phenomenon and it will cover domains with long sizes. At a first glance, it appears that NMR data

are in contradiction with the well described crystalline structure of $Al_{2-x}Sc_x(WO_4)_3$ solid solutions [8, 17, 18].

Single crystal X-ray diffraction of $Al_{2-x}Sc_x(WO_4)_3$

In order to make NMR and crystalline structure data self-consistent, we reinvestigated the crystalline structure of $Al_{2-x}Sc_x(WO_4)_3$ solid solutions in the form of single crystals. In the first approximation, the structure refinement is carried out within the framework of the structural model based on *Pbcn* space group. The refinement revealed that the chemical composition of the measured single-crystal sample is $Al_{0.42}Sc_{1.58}(WO_4)_3$, which is well consistent with the chemical analysis: $Al_{0.40}Sc_{1.60}(WO_4)_3$ in accordance with EDAX analysis. At room temperature the studied compound is orthorhombic with lattice parameters and volume values quite similar to those observed for $AlSc(WO_4)_3$ [4]. As it is expected the unit cell volume of the studied compound is larger than that of $AlSc(WO_4)_3$ because of the higher Sc:Al ratio ($V=1171\text{Å}^3$ versus 1134Å^3 , respectively). This is in agreement with data reported previously on the concentration dependence of the lattice parameters for $Al_{2-x}Sc_x(WO_4)_3$ single crystals [16]. In addition, the lattice parameters for single crystal and nanopowder $Al_{2-x}Sc_x(WO_4)_3$ with the same composition (i.e. $x\sim 1.5$) are $V=1171\text{Å}^3$ and $V=1190\text{Å}^3$, respectively.

Analyses of the structural similarity between each one of the end members and the studied solid solution have been performed by the program COMPSTRU at Bilbao Crystallographic Server. The measure of similarity (Δ) is defined as a function of the differences in atomic positions and the ratios between the corresponding lattice parameters of the structures [29, 30]. The calculated Δ -value indicates that the crystalline structure of $Al_{0.42}Sc_{1.58}(WO_4)_3$ is quite similar to that of $Sc_2(WO_4)_3$ with $\Delta = 0.004$, while for the structure of $Al_2(WO_4)_3$ this parameter is 0.014. The bond lengths Sc/Al – O vary in a slightly narrower range (from 1.999(5) to 2.050(4) Å) comparing with that in $AlSc(WO_4)_3$ (1.997 – 2.055Å).

Taking into account that the crystalline structure of the solid solution is described in the *Pbcn* space group a statistical distribution of Al^{3+} and Sc^{3+} among one crystallographic site should be assumed. This also means that the W ions as first metal neighbours will only form one type of surrounding of Al (Sc) position. However, the NMR

spectroscopy proves clearly that Al and Sc ions occupy two distinctly different sites. Therefore, the next level of structure refinement is based on a model, where the structure of the solid solution is described in one of the maximal non-isomorphic subgroups of *Pbcn* space group where the M atomic position will be split into two symmetrically non-equivalent ones. There are four orthorhombic subgroups of space group *Pbcn* (60): *P2₁2₁2* (18), *Pca2₁* (29), *Pnc2* (30) and *Pna2₁* (33), respectively. Structure refinements in *P2₁2₁2* (18), *Pca2₁* (29), *Pnc2*(30) and *Pna2₁* (33) space groups have been tested using the experimental data obtained for the studied sample and the results are presented in Table 2. The refinement indicators are similar,

which makes difficult the assignment of the right space group. The values of the Flack parameter vary between 0.15 – 0.35, but only for *P2₁2₁2* and *Pca2₁* space groups the uncertainty is relatively small. At first glance, this may indicate that the centrosymmetric space group is the correct one. However, it is worth mentioning that the value obtained for the Flack parameter is dependent on the Friedel coverage of the intensity data, approaching 0.5 for coverage of 100% and sticking near the starting value for coverage of 0%. For pseudo-centrosymmetric structures with heavy atoms in a centrosymmetric arrangement such as W, the obtained values of the Flack parameter are not strictly indicative (Table 2).

Table 2. Crystal data and structure refinement indicators for the studied composition, obtained for different space groups.

Space group	<i>P2₁2₁2</i> (18)	<i>Pca2₁</i> (29)	<i>Pnc2</i> (30)	<i>Pna2₁</i> (33)
Data/parameters	2861 / 158	2818 / 142	2757 / 158	2554 / 157
Goodness-of-fit on F ²	1.025	0.970	1.136	1.136
Final R indices [I > 2σ (I)]	R = 0.0239 R _w = 0.047	R = 0.0248 R _w = 0.054	R = 0.0242, R _w = 0.050	R = 0.0242, R _w = 0.053
Final R indices (all data)	R = 0.0337 R _w = 0.051	R = 0.0325 R _w = 0.059	R = 0.0316 R _w = 0.054	R = 0.0305 R _w = 0.057
Largest difference peak and hole	1.21 and -1.562 eÅ ³	1.308 and -1.322 eÅ ³	1.390 and -1.473 eÅ ³	1.107 and -1.982 eÅ ³
Flack x *	0.33(5)	0.35(5)	0.14(7)	0.26(8)
Displacement parameters	Anisotropic for all atom	Two atoms non positive defined	Two atoms non positive defined	Two atoms non positive defined

Table 3. Atomic coordinates, Wyckoff positions and equivalent isotropic displacement parameters for $Al_{0.42}Sc_{1.58}(WO_4)_3$, refined in *P2₁2₁2*.

	Wyckoff positions	SOF	x	y	z	U(eq)
M1(Sc1)	4c	0.72(3)	0.2824(5)	0.3803(4)	0.5005(6)	0.0126(14)
M1(Al1)	4c	0.28(3)	0.2824(5)	0.3803(4)	0.5005(6)	0.0126(14)
M2(Sc2)	4c	0.94(3)	0.2157(4)	0.6192(3)	0.9984(6)	0.0113(12)
M2(Al2)	4c	0.06(3)	0.2157(4)	0.6192(3)	0.9984(6)	0.0113(12)
W11	4c	1	0.36743(11)	0.64432(9)	0.35520(15)	0.0178(3)
W12	4c	1	0.13216(11)	0.35573(9)	0.14571(15)	0.0179(3)
W21	2b	1	0	0.5	0.7230(2)	0.0173(4)
W22	2a	1	0.5	0.5	0.7773(2)	0.0170(4)
O11	4c	1	0.3219(18)	0.5255(11)	0.4320(2)	0.0370(5)
O12	4c	1	0.1780(14)	0.4743(10)	1.0740(2)	0.0290(5)
O21	4c	1	0.3367(16)	0.6457(12)	1.1718(19)	0.0370(5)
O22	4c	1	0.1549(15)	0.3624(12)	0.3300(17)	0.0260(4)
O31	4c	1	0.2430(2)	0.2368(12)	0.5680(2)	0.0350(5)
O32	4c	1	0.2640(2)	0.7581(11)	0.9290(3)	0.0390(5)
O41	4c	1	0.4520(12)	0.3298(11)	0.3890(2)	0.0280(4)
O42	4c	1	0.0434(14)	0.6668(13)	1.1110(2)	0.0410(5)
O51	4c	1	0.0819(16)	0.5922(11)	0.8340(2)	0.0280(4)
O52	4c	1	0.4095(16)	0.4136(13)	0.6720(2)	0.0340(4)
O61	4c	1	0.1273(16)	0.4374(14)	0.6120(3)	0.0450(5)
O62	4c	1	0.3837(15)	0.5653(14)	0.8810(3)	0.0450(5)

Among several proposed space groups, we choose the structural model based on $P2_12_12$ space group since only refinement in this space group allows anisotropic description of the displacement parameters for all atoms. The atomic parameters of the studied compound in $P2_12_12$ are represented in Table 3. In this model, there are two metal ions positions, which ensure different geometry for the metal ions (Table 4, Fig. 5). The refinement shows that Al atoms occupy preferentially one of the positions (marked with M1, Table 3 and 4), while Sc atoms reside in both positions (marked with M1 and M2, Table 3 and 4).

Table 4. Selected bond lengths (Å) of $Al_{0.42}Sc_{1.58}(WO_4)_3$ refined in $P2_12_12$.

M1 – O61	1.956(17)	M2 – O32	1.986(15)
M1 – O31	2.017(16)	M2 – O21	2.026(15)
M1 – O22	2.025(17)	M2 – O51	2.034(17)
M1 – O41	2.032(15)	M2 – O42	2.046(16)
M1 – O11	2.040(16)	M2 – O12	2.056(15)
M1 – O52	2.062(18)	M2 – O62	2.066(17)

The preferential distribution of Al^{3+} among the two positions is consistent with the NMR data with splitting of Al lines in solid solutions of $Al_{2-x}Sc_x(WO_4)_3$. Due to the larger distance between Al/Sc ions, the effect of second metal neighbours can be neglected. This is supported by the experimental observations of the small effect of the first W and Mo neighbours on the chemical shift of ^{45}Sc , as was observed previously [21, 28]. In addition, both ^{27}Al and ^{45}Sc NMR parameters are more sensitive towards the local coordination environment in comparison with the effect of metal neighbours. The resonance at -4 ppm can be attributed to Al occupying the second position, while Al in the first position causes the resonance shift at -1 ppm. In addition, the newly found refined structure can also answer the question why the only parameter that is systematically changing with the Al-to-Sc ratio is the ^{27}Al NMR resonance intensity (relative intensities, Table 1). For $Al_{2-x}Sc_x(WO_4)_3$ with $x=1.5$, the relative part of the NMR signal of ^{27}Al at -4 ppm is 0.44 (Table 1), which is comparable with the relative part of Al in the M2-position determined from the crystal structure refinement: 0.06 (Table 3). The observation of one resonance signal for ^{45}Sc is consistent with homogeneous distribution of Sc over two positions. These results demonstrate that ^{27}Al MAS NMR

spectra allow quantification the distribution of Al over two crystallographic positions, established by single crystal X-ray diffraction (Table 1, Table 3).

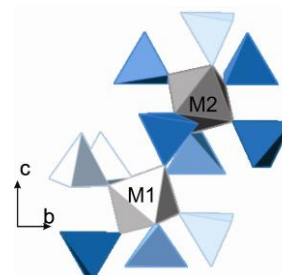


Fig. 5 Detailed view of M1 and M2 positions in the $P2_12_12$ space group.

CONCLUSION

The crystalline structure of $Al_{2-x}Sc_x(WO_4)_3$ solid solutions is being reconsidered. Single crystal X-ray diffraction shows that $Al_{2-x}Sc_x(WO_4)_3$ solid solutions crystallize in an orthorhombic space group $P2_12_12$, which is a non-isomorphic subgroup of $Pbcn$. In this structural model, there are two symmetrically non-equivalent positions: one of them is preferentially occupied by Al, while Sc resides homogeneously both positions. The distribution of Al and Sc over crystallographic positions is monitored by multinuclear ^{27}Al and ^{45}Sc MAS and MQMAS NMR spectroscopy. The coordination of Al and Sc in $Al_{2-x}Sc_x(WO_4)_3$ is an intrinsic property, which does not depend on the form of $Al_{2-x}Sc_x(WO_4)_3$ whether it is single crystal or nano-powder. The local cationic distribution in $Al_{2-x}Sc_x(WO_4)_3$ solid solutions can serve as a basis for reinterpretation of their thermal, conductive and optical properties.

Acknowledgements: The generous financial support of the Bulgarian Science Fund (projects UNA-17/2005, DRNF-02–13/2009 and DRNF-02–01/2009) is gratefully acknowledged.

REFERENCES

1. T. Sugimoto, Y. Aoki, E. Niwa, T. Hashimoto, Y. Morito, *J. Ceramic Soc. Japan* **115**, 176 (2007).
2. J. S. O. Evans, T. A. Mary, A. W. Sleight, *J. Solid State Chem.*, **137**, 148 (1998).
3. Y. Okazaki, T. Ueda, S. Tamura, N. Imanaka, G. Adachi, *Solid State Ionics*, **136–137**, 437 (2000).
4. J. Zhu, J. Yang, X. Cheng, *Solid State Sci.*, **14**, 187 (2012).
5. Y. Zhou, S. Adams, R. Rao, D. Edwards, A. Neiman and N. Pestereva, *Chem. Mater.*, **20**, 6335 (2008).

6. K. Petermann, P. Mitzscherlich, *EEE J. Quantum Elect.*, **23**, 1122 (1987).
7. N. Dasgupta, E. Sörge, B. Butler, T.-C. Wen, D. K. Shetty, L. K. Cambrea, D. C. Harris, *J. Mater. Sci.*, **47**, 6286 (2012).
8. K. Nassau, H. J. Levinstein, G. M. Loiacono, *J. Phys. Chem. Solids*, **26**, 1805 (1965).
9. K. Nassau, *Rare Earth Res.*, **3**, 331 (1964).
10. V. E. Plyushev, V. M. Amosov, *Doklady Akademii nauk SSSR*, **157**, 131 (1964).
11. M. Maczka, K. Hermanowicz, J. Hanuza, *J. Mol. Struct.*, **744-747**, 283 (2005).
12. Y. Ogata, K. Tsuda, T. Hashimoto, *Japanese J. Appl. Phys.*, **47**, 4664 (2008).
13. J. S. O. Evans, T. A. Mary, A.W. Sleight, *J. Solid State Chem.*, **133**, 580 (1997).
14. M. Maczka, K. Hermanowicz, A. Pietraszko, A. Yordanova, I. Koseva, *Opt. Mater.*, **36**, 658 (2014).
15. J. Zhu, J. Yang, X. Cheng, *Solid State Sci.*, **14**, 187 (2012).
16. M. Hiraiwa, S. Tamura, N. Imanaka, G. Adachi, H. Dabkowska, A. Dabkowski, *Solid State Ionics*, **137**, 427 (2000).
17. A. Yordanova, I. Koseva, N. Velichkova, D. Kovacheva, D. Rabadjieva, V. Nikolov, *Mater. Res. Bull.*, **47**, 1544 (2012).
18. D. Ivanova, V. Nikolov, P. Peshev, *J. Crystal Growth*, **308**, 84 (2007).
19. C. Lind, *Materials*, **5**, 1125 (2012).
20. S. E. Ashbrook, *Phys. Chem. Chem. Phys.*, **11**, 6892 (2009).
21. N. Kim, J. Stebbins, *Chem. Mater.*, **21**, 309 (2009).
22. E. Zhecheva, R. Stoyanova, S. Ivanova, V. Nikolov, *Solid State Sci.s*, **12**, 2010 (2010).
23. D. Nihtianova, N. Velichkova, R. Nikolova, I. Koseva, A. Yordanova, V. Nikolov, *Mater. Res. Bull.*, **46**, 2125 (2011).
24. Bruker Solids User Manual, ver. 002, 2009.
25. Agilent. CrysAlis PRO (version 1.171.35.15). Agilent Technologies Ltd, Yarnton England, 2010.
26. G. M. Sheldrick, *Acta. Cryst. A*, **64**, 112 (2008).
27. Crystal Maker (version 2.6.2, SN2080).
28. S. Balamurugan, U. Ch. Rodewald, T. Harmening, L. Wüllen, D. Mohr, H. Eckert, R. Pöttgen, *Z. Naturforsch.*, **65b**, 13 (2010).
29. G. Bergerhoff, M. Berndt, K. Brandenburg, T. Degen, *Acta Cryst.*, **B55**, 147 (1999).
30. S. Parsons, H. D. Flack, T. Wagner, *Acta Cryst. B*, **69**, 249 (2013).

ТВЪРДИ РАЗТВОРИ НА АЛУМИЕВО-СКАНДИЕВИ ВОЛФРАМАТИ $Al_{2-x}Sc_x(WO_4)_3$: РАЗПРЕДЕЛЕНИЕ НА Al И Sc НА ЛОКАЛНО НИВО

A. Йорданова¹, С. Симова², Й. Косева¹, Р. Николова³, В. Николов¹, Р. Стоянова^{1*}

¹ Институт по обща и неорганична химия, Българска академия на науките, 1113 София, България

² Институт по органична химия с Център по фитохимия, Българска академия на науките, ул. Акад. Г. Бончев, бл. 9, 1113 София, България

³ Институт по минералогия и кристалография „Акад. Иван Костов“, Българска академия на науките, ул. Акад. Г. Бончев, бл. 107, 1113 София, България

Постъпила на 27 април 2017 г.; Коригирана на 23 май 2017 г.

(Резюме)

За оценка на локалното разпределение на Al и Sc в смесени алуминиево-скандиеви волфраматни, интересни като материали с отрицателно термично разширение са използвани съвместно ЯМР метода „многоквантово възбуждане при въртене около магическия ъгъл“ (MQMAS) на ядрата ^{27}Al и ^{45}Sc и монокристална рентгенова дифракция. Изучаването на специфичните характеристики на локалното катионно разпределение е извършено на твърди разтвори $Al_{2-x}Sc_x(WO_4)_3$ ($0 \leq x \leq 2$) под формата на монокристали и нано-прахове. ЯМР спектрите на ^{27}Al MAS и MQMAS показват, че Al атоми в твърдите разтвори на $Al_{2-x}Sc_x(WO_4)_3$ приемат две ясно различаващи се една от друга координации. Обратно на Al атоми, ЯМР спектрите на ^{45}Sc MAS и MQMAS дават указание само за една координация на Sc атоми. Кристалната структура на $Al_{2-x}Sc_x(WO_4)_3$ е рафинирана в орторомбична симетрия с пространствена група $P2_12_12$, не-изоморфна подгрупа $P6_{3cn}$. В този структурен модел се различават две нееквивалентни Al/Sc позиции: едната от тях е предпочитано заета от Al йони, докато Sc йони могат да заемат и двете позиции. Показано е, че координацията на Al и Sc във волфраматите е присъщо свойство за образците, което не зависи от формата им - монокристал или нанопрах.

Experimental and DFT studies on the IR spectra and structure of 4-acetamidobenzoic acid (acedoben), its oxyanion and dianion

E. Velcheva*, B. Stamboliyska, S. Stoyanov

Institute of Organic Chemistry with Centre of Phytochemistry, Bulgarian Academy of Sciences, Acad. G. Bonchev Str., Block. 9, 1113 Sofia, Bulgaria

Received May 01, 2017; Revised May 26, 2017

Dedicated to Acad. Ivan Juchnovski on the occasion of his 80th birthday

The spectral and structural changes taking place during the course of the conversion of 4-acetamidobenzoic acid, HOOC-C₆H₄-NH-COCH₃, into the corresponding oxyanion, -OOC-C₆H₄-NH-COCH₃, and dianion, -OOC-C₆H₄-N-COCH₃, have been followed by both infrared spectra in DMSO solution and DFT/B3LYP/6-311+G(2df,p) calculation. The solvent effect was simulated by using self-consistent integral equation formalism variant (IEFPCM) model. The *trans* conformers (with respect to phenylene and methyl groups) have been calculated to be more stable than the *cis* ones in all species studied. The changes accompanying the first deprotonation concern mainly the carboxylato fragment; those resulting from the second one are spread over the whole dianion. Analysis of the atomic charge changes shows that over 70% of the first (oxyanionic) charge remains localized within the carboxylato fragment. The second (nitranionic) charge delocalizes over the acetyl (0.42 e⁻) and phenylene (0.19 e⁻) groups, nitranionic center (0.34 e⁻) and (0.05e⁻) carboxylate group.

Key words: IR; DFT; 4-acetamidobenzoic acid (acedoben); oxyanion; dianion

INTRODUCTION

4-Acetamidobenzoic acid (acedoben) molecule, simultaneously a carboxamide and a carboxylic acid, is an important conjugated compound of biological and medicinal interest. Acedoben (or its sodium or potassium salts) is contained in a number of pharmaceutical products as antiviral drug Isoprinosine, Deanol acetamidobenzoate, Fibroderm, Perlinsol Cutaneo. In a human body acedoben is a metabolite of *p*-aminobenzoic acid [1], benzocaine [2], *etc.*, so its biological properties and metabolic transformations have been extensively investigated during the last few decades [3]. Acedoben has multifunctional coordination sites with chelating and bridging ability and it has been widely used in coordination chemistry and crystal engineering [4,5].

Acedoben was first prepared by Hofmann in 1876 [6]. The solid-state IR and Raman spectra of acedoben are accessible on-line [7]. Only the frequencies of the amide carbonyl (C=O) and amino (N-H) stretching bands in solutions of the title molecule have been reported, included in series of substituted acetanilides, and were found to correlate with both Hammett's substituent constants [8,9] and certain indices computed within DFT method [9].

ATR FTIR spectroscopy has recently been used to detection *p*-acetamidobenzoic acid and *p*-aminobenzoic acid in human skin treated with essential oil formulations [10]. Lanthanide complexes with 4-acetamidobenzoate have been characterized by their IR spectra [6]. No detailed interpretations of IR spectra of 4-acetamidobenzoic acid and of its carboxylate anion has been performed.

The conversions of neutral molecule into anions, radical-anions, carbanions, azanion, *etc.* are accompanied by essential changes in the vibration spectra. So, these changes are very informative for the structural variations caused by the same conversions [11]. The title compound is an interesting and convenient object of the molecule → anion → dianion conversions investigations, as it contains the (-COOH) and (-CO-NH-) characteristic groups and can be easily converted into a carboxylate anion and dianion, stable in dimethyl sulfoxide (DMSO). In the literature we have found neither IR spectra, nor theoretically calculations for the title anionic species. The structure of large series of organic molecules and their anions have been successfully studied recently on the basis of experimental IR spectra combined with DFT computations ([12-16] and references therein). The purpose of the present investigation is to follow the spectral and structural changes,

* To whom all correspondence should be sent:
E-mail: ev@orgchm.bas.bg

caused by the conversion of 4-acetamidobenzoic acid molecule into the corresponding carboxylate anion and dianion, by means of both DFT computations and spectroscopic experiments.

EXPERIMENTAL AND COMPUTATIONS

Commercial 4-acetamidobenzoic acid (Aldrich, 98%) was used without further purification. The 4-acetamidobenzoate anion was prepared by adding solutions of the parent compound in dimethyl sulfoxide (DMSO) and DMSO- d_6 (Fluka) to an excess of dry sodium or potassium carbonate. The suspensions obtained were stirred for 1 min and then filtered through a syringe-filter. The conversion was practically complete (Fig. 1(A) and Fig. 1(B)). The dianion of 4-acetamidobenzoic acid was prepared by reacting DMSO and DMSO- d_6 solutions of the parent compound with an excess of dry alkali-metal methoxides and methoxides- d_3 . The conversion was also practically complete: in the spectra we found neither the bands of 4-acetamidobenzoic acid nor those of its anion (cf. Fig. 2(A-C)).

The IR spectra were recorded at a resolution of 1 cm^{-1} , by 50 scans on a Bruker Vector 22 FTIR spectrophotometer in a CaF_2 cell of 0.13 mm path length.

The quantum chemical calculations were performed using the Gaussian 09 package [17]. The geometry optimizations of the structures investigated were done without symmetry restrictions, using density functional theory (DFT). We employed B3LYP hybrid functional, which combines Becke's three-parameter nonlocal exchange with the correlation functional of Lee *et al.* [18,19], adopting 6-311+G(2df,p) basis sets. To estimate the effect of the solvent (DMSO) on the infrared spectra of studied species, we applied the integral equation formalism of polarizable continuum model (IEFPCM), proposed by Tomasi and coworkers [20,21].

The stationary points found on the molecular potential energy hypersurfaces were characterized using standard harmonic vibrational analysis. The theoretical vibrational spectra were interpreted by means of potential energy distributions (PEDs) using VEDA 4 program [22]. For a better correspondence between experimental and calculated values, we modified the results using the empirical scaling factors.

RESULTS AND DISCUSSION

Energy analysis

The structures of the most stable conformers of the three species studied are shown in Scheme 1. All structures with a subscript 1 in Scheme 1 correspond to the *trans*-type conformers (with respect to phenylene and methyl groups). According to the B3LYP/6-311+G(2df,p) calculations the *cis* conformers of molecule are less stable than the *trans* form by 11.6 kJ mol^{-1} . The energy difference between two *trans* conformers of molecule (A_1 and A_{1a}), differing by the direction of the carboxyl group, is 0.7 kJ mol^{-1} and they seem to be present simultaneously in solutions. The presence of the conformer A_1 in solid state was established by crystallographic analysis [23]. According to both experimental and theoretical [24] data, the *trans* conformer of the unsubstituted acetanilide is also the more stable one. Our calculations predict the both *trans* conformers of the oxyanion and dianion are the more stable (Scheme 1).

The calculated total energies of the studied species are as follow:

$E_{\text{tot}} = -629.063365971$ H for the 4-acetamidobenzoic acid molecule (A_1 in Scheme 1);

$E_{\text{tot}} = -628.511829360$ H for the 4-acetamidobenzoic acid oxyanion (B_1 in Scheme 1);

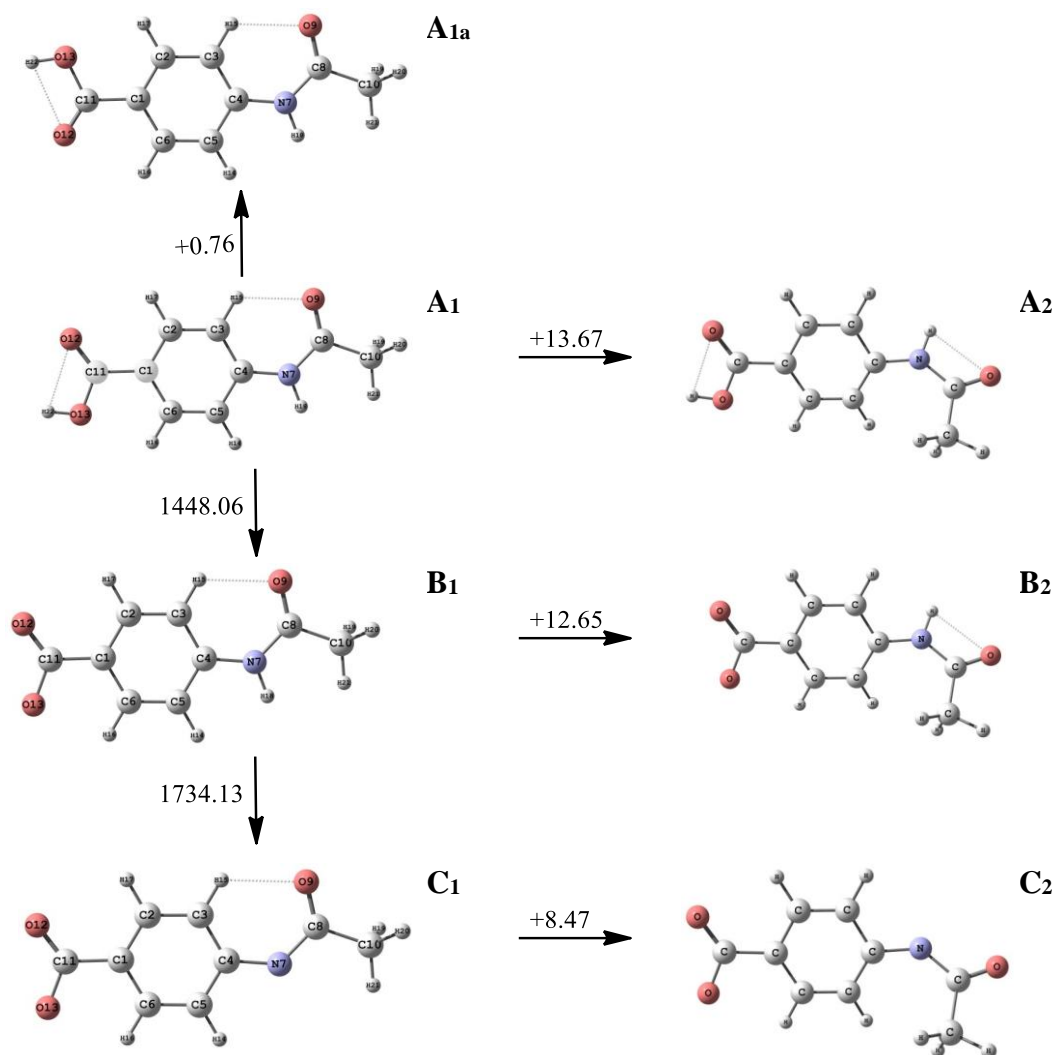
$E_{\text{tot}} = -627.851335706$ H for the 4-acetamidobenzoic acid dianion (C_1 in Scheme 1).

The following deprotonation energies correspond to the above values (see Scheme 1):

$E^d = E_{\text{tot}}(B_1) - E_{\text{tot}}(A_1) = 1448.05948249$ kJ mol^{-1} ;

$E^d = E_{\text{tot}}(C_1) - E_{\text{tot}}(B_1) = 1734.12622068$ kJ mol^{-1} .

The energy differences E^d is related to the gas-phase Brønsted acidities, and can be used as approximate measure of these acidities in polar aprotic solvents [25]: low $E^d \rightarrow$ high acidities \rightarrow low pKa values. For comparison, the first deprotonation energy is lower than E^d of paracetamol (1537.9 kJ mol^{-1} [24]) and higher than E^d of stronger acid acesulfame (1324.31 kJ mol^{-1} [12]). The second deprotonation energy is essentially higher, and can be compared with the second deprotonation energy of paracetamol (1880.2 kJ mol^{-1} [26]). This result is not surprising, having in mind that the products of the second deprotonation are in fact dianions.



Scheme 1. Conformers of the 4-acetamidobenzoic acid molecule, oxyanion and dianion. The values the arrows are the means energy differences in kJ mol^{-1} .

Infrared analysis

A fragment of the infrared spectrum of 4-acetamidobenzoic acid in DMSO-d_6 solution is shown in Fig. 1(A). The numeric data for the frequencies of the bands are listed in Table 1 together with the corresponding theoretical values for the most stable conformers of molecules. As can be seen, there is a good agreement between the scaled theoretical and experimental IR frequencies. The mean deviation between them is 11.1 cm^{-1} . No experimental data for the $\nu(\text{OH})$ and $\nu(\text{NH})$ bands were given in Table 1, as they are very broad because of the formation of hydrogen bonds mainly with solvent, like other carboxamides in DMSO [18,20]. The assignment of the experimental bands to the calculated normal modes in the C–H stretching region ($3100\text{--}2800 \text{ cm}^{-1}$) is not obvious

because there are fewer bands in the experimental spectrum than predicted by the calculations.

The highest frequency experimental bands observed in the IR spectrum ($3200\text{--}3000 \text{ cm}^{-1}$) are assigned to the aromatic C–H stretches, while the lower frequency bands are attributed to the methyl group motions. The $\nu(\text{C-H})$ bands are of low intensity in both the experimental and theoretical spectra.

The calculations resolved and located well the two carbonyl stretching vibrations, those of the carboxy and the amido group, at 1693 cm^{-1} and 1683 cm^{-1} , respectively. The shifting expected in this case should amount to a 10 cm^{-1} and it is in agreement with the experimental measured after having decomposed the complex band into components (1702 cm^{-1} , 1691 cm^{-1} , Table 1).

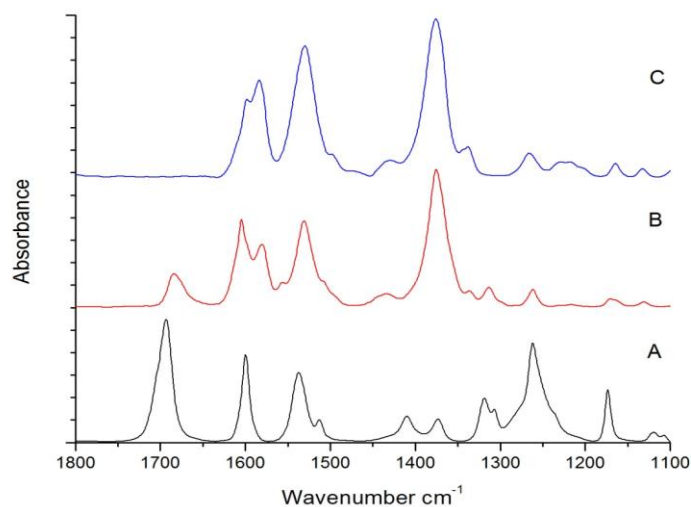


Fig. 1. Infrared spectra of : (A) 4-acetamidobenzoic acid, (B) its anion (with counter ion Na^+) and (C) its dianion (with counter ions Na^+), 0.09 mol l^{-1} in DMSO-d_6 .

Table 1. Theoretical (B3 LYP/6-311+G(2df,p) and experimental (solvent DMSO-d_6) vibrational frequencies (in cm^{-1}) and IR integrated intensities (A in km.mol^{-1}) of 4-acetamidobenzoic acid.

No.	$\nu_{\text{calc.}}^a$	A_{calc}	Approximative description ^b	$\nu_{\text{exp.}}^c$	
1.	3667	175.8	100 $\nu(\text{OH})$		
2.	3530	62.9	100 $\nu(\text{NH})$		
3.	3176	4.5	97 $\nu(\text{PhH})$		
4.	3134	1.6	97 $\nu(\text{PhH})$		
5.	3130	3.8	97 $\nu(\text{PhH})$	3048	w
6.	3098	10.7	97 $\nu(\text{PhH})$	3006	w
7.	3063	20.1	100 $\nu(\text{CH}_3)$		
8.	3044	4.7	100 $\nu(\text{CH}_3)$	2934	w
9.	2983	5.8	100 $\nu(\text{CH}_3)$	2856	w
10.	1693	645.8	78 $\nu(\text{C=O})$ (carboxy)	1702 ^d	s
11.	1683	558.9	61 $\nu(\text{C=O})$ (amid)	1691 ^d	vs
12.	1609	209.0	52 $\nu(\text{CC})$	1599	s
13.	1589	179.7	52 $\nu(\text{CC})$, 10 $\delta(\text{PhH})$		
14.	1516	256.7	54 $\delta(\text{HNC})$, 10 $\nu(\text{NC})$	1537	s
15.	1503	338.1	78 $\delta(\text{PhH})$, 10 $\delta(\text{CCC})$	1512	m
16.	1453	39.9	72 $\delta(\text{CH}_3)$, 12 $\nu(\text{PhH})$		
17.	1434	12.7	93 $\delta(\text{CH}_3)$		
18.	1408	88.5	30 $\nu(\text{CC})$, 26 $\delta(\text{PhH})$	1409	m
19.	1370	65.9	90 $\delta(\text{CH}_3)$		
20.	1337	188.7	28 $\nu(\text{C-O})$, 25 $\delta(\text{HOC})$, 13 $\nu(\text{C-COOH})$	1373	m
21.	1318	303.1	37 $\nu(\text{NC})$, 15 $\delta(\text{HNC})$, 13 $\nu(\text{CC})$	1318	m
22.	1308	169.3	69 $\delta(\text{PhH})$	1307	m
23.	1247	311.3	36 $\delta(\text{PhH})$, 20 $\nu(\text{Ph-C})$, 12 $\delta(\text{HNC})$,	1261	s
24.	1217	118.6	23 $\nu(\text{Ph-N})$, 22 $\nu(\text{NC})$, 19 $\nu(\text{C-CH}_3)$		
25.	1188	42.7	32 $\delta(\text{PhH})$, 22 $\delta(\text{HOC})$, 12 $\nu(\text{CC})$	1173	m
26.	1149	503.9	34 $\delta(\text{CCC})$, 28 $\delta(\text{PhH})$	1119	w
27.	1119	21.0	78 $\delta(\text{PhH})$, 15 $\nu(\text{CC})$	1108	
28.	1099	398.4	55 $\nu(\text{C-O})$, 13 $\nu(\text{CC})$, 12 $\delta(\text{HOC})$		
29.	1055	12.6	67 $\delta(\text{CH}_3)$, 19 $\delta(\text{NC=O})$		

^aScaled by 0.98. ^bVibrational modes: ν , stretching; δ , bendings. The numbers before the mode symbols indicate % contribution (10 or more) of a given mode to the corresponding normal vibration, according to the potential energy distribution. ^cRelative intensity: s, strong; m, moderate; w, weak; v, very. ^dMeasured after having decomposed the complex hands into components.

The theory reproduce qualitatively well the high integral intensities for the bands in the experimental spectrum, namely $\nu(\text{C}=\text{O})$ (carboxy) and $\nu(\text{C}=\text{O})$ (amid-I). DFT calculations predicted well also the IR frequencies measured in DMSO of the amide-II and amide-III vibrations. The amide-II mode $\delta(\text{HNC})$ is predicted to appear at 1516 cm^{-1} as a very intense band. Experimentally, a very strong

band was detected at 1537 cm^{-1} in DMSO. The stretching $\nu(\text{N}-\text{C})$ coupled with $\delta(\text{HNC})$ and $\nu(\text{CC})$, denoted as amide-III was predicted and measured as an intensity band at 1318 cm^{-1} .

The experimental spectrum of anion is shown on Fig. 1(B) and its numerical data are compared with theoretical values in Table 2.

Table 2. Theoretical (B3 LYP/6-311+G(2df,p) and experimental (solvent DMSO- d_6) vibrational frequencies (in cm^{-1}) and IR integrated intensities (A in $\text{km}\cdot\text{mol}^{-1}$) of 4-acetamidobenzoic acid.

No.	$\nu_{\text{calc.}}^a$	A_{calc}	Approximative description ^b	$\nu_{\text{exp.}}^c$	
1.	3538	55.8	100 $\nu(\text{NH})$		
2.	3172	1.2	97 $\nu(\text{PhH})$		
3.	3129	8.6	97 $\nu(\text{PhH})$		
4.	3122	7.2	97 $\nu(\text{PhH})$		
5.	3089	21.7	97 $\nu(\text{PhH})$	3049	w
6.	3064	23.4	100 $\nu(\text{CH}_3)$	2972	w
7.	3048	6.5	100 $\nu(\text{CH}_3)$		
8.	2987	8.8	100 $\nu(\text{CH}_3)$	2930	w
9.	1675	432.7	73 $\nu(\text{C}=\text{O})$, 10 $\delta(\text{HNC})$	2910	w
10.	1605	43.3	63 $\nu(\text{CC})$	1684	s
11.	1593	617.2	72 $\nu^{\text{as}}(\text{OCO})$	1604	vs
12.	1545	405.1	39 $\nu(\text{CC})$, 14 $\delta(\text{PhH})$	1580	s
13.	1507	656.5	38 $\delta(\text{HNC})$, 12 $\nu(\text{NC})$, 10 $\delta(\text{PhH})$		
14.	1497	98.7	68 $\delta(\text{PhH})$, 14 $\delta(\text{CCC})$	1531	vs
15.	1451	31.9	89 $\delta(\text{CH}_3)$	1512	w
16.	1433	12.4	92 $\delta(\text{CH}_3)$		
17.	1391	62.3	44 $\nu(\text{CC})$, 14 $\delta(\text{PhH})$	1435	w
18.	1369	680.0	72 $\nu^{\text{s}}(\text{OCO})$		
19.	1333	54.5	90 $\delta(\text{CH}_3)$	1375	vs
20.	1309	419.2	58 $\nu(\text{CC})$, 18 $\nu(\text{Ph-N})$		
21.	1293	40.0	83 $\delta(\text{PhH})$	1313	m
22.	1244	273.1	37 $\nu(\text{NC})$, 15 $\delta(\text{HNC})$, 13 $\nu(\text{CC})$		
23.	1211	3.2	36 $\nu(\text{Ph-N})$	1261	m
24.	1166	47.8	54 $\delta(\text{PhH})$, 14 $\nu(\text{CC})$		
25.	1115	33.3	44 $\delta(\text{CCC})$, 28 $\delta(\text{PhH})$	1170	w
26.	1100	19.3	76 $\delta(\text{PhH})$, 14 $\nu(\text{CC})$	1131	w
27.	1033	11.9	40 $\delta(\text{NCC})$, 33 $\delta(\text{CH}_3)$		
28.	1009	18.0	54 $\delta(\text{CCC})$		

^aScaled by 0.98. ^bVibrational modes: ν , stretching; δ , bendings; superscripts: s, symmetrical; as, asymmetrical.. The numbers before the mode symbols indicate % contribution (10 or more) of a given mode to the corresponding normal vibration, according to the potential energy distribution. ^cRelative intensity: s, strong; m, moderate, w, weak; v, very. ^dMeasured after having decomposed the complex bands into components.

As above we can find there a good agreement between experimental and scaled theoretical frequencies. The mean deviation between them is 10.2 cm^{-1} within the corresponding interval of $9\text{--}25\text{ cm}^{-1}$, typical for DFT calculations of frequencies for series of anions [12-16] (and references therein). Removing the proton after the conversion of the carboxy group into the carboxylate anion leads to equalization of the two CO bonds in the anion (and hence the disappearance of bands 10, Table 1). Two strong bands at 1583 and 1338 cm^{-1} , corresponding to the $\nu^{\text{as}}(\text{OCO})$ and $\nu^{\text{s}}(\text{OCO})$ vibrations appear instead of the $\nu(\text{C=O})$ (carboxy)

band at 1702 cm^{-1} and the formal $\nu(\text{C-O})$ band at 1373 cm^{-1} . In full agreement between theory and experiment, conversion of the studied molecule into the oxyanion has only a weak effect on the $\nu(\text{C=O})$ (amid-I) frequency: predicted decrease 8 cm^{-1} , measured 7 cm^{-1} . The conversion causes also a decrease in the $\delta(\text{HNC})$ (amide-II) frequency: predicted 13 cm^{-1} , measured 6 cm^{-1} (Tables 1 and 2). The $\nu(\text{C-N})$ (amide-III) band also undergoes a frequency decrease: predicted 9 cm^{-1} , measured 6 cm^{-1} (Tables 1 and 2). Theoretical and experimental IR data for the 4-acetamidobenzoic acid dianion are compared in Table 3.

Table 3. Theoretical (B3 LYP/6-311+G(2df,p) and experimental (solvent DMSO- d_6) vibrational frequencies (in cm^{-1}) and IR integrated intensities (A in $\text{km}\cdot\text{mol}^{-1}$) of 4-acetamidobenzoic acid dianion.

No.	$\nu_{\text{calc.}}^{\text{a}}$	$A_{\text{calc.}}$	Approximative description ^b	$\nu_{\text{exp.}}^{\text{c}}$	
1.	3153	3.3	97 $\nu(\text{PhH})$		
2.	3107	27.2	97 $\nu(\text{PhH})$		
3.	3095	19.0	97 $\nu(\text{PhH})$	3052	w
4.	3077	32.9	97 $\nu(\text{PhH})$	3026	w
5.	3042	47.8	100 $\nu(\text{CH}_3)$		
6.	2998	39.0	100 $\nu(\text{CH}_3)$	2936	w
7.	2951	68.1	100 $\nu(\text{CH}_3)$	2902	w
8.	1610	98.0	63 $\nu(\text{CC})$	1598	vs
9.	1567	528.6	42 $\nu^{\text{as}}(\text{O-C-O}), 16\ \nu(\text{CC})$	1583	vs
10.	1522	409.8	41 $\nu^{\text{as}}(\text{O-C-O}), 21\ \nu(\text{CC})$	1535 ^d	
11.	1519	1054.2	40 $\nu(\text{C=O}), 16\ \nu(\text{Ph-N})$	1528 ^d	vs
12.	1496	703.9	68 $\delta(\text{PhH})$	1496	sh
13.	1455	8.5	80 $\delta(\text{CH}_3)$	1469	vw
14.	1440	202.2	98 $\delta(\text{CH}_3)$	1429	w
15.	1411	32.7	39 $\delta(\text{CCC}), 22\delta(\text{PhH})$		
16.	1378	356.3	30 $\nu(\text{C-N}), 17\ \nu(\text{C=O})$	1376	vs
17.	1351	55.2	90 $\delta(\text{CH}_3)$		
18.	1332	2115.0	71 $\nu^{\text{s}}(\text{O-C-O})$	1338	m
19.	1297	46.2	75 $\delta(\text{PhH})$		
20.	1284	5.9	73 $\nu(\text{CC})$	1266	m
21.	1214	39.6	30 $\nu(\text{Ph-N}), 20\ \delta(\text{CCC})$	1230	w
22.	1163	111.4	55 $\delta(\text{PhH}), 24\ \nu(\text{CC})$	1164	w
23.	1124	192.4	55 $\delta(\text{PhH}), 24\ \nu(\text{CC})$	1132	w
24.	1099	21.4	76 $\delta(\text{PhH})$		
25.	1027	4.2	55 $\delta(\text{NCC}), 20\ \delta(\text{CH}_3)$		
26.	997	1.9	77 $\delta(\text{CCC})$		

^aScaled by 0.98. ^bVibrational modes: ν , stretching; δ , bendings; superscripts: s, symmetrical; as, asymmetrical. The numbers before the mode symbols indicate % contribution (10 or more) of a given mode to the corresponding normal vibration, according to the potential energy distribution. ^cRelative intensity: s, strong; m, moderate, w, weak; v, very. ^dMeasured after having decomposed the complex bands into components.

Again there is good agreement between experimental and scaled theoretical frequencies. The mean deviation between them is 9.1 cm⁻¹, this value being lower than these in case of the dianion of paracetamol [20]. The experimental spectrum of the dianion studied is shown in Fig. 2(C). Comparison with the other spectra of Fig. 2 shows that fundamental spectral changes accompany the second deprotonation of 4-acetamidobenzoic acid. There is no longer carbonyl band $\nu(\text{C}=\text{O})$ at the usual place. The theory predicts two new bands characterizing the carboxamido group in the dianion: very strong bands at 1519 cm⁻¹ and 1378 cm⁻¹. These very strong bands are actually present in the experimental spectrum (Fig. 2(C)): i.e., at 1531 cm⁻¹ and 1376 cm⁻¹. The approximate description of the corresponding normal vibrations (Table 3, nos. 11 and 16) are in agreement with the literature data. For the nitranions of acetanilide and of a series of ring-substituted acetanilides, Ognyanova *et al.* have assigned the very strong bands in the 1518-1533 cm⁻¹ spectral region as $\nu(\text{C}=\text{O})$ (amide-I) and the medium-to-strong bands at 1373-1382 cm⁻¹ $\nu(\text{C}-\text{N})$ (amide-III). In agreement

between theory and experiment, the second deprotonation of 4-acetamidobenzoic acid causes an increase in C-N stretching frequency $\nu(\text{C}-\text{N})$ and essential increase in the corresponding intensity $A(\text{C}-\text{N})$. The shift of this coordinate to higher frequency is obviously due to the significant shortening of the C-N bond, caused by the conversion of the acetanilide molecule into the azanion.

Structural analysis

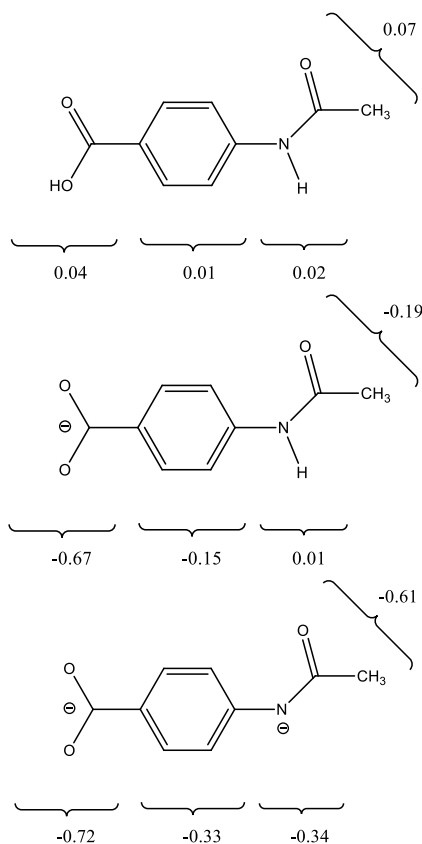
According to X-ray diffraction the plane of the acetamide group is oriented at 40.4° with respect to the benzene ring, whereas the plane of the carboxylic acid group is essentially coplanar with the benzene ring [21]. According to the calculations in the most stable conformers of the isolated molecule these groups are planar. The same groups in the isolated oxyanion and dianion have been predicted to be again planar. The theoretical and experimental bond lengths and angles in the 4-acetamidobenzoic acid and its oxyanion and dianion are listed in Table 4.

Table 4. Theoretical (B3LYP/6-311+G(2df,p)) and experimental bond lengths R (Å) and bond angles A (°) in the 4-acetamidobenzoic acid molecule, its oxyanion and dianion.

	Molecule		Δ^b	Anion	Δ^c	Dianion	Δ^d
	Experimental ^a	Theoretical		Theoretical		Theoretical	
<i>Bond lengths</i>							
R(C ⁴ ,C ⁵)	1.383(3)	1.400	0.017	1.398	-0.002	1.414	0.016
R(C ⁵ ,C ⁶)	1.379(2)	1.379	-0.001	1.385	0.007	1.387	0.002
R(C ¹ ,C ⁶)	1.382(3)	1.398	0.016	1.394	-0.004	1.399	0.005
R(C ¹ ,C ²)	1.392(3)	1.396	0.004	1.392	-0.004	1.396	0.004
R(C ² ,C ³)	1.384(3)	1.386	0.002	1.392	0.006	1.394	0.002
R(C ⁴ ,N ⁷)	1.420(3)	1.400	-0.020	1.420	0.02	1.394	-0.026
R(N ⁷ ,C ⁸)	1.350(2)	1.372	0.022	1.361	-0.011	1.326	-0.035
R(C ⁸ ,O ⁹)	1.219(2)	1.220	0.001	1.221	0.001	1.259	0.038
R(C ⁸ ,C ¹⁰)	1.505(3)	1.511	0.006	1.524	0.013	1.543	0.019
R(C ¹ ,C ¹¹)	1.481(3)	1.477	-0.004	1.549	0.072	1.539	-0.010
R(C ¹¹ ,O ¹²)	1.254(2)	1.214	-0.040	1.251	0.037	1.260	0.009
R(C ¹¹ ,O ¹³)	1.279(2)	1.349	0.070	1.250	-0.099	1.259	0.009
<i>Bond angles</i>							
A(C ⁴ ,C ⁵ ,C ⁶)	119.6(2)	120.5	0.9	120.4	-0.1	122.5	2.1
A(C ⁵ ,C ⁶ ,C ¹)	120.2(2)	120.5	0.3	121.0	0.5	121.4	0.4
A(C ⁶ ,C ¹ ,C ²)	119.4(2)	118.7	-0.7	117.7	-1	116.3	-1.4
A(C ¹ ,C ² ,C ⁶)	120.4(2)	121.2	0.8	122.2	1	122.7	0.5
A(C ⁶ ,C ¹ ,C ¹¹)	120.2(2)	119.7	-0.5	120.6	0.9	121.4	0.8
A(N ⁷ ,C ¹ ,C ²)	118.6(2)	116.9	-1.7	116.5	-0.4	116.3	-0.2
A(C ⁸ ,N ⁷ ,C ¹)	127.6(2)	129.7	2.1	130.8	1.1	123.5	-7.3
A(N ⁷ ,C ⁸ ,O ⁹)	123.3(2)	123.5	0.2	125.2	1.7	131.5	6.3
A(N ⁷ ,C ⁸ ,C ¹⁰)	115.0(2)	114.8	-0.2	114.4	-0.4	113.0	-1.4
A(C ¹ ,C ¹¹ ,O ²⁰)	119.7(2)	124.8	5.1	115.1	-9.7	116.4	1.3
A(C ⁴ ,C ¹¹ ,O ²¹)	117.2(2)	113.4	-3.8	115.3	1.9	116.4	1.1
A(O ²¹ ,C ¹¹ ,O ²²)		121.7		126.2	-5.5	125.2	1.0

^aSee Ref. [23]. ^bAlgebraic deviations between experimental and theoretical values. ^cAlgebraic deviations between theoretical values of the anion and molecule. ^dAlgebraic deviations between theoretical values of the dianion and anion.

As seen, there is a good agreement between the experimental and the theoretical values. Exceptions (deviations of 0.04 Å or more) are typical only for the carboxy group itself, whose atoms participate directly in hydrogen bond formation. The data in the Table 4 make it possible to conclude that the conversion of the molecule studied into corresponding anion are localized within the corboxy/carboxylate groups and the adjacent C-Ph bond. As in the carboxylate anion has two equal C-O bonds, the C=O bond undergo a lengthening of 0.037 Å and the C-O one undergo shortening of 0.099 Å. The C-Ph bond in the anion is with 0.072 longer than the same bonds in the molecule, as the carboxylate group is much less conjugated with the aromatic ring that the carboxy group. The OCO bond angel in the anion is with 7.8° larger than those in the molecule, because of the repulsion of the electronic densities in the carboxylate groups. The bond length changes that accompany the conversion of the oxyanion into the dianion are take place both at the azanionic center and next to it - shortening of the Ph-N and N-C and bonds and lengthening of the C=O and C-CH₃ bonds (Table 4). The net electric charges of certain fragments of the species studied are shown in Scheme 2.



Scheme 2. Mulliken net electric charges over fragments of 4-acetamidobenzoic acid molecule, its anion and dianion.

The corresponding charge changes accompanying the conversion molecule - oxyanion - dianion (Table 5) are also quite informative, and show that:

1. The first (oxyanionic) charge remains localized mainly within the carboxylate group while.
2. The second (nitranionic) charge spreads over the whole species.

Table 5. Electric charge changes accompanying the conversion of the 4-acetamidobenzoic acid molecule into the oxyanion and of the oxyanion into the dianion.

Charge changes of the fragments	-COOH/ Ph	NH/N-	COCH ₃	COO ⁻
$q_{\text{oxyanion}} - q_{\text{molecule}}$	-0.71	-0.16	-0.01	-0.12
$q_{\text{dianion}} - q_{\text{oxyanion}}$	-0.05	-0.18	-0.35	-0.42

CONCLUSION

The spectral and structural changes, caused by the conversion of the 4-acetamidobenzoic acid into the corresponding anion and dianion have been studied by IR spectra and calculations at B3LYP/6-311+G(2df,p) level of theory. A comparison of calculated with measured infrared data can be used as a test for the reliability of the structural predictions for various molecules and anions of this and similar types. These predictions can be very useful in cases of molecules and ions for which experimental structural parameters are inaccessible or unknown. IR spectral changes, which take place as a result of the conversion of molecule into anions, were adequate predicted by same theoretical method.

Acknowledgements: The financial support of this work by the National Science Fund of Bulgaria (Contracts RNF01/0110), Science Fund is gratefully acknowledged.

REFERENCES

1. C. Nortje, P. Jansen Van Rensburg, C. Cooke, E. Erasmus, *Bioanalysis*, **7**, 1211 (2015).
2. A. Szoke, W. L. Hayton, I. R. Schultz, *J. Pharm. Biomed. Anal.*, **16**, 69 (1997).
3. <https://www.wikigenes.org/e/chem/e/19266.html>
4. X. Yin, J. Fan, Z. H. Wang, S. R. Zheng, J. B. Tan, W. G. Zhang, *J. Solid State Chem.*, **184**, 1850 (2011) (and references therein).
5. J. Arriñez-Soriano, J. Albalad, J. Pérez-Carvajal, I. Imaz, F. Busqué, J. Juanhuix, D. Maspoch, *Cryst. Eng. Comm.*, **18**, 4196 (2016).

6. A. W. Hofmann, *Ber. Dtsch. Chem. Ges.*, **9**, 1302 (1876).
7. <http://sdbs.db.aist.go.jp>
8. J. Bennett, J. C. Maire, *J. Chem. Soc. B*, 309 (1971).
9. S. Ilieva, B. Hadjieva, B. Galabov, *J. Org. Chem.*, **67**, 6210 (2002).
10. L. H. Wang, J. X. Chen, *Microchim. Acta*, **168**, 93 (2010).
11. N. Juchnovski, I. G. Binev, in: The chemistry of functional groups, Suppl. C, S. Patai, Z. Rappoport (eds.), Wiley, New York, 1983.
12. A. D. Popova, E. A. Velcheva, B. A. Stamboliyska, *J. Mol. Struct.*, **1009**, 23 (2012).
13. E. A. Velcheva, B. A. Stamboliyska, P. J. Boyadjieva, *J. Mol. Struct.*, **963**, 57 (2010).
14. D. Popova, M. K. Georgieva, O. I. Petrov, K. V. Petrova, E. A. Velcheva, *Int. J. Quant. Chem.*, **107**, 1752 (2007).
15. S. Stoyanov, J. A. Tsenov, D. Y. Yancheva, *J. Mol. Struct.*, **42**, **1009** (2012).
16. S. Stoyanov, *J. Phys. Chem.*, **114**, 5149 (2010).
17. M. J. Frisch, G. W. Trucks, H. B. Schlegel, G. E. Scuseria, M. A. Robb, J. R. Cheeseman, G. Scalmani, V. Barone, B. Mennucci, G. A. Petersson, H. Nakatsuji, M. Caricato, X. Li, H. P. Hratchian, A. F. Izmaylov, J. Bloino, G. Zheng, J. L. Sonnenberg, M. Hada, M. Ehara, K. Toyota, R. Fukuda, J. Hasegawa, M. Ishida, T. Nakajima, Y. Honda, O. Kitao, H. Nakai, T. Vreven, J. A. Montgomery, Jr., J. E. Peralta, F. Ogliaro, M. Bearpark, J. J. Heyd, E. Brothers, K. N. Kudin, V. N. Staroverov, R. Kobayashi, J. Normand, K. Raghavachari, A. Rendell, J. C. Burant, S. S. Iyengar, J. Tomasi, M. Cossi, N. Rega, J. M. Millam, M. Klene, J. E. Knox, J. B. Cross, V. Bakken, C. Adamo, J. Jaramillo, R. Gomperts, R. E. Stratmann, O. Yazyev, A. J. Austin, R. Cammi, C. Pomelli, J. W. Ochterski, R. L. Martin, K. Morokuma, V. G. Zakrzewski, G. A. Voth, P. Salvador, J. J. Dannenberg, S. Dapprich, A. D. Daniels, Ö. Farkas, J. B. Foresman, J. V. Ortiz, J. Cioslowski, D. J. Fox, Gaussian 09, Revision A1, Gaussian Inc., Wallingford CT, 2009.
18. A. D. Becke, *J. Chem. Phys.*, **98**, 5648 (1993).
19. C. Lee, W. Yang, G. R. Parr, *Phys. Rev.*, **B37**, 785 (1998).
20. J. Tomasi, M. Perisco, *Chem. Rev.*, **94**, 2027 (1994).
21. J. Tomasi, B. Mennucci, E. J. Cancès, *J. Mol. Struct. (THEOCHEM)*, **464**, 211 (1999).
22. H. J. Michal, VEDA 4, Warsaw, 2004.
23. S. Kashino, T. Matsushita, T. Iwamoto, K. Yamaguchi, M. Haisa, *Acta Crystallogr.*, **C42**, 457 (1986).
24. E. Velcheva, Z. Glavcheva, B. Stamboliyska, *Bulg. Chem. Commun.*, **48**(3), 514 (2016).
25. V. M. Vlasov, L. A. Oshkina, *Org. React.*, **28**, (1993) 47.
26. I. G. Binev, P. J. Boyadjieva, Y. I. Binev, *J. Mol. Struct.*, **447**, 235 (1998).

ЕКСПЕРИМЕНТАЛНО И ТЕОРЕТИЧНО ИЗСЛЕДВАНЕ НА ИЧ СПЕКТРИ И СТРУКТУРА НА 4-АЦЕТАМИДОБЕНЗОЕНА КИСЕЛИНА (АЦЕДОБЕН), НЕЙНИТЕ ОКСИАНИОН И ДИАНИОН

Е. Велчева*, Б. Стамболийска, С. Стоянов

Институт по органична химия с Център по фитохимия, Българска академия на науките, ул. „Акад. Г. Бончев“, бл.9, 1113 София

Постъпила на 01 май 2017 г.; Коригирана на 26 май 2017 г.

(Резюме)

Спектралните и структурни промени, протичащи от превръщането на 4-ацетамидобензоена киселина, $\text{HOOC-C}_6\text{H}_4\text{-NH-COCH}_3$, в съответния оксианион, $^-\text{OOC-C}_6\text{H}_4\text{-NH-COCH}_3$ и дианион, $^-\text{OOC-C}_6\text{H}_4\text{-N}^-\text{-COCH}_3$ са проследени посредством ИЧ спектри в ДМСО разтворител и DFT/B3LYP/6-311+G (2df,p) изчисления. Ефектът на разтворителя е отчетен по IEFPCM модела. Установено е, че *транс*-формите (по отношение на фениленовите и метиловите групи) са по-стабилни от *цис*-формите при всички изследвани частици. Промените, придружаващи първото депротониране, засягат главно карбоксилатния фрагмент, докато тези, които произтичат от второто депротониране, са разпределени върху целия дианион. Анализът на промените в атомните заряди показва, че над 70% от първия (оксианионен) заряд остава локализиран в карбоксилатния фрагмент. Вторият (азанионен) заряд се делокизира върху ацетилната ($0.42 e^-$), фенилната ($0.19 e^-$) и карбоксилатната ($0.05 e^-$) групи и азанионения център ($0.34 e^-$).

Conformational and spectral properties of newly synthesized compounds obtained by reaction of alrestatin with 3-aminocycloalkanespiro-5-hydantoins

M. N. Marinov¹, S. M. Bakalova², R. Y. Prodanova¹, N. V. Markova^{2*}

¹ Agricultural University – Plovdiv, Faculty of Plant Protection and Agroecology, Department of General Chemistry, 4000 Plovdiv, 12 “Mendeleev” Blvd, Bulgaria

² Institute of Organic Chemistry with Centre of Phytochemistry, Bulgarian Academy of Sciences, 1113 Sofia, Bulgaria

Received April 18, 2017; Revised June 02, 2017

Dedicated to Acad. Ivan Juchnovski on the occasion of his 80th birthday

Synthesis of new heterocyclic compounds by reaction of alrestatin with 3-aminocyclopentanespiro-5-hydantoin and 3-aminocyclohexanespiro-5-hydantoin is presented. The structures of the products obtained are verified *via* IR, ¹H and ¹³C NMR spectroscopy. Conformational analysis of the newly synthesized compounds is performed at the B3LYP/6-31G(d,p) level both in the gas phase and in solution (DMSO) in order to find the most stable conformers about all single bonds. We find that rotation about the torsion angles O=C-CH₂ and C=O-NH is important in the conformational search. The most stable structure has the all *trans*-conformation. Two more rotamers of comparable energy are located upon rotation about angle O=C-CH₂. Calculated energy differences and rotation barriers between the three most stable rotamers in DMSO show that they all should be present in gas phase and solution in fast equilibrium, their population being strongly dependent on solvent polarity. The theoretically predicted IR, ¹H and ¹³C NMR spectra of the two compounds are close to experiment.

Key words: Conformational analysis; GIAO NMR computational; synthesis; alrestatin, 3-aminocycloalkanespiro-5-hydantoins

INTRODUCTION

Alrestatin / (1,3-dioxo-1*H*-benzo[*de*]isoquinolin-2(3*H*)-yl)acetic acid/ is the first orally effective aldose reductase inhibitor [1]. Different spirohydantoins are also known as compounds with a similar type of activity. Substituted indan, tetralin, chroman and thiochroman hydantoins [2] as well as (9'-fluorene)-spiro-5-hydantoin (spiro-(fluorene-9,4'-imidazolidine)-2',5'-dione) and its derivatives [3-5] should be mentioned in this regard.

The crystal structure and DFT calculations of the 3-aminocycloheptanespiro-5-hydantoin and 3-aminocyclooctanespiro-5-hydantoin [6] shows that two symmetrically nonequivalent molecules exist in the hydrogen bonding of the crystal lattice molecular packing due to the two different conformations of cycloheptane ring.

The aim of the current research is to elucidate the structure and conformational properties of two newly synthesized heterocyclic compounds with potential biological activity. The reaction of 3-aminocycloalkanespiro-5-hydantoins with alrestatin was studied for this purpose.

COMPUTATIONAL AND EXPERIMENTAL DETAILS

Quantum-chemical calculations

All calculations have been performed using the Gaussian 09 software package, G09, [7] with default optimization criteria. Conformational analyses and geometry optimizations in the gas phase and dimethylsulfoxide (DMSO) have been done using the hybrid B3LYP functional, which combines the threeparameter exchange functional of Becke [8] with the LYP correlation [9], at the 6-31G(d,p) basis set. Solvent effects are accounted for using the Polarizable Continuum Model, as implemented in G09 [10]. Vibrational frequency calculations have been performed for each structure to obtain vibrational zero point and thermal energies and to validate that the located structures correspond to energy minima with no imaginary frequency or to transition structures with a unique imaginary frequency. The calculations have been carried out without symmetry constraints by the gradient procedure.

* To whom all correspondence should be sent:
E-mail: nadya@orgchm.bas.bg

The populations (p_i) of the conformers are calculated by formula 1:

$$p_i = e^{-\Delta G_i / RT} / \sum_i e^{-\Delta G_i / RT} \quad (1)$$

In simulation of infrared (IR) spectra vibration frequencies are scaled by a factor of 0.945 to ensure better agreement with experimental values.

The methods currently used for prediction of proton and carbon chemical shielding in NMR spectra are *ab initio* (MP2, Hartee-Fock), and density functional (DFT) theory applying the gauge-including atomic orbitals (GIAO) approach [11,12] and PCM/B3LYP/6-31G(d) optimized geometry. Only the results at HF/6-31+G(2d,p) level of theory are presented in this paper because of the large deviations in chemical shift values (about 20 ppm) relative to experiment of the spiro-carbon atom obtained by all other methods. Isotropic magnetic shieldings are converted into chemical shifts by subtracting the corresponding isotropic magnetic shieldings of the reference compound tetramethylsilane (TMS): $\delta = \delta_{\text{calc}}(\text{TMS}) - \delta_{\text{calc}}$, calculated at the same level of theory.

General

All used chemicals have been purchased from Merck and Sigma-Aldrich. The melting points are determined by a SMP-10 digital melting point apparatus. The purity of the compounds has been checked by thin layer chromatography on Kieselgel 60 F₂₅₄, 0.2 mm Merck plates, eluent system (vol. ratio): ethyl acetate : petroleum ether = 1 : 2. The elemental analysis data are obtained with an automatic analyzer Carlo Erba 1106. The IR spectra are taken on a Perkin-Elmer FTIR-1600 spectrometer in KBr discs. The NMR spectra are recorded on a Bruker Avance II + 600 MHz spectrometer, operating at 600.130 and 150.903 MHz for ¹H and ¹³C, respectively, using the

standard Bruker software. The chemical shifts are referenced to tetramethylsilane (TMS). The measurements in DMSO-*d*₆ solutions are carried out at ambient temperature

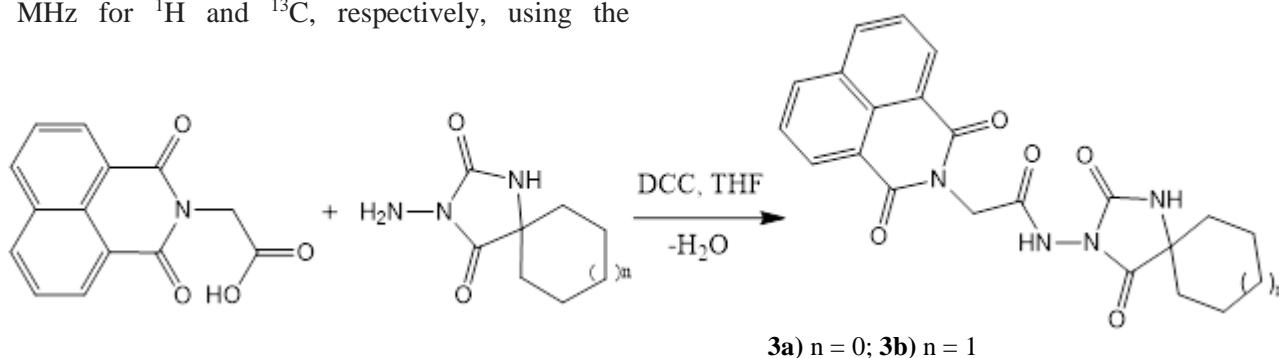
Synthesis of alrestatin derivatives with 3-aminocycloalkanespiro-5-hydantoins (Scheme 1):

A mixture of 2.55 g (0.01mol) of alrestatin (**1**) and 0.01 mol of the corresponding 3-aminospirohydantoins (**2a** and **2b**) has been dissolved in 50 ml of tetrahydrofuran with stirring at room temperature. *N,N'*-dicyclohexylcarbodiimide (DCC, 2.06 g, 0.01 mol) is added to the reaction mixture and the latter is left overnight. The *N,N'*-dicyclohexylcarbamide formed has been filtered off and 1 ml of glacial acetic acid is added to the filtrate for removing of the unreacted reagent. After filtration, the solvent is evaporated to dryness and the products obtained: 2-(1,3-dioxo-1*H*-benzo[*de*]isoquinolin-2(3*H*)-yl)-*N*-(2,4-dioxo-1,3-diazaspiro[4.4]nonan-3-yl)acetamide, **3a** (Yield = 58 %, M. p. = 206-207 °C, R_f = 0.57) and 2-(1,3-dioxo-1*H*-benzo[*de*]isoquinolin-2(3*H*)-yl)-*N*-(2,4-dioxo-1,3-diazaspiro[4.5]decan-3-yl)acetamide, **3b** (Yield = 69 %, M. p. = 189-190 °C, R_f = 0.63) are recrystallized from ethanol.

RESULTS AND DISCUSSION

3-aminocycloalkanespiro-5-hydantoins **3a** and **3b** can exist as mixtures of conformers. Since the used spectral methods give no possibility for identification of the different conformers, we perform quantum-chemical calculations to elucidate the structure of the newly synthesized compounds.

Full conformational analysis has been performed for compound **3a** for rotation about the O=C-CH₂

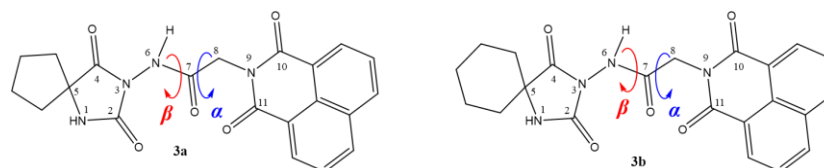


Scheme 1. Synthesis of alrestatin derivatives with 3-aminocycloalkanespiro-5-hydantoins

(α) and the C=O-NH (β) bonds as well as the two adjacent single bonds (Scheme 2) applying a step of 20° over a 360° range. The scans about the single bonds adjacent to the heterocyclic substituents show just a second, practically isoenergetic conformer at ca 180° . This result can be easily understood having in mind the symmetry of both heterocyclic substituents. On the other hand rotation about angle α (N9-C8-C7-N6) reveals the existence of three stable conformers. Located by the conformational scan minima have been further optimized to give $3a1$, $3a2$ and $3a3$, while located maxima have been optimized as transition structures. Rotation around angle β (N3-N6-C7-C8) and subsequent optimizations lead to the localization of two more conformers— $3\beta1$, $3\beta2$.

According to our calculations the relative stability of the conformers of compound **3a** in the gas phase decreases in the order $3a\alpha3$ (Fig. 1 and Table 1), $3a\alpha2$, $3a\alpha1$. The energy difference between $3a\alpha3$ and $3a\alpha2$ is very small and they are practically isoenergetic, while $3a\alpha1$ is less stable than $3a\alpha3$ by $1.16 \text{ kcal mol}^{-1}$. Conformers $3a\beta1$ and

$3a\beta2$ are of much higher energy and have not been considered further. That is why in the case of **3b** we have scanned only the rotation about the O=C-CH₂ bond, i.e. dihedral angle α (Figure 2). The stability sequence in the gas phase for compound **3b** is the same as that for **3a**: $3b\alpha3 > 3b\alpha2 > 3b\alpha1$. The relative free energy sequence of the conformers of compounds **3a** and **3b** in DMSO is changed in comparison to that in the gas phase (Table 1). The most stable structure of **3a** becomes conformer $3a\alpha1$ followed by $3a\alpha2$ ($0.79 \text{ kcal mol}^{-1}$) and $3a\alpha3$ ($1.03 \text{ kcal mol}^{-1}$). The energy differences between the most stable conformer $3a\alpha1$ and conformers $3a\beta1$ and $3a\beta2$ are insignificantly increased in comparison to the gas phase, being 1.73 and $5.81 \text{ kcal mol}^{-1}$, respectively. The percentage distribution of the conformers of **3a** in DMSO, calculated on the basis of their relative free energies using Equation 1, is as follows: 59.07% for $3a\alpha1$, 21.86% for $3a\alpha2$, 14.95% for $3a\alpha3$, 5.12% for $3a\beta1$ and 0.01% for $3a\beta2$, respectively.



Scheme 2. Structural formulas and atom numbering of the investigated compounds. Rotation angles which are important in the conformational analysis are denoted as α and β .

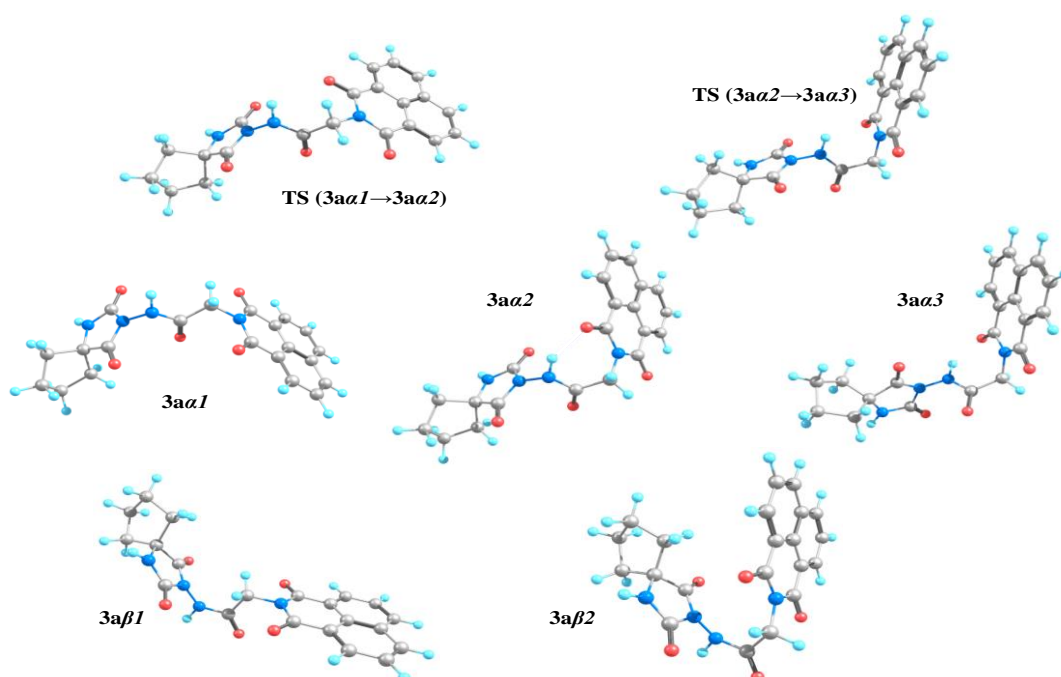


Fig. 1. PCM/B3LYP/6-31G(d,p) optimized structures of five conformers of compound **3a** in DMSO. The transition structures for rotation around angle α (Fig. 1) are presented as well.

The stability sequence of **3b** is also different in solution in comparison with the gas phase. The conformers are close in energy and at PCM/B3LYP/6-31G(d,p) level of theory conformer *3ba1* became the most stable structure, followed by the *3ba2* (0.31 kcal mol⁻¹) and the *3ba3* (0.41 kcal mol⁻¹) ones. The calculated values of the rotation barriers for compound **3a** in DMSO relative to the most stable conformer *3aa1* are given in Table 5. The free activation energy for the conversion *3aa1*→*3aa2* is 3.54 kcal mol⁻¹, while that for the *3aa2*→*3aa3* one is lower, 3.11 kcal mol⁻¹ (Fig. 4). According to these results the three lowest energy conformers of compounds **3a** in DMSO exist in equilibrium. Based on the calculated populations and the low energy barriers of rotation it can be concluded that in DMSO compound **3a** could exist as four conformers - mainly *3aa1* and in smaller concentrations of *3aa2*, *3aa3* and *3aβ1*. The picture is similar for compound **3b**.

The synthesis of the target compounds (**3a** and **3b**) is shown in Scheme 1. Alrestatin (**1**) is obtained in accordance with ref. [13]. The 3-aminocyclopentanespiro-5-hydantoin (**2a**) and the 3-aminocyclohexanespiro-5-hydantoin (**2b**) are prepared by treatment of the corresponding cycloalkanespiro-5-hydantoins (obtained *via* the Bucherer-Lieb method [14]) with concentrated hydrazine hydrate in accordance with Marinov *et al.* [15]. The interaction between the above mentioned compounds following the DCC-method [16] leads to the formation of products **3a** and **3b**.

The elemental analysis, IR and NMR spectral data of the synthesized compounds (**3a** and **3b**) are listed in Tables 2-4 respectively. The structural formulas and atom numbering of the compounds synthesized are presented in Scheme 2.

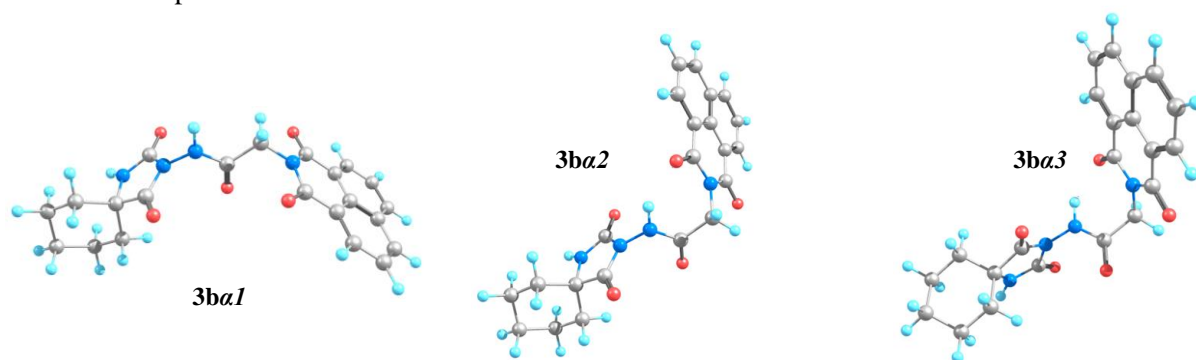


Fig. 2. PCM/B3LYP/6-31G(d,p) optimized structures of the three most stable isomers of compound **3b**.

Table 1. Relative free energies (kcal mol⁻¹) and torsion angles (°) of rotation about the CO-NH and CO-CH₂ bonds of the conformers of compounds **3a** and **3b** (Fig. 1 and Fig. 2.) calculated in the gas phase and in DMSO.

	PCM/B3LYP/6-31G(d,p)			B3LYP/6-31G(d,p)		
	ΔG_{298}	β	α	ΔG_{298}	β	α
3aa1	0.00	172.9	161.6	1.16	167.9	162.9
3aa2	0.79	174.1	-73.6	0.05	168.3	-80.6
3aa3	1.03	-179.8	65.8	0.00	-172.2	78.5
3aβ1	1.73	-7.3	-170.6	1.59	17.4	-173.4
3aβ2	5.81	-170.6	-47.8	4.10	-32.1	-47.4
TS (3aa1 → 3aa2)	3.54	-178.5	-130.4			
TS (3aa2 → 3aa3)	3.11	178.6	-10.4			
3ba1	0.00	173.8	163.3	1.43	167.9	162.6
3ba2	0.31	175.6	-70.8	0.13	168.3	-80.6
3ba3	0.41	-177.0	69.0	0.00	-172.6	78.1

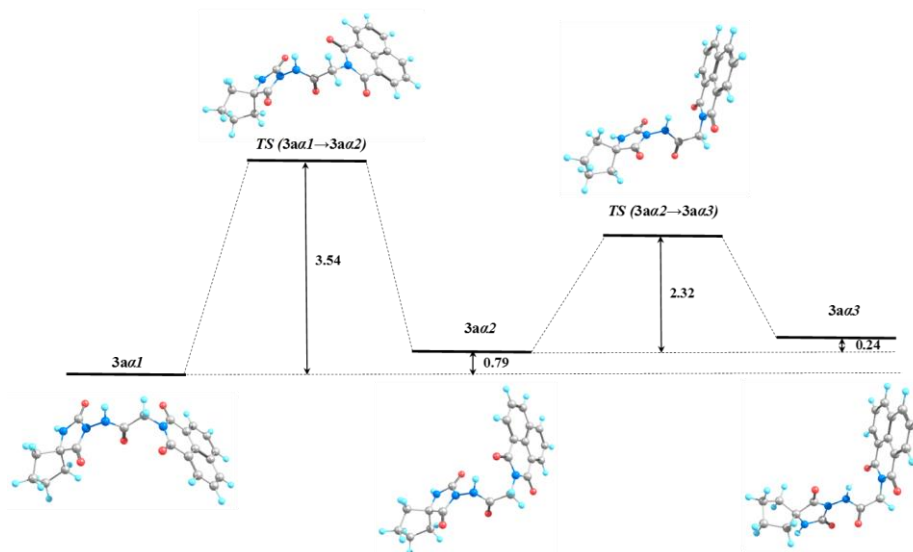


Fig. 3. PCM/B3LYP/6-31G(d,p) calculated free energy differences and rotation barriers (in kcal mol⁻¹) of the three most stable conformers of compound **3a** in DMSO.

As previously mentioned, quantum-chemical studies are performed using B3LYP functional and 6-31G(d,p) basis set in the gas phase and including solvent effects, as described in the computational section. The vibrational spectra of the all conformers of **3a** and **3b** were computed at B3LYP/6-31G(d,p) level also. Because of the fast equilibrium between the three most stable rotamers and the relatively similar predicted frequencies in their IR spectra we present selected vibration frequencies only for the most stable conformer, **3aα3** in the gas phase. Available experimental data for the vibrational frequencies of the two compounds in KBr are presented for comparison. All results are listed in Table 3. Our assignments for the DFT calculated frequencies are based upon analysis of the corresponding vibrational eigenvectors. Some modes such as NH and C=O stretching have been found to be characteristic. The analysis of the theoretically predicted spectra of the two compounds shows that they are in a good

agreement with experimental data. The augmentation of the cycloalkane ring in the molecule of **3a** to **3b** does not lead to the changes in IR spectra.

To elucidate the structure of newly synthesized compounds NMR quantum-chemical study is performed. We carry out calculations using the ab-initio (MP2), Hartee-Fock and different density functionals with a wide range of basis sets to find that HF results are closest to experimental data. MP2 and DFT do not reproduce accurately the chemical shifts of the spiro-carbon atom, the deviation from the experiment being about 20 ppm. Therefore, we present only the HF results in GIAO NMR calculations in DMSO. Because of the sensitivity of ¹³C NMR chemical shifts to the presence of polarization and diffuse functions in the basis set, the 6-31+G(2d,p) basis set is employed. GIAO NMR calculations in DMSO are performed for all conformers of the compounds studied.

Table 2. Elemental analysis data of compounds **3a** and **3b**.

Compound	Molecular formula	Elemental analysis, %					
		Calculated			Found		
		C	H	N	C	H	N
3a	C ₂₁ H ₁₈ N ₄ O ₅	62.06	4.46	13.79	62.35	4.23	13.57
3b	C ₂₂ H ₂₀ N ₄ O ₅	62.85	4.79	13.33	62.55	4.45	13.49

Table 3. Experimental IR data and selected frequencies calculated at B3LYP/6-31G(d,p) level (in italic) for compounds **3a** and **3b**. The calculated frequencies are given for the most stable isomer (**3aa3**) of the two compounds in the gas phase and are scaled by a factor of 0.945.

No	ν_{NH}	ν_{CH} (arom.)	ν_{as} (CH ₂)	ν_{s} (CH ₂)	$\nu_{\text{C=O}}$ (amide)	$\nu_{\text{C=O}}$	ν_{CC} (arom.)	ν_{CN} (imide)
3a	3328	3065	2933	2854	1698	1775, 1660	1590, 1537	1380
	3394	3030	3022	2935	1684	1793, 1627	1582, 1543	1369
3b	3328	3066	2933	2853	1696	1766, 1658	1590, 1537	1380
	3396	3030	3022	2935	1684	1792, 1627	1582, 1543	1368

Table 4. GIAO ¹H and ¹³C chemical shifts (δ /ppm) in DMSO of the most stable conformers of compounds **3a** and **3b** calculated at HF/6-31+G(2d,p) level and experimental data. The geometries are optimized at the PCM/B3LYP/6-31G(d,p) level in DMSO.

Nuclei	<i>Exptl.*</i> (DMSO- <i>d</i> ₆)	3aa1	<i>Exptl.*</i> (DMSO- <i>d</i> ₆)	3ba1
CH ₂ , cyclopentane/ cyclohexane	23.4, 32.6	26.1, 36.2	24.9-32.2	20.8-31.2
CH ₂ , methylene	43.3	39.7	42.4	39.7
spiro C-atom	52.4	60.0	50.2	56.1
CH, naphthalene	128.2- 138.5	122.9-141.7	127.8- 135.2	123.0- 141.2
C=O, spirohydantoin	159.2	157.2	158.2	157.4
C=O, naphthalene	165.5	171.4	163.6	171.6
C=O	171.2	175.0	169.4	174.9
C=O, spirohydantoin	209.6	182.9	207.5	180.8
m, 8H (10H), CH ₂	1.52-1.92	1.53-2.11	1.50-1.95	1.18-1.67
s, 2H, CH ₂	4.91	5.05	4.87	5.07
m, 6H, CH	7.59-7.94	8.23-9.56	7.68-7.90	8.23-9.65
s, 1H, NH	8.54	5.25	8.51	5.71
s, 1H, NH	11.12	7.28	10.82	7.31

*The assignments of ¹³C chemical shifts are confirmed by the DEPT-135 spectral data.

Due to the fact that the chemical shifts of the different conformers are relatively close we present the chemical shifts only of the most stable conformers of **3a** and **3b** in DMSO, *al*.

The augmentation of the cycloalkane ring in the molecule of **3b** relative to **3a** leads only to minor changes in ¹H and ¹³C NMR spectra (Table 4). Our theoretical results are in agreement with the ¹H and ¹³C NMR measurements in DMSO-*d*₆ solutions of compounds **3a** and **3b**. The exceptions are the chemical shifts of carbonyl group in spirohydantoin moiety as well as of the NH-protons, the theoretically predicted shifts being underestimated in comparison to the experimentally found ones.

CONCLUSIONS

New alrestatin derivatives with 3-amino cyclopentanespiro-5-hydantoin and 3-amino cyclohexanespiro-5-hydantoin are successfully

synthesized. The structures of the products obtained have been proven by physicochemical parameters, IR, ¹H and ¹³C NMR spectroscopy. The performed full computational analyses of the studied compounds about all single bonds show, that in the most stable conformers angle β is ca 180° while rotation about angle α leads to the three most stable conformers population is strongly dependent on solvent polarity. Calculated free energies for rotation about angle α suggest that these three conformers are in rapid equilibrium. Computationally predicted IR, ¹H and ¹³C NMR spectra of studied compounds are in good agreement with experiment.

Acknowledgements: Financial support by the Agricultural University – Plovdiv, Bulgaria (Contract 02-15) is gratefully acknowledged. The calculations were performed on the computer

system installed at the Institute of Organic Chemistry, Bulgarian Academy of Sciences with the financial support of the National Science Fund, Project "MADARA" (Grant DO 02-52/2008).

REFERENCES

1. D. Dvornik, N. Simard-Duquesne, M. Krami, K. Sestanj, K. H. Gabbay, J. H. Kinoshita, S. D. Varma, L. O. Merola, *Science*, **182**, 1146 (1973).
2. R. Sarges, R. C. Schnur, J. L. Belletire, M. J. Peterson, *J. Med. Chem.*, **31**, 230 (1988).
3. B. M. York, US Patent 4438272 (1984).
4. P. Bovy, A. Lenaers, M. Callaert, N. Herickx, C. Gillet, J. Roba, J. -M. Dethy, B. Callaert-Deveen, M. Janssens, *Eur. J. Med. Chem.*, **23**, 165 (1988).
5. P. Bovy, R. C. Gillet, A. Lenaers, P. Niebes, J. Roba, G. Lambelin, US Patent 4853401 (1989).
6. P. Todorov, R. Petrova, E. Naydenova, B. Shivachev, *Cent. Eur. J. Chem.*, **7**, 14 (2009).
7. M. J. Frisch, G. W. Trucks, H. B. Schlegel, G. E. Scuseria, M. A. Robb, J. R. Cheeseman, et al. Gaussian 09, Revision D.01. In: Gaussian, Inc., Wallingford CT, 2009.
8. A. Becke, *J. Chem. Phys.*, **98**, 5648 (1993).
9. C. Lee, W. Wang, R. Pople, *Phys. Rev. B*, **37** 785 (1988).
10. J. Tomasi, B. Mennucci, R. Cammi, *Chem. Rev.*, **105**, 2999 (2005).
11. R. Ditchfield, *Mol. Phys.*, **27**, 789 (1974).
12. K. Wolinski, J.F. Hinton, P. Pulay, *J. Am. Chem. Soc.*, **112**, 8251 (1990).
13. K. Sestanj, N. Simard-Duquesne, D. M. Dvornik, US Patent 3821383 (1974).
14. H. T. Bucherer, V. A. Lieb, *J. Prakt. Chem.*, **141**, 5 (1934).
15. M. Marinov, I. Kostova, E. Naydenova, R. Prodanova, P. Marinova, P. Penchev, N. Stoyanov, *Univ. of Ruse "Angel Kanchev" Proc.*, **54**, 62 (2015).
16. J. C. Sheehan, G. P. Hess, *J. Am. Chem. Soc.*, **77**, 1067 (1955).

КОНФОРМАЦИОННИ И СПЕКТРАЛНИ СВОЙСТВА НА НОВОСИНТЕЗИРАНИ СЪЕДИНЕНИЯ, ПОЛУЧЕНИ ПРИ РЕАКЦИЯ НА АЛРЕСТАТИН И 3-АМИНОЦИКЛОАЛКАНСПИРО-5-ХИДАНТОИНИ

М. Н. Маринов¹, С. М. Бакалова², Р. Й. Проданова¹, Н. В. Маркова^{2*}

¹ Аграрен университет – Пловдив, Факултет по растителна защита и агроекология, Катедра „Обща химия“, 4000 Пловдив, бул. „Менделеев“ 12, България

² Институт по органична химия с Център по фитохимия, Българска академия на науките, 1113 София, ул. „Акад. Г. Бончев“, бл. 9, България

Постъпила на 18 април 2017 г.; Коригирана на 02 юни 2017 г.

(Резюме)

Представен е синтез на нови хетероциклени съединения чрез реакция между алрестатин и 3-аминоциклопентанспиро-5-хидантоин и 3-аминоциклохексанспиро-5-хидантоин. Структурите на получените продукти са потвърдени с помощта на ИЧ, ¹H и ¹³C ЯМР спектроскопия. За да се локализира най-стабилните конформери на новосинтезираните съединения е направен конформационен анализ спрямо всички прости връзки на ниво V3LYP/6-31G(d,p) в газова фаза и в разтвор (диметил сулфоксид, ДМСО). Установено е, че въртенето около торзионните ъгли O=C-CH₂ и C=O-NH е важно при конформационния анализ. Най-стабилната структура има транс-конформация. Локализиран са още два конформера със сравнима енергия, при ротация около ъгъл O=C-CH₂. Изчислените в разтворител (ДМСО) енергетични разлики и бариери на ротация между трите най-стабилни ротамера показват, че те би трябвало да присъстват в разтвор, и се намират в бързо равновесие, като концентрациите им зависят от поляриността на разтворителя. Теоретично предсказаните ИЧ, ¹H и ¹³C ЯМР спектри на двете съединения са близки до експериментално установените.

Application of a RP-HPLC method for determination of chemical and physiological stability of two newly synthesized methoxy-benzoylhydrazone derivatives

B. I. Nikolova-Mladenova^{1*}, L. P. Peikova², M. B. Georgieva², Al. B. Zlatkov²

¹ Department of Chemistry, Faculty of Pharmacy, Medical University-Sofia, 2 Dunav str., 1000 Sofia, Bulgaria

² Department of Pharmaceutical chemistry, Faculty of Pharmacy, Medical University-Sofia, 2 Dunav str., 1000 Sofia, Bulgaria

Received May 1, 2017; Revised May 26, 2017

Dedicated to Acad. Ivan Juchnovski on the occasion of his 80th birthday

The study investigates the stability of novel aroylhydrazones containing susceptible to hydrolysis hydrazone group at conditions close to physiological. Two methoxy-derived hydrazones (3-methoxysalicylaldehyde benzoylhydrazone – 3M and 4-methoxysalicylaldehyde benzoylhydrazone – 4M) were dissolved in different buffer solutions (pH 2.0, 7.4 and 9.0) at 37 °C and aliquot samples were drawn at definite time intervals. Stability of the compounds was determined using precise, selective and validated RP-HPLC method. No changes in the structures were detected at pH= 7.4 and pH = 9.0, whereas an appearance of new peaks corresponding to the retention time of the supposed hydrolysis products was observed at pH 2.0. The results revealed chemical stability of the tested compounds at neutral and low alkali pH under physiological temperature and hydrolytic sensibility at strong acidic medium.

Key words: benzoylhydrazones; chemical stability; physiological stability; RP-HPLC

INTRODUCTION

Benzoylhydrazones are currently widely investigated from the viewpoint of their application as bioactive compounds. Many studies have discovered an extensive variety of biological activities such as anti-inflammatory, anti-malarial, analgesic, anti-oxidative, antimicrobial, and antiproliferative activity [1–10]. Hence, aroylhydrazones seem to be promising drug candidates with potential to be used in the treatment of some human diseases. Recently, the synthesis of some new methoxy-salicylaldehyde benzoylhydrazones and evaluation of their antiproliferative effect on a wide spectrum of human tumor cell lines was reported [9-10]. The investigations demonstrated that the presence of methoxy group in salicylaldehyde results in derivatives with high antiproliferative and antioxidant activity [4-6, 9-10].

The pharmaceutical stability of any promising drug candidate plays an important role in the process of the novel drug development. Many factors, such as air, heat, light, moisture as well as the inherent chemical susceptibility of a substance to hydrolysis affect the stability of compounds. The stability of a compound synthesized as a potential medicinal agent is related to the pharmacokinetic

behavior in the body and to the conditions for the formulation, storage, occurrence of toxic effects associated with degradation products and so on. Most of the compounds are fairly stable in the neutral pH value found in the intestine but can be unstable at the pH value found in the stomach [11]. Some aroylhydrazones also have been reported to be sensitive to hydrolysis in both acid and alkaline medium [12-13]. Thus in the development of new drugs early information of stability becomes essential for subsequent processes of optimization and selection of leading active structures and can prevent unnecessary costs on developing products that subsequently prove to be unstable. The aim of this study is to establish and apply a reversed phase liquid chromatography (RP-HPLC) method for investigation of the stability of recently synthesized benzoylhydrazone derivatives under physiological pH and temperature and for identification of their hydrolytic degradation products. The structures of the hydrazones are shown on Fig. 1.

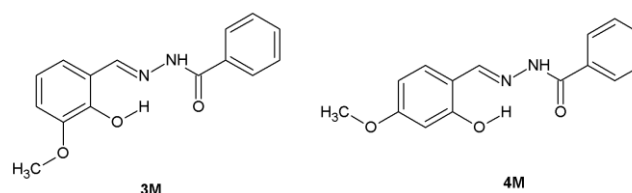


Fig. 1. Chemical structures of the investigated hydrazones **3M** (3-methoxysalicylaldehyde benzoylhydrazone) and **4M** (4-methoxysalicylaldehyde benzoylhydrazone).

* To whom all correspondence should be sent:
E-mail: boriananik@abv.bg

EXPERIMENTAL

Chemicals and reagents

3-methoxysalicylaldehyde, 4-methoxysalicylaldehyde and benzhydrazide used for the preparation of the 3-methoxysalicylaldehyde benzoylhydrazone (**3M**) and 4-methoxysalicylaldehyde benzoylhydrazone (**4M**) were purchased from Sigma-Aldrich and used without further purification. The investigated hydrazones were synthesized as already reported [9] by Schiff-base condensation in ethanol between 3-methoxysalicylaldehyde and benzhydrazide for **3M** and between 4-methoxysalicylaldehyde and benzhydrazide for **4M**. The structure and purity of the compounds **3M** and **4M** were confirmed by IR (Bruker Tensor 27 spectrophotometer), ^1H and ^{13}C NMR (Bruker Avance DRX 250 spectrophotometer) spectroscopy. The melting points were measured using a Buchi 535 apparatus. The necessary components used for the preparation of the mobile phase and the buffers were of analytical grade, whereas potassium dihydrogen phosphate dihydrate (Sigma-Aldrich), orthophosphoric acid (Merck) and methanol (Sigma-Aldrich) were of gradient grade.

Preparation of the sample solutions

Due to the poor solubility of the analyzed structures in water, methanol-buffer solutions were prepared at the necessary relevant ratio in order to obtain the desired pH values. A 10 mg sample of the model compounds was weighed and dissolved in the corresponding mixture of methanol and buffer with respective pH (2.0 or 7.4 or 9.0). The obtained solutions were thermostated and stirred in a micro reactor at 37 °C for a total time of 1440 min (24 hours). Aliquot samples of 20 μL of the analyzed solutions of **3M** and **4M** were taken at definite time intervals (15, 30, 60, 120, 240, 480 and 1440 min) and injected into the RP-HPLC system.

Instrumentation and chromatographic conditions

Chromatographic separation was performed on a modular HPLC system LC-10A Shimadzu (Japan) which consisted of a LC-10A pump, solvent degasser DGU-3A, Rheodyne injector with 20 μL loop, column oven CTO-10A, SPD-M10A UV detector with fixed wavelength and communication bus module CBM-10A. The analysis was achieved with a Luna 5u CB 100A C18 (250 mm x 4.6 mm), 5 μm particle size column used as a stationary

phase. The components were eluted isocratically with a mixture of methanol and phosphate buffer (0.5 M KH_2PO_4 , pH 4.0 adjusted with orthophosphoric acid) 65:35 v/v as the mobile phase at flow rate of 1.0 mL/min. The mobile phase was filtered through a 0.45 μm membrane filter and degassed. Detection was carried out by absorbance at 240 nm. The analysis was carried out at ambient column temperature and injection volume was 20 μL .

Preparation of the mobile phase buffer

6.80 g of potassium dihydrogen phosphate dehydrate ($\text{KH}_2\text{PO}_4 \cdot 2\text{H}_2\text{O}$) was dissolved in 1L of ultrapure water. An orthophosphoric acid solution (6 %) was used to adjust the pH to 4.0 (± 0.05). The mobile phase buffer was filtered through a membrane filter (0.20 μm) using a Millipore glass filter holder. The mobile phase buffer was used immediately after preparation or stored in the refrigerator in closed borosilicate glass bottles for a maximum of 24 hours.

Preparation of the buffers 2.0, 7.4 and 9.0

The buffers were prepared according to a procedure enlisted in European Pharmacopoeia 7.0 [14].

Validation procedure

The developed RP-HPLC method for the analysis of aroylhydrazones was tested with respect to following validation parameters: precision, linearity, accuracy and selectivity.

Precision: Precision of the method was tested by performing six independent sample solutions from each of the evaluated hydrazones. Each sample was injected three times. The final results are reported as relative standard deviations (RSD %).

Linearity: Linearity was determined within the range of 25-200 $\mu\text{g/mL}$ for both the hydrazones **3M** and **4M**. Calibration curves were created using 6 points covered 6 different concentrations of the hydrazones over the tested concentration range (25, 50, 75, 100, 150, 200). Linear regression was used to process the calibration data.

Accuracy: The solutions for injection were prepared using a placebo and stock solution of the tested structures. Six solutions were prepared from each of the two compounds. Each solution was injected onto the column three times. Accuracy is reported as a parameter recovery with relative standard deviations.

Selectivity: The selectivity was determined by comparing the chromatograms for the solutions of the tested **3M** and **4M** hydrazones with the solutions of the initial corresponding benzhydrazide and 3-methoxysalicylaldehyde (initial for **3M**) and 4-methoxysalicylaldehyde (initial for **4M**), alone and in mixture.

RESULTS AND DISCUSSION

In an attempt to determine the chemical stability and the stability at close to physiological conditions of the synthesized benzoylhydrazone derivatives **3M** and **4M** wide range of pH was chosen. The analyzed compounds were investigated for hydrolytic decomposition under physiological temperature of 37 °C and at pH 2.0, 7.4 and 9.0, namely the physiological pH in the stomach, blood plasma and intestines, respectively. Based on the chemical structure of the evaluated compounds the most probable change is the cleavage of the characteristic hydrazone group -CH=N-. Thus as referent substances were chosen the corresponding initial benzhydrazide and 3-methoxy- or 4-methoxysalicylaldehyde. For identification of the possible degradation and formation of new products an RP-HPLC method was developed and validated.

Validation of the developed RP-HPLC analytical procedure

The method was validated according to ICH Q2 (R1) guidelines [15]. The precision, linearity, accuracy and selectivity of the system were evaluated during the method validation. The obtained parameters for the two analyzed hydrazones are shown on Table 1.

Precision: The calculated RSD values for **3M** and **4M** for the assessment of the precision are 1-1.5 %, confirming that the method is precise.

Table 1. Validation parameters for compounds **3M** and **4M**.

	3M	4M	Criterion
Repeatability t_R (% RSD)*	0.15	0.25	$X < 1\%$
Resolution*	1.9	1.7	$R_{ij} > 1.5$
Precision (% RSD)#	1.5	1.0	$X < 5\%$
Linearity (correlation coefficient)§	0.9992	0.9989	$R > 0.9990$
Accuracy (%)#	100.2	99.98	$X = 100 \pm 5\%$
Selectivity	No interference	No interference	No interference

* Six injections.

Two samples, three injections of each solution

§ At 25, 50, 75, 100, 150 and 200 µg/mL concentration level.

% RSD: Relative standard deviation in %

Linearity: The correlation coefficients of linearity are 0.9992 for **3M** and 0.9989 for **4M**. The values indicate good correlation between the peak areas and the range of concentrations studied (Fig. 2).

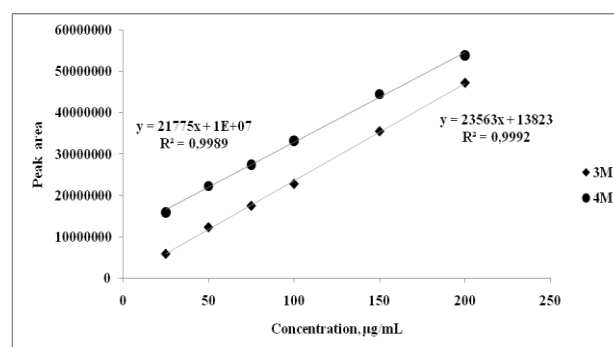


Fig. 2. Linearity of the developed RP-HPLC method.

Accuracy: The method was found to be accurate with recoveries of 99.98%–100.2%

Selectivity: The selectivity of the method is illustrated on the chromatograms on Fig. 3.

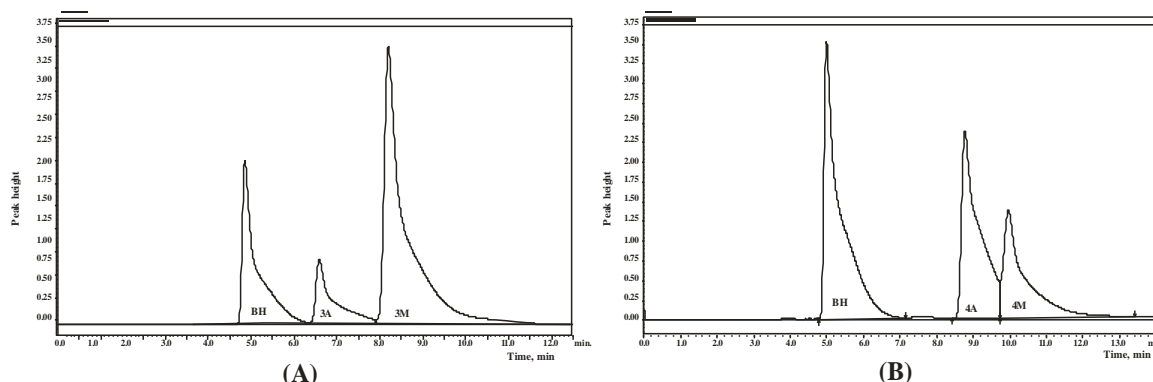


Fig. 3. Chromatogram of a model mixture of the tested **3M** and the corresponding benzhydrazide and 3-methoxysalicylaldehyde (A) and **4M** and the corresponding benzhydrazide and 4-methoxysalicylaldehyde (B).

It is evident that under the proposed chromatographic conditions each of the tested hydrazones (**3M** and **4M**) is completely separated from initial corresponding benzhydrazide (BH) and methoxy-salicylaldehyde (3A and 4A, respectively). No interferences were observed which indicates that the method is selective and could be used for their simultaneous identification.

Limit of quantitation and limit of detection: The limit of quantitation (LOQ) and limit of detection (LOD) were calculated from the standard deviations and slopes of the responses using a signal-to-noise ratio. The LOQs for **3M** and **4M** were found to be 1.0 µg/mL and 0.8 µg/mL, while the LODs were 0.2 µg/mL and 0.1 µg/mL, respectively.

Chemical stability

By definition, the chemical stability is the tendency of a substance to resist change or decomposition due to internal reaction, or due to the action of air, humidity, heat, light, pressure, etc. All compounds presented in this paper have been stored for 6 months at room temperature with access of air and light. It was determined that the compounds kept their physical and chemical

properties unchanged under these conditions. Thus the tested compounds may be considered as chemically stable.

Physiological stability

An important factor influencing the performance of the molecules in the organism is their hydrolytic stability at physiological conditions, such as: body temperature of 37 °C and physiological pH of 2.0 (in stomach), 7.4 (in blood plasma) and 9.0 (in intestine) [16]. The processed according to the above described procedure samples were injected into the RP-HPLC system and the corresponding chromatograms were obtained. The stability of **3M** and **4M** was firstly studied in alkaline solutions. For both of hydrazones no new peaks were observed at pH 7.4 and 9.0 for the tested period of 1440 min (24 h). This leads to conclusion that no hydrolysis of the hydrazones exists at these conditions. The analyzed **3M** and **4M** hydrazones are stable in alkaline medium under physiological temperature. The resulted chromatograms of the conducted stability studies at a temperature of 37 °C and pH=7.4 (blood plasma) and pH 9.0 (intestine) are presented on Figs. 4 and 5.

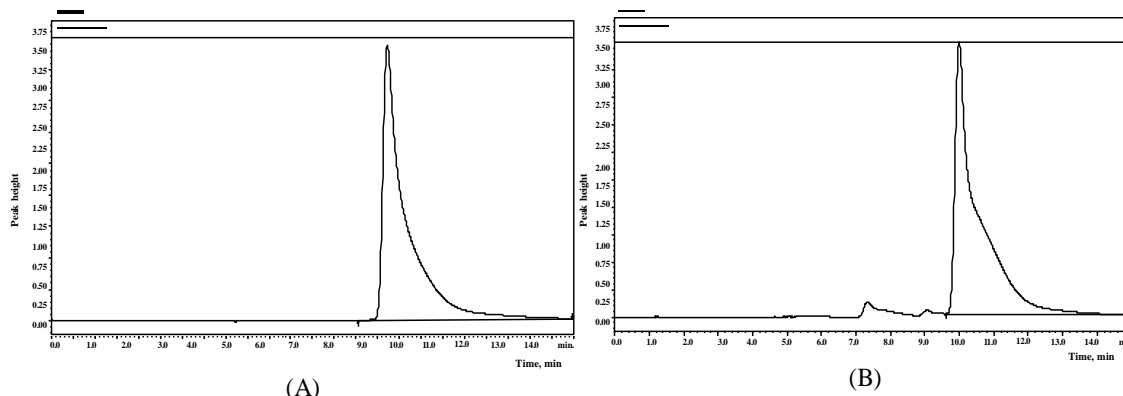


Fig. 4. Representative chromatograms of the analyzed **3M** at pH 7.4 (A) and 9.0 (B).

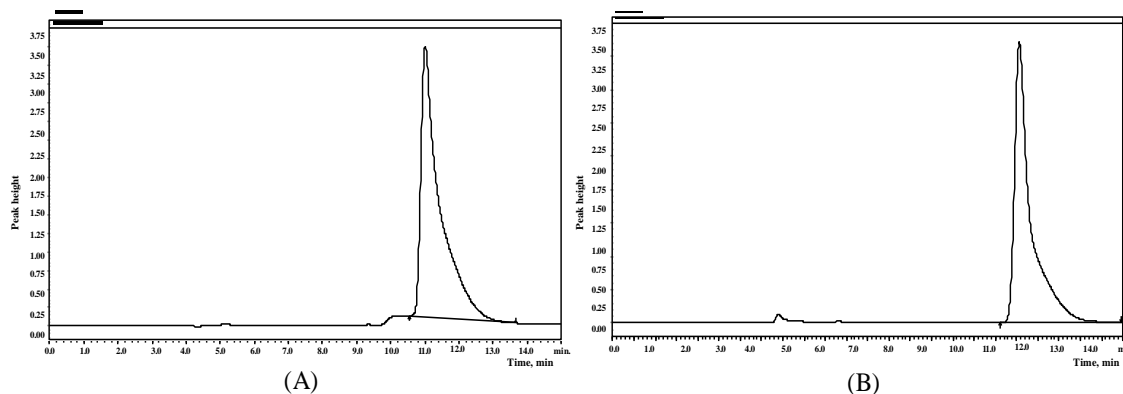


Fig. 5. Representative chromatograms of the analyzed **4M** at pH 7.4 (A) and 9.0 (B).

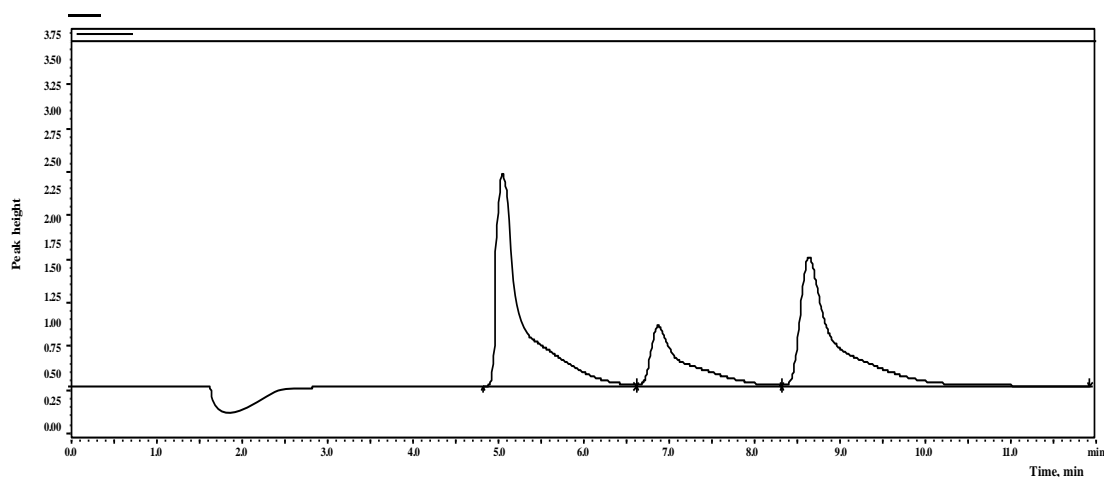


Fig. 6. Representative chromatogram of the analyzed **3M** at pH 2.0 at 30 minute.

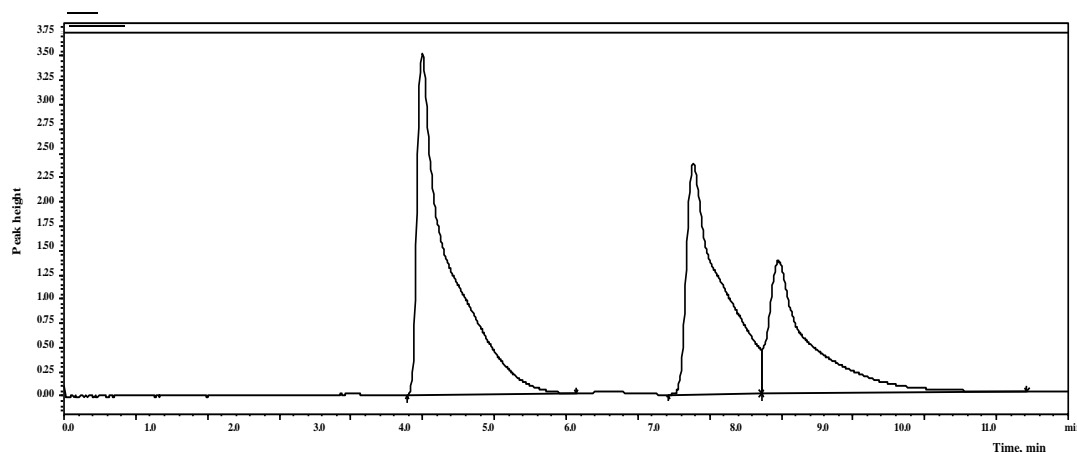


Fig. 7. Representative chromatogram of the analyzed **4M** at pH 2.0 at 30 minute.

The stability of **3M** and **4M** was also studied in the strong acidic medium (pH 2.0). At the 30th min of incubation at these conditions hydrolytic decomposition of the hydrazones was determined. An appearance of two new peaks due to the degradation products was observed. Both hydrazones hydrolyzed to corresponding initial benzhydrazide and 3-methoxy- or 4-methoxysalicylaldehyde. The resulted chromatograms of the conducted stability studies for **3M** and **4M** at a temperature of 37 °C and pH=2.0 (stomach) are presented on Figs. 6 and 7.

In addition a kinetic study of the established degradation for both analyzed products was performed. The corresponding time dependence curves for degree of degradation of the compounds at pH = 2 and temperature of 37 °C was drawn and presented on Fig. 8. The graphical dependency reveals a fast hydrolysis under the evaluated conditions for a period of 24 hours. The obtained

results correspond to a first degree polynomial dependency of the degradation with R^2 of 0.925 and R^2 of 0.939, for the analyzed product **3M** and **4M**, respectively.

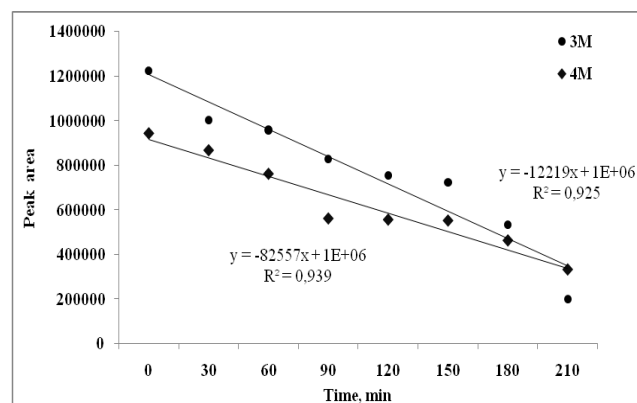


Fig. 8. Time dependent degradation of **3M** and **4M** at pH 2.0 and 37 °C.

CONCLUSION

An isocratic RP-HPLC method for determination of the chemical stability and stability under close to physiological conditions of two benzoylhydrazones was developed and validated. The proposed method was found to be accurate, precise, reproducible and specific. The results indicate that the tested compounds are stable at moderate and low alkali pH and physiological temperature of 37 °C, but they are susceptible to hydrolysis in strong acidic media of the stomach. The decomposition of the 3M and 4M hydrazones proceeds through the hydrolysis of hydrazone bond. The products of this reaction have been detected in chromatograms – the corresponding initial benzhydrazide and methoxy-salicylaldehydes, used in the synthesis

Acknowledgements: Financial support by the Medical University of Sofia (Council of Medical Science, Project №540/21.01.2016, Grant 49/2016) is gratefully acknowledged.

REFERENCES

1. S. Rollas, S. G. Küçükgülzel, *Molecules*, **12**(8), 1910 (2007).
2. K. Padmini, P. J. Preethi, M. Divya, P. Rohini, M. Lohita, K. Swetha, P. Kaladar, *Int. J. Pharm. Res. Rev.*, **2**(8), 43 (2013).
3. A. Walcourt, M. Loyevsky, D. B. Lovejoy, V. R. Gordeuk, D. R. Richardson, *Int. J. Biochem. Cell Biol.* **36**, 401 (2004).
4. N. G. Hristova-Avakumova, B. I. Nikolova-Mladenova, V. A. Hadjimitova, *Bulg. Chem. Comm.*, **47**(4), 1053 (2015).
5. V. Hadjimitova, N. Avakumova, T. Traykov, *Luminescence*, **29**(S1), 60 (2014).
6. N. Avakumova, V. Hadjimitova, T. Traykov, *Luminescence*, **29**(S1), 60 (2014).
7. T. B. Chaston, R. N. Watts, J. Yuan, D. R. Richardson, *Clin. Cancer Res.*, **10**(21), 7365 (2004).
8. A. M. Pieczonka, A. Strzelczyk, B. Sadowska, G. Młostoń, P. Stączek, *Eur. J. Med. Chem.*, **64**, 389 (2013).
9. B. Nikolova-Mladenova, N. Halachev, R. Iankova, G. Momekov, D. Ivanov, *J. Arzneim.-Forsch.*, **61**(12), 714 (2011).
10. B. Nikolova-Mladenova, G. Momekov, D. Ivanov, A. Bakalova, *J. Appl. Biomed.*, in press (2017).
11. M. Zajac, A. Sobczak, W. Malinka, A. Redzicka, *Acta Pol Pharm.*, **67**(1), 27 (2014).
12. P. Kovarikova, M. Mokry, J. Klimes, K. Vavrova, *J. Pharm. Biomed. Anal.*, **40**, 105 (2006).
13. P. Kovarikova, Z. Mrkvickova, J. Klimes, *J. Pharm. Biomed. Anal.*, **47**, 360 (2008).
14. European Pharmacopoeia 7.0.
15. International Council for Harmonization, Expert Working Group, 2005. Validation of Analytical Procedures: Text and Methodology Q2(R1).
16. F. Kong, R. P. Singh, *J. Food Sci.*, **73**(5), 67 (2008).

ПРИЛОЖЕНИЕ НА RP-HPLC МЕТОД ЗА ОПРЕДЕЛЯНЕ НА ХИМИЧНАТА И ФИЗИОЛОГИЧНАТА СТАБИЛНОСТ НА ДВА НОВОСИНТЕЗИРАНИ МЕТОКСИПРОИЗВОДНИ БЕНЗОИЛХИДРАЗОНА

Б. И. Николова-Младенова^{1*}, Л. П. Пейкова², М. Б. Георгиева², Ал. Б. Златков²

¹ Катедра "Химия", Фармацевтичен факултет, Медицински университет - София, ул. Дунав 2, София 1000, България

² Катедра "Фармацевтична химия", Фармацевтичен факултет, Медицински университет - София, ул. Дунав 2, София 1000, България

Постъпила на 1 май 2017 г.; Коригирана на 26 май 2017 г.

(Резюме)

Проучването изследва стабилността на нови ароилхидразони, съдържащи хидразонова група, чувствителна към хидролиза, при условия близки до физиологичните. Два метокси-производни хидразона (3-метоксисалицилалдехид бензоилхидразон – 3M и 4-метоксисалицилалдехид бензоилхидразон – 4M) бяха разтворени в различни буферни разтвори (pH 2.0, 7.4 и 9.0) при 37 °C и аликвотни проби от тях бяха изтеглени на определени интервали от време. Стабилността на съединенията беше определена чрез използването на точен, селективен и валидиран RP-HPLC метод. Не бяха установени промени в структурите при pH = 7.4 и pH = 9.0, докато при pH = 2.0 хидразоните се хидролизират и се наблюдава появата на нови пикове, съответстващи на времето на задържане на хидролизните продукти. Резултатите показват химична стабилност на тестваните съединения при неутрално и нискоалкално pH и хидролизна чувствителност в силно киселинна среда.

In silico drug likeness and *in vitro* cytotoxic activity of some 3,5-disubstituted hydantoin and spirohydantoin

B. I. Nikolova-Mladenova*, A. G. Bakalova

Department of Chemistry, Faculty of Pharmacy, Medical University-Sofia, 2 Dunav Str., 1000 Sofia, Bulgaria

Received April 30, 2017; Revised May 28, 2017

Dedicated to Acad. Ivan Juchnovski on the occasion of his 80th birthday

The study presents the comparative evaluation of drug-like properties of six hydantoin and spirohydantoin derivatives. Some of the compounds were designed by replacement of the hydrogen atom from NH-3(hydantoin ring) with amine group, namely 3-amino- α -tetralonespiro-5'-hydantoin, 3-amino-2-indanespiro-5'-hydantoin, 3-amino-5-methyl-5-phenylhydantoin, 3-amino-5-methyl-5-(4-pyridyl)hydantoin. The other two compounds were spirohydantoin with S-containing cycloalkane rings - 3-thiolanespiro-5'-hydantoin and 4-thio-1H-tetrahydropyranspiro-5'-hydantoin. The drug applicable properties of the reported organic compounds, essential for drug pharmacokinetics in the human body, were estimated with the Lipinski's rule of five. The value of LogP and the residual parameters of drug likeness were estimated with the method based on group contributions. The approach is used only as an initial step in drug discovery, to find the main candidates with heartening properties for further amplification. Some of the compounds were further tested for *in vitro* cytotoxicity on four human tumor cell lines SKW-3, HL-60, LAMA-84 and EJ. The tested spirohydantoin exerted concentration dependent cytotoxic activity on all human tumor cell lines. The most significant cytotoxicity was observed for 4-thio-1H-tetrahydropyranspiro-5'-hydantoin which inhibited the viability of tested cells at low micromolar concentrations.

Key words: *in silico* evaluation; LogP values; Lipinski's rule; cytotoxic activity

INTRODUCTION

Hydantoin derivatives possess a variety of pharmacological properties. Depending on the nature of the substituents in the hydantoin ring they exhibited fungicidal, herbicidal, antitumor, anti-inflammatory, anti-HIV, antiarrhythmic, and antihypertensive activities [1-7]. Hydantoin like 5-hydroxyhydantoin and 5-methyl-5-hydroxyhydantoin serve as blocking lesions for DNA polymerases [8]. 5-(2-Phenyl-3-indolal)-2-thiohydantoin have shown inhibitory activity on several cancer lines organized into subpanels representing leukemia, melanoma, and cancer of lung, colon, kidney, ovary, breast, prostate and central nervous system by the National Cancer Institute anti-cancer drug screening program [9]. Some spirohydantoin derivatives showed antimicrobial, antifungal, anti-inflammatory, antidiabetic, antiepileptic, antiproliferative activities and can act as new psychotropic agents (antidepressants, anxiolytics and antipsychotics) [10].

Modification of known bioactive structures by including many active groups and substituents is widely used approach in discovery of new potential

drugs. As a result, the newly synthesized compounds tend to have higher molecular weight, high lipophilicity and low aqueous solubility which results in poor bioavailability. Another disadvantage in the development of novel "drug-like" compounds is the huge number of required *in vitro* and *in vivo* examinations. Through the last years, a lot of *in silico* methods were discovered which significantly reduce the number of *in vivo* studies required [11]. The *in silico* design allows the screening of compounds against potential targets and determines the most promising ones with applicable molecular weight, lipophilicity, hydrogen bond donors/acceptors, solubility, and other related properties. The lipophilicity is the main characteristic, affecting the membrane permeability and oral bioavailability of the compounds. An accepted measure of lipophilicity is LogP and compounds demonstrating LogP > 3.5 usually have poor aqueous solubility [12]. Decreasing of lipophilicity improves solvation potential by increasing solvent-solute interactions in aqueous media.

This paper presents the evaluation of *in silico* biological activity of six 3,5-disubstituted hydantoin and spirohydantoin. The important molecular properties were calculated to reveal how

* To whom all correspondence should be sent:
E-mail: boriananik@abv.bg

the incorporation of different substituents affects the lipophilicity of the compounds. Furthermore some of the derivatives were tested for *in vitro* cytotoxicity on a panel of four human tumor cell lines SKW-3, HL-60, LAMA-84 and EJ by MTT-dye reduction assay.

EXPERIMENTAL

Design of the compounds

Six substituted hydantoin and spirohydantoin derivatives were examined. 3'-amino- α -tetralonespiro-5'-hydantoin (**1**), 3'-amino-2-indanespiro-5'-hydantoin (**2**), 3-amino-5-methyl-5-phenylhydantoin (**3**) and 3-amino-5-methyl-5-(4-pyridyl)hydantoin (**4**) were designed by replacement of the hydrogen atom from NH-3 (hydantoin ring) with amine group. 3-thiolanespiro-5'-hydantoin (**5**) and 4-thio-1H-tetrahydropyranspiro-5'-hydantoin (**6**) were spirohydantoins with S-containing cycloalkane rings. All amino hydantoin derivatives (**1-4**) were synthesized by Davidson method with some modifications. The S-containing hydantoins (**5-6**) were prepared by interaction of thiolane-3-one and tetrahydro-1H-thiopyran-4-one with NaCN and (NH₄)₂CO₃ in aqueous ethanol. The obtaining and the characterization of the compounds by elemental analysis, IR, NMR spectra, mass spectral analysis, X-ray diffraction method etc. were described in our previously published articles [13-15].

Calculations of Molecular Characteristics

The drug applicable properties of the reported organic compounds, essential for drug pharmacokinetics in the human body, were estimated with the Lipinski's rule of five [16-17] which states that the most "drug-like" molecules have LogP ≤ 5 , molecular weight (M_w) ≤ 500 , number of hydrogen bond acceptors (O and N atoms) ≤ 10 and number of hydrogen bond donors (OH and NH groups) ≤ 5 . Molecular volume and molecular polar surface area (PSA) are also very useful parameters for prediction of drug transport properties. The polar surface area is defined as a sum of surfaces of polar atoms (usually oxygens, nitrogens and attached hydrogens) in a molecule. The number of rotatable bonds determines flexibility of the molecules. The value of LogP and the residual parameters of drug likeness, as well as the PSA, were reckoned on the method based on group contributions [18]. These have been obtained by fitting the values of the calculated LogP with

experimental LogP for a set of more than twelve thousand, mostly drug-like molecules. The percentage of absorption (% ABS) was estimated using the equation:

$$\% \text{ ABS} = 109 - (0.345 \times \text{PSA}).$$

Cell lines and Cytotoxicity assessment

The cell lines used in this study - SKW-3 (human T-cell leukemia, established from peripheral blood of a 61-year-old man with T-cell lymphocytic leukemia), HL-60 (acute myeloid leukemia, established from the peripheral blood of a patient with acute promyelocyte leukemia), LAMA-84 (human chronic myeloid leukemia, established from peripheral blood of a 29-year-old woman with chronic myeloid leukemia) and EJ (urinary bladder carcinoma, established from an invasive endometrioid adenocarcinoma of the uterine corpus in a 56-year-old patient) were purchased from the German Collection of Microorganisms and Cell Cultures. The cells were grown as a suspension-type cultures under standard conditions - RPMI 1640 liquid medium supplemented with 10% fetal bovine serum (FBS) and 2 mM L-glutamine, in cell culture flasks, housed at 37°C in an incubator "BB 16-Function Line" Heraeus with humidified atmosphere and 5% carbon dioxide. Cell cultures were maintained in logarithmic growth phase by supplementation with fresh medium two or three times weekly.

Cytotoxicity Assessment (MTT-dye Reduction Assay)

The cytotoxic activity of the tested compounds was assessed using the MTT [3-(4,5-dimethylthiazol-2-yl)-2,5-diphenyltetrazolium bromide] dye reduction assay as described by Mossman [19]. The method is based on the reduction of the yellow tetrazolium salt MTT to a violet formazan via the mitochondrial succinate dehydrogenase in viable cells. In brief, exponentially growing cells were seeded in 96-well flat-bottomed microplates (100 μ L/well at a density of 3.5×10^5 cells/mL for the adherent and 1×10^5 cells/mL for the suspension cell lines) and allowed to grow for 24 h prior the exposure to the studied compounds. Stock solutions of the organic compounds were dissolved in DMSO and diluted in RPMI-1640 growth medium. At the final dilutions the solvent concentration never exceeded 0.5%. Cells were exposed to the tested compounds for 72 h, whereby for each concentration a set of 8

separate wells was used. Every test was run in triplicate, i.e. in three separate microplates. After the incubation with the test compounds 10 μ L MTT solution (10 mg/mL in PBS) aliquots were added to each well. The microplates were further incubated for 4 h at 37°C and the MTT-formazan crystals formed were dissolved by adding 100 μ L/well 5% HCOOH in 2-propanol. Absorption of the samples was measured by an ELISA reader (Uniscan Titertec) at 580 nm. Survival fraction was calculated as percentage of the untreated control. The experimental data were processed using GraphPad Prizm software and were fitted to sigmoidal concentration/response curves. Cisplatin

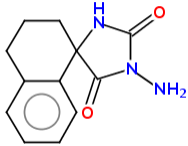
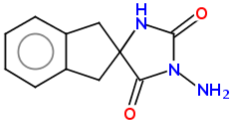
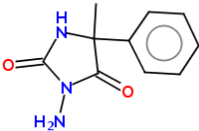
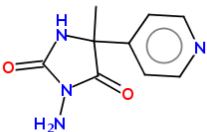
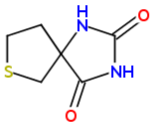
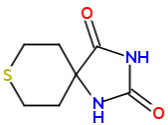
and melphalan were used as referent cytotoxic drugs throughout the pharmacological assay

RESULTS AND DISCUSSION

In silico Evaluation of Drug Likeness

The comparative evaluation of *in silico* biological activity of six 3,5-disubstituted hydantoin and spirohydantoin derivatives was presented. The compounds and their characteristics used for evaluation of drug similarity on the base of Lipinski's rule are presented in Table 1.

Table 1. Chemical structures and parameters of evaluation of the tested hydantoin and spirohydantoin derivatives with Lipinski's rule of five.

No	Structure	LogP <5	M _w <500	O,N <10	OH,N H <5	Rot. bond	Volume	TPSA (Å ²) <140	% ABS
1		0.99	231.25	5	3	0	203.71	75.43	82.98
2		0.41	217.23	5	3	0	186.91	75.43	82.98
3		0.59	205.22	5	3	1	180.71	75.43	82.98
4		-0.70	206.21	6	3	1	176.55	88.32	78.53
5		-0.35	172.21	4	2	0	138.76	58.20	88.92
6		-0.08	186.24	4	2	0	155.56	58.20	88.92

The calculations show that all derivatives observed boundary conditions of the "rule of Lipinski" and did not violate any of the listed criteria. LogP value is used in medicinal chemistry to predict the solubility of a potential drug

In general, spirohydantoins with S-containing cycloalkane ring have lower lipophilicity with negative LogP values. The LogP values of hydantoins ranged between -0.70 and 0.99. The replacement of benzene nuclei of (3) by pyridine nuclei in compound (4) notably reduces the LogP with more than 1 unit. All compounds possess low lipophilicity with values of LogP < 1, therefore they will have a good solubility in water and other polar liquids as blood and blood plasma. The molecular weight and molecular volume give information for the size of the molecules. The substituents slightly change the molecular weight but all derivatives are small drug-like molecules with M_w between 172 and 231. They are not very flexible as the number of rotatable bonds is between 0 and 1. The number of hydrogen bond donors and acceptors affects the value of polar surface area. All derivatives show a PSA of less than 140 Å², indicating a good permeability of the compounds in the cellular plasma membrane. Moreover the compounds demonstrated a PSA less than 90 Å² and thus are capable to penetrate the blood-brain barrier [20-22].

The *in silico* evaluation was used only as a first step in drug discovery, to find the leading candidates with encouraging properties for further amplification. The hydantoins, (2) and (3), with positive LogP and the spirohydantoins (5) and (6), with negative LogP values and lowest molecular weight were tested *in vitro* on four human tumor cell lines.

In Vitro Cytotoxicity

The derivatives, 3'-amino-2-indanespiro-5'-hydantoin (2), 3-amino-5-methyl-5-phenylhydantoin (3), 3-thiolanespiro-5'-hydantoin (5) and 4-thio-1H-tetrahydro-pyranspiro-5'-hydantoin (6) were tested for *in vitro* cytotoxicity. The cytotoxic potential of the compounds against the human leukemic cell lines SKW-3 (human T-cell leukemia), HL-60 (acute myeloid leukemia), LAMA-84 (human chronic myeloid leukemia) and EJ (urinary bladder carcinoma) was studied using the standard MTT-dye reduction assay for cell viability. Throughout the screening investigation the data about the compounds were compared with the referent agent cisplatin and the clinically

utilized antineoplastic drug melphalan (2-amino-3-[4-bis(2-chloroethyl) amino] phenylpropanoic acid). The corresponding IC₅₀ values obtained are shown in Table 2.

Table 2. Cytotoxicity of the compounds (2), (3), (5), (6) in some human tumor cell lines.

Compound	IC ₅₀ values (μM)			
	SKW-3 ^a	HL-60 ^b	LAMA-84 ^c	EJ ^d
2	-	> 200	> 200	-
3	-	> 200	> 200	-
5	114.0	> 200	174.5	115.2
6	92.6	180.9	101.1	143.5
cisplatin	11.4	8.7	10.2	16.9
melphalan	31.3	18.5	22.1	-

^aT-cell leukemia; ^bAcute myeloid leukemia; ^cHuman chronic myeloid leukemia; ^dUrinary bladder carcinoma

IC₅₀ values were calculated as concentrations of the tested compounds causing 50% decrease of cell survival. The hydantoins (2) and (3) showed lack of cytotoxic effects on tested cell lines. In contrast spirohydantoins (5) and (6) exerted concentration dependent cytotoxic activity on all human tumor cell lines. Probably the lower molecular weight and the lower lipophilicity affect positively the cytotoxicity. The most significant cytotoxicity was observed for the compound 4-thio-1H-tetrahydropyranspiro-5'-hydantoin (6), which inhibited the viability of tested cells at low micromolar concentrations.

CONCLUSION

Six 3,5-disubstituted hydantoin and spirohydantoin derivatives were studied for lipophilicity using the "rule of Lipinski". The compounds have a good solubility in water and other polar liquids as blood and blood plasma and a good permeability in the cellular plasma membrane. Four of them were tested *in vitro* on some human tumor cell lines in comparison with referent drugs cisplatin and melphalan. The tested spirohydantoins exerted concentration dependent cytotoxic activity on the used human tumor cell lines. The most significant cytotoxicity was observed for the compound 4-thio-1H-tetrahydropyranspiro-5'-hydantoin.

Acknowledgements: Financial support by the Medical University of Sofia (Council of Medical Science, Grant 51/27.05.2016) is gratefully acknowledged

REFERENCES

1. T. R. Rodgers, M. P. LaMontagne, A. Markovac, A. B. Ash, *J. Med. Chem.*, **20**(4), 591 (1977).
2. C. Carmi, A. Cavazzoni, V. Zuliani, A. Lodola, F. Bordi, P. V. Plazzi, *Bioorg. Med. Chem. Lett.*, **16**, 4021 (2006).
3. S. S. Hah, H. M. Kim, R. A. Sumbad, P. T. Henderson, *Bioorg. Med. Chem. Lett.*, **15**, 3627 (2005).
4. K. I. Ahmed, *Carbohydr. Res.*, **306**(4), 567 (1998).
5. R. N. Comber, R. C. Reynolds, J. D. Friedrich, R. A. Manguikian, R.W. Buckheit, J. J. W. Truss, et. al., *J. Med. Chem.*, **35**, 3567 (1992).
6. J. Knabe, J. Baldauf, A. Ahlhem, *Pharmazie*, **52**, 912 (1997).
7. J. C. Menendez, M. P. Diaz, C. Bellver, M. M. Sollhuber, *Eur. J. Med. Chem.*, **27**, 61(1992).
8. F-L. Yu, C. H. Schwalbe, D. J. Watkin, *Acta Cryst.*, **C60**: 714 (2004).
9. G. Ogrucildiz, I. Boz, O. Unsalan, *Opt. Spectrosc.*, **112**(5), 665 (2012).
10. L. K. Abdulrahman, M. M. Al-Mously, M. L. Al-Mosuli, K. K. Al-Azzawii, *Int. J. Pharm. Pharmac., Sci.*, **5**, 494 (2013).
11. V. H. Thomas, S. Bhattachar, L. Hitchingham, P. Zocharski, M. Naath, N. Surendran, C. L. Stoner, A. El-Kattan, *Exp. Opin. Drug Metab. Toxicol.*, **2**(4), 591 (2006).
12. K. A. Dehring, H. L. Workman, K. D. Miller, A. Mandagere, S. K. Poole, *J. Pharm. Biomed. Anal.*, **36**(3), 447 (2004).
13. A. Bakalova, R. Petrova, B. Shivachev, H. Varbanov, *J. Coord. Chem.*, **60**, 15, 1701 (2007).
14. H. Varbanov, R. Buyukliev, A. Bakalova, A. Roller, *Acta Cryst.*, **E65**, 953 (2009).
15. A. Bakalova, R. Buyukliev, G. Momekov, *J. Molec. Struct.*, **1091**, 118 (2015).
16. C. A. Lipinski, *Drug Disc. Today Technol.*, **1**(4), 337 (2004).
17. C. A. Lipinski, F. Lombardo, B.W. Dominy, P.J. Feeney, *Adv. Drug. Deliv. Rev.*, **46**(1-3), 3 (2002).
18. Molinspiration Cheminformatics, www.molinspiration.com. (2016).
19. T. Mosmann, *J. Immunol. Meth.*, **65**, 55 (1983).
20. R. M. Feng, *Curr. Drug. Metab.*, **3**, 647 (2002).
21. S. A. Hitchcock, L. D. Pennington, *J. Med. Chem.*, **49**(26), 7559 (2006).
22. D. F. Veber, S. R. Johnson, H.-Y. Cheng, B. R. Smith, K. W. Ward, K. D. Kopple, *J. Med. Chem.*, **45**, 2615 (2002).

IN SILICO ЛЕКАРСТВЕНО ПОДОБИЕ И IN VITRO ЦИТОТОКСИЧНА АКТИВНОСТ НА НЯКОИ 3,5-ДИЗАМЕСТЕНИ ХИДАНТОИНИ И СПИРОХИДАНТОИНИ

Б. И. Николова-Младенова*, А. Г. Бакалова

Катедра "Химия", Фармацевтичен факултет, Медицински университет - София, ул. Дунав 2, София 1000, България

Постъпила на 30 април 2017 г.; Коригирана на 28 май 2017 г.

(Резюме)

Изследването представя сравнителна оценка на лекарственото подобие на шест хидантоинови и спирохидантоинови производни. Някои от съединенията са получени чрез заместване на водородния атом от хидантоиновия пръстен (NH-3) с amino група, а именно 3-амино- α -тетралонспиро-5'-хидантоин, 3-амино-2-инданспиро-5'-хидантоин, 3-амино-5-метил-5-фенилхидантоин, 3-амино-5-метил-5-(4-пиридил)хидантоин. Другите две съединения са спирохидантоини със S-съдържащи циклоалканови пръстени - 3-тиоланспиро-5'-хидантоин и 4-тио-1H-тетраhydroпиран-спиро-5'-хидантоин. Важните свойства за лекарственото подобие на изследваните органични съединения, които влияят върху фармакокинетиката на съединенията в човешкото тяло, са определени с правилото на Липински. Стойността на LogP и останалите параметри на лекарствената прилика бяха оценени чрез метод, базиран на приноса на отделните групи. Теоретичният подход се използва само като начален етап в търсенето на нови лекарствени вещества. Някои от съединенията допълнително са изследвани *in vitro* за цитотоксична активност върху четири човешки туморни клетъчни линии - SKW-3, HL-60, LAMA-84 и EJ. Тестваните спирохидантоини проявяват концентрационно зависима цитотоксична активност върху всички човешки туморни клетъчни линии. Най-висока е цитотоксичността на 4-тио-1H-тетраhydroпиранспиро-5'-хидантоин, който инхибира жизнеспособността на изследваните клетки при ниски микромолярни концентрации.

Synthesis, physico-chemical investigation, DFT calculations and cytotoxic activity of palladium complexes with 3'-amino-4-thio-1H-tetrahydropyranspiro-5'-hydantoin

E. Cherneva^{1*}, R. T. Buyukliev¹, N. Burdzhiev², R. Michailova³, A. G. Bakalova¹

¹ Department of Chemistry, Faculty of Pharmacy, Medical University - Sofia, 2 Dunav Str., 1000 Sofia, Bulgaria

² Department of Organic Chemistry and Pharmacognosy, Faculty of Chemistry and Pharmacy, Sofia University, 1 James Bourchier Blvd., 1164 Sofia, Bulgaria

³ Department of Pharmacology, Pharmacotherapy and Toxicology, Faculty of Pharmacy, Medical University - Sofia, 2 Dunav Str., 1000 Sofia, Bulgaria

Received April 30, 2017; Revised May 26, 2017

Dedicated to Acad. Ivan Juchnovski on the occasion of his 80th birthday

A new organic compound - 3'-amino-4-thio-1H-tetrahydropyranspiro-5'-hydantoin and two new Pd(II) and Pd(IV) complexes were prepared and investigated by elemental analyses, IR and NMR spectral analyses. The structure geometries of the ligand and its palladium complexes were obtained using the hybrid DFT method. 6-311++G** set was used for the optimization of the geometry of the ligand, while for the Pd(II) and Pd(IV) complexes LANL2DZ basis set was utilized. According to the calculations data the geometry of the Pd(II) complex is square planar and of the Pd(IV) complex is distorted octahedral. The complexes were tested for cytotoxicity *in vitro* on five human tumor cell lines. The compounds tested exerted concentration dependent cytotoxic effects against the human tumor cell lines.

Key words: palladium complexes; amino-spiro-5'-hydantoins; DFT calculations; cytotoxic activity

INTRODUCTION

Platinum complexes are the most widely used drugs for the treatment of cancer. Cisplatin together with the second generation drug carboplatin and with the third generation drug oxaliplatin are widely used in worldwide [1]. All other clinically used platinum drugs have limited use in the world. Pt²⁺ and Pd²⁺ ions have similar chemical properties and modes of coordination forming square planar complexes [2,3]. The palladium compounds are more labile from both a thermodynamic and a kinetic point of view with respect to corresponding platinum compounds [4]. Palladium-based drugs can undergo a rapid hydrolysis before they reach the DNA target; this results in both a low antitumor activity or even inactivity and toxicity [5]. But some palladium complexes show significant antitumor activity in normal tumor cells and lower resistance of tumor cells to clinical treatments as well as lower side effects. Mononuclear palladium complexes with aromatic N-containing ligands, amino acid ligands, S-donor ligands, and P-containing ligands have respective qualities and properties due to the different structures and properties of the ligands [6].

The aim of this article is to synthesis, spectroscopic and theoretical study of new palladium complexes with 3'-amino-4-thio-1H-tetrahydropyranspiro-5'-hydantoin as carrier ligand. The spectroscopic study includes IR and NMR spectral investigation. The theoretical study comprehends the using of DFT calculations employing the B3LYP hybrid functional and 6-311++G** set for the ligand and LANL2DZ basis set for the palladium complexes. The ligand and the palladium complexes were investigated for cytotoxic activity on some human tumour cell lines.

MATERIALS AND METHODS

All chemicals were purchased from Fluka (UK) and Sigma-Aldrich. The newly synthesized Pd(II) and Pd(IV) complexes were characterized by elemental analyses, melting points, IR and NMR spectra. The elemental analyses were carried out on a "EuroEA 3000 – Single", EuroVectorSpA apparatus (Milan, Italy). Corrected melting points were determined, using a Bushi 535 apparatus (BushiLabortechnik AG, Flawil, Switzerland). The IR spectra were recorded on Thermo Scientific Nicolet iS10 spectrophotometer (Thermo Scientific, USA) in the range of 4000-400 cm⁻¹ as Attenuated Total Reflection Fourier Transform Infrared Spectroscopy (ATR-FTIR). The ¹H and ¹³C NMR spectra were recorded on a Bruker WM 500 (500

* To whom all correspondence should be sent:
E-mail: e.d.cherneva@gmail.com

MHz) spectrometer. Because the solubility of the complexes (1) and (2) is highly insufficient in DMSO, only ^1H NMR spectra of the palladium complexes were recorded. Intensities of reported IR bands are defined as br = broad, s = strong, m = medium, w = weak and sh- shoulder. The splitting of proton resonances in the ^1H NMR spectra is defined as s = singlet, bs = broad singlet, d = doublet, t = triplet, q = quartet and m = multiplet.

Synthesis of 3'-amino-4-thio-1H-tetrahydropyranspiro-5'-hydantoin

The synthesis and structure of 4-thio-1H-tetrahydropyranspiro-5'-hydantoin were described in details in our previously published work [7]. 4-thio-1H-tetrahydropyranspiro-5'-hydantoin (1.86 g) is dissolved in 20 mL 96% hydrazine-hydrate. The solution was heated with reflux condenser 4 hours. After that the mixture was poured in 50 mL of water and cooled below 0°C . After 24 hours the resulting crystals were filtered off and recrystallized from ethanol. IR (ATR): 3335 w, 3287 br, 3224 sh, 1781 m, 1707 s, 1609 m, 1411 w, 623 w. ^1H NMR (500 MHz, DMSO- d_6): 8.65 (s, 1H, NH); 4.66 (s, 2H, NH_2); 2.82-2.76 (m, 2H, $\text{CH}_2\text{-S(ax)}$); 2.62-2.59 (m, 2H, $\text{CH}_2\text{-S(eq)}$); 1.92-1.88 (m, 2H, $\text{CH}_2\text{-C(ax)}$); 1.75-1.72 (m, 2H, $\text{CH}_2\text{-C(eq)}$). ^{13}C NMR (125 MHz, DMSO- d_6): 174.6 (CO-2'); 156.0 (CO-4'); 58.5 (C-5'); 34.6 (C-3 + C-5); 23.0 (C-2 + C-6).

Synthesis of cis-bis(3'-amino-4-thio-1H-tetrahydropyranspiro-5'-hydantoin)-dichlorido palladium(II) – cis-[PdL₂Cl₂](1)

Two solutions of $\text{K}_2[\text{PdCl}_4]$ and 3'-amino-4-thio-1H-tetrahydropyranspiro-5'-hydantoin were prepared for the synthesis of the complex *cis*-[PdL₂Cl₂]. A 4 ml ethanol solution of the L (0.1344 g, 0.6137 mmol) was added dropwise to 5 ml aqueous solution of $\text{K}_2[\text{PdCl}_4]$ (0.0998 g, 0.3058 mmol) at constant stirring. The homogenous solution was stirred for 6 hours. A light-yellow product was obtained, filtered off and dried in a vacuum desiccator. IR (ATR): 3325 w, 3250 br, 3220 sh, 1775 m, 1720 s, 1604 m, 1412 w, 647 w. ^1H -NMR (500 MHz, DMSO- d_6): 8.65 (s, 1H, NH); 4.59 (bs, 2H, NH_2); 2.98-2.89 (m, 2H, $\text{CH}_2\text{-S(ax)}$); 2.76-2.70 (m, 2H, $\text{CH}_2\text{-S(eq)}$); 2.02-1.98 (m, 2H, $\text{CH}_2\text{-C(ax)}$); 1.83-1.79 (m, 2H, $\text{CH}_2\text{-C(eq)}$).

Synthesis of cis-bis(3'-amino-4-thio-1H-tetrahydropyranspiro-5'-hydantoin) dichlorido palladium(IV) – cis-[PdL₂Cl₄](2)

Two solutions of $\text{K}_2[\text{PdCl}_6]$ and 3'-amino-4-thio-1H-tetrahydropyranspiro-5'-hydantoin were prepared for the synthesis of the complex *cis*-[PdL₂Cl₄]. A 5 ml ethanol solution of the L (0.1106 g, 0.5050 mmol) was added dropwise to 5 ml aqueous solution of $\text{K}_2[\text{PdCl}_6]$ (0.1010 g, 0.2540 mmol) at constant stirring. The homogenous solution was stirred for 6 hours. A light-yellow product was obtained, filtered off, washed several times with water and dried in a vacuum desiccator. IR (ATR): 3331 w, 3251 br, 3220 sh, 1775 m, 1720 s, 1604 w, 1412 w, 648 w. ^1H NMR (500 MHz, DMSO- d_6): 8.62 (s, 1H, NH); 4.60 (bs, 2H, NH_2); 2.92-2.86 (m, 2H, $\text{CH}_2\text{-S(ax)}$); 2.70-2.66 (m, 2H, $\text{CH}_2\text{-S(eq)}$); 1.99-1.93 (m, 2H, $\text{CH}_2\text{-C(ax)}$); 1.81-1.75 (m, 2H, $\text{CH}_2\text{-C(eq)}$).

Computational details

All theoretical calculations were performed using the Gaussian 09 package [8] of programs. Optimization of the structures of the ligand 3'-amino-thio-1H-tetrahydropyranspiro-5'-hydantoin and possible conformers of Pd(II) and Pd(IV) complexes were carried out by DFT calculations, employing the B3LYP (Becke's three-parameter non-local exchange [9]) and Lee et al. correlation [10] hybrid functional and 6-311++G** set for the ligand and LANL2DZ basis set for the palladium complexes. The B3LYP hybrid functional [11, 12] was used because of its high accuracy. The basis set LANL2DZ was chosen to include the pseudopotential of the core electrons in atoms of heavy elements like platinum, palladium etc. and it is compatible with all other organic elements (C, N, H, O, Hal).

Cell culture conditions

The following cell lines were used for the experiments: (i) Hep-G2(Human Caucasian hepatocyte carcinoma, isolated from a liver biopsy of a male Caucasian aged 15 years, with a well differentiated hepatocellular carcinoma); (ii) REH(acute lymphoblastic leukemia, established from the peripheral blood of a 15-year-old North African girl with acute lymphoblastic leukemia in 1973); (iii) MDA-MB-231(human breast cancer cell line, established in 1973 from the pleural effusion of a 51-year-old woman with breast carcinoma); (iv) HL-60(acute myeloid leukemia,

established from the peripheral blood of a patient with acute promyelocyte leukemia); (v) EJ (human urinary bladder carcinoma). EJ cells (also designated MGH-U1) were originally isolated from a high grade (G3) invasive bladder carcinoma. These cell lines have been well validated in our laboratory as a proper test system for platinum agents. The EJ cell line has been obtained from the unit of Toxicology and Chemotherapy at the Deutsches Krebsforschungszentrum. The other cell lines were obtained from DSMZ German Collection of Microorganisms and Cell Cultures. Their DSMZ catalogue numbers are as follows: Hep-G2 (ACC 180), REH (ACC 22), MDA-MB-231 (ACC 73) and HL-60 (ACC 3).

Cytotoxicity assessment

Cytotoxicity of the compounds was assessed using the MTT [3-(4,5-dimethylthiazol-2-yl)-2,5-diphenyltetrazolium bromide] dye reduction assay as described by Mossman [13] with some modifications [14]. Exponentially growing cells were seeded in 96-well microplates (100 μL /well at a density of 3.5×10^5 cells/mL for the adherent and 1×10^5 cells/mL for the suspension cell lines) and allowed to grow for 24 h prior the exposure to the studied compounds. Stock solutions of the ligand and its Pd(II) and Pd(IV) complexes were freshly dissolved in DMSO and then promptly diluted in RMPI-1640 growth medium, immediately before

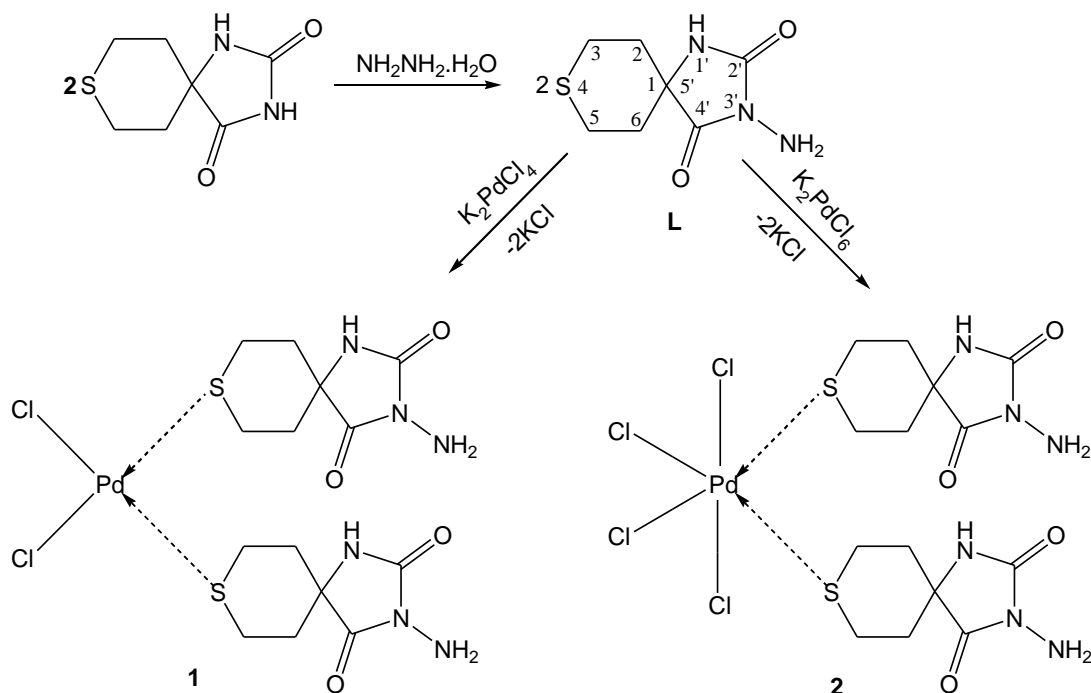
treatment of cells. At the final dilutions the solvent concentration never exceeded 0.5%. Cells were exposed to the tested compounds for 72 h, whereby for each concentration a set of 8 separate wells was used. Every test was run in triplicate, i.e. in three separate microplates. After incubation with the tested compounds MTT solution (10 mg/mL in PBS) aliquots were added to each well. The plates were further incubated for 4 h at 37°C and the formazan crystals formed were dissolved by adding 110 μL of 5% HCOOH in 2-propanol. Absorption of the samples was measured by an ELISA reader (UniscanTitertec) at 580 nm. Survival fraction was calculated as percentage of the untreated control. In addition IC₅₀ values were calculated from the concentration-response curves. The experimental data was processed using GraphPadPrizm software and was fitted to sigmoidal concentration/response curves *via* non-linear regression.

RESULTS AND DISCUSSION

Synthesis

The ligand and its new palladium complexes were prepared according to the Scheme 1.

The elemental analyses of the complexes (**1**) and (**2**) were in good agreement with the corresponding chemical formulas – *cis*-[Pd(C₇H₁₁N₃O₂S)₂Cl₂] and *cis*-[Pd(C₇H₁₁N₃O₂S)₂Cl₄]. The data from elemental analyses and some physical properties are summarized in Table 1.



Scheme 1. Synthesis of the ligand (**L**) and complexes (**1**) and (**2**).

Table 1. Physico-chemical data of the prepared compounds.

Compound	Molecular formula	MW	Yield ^a (%)	M.p. ^b (dec.) (°C)	Elemental analysis		
					% Calc.	% Found	
					C	H	N
Ligand	C ₇ H ₁₁ N ₃ O ₂ S	201	55	236	41.79 (42.00)	5.47 (5.81)	20.89 (21.03)
(1)	C ₁₄ H ₂₂ N ₆ O ₄ S ₂ Cl ₂ Pd	579.30	87	265	29.00 (30.38)	3.80 (4.16)	14.50 (14.49)
(2)	C ₁₄ H ₂₂ N ₆ O ₄ S ₂ Cl ₄ Pd	650.20	65	218	25.84 (26.05)	3.38 (3.68)	12.92 (12.70)

^aYield of analytically pure product; ^bMp of analytically pure product

IR spectral analysis

Due to the intermolecular hydrogen bonds of the ligand, the stretching vibrations of $\nu(\text{NH})$ and $\nu(\text{NH}_2)$ appear at the broad absorption band in the range of 3300 - 3150 cm^{-1} . The bands are slightly shifted to higher frequencies in the palladium complexes. Deformation vibrations of NH_2 and NH groups in the ligand at 1609 and 1411 cm^{-1} are not affected in the complexes (1604 cm^{-1} and 1412 cm^{-1} resp.) It proves that nitrogen atom from the NH_2 group is not participated in the coordination with metal ions. Upon the coordination of the sulphur atom to the metal ions the stretching vibration of the C-S bond is shifted from 623 cm^{-1} to 647 and 648 cm^{-1} respectively.

NMR spectral analysis

It is not possible to record ^{13}C NMR spectra of Pd (II) and Pd (IV) complexes due to their very poor solubility in DMSO- d_6 . In their proton NMR spectra, there is not visible shifting of N-NH₂ protons, which is proof for lack of complexation between metal cation and nitrogen from NH_2 group. NH-(1') chemical shift is not influenced. There is a shifting of CH₂ groups in the complexes in comparison with the metal-free ligand. Thus, in Pd(II) complex, chemical shifts of axial S-CH₂ protons are moved with approximately 0.15 ppm and equatorial ones are moved with 0.13 ppm. In CH₂-C(1) protons this difference is similar: 0.10 ppm for axial and 0.08 ppm for equatorial protons. In the Pd(IV) complex, the differences of chemical shifts of S-CH₂ protons are respectively 0.10 ppm for axial and 0.08 ppm for equatorial. For CH₂-C(1) protons the differences are 0.08 ppm for axial and 0.05 ppm for equatorial protons. Atom numbering is in accordance with Scheme 1.

Theoretical analysis

The optimized geometry of the ligand and the complexes **(1)**, **(2)** and atom numbering were shown on Figs.1-3.

Gas phase optimized geometry of the compounds were obtained at B3LYP hybrid functional and 6-311++G**set for ligand and LANL2DZ basis set for the Pd complexes. The theoretical calculations showed that the atoms in the ligand are lying in two planes oriented perpendicularly to each other as expected. The first one comprises the hydantoin fragment together with NH_2 group and the other – the tetrahydrothiopyran ring (Fig. 1). The angles around the Pd center suggest square planar coordination environment in the complex **(1)** and a distorted octahedral geometry in the complex **(2)** (Figs. 2, 3). Each complex has two molecules of the ligand bonded to the metal center through the sulfur atom. In both complexes ligand (**L**) is stretched above the plane formed by the metal ion, Cl₁, Cl₂, S₃, S₂₇ while the second one is beneath the plane.

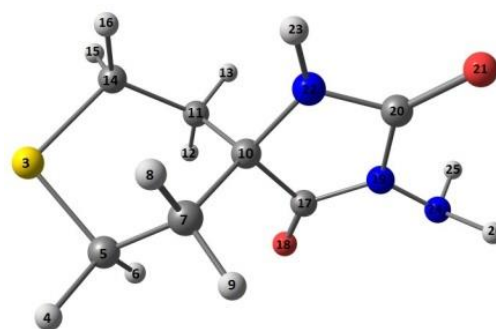


Fig. 1. Optimized geometry of the ligand, performed at B3LYP/6-311++G**set.

The coordination leads to small changes in geometry parameters (Table 2).

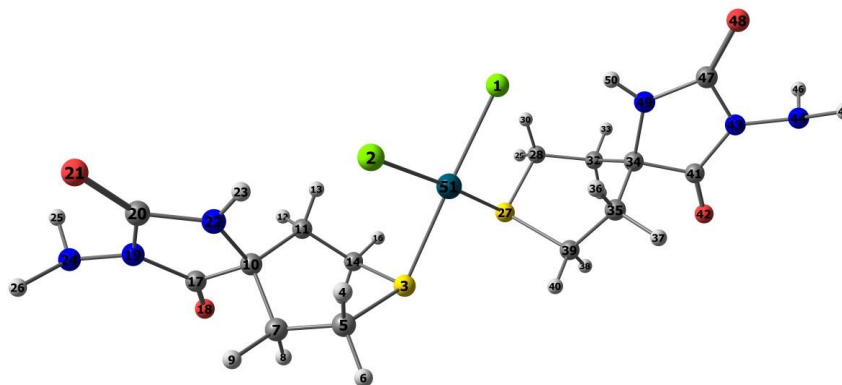


Fig. 2. Optimized geometry of the complex (1), performed at B3LYP/LANL2DZ basis set.

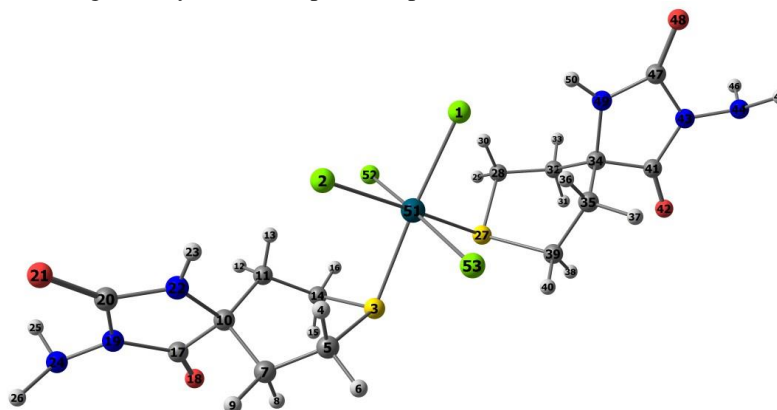


Fig. 3. Optimized geometry of the complex (2), performed at B3LYP/LANL2DZ basis set.

Table 2. Selected calculated geometry parameters.

Parameters	Ligand(L)	Complex (1)	Complex (2)
μ (D)	1.94	7.52	6.56
Bond lengths (Å)			
Pd-Cl ₁	-	2.39	2.41
Pd-Cl ₂	-	2.39	2.41
Pd-S ₃	-	2.48	2.52
Pd-S ₂₇	-	2.48	2.52
C ₅ -S ₃	1.84	1.92	1.92
C ₁₄ -S ₃	1.84	1.91	1.91
C ₂₈ -S ₂₇	-	1.92	1.92
C ₃₉ -S ₂₇	-	1.91	1.91
Angles (°)			
Cl ₁ -Pd-Cl ₂	-	89.8	88.4
S ₃ -Pd-Cl ₂	-	93.2	93.4
S ₂₇ -Pd-Cl ₁	-	93.2	93.4
S ₃ -Pd-S ₂₇	-	83.7	84.9
Dihedral angles (°)			
C ₅ -S ₃ -Pd-Cl ₂	-	-13.6	-33.0
C ₅ -S ₃ -Pd-S ₂₇	-	165.9	150.7
C ₁₄ -S ₃ -Pd-S ₂₇	-	-89.2	-103.2
C ₂₈ -S ₂₇ -Pd-Cl ₁	-	-13.6	-33.0
C ₃₉ -S ₂₇ -Pd-Cl ₁	-	91.1	72.9

In the complexes S-C bonds length increase than those in the ligand by 0.08 Å. For the Pd(II)

complex the two Pd-Cl bonds are equal, but they are slightly shorter than those calculated for Pd(IV) complex by 0.02 Å. It is similar for the Pd-S bonds, in complex (2) they are longer, which could be explained with the different coordination number. Bonds lengths are in agreement with those reported for the analogous complexes [15].

Pharmacological screening

The ligand (L) and the complexes (1,2) were tested for cytotoxic activity on five human tumor cell lines. The tested organic compound (L) and complexes (1,2) exerted cytotoxic effect after 72 h continuous exposure, whereby the individual chemosensitivity varied among the different cell lines. The complex (1) showed higher cytotoxic activity than the ligand (L) and complex (2) on REH cell line. The complex (2) presented better cytotoxic activity than the ligand and complex (1) on MDA-MB-231 and EJ cell lines. This can be explained by the fact that palladium complexes have a similar mechanism of action as platinum complexes. The results are summarized in Table 3.

Table 3. Cytotoxicity of the ligand (**L**) and complexes (**1,2**) in comparison with referent drug cisplatin in two human tumour cell lines.

Cell line	IC ₅₀ values(μM)				
	Hep-G2 ^a	REH ^b	MDA-MB- 231 ^c	HL-60 ^d	EJ ^e
Compound					
Ligand	> 200	> 200	> 200	> 200	> 200
Complex (1)	> 200	137.5	> 200	> 200	196.3
Complex (2)	> 200	> 200	188.7	> 200	144.1
Cisplatin	12.0	1.07	31.6	8.7	10.2

^ahuman hepatocyte carcinoma; ^bacute lymphoblastic leukemia; ^chuman breast cancer; ^dacute myeloid leukemia;

^ehuman urinary bladder carcinoma

CONCLUSION

A new organic compound - 3'-amino-4-thio-1H-tetrahydropyranspiro-5'-hydantoin and two new Pd(II) and Pd(IV) complexes were synthesized. The chemical formulas were investigated by elemental analyses, IR and NMR spectral analyses. The geometry of the ligand and its palladium complexes were optimized, using the DFT method, employing the B3LYP with 6-311++G** basis set for the ligand and LANL2DZ basis set for the complexes. From the results obtained the coordination mode of the ligand with the palladium ions is realized by the sulphur atom from the tetrahydrothiopyran ring. The compounds were tested for cytotoxic activity on five human tumour cell lines. According to the IC₅₀ values of the compounds, palladium complexes are more active than the ligand. Complex (**1**) is more active than complex (**2**) on REH tumour cell line, but complex (**2**) is more active than the complex (**1**) on MDA-MB-231 and EJ cell lines.

REFERENCES

1. T. C. Johnstone, K. Suntharalingam, S. J. Lippard, *Chem. Rev.*, **116**, 3436 (2016).
2. N. T. Abdel Ghani, A. M. Mansour, *J. Mol. Struct.*, **991**, 108 (2011).
3. S. Rubino, R. Busà, A. Attanzio, R. Alduina, Vita Di Stefano, M. A. Girasolo, S. Orecchio, L. Tesoriere, *Bioorg. Med. Chem.*, **25**, 2378 (2017).
4. E.J. Gao, K.H. Wang, X.F. Gu, Y. Yu, Y.G. Sun, W.Z. Zhang, H.X. Yin, Q. Wu, M.C. Zhu, X.M. Yan, *J. Inorg. Biochem.*, **101**, 1404 (2007).
5. M. Fanelli, M. Formica, V. Fusi, L. Giorgi, M. Micheloni, P. Paoli, *Coord. Chem. Rev.*, **310**, 41 (2016).
6. E. Gao, C. Liu, M. Zhu, H. Lin, Q. Wu, L. Liu., *Anti-Cancer Agents in Medicinal Chemistry*, **9**, 356, 2009.
7. A. Bakalova, B. Nikolova-Mladenova, R. Buyukliev, E. Cherneva, G. Momekov, D. Ivanov, *Chem. Pap.*, **70**, 93 (2016).
8. M. J. Frisch, G. W. Trucks, H. B. Schlegel, G. E. Scuseria, M. A. Robb, J. R. Cheeseman, G. Scalmani, V. Barone, B. Mennucci, G. A. Petersson, H. Nakatsuji, M. Caricato, X. Li, H. P. Hratchian, A. F. Izmaylov, J. Bloino, G. Zheng, J. L. Sonnenberg, M. Hada, M. Ehara, K. Toyota, R. Fukuda, J. Hasegawa, M. Ishida, T. Nakajima, Y. Honda, O. Kitao, H. Nakai, T. Vreven, J. A. Montgomery, Jr., J. E. Peralta, F. Ogliaro, M. Bearpark, J. J. Heyd, E. Brothers, K. N. Kudin, V. N. Staroverov, R. Kobayashi, J. Normand, K. Raghavachari, A. Rendell, J. C. Burant, S. S. Iyengar, J. Tomasi, M. Cossi, N. Rega, J. M. Millam, M. Klene, J. E. Knox, J. B. Cross, V. Bakken, C. Adamo, J. Jaramillo, R. Gomperts, R. E. Stratmann, O. Yazyev, A. J. Austin, R. Cammi, C. Pomelli, J. W. Ochterski, R. L. Martin, K. Morokuma, V. G. Zakrzewski, G. A. Voth, P. Salvador, J. J. Dannenberg, S. Dapprich, A. D. Daniels, O. Farkas, J. B. Foresman, J. V. Ortiz, J. Cioslowski, and D. J. Fox, Gaussian 09, Revision A.1, Gaussian Inc., Wallingford CT, 2009.
9. P. J. Stephens, F. J. Devlin, C. F. Chabalowski, M. J. Frisch, *J. Phys. Chem.*, **98**, 11623 (1994).
10. C. T. Lee, W. T. Yang, R. G. Parr, *Phys. Rev.*, **B**, **37**, 785 (1988).
11. A. Becke, *Phys. Rev. A*, **38**, 3098 (1988).
12. A. Becke, *J. Chem. Phys.*, **96**, 2155 (1992).
13. T. Mosmann, *J. Immunol. Methods*, **65**, 55 (1983).
14. S. Konstantinov, H. Eibl, M. Berger, *Br. J. Haemat.*, **107**, 365 (1999).
15. P. Bharati, A. Bharti, P. Nath, S. Kumari, N.K. Singh, M.K. Bharty, *Inorg. Chim. Acta*, **443**, 160 (2016)

СИНТЕЗ, ФИЗИКО-ХИМИЧНО ОХАРАКТЕРИЗИРАНЕ, ТЕОРЕТИЧНО ИЗСЛЕДВАНЕ И ЦИТОТОКСИЧНА АКТИВНОСТ НА ПАЛАДИЕВИ КОМПЛЕКСИ С 3'-АМИНО-4-ТИО-1Н-ТЕТРАХИДРОПИРАНСПИРО-5'-ХИДАНТОИН

Е. Чернева^{1*}, Р. Т. Буюклиев¹, Н. Бурджиев², Р. Михайлова³, А. Г. Бакалова¹

¹ Катедра "Химия", Фармацевтичен факултет, Медицински университет - София,
ул. „Дунав“ 2, 1000 София, България

² Катедра "Химия и фармакогнозия", Факултет по химия и фармация, Софийски Университет, бул. „Джеймс Баучер“ 1, 1164 София, България

³ Катедра по фармакология, фармакотерапия и токсикология, Фармацевтичен факултет, Медицински университет - София, ул. „Дунав“ 2, 1000 София, България

Постъпила на 30 април 2017 г.; Коригирана на 26 май 2017 г.

(Резюме)

Синтезирани и изследвани са едно ново органично съединение - 3'-амино-4-тио-1Н-тетраhydroпиранспиро-5'-хидантоин и два нови комплекса на Pd(II) и Pd(IV) чрез елементарен анализ, ИЧ и ЯМР спектрални методи. Геометрията на лиганда и на неговите паладиеви комплекси е изследвана с помощта на хибриден DFT метод. Използван е 6-311++G** базисен сет за оптимизиране геометрията на лиганда, докато за комплексите на Pd(II) и Pd(IV) е използван LANL2DZ базисен сет. Според изчислените данни, геометрията на комплекса на Pd(II) е квадратно планарна, а на комплекса на Pd(IV) е деформиран октаедър. Комплексите бяха тествани *in vitro* за цитотоксичност върху пет човешки туморни клетъчни линии. Новосинтезираните съединения проявяват концентрационно зависима цитотоксична активност върху изследваните човешки туморни клетъчни линии.

Chemical composition of propolis and American foulbrood: Is there any relationship?

M. Popova, D. Antonova, V. Bankova*

Institute of Organic Chemistry with Centre of Phytochemistry, Bulgarian Academy of Sciences, Acad. G. Bonchev str. Bl 9, 1113 Sofia, Bulgaria

Received May 03, 2017; Revised May 19, 2017

Dedicated to Acad. Ivan Juchnovski on the occasion of his 80th birthday

American foulbrood (AFB) is the most destructive brood diseases of honeybees, causing significant losses to beekeepers. Propolis is an important element of the bee colony social immunity and has demonstrated activity against the causative agent of AFB *Paenibacillus larvae*. However, knowledge on the relationship between propolis chemical composition and the health of the bee colony is still scarce. We studied by GC-MS the chemical profiles of propolis samples from healthy bee colonies and colonies with clinical symptoms of AFB. Healthy colonies produced propolis with higher content of balsam. Although the qualitative composition of all samples was the same, there were quantitative differences: propolis from healthy colonies contained much higher levels (statistically significant, $p < 0.01$) of ferulic acid and coniferyl benzoate, than the propolis from colonies with AFB. Our results are only preliminary, further research should be performed to clarify whether these differences are indeed related to the health of the colonies.

Key words: propolis; American foulbrood; GC-MS

INTRODUCTION

Propolis (bee glue) is a sticky material collected by honeybees from plants and used in the hive both as building material and chemical defense against infections. It is well known to possess diverse beneficial biological activities, such as antimicrobial, immunostimulating, antitumor, antiinflammatory, etc., and is widely used in health foods and over-the-counter preparations [1,2]. Recently, propolis has been attracting growing attention with respect to its potential to combat bee pathogens and the possibility to replace pesticides and antibiotics in beekeeping [3]. Several studies revealed the role of propolis as an important element of bees' "social immunity" [4]. Propolis extracts have been found to act against varroa mites [5,6], and extracts as well as some individual propolis constituents demonstrated *in vitro* significant activity against the causative agent of American Foulbrood [7,8]. American Foulbrood (AFB) is an infectious disease of honeybees caused by *Paenibacillus larvae*, a gram positive spore forming bacterium which is distributed worldwide [9]. AFB is considered the most destructive brood disease [10]. Some antibiotics are effective against *P.larvae* but antibiotics are poorly metabolized by honeybees, and their residues or those of their metabolites can be stable in honey for over a year

[11]. Moreover, the use of antibiotics in beekeeping is banned in the EU countries. The current most typical solution to deal with an AFB affliction is to burn the entire hive [12]. Thus, finding alternatives is an important issue in beekeeping.

Although propolis is known to be a defensive material against microorganisms, the knowledge on the relationship between propolis chemical composition and the health of the bee colony is still scarce. We have recently found a significant difference between the composition of propolis of colonies susceptible and resistant against *Varroa destructor* in France [13]. In the present study, we continued our attempt to clarify some aspects of the relationship propolis chemistry-colony health, studying the chemical composition of propolis (by GC-MS) and correlating it with health issues of the colonies, specifically the presence or lack of clinical symptoms of AFB.

EXPERIMENTAL

Propolis samples

Propolis samples were collected in Northern parts of Sweden by Prof. Ingemar Fries, Swedish University of Agricultural Sciences, Uppsala, Sweden. Five samples, 1 - 5 were collected from healthy colonies and three samples: 6, 7 and 8, from colonies with clinical symptoms of AFB.

* To whom all correspondence should be sent:
E-mail: bankova@orgchm.bas.bg

Propolis extraction

Frozen propolis (freezer) was grated and 1 g was dissolved in 30 mL 70% ethanol in a 100 mL flask and left for 24 h at room temperature. The extract was filtered and the extraction was repeated. The two extracts were combined and diluted to 100 mL with 70% ethanol in a volumetric flask.

Balsam percentage

From each crude sample, three parallel extracts with 70% ethanol were prepared as described above. Two mL of each were evaporated to dryness *in vacuo* until constant weight, and the percentages of balsam in the extracts were calculated as the ethanol soluble fraction. The mean of the three values was determined.

GC-MS analysis

5 mg of the propolis dry extract was dissolved in 50 μ L of dry (water-free) pyridine, and 75 μ L of bis(trimethylsilyl)-trifluoroacetamide (BSTFA) were added. The mixture was heated at 80 °C for 20 min and analyzed by GC-MS. The GC-MS analysis was performed with a Hewlett-Packard gas chromatograph 5890 series II Plus linked to a Hewlett-Packard 5972 mass spectrometer system equipped with a 30 m long, 0.25 mm i.d. and 0.5- μ m film thickness HP5-MS capillary column. The temperature was programmed from 60 to 300 °C at a rate of 5 °C/min, and a 10 min hold at 300 °C. Helium was used as a carrier gas at a flow rate of 0.8 mL/min. The split ratio was 1:10, the injector temperature 280 °C, the interface temperature 300 °C and the ionisation voltage 70 eV, as described elsewhere [13]. Identification of the compounds was performed using comparison of mass spectra and retention times of reference compounds (21 compounds), and the rest was tentatively identified using their mass spectra and retention time analysis. The semi-quantification was carried out by internal normalisation with the area of each compound. The addition of individual areas of the compounds corresponds to 100% area.

RESULTS AND DISCUSSION

We studied 5 healthy and 3 American foulbrood infected colonies, starting with the content of balsam. The extract with 70% ethanol is known as propolis balsam and contains the biologically active secondary plant metabolites of the resins collected

by bees [14]. The undissolved material consists mainly of waxes and mechanical impurities. The balsam percentage characterizes the amount of resins that bees have collected from plants and used to produce propolis. The balsam content of the studied samples is presented in Table 1. The mean value of the percentage of propolis balsam in the bee glue of colonies with AFB was significantly lower, compared to healthy colonies: 55% against 72% ($p = 0.008$). This is an indication that honeybees from infected colonies have allocated lesser resources to resin collection, than bees from healthy colonies. The reason for this fact however remains unclear.

By GC-MS, we were able to identify completely or tentatively over 70 individual compounds in the studied samples (data not shown). The chemical profiles of all eight samples were very similar qualitatively and quantitatively. They were all of practically pure trembling aspen (*Populus tremula*) origin and thus displayed a very low flavonoids concentration [15,16]. Instead, they contained high amounts of phenolic acids and their esters, and the typical aspen chemical markers: glycerol esters of substituted cinnamic acids. The chemical profiles of the studied samples can be represented in a concise manner by the percentage of the main structural groups of chemical constituents (Table 1): aromatic acids (major components [MC] coumaric, ferulic and benzoic acid), esters of aromatic acids (MC benzyl *p*-coumarate and coniferyl benzoate), flavonoids, including chalcones, flavones/flavonols, and flavanones/dihydroflavonols (no individual flavonoid was found in amount over 2%, most were under 1%); glycerol esters of cinnamic acids (MC 2-acetyl-1,3-di-*p*-coumaroylglycerol), and sugars, fatty acids and others (all minor components under 0.5% of total ion current)

The large amount of data obtained from the GC-MS studies were analyzed using Principle Component Analysis (PCA). The central idea of PCA is to reduce the dimensionality of a data set in which there are a large number of correlated variables, while retaining as much as possible the total information. We selected for PCA analysis the relative amounts of the main groups of chemical constituents of propolis: aromatic acids, phenolic acid esters, flavonoids, sugars, and others. The application of PCA produced a two-dimensional plot (Fig. 1) which covered 94% of the total variation and formed two distinct groups of samples: from healthy colonies and from colonies with clinical symptoms of AFB.

Table 1. Balsam content and chemical composition (compound groups, GC/MS, percentage of TIC) of propolis from healthy and AFB infected colonies

Compound	1	2	3	4	5	6	7	8
	CLEAN				American Foulbrood			
Balsam content	68,1	79,8	69,7	66,4	76,00	51,3	51	62,5
Aromatic acids	32,0	39,1	32,6	29,9	32,2	25,8	24,9	28,8
Esters of aromatic acids	28,1	26,7	29,6	17,4	25,2	12,7	16,5	19,0
Chalcones	1,4	0,6	1,3	5,2	2,8	3,5	1,8	1,3
Flavanones and dihydroflavonols	0,1	0	0,2	0,8	0,7	0,4	0,1	0,1
Flavones and flavonols	1,2	0,3	0,8	6,9	2,0	5,8	1,8	0,5
Glycerols esters of cinnamic acids	7,9	8,0	10,3	9,7	10,0	13,9	7,1	11,0
Sugars	7,1	5,0	3,7	7,2	4,2	6,1	17,1	17,4
Fatty acids	0,4	0,4	0,4	0,8	0,6	2,0	1,9	0,9
Others	3,6	3,7	3,4	4,7	4,1	4,0	3,6	4,0

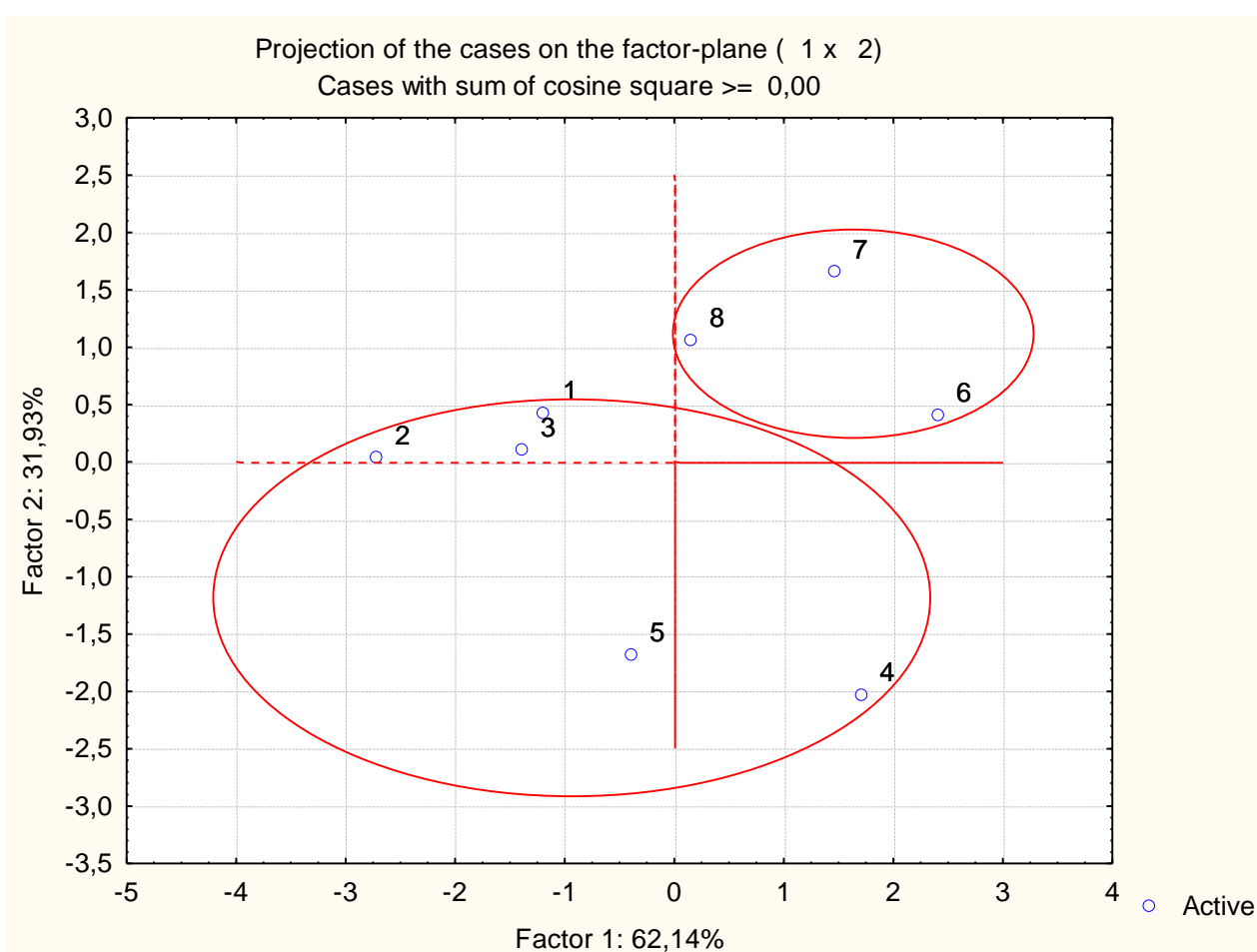


Fig. 1. PCA of propolis secondary metabolite profiles from healthy and AFB infected colonies. 1–5, samples from healthy colonies; 6–8, samples from infected colonies.

Looking into detail, it became evident that the chemical difference between propolis of healthy and AFB infected colonies are less obvious than the ones in balsam content. The most substantial distinction between the two groups was the content of two individual propolis constituents: propolis from healthy colonies contained much higher levels (statistically significant, $p < 0.01$) of ferulic acid and

the benzoic acid ester coniferyl benzoate, than the propolis from colonies with AFB (Fig. 2). Especially the concentration of coniferyl benzoate was 3 – 4 times higher. Recently we found considerable activity of some propolis flavonoids and phenolic acid esters against *P. larvae*. Those active compounds were isolated from propolis originating from *P. nigra* and are practically absent

in aspen (*P. tremula*) propolis. It is interesting to note that coniferyl alcohol and some of its esters have antibacterial activities [17,18].

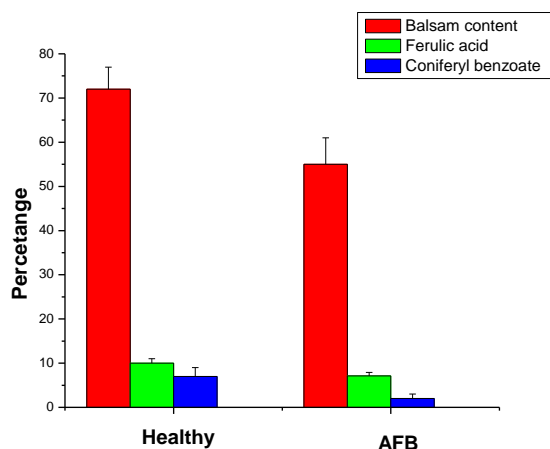


Fig. 2. Content of balsam, ferulic acid and coniferyl benzoate in propolis from healthy and AFB infected colonies.

CONCLUSIONS

Our results are only preliminary and they cannot give an unambiguous answer to the question about the possible relationship between propolis chemical composition and bee colony health. Nevertheless, they give some indications that such a relationship might be present. We established that chemical differences exist between propolis from colonies with AFB and healthy colonies. Further research should be performed to clarify whether these differences are indeed related to the health of the colonies. Special attention should be paid to the specific compounds that are more abundant in healthy colonies

Acknowledgements: This study was supported by the European Union-funded 7th Framework Project BEE DOC, Grant Agreement 244956 and the Bulgarian Science Fund, Contract DKOF 7RP

02/15. The authors are grateful to Prof. Ingemar Fries for providing the propolis samples.

REFERENCES

1. P. G. Pietta, C. Gardana, A. M. Pietta, *Fitoterapia*, **73**, S7 (2002).
2. J. M. Sforcin, V. Bankova, *J. Ethnopharmacol.*, **133**, 253 (2011).
3. A. Ariba, B. Babbay, *J. Entomol.*, **8**(10), 1 (2011).
4. R. S. Borba, K. K. Klyczek, K. L. Mogen, M. Spivak, *J. Exp. Biology*, **218**, 3689 (2015).
5. N. Damiani, N. J. Fernández, L. M. Maldonado, A. R. Álvarez, M. J. Eguaras, J. A. Marcangeliet, *Parasitol. Res.*, **107**, 31 (2010).
6. N. Drescher, A.-M. Klein, P. Neumann, O. Yañez, S. D. Leonhardt, *Insects*, **8**, 15 (2017).
7. K. Bilikova, M. Popova, B. Trusheva, V. Bankova, *Apidologie*, **44**, 278 (2013).
8. V. A. Isidorov, K. Buczek, G. Zambrowski, K. Miastkowski, I. Swiecicka, *Apidologie* (2017). doi:10.1007/s13592-016-0485-z.
9. E. Genersch, *J. Invertebr. Pathol.*, **103**, S10 (2010).
10. B. J. Morrissey, T. Helgason, L. Poppinga, A. Funfhaus, E. Genersch, G. E. Budge, *Environ. Microbiol.*, **17**, 1414 (2015).
11. W. Reybroeck, E. Daeseleire, H. F. De Brabander, L. Herman, *Vet. Microbiol.*, **158**, 1 (2012).
12. E. N. Grady, J. MacDonald, L. Liu, A. Richman, Z.-C. Yuan, *Microb. Cell Fact.*, **15**, 203 (2016).
13. M. Popova, M. Reyes, Y. Le Conte, V. Bankova, *Nat. Prod. Res.*, **28**, 788 (2014).
14. M. Popova, V. Bankova, D. Butovska, V. Petkov, B. Nikolova-Damyanova, A. G. Sabatini, G. L. Marcazzan, S. Bogdanov, *Phytochem. Anal.*, **15**, 235 (2004).
15. M. Popova, B. Trusheva, R. Khismatullin, N. Gavrilova, G. Legotkina, J. Lyapunov, V. Bankova, *Nat. Prod. Commun.*, **8**, 617 (2013).
16. V. A. Isidorov, L. Szczepaniak, S. Bakier, *Food Chemistry*, **142**, 101 (2014).
17. M. S. Barber, V. S. McConnell, B. S. DeCaux, *Phytochemistry*, **54**, 53 (2000).
18. Y. Yu, Q.-W. Zhang, Y.-T. Wang, S.-P. Li, *J. Chin. Pharm. Sci.*, **16**, 197 (2007).

СЪСТАВ НА ПРОПОЛИСА И АМЕРИКАНСКИ ГНИЛЕЦ: ИМА ЛИ ВРЪЗКА?

М. Попова, Д. Антонова, В. Банкова*

Институт по органична химия с Център по фитохимия, Българска академия на науките, ул. Акад. Г. Бончев, бл. 9, 1113 София

Постъпила на 3 май 2017 г.; Коригирана на 19 май 2017 г.

(Резюме)

Американският гнилец (АГ) е най-разрушителното заболяване, засягащо пчелното пило и причинява значителни загуби на пчеларските стопанства. Прополисът е важен елемент от социалния имунитет на пчелните семейства и е показал активност срещу причинителя на АГ *Paenibacillus larvae*. При все това познанията за връзката между химичния състав на прополиса и здравето на пчелното семейство са много ограничени. С помощта на газова хроматография – маспектрометрия ние изучихме химичните профили на прополиси от здрави кошери и от такива с клинични симптоми на АГ. Оказа се, че здравите пчелни семейства произвеждат прополис със значително по-високо съдържание на балсам. Макар че качественият състав на всички прополиси беше практически идентичен, бяха намерени количествени различия – прополисът на здравите пчелни семейства съдържаше по-висок процент (статистически значими различия, $p < 0.01$) ферулова киселина и кониферилбензоат в сравнение с болните от АГ. Получените резултати са само предварителни и са необходими по-нататъшни изследвания, за да се изясни дали тези различия наистина са свързани със здравето на пчелните семейства.

Phenolic constituents and antioxidant capacity of *Inula oculus-christi* from Bulgaria

A. Trendafilova^{1*}, M. Todorova¹, V. Ivanova¹, I. Aneva²

¹ Institute of Organic Chemistry with Centre of Phytochemistry, Bulgarian Academy of Sciences, Acad. G. Bonchev Str., bl. 9, 1113 Sofia, Bulgaria

² Institute of Biodiversity and Ecosystem Research, Bulgarian Academy of Sciences, 2 Gagarin Str., 1113 Sofia, Bulgaria

Received May 01, 2017; Revised May 30, 2017

Dedicated to Acad. Ivan Juchnovski on the occasion of his 80th birthday

The aim of this study was to evaluate the total phenolic and flavonoid contents and antioxidant capacity of different *Inula oculus-christi* extracts and to isolate the potential antioxidant compounds. The methanol extract from flowers showed the highest total phenolic (68.34±0.66 mg GAE/g DE) and flavonoid (42.63±0.75 mg CE/g DE) contents, and the highest antioxidant capacity compared to other extracts through DPPH and ABTS assays (1.167±0.007 and 0.582±0.010 mM TE/ g DE, resp.). Six flavones (apigenin, luteolin, hispidulin, nepetin, scutellarein-4'-methyl ether and jaceosidin), two flavone glucosides (nepetrin and hispidulin-7-O-glucoside), chlorogenic acid and 3,5-dicaffeoylquinic acid were isolated from the most active extract. Their structures were established by spectroscopic methods. With exception of hispidulin, all identified compounds were found for the first time in the studied species.

Key words: *Inula oculus-christi*; Asteraceae, phenolics; flavonoids; DPPH; ABTS assays

INTRODUCTION

Free radicals and reactive oxygen species are known to be the major reason for various chronic and degenerative diseases associated with oxidative stress, such as diabetes mellitus, inflammation, cancer, hypertension, atherosclerosis, cardiovascular and neurodegenerative diseases [1]. Recently, plants and plant-derived antioxidants (vitamins, flavonoids and phenolic acids) have received growing attention, since they play an important role as preventive agents against damage caused due to oxidative stress with long-term physiological benefits without any harmful side effects [2]. The genus *Inula* (Asteraceae) comprises about 100 species widespread in temperate regions of Europe, Africa and Asia. Many *Inula* species are frequently used in traditional medicines throughout the world and reports on their ethnopharmacological applications have been recently reviewed [3]. Plants belonging to this genus have shown to possess various biological activities - antitumor, antiinflammatory, antibacterial, antiproliferative, antitussive, antidiabetic and hepatoprotective, etc., which were attributed to the abundance of bioactive components mainly sesquiterpene lactones, phenolic acids, and flavonoids [3,4]. *I. oculus-*

christi is native to Iran, the Caucasus, Turkey, eastern Central Europe, Austria and the Balkan Peninsula [5]. Literature survey revealed several articles dealing mainly with the content of sesquiterpene lactones and their cytotoxic, antitumor and acetylcholinesterase activities [6-9]. A little is known about antioxidant properties of this species and the content of phenolic compounds. To the best of our knowledge, only hispidulin in *I. oculus-christi* from Serbia [6] and a DPPH scavenging activity of aqueous extracts of the species from Turkey [10] have been reported.

Continuing our research on *Inula* species, growing in Bulgaria we have focused our attention on the phenolic constituents and antioxidant capacity of *I. oculus-christi*.

EXPERIMENTAL

Plant material

Wild growing *I. oculus-christi* was collected in full flowering stage in July 2016 from western Rhodope Mts in Bulgaria. The plant was identified by Dr. Ina Aneva (Institute of Biodiversity and Ecosystem Research, BAS, Sofia). A voucher specimen (SOM 1360) has been deposited in the Herbarium of the Institute of Biodiversity and Ecosystem Research, BAS, Sofia, Bulgaria.

* To whom all correspondence should be sent:
E-mail: trendaf@orgchm.bas.bg

Extraction and isolation

Air-dried and powdered flowers (180 g) from *I. oculus-christi* were sequentially extracted with chloroform (2 x 2L) and methanol (2 x 1L) at room temperature for 24 hrs each. After filtration, the solvent from the combined extracts was evaporated under vacuum to give corresponding chloroform (7.4 g) and methanol (10.6 g) extracts. A portion of methanol extract (2.5 g) was dissolved in CH₃OH (15 ml) and centrifuged at 5800 rpm in order to remove insoluble parts. Clear methanolic solution was concentrated up to 5 ml and subjected to a Sephadex LH-20 column (equilibrated with CH₃OH) to give two main fractions A (1.5 g) and B (0.3 g). Fraction B was further applied to MPLC on LiChroprep RP-18 and eluted with increasing concentrations of CH₃OH in H₂O (20 to 80%). Further purification of selected fractions by MPLC (LiChroprep RP-18, CH₃OH/H₂O, 50:50) and/or prep. TLC (Silica gel, CHCl₃/CH₃OH, 10:1) yielded individual compounds: **1** (2.8 mg), **2** (5.3 mg), **3** (2.3 mg), **4** (12.3 mg), **5** (2.1 mg), **6** (2.2 mg), **7** (5.1 mg), **8** (4.6 mg), **9** (10.2 mg), and **10** (16.3 mg).

Chloroform and methanol extracts (0.41 and 0.49 g, respectively) from leaves of *I. oculus-christi* were obtained from 10 g of dry plant material using the same procedure. TLC comparison of the methanol extracts obtained from leaves and flowers was performed on Silica gel using Toluene/Dioxane/CH₃COOH (90:25:4) and EtOAc/HCOOH/CH₃COOH/H₂O (100:11:11:26) followed by spraying with NP/PEG reagent and UV visualization at 366 nm [11].

Determination of total phenolic content (TPC)

Total phenolic content (TPC) was measured using Folin–Ciocalteu method [12]. Gallic acid was used as a standard compound and TPC was expressed as mg gallic acid equivalents (GAE) per 1 g of dry extract.

Determination of total flavonoid content (TFC)

Total flavonoid content was measured using a colorimetric assay developed previously [13]. (+)-Catechin was used as a standard compound and TFC was expressed as mg catechin equivalents per 1 g of dry extract.

Determination of antioxidant capacity

DPPH (1,1-diphenyl-2-picrylhydrazyl) and ABTS (2,2'-azinobis (3)-ethylbenzthiazoline-6-

sulfonic acid) radical scavenging activities were determined according to the previously described methods [14]. Results were expressed as Trolox equivalent antioxidant capacity (mM Trolox equivalents per gram dry extract, mM TE/g DE), using calibration curve (absorption vs. concentration) of Trolox dissolved in methanol at different concentrations.

Statistical analysis

All data were reported as means ± standard deviation (SD) using at three independent measurements. Analysis of variance with a confidence interval of 95% was performed using MS Excel software.

RESULTS AND DISCUSSION

Phenolic compounds and flavonoids contribute to the overall antioxidant potential of plants, so that the chloroform and methanol extracts of the leaves and flowers of *I. oculus-christi* were analyzed for their total phenolic and flavonoid contents (Table 1). Total phenol content was expressed as mg GAE/g DE. The highest amount of phenolics was detected in methanol extracts. Leaves and flowers contained almost equal amounts of phenolics (68.34±0.66 and 66.95±1.13 mg GAE/g DE, respectively). Flavonoid content was expressed as mg catechin equivalents per gram of dry extract (mg CE/g DE) and its values varied widely for both solvents used and in the different plant parts. The methanol extract from flowers was the richest of in flavonoids (42.63±0.75 mg CE/g DE).

Antioxidant capacity of plants is commonly evaluated using more than one method to measure various oxidation products [15]. In this study, DPPH and ABTS^{•+} assays were used to estimate free radical scavenging properties of the studied extracts and the obtained results were expressed as mM Trolox equivalents per gram of dry extracts (mM TE/g DE (Table 1). Antioxidant capacity of the studied extracts measured by the DPPH method ranged from 0.023 to 1.167 mM TE/g DE. As shown in Table 1, methanol extract from flowers showed the highest radical scavenging activity, followed by methanol extract from leaves, while chloroform extract from leaves was almost inactive. Lower antioxidant capacities were determined by ABTS^{•+} assay and the values varied between 0.056 and 0.582 mM TE/g DE. The different antioxidant activity levels obtained from the assays probably due to the difference in the ability of antioxidant

compounds in the extracts to quench ABTS and DPPH free radicals in *in vitro* systems. A good correlation was observed between antioxidant capacity assessed with the DPPH and ABTS tests and phenolic content in studied extracts ($R^2 = 0.9726$ and 0.9684 , respectively).

The most active methanol extract obtained from flowers was worked up for isolation of the Sephadex LH-20 and further purification afforded apigenin (**1**) [16, 17], luteolin (**2**) [16-19], scutellarein-4'-methyl ether (**3**) [20], nepetin (**4**) individual compounds. Column chromatography on [18, 19], jaceosidin (**5**) [21], hispidulin (**6**) [19, 22], nepetrin (**7**) [22], hispidulin-7-glucoside (**8**) [23], chlorogenic acid (**9**) [24] and 3,5-dicaffeoylquinic acid (**10**) [24] (Fig. 1). The isolated compounds were identified using spectral data (UV, ^1H NMR and MS) compared with those published in the

literature. TLC comparison of the methanol extracts obtained from leaves and flowers of *I. oculus-christi* in the presence of the isolated compounds did not show significant qualitative differences.

The results described above showed that *I. oculus-christi* was characterized by the presence of flavones (**1-8**) and caffeoylquinic acid derivatives (**9** and **10**). Compounds **3-8** were substituted at C-6 with hydroxyl or methoxyl group. With exception of jaceosidin (**5**), all isolated flavonoids have been previously found in species of genus *Inula* such as *I. britannica*, *I. japonica*, *I. helenium*, *I. salsoides*, *I. helenium*, *I. viscosa*, *I. germanica*, etc. [3, 4, 25, 26]. Mono- and dicaffeoylquinic acid derivatives are widespread in the plant kingdom including *Inula* species. Phenolic acids **9** and **10** have been detected previously in *I. viscosa*, *I. britannica*, *I. helenium*, *I. cappa*, etc. [3, 4]. It is worth also to

Table 1. Total phenolic content (TPC), total flavonoid content (TFC) and antioxidant capacity (ABTS and DPPH assay) of different *I. oculus-christi* extracts.

Sample	Extract	TPC [mg GAE/g DE]	TFC [mg CE/g DE]	Antioxidant capacity [mM TE/g DE]	
				ABTS	DPPH
leaves	CHCl ₃	5.48±0.62 ^a	4.90±0.16 ^a	0.056±0.003 ^a	0.023±0.001 ^a
flowers	CHCl ₃	18.31±1.63 ^b	16.08±1.10 ^b	0.105±0.003 ^b	0.076±0.002 ^b
leaves	MeOH	66.95±1.13 ^c	19.12±1.34 ^c	0.470±0.009 ^c	0.981±0.003 ^c
flowers	MeOH	68.34±0.66 ^c	42.63±0.75 ^d	0.582±0.010 ^d	1.167±0.007 ^d

Values are means ± SD. Different letters in same columns are significantly different at $p < 0.05$

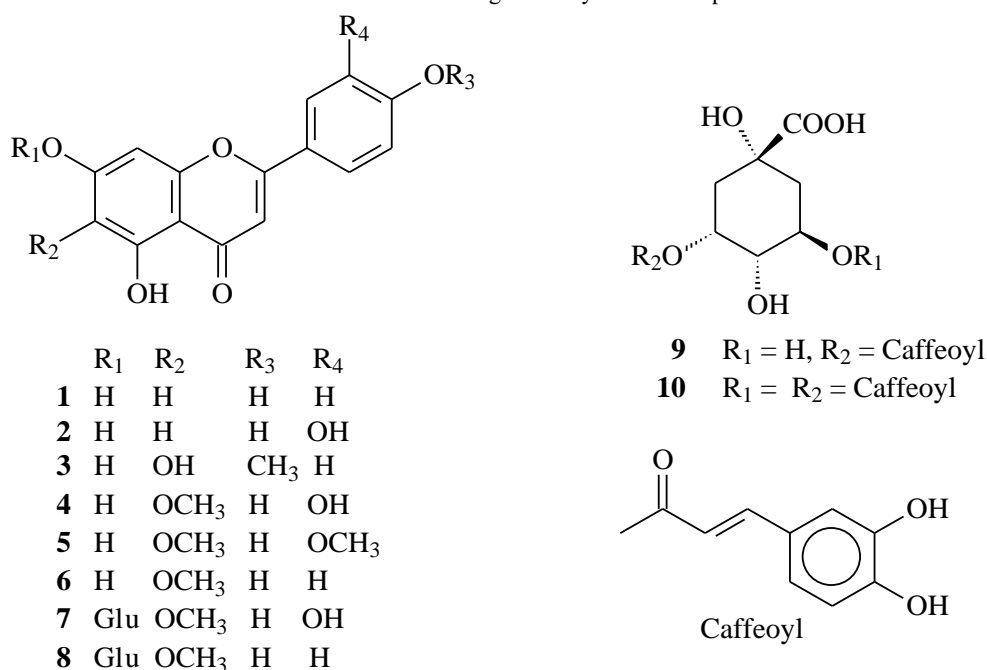


Fig. 1. Structures of the isolated compounds

mention that besides hispidulin (7) [6] all other isolated compounds were registered for the first time in *I. oculus-christi*.

CONCLUSION

The highest antioxidant capacity of the methanol extract obtained from flowers of *I. oculus-christi* could be attributed to the high content of phenolic components such as caffeoylquinic acid derivatives and flavonoids. Moreover, the domination of C-6 substituted flavonoids in *I. oculus-christi* is in accordance with the known flavonoid patterns of *Inula* species, i.e. they could be assumed as chemotaxonomic markers.

Acknowledgements: This work was supported by the National Science Fund, Ministry of Education and Science, Bulgaria, Project DN 09/11.

REFERENCES

1. J. M. McCord, *Am. J. Med.* **108**, 652 (2000).
2. S. Alok, S.K. Jain, A. Verma, M. Kumar, A. Mahor, M. Sabharwal, *Asian Pac. J. Trop. Biomed.*, **4**, 78 (2014).
3. A. M. L. Seca, A. Grigore, D. C. G. A. Pinto, A. M. S. Silva, *J. Ethnopharmacol.*, **154**, 286 (2014).
4. A. M. L. Seca, D. C. G. A. Pinto, A. M. S. Silva, *Chemistry & Biodiversity*, **12**, 859 (2015).
5. http://en.hortipedia.com/wiki/Inula_oculus-christi
6. V. Vajs, M. Neveščanin, S. Macura, N. Juranić, N. Menković, S. Milosavljević, *Fitoterapia*, **74**, 508 (2003).
7. M. Mosaddegh, M. H. Moghadam, S. Ghafari, F. Naghibi, S.N. Ostad, R.W. Read, *Nat. Prod. Commun.*, **5**, 511 (2010).
8. M. H. Moghadam, F. Naghibi, A. Atoofi, M. A. Rezaie, M. Irani, M. Mosaddegh, *Z. Naturforsch.*, **68c**, 108 (2013).
9. H. Hajimehdipoor, M. Mosaddegh, F. Naghibi, A. Haeri, M. Hamzeloo-Moghadam, *An. Acad. Bras. Cien.*, **86**, 801 (2014).
10. S. Berk, B. Tepe, S. Arslan, *Afr. J. Pharm. Pharmacol.*, **5**, 1695 (2011).
11. H. Wagner, S. Bladt, *Plant Drug Analysis. A Thin Layer Chromatography Atlas. Second Edition*, Springer-Verlag, Brooklyn, New York, 1996.
12. K. M. Yoo, Ch. H. Lee, H. Lee, B. K. Moon, Ch. Y. Lee, *Food Chem.*, **106**, 929 (2008).
13. J. Zhishen, T. Mengcheng, W. Jianming, *Food Chem.*, **64**, 555 (1999).
14. A. Marchev, I. Ivanov, P. Denev, M. Nikolova, V. Gochev, A. Stoyanova, A. Pavlov, V. Georgiev, *J. BioSci. Biotechnol.*, **4**, 219 (2015).
15. K. Schlesier, M. Harwat, V. Böhm, R. Bitsch, *Free Radic Res.*, **36**, 177 (2002).
16. T. Fossen, Ø. M. Andersen, in: *Flavonoids – Chemistry, Biochemistry and Applications*, Ø. M. Andersen, K. R. Markham (eds.), Taylor & Francis, USA (2005).
17. K. R. Markham, H. Geiger, in: *The Flavonoids - Advances in Research 1986-1990*, J. B. Harborne (ed.), Chapman and Hall, London (1993).
18. N. Bai, Z. Zhou, N. Zhu, L. Zhang, Z. Quan, K. He, Q. Y. Zheng, C.-T. Ho, *J. Food Lipids*, **12**, 141 (2005).
19. G. Flamini, E. Antognoli, I. Morelli, *Phytochemistry*, **57**, 559 (2001).
20. H. Sabina, R. Aliya, *Pak. J. Bot.*, **41**, 1927 (2009).
21. L. Hammoud, R. Seghiri, S. Benayache, P. Mosset, A. Lobstein, M. Chaabi, F. León, I. Brouard, J. Bermejo, F. Benayache, *Nat Prod Res.*, **26**, 203 (2012).
22. S. Shi, Y. Ma, Y. Zhang, L. Liu, Q. Liu, M. Peng, X. Xiong, *Sep. Puri. Technol.*, **89**, 225 (2012).
23. I. Fernandez, B. Garcia, J. R. Pedro, A. Varea, *Phytochemistry*, **30**, 1030 (1991).
24. H. Morishita, H. Iwahashi, N. Osaka, R. Kido, *J. Chromatography A*, **315**, 253 (1984).
25. E. Wollenweber, M. Dörr, H. Fritz, K. M. Valant-Vetschera, *Z. Naturforsch.*, **52c**, 137 (1997).
26. E. Wollenweber, M. Christ, R. H. Dunstan, J. N. Roitman, J. F. Stevens, *Z. Naturforsch.*, **60c**, 671 (2005).

ФЕНОЛНИ СЪЕДИНЕНИЯ И АНТИОКСИДАНТЕН КАПАЦИТЕТ НА *INULA OCULUS-CHRISTI* ОТ БЪЛГАРИЯ

А. Трендафилова^{1*}, М. Тодорова¹, В. Иванова¹, И. Анева²

¹ *Институт по органична химия с Център по фитохимия, Българска академия на науките, ул. "Акад. Г. Бончев", бл. 9, 1113 София, България*

² *Институт по биоразнообразие и екосистемни изследвания, Българска академия на науките, ул. "Гагарин" 2, 1113 София, България*

Постъпила на 1 май 2017 г.; Коригирана на 30 май 2017 г.

(Резюме)

Целта на това изследване е да се определи тоталното фенолно и флавоноидно съдържание и антиоксидантния капацитет на различни екстракти от *Inula oculus-christi*, както и да се изолират потенциалните антиоксидантни съединения. Метанолният екстракт получен от цветовете на растението показва най-високо тотално съдържание на фенолни съединения (68.34 ± 0.66 mg GAE/g DE) и флавоноиди (42.63 ± 0.75 mg CE/g DE) и най-висок антиоксидантен капацитет спрямо DPPH and ABTS радикали (1.167 ± 0.007 and 0.582 ± 0.010 mM TE/g DE, съответно). Шест флавона (апигенин, лутеолин, хиспидулин, непетин, скутелареин-4'-метил етер и яйцеозидин), два флавонови глюкозида (непетрин и хиспидулин-7-О-глюкозид), хлорогенова и 3,5-дикафеоилхинова киселини бяха изолирани от най-активния екстракт. Тяхната структура е определена с помощта на спектрални методи. С изключение на хиспидулин, всички идентифицирани съединения се откриват за първи път в изследваното растение.

IR study on the electrochemical reduction of nimesulide

S. Stoyanov*, D. Yancheva, A. Kosateva

Department of Structural Organic Analysis, Institute of Organic Chemistry with Centre of Phytochemistry,
Bulgarian Academy of Sciences, Acad. G. Bonchev Str., build. 9, 1113 Sofia, Bulgaria

Received May 01, 2017; Revised May 31, 2017

Dedicated to Acad. Ivan Juchnovski on the occasion of his 80th birthday

The electrochemical reduction of the nonsteroidal anti-inflammatory drug nimesulide, N-(4-nitro-2-phenoxyphenyl)-methanesulfone anilide, was performed in DMSO-d₆ solution and the IR spectral changes arising from the conversion were monitored. The spectral studies showed that in these conditions, electrochemical reduction leads to considerable decrease of the N-O and S-O stretching frequencies, increase of the C-NO₂ stretching frequency and disappearance of $\delta(\text{N-H})$. Based on comparison with theoretically predicted spectra of possible reduction products, the observed changes were attributed to the generation of dianion radical of nimesulide. The IR frequency shifts indicated that essential structural changes in the nitro, sulfonamide group and the phenyl ring connecting them have occurred as a result of the reduction. NBO charge and spin density calculations showed that 71% of the spin density is localized into the nitro group of the dianion radical, whereas 87% of the anionic charge is concentrated into the sulfonamide fragment.

Key words: nimesulide; nitro reduction; electrochemical reduction; IR spectroscopy; dianion radical

INTRODUCTION

N-(4-nitro-2-phenoxyphenyl)-methanesulfone anilide (**1**) is a nonsteroidal anti-inflammatory drug (NSAID) that has potent analgesic, anti-inflammatory and antipyretic activities on oral and rectal administration [1]. It is a preferential cyclooxygenase-2 (COX-2) inhibitor hence inhibits the synthesis of destructive prostaglandins and spares cytoprotective prostaglandins [2]. In addition, some studies had mainly attributed the selective inhibition of COX-2 and the anti-inflammatory effect of nimesulide to its radical scavenger behaviour, which may be explained by the presence of a methanesulfonamide group that has strong interactions with the COX-2 enzyme [1,3].

Nimesulide as other nitroaromatic drugs, has been associated with rare and unpredictable but serious hepatic adverse reactions [4,5]. What the nitroaromatic drugs have in common is their potential to undergo multistep nitroreductive bioactivation (6-electron transfer) that produces the potentially hazardous nitroanion radical, nitroso intermediate, and N-hydroxy derivative. These intermediates have been associated with increased oxidant stress and targeting of nucleophilic residues on proteins and nucleic acids [5]. It was shown that in humans nimesulide is oxidatively metabolized to 4'-hydroxynimesulide but also nitroreduced to the amine (with subsequent conjugation) [6,7].

However, the role of the reactive intermediates, resulting from the transformation could not be clarified, presumably due to their short life-time and inability to detect them by conventional analysis of metabolites [8]. In addition, it is not known which nitroreductase(s) play a role in these reactions. In rats, nimesulide was reduced to its amino metabolite, similar to humans [9]. Interestingly, anaerobic incubation increased the nitroreductive pathway, while the formation of 4'-hydroxylated nimesulide (CYP-mediated and therefore oxygen-dependent) was completely blocked. Under anaerobic conditions, the nitroreductive pathway is enhanced, while the formation of 4'-hydroxylated nimesulide, which is mediated by CYP in presence of oxygen, is blocked [5,9]. Given the complexity of the multiple competing reactions, it was suggested that the imbalance between the oxidative and reducing pathways of nimesulide and the relative abundance of molecular oxygen might be the crucial starting events in the pro-toxic processes in the liver [5].

The redox behaviour of nimesulide was previously studied by cyclic voltametry in efforts to understand its metabolism and mechanism of hepatotoxicity [10-12]. These electrochemical measurements showed that the reduction of nimesulide is strongly dependent on the nature of the media, following different reduction behavior. It was demonstrated that a stable free radical product was successfully electrogenerated in mixed

* To whom all correspondence should be sent:
E-mail: S_Stoyanov@orgchm.bas.bg

media, containing DMF(60%) and citrate buffer (40%), while in protic mixture of Britton Rhobinson buffer (70%) and KCl-ethanol solution (30%) a radical species could be observed only in strong alkaline media (pH 12) [12]. In protic medium at pH 9, nimesulide was converted directly to hydroxylamine [12].

Monitoring of the IR spectral changes in the course of electrochemical reduction of nimesulide offers a convenient way to complement the information gathered by the cyclovoltametric studies. Earlier studies has proven that the structural changes arising from the conversion of various organic carbonyl, nitrile and nitro compounds can be reliably described based on the observed shifts of their characteristic IR absorptions, especially when supported by theoretical computations [13-23]. Herein we present our study on the IR spectral and structural changes related to the electrochemical reduction of nimesulide.

EXPERIMENTAL AND COMPUTATIONS

Nimesulide (99%), tetrabutylammonium bromide (99%) and spectral quality DMSO-d₆ were purchased from Sigma-Aldrich Co. All spectra were measured on a Bruker Tensor 27 FT spectrometer by accumulating 64 scans at 2 cm⁻¹ resolution. The electrochemical transformation of nimesulide was performed in a special CaF₂ cell with platinum electrodes, filled with 0.1 M solution of nimesulide in DMSO-d₆ and equavimolar amount of tetrabutylammonium bromide. 4.5 V voltage was applied, and the spectra were measured in 10 minutes interval. The measurements were carried out for 75 min to gain maximum conversion. After that the polarity of electrodes was reversed and the measurements continued for the same interval.

All quantum chemistry calculations were performed using Gaussian 09 package of programs [24]. Geometry and vibrational frequencies of the species studied were performed by an analytical gradient technique without any symmetry constraint. All the results were obtained using the density functional theory (DFT), employing the B3LYP (Becke's three-parameter non-local exchange correlation) functional [25], 6-311++G** and 6-311++G(2df,2dp) basis sets. Incorporation of DMSO solvent was performed by the Integral Equation Formalism of Polarizable Continuum Model (IEFPCM) [26,27]. The stationary points found on the potential energy hypersurfaces for

each structure were characterized using the standard harmonic vibrational analysis. A standard least-squares program has been used to calculate single parameter regression indices. The absence of imaginary frequencies confirmed that the stationary points corresponded to local minima on the potential hypersurfaces.

RESULTS AND DISCUSSION

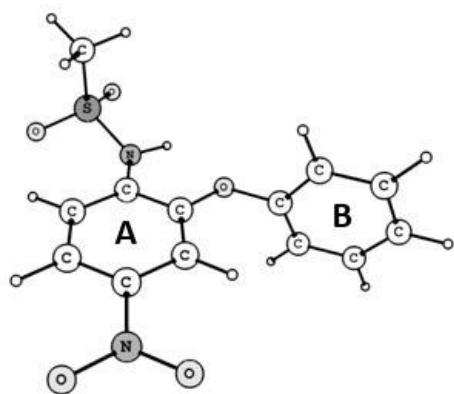
The IR spectral measurements during electrochemical reduction are typically performed in DMSO-d₆ solution with tetrabutylammonium bromide as electrolyte salt [13-23]. In these conditions it is expected that the radical anion product will be generated and stabilized in measurable amounts. In order to achieve an accurate and reliable description of the changes resulting from the electrochemical reduction of nimesulide, several initial studies were done prior the IR measurements:

- (i) Optimization of the molecular structure of nimesulide and possible reduction products,
- (ii) Assignment of the characteristic IR bands of nimesulide in DMSO-d₆ solution,
- (iii) Prediction of the IR spectra of possible reduction products.

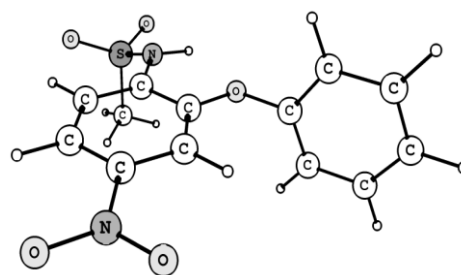
Having in mind the strong dependence of the reduction behavior on the nature of the media, we took into account a radical anion resulting from one-electron reduction (**2**) and a dianion radical resulting from one-electron reduction accompanied by deprotonation (**3**) in the analysis of possible reduction products.

Optimization of the molecular structure of nimesulide and possible reduction products

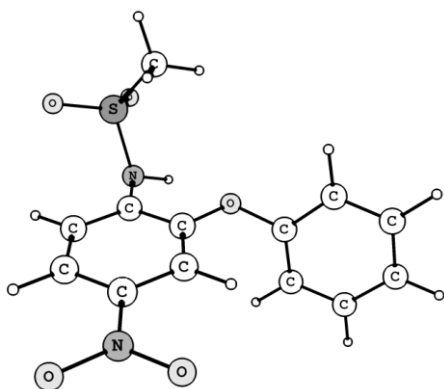
X-ray studies have reported three polymorphic forms of nimesulide, which are distinguished by different steric positions of the sulfonamide fragment and ring B [28-31]. Our computations showed that nimesulide has two stable conformations in DMSO solution differing by the torsion angle of the sulfomethyl group (Figure 1). In both forms the nitro and amino group lie in the plane of benzene ring A. Ring B lies in another plane with dihedral angle 77° towards ring A. The structure is stabilized by formation of an intramolecular hydrogen bond between the sulfonamide N-H and the phenoxy O-atom. The sulfomethyl group might be above (**1a**) or below (**1b**) the plane of benzene ring A. The two forms give indiscernible IR spectra.



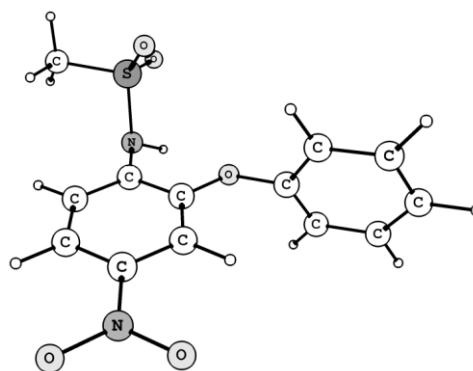
Nimesulide molecule **1a**



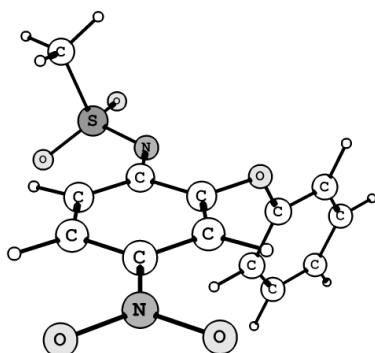
Nimesulide molecule **1b** ($\Delta E = + 0.003 \text{ kJ.mol}^{-1}$)



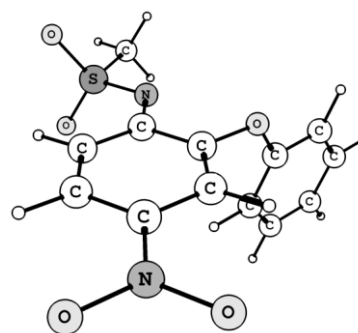
Radical anion **2a**



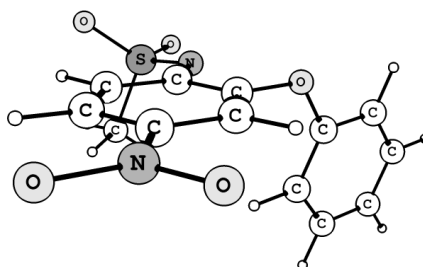
Radical anion **2b** ($\Delta E = + 4.97 \text{ kJ.mol}^{-1}$)



Dianion radical **3a**



Dianion radical **3b** ($\Delta E = + 0.21 \text{ kJ.mol}^{-1}$)



Dianion radical **3c** ($\Delta E = + 0.32 \text{ kJ.mol}^{-1}$)

Fig. 1. Different possible conformers of nimesulide molecule **1**, its radical-anion **2**, and dianion-radical **3**, computed at 6-311++G** theory level.

The conformational flexibility of the radical species is also considerable as can be seen by the small energy differences between their conformers. Two stable conformations of radical anion **2** were found (Figure 1) resembling closely those of the neutral nimesulide. The theoretical data for dianion radical **3** showed the presence of at least three conformers, which are characterized by very low energy differences (Figure 1).

Assignment of the characteristic IR bands of nimesulide in DMSO-d₆ solution

The strongest and most characteristic bands of nimesulide were observed in the 1700-1100 cm⁻¹ region (Figure 2). The bands at 1523 and 1340 cm⁻¹ (Table 1) can be assigned to the nitro asymmetrical and symmetrical vibration.

Table 1. Theoretical and experimental frequencies and intensities for nimesulide molecule **1**.

No	Theoretical data (B3LYP/6-311++G(2df,2dp))			Experimental data (DMSO-d ₆ ^a)	
	$\nu_{\text{theor.}}^b$	A ^c	Approximate description ^d	$\nu_{\text{exp.}}$	A ^e
1.	3396	197	$\nu(\text{N-H})$	- ^f	- ^f
2.	3098	12	$\nu_{\text{PhA}}(\text{C-H})$	- ^g	- ^g
3.	3097	4	$\nu_{\text{PhA}}(\text{C-H})$	- ^g	- ^g
4.	3086	2	$\nu_{\text{PhA}}(\text{C-H})$	- ^g	- ^g
5.	3063	4	$\nu_{\text{PhB}}(\text{C-H})$	- ^g	- ^g
6.	3058	12	$\nu_{\text{PhB}}(\text{C-H})$	- ^g	- ^g
7.	3053	23	$\nu_{\text{PhB}}(\text{C-H})$	- ^g	- ^g
8.	3045	8	$\nu_{\text{PhB}}(\text{C-H})$	- ^g	- ^g
9.	3038	0	$\nu^{\text{as}}(\text{CH}_3)$	- ^g	- ^g
10.	3037	0	$\nu_{\text{PhA}}(\text{C-H}), \nu_{\text{PhB}}(\text{C-H})$	- ^g	- ^g
11.	3026	1	$\nu^{\text{as}}(\text{CH}_3)$	- ^g	- ^g
12.	2937	0	$\nu^{\text{s}}(\text{CH}_3)$	- ^g	- ^g
13.	1607	4	$\nu_{\text{PhA}}(\text{C=C}), \nu_{\text{PhB}}(\text{C=C})$	- ^g	- ^g
14.	1601	11	$\nu_{\text{PhB}}(\text{C=C})$	- ^g	- ^g
15.	1598	67	$\nu_{\text{PhA}}(\text{C=C}), \nu_{\text{PhB}}(\text{C=C})$	1597	m
16.	1593	194	$\nu_{\text{PhA}}(\text{C=C}), \nu_{\text{PhB}}(\text{C=C})$	1587	m
17.	1507	550	$\nu^{\text{as}}(\text{NO}_2), \delta(\text{N-H})$	1523	s
18.	1500	88	$\delta_{\text{PhB}}(\text{C-H})$	1501	sh
19.	1499	431	$\delta_{\text{PhB}}(\text{CH}), \nu^{\text{as}}(\text{NO}_2)$	1490	s
20.	1467	3	$\delta_{\text{PhB}}(\text{CH})$	- ^g	- ^g
21.	1443	107	$\delta(\text{NH})$	1457	w, br
22.	1433	5	$\delta^{\text{as}}(\text{CH}_3)$	- ^g	- ^g
23.	1432	9	$\delta^{\text{as}}(\text{CH}_3)$	- ^g	- ^g
24.	1413	214	$\delta(\text{N-H}), \nu_{\text{PhA}}(\text{C=C})$	1411	w, br
25.	1356	69	$\nu_{\text{PhA}}(\text{C=C}), \nu(\text{C-N})$	- ^g	- ^g
26.	1345	14	$\delta^{\text{s}}(\text{CH}_3)$	- ^g	- ^g
27.	1337	0	$\delta_{\text{PhB}}(\text{CH})$	- ^g	- ^g
28.	1329	901	$\nu^{\text{s}}(\text{NO}_2), \delta^{\text{PhB}}(\text{CH})$	1340	vs
29.	1312	10	$\delta_{\text{PhB}}(\text{CH})$	- ^g	- ^g
30.	1308	466	$\nu^{\text{as}}(\text{SO}_2), \delta_{\text{PhB}}(\text{CH})$	1291	w
31.	1291	387	$\nu(\text{C-NH}), \delta_{\text{PhB}}(\text{CH})$	1281	w
32.	1257	736	$\nu(\text{C-OC}), \delta_{\text{PhA}}(\text{CH})$	1250	m
33.	1227	344	$\nu(\text{C-OC}), \delta_{\text{PhB}}(\text{CH})$	1217	m
34.	1199	52	$\delta_{\text{PhA}}(\text{CH}), \delta(\text{C-OC})$	- ^g	- ^g
35.	1182	34	$\delta_{\text{PhA}}(\text{CH}), \delta(\text{C-OC})$	- ^g	- ^g
36.	1181	2	$\delta_{\text{PhB}}(\text{CH})$	- ^g	- ^g
37.	1157	41	$\delta_{\text{PhA}}(\text{CH})$	- ^g	- ^g
38. ^h	1139	471	$\nu^{\text{s}}(\text{SO}_2)$	1159	s
MADⁱ	-	-	-	9.5	-

^a Measured after having decomposed the complex bands into components; ^b Infrared frequencies [cm⁻¹] scaled by Eqn. (1). ^c Predicted intensities [km.mol⁻¹]; ^d Vibrational modes: ν , stretching; δ , in-plane bending; γ , out-of-plane bending; superscripts: s, symmetrical; as – asymmetrical; PhA, phenyl ring A; PhB - phenyl ring B; ^e Relative intensities: vw, very weak; w, weak; m, moderate; s, strong; vs, very strong; sh, shoulder; br, broad; ^f This frequency was removed from correlation analysis, because there is significant association between the amide group and the solvent molecules; ^g These bands were not detected in the IR spectrum; ^h Followed by 28 lower-frequency vibrations that could not be observed experimentally due to self-absorptions of DMSO-d₆ below 1100 cm⁻¹; ⁱ Mean Absolute Deviation between theoretically predicted and experimentally observed vibrational frequencies.

Two weaker bands observed at 1291 and 1159 cm^{-1} could be attributed to the asymmetrical and symmetrical stretching of the SO_2 group. The NH deformation is characterized by a weak broad band with maximum at 1411 cm^{-1} . The bands for C-N and S-N stretching are expected below 1100 cm^{-1} and could not be observed due to self-absorptions of DMSO-d_6 .

The experimental IR frequencies were accurately reproduced by the IEF-PCM B3LYP/6-311++G(2df,2dp) calculations. After comparison of the theoretical frequencies to the experimental values the following scaling equation was obtained:

$$\nu^{\text{scaled}} = 0.92992 + 84.2 \left(\text{cm}^{-1} \right)$$

It was applied in the following IR analysis to scale the native theoretical frequencies of the radical species **2** and **3** calculated at same theory level.

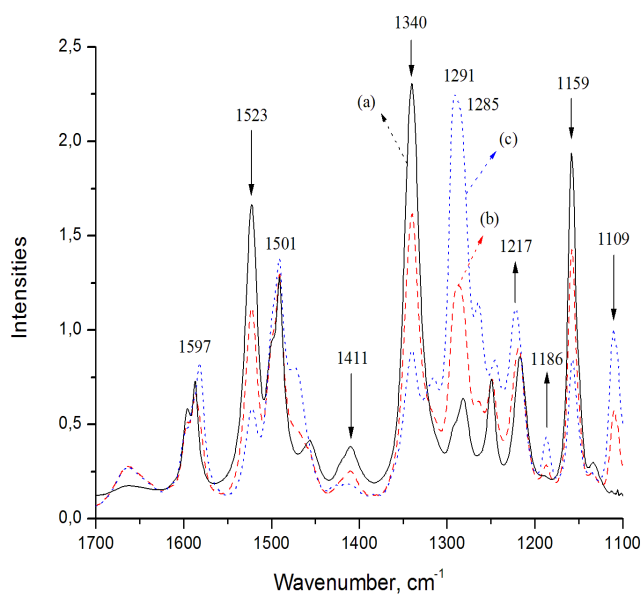


Fig. 2. IR spectra of nimesulide before reduction, $t = 0$ min (a) and in the course of electrochemical reduction, $t = 30$ min (b), $t = 75$ min (c).

IR measurements in the course of electrochemical reduction of nimesulide

In the course of electrochemical reduction of nimesulide, the intensities of the bands at 1523 and 1340 cm^{-1} decreased (Figure 2). The same was observed also for the band of the SO_2 symmetrical stretching at 1159 cm^{-1} . The band for NH deformation at 1411 cm^{-1} nearly disappeared. In the

same time, new bands appeared at 1291, 1217, 1186 and 1109 cm^{-1} . Two new bands – at 1225 and 1347 cm^{-1} , were detected like shoulders.

The intensities of the newly appeared bands gradually increased over time. Reversal in the polarity of the electrolysis cell restored the original spectrum of **1** which led to the conclusion that the observed spectral changes are due to reduction of nimesulide and not to products of radical recombination or other chemical transformations.

Interpretation of the IR data

Due to the broadening and overlapping of the bands, the assignment of the exact positions of experimental bands was done by second derivative analysis and curve fitting procedure. The frequencies of all bands appearing in the course of electrochemical reduction of nimesulide were thoroughly compared with the theoretically calculated frequencies of possible products – radical anion **2** and radical dianion **3**.

According to the theoretically calculated frequencies of **2** and **3**, in both cases of $\nu^{\text{as}}(\text{NO}_2)$ and $\nu^{\text{s}}(\text{NO}_2)$ should strongly decrease, while $\nu(\text{C}-\text{NO}_2)$ should considerably increase. The positions of the phenyl bands are not expected to change strongly. However, the magnitude of the nitro frequencies shift and the spectral changes concerning the other functional groups allow discrimination between the two products.

Upon conversion in **2**, the band for $\nu^{\text{as}}(\text{NO}_2)$ is expected to appear at 1257 cm^{-1} ($\Delta\nu = -273 \text{ cm}^{-1}$); $\nu^{\text{s}}(\text{NO}_2)$ – at 1055 cm^{-1} ($\Delta\nu = -274 \text{ cm}^{-1}$); and $\nu(\text{C}-\text{NO}_2)$ – at 1365 cm^{-1} ($\Delta\nu = +265 \text{ cm}^{-1}$) (Table S1). These changes are similar to those, observed earlier for other nitrophenyl derivatives [13-16,22,23]. The band for $\delta(\text{N}-\text{H})$ is expected to shift only slightly. $\nu^{\text{as}}(\text{SO}_2)$ and $\nu^{\text{s}}(\text{SO}_2)$ should be lowered weakly, only by 19 and 2 cm^{-1} .

Conversion in **3** should lead to the following changes: the band for $\nu^{\text{as}}(\text{NO}_2)$ would shift to 1227 cm^{-1} ($\Delta\nu = -303 \text{ cm}^{-1}$); $\nu^{\text{s}}(\text{NO}_2)$ – to 1057 cm^{-1} ($\Delta\nu = -283 \text{ cm}^{-1}$); and $\nu(\text{C}-\text{NO}_2)$ – to 1348 cm^{-1} ($\Delta\nu = +248 \text{ cm}^{-1}$) (Table 2). The band for $\delta(\text{N}-\text{H})$ should disappear as a result of deprotonation, while $\nu^{\text{as}}(\text{SO}_2)$ and $\nu^{\text{s}}(\text{SO}_2)$ should be lowered significantly by 105 and 75 cm^{-1} . $\nu(\text{C}-\text{NSO}_2)$ should produce a very strong band at 1298 cm^{-1} .

Based on these assignments, better matching was found with the spectrum of radical dianion **3**

(Table 2). The experimental bands at 1347 and 1225 cm^{-1} were attributed to $\nu(\text{C-NO}_2)$ and $\nu^{\text{as}}(\text{NO}_2)$ of radical dianion **3**. Deprotonation was evidenced by the nearly complete disappearance of the band for $\delta(\text{N-H})$. Another prove for the conversion of **1** in **3** was found in the appearance of the strong doublet with maximum around 1290 cm^{-1} (1294

and 1285 cm^{-1} after deconvolution) which agrees well with the predicted positions and strong intensities of $\nu(\text{C-NSO}_2)$ and $\nu_{\text{PhA}}(\text{C=C})$ - number 26 and 27 in Table 2. Therefore it was concluded that the one-electron reduction of nimesulide proceeded with deprotonation.

Table 2. Theoretical and experimental frequencies and intensities for nimesulide dianion radical **3a**.

No	Theoretical data (B3LYP/6-311++G(2df,2dp))			Experimental data (DMSO-d ₆ ^a)	
	$\nu_{\text{theor.}}$ ^b	A ^c	Approximate description ^d	$\nu_{\text{exp.}}$	A ^e
1.	3079	1	$\nu_{\text{PhA}}(\text{C-H})$	- ^f	- ^f
2.	3074	5	$\nu_{\text{PhA}}(\text{C-H})$	- ^f	- ^f
3.	3063	3	$\nu_{\text{PhB}}(\text{C-H})$	- ^f	- ^f
4.	3055	4	$\nu_{\text{PhA}}(\text{C-H})$	- ^f	- ^f
5.	3054	24	$\nu_{\text{PhB}}(\text{C-H})$	- ^f	- ^f
6.	3046	33	$\nu_{\text{PhA}}(\text{C-H})$	- ^f	- ^f
7.	3034	16	$\nu_{\text{PhB}}(\text{C-H})$	- ^f	- ^f
8.	3028	4	$\nu_{\text{PhB}}(\text{C-H})$	- ^f	- ^f
9.	3020	7	$\nu^{\text{as}}(\text{CH}_3)$	- ^f	- ^f
10.	3013	10	$\nu^{\text{as}}(\text{CH}_3)$	- ^f	- ^f
11.	2929	11	$\nu^{\text{s}}(\text{CH}_3)$	- ^f	- ^f
12.	1603	124	$\nu^{\text{s}}(\text{CH}_3)$	1599	sh
13.	1592	35	$\nu_{\text{PhB}}(\text{C=C})$	1590	sh
14.	1578	50	$\nu_{\text{PhB}}(\text{C=C})$	1581	m
15.	1528	1	$\nu_{\text{PhA}}(\text{C=C})$	- ^f	- ^f
16.	1496	176	$\nu_{\text{PhA}}(\text{C=C})$	1500	sh
17.	1484	455	$\delta_{\text{PhA}}(\text{C-H})$	1492	s
18.	1467	1	$\delta_{\text{PhB}}(\text{C-H})$	1474	m
19.	1438	5	$\delta^{\text{as}}(\text{CH}_3)$	- ^f	- ^f
20.	1436	2	$\delta^{\text{as}}(\text{CH}_3)$	- ^f	- ^f
21.	1425	42	$\nu_{\text{PhA}}(\text{C=C}); \delta_{\text{PhA}}(\text{C-H})$	- ^f	- ^f
22.	1348	395	$\nu(\text{C-NO}_2); \delta_{\text{PhA}}(\text{C-H})$	1347	m
23.	1343	24	$\delta_{\text{PhB}}(\text{C-H})$	- ^f	- ^f
24.	1326	107	$\delta^{\text{s}}(\text{CH}_3)$	1323	m
25.	1316	14	$\nu_{\text{PhA}}(\text{C=C}); \delta_{\text{PhA}}(\text{C-H})$	1313	m
26.	1298	732	$\nu(\text{C-NSO}_2); \delta_{\text{PhA}}(\text{C-H})$	1294	vs, sh
27.	1293	714	$\nu_{\text{PhA}}(\text{C=C}); \delta_{\text{PhA}}(\text{C-H})$	1285	vs, sh
28.	1248	84	$\delta^{\text{PhB}}(\text{C-H})$	1264	m
29.	1236	520	$\nu(\text{C-OC}), \delta_{\text{PhA}}(\text{C-H})$	1246	m
30.	1227	331	$\nu^{\text{as}}(\text{NO}_2), \delta_{\text{PhA}}(\text{CH})$	1225	m
31.	1188	208	$\nu(\text{CO-C}), \delta_{\text{PhA}}(\text{C-H})$	1191	w
32.	1183	34	$\delta_{\text{PhB}}(\text{C-H})$	1188	w
33.	1178	484	$\nu^{\text{as}}(\text{SO}_2), \delta_{\text{PhA}}(\text{C-H})$	1186	w
34.	1175	5	$\delta_{\text{PhB}}(\text{C-H})$	- ^f	- ^f
35.	1137	165	$\delta_{\text{PhA}}(\text{C-H})$	- ^f	m
36.	1104	18	$\delta_{\text{PhB}}(\text{C-H})$	- ^f	m
37.	1085	390	$\nu^{\text{s}}(\text{SO}_2)$	1109	- ^f
38. ^g	1058	12	$\nu^{\text{s}}(\text{NO}_2)$	- ^f	- ^f
MAD ^h	-	-	-	8.6	-

^a Measured after having decomposed the complex bands into components; ^b Infrared frequencies [cm^{-1}] scaled by Eqn. (1); ^c Predicted intensities [km.mol^{-1}]; ^d Vibrational modes: ν , stretching; δ , in-plane bending; superscripts: s, symmetrical; as, asymmetrical; PhA, phenyl ring A; PhB - phenyl ring B; ^e Relative intensities: w, weak; m, moderate; s, strong; vs, very strong; sh, shoulder; ^f These bands were not detected in the IR spectrum; ^g Followed by 28 lower-frequency vibrations that could not be observed experimentally due to self-absorptions of DMSO-d₆ below 1100 cm^{-1} ; ^h Mean Absolute Deviation between theoretically predicted and experimentally observed vibrational frequencies.

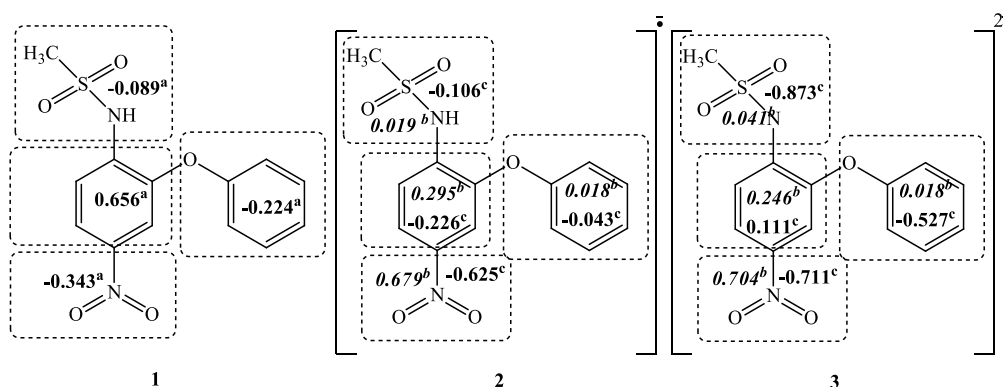


Fig. 3. Electron density distribution over fragments in nimesulide molecule **1** and its radical species **2** and **3**.

^aNBO net electronic charges. ^bNBO electron spin density (in italics). ^cNBO electronic charge changes $\Delta q_i = q_i$ (radical) - q_i (molecule).

Structural analysis

The observed shifting of the bands of nitro and sulfonyl groups is in good agreement with the predicted changes in bond lengths. The S-O bonds are affected insignificantly by conversion in **2**, while conversion in **3** causes 0.025-0.032 Å lengthening of the S-O bonds and 0.008 Å shortening of the C-NSO₂ bond.

NBO electronic charges and spin density distribution over fragments of the studied species are shown in Figure 3. In the radical anion **2** 68% of the spin density and 63% from the anionic charge are concentrated into the nitro group (Figure 3). It can be concluded, that the structure of **2** is determined mainly by the localization of the single electron in the nitrophenyl fragment (96%). The results presented for dianion radical **3** are also indicative – 71% of the spin density is localized into the nitro group, whereas 87% of the anionic charge is concentrated into the sulfonamide fragment.

It can be summarized, that the topological characteristics of the structure determine sulfonyl group to be a weak competitor of the nitro group for the odd electron distribution and the opposite – the nitro group to be a weak competitor of the sulfonyl one for the anionic charge distribution.

CONCLUSION

The IR spectral changes arising in the course of electrochemical reduction of nimesulide, were studied in DMSO-d₆ solution with tetrabutylammonium bromide as electrolyte salt. Based on comparison with theoretically predicted spectra of possible reduction products, *i.e.* (i) radical anion resulting from one-electron reduction and (ii) dianion radical resulting from one-electron reduction accompanied by deprotonation, it was concluded that in these conditions the

electrochemical reduction of nimesulide leads to the generation of a dianion radical. A reliable interpretation of the spectral data was achieved by a combined experimental and theoretical IR approach. It was shown that conversion of nimesulide into dianion radical caused significant spectral and structural changes in the nitro and sulfonamide group and the phenyl ring connecting them. According to the NBO calculations, the major part of the spin density is localized into the nitro group of the dianion radical, whereas the most of the anionic charge is concentrated into the sulfonamide fragment.

Acknowledgements: The financial support of this work by the National Science Fund of Bulgaria (Contracts RNF01/0110), Science Fund is gratefully acknowledged.

Electronic Supplementary Data available here.

REFERENCES

1. H. Suleyman, E. Cadirci, A. Albayrak, Z. Halici, *Curr. Med. Chem.*, **15**, 278 (2008).
2. S. Agrawal, S. S. Pancholi, N. K. Jain, G. P. Agrawal, *Int. J. Pharm.*, **274**, 149 (2004).
3. G. F. Fabiola, V. Pattabhi, K. Nagarajan, *Bioorg. Med. Chem.*, **6**, 2337 (1998).
4. U. A. Boelsterli, *Int. J. Clin. Pract.*, **128**, 30 (2002).
5. U. A. Boelsterli, H. K. Ho, S. Zhou, K. Y. Leow, *Curr. Drug Metabol.*, **7**, 715 (2006).
6. R. Davis, R. N. Brogden, *Drugs*, **48**, 431 (1994).
7. A. Bernareggi, *Clin. Pharmacokinet.*, **35**, 247 (1998).
8. R. S. Borges, R.F. Matos, A.S. Carneiro, J.P. Oliveira, A.M.J.C. Neto, M.C. Monteiro, *J. Mol. Model.*, **21**, 166 (2015).
9. S. G. Kucukguzel, I. Kucukguzel, B. Oral, S. Sezen, S. Rollas, *Eur. J. Drug Metab. Pharmacokinet.*, **30**, 127 (2005).

10. F. W. P. Ribeiro, T. R. V. Soares, S. do N. Oliveira, L. C. Melo, J. E. Soares, H. Becker, D. De Souza, P. de Lima-Neto, A. N. Correia, *J. Anal. Chem.*, **69**, 62 (2014).
11. A. Alvarez-Lueje, P. Vasquez, L.J. Núñez-Vergara, J.A. Squella, *Electro-anal.*, **9**, 1209 (1997).
12. J. Squella, P. Gonzalez, S. Bollo, L. Núñez-Vergara, *Pharm Res.*, **16**, 161 (1999).
13. I. N. Juchnovski, Ch. Tsvetanov, I. Panayotov, *Monatsh. Chem.*, **100**, 1980 (1969).
14. I. N. Juchnovski, I. Binev, *Chem. Phys. Lett.*, **12**, 40 (1971).
15. I. Juchnovski, I. Binev, A. Fattah Nazir, J. Tsenov, *Commun. Depart. Chem. Bulg. Acad. Sci.*, **12**, 500 (1979).
16. I. N. Juchnovski, T. M. Kolev, I. G. Binev, *Dokl. Bulg. Acad. Sci.*, **30**, 1017(1977).
17. I. Juchnovski, T. Kolev, I. Rashkov, *Spectrosc. Lett.*, **18**, 171 (1985).
18. I. Juchnovski, T. Kolev, *Spectrosc. Lett.*, **19**, 529 (1986).
19. I. Juchnovski, T. Kolev, *Spectrosc. Lett.*, **19**, 1183 (1986).
20. I. Juchnovski, Ts. Kolev, *Spectrosc. Lett.*, **18**, 481 (1985).
21. I. N. Juchnovski, V. Ognyanova, G. N. Andreev, *Spectrosc. Lett.*, **27**, 1299 (1994).
22. S. Stoyanov, *J. Phys. Chem.*, **114**, 5149 (2010).
23. S. S. Stoyanov, D. Y. Yancheva, B. Stamboliyska, *Comp. Theor. Chem.*, **1046**, 57 (2014).
24. M.J. Frisch, G.W. Trucks, H.B. Schlegel, G.E. Scuseria, M.A. Robb, J.R. Cheeseman, V.G. Zakrzewski, J.A. Montgomery, R.E.S. Jr., J.C. Burant, S. Dapprich, J.M. Millam, A.D. Daniels, K.N. Kudin, M.C. Strain, O. Farkas, J. Tomasi, V. Barone, M. Cossi, R. Cammi, B. Mennucci, C. Pomelli, C. Adamo, S. Clifford, J. Ochterski, G.A. Petersson, P.Y. Ayala, Q. Cui, K. Morokuma, D.K. Malick, A.D. Rabuck, K. Raghavachari, J.B. Foresman, J. Cioslowski, J.V. Ortiz, A.G. Baboul, B.B. Stefanov, G. Liu, A. Liashenko, P. Piskorz, I. Komaromi, R. Gomperts, R.L. Martin, D.J. Fox, T. Keith, M.A. Al-Laham, C.Y. Peng, A. Nanayakkara, C. Gonzalez, M. Challacombe, P.M.W. Gill, B. Johnson, W. Chen, M.W. Wong, J.L. Andres, M. Head-Gordon, E.S. Replogle, J.A. Pople, Gaussian98, Gaussian, Inc., Pittsburgh PA, 1998.
25. P. J. Stephens, F. J. Devlin, C. F. Chabalowsky, M. J. Frisch, *J. Phys. Chem.*, **98**, 623 (1994).
26. J. Tomasi, B. Mennucci, E.J. Cancas, *J. Mol. Struct. (THEOCHEM)*, **464**, 211 (1999).
27. J. Tomasi, M. Perisco, *Chem. Rev.*, **94**, 2027 (1994).
28. P. Bergese, E. Bontempi, I. Colombo, D. Gervasoni, L. Depero, *Compos Sci. Technol.*, **63**, 1197 (2003).
29. L. Dupont, B. Pirrotte, B. Masereel, J. Delarge, J.Geczy, Nimesulide, *J Acta Cryst C*, **51**, 507 (1995).
30. C. Michaux, C. Charlier, F. Julemont, B. Norberg, J.-M. Dogne, B. Pirotte, F. Durant, *Acta Cryst.*, **E57**, o1012 (2001).
31. P. Sanphui, B. Sarma, A. Nangia, *J. Pharm. Sci.*, **100**, 2287 (2011).

ИЧ СПЕКТРАЛНО ИЗСЛЕДВАНЕ НА ЕЛЕКТРОХИМИЧНАТА РЕДУКЦИЯ НА НИМЕЗУЛИД

С. Стоянов*, Д. Янчева, А. Косатева

Лаборатория „Структурен органичен анализ“, Институт по органична химия с център по фитохимия, Българска академия на науките, ул. „Акад. Г. Бончев“, бл. 9, 1113 София, България

Постъпила на 01 май 2017 г.; Коригирана на 31 май 2017 г.

(Резюме)

Електрохимичната редукция на нестероидното противовъзпалително лекарство нимезулид, N-(4-нитро-2-феноксифенил)-метансулфонамид, беше проведена в разтвор на DMSO-d₆ и бяха проследени ИЧ спектралните промени, породени от превръщането. Спектралните изследвания показаха, че при тези условия електрохимичната редукция води до значително понижение на N-O и S-O валентните честоти, повишаване на C-NO₂ валентната честота и изчезване на δ(N-H). Въз основа на сравнението с теоретично предсказаните спектри на възможните редукционни продукти, наблюдаваните промени са отдадени на генерирането на дианион-радикал на нимезулида. Отместванията на ИЧ ивици свидетелстват, че в резултат на редукцията са настъпили значителни структурни промени в нитро-, сулфонамидната група и фенилното ядро, свързвано с тях. Според изчислените натурални заряди и спинова плътност, 71% от спиновата плътност е съсредоточена в нитрогрупата на дианион-радикала, докато 87% от анионния заряд е локализиран в сулфонамидния фрагмент.

IIA/IIB group metal cations hosted by β -cyclodextrin: a DFT study

V. Nikolova^{1*}, S. Angelova², T. Dudev¹

¹ Faculty of Chemistry and Pharmacy, Sofia University "St. Kl. Ohridski", 1164 Sofia, Bulgaria

² Institute of Organic Chemistry with Centre of Phytochemistry, Bulgarian Academy of Sciences, 1113 Sofia, Bulgaria

Received April 28, 2017; Revised June 01, 2017

Dedicated to Acad. Ivan Juchnovski on the occasion of his 80th birthday

Although there is a lot of information about cyclodextrins (CDs) and their coordination complexes, there are still many open questions concerning the factors influencing the processes of their metal binding and selectivity. The purpose of this study is to clarify the factors that drive the formation of β CDs - metal ion complexes. A DFT computational study of complexes of β CDs with IIA/IIB group metal cations (Be^{2+} , Mg^{2+} , Ca^{2+} , Sr^{2+} , Ba^{2+} , Zn^{2+} , Cd^{2+} , Hg^{2+}) was performed to determine the main factors (ionic radius, preferred coordination number and degree of hydration of the metal cation, dielectric constant of the medium, etc.) controlling the processes of metal binding and selectivity in these systems.

Key words: cyclodextrin; metal cations, metal binding; selectivity; DFT calculations

INTRODUCTION

Some of the most commonly used molecules in the host-guest interactions are cyclodextrins (CDs). They are macromolecules which possess amphoteric properties, because they have hydrophobic cavity and hydrophilic outer surface. The natural CDs consist of 6, 7 or 8 glucopyranose units and are referred to as α CD, β CD and γ CD, respectively [1]. The form of cyclodextrins is truncated cone because of the chair conformation of the glucopyranose units [2]. For industrial use CDs are manufactured by enzymatic degradation of starch [3]. All three major types naturally occurring CDs have the same side rim depth – about 0.8 nm, but they have different cavity diameters (empty diameters between anomeric oxygen atoms) - 0.5, 0.6 and 0.8 nm for α CD, β CD and γ CDs, respectively [4]. Due to the large number of OH-groups CDs are soluble in water and the solubility of the α CD, β CD and γ CD under normal conditions is approximately 13%, 2% and 26% (145 g/l, 18.5 g/l and 232 g/l, respectively) [5]. One of the most important properties of CDs is their ability to accommodate different molecules inside their cavity [3,6,7], as the size of molecules that can be placed inside (hosted) is determined by the CDs cavity size. As a result, these molecules have found a number of applications in a wide range of fields. In the pharmaceutical industry CDs are primarily

used as complexing agents to increase the water solubility of poorly water-soluble drugs and to increase their bioavailability and stability [2,8,9]. For example, β CD is used as an agent to increase the solubility and reduce the adverse side effects (gastrointestinal irritation) of the Piroxicam (belonging to the group of nonsteroidal anti-inflammatory drugs), its faster absorption and thus faster analgesic effect [10]. CDs can alter the chemical stability of drugs - may slow down or accelerate their degradation or influence their reactivity. For example, doxorubicin (an antitumor drug) is unstable in aqueous medium and complexation with β CD or γ CD significantly increases its stability [11]. CDs inclusion complexes with metals, where CD acts as a ligand from the first coordination sphere, are described in the literature. One of the most interesting examples is the complex of β CD with Cu^{2+} , which also include Li^+ [12]. β CD may also form complexes with metal ions in which it is in the second coordination sphere: for instance adducts of ferrocene and β CD, described by Breslow [13]. Zhang et al. [14] investigated complexes of β CD with M^{2+} (Fe^{2+} , Co^{2+} , Ni^{2+} , Cu^{2+} and Zn^{2+}) and demonstrated that these complexes have catalytic properties in aldol condensation reaction. Stachowicz et al. [15] studied computationally the complexes of β CD with some metal cations (Na^+ , Cu^+ , Mg^{2+} , Zn^{2+} and Al^{3+}) at the B3LYP/6-31G* level and revealed the structure of the formed host-guest complexes.

* To whom all correspondence should be sent:
E-mail: ohtvd@chem.uni-sofia.bg

The aims of the present study are: (a) to clarify whether the properties of the metal ion influence the process of metal - β CD complexation; (b) to verify how dielectric properties of the medium affect the process of metal binding and the selectivity in these complexes; (c) to check which type of coordination mode of β CD (as first or second coordination sphere) is more favorable. In achieving these aims, we conducted DFT calculations combined with the PCM computations (Polarizable Continuum Model) for the complexes of β CD with IIA/IIB group metal ions.

COMPUTATIONAL DETAILS

All calculations in this work were performed by using Gaussian 09 quantum chemistry package [16]. For geometry optimization of the β CD molecule and its complexes with metal ions M062X functional was employed [17]. The computations were performed with the 6-31G(d,p) basis set [18] for the lighter atoms (C, O, H, Be, Mg, Ca, Zn) and with SDD pseudopotential [19,20] for Sr, Ba, Cd and Hg. In our previous study this combination of functional and basis set (M062X/6-31G(d,p)) has been proven to reproduce accurately metal–oxygen atoms distances in a metal complex with ligand resembling CD molecule [21]. For each optimized structure frequency calculations were performed at the same level of theory. No imaginary frequency was found for the lowest energy configurations of any of the optimized structures. The scaled by an empirical factor of 0.979 vibrational frequencies were used to compute the thermal energies, E_{th} , including zero-point energy, and entropies, S . The free energy of complex formation in the gas phase at $T=298.15$ K, ΔG^1 , was calculated by equation (1):

$$\Delta G^1 = \Delta E_{el} + \Delta E_{th} + \Delta PV - T\Delta S \quad (1)$$

where the terms ΔE_{el} , ΔE_{th} and ΔS are differences between the respective values of energies of the products and reactants, and the term ΔPV is a work term.

Solvation effects were accounted for by employing the Polarizable Continuum Model (PCM) [22,23] method. The fully optimized structure of each molecule/complex in the gas phase was subjected to a single point calculation in water ($\epsilon \approx 80$). The free energy of the complex formation in water was obtained by equation (2), where ΔG_{solv}^{80} (Products) and ΔG_{solv}^{80} (Reactants) are differences between the gas-phase and PCM calculated energies for the products (complexes) and reactants (β CD and metal cations), respectively:

$$\Delta G^{80} = \Delta G^1 + \Delta G_{solv}^{80}(\text{Prod.}) - \Delta G_{solv}^{80}(\text{React.}) \quad (2)$$

The calculated values of ΔG^{80} can be positive or negative: if the obtained value is positive, then the complex formation is thermodynamically unfavorable; if ΔG^{80} value is negative, then the process is thermodynamically favorable.

The PyMOL molecular graphics system was used for generating the molecular graphics images [24].

RESULTS AND DISCUSSION

β CD

Figure 1 presents the lowest-energy optimized structure of β CD in two projections – a view from the narrow rim and a side view. The β CD system possesses nearly 7-fold symmetry with main symmetry z-axis passing through the centre of the β CD and perpendicular to the mean plane of the oxygen atoms from the primary OH groups. Hydrogen bonds are formed at the trimmed with OH groups rims (upper/narrow and lower/wide rim); these at the narrow rim are stronger than their wide-rim counterparts.

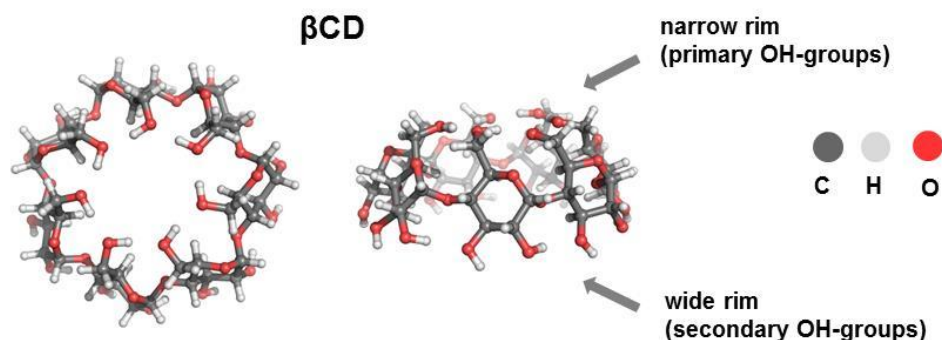


Fig. 1. Optimized structure of β CD in two projections: side view and view from the narrow rim.

The orientation of intramolecular hydrogen bonds at both rims is opposite: looking from the narrow rim side the orientation of the narrow rim hydrogen bonds is counter-clockwise, while the wide rim hydrogen bonds is clockwise.

β CD as a first-shell ligand for IIA/IIB group metal cations: $[\beta\text{CD}-\text{M}]^{2+}$ complexes

Formation of $[\beta\text{CD}-\text{M}]^{2+}$ complexes (M = IIA/IIB group metal) where β CD acts as a first-shell ligand to the metal cation, was studied. The optimization of the $[\beta\text{CD}-\text{M}]^{2+}$ structures was initiated from geometry with the preferred metal cation positioning- at the center of the narrow rim plane of the optimized structure of the free β CD. The optimized structures of the resultant metal complexes are shown in Figure 2. The initial shape of truncated cone becomes distorted for all metal cations. The mode of metal binding to the host cyclodextrin depends on the ionic radius of the guest cation: bulkier cations tend to coordinate to larger number of hydroxyl groups from the narrow rim while smaller cations prefer smaller number of binding partners, so the final geometries of the $[\beta\text{CD}-\text{M}]^{2+}$ complexes differ. Be^{2+} and Zn^{2+} are three-coordinated having only three adjacent hydroxyl partners, Ba^{2+} exhibit coordination number of 5 in the complex, while the rest of the cations have coordination number of 4. The $\text{M}-\text{O}_{\beta\text{CD}}$ distances, ionic radii of metal cations and free energies of complex formation in the gas-phase and water environment are presented in Table 1.

Table 1. $\text{M}-\text{O}_{\beta\text{CD}}$ distances (Å), ionic radii of metal cations (Å) and Gibbs free energies (in kcal/mol) in the gas phase (superscript 1) and water environment (superscript 80) calculated for the metal complex formation reaction, $\beta\text{CD} + \text{M}^{2+} \rightarrow [\beta\text{CD}-\text{M}]^{2+}$

Metal cation	$\text{M}-\text{O}_{\beta\text{CD}}$	ionic radius ^a	ΔG^1	ΔG^{80}
Be^{2+}	1.56	0.27	-439.9	-116.6
Mg^{2+}	2.02	0.72	-300.7	-31.8
Ca^{2+}	2.34	1.00	-219.9	-4.5
Sr^{2+}	2.46	1.18	-179.7	13.6
Ba^{2+}	2.73	1.35	-155.8	32.7
Zn^{2+}	2.64	0.74	-331.9	-24.0
Cd^{2+}	2.30	0.95	-259.0	29.5
Hg^{2+}	2.40	1.02	-273.3	54.2

^aIonic radius in tetracoordinated Be^{2+} complexes and hexacoordinated complexes for the rest of the dications; from Shannon, 1976 [25].

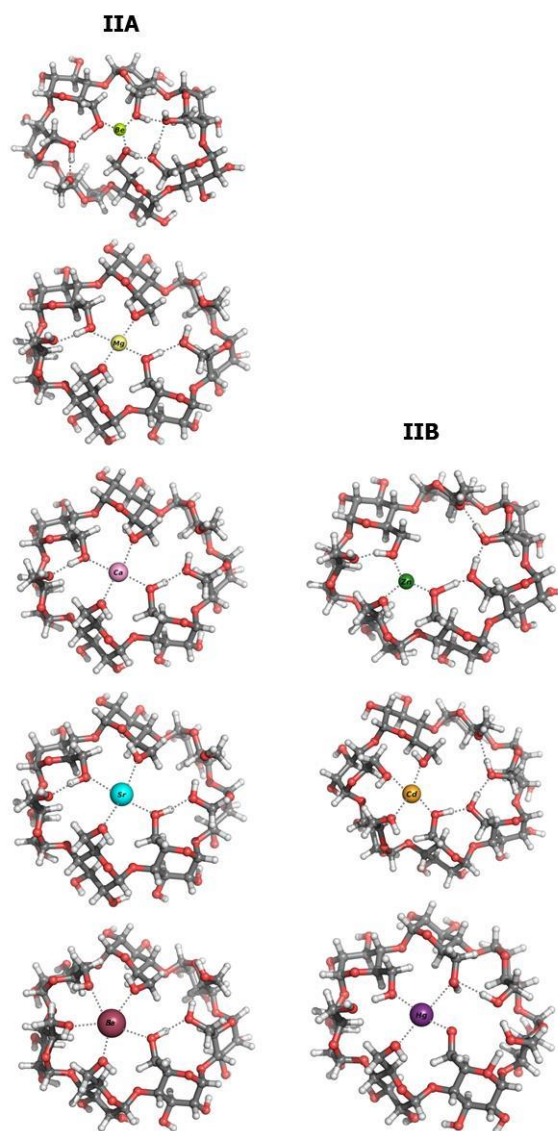


Fig. 2. M062X/6-31G(d,p) fully optimized structures of $[\beta\text{CD}-\text{M}]^{2+}$ complexes in the gas phase.

As the data in Table 1 reveal, the smaller the cationic radius (and higher the respective charge density of the cation) the more thermodynamically favorable is the complex formation in the respective subgroup (lower free energy values for the smaller cations than their bulkier counterparts in each subgroup). The results obtained demonstrate that all the reactions in the gas phase are favorable characterized with quite large negative formation free energies ΔG^1 . Solvation effects, however, significantly attenuate the free energy gains in the gas phase and render some reactions unfavorable in aqueous solution (positive ΔG^{80} values for the Sr^{2+} , Ba^{2+} , Cd^{2+} and Hg^{2+} complex formation). In comparing the magnitude of ΔG^1 and ΔG^{80} between IIA and IIB subgroups, the role of charge-accepting ability of the guest cation in complex formation

stands out. Cations from the B subgroup are better electron density acceptors than their counterparts from the A subgroup with similar ionic radii due to favorable hybridization between the valence s-orbital and highest occupied d-orbitals resulting in low-lying electron-receptive orbitals. For example, between Zn^{2+} and Mg^{2+} , two cations with virtually identical ionic radii (0.74 and 0.72 Å, respectively), the complex of the former is more stable in the gas phase characterized by lower ΔG^1 value than that of the latter. The same trend is observed for Cd^{2+} and Ca^{2+} , and Hg^{2+} and Sr^{2+} in the gas phase (ΔG^1 values). The series of cations with similar ionic radii (Mg^{2+} , Ca^{2+} , Sr^{2+} vs. Zn^{2+} , Cd^{2+} , Hg^{2+}) show the opposite trend in ΔG^{80} values. The explanation lies in the difference in the desolvation penalties for these metal cations.

β CD as a ligand for monohydrated IIA/IIB group metal cations: $[\beta\text{CD}-\text{M}-\text{H}_2\text{O}]^{2+}$ complexes

The effect of metal hydration on complexation process was studied by employing supramolecular approach. Formation of $[\beta\text{CD}-\text{M}-\text{H}_2\text{O}]^{2+}$, where βCD acts as a ligand to monohydrated $[\text{M}-\text{H}_2\text{O}]^{2+}$ metal cation (Figure 3), was studied. The $\text{M}-\text{O}_{\beta\text{CD}}$ and $\text{M}-\text{O}_{\text{H}_2\text{O}}$ distances, ionic radii of metal cations and free energies of complex formation are listed in Table 2. The addition of one water molecule affects slightly the distances $\text{M}-\text{O}_{\beta\text{CD}}$, and almost all of them (except for the zinc complex) slightly increase (0.02 ÷ 0.08 Å). $\text{M}-\text{O}_{\text{H}_2\text{O}}$ distances have similar values to the respective $\text{M}-\text{O}_{\beta\text{CD}}$ ones. The dependence of ΔG^1 on the ionic radius is the same as in the complexes without added H_2O molecule, but ΔG^1 values here fall in a narrow range (the lowest value is $-320.6 \text{ kcal mol}^{-1}$, and the highest is $-131.4 \text{ kcal mol}^{-1}$).

Table 2. $\text{M}-\text{O}_{\beta\text{CD}}$ and $\text{M}-\text{O}_{\text{H}_2\text{O}}$ distances (Å), ionic radii of metal cations (Å) and Gibbs free energies (in kcal/mol) in the gas phase (superscript 1) and water environment (superscript 80) calculated for the monohydrated metal complex formation reaction, $\beta\text{CD} + [\text{M}-\text{H}_2\text{O}]^{2+} \rightarrow [\beta\text{CD}-\text{M}-\text{H}_2\text{O}]^{2+}$.

Metal cation	$\text{M}-\text{O}_{\beta\text{CD}}$	$\text{M}-\text{O}_{\text{H}_2\text{O}}$	ionic radius ^a	ΔG^1	ΔG^{80}
Be^{2+}	1.63	1.68	0.27	-320.6	-100.8
Mg^{2+}	2.05	2.04	0.72	-244.6	-32.0
Ca^{2+}	2.36	2.37	1.00	-189.0	-5.3
Sr^{2+}	2.49	2.49	1.18	-151.2	14.0
Ba^{2+}	2.76	2.64	1.35	-131.4	28.5
Zn^{2+}	1.96	2.04	0.74	-252.7	-26.6
Cd^{2+}	2.29	2.29	0.95	-199.3	179.3
Hg^{2+}	2.42	2.54	1.02	-195.6	51.7

^aIonic radius in tetracoordinated Be^{2+} complexes and hexacoordinated complexes for the rest of the dications; from Shannon, 1976 [25].

Four positive ΔG^{80} values are observed, i.e. the water molecule addition does not render complex formation with Sr^{2+} , Ba^{2+} , Cd^{2+} and Hg^{2+} favorable.

β CD as a ligand for hexahydrated IIA/IIB group metal cations: $[\beta\text{CD}-\text{M}(\text{H}_2\text{O})_6]^{2+}$ complexes

The group II metals in their +2 oxidation state have a hydration number of 6 (except Be^{2+}) with octahedral arrangement of the water ligands (Figure 4). Magnesium hexaaqua complex, $[\text{Mg}(\text{H}_2\text{O})_6]^{2+}$, was modeled as a representative of the hydrated metal species from the series and taken for further evaluations.

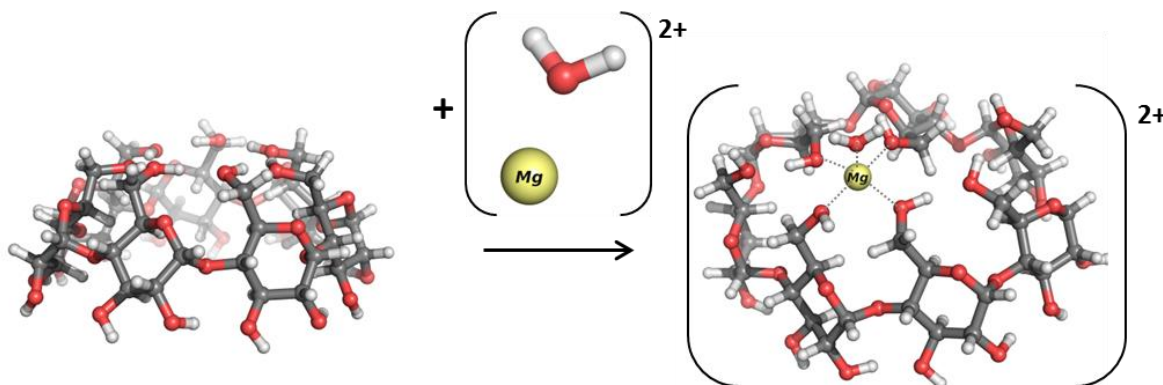


Fig. 3. $[\beta\text{CD}-\text{Mg}-\text{H}_2\text{O}]^{2+}$ complex formation reaction.

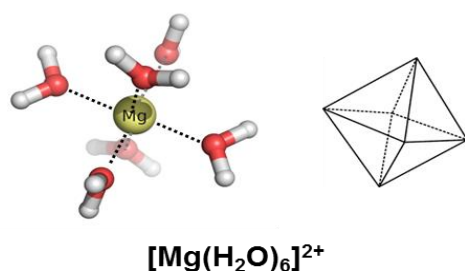


Fig. 4. Magnesium hexaaqua complex $[\text{Mg}(\text{H}_2\text{O})_6]^{2+}$; $\text{M}-\text{O}_{\text{H}_2\text{O}} = 2.06 \text{ \AA}$

Two complexes of hexaaqua magnesium ion with βCD were modeled and the metal binding affinities of different localities of the host cavity were probed:

(1) $[\text{Mg}(\text{H}_2\text{O})_6]^{2+}$ complex is entirely buried inside the cavity;

(2) $[\text{Mg}(\text{H}_2\text{O})_6]^{2+}$ ion is located outside the cavity, near the narrow rim of the βCD , and only one of the water molecules is located inside the cavity of the βCD .

The overall shapes of the discussed complexes, as well as their relative stability are shown in Figure 5 and Table 3. As the calculations reveal, the structure where the $[\text{Mg}(\text{H}_2\text{O})_6]^{2+}$ ion is placed inside the cavity of the βCD is more stable and advantageous in the gas phase.

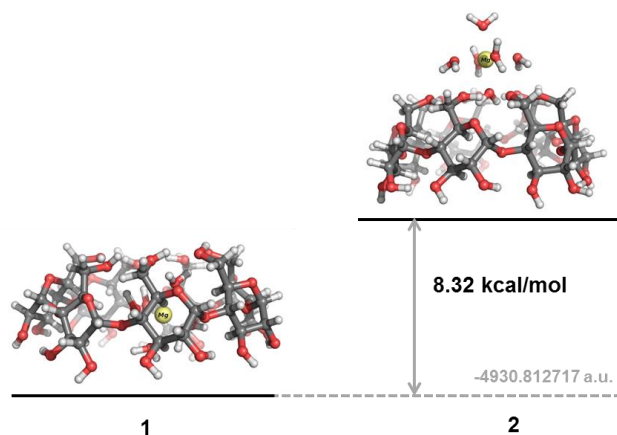


Fig. 5. Optimized structures and relative stabilities of the $[\beta\text{CD}-\text{Mg}(\text{H}_2\text{O})_6]^{2+}$ complexes.

Table 3. Calculated Gibbs free energies in the gas phase (ΔG^1) and in water environment (ΔG^{80}) (in kcal mol^{-1}) for $[\beta\text{CD}-\text{Mg}(\text{H}_2\text{O})_6]^{2+}$ complex formation, $\beta\text{CD} + [\text{Mg}(\text{H}_2\text{O})_6]^{2+} \rightarrow [\beta\text{CD}-\text{Mg}(\text{H}_2\text{O})_6]^{2+}$

Complex	ΔG^1	ΔG^{80}
1	-84.79	-10.31
2	-76.47	-12.76

Note that the metal binding to the host molecule in both locations is favorable as evidenced by the negative values of ΔG^1 and ΔG^{80} in Table 3, but the interaction free energies are less negative than those of the respective host-(bare-guest) complexation (Table 1).

CONCLUSION

The presented results confirm that the complex formation process between IIA and IIB group metal cations and βCD is thermodynamically favorable. Coordination of hydrated metal ions into the hydrophobic cavity of the βCD is also possible, with pronounced preference for metals with small ionic radii. Complexation free energies are strongly affected by the dielectric properties of the medium: increasing the dielectric constant of the surroundings attenuates the free energy gains on complexation. Regardless of whether the metal ion is hydrated or not, the most advantageous position in the cavity is close to the narrow rim of the cyclodextrin, where the negative charge is concentrated.

REFERENCES

1. A. Vyas, S. Saraf, S. Saraf, *J. Inc. Phen. Macroc. Chem.*, **62**, 23 (2008).
2. A. Magnúsdóttir, M. Másson, T. Loftsson, *J. Incl. Phenom. Macroc. Chem.*, **44**, 213 (2002).
3. J. Szejtli, *Chem. Rev.*, **98**, 1743 (1998).
4. L. Sharma, A. Sharma, *Eur. J Biochem.* **268** 2456 (2001).
5. J. L. Atwood, et al. (eds). *Comprehensive Supramolecular Chemistry Vol. 3: Cyclodextrins* Pergamon, New York, 1996.
6. G. Chen, M. Jiang, *Chem. Soc. Rev.*, **40**, 2254 (2011).
7. K. A. Connors, *Chem. Rev.*, **97**, 1325 (1997).
8. R. Challa, A. Abuja, J. Ali, R. K. Khar, *AAPS Pharm. Sci. Tech.*, **6** (2) (2005).
9. M. Davis; M. Brewster, *Nature Reviews Drug Discovery*, **3**, 1023 (2004).
10. C. Lee, J. Balfour, *Drugs*, **48**(6), 907 (1994).
11. R. Anand, F. Manoli, I. Manet, S. Daoud-Mahammed, V. Agostoni, R. Gref, S. Monti, *Photochem. Photobiol. Sci.*, **11**, 1285 (2012).
12. R. Fuchs; N. Habermann; P. Klüfers, *Angew. Chem. Int. Ed. Engl.*, **32**(6), 852 (1993).
13. B. Siegel; R. Breslow, *J. Am. Chem. Soc.*, **97**, 6869 (1975).
14. Y. Zhang, W. Xu, *Synth. Commun.*, **19**, 1291 (1989).
15. A. Stachowicz, A. Styrz, J. Korchowiec, A. Modarelli, M. Rogalski, *Theor. Chem. Acc.*, **120**, 215 (2011).

16. Gaussian 09, revision D.01 (Gaussian, Inc, Wallingford CT, 2009).
17. Y. Zhao, D. G. Truhlar, *Theor. Chem. Account.*, **120**, 215 (2006).
18. (a) R. Ditchfield, W. Hehre, J. Pople, *J. Chem. Phys.*, **54**, 724 (1971); (b) P. Hariharan J. Pople, *Theor. Chem. Acc.*, **28**, 213 (1973).
19. T. Dunning; P. Hay, in *Modern Theoretical Chemistry*, H. Schaefer III, Plenum (ed.), Vol. 3 New York, 1977.
20. G. Igel-Mann; H. Stoll; H. Preuss, *Mol. Phys.*, **65**, 1321 (1988).
21. S. Angelova, V. Nikolova, N. Molla, T. Dudev, *Inorg. Chem.*, **56(4)**, 1981 (2017).
22. S. Miertuš; E. Scrocco; J. Tomasi, *Chem. Phys.*, **55**, 117 (1981).
23. S. Miertuš; J. Tomasi, *Chem. Phys.*, **65**, 239 (1982).
24. The PyMOL Molecular Graphics System, Version 1.7.6.6, Schrödinger, LLC
25. R. D Shannon, *Acta Cryst.*, **A32**, 751 (1976).

КОМПЛЕКСООБРАЗУВАНЕ МЕЖДУ МЕТАЛНИ ЙОНИ ОТ ПА/ІВ ГРУПИ И β -ЦИКЛОДЕКСТРИН: ИЗСЛЕДВАНЕ С ТЕОРИЯ НА ФУНКЦИОНАЛА НА ПЛЪТНОСТТА

В. Николова^{1*}, С. Ангелова², Т. Дудев¹

¹ Факултет по химия и фармация, СУ "Св. Климент Охридски", 1164 София, България
² Институт по органична химия с Център по фитохимия, Българска академия на науките, бл. 9, 1113 София, България

Постъпила на 28 април 2017 г.; Коригирана на 1 юни 2017 г.

(Резюме)

Въпреки че има много информация за циклодекстрините и техните координационни комплекси, все още много въпроси, свързани с факторите, определящи процесите на тяхното метално свързване и селективност остават неизяснени. Целта на това изследване е да се уточнят факторите, ръководещи формирането на комплекси на β -циклодекстрин и метални йони. Проведено е изследване на комплекси на β -циклодекстрин с метални йони от ПА/ІВ група (Be^{2+} , Mg^{2+} , Ca^{2+} , Sr^{2+} , Ba^{2+} , Zn^{2+} , Cd^{2+} , Hg^{2+}) с използване на метода на Теория на Функционала на Плътността (ТФП). Определени са основните фактори (йонен радиус, предпочитано координационно число, степен на хидратация на металния катион и диелектрична константа на средата), които контролират процесите на метално свързване и селективност в тези системи.

Computational study of *exo*-selective Diels-Alder cycloadditions, catalyzed by aluminum chloride

S. M. Bakalova*, J. Kaneti, N. Markova

Institute of organic chemistry with Centre of phytochemistry Bulgarian Academy of Sciences, Acad. G. Bonchev str., Block 9, 1113 Sofia, Bulgaria

Received April 18, 2017; Revised June 02, 2017

Dedicated to Acad. Ivan Juchnovski on the occasion of his 80th birthday

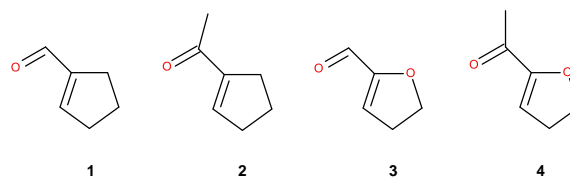
The aluminum chloride catalyzed *exo*-selective Diels-Alder reaction of cyclopentadiene with four dienophiles, with the reactive double bond in a five-membered cyclopentene or dihydrofuran ring, is studied computationally by M06-2x/6-311G(d,p) density functional theory. The electron-withdrawing group in these dienophiles is a carbonyl group, aldehyde or methyl ketone, at the reactive double bond, capable to form complexes by coordination of AlCl₃. The predicted stabilization energy of the complexes is in the range of 25 to 37 kcal.mol⁻¹. Present calculations predict stereoselectivities in very good agreement with experiment for the studied cyclopentene dienophiles. In the cases of dihydrofuran dienophiles calculated selectivities are higher than determined by experiment, although the observed trend of selectivity change between the two dihydrofuran dienophiles is predicted correctly. Free energy differences between located transition structures are interpreted mainly on the basis of steric repulsion. The majority of the studied reaction channels follow a concerted non-synchronous mechanism. In a few cases of highly asynchronous transition structures calculations predict a two-step mechanism.

Key words: *exo*-selectivity; Diels-Alder; DFT; cyclopentenal; dihydrofurfural; aluminum chloride; catalysis

INTRODUCTION

The most significant feature of the Diels-Alder cycloaddition reaction, discovered a century ago, [1] is its capability to generate up to four stereogenic centers in a single reaction step. Indeed, this reaction capability has been and currently is still the focus of intense scrutiny both experimentally and theoretically. The creation of essential natural and biomimetic products is based to a significant extent on Diels – Alder type condensed ring syntheses, due to their high and predictable stereoselectivity. With [4+2] cycloadditions, the predominant stereochemical outcome consists of *endo* – Diels-Alder adducts [2]. In certain cases of synthetic design, this preference may happen to be undesirable. Therefore, cycloadditions of the [4+2] type with *exo* preference are of special interest to synthetic planners. For this reason we attempt to understand the origins of *exo*-selectivity by means of computational theoretical chemistry, applied to some experimentally known examples of this kind of reaction [3-7]. The uncatalyzed reactions of cyclopenten-1-al **1** and the corresponding methylketone **2** with cyclopentadiene, CPD, produce the corresponding adducts with *exo/endo*

selectivity up to 5:1 for the aldehyde, but with practically equal amounts of *exo* and *endo* adducts with the enone [3]. 4,5-Dihydrofurfural **3** and 2-acetyl-4,5-dihydrofuran **4** as dienophiles, Scheme 1, give with CPD, in the presence of dimethylaluminum chloride predominantly the *exo*-adduct [3].



Scheme 1. Studied dienophiles in their *s-cis* conformations.

The observed low to moderate selectivity of uncatalyzed additions is increased upon Lewis acid catalysis [3]. We model computationally the reactions of the above dienophiles with CPD catalyzed by AlCl₃ in the attempt to understand the role of Lewis catalysts in reaction stereoselectivity.

COMPUTATIONAL DETAILS

We study reaction potential energy profiles and surfaces using the Gaussian 09 program system [8]. Our model uses M06-2x/6-311G(d,p) [9]

* To whom all correspondence should be sent:
E-mail: bakalova@orgchm.bas.bg

calculations to search for minima and transition structures, TSs, on the reaction potential energy surfaces, PES, using the default Berny algorithm and tight optimization criteria [8,10]. Located stationary structures are further identified by vibrational analysis to ensure the presence of a unique imaginary frequency in TSs and no imaginary frequency in the minima. In addition, we characterize TSs by following intrinsic reaction coordinates, IRC, [11–13] to acquire additional information regarding the reaction mechanism from curvatures of the energy profiles. To compute kinetic stereoselectivities of each diastereoisomeric reaction channel, we calculate their respective Gibbs free energies and determine the overall reaction stereochemical distribution from the relative $\Delta\Delta G^\ddagger$ [14,15]. Relative free energies and kinetic stereoselectivities are calculated at the experimental temperature of 195 K for better comparison with experimental results. [3] The catalytic Lewis acid in our models is AlCl_3 , a simplification for Et_2AlCl used in experiments [3]. Solvent effects are accounted for using the PCM model [16] as implemented in Gaussian 09.

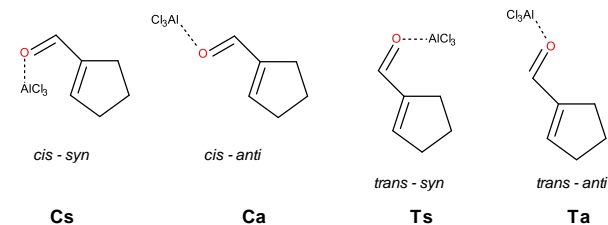
RESULTS AND DISCUSSION

Dienophiles **1** – **4** (Scheme 1) can exist as mixtures of *s-cis* and *s-trans* isomers, denoted further as C and T. Our calculations show that dienophiles **1** – **3** in dichloromethane (DCM) have an energetic preference for the *s-trans* conformation, with the energy difference between conformers decreasing from **1** to **3**, while for dienophile **4** the *s-cis* rotamer is more stable.

We initiate our modeling of Lewis acid (LA) catalysis of the [4+2] addition with optimization of the structures of the reactant dienophile complexes with AlCl_3 as starting PES minima of the reaction. Structures of AlCl_3 complexes are determined by the direction of free electron pairs of carbonyl oxygen atoms, as shown on Scheme 2, and denoted for convenience as *syn* and *anti* relative to the C=C bond. Thus complex **Ca** stands for a complex with *s-cis* conformation and *anti* orientation of the LA relative to the reactive double bond of the dienophile complex. The free energies of complexes with respect to the reactants, as well as their relative free energies are listed in Table 1.

The data in Table 1 shows that the most stable complexes of the cyclopentene dienophiles **1** and **2** have the *s-trans* conformation with *anti* orientation of AlCl_3 . On the other hand, the most stable complexes of the 4,5-dihydrofuran dienophiles **3**

and **4** have the *s-trans* conformation with *syn* orientation of the LA, although the energy difference between complexes **Ta** and **Ts** in the case of dienophile **3** is minimal.



Scheme 2. *Syn*- and *anti*-complexes of **1** with AlCl_3 .

The more simple examples of *exo*-selective dienophiles are the two 1-carbonyl derivatives of cyclopentene **1** and **2**. Calculated relative free energies of TSs for their additions to CPD are listed in Tables 2 and 3, resp. The favored diastereoisomeric TSs with **1** are shown in Fig. 1 along with their corresponding free energy differences and kinetic percentage contributions at 195 K.

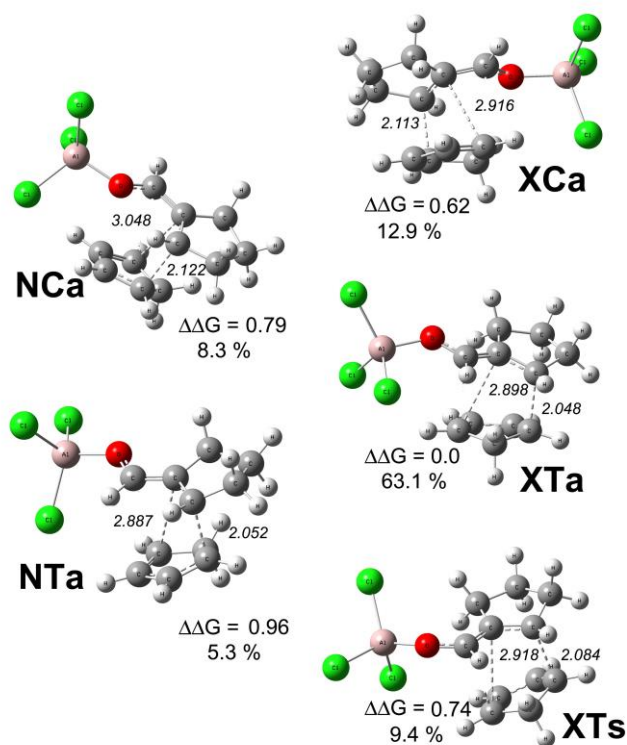
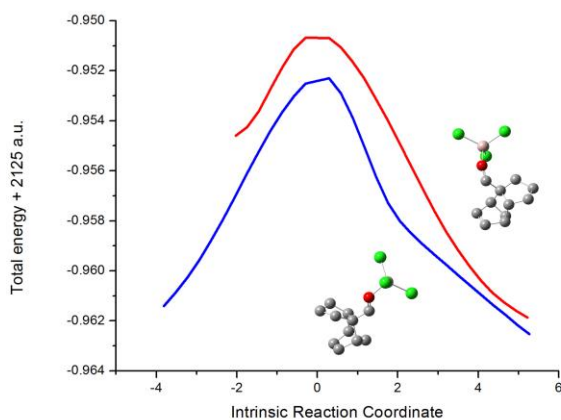


Fig. 1. Energetically preferred transition structures for the AlCl_3 catalyzed addition of **1** to CPD, favored *exo*-isomers on the right. Incipient C-C bonds are denoted by dash lines. The shown relative TS free energies are in $\text{kcal}\cdot\text{mol}^{-1}$ at 195 K. Calculated kinetic product percentage distributions are at 195 K as well.

Table 1. Stabilization and relative energies of AlCl₃ complexes of the dienophiles in kcal.mol⁻¹ at 298K and 195K. Stabilization energies are relative to free dienophiles **1** – **4** and isolated AlCl₃.

	$\Delta\Delta G_{298}$		$\Delta\Delta G_{195}$		$\Delta\Delta G_{298}$		$\Delta\Delta G_{195}$	
	1				2			
Ca	-30.50	3.13	-34.57	3.11	-32.58	1.18	-36.82	1.09
Cs	-28.35	5.28	-32.60	5.08	-31.36	2.40	-35.60	2.31
Ta	-33.63	0.00	-37.68	0.00	-33.76	0.00	-37.91	0.00
Ts	-31.27	2.36	-35.64	2.04	-32.16	1.60	-36.21	1.70
	3				4			
Ca	-26.86	2.23	-30.89	2.47	-30.82	0.00	-34.55	0.39
Cs	-25.00	4.08	-29.14	4.22	-28.53	2.29	-32.60	2.34
Ta	-29.00	0.08	-33.01	0.35	-28.51	2.32	-32.77	2.17
Ts	-29.08	0.00	-33.36	0.00	-30.67	0.16	-34.94	0.00

Energetically preferred *exo* TSs, contributing to more of 70% of the reaction *exo* outcome, Fig. 1, have the *s-trans* conformation following the relative stability of the LA complexes (Table 1). The most stable *endo* TS however prefers the *s-cis* conformation. The *anti*-orientation of LA is preferred in all TSs. Calculated *exo* : *endo* ratio via all 8 TSs at 195K, 85.44 : 14.56, is in a very good agreement with the experimentally found one, 87.5 : 12.5. [3]. A computation of IRCs from favored *endo* and *exo* TSs is given on Fig. 2. The resulting smooth IRC energy profiles indicate concerted non-synchronous reaction mechanisms.

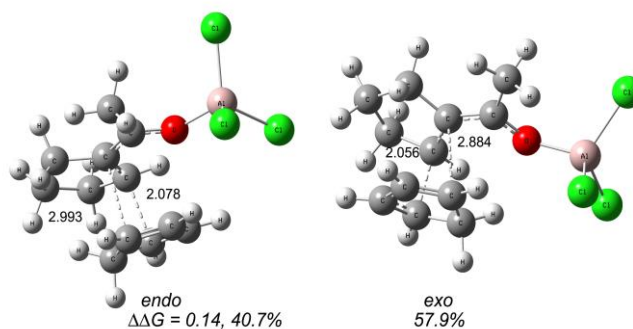
**Fig. 2.** Intrinsic reaction coordinate following for the AlCl₃ catalyzed addition of **1** to CPD, the upper red curve refers to a NT addition, and the bottom blue curve to the XT favored addition. Optimized product structures are shown on the right (product) side of the graphic. Hydrogen atoms are removed for clarity

The less favored TS *endo*-isomers, Fig. 1, left, also indicate the reason for the observed diastereoselectivity, even though these structures satisfy the Alder-rule [2] for “maximum accumulation of unsaturation”, or stacked π -bonds. The bulk of AlCl₃ catalyst, bound to the electron-withdrawing group, brings a strong disadvantage to the corresponding TSs due to steric repulsion.

Fig. 3 depicts favored TSs for the reaction of **2** and CPD with their corresponding kinetic contributions to the reaction stereochemical outcome. Energetically preferred TSs in the case of dienophile **2** have the *s-cis* conformation (Table 2, Fig. 3), although the *s-trans* reactant complexes are more stable than the *s-cis* ones (Table 1).

Table 2. Relative free energies of TSs for the addition of **1** to CPD, kcal.mol⁻¹, and selected geometry parameters, incipient bonds d₁ and d₂, numbered in the order of their formation, in Å. *Endo* is denoted N, while *exo* is X. Reaction asynchronicity may be deduced from the difference between lengths of incipient C-C bonds, d₂-d₁, or from their ratio d₂/d₁.

	$\Delta\Delta G$	$\Delta\Delta G$	d ₁	d ₂	d ₂ -d ₁	d ₂ /d ₁
	298	195				
NCa	0.88	0.79	2.122	3.048	0.926	1.436
NCs	3.59	3.52	2.159	2.981	0.822	1.381
NTa	1.06	0.96	2.052	2.887	0.835	1.407
NTs	1.89	1.63	2.051	2.973	0.922	1.450
XCa	0.58	0.62	2.113	2.916	0.803	1.380
XCs	3.02	2.89	2.145	2.952	0.807	1.376
XTa	0.00	0.00	2.048	2.898	0.850	1.415
XTs	0.90	0.74	2.084	2.918	0.834	1.400

**Fig. 3.** Dominant TSs for the model reaction of **2** with CPD, catalyzed by AlCl₃. Relative free energies, in kcal.mol⁻¹, and product percentage distributions are at the experimental temperature, 195 K.

Moreover, at difference to dienophile **1**, only two TSs, **NCa** and **XCa**, contribute to the reaction outcome. The relative stabilities of **NCa** and **NCs**, as well as of **XCa** and **XCs** correspond to these of the *anti* – *syn* isomers of LA complexes, **NCs** being additionally hindered by repulsive interaction with CPD. The *s-trans* isomers, **XT**, suffer a repulsive interaction between their methyl group and the CH₂ fragment of CPD. Calculated *exo* : *endo* ratio via all 8 TSs at 195 K, 41.8 : 58.2, is in reasonable agreement with the experimentally found one, 50 : 50. [3]. Note that the energy difference between **NCa** and **XCa** of only 0.14 kcal.mol⁻¹ is about the limit of precision of DFT computations. IRC analyses indicate that both **XCa** and **NCa** products are the result of concerted reactions.

Table 3. Relative free energies for TSs for the addition of **2** to CPD, kcal mol⁻¹, and selected geometry parameters (incipient bonds), Å. For notations see Table 2.

TS	$\Delta\Delta G$	$\Delta\Delta G$	d_1	d_2	d_2-d_1	d_2/d_1
	298	195				
NCa	0.00	0.00	2.078	2.993	0.915	1.440
NCs	1.94	1.99	2.109	2.962	0.853	1.404
NTa	3.41	3.03	2.019	2.864	0.845	1.419
NTs	4.75	4.21	2.016	2.964	0.948	1.470
XCa	0.27	0.14	2.056	2.884	0.828	1.403
XCs	1.56	1.55	2.077	2.884	0.807	1.389
XTa	3.28	2.94	2.056	2.923	0.867	1.422
XTs	4.76	4.15	2.050	2.894	0.844	1.412

Experimentally determined *exo*-selectivity at 195 K is significantly higher in the [4+2] additions of 4,5-dihydrofurfural **3** (*exo* : *endo* = 97.5 : 2.5) and 4,5-dihydro-2-furylmethylketone **4** (*exo* : *endo* = 93.8 : 6.2) to CPD than in the corresponding reactions of carbonyl-substituted hydrocarbons **1** and **2** [3].

Our M06-2x/6-311G(d,p) model calculations with the AlCl₃ catalyst show overestimated *exo* – selectivity for **3** and **4**, while indicating increased asynchronicity of the favored TSs for the latter reactions, Fig. 4.

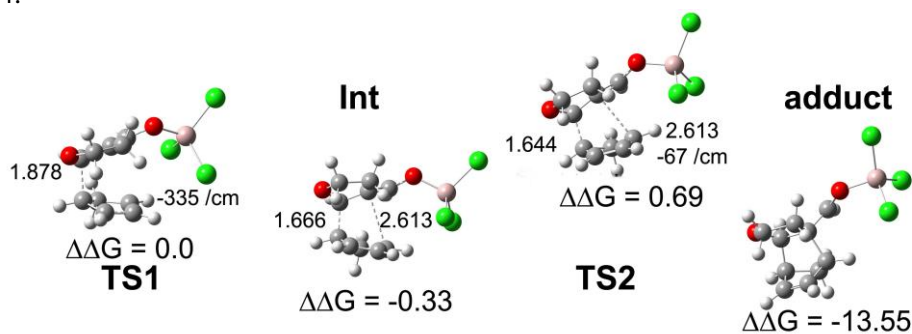


Fig. 5. Calculated Gibbs free energies of PES stationary points around the rate-determining **TS1** of 4,5-dihydrofurfural with CPD, left, at the experimental temperature, 195 K, catalyzed by AlCl₃. Relative energies are in kcal.mol⁻¹, incipient C-C bond lengths (dashed lines) are in Å. The imaginary frequencies of the two TSs (as negative, in cm⁻¹) are also shown. The final product is at the right, with free energy out of scale.

IRC following for the *endo*-TSs shows that the studied [4+2] addition is still a concerted though nonsynchronous reaction. In the two most stable *exo*-TSs the d_2/d_1 ratio is significantly increased to 1.593 for dienophile **3**, and 1.574 for dienophile **4**. IRC following for **4** shows that the reaction still remains a concerted single step addition, while for **3** the product branch of the IRC arrives first at an intermediate, which is ca. 0.5 kcal mol⁻¹ lower in energy than the TS. Next we find a second TS, indicating that at a ratio of $d_2/d_1 \geq 1.57$ the concerted mechanism becomes a two-step one, see Fig. 5.

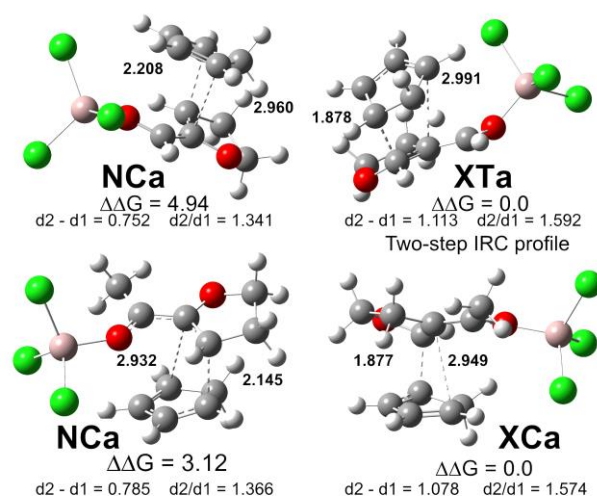


Fig. 4. Most stable *endo* and *exo* TSs for the [4+2] additions of **3** (upper row) and **4** to CPD catalyzed by AlCl₃. Incipient C-C bonds are indicated by dashed lines, with corresponding distances in Å. Relative free energy differences in kcal.mol⁻¹ are at the experimental temperature, 195 K.

Nevertheless, present calculations predict correctly the experimentally observed reduction of selectivity in the reaction of the methyl substituted dienophile **4** relative to **3** [3].

CONCLUSIONS

Synthetically important *exo*-selective Diels – Alder additions are reproduced reasonably well using contemporary DFT calculations. This can be meaningful in view of possible synthetic planning of condensed ring compounds, such as alkaloid and polysaccharide systems, [3-7] requiring *exo*-junctions. With the studied dienophiles **1** – **4**, *exo*-selectivity is mostly the result of steric interactions, although the cyclic dienophile C=C bonds with attached electron-withdrawing carbonyl groups could also contribute by reaction strain. [17] Lewis acid catalysis, while enhancing selectivity, does not fundamentally change the reaction outcome, even in the cases of mechanistic changes from a nonsynchronous concerted to a biradicaloid two-step reaction energy profile.

Acknowledgements: A part of the reported computations has been carried out on the MADARA HPC cluster, IOCCP, acquired under Project RNF01/0110 (2009-2011) of the National Science Fund of Bulgaria.

REFERENCES

1. O. Diels, K. Alder, *J. Liebig's Ann. Chem.*, **460**, 98 (1928).
2. K. Alder, G. Stein, *Angew. Chem.* **50**, 510 (1937).
3. K. S. Kim, Y. H. Joo, *Bull. Korean Chem. Soc.*, **20**, 385 (1999).
4. W. Adam, L. Hasemann, *Tetrahedron Lett.*, **32**, 7033 (1991).
5. F. Fotiadu, F. Michel, G. Buono, *Tetrahedron Lett.*, **31**, 4863 (1990).
6. F. Fotiadu, O. Pardigon, G. Buono, M. Le Corre, A. Hercouet, *Tetrahedron Lett.*, **40**, 867 (1999).
7. E. Fosu, R. Tia, E. Adei, *Tetrahedron*, **72**, 8261 (2016).
8. Gaussian 09 Rev. D.01: M. J. Frisch, G. W. Trucks, H. B. Schlegel, G. E. Scuseria, M. A. Robb, J. R. Cheeseman, G. Scalmani, V. Barone, B. Mennucci, G. A. Petersson, H. Nakatsuji, M. Caricato, X. Li, H. P. Hratchian, A. F. Izmaylov, J. Bloino, G. Zheng, J. L. Sonnenberg, M. Hada, M. Ehara, K. Toyota, R. Fukuda, J. Hasegawa, M. Ishida, T. Nakajima, Y. Honda, O. Kitao, H. Nakai, T. Vreven, J. A. Montgomery, Jr., J. E. Peralta, F. Ogliaro, M. Bearpark, J. J. Heyd, E. Brothers, K. N. Kudin, V. N. Staroverov, T. Keith, R. Kobayashi, J. Normand, K. Raghavachari, A. Rendell, J. C. Burant, S. S. Iyengar, J. Tomasi, M. Cossi, N. Rega, J. M. Millam, M. Klene, J. E. Knox, J. B. Cross, V. Bakken, C. Adamo, J. Jaramillo, R. Gomperts, R. E. Stratmann, O. Yazyev, A. J. Austin, R. Cammi, C. Pomelli, J. W. Ochterski, R. L. Martin, K. Morokuma, V. G. Zakrzewski, G. A. Voth, P. Salvador, J. J. Dannenberg, S. Dapprich, A. D. Daniels, O. Farkas, J. B. Foresman, J. V. Ortiz, J. Cioslowski, D. J. Fox, Gaussian, Inc., Wallingford CT, 2013.
9. Y. Zhao, D. G. Truhlar, *Acc. Chem. Res.*, **41**, 157 (2008).
10. H. B. Schlegel, *J. Comput. Chem.*, **3**, 214 (1982).
11. X. Li, M. J. Frisch, *J. Chem. Theory Comput.*, **2**, 835 (2006).
12. H. P. Hratchian, H. B. Schlegel, *J. Chem. Phys.*, **120**, 9918 (2004).
13. H. P. Hratchian, H. B. Schlegel, *J. Chem. Theory Comput.*, **1**, 61 (2005).
14. S. Shaik, H. B. Schlegel, S. Wolfe, *Theoretical aspects of physical organic chemistry*, Wiley, 1992.
15. T. Lowry, K. S. Richardson, *Mechanism and Theory in Organic Chemistry*, 3rd ed., Harper & Row, 1987.
16. J. Tomasi, B. Mennucci, R. Cammi, *Chem. Rev.*, **105**, 2999 (2005).
17. F. M. Bickelhaupt, K. N. Houk, *Angew. Chem. Int. Ed.* 10.1002/anie.201701486,

ТЕОРЕТИЧНО ИЗСЛЕДВАНЕ НА ЕКЗО-СЕЛЕКТИВНИ ПРИСЪЕДИНЯВАНИЯ ПО ДИЛС – АЛДЕР, КАТАЛИЗИРАНИ ОТ АЛУМИНИЕВ ХЛОРИД

С. М. Бакалова*, Х. Канети, Н. Маркова

*Институт по органична химия с Център по фитохимия, Българска академия на науките,
1113 София, България*

Постъпила на 18 април 2017 г.; Коригирана на 2 юни 2017 г.

(Резюме)

Изследвана е катализираната от алуминиев хлорид екзо-селективна реакция на Дилс-Алдер между циклопентадиен и четири диенофила с петатомни пръстени, циклопентен и дихидрофуран, съдържащи диенофилната двойна връзка. Използвана е теорията на функционала на плътността в приближение M06-2x/6-311G(d,p). Електронакцепторната група на използваните диенофили е карбонил, алдехид или кетон, свързан пряко с двойната връзка и способен да образува комплекси чрез координиране с алуминиев хлорид. Стабилизиращите енергии на тези комплекси са в рамките на 25 до 37 ккал.мол⁻¹. Пресмятанията предсказват много добре наблюдаваната експериментално селективност на циклопентеновите диенофили, но преувеличават резултатите за дихидрофурановите производни. Независимо от това е предсказано правилно намаляването на селективността при ацетил-4,5-дихидрофуран в сравнение с 4,5-дихидрофурфурал. Разликата между изчислените свободни енергии на намерените преходни структури за реакциите се обяснява главно със стерични взаимодействия. Повечето от изследваните реакционни пътища отговарят на съгласуван несинхронен механизъм. В малкото случаи на силно асинхронни преходни структури пресмятанията предсказват двустепенен механизъм на реакцията.

Synthesis and properties of several Betti bases as potential drugs

N. V. Georgieva^{1*}, Z. L. Yaneva¹, S. D. Simova², G. D. Nikolova³

¹ Chemistry Unit, Department of Pharmacology, Animal Physiology and Physiological Chemistry, Faculty of Veterinary Medicine, Trakia University, Students Campus, Stara Zagora 6000, Bulgaria

² Institute of Organic Chemistry with Centre of Phytochemistry, Bulgarian Academy of Sciences, Acad. G. Bonchev street, bl. 9, 1113 Sofia, Bulgaria

³ Department of Medical Chemistry and Biochemistry, Faculty of Medicine, Trakia University, Armejska Str., 11, Stara Zagora 6000, Bulgaria

Received April 18, 2017; Revised June 2, 2017

Dedicated to Acad. Ivan Juchnovski on the occasion of his 80th birthday

The aim of the present study was to synthesize several Betti bases by a modified Betti reaction, to develop analytical methods for the quantitative determination and testing the microbiological and antioxidant activities. For the modification of the Betti reaction we used primary heterocyclic amine, aromatic aldehydes, 8-quinolinol and halogen-substituted aromatic aldehydes. Betti bases were obtained at yield 80-98% and characterized by elemental analysis and NMR spectra. The applied analytical methods for quantitative determination of the studied Betti bases offered short analysis time, high precision, high linearity and satisfactory limit of detection (LOD) and limit of quantification (LOQ) values. The microbiological activity of studied Betti bases was tested against 23 test strains pathogenic microorganisms (different gram positive and gram negative). The microbiological screening proved their selective microbiological activity. According to the EPR study, the Betti bases possess radical structure and are likely to exhibit antioxidant activity. We assume that the potential of the presented Betti bases as a pharmacological compound is promising.

Key words: Betti bases; 8-quinolinol; UV-VIS spectroscopy, EPR spectroscopy; HPLC

INTRODUCTION

Quinolones are extensively investigated as broad spectrum anti-bacterial, anti-diabetic, anti-convulsant, anti-inflammatory, anti-viral, anti-fungal and anti-HIV agents [1–8]. In vitro studies show that the hydrochlorides of the Mannich bases of 8-hydroxyquinoline and 7-diethylaminomethyl-8-hydroxyquinoline exhibit high cytotoxic activity against human cancer cells of leukemia and myeloma, as well as other tumors [6, 8]. The scientific literature presents reports demonstrating the antioxidant activity of quinoline-8-ol derivatives [9, 10]. The study of Betti bases chemistry started at the beginning of the 20th century. The reaction of primary aromatic amines with benzaldehyde and phenols or naphthols is called a Betti reaction although it represents a special case of the Mannich reaction and the products (aminonaphthols) obtained are known as Betti bases [11–15]. These bases have interesting biological applications, such as antibacterial, hypotensive, and bradycardic agents [3, 16–19]. The optically active Betti bases can be used as ligands to chelate with organometallic reagents in

different reactions to provide highly efficient complex compounds [20–22]. However, various modifications have been made to prepare Betti base derivatives by using other naphthols or phenols, quinolins, and amines [23–25]. Many procedures for Betti reactions have also been successfully developed [26–31].

In our previous investigations we have found growth regulating activity of synthesized by us 7-aminobenzyl-8-hydroxyquinolines [32] and microbiological activity against a reference *Staphylococcus aureus* strain of the synthesized by us 2,5,7-substituted derivatives of 8-quinolinol [33].

The aim of the present study was to synthesize several Betti bases by a modified Betti reaction, to develop analytical methods for its quantitative determination and to test its microbiological and antioxidant activities.

EXPERIMENTAL

Reagents

The halogen-substituted aromatic aldehydes, quinolin-8-ol and 2-amino-6-methylpyridine used in the syntheses are commercially available (Fluka, Merck, Germany, > 99%) with analytical reagent

* To whom all correspondence should be sent:
E-mail: nvgeorgieva@vmf.uni-sz.bg

grade. The amino benzylation of quinolin-8-ol was carried out by modified by us Betti reaction: three-component Mannich-type condensation of 8-hydroxyquinoline (0.01mol), chloro-, fluoro- and bromo-substituted benzaldehydes (0.01mol), 2-amino-6-methylpyridin-2-amino-6-methylpyridine (0.01mol) in absolute ethanol according to the scheme (Fig. 1):

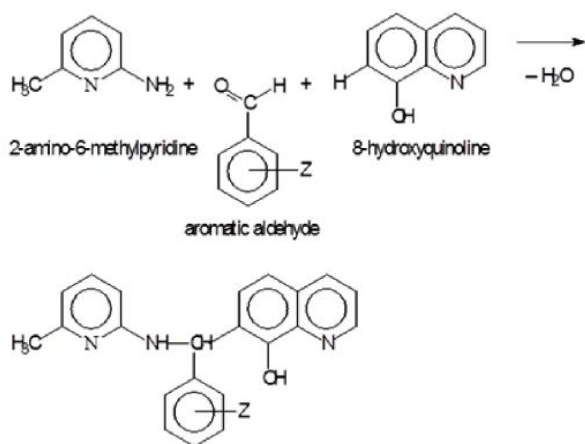


Fig. 1. Scheme of the reaction for the syntheses of 7-[(6-methylpyridin-2-ylamino)(halogenophenyl)methyl]quinolin-8-ols, where Z is: 2-chloro; 3-chloro; 4-chloro; 2,4-dichloro; 2-bromo; 3-brom; 4-bromo and 2-fluoro.

The reaction mixtures were allowed to stand for 21 days at room temperature in a closed flask and the time (in hours) required for the precipitation of the products was reported. After completion of the process, the separated solid phase was filtered (no earlier than 21 days) and purified by recrystallization from an organic solvent (preferably a mixture of ethanol and acetone in the ratio 1:1).

NMR spectroscopy

¹H (600.1 and 250.1 MHz), ¹³C (150.9 MHz) and ¹⁵N (60.8 MHz) NMR spectra were acquired on Bruker AVANCE AV600 II+ and DRX 250 NMR spectrometers. All spectra were recorded in DMSO-d₆ at room temperature. Chemical shifts are referenced to the residual solvent ¹H (2.51 ppm) and ¹³C (39.50 ppm) signals. Inverse detected ¹⁵N NMR chemical shifts are referenced to external liquid NH₃. Unambiguous assignment of the NMR signals was made on the basis of the gradient enhanced versions of COSY, TOCSY, NOESY (ROESY), HSQC and HMBC experiments; Bruker TOPSPIN 3.5p11 pulse library: cosygpmfqq, dipsi2etgpsi, noesygpshz, hsqcedetgpsi.sp.3 and hmbcgp(lp)ndqf, 2015.

UV-VIS Spectrophotometry

Standard stock solutions (100 µg/ml) were prepared by dissolving the appropriate amount of 7-[(6-methylpyridin-2-ylamino)(2,4-dichlorophenyl)methyl]quinolin-8-ol (Bt4) in ethanol:HCl (pH 1.0). Working standard solutions (1–100 µg/mL) were prepared daily. The concentrations of Bt4 were measured with UV-VIS spectrophotometer DR 5000 Hach Lange (Germany), supplied with 10 mm quartz cells. All spectra were recorded in the UV region at λ 204 nm with 2 nm slit width, 900 nm min⁻¹ scan speed and very high smoothing.

HPLC Study

RP-HPLC system comprising of a Hypersil BDS C18 (5 µM, 4.6 x 150 mm) column, Surveyor LC Pump Plus, PDA detector, and Surveyor Autosampler Plus (Thermo Fisher Scientific) was used. The used mobile phase consisted of a mixture of MeOH:H₂O (40:60, v/v). The samples were monitored at 204 nm. The buffer pH was adjusted to 3.2 with H₃PO₄. The volume injected into the HPLC column was 20 µl.

All UV/VIS spectrophotometric and HPLC analyses were made in triplicate. The experimental data was analyzed by regression analyses and determination of the corresponding correlation coefficients (R²) and relative standard deviation (RSD, %). The efficiency and accuracy of the developed UV/VIS and HPLC methods was estimated based on the calculated limit of detection (LOD) and limit of quantification (LOQ).

Microbiological activity

The obtained solid substances of the Betti bases were diluted in N,N'-dimethylformamide (DMF) and their microbiological activity was tested at concentrations of 4-500 µg/mL with Mueller-Hinton agar medium, against 23 strains of pathogenic microorganisms: *Listeria 215*, *Listeria 362*, *Listeria 1094*, *Swine erysipelas*, *Staphylococcus 1*, *Staphyloc. 5*, *Staphyloc. 42*, *Staphyloc. 78*, *Staphyloc. 119*, *Bact. megat 10*, *Bact. megat 11*, *Bact. megat 16*, *Bact. megat 39*, *Bact. cereus 12*, *Past. mult. 10*, *Past. mult. SHp*, *Past. mult. R II*, *Salm. Dublin*, *Salm. Gollinarum 200*, *Salm. Enter 4767*, *E. coli 21*, *E. coli 56*, *E. coli 94*. The inoculation of the test strains was conducted in Stuart equipment with 23 nests. After the inoculation and the development of the bacterial culture in agar, the samples were incubated at 37°C for several days.

The Betti base solutions were prepared for each petri dish separately with dissolved agar. Sterilized petri dishes and agar medium were used in the present work. The antibacterial activities of the compounds were evaluated by measuring the zone of inhibition on nutrient agar plate. The microbiological activities were tested for at least three times against all microorganisms and average values have been reported. Muller Hinton agar was used in the anti-bacterial study.

Electron paramagnetic resonance (EPR) study

EPR measurements were performed at room temperature on an X-band EMX_{micro}, spectrometer Bruker, Germany, equipped with standard Resonator. All EPR experiments were carried out in triplicate and repeated. Spectral processing was performed using Bruker WIN-EPR and SimFonia software. For the EPR study, direct EPR spectroscopy methods were used to investigate the antioxidant properties of 7-((6-methylpyridin-2-ylamino)(2,4-dichlorophenyl)methyl)quinolin-8-ol (Bt 4). By a direct EPR spectroscopy an EPR singlet signal was registered in the powdered form of Bt 4. Quartz capillaries were used as sample tubes. Sample tubes were filled with each powdered form and placed in the EPR microwave cavity. The EPR spectra of the Betti base in a powdered form were recorded at the following spectrometer settings: receiver gain 2×10^3 , power 1.64 mW, center field 3513.50 G, sweep width 200 G, time constant 163.84 ms, sweep time 61.44 s, modulation amplitude 10 G, 5 scans per sample.

RESULTS AND DISCUSSION

Synthesis

As a result of the condensation between 2-amino-6-methylpyridin, 8-quinolinol and halogen-substituted aromatic aldehydes, eight 7-[(6-methylpyridin-2-ylamino)(halogenophenyl)methyl]quinolin-8-ols, with a common formula presented

in Fig. 2, were obtained. The Betti bases, purified from the organic solvent are crystalline substances. The data for the common molecular formula, molecular mass, melting point, elemental analysis and yield of the newly synthesized derivatives of 8-hydroxyquinoline are presented in Table 1. It was established that the time required for extraction of the reaction products at room temperature is inversely proportional to their yield. The longer settling time could be explained by steric hindrance, as in the chemical structures of each of the Betti bases there is a substituent on the 2-position of the benzene ring.

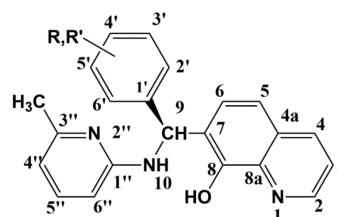


Fig. 2. Common formula of the Betti bases, where R is a substituent from 2-chloro (Bt1), 3-chloro (Bt2), 4-chloro (Bt3), 2-bromo (Bt5), 3-bromo (Bt6), 4-bromo (Bt7), 2-fluoro (Bt8) and R,R' is 2,4-dichloro (Bt4).

Confirmation of the Structure of the Betti Bases

The structures of the studied Betti bases were confirmed by their NMR spectra. They are also characterized by their melting point determined by Kofler microscope and by elemental analysis - nitrogen, carbon and hydrogen were determined (Table 1).

The NMR spectral assignment for the individual compounds is presented below:

R = 2'-Cl (Bt1): ¹H NMR (250 MHz, DMSO-*d*₆) δ 9.93 (s, 1H, OH), 8.85 (dd, *J* = 4.2, 1.6 Hz, 1H, H-2), 8.30 (dd, *J* = 8.3, 1.6 Hz, 1H, H-4), 7.54 (dd, *J* = 8.3, 4.2 Hz, 1H, H-3), 7.48 – 7.23 (m, 8H), 7.10 (d, *J* = 7.8 Hz, 1H, NH-10), 6.98 (d, *J* = 7.8 Hz, 1H, H-9), 6.45 – 6.30 (m, 2H), 2.19 (s, 3H).

Table 1. Properties of the studied Betti bases with common formula shown in Fig. 2.

Betti bases	Bt1	Bt2	Bt3	Bt4	Bt5	Bt6	Bt7	Bt8
Empirical formula	C ₂₂ H ₁₈ ClN ₃ O	C ₂₂ H ₁₈ ClN ₃ O	C ₂₂ H ₁₈ ClN ₃ O	C ₂₂ H ₁₇ Cl ₂ N ₃ O	C ₂₂ H ₁₈ BrN ₃ O	C ₂₂ H ₁₈ BrN ₃ O	C ₂₂ H ₁₈ BrN ₃ O	C ₂₂ H ₁₈ FN ₃ O
MG	375.85	375.85	375.85	410.3	420.31	420.31	420.31	359.40
Time, h	96	17	12	33	39	22	19	15
M.P., °C	183-185	154-156	144-146	184-186	185-187	172-174	151-153	181-183
Yd, %	80	93	95	98	88	90	93	98
%,N Calc.	11.18	11.18	11.18	10.24	10.00	10.00	10.00	11.69
%,N Found	11.03	11.52	11.10	10.39	9.75	10.25	10.36	11.73
%,C Calc.	70.30	70.30	70.30	64.40	62.87	62.87	62.87	73.52
%,C Found	70.00	69.78	70.10	64.22	62.83	62.55	62.38	73.72
%,H Calc.	4.83	4.83	4.83	4.18	4.32	4.32	4.32	5.05
%,H Found	5.00	4.99	4.86	3.94	4.53	4.42	4.46	4.75

2nd isomer (25%) - 8.88 (dd, $J = 4.1, 1.6$ Hz), 8.46 (dd, $J = 8.8, 1.6$ Hz), 7.62 (dd, $J = 8.8, 4.1$ Hz), 6.98 (d, $J = 8.0$ Hz), 6.85 (d, $J = 8.0$ Hz), 2.24 (s).

R = 3'-Cl (Bt2): ¹H NMR (250 MHz, DMSO-*d*₆) δ 10.03 (s, 1H, OH), 8.86 (dd, $J = 4.2, 1.7$ Hz, 1H, H-2), 8.29 (dd, $J = 8.4, 1.6$ Hz, 1H, H-4), 7.66 (d, $J = 8.6$ Hz, 1H, H-6), 7.54 (dd, $J = 8.3, 4.2$ Hz, 1H, H-3), 7.42 (d, $J = 8.6$ Hz, 1H, H-5), 7.42 (m, 1H, H-2'), 7.39 – 7.19 (m, 6H), 6.88 (d, $J = 8.9$ Hz, 1H, H-9), 6.48 (d, $J = 8.4$ Hz, 1H, H-6''), 6.38 (d, $J = 7.2$ Hz, 1H, H-4''), 2.23 (s, 3H).

R = 4'-Cl (Bt3): ¹H NMR (600.1 MHz, DMSO-*d*₆) δ 10.08 (s, 1H, OH), 8.86 (dd, $J = 4.2, 1.6$ Hz, 1H, H-2), 8.29 (dd, $J = 8.3, 1.6$ Hz, 1H, H-4), 7.64 (d, $J = 8.6$ Hz, 1H, H-6), 7.54 (dd, $J = 8.3, 4.2$ Hz, 1H, H-3), 7.41 (d, $J = 8.6$ Hz, 1H, H-5), 7.38;7.35 (AA'XX', 4H, H-2',3',5',6'), 7.31 (d, $J = 8.9$ Hz, 1H, NH-10), 7.28 (dd, $J = 8.3, 7.3$ Hz, 1H, H-5''), 6.85 (d, $J = 8.7$ Hz, 1H, H-9), 6.46 (d, $J = 8.3$ Hz, 1H, H-6''), 6.36 (d, $J = 7.2$ Hz, 1H, H-4''), 2.22 (s, 3H, CH₃-3''); ¹³C NMR (150.9 MHz, DMSO-*d*₆) δ 157.43 (C-1''), 155.68 (C-3''), 149.60 (C-8), 148.31 (C-2), 142.78 (C-1'), 138.11 (C-8a), 137.24 (C-5''), 136.04 (C-4), 130.97 (C-4'), 128.92 (C-2',6'), 128.10 (C-3',5'), 127.52 (C-4a), 126.61 (C-6), 125.36 ((C-7), 121.72 (C-3), 117.46 (C-5), 111.31 (C-4''), 105.26 (C-6''), 51.06 (C-9), 24.24 (CH₃-3''); ¹⁵N NMR (60.8 MHz, DMSO-*d*₆) δ 296 (N-1), 91 (d, $J = 92$, N-10), 266 (N-2'').

R, R' = 2',4'-Cl (Bt4): ¹H NMR (250 MHz, DMSO-*d*₆) δ 10.00 (s, 1H, OH), 8.85 (dd, $J = 4.2, 1.7$ Hz, 1H, H-2), 8.30 (dd, $J = 8.4, 1.7$ Hz, 1H, H-4), 7.56 (d, $J = 2.0$ Hz, 1H, H-3'), 7.54 (dd, $J = 8.3, 4.2$ Hz, 1H, H-3), 7.45 (d, $J = 8.4$ Hz, 1H, H-6'), 7.40 (dd, $J = 8.4, 2.0$ Hz, 1H, H-5'), 7.38 (d, $J = 8.5, 1H, H-5$), 7.32 (d, $J = 8.5, 1H, H-6$), 7.27 (dd, $J = 8.5, 7.5$ Hz, 1H, H-5''), 7.15 (d, $J = 7.6$ Hz, 1H, NH-10), 6.95 (d, $J = 7.6$ Hz, 1H, H-9), 6.40 (d, $J = 8.6$ Hz, 1H, H-6''), 6.36 (d, $J = 7.5$ Hz, 1H, H-4''), 2.19 (s, 3H).

R = 2'-Br (Bt5): ¹H NMR (250 MHz, DMSO-*d*₆) δ 9.93 (s, 1H), 8.85 (dd, $J = 4.1, 1.6$ Hz, 1H, H-2), 8.29 (dd, $J = 8.4, 1.7$ Hz, 1H, H-4), 7.61 (m, 1H, H-3'), 7.53 (dd, $J = 8.4, 4.1$ Hz, 1H, H-3), 7.45 – 7.16 (m, 7H), 7.10 (d, $J = 7.7$ Hz, 1H, NH-10), 6.91 (d, $J = 7.7$ Hz, 1H, H-9), 6.37 (m, 2H), 2.19 (s, 3H).

2nd isomer (21%) 8.88 (dd, $J = 4.1, 1.5$ Hz), 8.46 (dd, $J = 8.7, 1.5$ Hz), 7.62 (m), 6.98 (d, $J = 8.1$ Hz), 6.83 (d, $J = 8.1$ Hz), 2.25 (s).

R = 3'-Br (Bt6): ¹H NMR (250 MHz, DMSO-*d*₆) δ 10.04 (s, 1H), 8.86 (dd, $J = 4.2, 1.7$ Hz, 1H, H-2), 8.29 (dd, $J = 8.3, 1.6$ Hz, 1H, H-4), 7.66 (d, J

= 8.5 Hz, 1H, H-6), 7.57 (m, 1H, H-2'), 7.54 (dd, $J = 8.3, 4.2$ Hz, 1H, H-3), 7.42 (d, $J = 8.5$ Hz, 1H, H-5), 7.41 – 7.21 (m, 5H), 6.88 (d, $J = 8.9$ Hz, 1H, H-9), 6.47 (d, $J = 8.2$ Hz, 1H, H-6''), 6.38 (d, $J = 7.1$ Hz, 1H, H-4''), 2.23 (s, 3H).

R = 4'-Br (Bt7): ¹H NMR (250 MHz, DMSO-*d*₆) δ 10.02 (s, 1H), 8.85 (dd, $J = 4.2, 1.6$ Hz, 1H, H-2), 8.28 (dd, $J = 8.4, 1.7$ Hz, 1H, H-4), 7.64 (d, $J = 8.5$ Hz, 1H, H-6), 7.53 (dd, $J = 8.3, 4.2$ Hz, 1H, H-3), 7.48 (d, $J = 8.5$ Hz, 1H, H-5), 7.50 – 7.25 (m, 5H), 6.84 (d, $J = 8.7$ Hz, 1H, H-9), 6.46 (d, $J = 8.3$ Hz, 1H, H-6''), 6.37 (d, $J = 7.1$ Hz, 1H, H-4''), 2.23 (s, 3H).

R = 2'-F (Bt8): ¹H NMR (600 MHz, DMSO-*d*₆) δ 10.00 (s, 1H, OH), 8.84 (dd, $J = 4.1, 1.6$ Hz, 1H, H-2), 8.29 (dd, $J = 8.3, 1.6$ Hz, 1H, H-4), 7.54 (d, $J = 8.5$ Hz, 1H, H-6), 7.53 (dd, $J = 8.5, 4.1$ Hz, 1H, H-3), 7.40 (d, $J = 8.9$ Hz, 1H, H-5), 7.38 (m, 1H, H-6'), 7.27 (dd, $J = 8.3, 7.2$ Hz, 1H, H-5''), m, 1H, H-4'), 7.20 (d, $J = 8.4$ Hz, 1H, NH-10), 7.13 (m, 2H, H-3',5'), 7.04 (d, $J = 8.4$ Hz, 1H, C-9), 6.44 (d, $J = 8.3$ Hz, 1H, H-6''), 6.35 (dt, $J = 7.2, 0.7$ Hz, 1H, H-4''), 2.20 (s, 3H); ¹³C NMR (150.9 MHz, DMSO-*d*₆) δ 160.12 (C-2' d, $J = 245.4$), 157.24 (C-1''), 155.62 (C-3''), 149.87 (C-8), 148.25 (C-2), 138.05 (C-8a), 137.11 (C-5''), 136.03 (C-4), 130.35 (C-1' d, $J = 14.2$), 128.94 (C-6' d, $J = 4.3$), 128.60 (C-4' d, $J = 7.9$), 127.58 (C-4a), 126.75 (C-6), 124.33 (C-7), 124.06 (C-5' d, $J = 3.4$), 121.69 (C-3), 116.99 (C-5), 115.20 (C-3' d, $J = 21.5$), 111.19 (C-4''), 105.28 (C-6''), 46.21 (C-9 d, $J = 3.6$), 24.28 (CH₃-2''); ¹⁵N NMR (60.8 MHz, DMSO-*d*₆) δ 296 (N-1), 88 (d, $J = 90$, N-10), 266 (N-2'').

2nd isomer (12%) - 8.87 (dd, $J = 4.1, 1.6$ Hz), 8.48 (dd, $J = 8.7, 1.6$ Hz), 7.61 (dd, $J = 8.7, 4.1$ Hz), 6.42 (dt, $J = 8.3, 0.7$ Hz, 1H, H-4''), 6.38 (dt, $J = 7.1, 0.7$ Hz, 1H, H-4''), 2.24 (s).

For the ortho (2') substituted derivatives two sets of signals are registered due to the hindered rotation around the C-9-C-1' bond. The ratio of the two observed atropisomers depends on the nature of the substituents and on the temperature.

UV/VIS and HPLC methods for determination of 7-[(6-methylpyridin-2-ylamino) (2,4-dichlorophenyl)methyl]quinolin-8-ol (Bt4) in liquid phase

The UV/VIS spectra of Bt4 in acidic ethanol solutions (pH 1.0, Fig. 3 a,b) displayed maximum absorbance peaks in the UV region at $\lambda = 204$ nm for the entire concentration range 1-100 $\mu\text{g/ml}$.

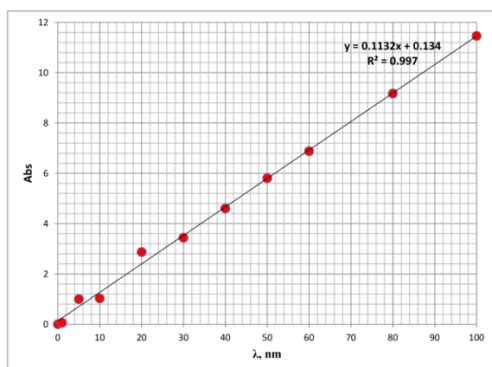


Fig. 3a. UV/VIS calibration curve.

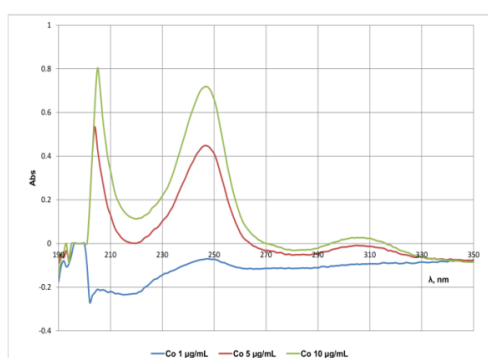


Fig. 3b. UV/VIS spectra of Bt4.

The obtained standard curve for Bt4 was linear over the tested range of initial concentrations C_0 1 - 100 $\mu\text{g/ml}$. The high value of the calculated correlation coefficient - R^2 0.9970, and the well-resolved UV absorption peaks of the heterocyclic compound proved the applicability of this method for determination of Bt4 concentrations in aqueous medium in the range C_0 1 - 100 $\mu\text{g/ml}$.

The HPLC experiments were conducted with ten Bt4 standard solutions in the concentration range 10 - 100 $\mu\text{g/ml}$. The used mobile phase consisted of methanol:H₂O (40:60, v/v). Optimal performance was obtained at a flow rate of 0.8 ml/min. The effect of temperature on the separation process was studied in the range 18 - 30°C. Satisfactory peak resolution and optimum analyses time were established at 30°C, at wavelength $\lambda=204$ nm. Bt4 was successfully detected within 1.5 min (Fig. 4 a,b). The standard calibration curve plotted, based on the spectral peak areas, characterized with a high correlation coefficient R^2 0.9825 and the following linear equation:

$$y = 3110.8x + 16864$$

Table 2. Values of the characteristic parameters and error functions for the UV/VIS and HPLC methods.

Method	R^2	SD	S_x	S_y	LOQ, $\mu\text{g/mL}$	LOD, $\mu\text{g/mL}$
UV/VIS	0.9969	0.2201	0.0021	0.0999	2.9117	8.8233
HPLC	0.9825	14704	138.5093	6672.28	7.0782	21.4491

S_x – standard deviation of the slope; S_y – standard deviation of the intercept

The obtained HPLC chromatograms did not contain any interference peaks, which could influence the quantitative results. Besides, the base line is straight and stable with lower signal noise. The correlation regression coefficient of the obtained standard calibration curve at these HPLC conditions was sufficiently high, although lower than that of the UV/VIS method.

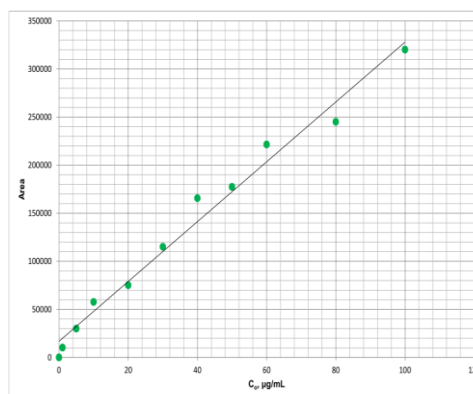


Fig. 4a. HPLC calibration curve.

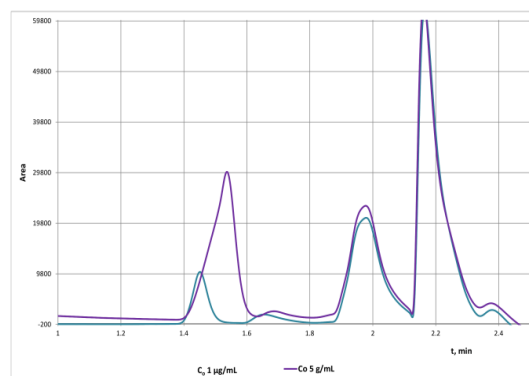


Fig. 4b. HPLC spectra of Bt4.

The values of LOD and LOQ were estimated according to the guidelines of the International Conference on Harmonization of Technical Requirements for Registration of Pharmaceuticals for Human Use (ICH) based on the standard deviation of the response and the slope of the calibration curve of the analyte [34]. The values of these parameters are presented in Table 2.

The comparative analyses of the obtained experimental results revealed that the developed and applied UV/VIS spectrophotometric method characterized with the highest correlation coefficient and lowest SD value.

Table 3. Microbiological activities of the studied Betti bases – MIC, $\mu\text{g/mL}$.

Test strains	Bt1, $\mu\text{g/mL}$	Bt2, $\mu\text{g/mL}$	Bt3, $\mu\text{g/mL}$	Bt4, $\mu\text{g/mL}$	Bt5, $\mu\text{g/mL}$	Bt6, $\mu\text{g/mL}$	Bt7, $\mu\text{g/mL}$	Bt8, $\mu\text{g/mL}$
<i>Listeria 212</i>	32	250	250	500	125	4	4/500	0
<i>Listeria 362</i>	32	500	500	+	250	500	500	250
<i>Listeria 1094</i>	32	250	500	500	250	250	250	250
<i>Swine erysipelas</i>	125	250	500	500	125	250	250	500
<i>Staphylococcus 1</i>	64	250	250	500	125	+	500	250
<i>Staphylococcus 5</i>	64	500	500	500	125	+	500	250
<i>Staphylococcus 42</i>	64	500	500	500	500	+	+	250
<i>Staphylococcus 78</i>	64	500	500	500	125	+	250	250
<i>Staphylococcus119</i>	64	+	250	500	125	+	250	250
<i>Bact. megat 10</i>	64	500	500	500	250	500	500	250
<i>Bact. megat 11</i>	64	500	500	500	500	500	500	500
<i>Bact. megat 39</i>	64	500	500	500	250	500	500	250
<i>Bact. megat 16</i>	64	500	500	500	125	500	500	250
<i>Bact. cereus 12</i>	64	+	+	+	+	500	500	500
<i>Past. mult. 10</i>	0	4	4	+	4	4	4	4
<i>Past. mult. SHp</i>	0	4	4	+	8	8	8	4
<i>Past. mult. R II</i>	0	4	4	+	8	8	8	8
<i>Salm. Dublin</i>	250	+	+	+	+	+	+	+
<i>S. Gollinarum200</i>	250	500	+	+	+	+	+	+
<i>Salm.enter4767</i>	250	+	+	+	+	+	+	+
<i>E. coli 21</i>	250	+	+	+	500	500	+	64
<i>E. coli 56</i>	500	+	+	+	+	+	+	64
<i>E. coli 94</i>	500	+	+	+	+	+	+	64

“+” - registered growth of the tested pathogenic strains in the entire concentration range (4-500 $\mu\text{g/mL}$)

“0” - not registered growth of the tested pathogenic strains in the entire concentration range (4-500 $\mu\text{g/mL}$)

Besides, the determined LOD and LOQ values were the lowest. According to the spectra presented in Fig. 4b, however, solutions with Bt4 concentration lower than 5.0 $\mu\text{g/mL}$ are characterized with not well resolved spectral peaks, i.e. the accuracy of the method below this limit is unsatisfactory. Among the basic advantages of the UV/VIS method is its cost-effectiveness and rapidity.

Regarding the developed HPLC methodology, and based on the data from Table 2, it could be concluded that it is characterized with lower accuracy and efficiency as the determined RSD, LOD and LOQ values were higher as compared to those of the UV/VIS method. The HPLC spectral data of Bt4 (Fig. 4b) revealed that its spectral peaks are characterized with great area. Besides, they were significantly more pronounced in the entire tested concentration range as compared to the UV/VIS peaks. The presence of two secondary peaks (at 2 and 2.2 min) could be attributed to the detection of methanol, as the area and height of these peaks remain constant at different initial Bt4 concentrations, which does not influence the analytical results. According to the spectra presented in Fig. 4b, the solutions with Bt4 concentration 1.0 $\mu\text{g/mL}$ are characterized with a very well resolved spectral peak, i.e. the accuracy

of the method is satisfactory. Another advantage of the HPLC method is the registered short retention time – 1.5 min.

Biological activities

Considering the wide range of biological activities of compounds containing phenolic hydroxyl group, including 8-hydroxyquinoline [1–8] and the physiological activity of the amino derivatives of the pyridine series [2–4, 11], we predicted high biological activity of the synthesized Betti bases. The results of the microbiological screening are presented in Table 3, where the compounds are denoted as in Table 1. The present study established that the microbiological activity depends on the number and position of the halogen-substitute in the benzene ring of the studied Betti bases. The presence of Cl-atom on position 2 of the benzene ring (Bt1) raised the bacteriostatic activity against all tested strains, as compared to the other Betti bases. All studied Betti bases, except Bt4, showed a bacteriostatic activity against test strains *Past. Mult.* in low concentrations (Table 3). Probably, the accumulation of Cl-atoms in the benzene ring of the Betti bases decreases the bacteriostatic activity. The presence of F-atom on position 2 of the benzene ring (Bt8) raised the bacteriostatic activity against *E. coli* strain (64

µg/mL, Table 3). The results of the microbiological screening of the studied Betti bases showed that they possess selective microbiological activity.

The established microbiological activity of the studied [(6-methylpyridine-2ylamino)(halogenophenyl)methyl]quinolin-8-ols was probably due, on the one hand to the presence of a quinoline ring in their molecular structure, and on the other - to the possibility of the -OH group on 8-position of the quinoline ring to form chelate complexes with traces of ions of some d-elements. Probably, the chelate complexes of 3d-elements and the derivatives of 8-hydroxyquinoline, which penetrated into the bacterial cell, lead to disturbance of the endo-cellular esterase within the cell, and caused violations of the metabolism of vital for the microorganisms enzymes. These observations of the prepared Betti bases correspond to those reported by other research teams [35]. The microbiological activity may also be due to the ability of 8-hydroxyquinoline derivatives to capture free radicals (spin - trap) [10], which allows us to continue our research in this direction and to investigate the antioxidant activity of Bt4.

EPR spectroscopy of Bt4

By a direct EPR spectroscopy, the EPR singlet signal, registered in the powdered forms of Bt4, exhibited almost a symmetrical single EPR signal (Fig. 5). According to it, the intensive central singlet in the EPR spectrum characterized with a g factor 1.9737 ± 0.0002 and width - 43 mT (Fig. 5).

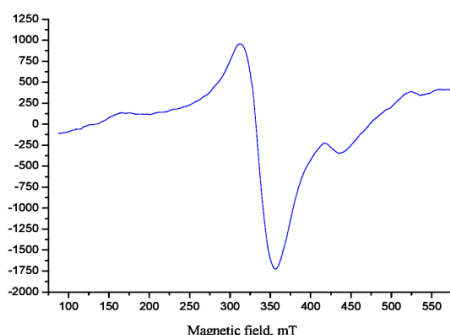


Fig. 5. EPR singlet signal in the powdered form of Bt4.

According to the registered EPR spectrum, Bt4 possesses radical structure. Considering the presence of a phenolic group in its structure (Fig. 2), we suppose that this group is involved in the formation of radical species and it could possibly capture reactive oxygen species (ROS), i.e. exhibit antioxidant activity. It is known that ROS such as superoxide radicals (O_2^-), hydroxyl radicals ($\bullet OH$) and hydrogen peroxide (H_2O_2) play a key role in human cancer development and has gained much

support recently. They have been shown to possess several characteristics of carcinogens [36, 37].

Further, we hypothesized that the antioxidant action of the studied [(6-methylpyridin-2ylamino)(2,4-dichlorophenyl)methyl]quinolin-8-ol may be responsible for the beneficial effects of this compound, thus the other 6-methylpyridin-2ylamino(halogenophenyl) methyl]quinolin-8-ols could be used as antioxidants. According to the result obtained in this study, the compounds tested can probably be used for the treatment of diseases associated with oxidative stress.

CONCLUSION

We investigated a three-component reaction of 8-hydroxyquinoline, halogeno-substituted benzaldehydes and 2-amino-6-methylpyridine, found a convenient methodology for the synthesis and efficient analytical methods for quantification in liquid phase of new type of Betti bases. The potential applications of this reaction in synthetic and medicinal chemistry might be significant. We assume that the potential of the studied Betti bases as pharmacological compounds is promising.

Acknowledgements: The study was supported financially by Scientific Project №14-15, Faculty of Veterinary Medicine, Trakia University, Stara Zagora, Bulgaria; The work was also supported by Projects UNA-17/2005 and DRNF-0213/2009 of Bulgarian National Science Fund, Sofia, Bulgaria.

REFERENCES

1. V. Oliveri, G. Vecchio, *EJMECH.*, **120**, 252 (2016).
2. N. N. Chopde, *Int. J. Pharm. Pharm. Sci.*, **5**, 541 (2014).
3. C. Cardellicchio, M. A. Capozzi, F. Naso, *Tetrahedron: Asymmetry*, **21**, 507 (2010).
4. B. P. Mathew, A. Kumar, S. Sharma, P. K. Shukla, M. Nath, *EJMECH*, **45**, 1502 (2010).
5. R. Musiol, M. Serda M, S. Hensel-Bielowka, U. J. Polanski, *Curr. Med. Chem.*, **17**, 1960 (2010).
6. X. H. Ma, X. Y. Zhang, J. J. Tan, W. Z. Chen, C. X. Wang, *Acta Pharmacol. Sin.*, **25**, 950 (2004).
7. A. Y. Shen, S. N. Wu, C. T. Chiu, *J. Pharm. Pharmacol.*, **51**, 543 (1999).
8. I. M. Awad, A. A. Aly, A. M. Abdel-Alim, R. A. Ab, S. H. Ahmed, *J. Inorg. Biochem.*, **33**, 77 (1988).
9. S. Ariyasu, A. Sawa, A. Morita, K. Hanaya, M. Hoshi, I. Takahashi, B. Wang, S. Aoki, *Bioorg. Med. Chem.*, **22**, 3891 (2014).
10. O. Varagupta, P. Boonchoong, Y. Wongkrajang, *Bioorg. Med. Chem.*, **8**, 2617 (2000).

11. M. Betti, *Org. Synth. Coll.*, **1**, 381 (1944).
12. J. P. Phillips, R. W. Keown, Q. Fernando, *J. Org. Chem.*, **19**, 907 (1954).
13. J. P. Phillips, *Chem. Rev.*, **56**, 271 (1956).
14. J. P. Phillips, J. P. Barral, *J. Org. Chem.*, **21**, 692 (1956).
15. J. P. Phillips, J. T. Leach, *Trans. Ky. Acad. Sci.*, **24**, 95 (1964).
16. C. Cardellicchio, M. A. Capozzi, A. Faso, *Tetrahedron: Asymmetry*, **21**, 507 (2010).
17. M. Salamone, R. Amorati, S. Menichetti, C. Viglianisi, M. Bietti, *J. Org. Chem.*, **79**, 6196 (2014).
18. P. F. Kaiser, J. M. White, C. A. Hutton, *J. Am. Chem. Soc.*, **130**, 16450 (2008).
19. G. Cheng, X. Wang, R. Zhu, C. Shao, J. Xu, Y. Hu, *J. Org. Chem.*, **76**, 2694 (2011).
20. V. Prachayasittikul, S. Prachayasittikul, S. Ruchirawat, V. Prachayasittikul, *Drug Des. Devel. Ther.*, **7**, 1157 (2013).
21. H. Wang, Y. Dong, J. Sun, X. Xu, R. Li, J. Hu, *J. Org. Chem.*, **70**, 1897 (2005).
22. H. Wei, L. Yin, H. Luo, X. Li, A. S. Chan, *Chirality*, **23**, 222 (2011).
23. C. Cimarrelli, D. Fratoni, A. Mazzanti, G. Palmieri, *Tetrahedron: Asymmetry*, **22**, 591 (2011).
24. I. Szatmári, F. Fülöp, *Tetrahedron*, **69**, 1255 (2013).
25. M. Marinova, K. Kostova, P. Tzvetkova, M. Tavlinova-Kirilova, A. Chimov, R. Nikolova, B. Shivachev, V. Dimitrov, *Tetrahedron: Asymmetry*, **24**, 1453 (2013).
26. A. Shahrifa, R. Teimuri-Mofrad, M. Gholamhosseini-Nazari, *Mol. Diversity*, **19**, 87 (2015).
27. R. Teimuri-Mofrad, A. Shahrifa, M. Gholamhosseini-Nazari, N. Arsalani, *Res. Chem. Intermed.*, **42**, 3425 (2016).
28. M. Shafiee, A. R. Khosropour, I. Mohammadpoor-Baltork, M. Moghadam, S. Tangestaninejad, V. Mirkhani, *Tetrahedron Lett.*, **53**, 3086 (2012).
29. A. Kumar, M. K. Gupta, M. Kumar, *Tetrahedron Lett.*, **51**, 1582 (2010).
30. J. P. Errico, B. Mugrage, I. Turchi, M. Sills, J. Ong, J. Allocco, P. Wines, *Patent* WO2011/85126 (2011).
31. R. A. Mekheimer, A. M. Asiri, A. M. Abdel Hameed, R. R. Awed, K. U. Sadek, *Green Processing and Synthesis*, **5**, 365 (2016).
32. I. Sergiev, N. Georgieva, A. Alexieva, E. Karanov, I. Petkov, *J. Ecol. Sci. - Ecology and Future*, **4**, 42 (2007).
33. A. Pavlov, N. Takuchev, N. Georgieva, *Biotechnol. Biotechnol. Equip.*, **26**(SE), 164 (2012).
34. International Conference on Harmonisation of Technical Requirements for Registration of Pharmaceuticals for Human Use, ICH Harmonized Tripartite Guideline, Validation of Analytical Procedures: Text and methodology, Q2 (R1), 1 (2005).
35. G. L. Grunewald, V. H. Dahanukar, R. K. Jalluri, K. R. Criscione, *J. Med. Chem.*, **42**, 3315 (1999).
36. P. A. Cerutti, *Lancet*, **344**, 862 (1994).
37. R. H. Burdon, *Free Radic. Biol. Med.*, **18**, 775 (1995).

СИНТЕЗ И СВОЙСТВА НА НЯКОИ БЕТИ БАЗИ КАТО ПОТЕНЦИАЛНИ ЛЕКАРСТВЕНИ ПРЕПАРАТИ

Н. Георгиева^{1*}, З. Янева¹, С. Симова², Г. Николова³

¹ Ветеринарно-медицински факултет, Тракийски университет, Студентски град, 6000 Стара Загора, България

² Институт по органична химия с Център по фитохимия, Българска академия на науките, ул. Акад. Г. Бончев, бл. 9, 1113 София, България

³ Медицински факултет, Тракийски университет, ул. „Армейска“ 11, 6000 Стара Загора, България

Постъпила на 18 април 2017 г.; Коригирана на 02 юни 2017 г.

(Резюме)

Целта на настоящето изследване бе да се синтезират Бети бази чрез модифицирана реакция на Бети, да се разработят аналитични методи за количествено определяне и тестване на тяхната микробиологична и антиоксидантна активности. За модификацията на реакцията на Бети ние използвахме първичен хетероцикличен амин, 8-хидроксихинолин и халогено-заместени ароматни алдехиди. Приложените аналитични методи за количествено определяне на изследваните Бети бази са с висока точност, висока линейност и задоволителни стойности на граница на откриване (LOD) и граница на количествено определяне (LOQ). Бети базите бяха получени с добив 80-98% и охарактеризирани чрез елементарен анализ и ЯМР спектри. Тяхната микробиологична активност бе тествана срещу 23 патогенни щамове микроорганизми (различни грам-положителни и грам-отрицателни). Микробиологичният скрининг доказа тяхната селективна микробиологична активност. Според ЕПР изследването Бети базите притежават радикалова структура и вероятно проявяват антиоксидантна активност. Ние предполагаем, че потенциалът на представените Бети бази като фармакологични препарати е голям.

Chemical profile of *Artemisia annua* from the region of Sliven, Bulgaria. A preliminary NMR study

V. Kurteva*, A. Trendafilova, S. Simova

Institute of Organic Chemistry with Centre of Phytochemistry, Bulgarian Academy of Sciences, Acad. G. Bonchev street, bl. 9, 1113 Sofia, Bulgaria

Received April 28, 2017; Revised June 05, 2017

Dedicated to Acad. Ivan Juchnovski on the occasion of his 80th birthday

A preliminary study on the chemical profile of hexane extracts of the areal part of *Artemisia annua* from the region of Bulgarian town Sliven by NMR spectroscopy is performed. The presence of a number of main components is found using NMR spectra of authentic samples and comparison with literature data. Estimation of the artemisinin quantity is made.

Key words: *Artemisia annua*; Sliven region; artemisinin; sesquiterpenes; NMR

INTRODUCTION

Artemisia annua L. (Chinese sweet wormwood, family Asteraceae) is indigenous to China. The species is also found as native to Korea, Japan, Myanmar, Northern India, Vietnam, and Southern Siberia throughout Eastern Europe and is cultivated in many parts of the World as well, like equatorial Africa, Argentina, Europe and India [1]. *A. annua* L. is used in traditional medicine for the treatment of malaria, cough, cold, and diarrhea. Whole flowering plant parts are also known to possess anthelmintic, antipyretic, antiseptic, carminative, antispasmodic, stimulant, tonic, and stomachic properties. World Health Organization has recommended *A. annua* as antimalarial drug [1].

A. annua has become the subject of intensive phytochemical evaluation following the discovery of the antimalarial drug artemisinin [1–3]. Phytochemical studies of *A. annua* have resulted in identification of more than 600 compounds including terpenoids (like sesquiterpene lactones), coumarins, phenolics, flavonoids, essential oils, etc. [2]. *A. annua* is the only known source of artemisinin (Qinghaosu). This sesquiterpene lactone is also effective in other infectious diseases such as schistosomiasis, HIV, hepatitis-B, leishmaniasis, and against a variety of cancer cell lines [1, 4–7].

Analysis of artemisinin is a challenging problem since the compound is present in low concentration in the plant; it is thermolabile, acid sensitive and unstable and lacks chromophoric groups. Various conventional and unconventional methods have

been developed in order to detect and quantify artemisinin [8], including NMR spectroscopy [9]. The popularity of quantitative NMR (qNMR) has grown substantially over the past two decades, as it can provide absolute or relative quantification of multiple metabolites within a sample without prior separation of components [10, 11].

Literature survey for wild growing *A. annua* from Bulgaria revealed only few articles on essential oil composition [12–15] and surface flavonoid aglycones [16]. Surprisingly, the content of artemisinin in Bulgarian species has not been investigated so far. The aim of this study was to determine the amount of artemisinin in *A. annua* from the region of Sliven in Bulgaria as well as to identify its accompanying compounds.

EXPERIMENTAL

Materials and methods

All solvents were purchased from Aldrich and LabScan and were used without purification. Merck Silica gel 60 (0.040-0.063 mm) was used for flash chromatography fractionation of the total extract. Salophene, a calibration substance of Reichert (Vienna) Kofler block for determination of melting points, was found to be a suitable standard for NMR quantitation of artemisinin.

Plant material

Plant material was collected in full flowering stage from the region of Sliven town in 2015. The aerial parts were air-dried and kept in dark place.

* To whom all correspondence should be sent:
E-mail: vkurteva@orgchm.bas.bg

Extraction and Fractionation

Air-dried aerial parts (300 g) were extracted in hexane (1 L) at room temperature for 48 hrs. The solid phase was removed by filtration and the solvent was evaporated under vacuum at 25 °C to give the yellowish oily residue (305 mg from 200 ml extract; 0.51%; average from three independent experiments collecting 17-19 fractions each). The crude residue was fractionated by flash chromatography on silica gel (1:100) by using a mobile phase with a gradient of polarity from hexane through dichloromethane to 5% acetone in dichloromethane.

NMR spectra

The NMR spectra were recorded on a Bruker Avance II+ 600 spectrometer (Rheinstetten, Germany) using Topspin 3.5p16 in CDCl₃ at 20 °C. The chemical shifts are quoted as δ -values in ppm against internal tetramethylsilane (TMS). Spectral width of 16 ppm on 32K points was acquired and processed with zero filling on 64K points. 64 scans were acquired for all individual fractions.

For estimation of the artemisinin quantity to a solution of 16 mg artemisinin containing fraction in 0.5 ml in CDCl₃ 1.6 mg salophene (5×10^{-3} mmol) was added. In the proton spectrum of the mixture the integral of the artemisinin signal at 3.4 ppm amounted 0.62 as compared to the salophene azomethine protons at 10.5 ppm (equal to 2) providing estimation for the quantity of artemisinin as 0.88 mg (3×10^{-3} mmol, 62% in respect to salophene).

RESULTS AND DISCUSSION

The aerial part of *Artemisia annua*, collected in full flowering stage from the region of Bulgarian town Sliven, was extracted with hexane, fractionated by flash chromatography and analysed by NMR spectroscopy. The proton NMR spectrum of the total extract provides a complicated picture with a number of overlapped signals in many areas, which hampers a reliable components' assignment. The anti-malarial drug artemisinin was detected only in a single fraction eluted by 2% acetone in dichloromethane. In the ¹H NMR spectrum of the latter a characteristic doublet of quartets in an area clear of other signals at 3.4 ppm was found, while this area is quite overlapped in the total extract, analogously no free area for the other expected artemisinin signals was found [17]. A selective TOCSY experiment starting at the proton at 3.4 ppm proved that it does belong to artemisinin via the coincidence of the chemical shifts of several neighbouring protons (methyls at 1.21/1.00 ppm, methynes at 1.78/1.25 ppm and methylenes at 1.87/1.08 ppm and 1.78/1.07 ppm) with literature data (Fig. 1). The amount of artemisinin was roughly estimated by comparison with salophen as an internal standard (Fig. 2). The integral intensity of the signal at 3.4 ppm was determined as 0.62 to the two salophen imine protons, which represents 5.5 wt.% of the fraction, 0.29 wt.% of the total extract, and 0.0015 wt.% of the dry plant. The obtained results showed very low amount of artemisinin in *A. annua* from Bulgaria when compared with the data published in the literature,

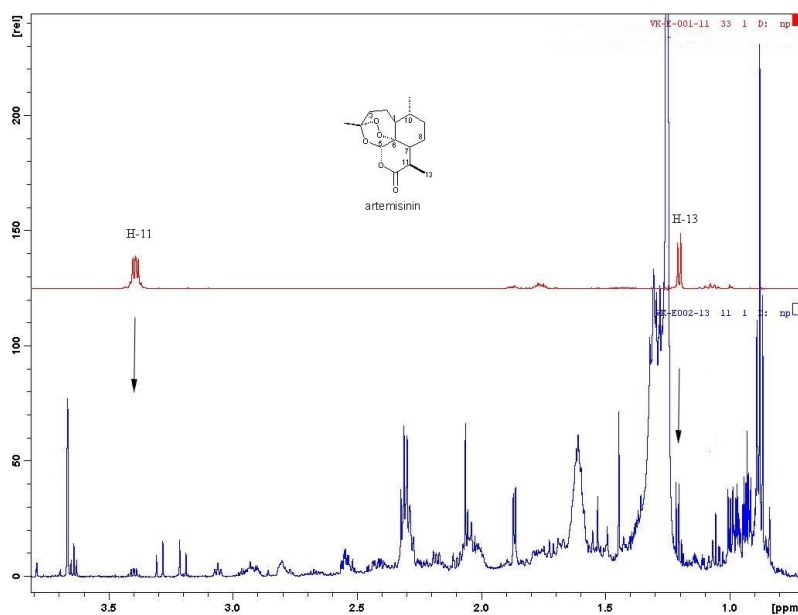


Fig. 1. Aliphatic part of ¹H (down) and selective ¹H-¹H TOCSY (up) spectra of artemisinin containing fraction.

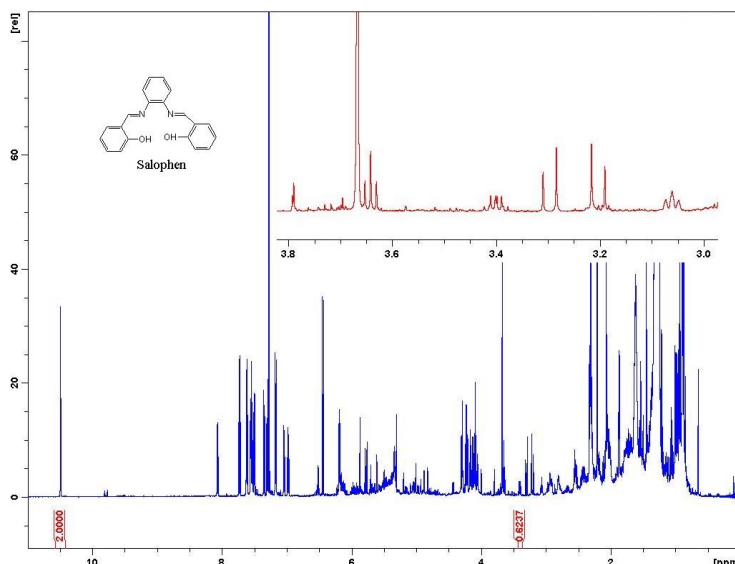


Fig. 2. ^1H NMR spectrum of artemisinin containing fraction with addition of salophene.

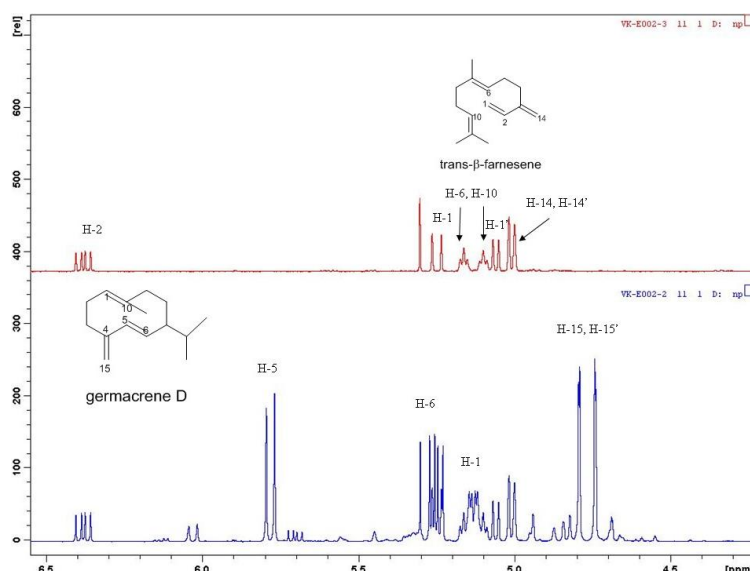


Fig. 4. Partial ^1H NMR spectra of *trans*- β -farnesene and germacrene D containing fraction (down) and *trans*- β -farnesene (up) [21].

indicating highly variable content of this lactone (0.01% – 1% depending on variety) [1, 2].

In addition to artemisinin, several other components were determined in the hexane extract (Fig. 3). Their structures were principally elucidated by comparison of their ^1H NMR spectra with those published in the literature.

Two sesquiterpene hydrocarbons were found in the less polar fractions, eluted by pure hexane. *Trans*- β -farnesene was identified by characteristic signals for a vinyl group (δ 6.36 dd, 5.24d, 5.06 d), exomethylene double bond (δ 5.01 brs and 4.99 brs) and two olefinic protons at δ 5.17 and 5.10 (Fig. 4) [21]. The structure of the other compound, germacrene D was deduced from the characteristic signals for double bonds in 10-membered ring:

trisubstituted C-1/C-10 (δ 5.13, H-1 and 1.52, H-14), *trans*-disubstituted C-5/C-6 (δ 5.78, d, H-5 and 5.26, dd, H-6, $J_{5,6} = 16$ Hz), and exomethylene C-4/C-15 (δ 4.74 brs and 4.79 brs) [22].

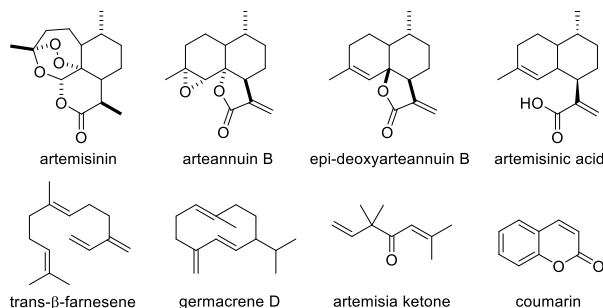


Fig. 3. Detected components in hexane extract of *Artemisia annua* from Sliven region.

The presence of monoterpene ketone artemisia ketone in a fraction eluted by dichloromethane/hexane 1:1 mixture was confirmed by comparison with the ^1H NMR spectrum of the authentic standard (Fig. 5). *Trans*- β -farnesene, germacrene D and artemisia ketone are typical volatile components of *A. annua* essential oils and their presence in hexane extracts is not surprising.

Three sesquiterpenes with cadinane skeleton, arteannuin B, *epi*-deoxyarteannuin B and artemisinic acid, were detected in fractions eluted with 2% acetone in dichloromethane. ^1H NMR spectra (Fig. 6) of arteannuin B and *epi*-deoxyarteannuin B contain signals characteristic for α -exomethylene- γ -lactones (H-13/13', δ 6.16/5.43 d and 6.17/5.56 d, respectively). Their spectra differ

in the multiplicity and chemical shifts of some other signals. Thus, H-7 methyne at δ 2.74 in the spectrum of arteannuin B exhibits allylic coupling with H-13/13' ($J = 3.1$ Hz), which requires *trans*-fusion of the lactone ring, while the observed smaller allylic constants ($J_{7,13} = J_{7,13'} = 1.2$ Hz) in the spectrum of *epi*-deoxyarteannuin B corresponds to *cis*-fusion of the lactone ring. The signals at δ 5.28 brs and 1.67 s (CH_3) confirmed the presence of a trisubstituted C-4/C-5 double bond in the structure of *epi*-deoxyarteannuin B. These signals are missing in the spectrum of arteannuin B. Instead, two new singlets appear at δ 2.68 and 1.34 (CH_3), indicating the presence of a methyl-substituted epoxy ring. All these data are in agreement with those reported previously [18, 19].

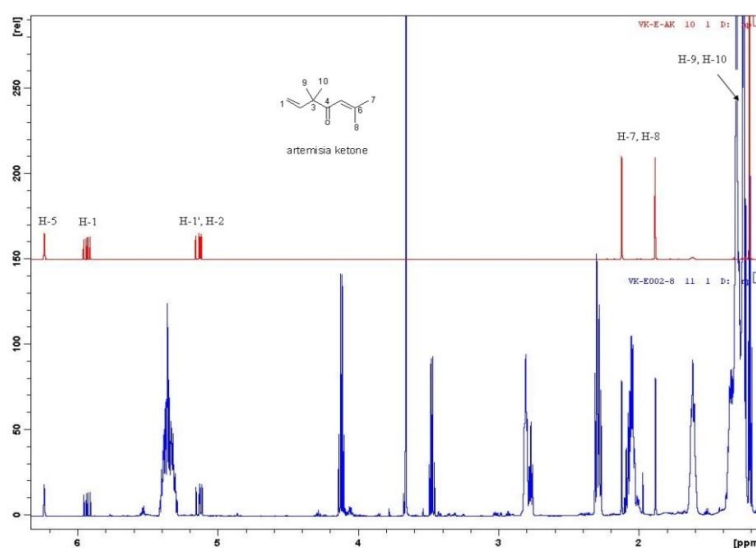


Fig. 5. ^1H NMR spectra of artemisia ketone containing fraction (down) and authentic sample of artemisia ketone (up).

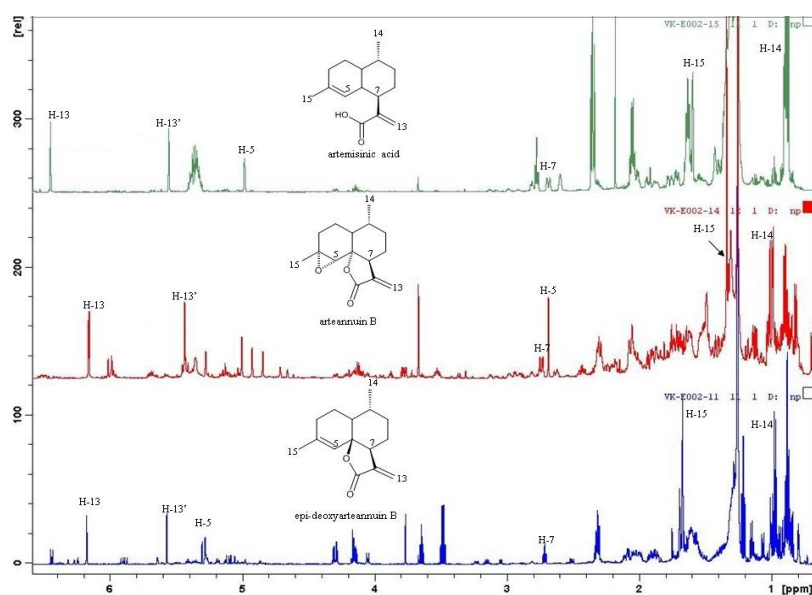


Fig. 6. ^1H NMR spectra of *epi*-deoxyarteannuin B (down), arteannuin B (middle), and artemisinic acid (up) containing fractions.

Table 1. Main constituents in the hexane extract of *Artemisia annua* from the region of Sliven, Bulgaria, detected by relevant 1D and 2D NMR spectra and literature comparison.

Component	Selected $^1\text{H}/^{13}\text{C}$ signals in ppm (multiplicity, coupling constants)
artemisinin	3.40 (dq, 5.2,7.2), 1.21 (d, 7.2)
arteannuin B	6.16 (d, 3.1), 5.43 (d, 3.1), 2.74 (dq, 12.4, 3.1), 2.68 (s), 1.34 (s), 0.99 (d, 6.0)
epi-deoxyarteannuin B	6.17 (d, 1.2), 5.57 (d, 1.2), 5.28 (brs), 2.71 (tt, 6.8, 1.2), 1.67 (s)
artemisinic acid	6.45 (brs), 5.55 (t, 1.5), 4.98 (s), 2.69 (dt, 12.3, 3.6), 2.60 (brs), 1.59 (brs), 6.38 (dd, 10.9, 17.6), 5.25 (d, 17.6), 5.16 (brt, 6.6), 5.10 (brt, 6.9), 5.06 (d, 10.9), 5.02 (brs), 5.00 (brs)
<i>trans</i> - β -farnesene	5.13 (m), 5.78 (d, 15.8), 5.25 (dd, 15.8, 10.0), 4.74 (d, 2.3), 4.79 (d, 2.3), 1.51 (s), 0.86 (d, 6.7), 0.81 (d, 6.8)
germacrene D	6.24 (quint, 1.3), 5.93 (dd, 17.5, 10.7), 5.15 (dd, 17.4, 0.9), 5.13 (dd, 10.6, 0.9), 2.12 (d, 1.3), 1.89 (d, 1.3), 1.22 (s)
artemisia ketone	7.72 (d, 9.5), 7.54 (ddd, 8.4,7.4,7.2), 7.50 (dd, 7.7,1.5), 7.34 (d, 8.3), 7.29 (td, 7.5, 1.0), 6.43 (d, 9.5)
coumarin	4.12 (q, 7.1), 3.66 (s) 2.81/2.77 (t, 7.0), 2.35/2.30/2.28 (t, 7.5), 2.06 (m), 1.62 (m), 0.89 (t, 6.8), 0.88 (t, 7.1),
fatty acids and esters	0.98 (t, 7.5), 2.08 (m), 2.81 (brt, 6.2)

The ^1H NMR spectrum of the biogenetic precursor of artemisinin, artemisinic acid (Fig. 6), is very similar to that of *epi*-deoxyarteannuin B. However, H-5 is shifted upfield (δ 4.98) and H-13 and H-13' - downfield (δ 6.44 and 5.55) suggesting the presence of an α,β -unsaturated acid instead of a lactone ring [20].

Finally, sizeable amounts of coumarin are easily identified in several fractions eluted by 2% acetone in dichloromethane by their characteristic signals in the aromatic area (δ 6.40 – 7.80) [22].

Main components in the hexane extract constitute a mixture of fatty acids (FA), methyl and ethyl esters of fatty acids. The NMR spectra show the presence of both saturated and differently unsaturated fatty acids, including approximately 25% of ω -3 polyunsaturated FA, determined from the ratio of the integral intensities of the methyl groups at 0.97 and 0.88 ppm.

The characteristic signals described above are listed on Table 1.

CONCLUSION

A preliminary study on the chemical profile of hexane extracts of the areal part of *Artemisia annua* from the region of Sliven town performed by NMR spectroscopy show the presence of several components: fatty acid and their methyl and ethyl esters, sesquiterpenes *trans*- β -farnesene, germacrene D, artemisinin, arteannuin B, *epi*-deoxyarteannuin B, and artemisinic acid, irregular terpene artemisia ketone, and the fragrant compound coumarin. The amount of artemisinin in the extract of the Bulgarian plant is estimated and is found to be very low in respect to its content in plants from other regions.

Acknowledgements: The financial support by The Bulgarian Science Fund, projects UNA-17/2005 and DRNF-02-13/2009, is gratefully acknowledged. The authors are also thankful to Dr. Ergun Atay, Siberica Life Ltd., for supplied dry plant material.

REFERENCES

1. *Artemisia annua* – Pharmacology and Biotechnology, T. Aftab, J. F. S. Ferreira, M. M. A. Khan, M. Naeem, (eds.), Springer-Verlag, Berlin, Heidelberg, 2014.
2. G. D. Brown, *Molecules*, **15**, 7603 (2010).
3. P. Newton, N. White, *Ann. Rev. Med.*, **50**, 179 (1999).
4. S. Borrmann, N. Szlezák, J.-F. Faucher, P.-B. Matsiegui, R. Neubauer, R. K. Binder, B. Lell, P. G. Kreamer, *J. Infect. Dis.*, **184**, 1363 (2001).
5. R. Sen, S. Bandyopadhyay, A. Dutta, G. Mandal, S. Ganguly, P. Saha, M. Chatterjee, *J. Med. Microbiol.*, **56**, 1213 (2007).
6. N. P. Singh, H. Lai, *Life Sci.*, **70**, 49 (2001).
7. M. P. Crespo-Ortiz, M. Q. Wei, *J. Biomed. Biotechnol.*, Article ID 2475972012 (2012).
8. P. Christen, J. L. Veuthey, *Curr. Med. Chem.*, **8**, 1827 (2001).
9. P. C. Castilho, S. C. Gouveia, A. I. Rodrigues, *Phytochem. Anal.*, **19**, 329 (2008).
10. S. K. Bharti, R. Roy, *TrAC Trends Anal. Chem.*, **35**, 5 (2012).
11. G. F. Pauli, Shao-Nong Chen, Ch. Simmler, D. C. Lankin, T. Gödecke, B. U. Jaki, J. B. Friesen, J. B. McAlpine, J. G. Napolitano, *J. Med. Chem.* 2014, **57**, 9220–9231
12. E. Tsankova, I. Ognyanov, *Italiana Essenze, Profumi, Piante Officinale, Aromi, Saponi, Cosmetici, Aerosol*, **58**, 502 (1976).

13. N. Genov, E. Georgiev, *Naunchi Trudove - Vissh Institut po Khranitelna i Vkusova Promishlenost, Plovdiv*, **30**, 141 (1983).
14. G. D. Pham, *Tap. Chi. Duoc. Hoc.*, **11** (2003).
15. R. Tzenkova, Z. Kamenarska, A. Draganov, A. Atanassov, *Biotechnol. Biotechnol. Equip.*, **24**, 1833 (2010).
16. M. Nikolova, R. Gevrenova, S. Ivancheva, *J. Serb. Chem. Soc.*, **69**, 571 (2004).
17. H.-D. Hao, Y. Li, W.-B. Han, Y. Wu, *Org. Lett.*, **13**, 4212 (2011).
18. P. K. Agrawal, R. A. Vishwakarma, D. C. Jain, R. Roy, *Phytochemistry*, **30**, 3469 (1991).
19. L.-K. Sy, G. D. Brown, *Phytochemistry*, **58**, 1159 (2001).
20. S.-U. Kim, j. Han, Y.-H. Lim, *Planta Med.*, **62**, 460 (1996).
21. E. Simionatto, C. Porto, C. Z. Stüker, I. I. Dalcol, U. F. da Silva, *Quim. Nova*, **30**, 1923 (2007).
22. F. Boeck, M. Blazejak, M. R. Anneser, L. Hintermann, *Beilstein J. Org. Chem.*, **8**, 1630 (2012).

ХИМИЧЕН ПРОФИЛ НА *ARTEMISIA ANNUA* ОТ РЕГИОНА НА ГР. СЛИВЕН, БЪЛГАРИЯ. ПРЕДВАРИТЕЛНО ЯМР ИЗСЛЕДВАНЕ

В. Куртева*, А. Трендафилова, С. Симова

*Институт по органична химия с Център по фитохимия, Българска академия на науките,
ул. Акад. Г. Бончев, бл. 9, 1113 София, България*

Постъпила на 28 април 2017 г.; Коригирана на 05 юни 2017 г.

(Резюме)

Проведено е предварително изследване на химичния профил на хексанов екстракт на надземните части на *Artemisia annua* от региона на град Сливен, България, посредством ЯМР спектроскопия. Идентифицирани са основните компоненти чрез сравнение с автентични проби и литературни данни. Направена е оценка на количеството на артемизинин в екстракта.

Preliminary NMR and chemometric study of pine jams used as medicinal remedies

D. Gerginova, D. Dimova, S. Simova*

Institute of Organic Chemistry with Centre of Phytochemistry, Bulgarian Academy of Sciences, Acad. G. Bonchev street, bl. 9, 1113 Sofia, Bulgaria

Received May 3, 2017; Revised June 5, 2017

Dedicated to Acad. Ivan Juchnovski on the occasion of his 80th birthday

Chemical profile of pine cone and pine bud jam is determined using ¹H and ¹³C NMR spectra. Principal component and cluster analysis of 41 detected organic ingredients allow discrimination of jam from honey. Difference in the chemical profile of the two jams is found.

Key words: pine cone and bud; honey; ¹H nuclear magnetic resonance; ¹³C NMR; cluster analysis, PCA

INTRODUCTION

Pine jam, also known as “pine honey” or pine elixir, does not originate from bee activity, but is made from pine cones or buds. Both products are delicious due to their unique aroma of a pine forest. Additionally they are healthy and a worthy substitute of honey. Pine jams are often used in traditional medicine as therapeutic agents against respiratory viral diseases and/or for strengthening of the immune system, very popular in Eastern Europe, Russia and Georgia. Despite abundant information on the chemical composition [1] and biological activities [2] of the *Pinus* species, jams are only poorly studied. We were able to find only two publications in the literature so far – one devoted to their antioxidant and antimicrobial properties [3] and one to characterization of the detected volatile components [4]. The traditional medical use of pine jams and honeys is very often quite close, however, their prize and actual activity differs considerably. That is why the aim of the present work is to determine the main components in pine jams from cones and buds using NMR spectroscopy and to test the suitability of unsupervised chemometric methods to distinguish pine jams from honey types.

EXPERIMENTAL

Sample preparation

Pine jams and honeys were bought from the local market. 0.5 g of jam or honey was dissolved in 0.5 ml D₂O, containing 0.02 v. % sodium salt of

trimethylsilylpropionic acid-d₄ (TSPA) for internal standard and 0.02 v. % of NaN₃ as a preservative.

Spectral Parameters

¹H (600.01 MHz) and ¹³C (150.88) NMR spectra have been acquired on an AVANCE AV600 II+ NMR spectrometer using topspin v.3 pl 6. All spectra have been recorded in D₂O at 293.0±0.1 K. TSPA-d₄ has been used as an internal reference with chemical shifts at 0.0 ppm and -2.63 ppm for ¹H and ¹³C, respectively. Following acquisition parameters have been used for ¹H NMR: spectral width of 13.6 ppm (transmitter frequency at 4.84 ppm) on 64 K data points – FID resolution of 0.3 Hz and acquisition time 2.58 s; 60⁰ pulses of 7.2 μs duration; relaxation delay of 4 s; 16 dummy and 256 scans. Zero filling by a factor of 2 and exponential multiplication by a line broadening of 0.3 Hz has been applied. Manual processing and careful manual phasing of the spectra ensured that the integrals have minimal distortion and thus contribute to the quantitative reproducibility. Standard ¹³C NMR parameters have been used - spectral width 238.9 ppm, 32 K data points, 60⁰ pulses of 6.5 μs duration; relaxation delay of 2.0 s; 4048 scans. Assignment of the signals has been made on the basis of the gradient enhanced versions of TOCSY, standard and semi-selective HSQC [5].

Preparation of data for chemometrics

A combined ¹H/¹³C method was used to obtain reliable semi-quantitative data for characterization of the pine jams and their differentiation from the honey types. Quantitation relies on the intensities of the ¹³C NMR signals utilizing the much higher

* To whom all correspondence should be sent:
E-mail: sds@orgchem.bas.bg

dispersion (Fig. 2) of the signals in the carbon than in the ^1H spectra (Fig. 1). The region of the anomeric carbon atoms (106–83 ppm) contains a number of non-overlapped signals for most of the saccharides. Additionally, ^{13}C intensities for several typical honey ingredients as quercitol [6], butanediol [7] and proline [8] as well as for 15 unidentified constituents were determined (see Table S1). One carbon signal was chosen for every of the 41 components (Table 1). Reducing sugars were also represented by one non-overlapped signal taking into account the quantities of the corresponding epimers from the NMR spectra of the individual sugars in D_2O . The molar mass of all components was taken into account in order to determine the amount of the individual ingredients. Diffusion NMR spectra indicate that the unidentified components have diffusion coefficients in the range between mono- and disaccharides, and a tentative molar mass of 200 was ascribed to all of them. Additional adjustment of all carbon intensities was made via comparison with the integration results of several proton signals against TSPA.

Chemometric analysis

Chemometric analysis [9, 10] was applied in order to test the possibility to differentiate pine jams from honey varieties. Taking into account the limited number of samples unsupervised pattern recognition via cluster analysis (CA) and principle component analysis (PCA) were applied using the algorithms offered by EXCEL [11], SIMCA14 [12] and Past3 [13] statistical software.

Cluster analysis allows grouping of a set of objects in such a way that objects in the same group are more similar to each other than to those in other groups. Very popular is the “connectivity model” that uses hierarchical clustering based on distance connectivity represented by a dendrogram (e.g. Fig. 4A). The x-axis marks the distance at which the clusters merge, while the investigated objects are disposed along the y-axis preventing cluster mixing, accompanied by a table presenting the distances between the objects. The Ward's minimum variance method was found most appropriate for the jam-honey discrimination. Principal components analysis is the most often applied procedure for identifying a smaller number of uncorrelated variables, called “principal components”, from a large set of data. The goal of PCA is to explain the maximum amount of variance with the fewest number of principal components. These are linear combinations called usually factors being better descriptors than the original chemical or physical measurements, allowing easier visualization of the obtained results. In the case of a limited number of samples n as in our investigation ($n=5$) the number of derived factors is confined to $n-1$.

RESULTS AND DISCUSSION

NMR chemical profiling

The ^1H and ^{13}C NMR chemical shifts were obtained from the corresponding 1D NMR spectra of the five remedies. They are presented in Figs. 1 and 2 with annotation of the saccharide components in the corresponding anomeric spectral areas.

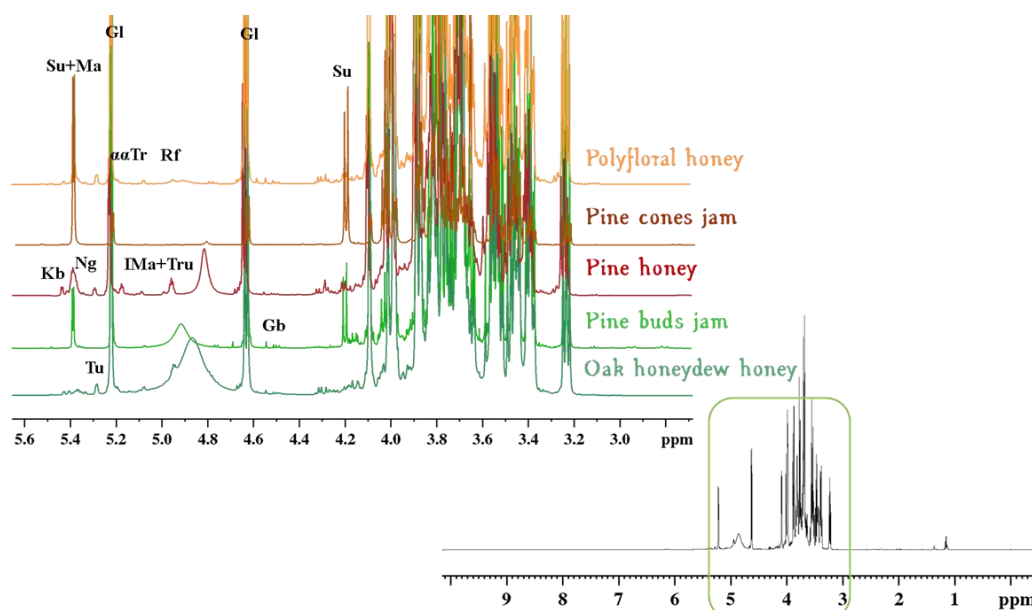


Fig. 1. ^1H NMR spectra of the investigated jams and honeys with expansion of the sugar region.

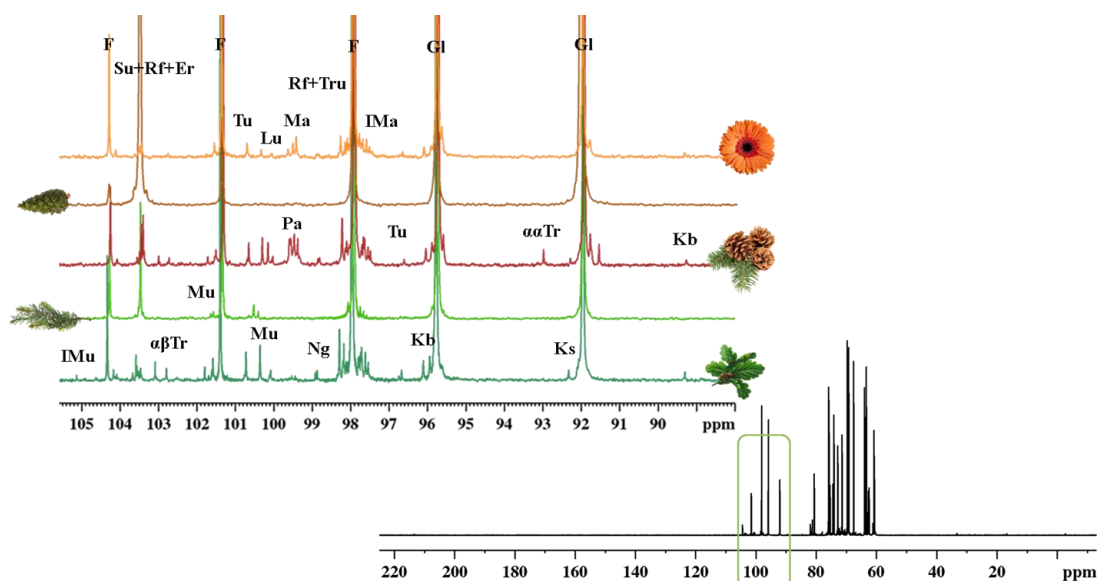


Fig. 2. ^{13}C NMR spectra of the investigated jams and honeys with expansion of the anomeric sugar region.

Use of the gradient version of the HSQC technique with high resolution in the indirect dimension and comparison with previously made sugar profiling [14, 15] and literature data [16] assures the unambiguous identification of the organic ingredients - carbohydrates, amino acids and some other detectable components. The profile of two jams is compared with the data of three previously studied types of honey [14, 15] – pine honeydew, oak honeydew and polyfloral honey. The chemical shifts used for quantitation of the detected organic ingredients are presented in Table 1 and the chemical profiles are visualized in Fig. 3.

Chemometric analysis

The input data set with normalized intensities for 41 detected organic ingredients in the five investigated natural remedies is presented in Table S1. The data is first standardized by the z-transform procedure to eliminate the parameter dimension

impact on the classification and interpretation results. For hierarchical aggregation of the samples into a cluster the Ward's method is used. The standardized component quantities, presented in Fig. 3, cluster in two statistically significant groups for the five studied samples. One is for the studied honeys and the other - for the jams (Fig. 4A) with Euclidean distances between the different elements presented on Fig. 4B. Principle component analysis identifies two factors responsible for 75% of the total variance in the chemical composition of honey and jam. The results are visualized in a 3D PCA plot on Fig. 4C and listed in Table 2S. The first factor, accounting for 51% of the explained system variance correlates with the main di- and trisachacharides characteristic for honey, quercitol, 2,3-butanediol and several unidentified components while the second factor, responsible for 23% is connected to the quantities of proline, several less common saccharides and the unrecognized components U1 and U10.

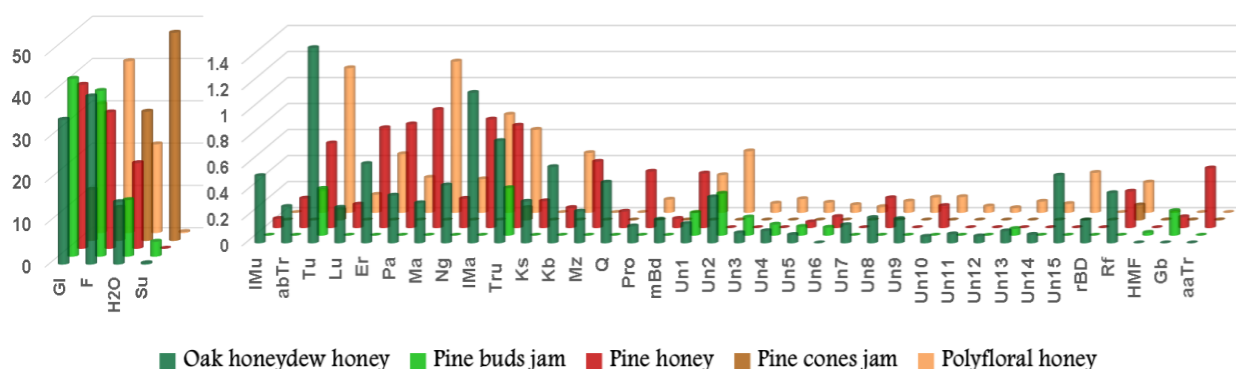


Fig. 3. Chemical profile of the studied natural remedies (in g/100g jam or honey), representing the semi-quantitative data obtained from the ^1H and ^{13}C NMR spectra.

Table 1. Chemical shifts of the carbon signals used for quantitation and their attached protons (in ppm), acronyms of the different organic ingredients, α/β ratio of the reducing sugars and proton signals used for adjustment of the carbon intensities.

<i>Component</i>	$\delta^{13}C$	δ^1H	<i>Acronym</i>	$\alpha:\beta$ Ratio	<i>Used δ^1H</i>
Isomaltulose	104.64	-	IMu	0.164	
$\alpha\beta$-Trehalose	102.79	4.63	$\alpha\beta$ Tr		
Gentiobiose	102.49	4.47	Gb	0.364	
Turanose	100.72	5.29	Tu	0.444	5.29
Leucrose	100.11	5.09	Lu		5.09
Erlose	99.67	5.38	Er		
Panose	99.64	5.38	Pa	0.615	
Maltose	99.54	5.38	Ma	0.417	
Nigerose	98.87	5.33	Ng	0.583	
Isomaltose	97.73	4.95	IMa	0.636	
Trehalulose	97.71	-	Tru		
$\alpha\alpha$-Trehalose	93.00	5.17	$\alpha\alpha$ Tr		
Isokestose	92.31	5.41	1-Ks		
Kojibiose	89.30	5.43	Kb	0.415	5.43
Melezitose	83.24	4.29	Mz		
Sucrose	76.21	4.21	Su		
Raffinose	76.14	4.22	Rf		4.99
Glucose	75.75	3.45	Gl	0.600	4.64
Fructose	67.45	3.78	F	0.688	4.10
Quercitol	33.20	1.98/1.80	Q		
Proline	23.71	1.99	Pro		
meso-Butanediol	16.72	1.13	mBd		
racemic Butanediol	17.80	1.13	rBd		
Unidentified compounds*	103.46	-	U1		
	97.79	-	U2		
	101.69	-	U3		
	101.22	5.23	U4		
	96.74	5.48	U5		
Hydroxymethyl-furfural	-	9.44	HMF		9.44

* Additional compounds U6-U15 (102.26; 104.08; 103.66; 103.55; 103.44; 103.38; 102.86; 100.77; 99.26; 98.17).

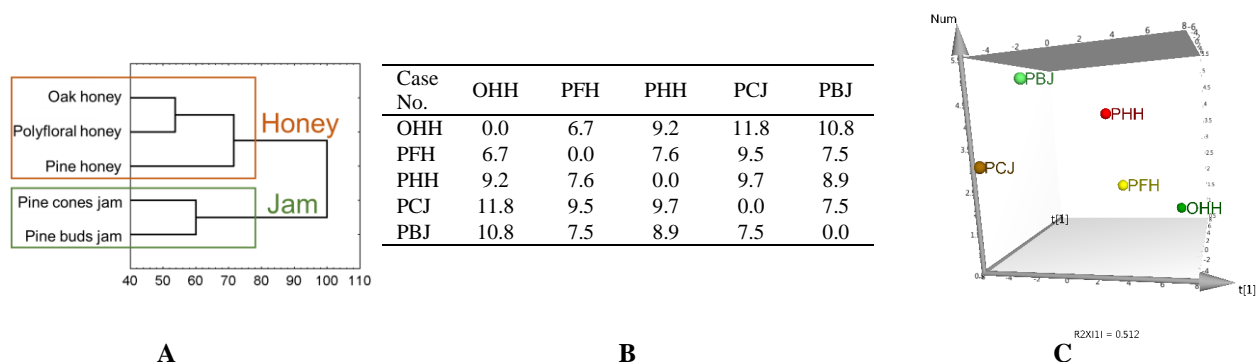


Fig. 4. Visualization of the multivariate analysis. A) Hierarchical dendrogram for clustering of 41 ingredients; B) Table of distances between different objects; C) PCA 3D score plot for: PCJ – pine cone jam; PBJ – pine bud jam, PHH – pine honeydew honey; PFH – polyfloral honey; OHH - oak honeydew honey.

The observed differences in the chemical profile of the two studied jams can be best visualized by the Nightingale's "rose diagram".

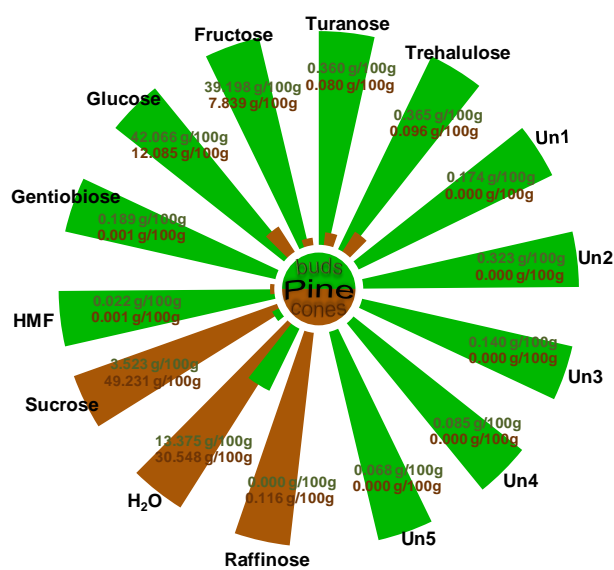


Fig. 5. Nightingale's diagram.

CONCLUSION

Significant difference in the carbohydrate profile of the studied jams has been detected. The jams are characterized generally by a lower content of di- and trisaccharides compared to honeys. Higher amounts in the jams only of saccharose and gentiobiose were determined. Pine cone jam contains appreciable amount of sucrose, while pine bud jam is rich in gentiobiose. The combination of NMR spectroscopy with chemometric methods is a power tool not only to detect adulteration, to distinguish geographical and botanical origin of honey but also to discriminate jam from homey, provoking more detailed analysis of pine jams.

Acknowledgements: Financial support of the Bulgarian National Science Fund (Projects UNA-

17/2005 and DRNF-0213/2009) is gratefully acknowledged. D. Dimova thanks project BG05M20P001-2.002-0001 of the Ministry of Education for providing a stipend for student practice.

Electronic Supplementary Data available here.

REFERENCES

1. A. Rogachev, N. Salakhutdinov, *Chem & Biodiv*, **12**, 1 (2015).
2. Bo Li, Yun-Heng Shen, Yi-Ren He, Wei-Dong Zhang, *Chem & Biodiv*, **10**, 2133 (2013).
3. L. Deac, A. Farcas, D. Vodnar, M. Tofana, S. Socaci, *Bulletin UASVM Food Science and Technology*, **71**, 77 (2014).
4. C. A. Semeniu, C. R. Pop, A. Rotar, L. Stan, S. Socaci, S. Muste, V. Mireşan, *CYTA – J. Food*, **14**, 213 (2016).
5. Bruker pulse library programs: dipsi2etgpsi, hsqcetdtpsp.3, shsqcetgpsisp2.2
6. S. Simova, A. Atanassov, M. Shishiniova, V. Bankova, *Food Chem.*, **134**, 1706 (2012).
7. A. Soria, M. Gonzalez, C. Lorenzo, I. Martinez-Castro, J. Sanz, *Food Chem.*, **85**, 121 (2004).
8. C. Truzzi, A. Annibaldi, S. Illuminati, C. Finale, G. Scarponi, *Food Chem.*, **150**, 477 (2014).
9. M. Nedyalkova, B. Donkova, V. Simeonov, *J. AOAC Int.*, **100**, 359 (2017).
10. R. Broa, A. Smilde, *Anal. Methods*, **6**, 2812 (2014).
11. Microsoft Excel 2010
12. SIMCA 14.X, <http://umetrics.com/products/simca>, last access 28.04.2017
13. Past 3, V. 3.15, last access 28.04.2017; link: <https://folk.uio.no/ohammer/past/index.html>,
14. D. Gerginova, BS Thesis, UCTM, Sofia, 2016.
15. D. Gerginova, M. Popova, V. Bankova, S. Simova – unpublished data.
16. B. Petersen, O. Hindsgaul, S. Meier, *Analyst*, **139**, 401 (2014).

**ИЗСЛЕДВАНЕ НА БОРОВИ СЛАДКА ИЗПОЛЗВАНИ В НАРОДНАТА МЕДИЦИНА
ПОСРЕДСТВОМ ЯМР И ХЕМОМЕТРИЯ**

Д. Гергинова, Д. Димова, С. Симова*

*Институт по органична химия с Център по фитохимия, Българска академия на науките,
ул. Акад. Г. Бончев, бл. 9, 1113 София, България*

Постъпила на 3 май 2017 г.; Коригирана на 5 юни 2017 г.

(Резюме)

Проведено е начално изследване на химичния профил на сладко от борови шишарки и от борови връхчета посредством ^1H and ^{13}C ЯМР спектроскопия. Анализ на главните компоненти и клъстерен анализ на 41 органични съставки позволява разграничаване на сладко от пчелен мед. Открити са разлики в химичния профил на двете борови сладка.

Cytotoxicity assay and intracellular localization of 2-carbamido-1,3-indandione in Balb/c 3T3 cells

N. Markova^{1*}, A. Georgieva², I. Philipova¹, I. Angelov¹, V. Enchev¹, A. Kril²

¹ Institute of Organic Chemistry with Centre of Phytochemistry, Bulgarian Academy of Sciences, Acad. G. Bonchev street, bl. 9, 1113 Sofia, Bulgaria

² Institute of Experimental Morphology, Pathology and Anthropology with Museum, Bulgarian Academy of Sciences, Sofia, Bulgaria

Received May 3, 2017; Revised May 23, 2017,

Dedicated to Acad. Ivan Juchnovski on the occasion of his 80th anniversary

Cytotoxicity assay of 2-carbamido-1,3-indandione (CAID) has been performed by means of the validated Balb/c 3T3 Neutral Red Uptake Test. In addition, the intracellular localization of CAID in murine embryonic fibroblasts, studied by fluorescence microscopy, is reported. The results indicate complete absence of toxicity of CAID to immortalized normal mammalian embryonic cells and high affinity for binding to nucleic acids. Fluorescence microscopic examination demonstrate the affinity of the 2-carboxamide-indane-1,3-dione to DNA- and RNA-containing cellular structures. To elucidate the affinity of CAID to nucleic acids, the B3LYP/6-31G(d,p) calculations were performed. According to the calculations CAID is preferably associated to nucleotides phosphate group.

Key words: 2-carbamido-1,3-indandione; anti-proliferative activity; malignant cells

INTRODUCTION

2-Substituted 1,3-indandiones have been a subject of investigations due to their pharmacological properties [1] and a wide range of biological activities such as anti-inflammatory [2] and antitumor [3,4] activity. Dimmock et al. [4] show that 2-benzylidene-1,3-indandiones are cytotoxic to several malignant cell lines and also display preferential toxicity to various neoplasms rather than to the normal cells.

2-Carbamido-1,3-indandione (CAID) belongs to the 1,3-indandione group. CAID shows relatively high photostability and because of its strong absorption in UVA and UVB spectral region it is a promising sunscreen candidate. Our previous work [5] also indicates that the compound has a potential and is suitable for use as a fluorescent molecular probe for investigation of different biomolecules.

Thus, the aim of this study, as an essential part of an ongoing investigation on the antitumor activity of 2-carbamido-1,3-indandione is to present data about its cytotoxicity to normal cells such as Balb/c 3T3 cell line. In addition, the intracellular localization of CAID in murine embryonic fibroblasts, studied by fluorescence microscopy, is reported.

MATERIALS AND METHODS

Synthesis of 2-carbamido-1,3-indandione

2-Carbamido-1,3-indandione was synthesized applying a known procedure [6]. Condensation of diethyl phthalate with acetonitrile in the presence of sodium methoxide afforded 1,3-dioxo-2-indancarboxitril in 91% yield. Subsequent hydrolysis with concentrated sulfuric acid resulted in the desired amide in 64 % yield after recrystallized from methanol.

Steady-state spectral measurements

The photophysical properties, absorbance and fluorescence, of CAID were investigated in ethanol and dimethylsulfoxide, solvents suitable for biological applications. UV-visible spectra were recorded with a Perkin Elmer Lambda 25 UV/Vis Spectrometer. Fluorescence spectra were recorded with a Perkin Elmer LS-55 Luminescence Spectrometer.

Cell lines and culture conditions

Balb/c 3T3 cell line was used for assessment of the cytotoxicity of CAID. Cells were cultured in Dulbecco's Modified Eagle's Medium with low glucose (1.0 g/L) containing L-glutamine and

* To whom all correspondence should be sent:
E-mail: nadya@orgchem.bas.bg

sodium pyruvate (DMEM, Sigma-Aldrich). The culture medium was supplemented with 10% fetal bovine serum - FBS (Gibco; BioWhittaker) and antibiotics (penicillin 100 UI/ml and streptomycin, 100 µg/ml, AppliChem). The cultures were maintained in plastic flasks with a growth surface area 25 cm² and 75 cm² (Orange Scientific, Belgium). Cultivation was performed in an incubator at 37°C, 5% CO₂ and 95% relative humidity. Solution containing 0.05% trypsin (Gibco) and 0,025% ethylenediamine tetraacetic acid (EDTA, FlowLab, Australia) was used for cell dissociation. Disposable plastic consumables (tissue culture flasks, containers, filtration systems, tissue culture plates, etc.) were purchased from Orange Scientific, Belgium.

Cytotoxicity testing (Balb/c 3T3 Neutral Red Uptake Test)

Cytotoxic effect of the 2-carboxamide-indane-1,3-dione was studied by Balb/c /c 3T3 Neutral Red Uptake Test (3T3 NRU test) as described previously [7,8]. Briefly, cells were suspended in growth medium with 10% FBS and seeded in 96-well plates (1x10⁴ cells/well). After 24-hour incubation period, the cell cultures were treated with indandione in growth medium containing 5% FBS. Cells were treated with eight different concentrations of the tested compound (dilution factor - $7\sqrt{10} = 1.389$; 6 wells for each concentration) for 24 hours. Untreated (control) cultures were grown for the same conditions in the growth medium with 5% FBS. The morphology of the cell cultures were monitored by inverted microscope. After washing with PBS control and treated cell cultures were incubated for 3 hours in a culture medium containing 0.25 µg/mL neutral red. The absorbed intracellular vital dye was extracted by adding a solution containing 50% ethanol, 49% water and 1% acetic acid. The cytotoxic effect of the test substance was presented as a concentration-dependent decrease of the amount of absorbed vital dye – neutral red. The optical density of the control and treated cultures was measured using an ELISA spectrophotometer (TECAN, SunriseTM, Grödig / Salzburg, Austria) at a wavelength of 540 nm. The relative survival of the treated cells compared to the control was calculated for each concentration using the following formula:

$$\text{Cell viability (\%)} = \frac{\text{Optical density (OD)}_{540} \text{ (experimental)}}{\text{OD}_{540} \text{ (control)}} \times 100.$$

Fluorescent microscopy

BALB/c 3T3 cells were suspended in growth medium on sterile diagnostic slides with teflon rings and incubated in a moist chamber at 37.5°C and 5% CO₂ for 24 hours. Growth medium was removed and cells were treated with four different concentrations of 2-carboxamide-indane-1,3-dione - 100 µM, 50 µM, 10 µM and 1 µM. After 24 h treatment, cells were washed with PBS, dried at room temperature, fixed in ice cold acetone for 20 min. and covered with glass coverslips. The preparations were observed by a fluorescence microscope Leica DM 5000 B.

Statistical analysis

Data are presented as mean ± standard deviation (SD). Statistical significance of differences between the viability of the cells treated with different concentrations and the control cells was evaluated by one-way analysis of variance (ANOVA), followed by Bonferroni's test using the GraphPAD PRISM software, version 5 (GraphPad Software Inc., San Diego, USA). Values * p < 0.05, ** p < 0.01 and *** p < 0.001 were considered statistically significant.

Quantum chemical calculations

The geometries of the two 2-carbamido-1,3-indandione tautomers were optimized at the MP2/6-31+G(d,p) level. Solvent effect (ethanol and dimethylsulfoxide, DMSO) was accounted by using the self-consistent reaction field method with the conductor polarizable continuum model (CPCM) formalism. The stationary-point geometries were fully optimized in the reaction field of the implicit solvent. The minima and transition state were confirmed to have zero and one imaginary frequency, respectively. The values of Gibbs free energies (ΔG) and activation barrier (ΔG[#]) were calculated at temperature 298.15 K. The percent content of tautomers is: content % = 100.p_i

where $p_i = \frac{e^{-\Delta G_i / RT}}{\sum_i e^{-\Delta G_i / RT}}$. The classical rate

constants of the forward (k_f) and the reverse (k_r) tautomerization reactions were obtained using the Eyring equation. Because of the size of the structures studied, the geometries of complexes of 2-carbamido-1,3-indandione with uridine monophosphate or guanosine monophosphate were optimized at B3LYP/6-31G(d,p) level without any constrains.

According to Alcolea Palafox [9-11], the B3LYP functional and 6-31G(d,p) basis set represents a compromise between accuracy and computational cost and thus B3LYP/6-31G(d,p) has been used in the majority of the calculations. The program package GAMESS [12] was used to perform the quantum chemical calculations.

RESULTS AND DISCUSSION

Two enol tautomeric forms of 2-carbamido-1,3-indandione coexist in different solutions [4, 12]: 2-(hydroxyl-aminomethylidene)-indan-1,3-dione (A) and 2-carboxamide-1-hydroxy-3-oxo-indan (B) (Fig. 1). According to our CPCM/MP2/6-31+G(d) calculations in ethanol and DMSO solutions the ratio of the tautomers is A : B = 60 : 40 (Table 1). Tautomer A converts into tautomer B and vice versa by means of very fast intramolecular proton transfer reaction. The rate constants are of order 10^8 (Table 1).

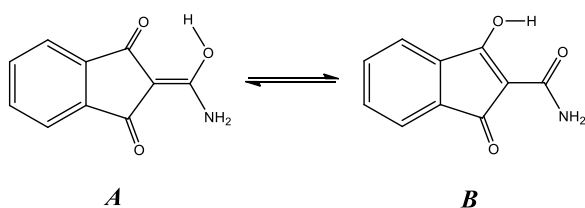


Fig. 1. Equilibrium between tautomeric forms 2-(hydroxylaminomethylidene)-indan-1,3-dione (A) and 2-carboxamide-1-hydroxy-3-oxo-indan (B).

Table 1. CPCM/MP2/6-31+G(d) calculated energy difference ΔG_{293} for the tautomers of CAID and energy barrier ΔG^\ddagger (kcal mol⁻¹) of intramolecular proton transfer in ethanol or DMSO solution, % contents of the tautomers and rate constants of the forward (k_f) and reverse (k_r) reactions (s⁻¹).

Solvent	ΔG_{293}	% content	ΔG^\ddagger	k
ethanol	0.26	60.8 % A	1.23 A→B	$k_f = 6.08 \times 10^8$
		39.2 % B	0.97 B→A	$k_r = 9.93 \times 10^8$
DMSO	0.21	58.8 % A	1.95 A→B	$k_f = 1.56 \times 10^8$
		41.2 % B	1.74 B→A	$k_r = 2.32 \times 10^8$

The electronic absorption spectra of CAID were recorded in ethanol (EtOH) and dimethylsulfoxide (DMSO). The absorption spectra (Fig. 2) showed characteristic absorption band in the UV-A region with slightly dependence on solvent. The absorption maxima for CAID solved in EtOH are at 374 nm and in DMSO - at 376 nm.

Fluorescence emission spectra for CAID were recorded at excitation 330 nm in both solvents at concentration 10 μ M (Fig. 2). The fluorescence emission maxima are red shifted as compared to the absorption maxima with a shift of 140 nm for both solvents. The fluorescence spectra are stable in time with good fluorescence quantum yield, which is an advantage in further studies for biological applications of CAID.

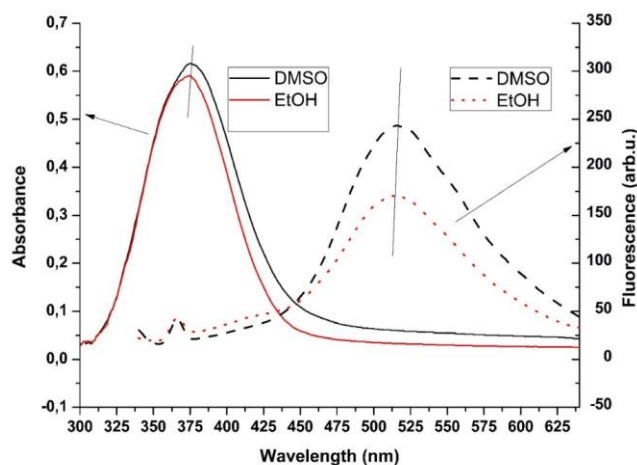


Fig. 2. Absorption (left) and emission (right) spectra of CAID in ethanol (EtOH) and dimethylsulfoxide (DMSO)

Balb/c 3T3 Neutral Red uptake test

Cytotoxic effect of 2-carboxamide-indane-1,3-dione was studied on non-tumorigenic cell line of mouse embryo fibroblasts Balb/c 3T3 by applying Neutral Red Uptake test. The cells were exposed to eight different concentrations of the tested compound for 24 hours. Light microscopic examination showed that CAID did not induce significant changes in morphology and growth properties of the cells. Results of the Neutral Red Uptake test confirmed the data from the microscopic examination and indicated that 2-carboxamide-indane-1,3-dione did not induce statistically significant reduction of the cell viability as compared to the control (Fig. 3).

The results of the study show that the 2-carboxamide-indane-1,3-dione is not toxic to the cells of the Balb/c 3T3 cell line. Fluorescence properties of the 2-carboxamide-indane-1,3-dione were used for study of CAID ability to penetrate through cellular membranes and to establish its intracellular localization (Fig. 4).

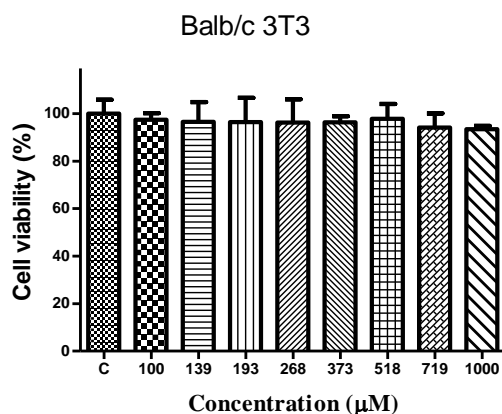


Fig. 3. Cytotoxicity of 2-carboxamide-indane-1,3-dione on Balb/c 3T3 cells line after 24 hours of treatment.

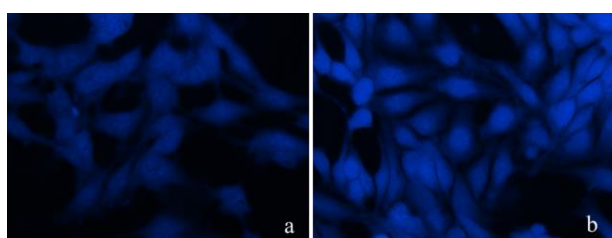


Fig. 4. Fluorescence microscopy of Balb/c 3T3 cells after 24-hour treatment with 1 µM CAID: a) control; b) cells treated 2-carboxamide-indane-1,3-dione.

Fluorescence microscopic examination indicated that the tested substance penetrates into Balb/c 3T3 cells and strongest fluorescent signal was established in the cell nucleus and nucleoli, demonstrating the affinity of the 2-carboxamide-

indane-1,3-dione to DNA- and RNA-containing cellular structures as nuclei and nucleoli.

To elucidate the affinity of CAID to nucleic acids, the DFT calculations were performed. We have modeled complexes between CAID and two nucleotides (with purine and pyrimidine nitrogen-containing nucleobases) – uridine monophosphate (UMP) and guanosine monophosphate (GMP). There are two possible site of association of CAID to nucleotide by hydrogen bonding - to nucleobases (UMP-CAID and GMP-CAID) or to phosphate group (CAID-GMP and CAID-GMP). The complexes formed are shown in Fig. 5. According to B3LYP/6-31G(d,p) calculations the more stable complex is CAID-UMP (by 3.09 kcal mol⁻¹) where 2-carboxamide-indane-1,3-dione is associated to UMP by phosphate group. In the case of GMP-complexes the two complexes are close by energy but the GMP-CAID are the more stable one by 0.12 kcal mol⁻¹.

To account for the possibility of the formation of intermolecular hydrogen bonding between CAID and nucleotides, the interaction energies (E_{int} 's) for the complex are considered: luorescence microscopic examination indicated that the tested substance penetrates into Balb/c 3T3 cells and strongest fluorescent signal was established in the cell nucleus and nucleoli, demonstrating the affinity of the 2-carboxamide-indane-1,3-dione to DNA- and RNA-containing cellular structures as nuclei and nucleoli.

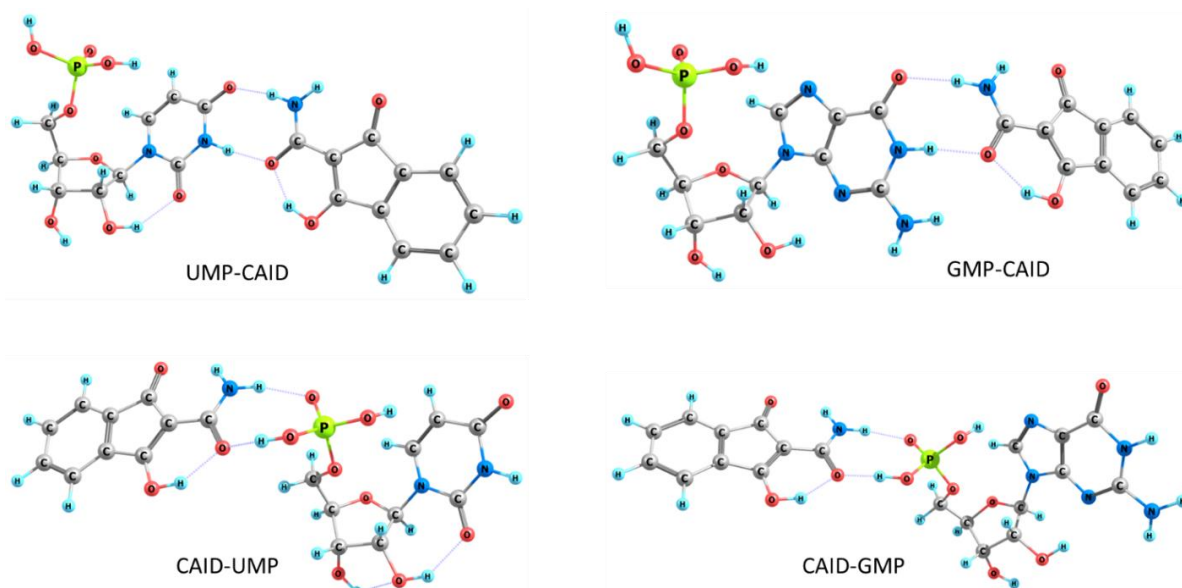


Fig. 5. Complexes of tautomer **B** (2-carboxamide-1-hydroxy-3-oxo-indan) (CAID) with: guanosine monophosphate (GMP) and uridine monophosphate (UMP).

To elucidate the affinity of CAID to nucleic acids, the DFT calculations were performed. We have modeled complexes between CAID and two nucleotides (with purine and pyrimidine nitrogen-containing nucleobases) – uridine monophosphate (UMP) and guanosine monophosphate (GMP). There are two possible site of association of CAID to nucleotide by hydrogen bonding - to nucleobases (UMP-CAID and GMP-CAID) or to phosphate group (CAID-GMP and CAID-GMP). The complexes formed are shown in Fig. 5. According to B3LYP/6-31G(d,p) calculations the more stable complex is CAID-UMP (by 3.09 kcal mol⁻¹) where 2-carboxamide-indane-1,3-dione is associated to UMP by phosphate group. In the case of GMP-complexes the two complexes are close by energy but the GMP-CAID are the more stable one by 0.12 kcal mol⁻¹.

To account for the possibility of the formation of intermolecular hydrogen bonding between CAID and nucleotides, the interaction energies (E_{int} 's) for the complex are considered:

$$\Delta E_{\text{int}} = E_{\text{CAID}} + E_{\text{GMP(UMP)}} - E_{\text{complex}}, \quad (1)$$

where the complexes are GMP-CAID, CAID-GMP, CAID-UMP and UMP-CAID (Figure 5).

According to eq. (1) the obtained values for E_{int} (in kcal mol⁻¹) are: 18.10 (GMP-CAID), 17.97 (CAID-GMP), 14.69 (UMP-CAID) and 17.77 (CAID-UMP). The results show that the association of CAID to the phosphate group in the two types of nucleotides is more probable. However, the favorite nucleotide is GMP

CONCLUSION

The results from the present study, namely complete absence of toxicity towards immortalized normal mammalian cells and high affinity for binding to nucleic acids makes 2-carboxamide-indane-1,3-dione a promising candidate for investigations on its antiproliferative activity to malignant cells. Fluorescence microscopic examination demonstrate the affinity of the 2-carboxamide-indane-1,3-dione to DNA- and RNA-containing cellular structures. According to our

DFT calculations tautomer B of CAID is preferably associated to nucleotides phosphate group.

Acknowledgements: This work is supported by the National Science Fund of Bulgarian Ministry of Education and Science (Grant: DFNI-B02/9/2014). The calculations were performed on the computer system installed at the Institute of Organic Chemistry, Bulgarian Academy of Sciences with the financial support of the National Science Fund, Project MADARA.

REFERENCES

1. V. Enchev, *Chem. Papers*, **48**, 219 (1994).
2. H. van der Goot, Ch. J. Eriks, and P. J. van Rhijn-van der Schaar, *Eur. J. Med. Chem.*, **13**, 425 (1978).
3. Y. Letourneux, L. Sparfel, C. Roussakis, *Eur. J. Med. Chem.*, **19**, 535 (1984).
4. H. N. Pati, U. Das, H. Sakagami, M. Kawase, Q. Chu, Q. Wang, J. P. Stables, J. R. Dimmock, *Arch. Pharm. Chem. Life Sci.*, **9**, 535 (2010).
5. V. Enchev, I. Angelov, V. Mantareva, N. Markova, *J. Fluorescence*, **25**, 1601 (2015)
6. R.L. Horton, K.C. Murdock, *J. Org. Chem.*, **25**, 938 (1960).
7. E. Borenfreund, J. A. Puerner, *Toxicol. Lett.*, **24**, 119 (1985)
8. European Centre for the Validation of Alternative Methods (ECVAM). 3T3 Neutral Red Uptake (NRU) Phototoxicity Assay. DB-ALM Protocol №78. http://ecvam-dbalm.jrc.ec.europa.eu/public_view_doc2.cfm?id=736F27E9E9F7A9D869FB48087878D2497180BB0BC12CB10496CDA74B54630A05A3291B895581F634 [Accessed on March 16, 2016].
9. M. Alcolea Palafox, *J. Biomol. Struct. Dyn.*, **32**, 831 (2014).
10. M. C. Alvarez-Ros, M. Alcolea Palafox, *J. Mol. Struct.*, **1047**, 358 (2013).
11. M. Alcolea Palafox, N. Iza, M. de la Fuente, R. Navarro, *J. Phys. Chem., B* **113**, 2459 (2009).
12. M. W. Schmidt, K. K. Baldrige, J. A. Boatz, S. T. Elbert, M. S. Gordon, J. H. Jensen, S. Koseki, N. Matsunaga, K. A. Nguyen, S. Su, T.L. Windus, M. Dupuis, J. A. Montgomery, *J. Comput. Chem.*, **14**, 1347 (1993).
13. V. Enchev, I. Abrahams, S. Angelova, G. Ivanova, *J. Mol. Struct. Theochem*, **719**, 169 (2005).

ИЗСЛЕДВАНЕ НА ЦИТОТОКСИЧНОСТТА И ВЪТРЕКЛЕТЪЧНАТА ЛОКАЛИЗАЦИЯ НА 2-КАРБАМИДО-1,3-ИНДАНДИОН В BALB/C 3T3 КЛЕТКИ

Н. Маркова^{1*}, А. Георгиева², И. Филипова¹, И. Ангелов¹, В. Енчев¹, А. Крил²

¹ *Институт по органична химия с Център по фитохимия, Българска академия на науките, ул. Акад. Г. Бончев, бл. 9, 1113 София, България*

² *Институт по експериментална морфология, патология и антропология с музей, Българска академия на науките, 1113 София, България*

Постъпила на 1 май 2017 г.; Коригирана на 23 май 2017 г.

(Резюме)

Изследването за цитотоксичност на 2-карбамидо-1,3-индандион (CAID) към Balb/c клетки беше извършено чрез валидизирания Balb/c 3T3 Neutral Red Uptake Test. Представени са и данни от флуоресцентното микроскопско изследване за вътреклетъчната локализация на CAID в ембрионални фибробласти от мишка. Резултатите показват пълно отсъствие на токсичен ефект на CAID към имортализирани ембрионални клетки от бозайник и подчертан афинитет за свързване с нуклеиновите киселини. Изследването с флуоресцентна микроскопия показва, че 2-карбоксамид-индан-1,3-дион се свързва приоритетно към клетъчни органели, съдържащи ДНК и РНК. За да се изясни свързването на CAID към нуклеиновите киселини, бяха проведени теоретични изследвания на ниво B3LYP/6-31G(d,p), които показват, че CAID се свързва приоритетно с фосфатната група от нуклеотида..

Semisynthesis of human insulin: transpeptidation or coupling mechanism?

P. Nikolova¹, Ch. Georgieva¹, G. Dimitrov¹, I. Stoineva^{2*}

¹Sopharma Pharmaceutical, Sofia, Rojen 16, Bulgaria

²Institute of Organic Chemistry with Centre of Phytochemistry, Bulgarian Academy of Sciences, 1113 Sofia, Bulgaria

Received April 30, 2017; Revised June 06, 2017

Dedicated to Acad. Ivan Juchnovski on the occasion of his 80th birthday

The polypeptides and proteins were responsible for essentially all the activities of the biological world. Insulin as a polypeptide hormone involved in the regulation of blood sugar, and is an important objective of modern biomedical research. Herein, we report the semisynthetic transformation of porcine into human insulin. A simple HPLC method and different analysis were used to obtain the evidence for the detailed mechanism of trypsin catalyzed reaction of semisynthetic transformation of animal insulin.

Key words: porcine insulin; human insulin; trypsin; enzyme transformation; HPLC

INTRODUCTION

Many publications reflect of important role of the insulin in the development of peptide chemistry, pharmacology, cell signaling and structural biology. These discoveries have provided a steadily improved quantity and quality of life for those afflicted with diabetes [1].

The interest in the synthesis of insulin and insulin analogues by chemical methods has recently increased owing to improvements in reagents, resins and methodology [2, 3]. Two methodologies were validated as effective methods of insulin synthesis: chemical/semisynthetic synthesis or using recombinant DNA-based technology.

Difference between human and porcine insulin is at the B- chain (Thr instead of Ala) of the polypeptide. The mechanism of semisynthetic transformation of porcine into human insulin is not clear till now.

The conclusion of Rose et al [4] is that the transformation occurs, by a mechanism involving hydrolysis followed by coupling, and not by direct transpeptidation as has been previously found the case for another similar systems [5].

Where is the true, in the mechanism involving hydrolysis followed by coupling, or direct transpeptidation?

The aim of this paper is to find the evidence for the mechanism of enzyme catalyzed transformation of animal into human insulin.

EXPERIMENTAL

Materials and Methods

Trypsin LKB (TPCK), trifluoroacetic acid (TFA), 1, 4–butanediol 1, 5–pentanediol, 1, 6–hexanediol, H-Thr-OMe, porcine and human insulin reference standard (United States Pharmacopeia) were obtained from Sigma - Aldrich (Germany). The enzyme activity of trypsin was determined according [6]. HCl, CH₃COOH, CH₃COCH₃, CaCO₃, NaOH, CH₃CN – gradient grade for HPLC were obtained from Merck (Germany). Monocomponent porcine insulin № 21002 (Sopharma) was used in reactions of enzymatic transformation.

Amino acid analyses

The amino acid content of insulin samples were calculated by using a BIOTRONIK automatic analyzer model 6001 after 24 h, 48 h and 72 h of hydrolysis in 6 M HCl in evacuated sealed tubes at 110° C.

HPLC analysis

The samples were chromatographed on HPLC Shimadzu Model LC 2010 A with UV detector. Zorbax -300 SB-C₈ column, 4,6 x 250 mm, 5 μm and guard column Zorbax -300 SB-C₈ column, 4,6 x 12,5 mm, 5 μm, with a 28 -50 % linear gradient

* To whom all correspondence should be sent:
E-mail: ane@orgchem.bas.bg

of 0,1% TFA/water - 0,1% CH₃CN /water for 55 minutes were used for monitoring of the studied reactions. The flow rate was 1 ml/min and the absorbance was monitored at 214 nm.

RESULTS AND DISCUSSION

Over the many years semisynthesis has been the predominant synthetic method in the preparation of human insulin or insulin analogs [7-14]. One of the strategies is to use targeted enzymatic, or chemical degradation of native insulin as a starting point for synthesis of the desired analog.

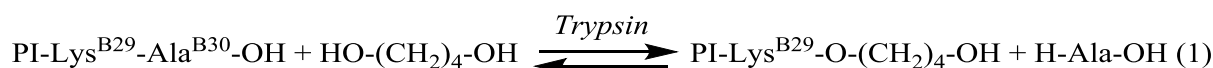
For the semisynthetic transformation of porcine insulin into insulin of human sequence three extreme mechanistic cases may be considered [1]:

(i) the reaction proceeds via aminolysis of the acyl-enzyme intermediate (i.e. via transpeptidation) without prior hydrolysis to des-Ala-B30-insulin;

(ii) porcine insulin is hydrolysed to des-Ala-B30-insulin, which then undergoes immediate coupling to give product;

(iii) porcine insulin, and there after acyl-enzyme intermediate, is hydrolysed reversibly to des-Ala-B30-insulin.

In this paper the trypsin (T) catalyzed reaction of transformation of porcine into human insulin was carry out in the mixed organic solvent N,N-dimethylacetamide and differend diols:1,4-butanediol, 1,5-pentanediol, 1,6- hexanediol in the ratio 1:1 (v/v), in the presence of H-Thr-OMe, at 12-15°C. The best result was obtained by using 1,4-butanediol. The experimental dates in the absence of the H-Thr-OMe showed that 1,4-butanediol reacts as a nucleophile in the formation of des-Ala-insulin-4 hydroxy-butyl-ester and free alanine was released according the equation (1):



Formation of the porcine des-Ala-insulin-butyl ester was monitored by HPLC analysis of the reaction components Fig. 1. Such kind of reaction of porcine insulin in the presence of alcohol is experimentally registered for the first time.

Kinetic of the reaction was followed at 214 nm by measurements of the concentration changes of the starting porcine insulin and formation of ester of des-Ala-insulin Fig. 2. Amino acid analysis of porcine des-Ala-insulin (theoretical values in brackets) give: Lys 0,98 (1), His 1,8 (2), Arg 0,87 (1), Asp 3,12 (3), Thr 2,03 (2), Ser 2,79 (3), Glu 6,87 (7), Pro 1,19 (1), Gly 4,15 (4), Ala 1,16 (1), CySO₃H 5,68 (6), Val 3,73 (4), Ile 1,68 (2), Leu 6,33 (6), Tyr 3,78 (4) and Phe 3,21 (3).These data cofirms the absence of one alanine in molecule of the porsine insulin.

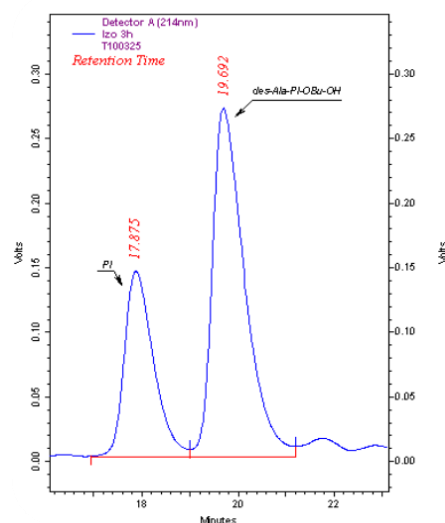


Fig.1. Representative HPLC chromatogram of the formation of butyl ester of porcine des-Ala-insulin, PI-porcine insulin; column Zorbax -300 SB-C₈ 4,6 x 250 mm, linear gradient for 55 min, 0,1% TFA/water-0,1% CH₃CN/water , flow rate 1 ml/min, detection at 214 nm.

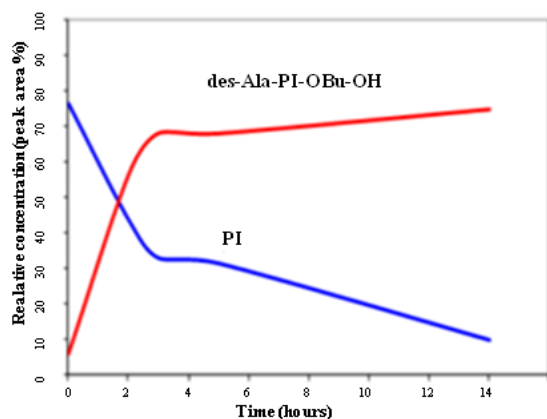
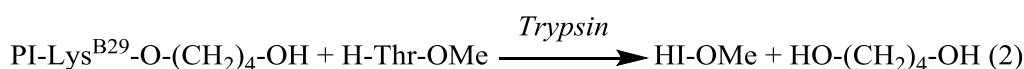


Fig.2. Time dependence of the concentration changes in trypsin catalyzed reaction of the hydrolysis of porcine insulin in the presence of 1,4-butanediol. Reaction conditions: 100 mg porcine insulin dissolved in 0.5 ml 10 M CH₃COOH, 2 ml N, N-dimethylacetamide / 1,4-butanediol (1:1 v/v), 10 mg (4, 2 x 10⁻⁷ mol) trypsin, 12°C.



When the reaction was carry out in the presence of H-Thr-OMe equation (2), we observed very fast disappearance of the kinetically controlled obtained des-Ala-insulin-4 hydroxy-butyl-esteris Fig 3.

This is a key factor in the enzymatic catalyzed synthesis of human insulin, leading to short reaction time and low side reaction products. The 1, 4-butanediol only accelerate the reaction and is released in the end without of change. We can conclude that it reacts as a catalyst of the transformation reaction. The yield of human insulin methyl ester varies from 68 % to 82% depending on the experimental conditions, as amount of enzyme, ratio of reagents or solvents and temperature.

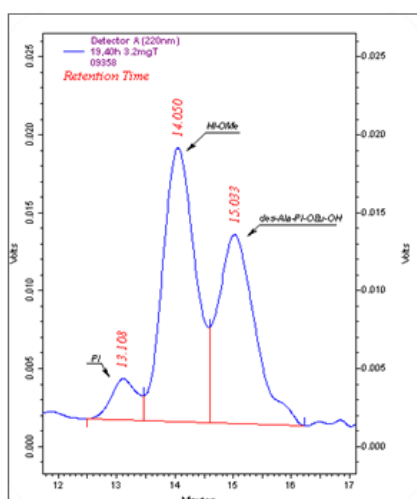


Fig.3. HPLC chromatogram of the formation of human insulin methyl ester from porcine insulin in the trypsin catalyzed reaction. Reaction conditions:100 mg porcine insulin dissolved in 0.5 ml 10 M CH₃COOH, 2 ml N,N – dimethylacetamide / 1,4- butanediol (1:1 v/v), 0.343 g (2,57x10⁻³ mol) H-Thr-OMe, 10 mg (4 x 10⁻⁷ mol) trypsin, 12°C.

CONCLUSION

The results in this study point unambiguously that enzymatic catalyzed semisynthesis of human insulin pass under coupling mechanism. As to our knowledge such direct involve of alcohol in formation of reactive intermediate compound, accelerating the reaction was registered for the first time experimentally.

Acknowledgements: The authors would like to acknowledge to the late Prof. D. Petkov for fruitful discussion and advices on the present work.

REFERENCES

1. D. R. Owens, B. Zinman, G. B. Bolli, *The Lancet*, **358**, 739 (2001).
2. A. N. Zaykov, J. P. Mayer, R. D. DiMarchi, *Nat. Rev. Drug Discov.*, **15**, 425 (2016).
3. A. N. Zaykov, J. P. Mayer, V. M. Gelfanov, R. D. DiMarchi, *ACS Chem. Biol.*, **9**, 683 (2014).
4. K. Rose, J. Gladstone, R. E. Offord, *Biochem. J.*, **220**, 189 (1984).
5. K. Rose, R. Stöcklin, L. A. Savoy, P. O. Regamey, R. E Offord, P. Vuagnat, J. Markussen, *Protein Eng.*, **4**, 409 (1991).
6. H. Bergmeyer, K. Gawehn, M. Grassl, *Methods of Enzymatic Analysis*, H. U. Bergmeyer (ed.), Academic Press, New York, 197, p. 4515.
7. M. A. Rittenberg, *Science*, **177**, 623 (1972).
8. K. Inouye, K. Watanabe, K. Morihara, Y. Tochino, T. Kanaya, J. Emura, S. Sakakibara, *J. Am. Chem. Soc.*, **101**, 751 (1979).

9. K. Morihara, T. Oka, H. Tsuzuki, *Nature*, **280**, 412 (1979).
10. K. Morihara, T. Oka, H. Tsuzuki, Washington, DC, *U.S. Patent* 4 511 505. (1985).
11. U. Yoshihiko, K. Morihara, *Biotech. Bioeng.*, **33**, 126 (1989).
12. K. Morihara, *J. Mol. Recognit.*, **3**, 181 (1990).
13. J. G. Ding, D. F. Cui, Y. S. Zhang, *Acta Bioch. Bioph. Sin.*, **35**, 215 (2003).
14. J. P. Mayer, F. Zhang, R. D. DiMarchi, *Biopolymers* **88**, 687 (2007).

СЕМИСИНТЕЗ НА ЧОВЕШКИ ИНСУЛИН: ТРАНСПЕПТИДИРАНЕ ИЛИ КОНДЕНЗАЦИОНЕН МЕХАНИЗЪМ?

П. Николова¹, Х. Георгиева¹, Г. Димитров¹, И. Стойнева^{2*}

¹ Софарма ООД, бул. Рожен 16, София, България

² Институт по Органична Химия с Център по Фитохимия (ИОХЦФ), Българска Академия на Науките,
ул. "Акад. Г. Бончев" бл. 9, 1113 София, България

Постъпила на 30 април 2017 г.; Коригирана на 06 юни 2017 г.

(Резюме)

Полипептидите и протеините имат голямо значение за почти всички процеси в биологичния свят. Инсулинът като полипептиден хормон, участващ в регулирането на кръвната захар, е обект на интензивни изследвания в съвременната биомедицина. Цел на това изследване е да се установи детайлният механизъм по който протича ензимно катализираната трансформация на свински в човешки инсулин. Високо-ефективна течна хроматография, (ВЕТХ) аминокиселинен анализ (АА) и кинетични изследвания бяха използвани за определяне на механизма по който се осъществява катализирана от трипсин реакция на трансформация на животински в човешки инсулин. Установено беше, че при избраните от нас експериментални условия, реакцията протича по кондензационен механизъм.

Chemical composition and nutritional value of seeds from new quinoa accessions, cultivated in Egypt

H. Barakat¹, I. Khalifa¹, G. A. Ghazal¹, A. Shams², P. N. Denev^{3*}

¹ Department of Food Technology, Faculty of Agriculture, Benha University, Moshtohor, 13736 Qaliuobia, Egypt

² Crop Intensification Research Department (CIRD), Field Crops Research Institute (FCRI), Agricultural Research Center (ARC), Giza, Egypt.

³ Institute of Organic Chemistry with Centre of Phytochemistry – Bulgarian Academy of Sciences, Laboratory of Biologically Active Substances, 139 “Ruski” blvd., 4000 –Plovdiv, Bulgaria

Received April 26, 2017; Revised June 13, 2017

Dedicated to Acad. Ivan Juchnovski on the occasion of his 80th birthday

Quinoa (*Chenopodium quinoa* Willd) is a plant that recently have been successfully grown in Egypt, providing seeds rich in nutrients and bioactive compounds. Present study aimed the characterization of chemical composition, nutritional value, amino acid and fatty acid profiles of selected quinoa accessions (Shams17-2, Shams16 and Shams14) cultivated in Egypt. Moisture, ash, crude protein, crude fat, crude fiber and carbohydrate contents of quinoa seeds were ranged from 10.74 to 11.77%, 3.22 to 3.87%, 11.15 to 17.81%, 4.01 to 6.14%, 6.30 to 8.24 and 56.69 to 66.07%, respectively. Shams17-2 was the richest source of Mg, K and Fe while Shams16 was the richest in Na and Zn. The highest amount of total amino acids was recorded in Shams17-2, whereas the highest content of essential amino acids was found in Shams14. Seeds from Shams17-2 were distinctive with the highest amount of non-essential amino acids. The unsaturated fatty acids content of quinoa oils was 86.60, 87.07 and 85.05% while the saturated fatty acids recorded 10.90, 9.44 and 10.75% for Shams17-2, Shams16 and Shams14, respectively. It could be concluded that quinoa seeds from the new accessions, cultivated in Egypt are a good source of essential nutrients such as minerals, essential amino acids and essential fatty acids.

Key words: Quinoa; chemical composition; nutritional value; fatty acids; amino acids

INTRODUCTION

Quinoa is a grain-like food nowadays referred as a pseudo-cereal. Its use as food is dated back to the Andean civilization and presently it is cultivated in different environmental conditions [1]. Besides their high nutritional value, quinoa seeds (QS) are rich source of different phytochemicals. A recent study reported that a serving portion of quinoa (~40 g) meets a significant part of the daily recommendation intake for essential nutrients - mainly vitamins, minerals and essential amino acids [2]. Quinoa flour is suitable for preparation of different food-stuffs and in particular bakery products (bread, cookies, biscuits, noodles, pasta, pancakes and others) [3], as well as fermented products [4]. In the meanwhile, quinoa has been rapidly gaining recognition as a functional food, thus its chemical constituents and therapeutic properties were recently spotlighted [5]. The Food and Agriculture Organization of the United Nations (FAO) launched the international year of quinoa in

2013 to promote the production and revalorization of this valuable crop [6]. QS are rich in protein, lipids and ash. Their high protein content range from 13.1 to 16.7% and is higher than those of rice, barley, corn and rye, and close to that of wheat [7]. Quinoa protein is referred as a high-quality protein with higher content of lysine, methionine and threonine compared to wheat and maize [8]. Carbohydrate content of QS is similar to that of wheat and starch is the major carbohydrate component constituting 32%–69% of the available carbohydrates. The content of total dietary fiber (7.0–11.7%) and soluble fiber content (1.3–6.1%) in quinoa seeds are close to these in wheat [1]. Lipid content of QS (5.5–7.4%) is higher than wheat (1.7%) and rice (0.7%), making quinoa an adequate source of functional lipids [9]. QS contain more vitamin E, vitamin C, riboflavin (B₂), pyridoxine (B₆) and folic acid than wheat, rice, barley and corn [9, 10], besides its high content of calcium, magnesium, iron, copper and zinc. Moreover, calcium, magnesium, and potassium are found in quinoa in bioavailable forms, thus their contents are considered to be adequate for a

* To whom all correspondence should be sent:
E-mail: petkodenev@yahoo.com

balanced diet [5,11]. QS are gluten-free which is beneficial for the high-risk consumer group with celiac disease. Valuable bioactive compounds exhibiting antifungal, antiviral, anticancer, hypocholesterolemic, hypoglycemic, antithrombotic, diuretic and anti-inflammatory activities such as saponins have been identified in QS [12]. Different polyphenols such as phenolic acids and flavonoids (quercetin, kaempferol and their glycosides) have been found in QS, as well [13-15]. Phytoecdysteroids in QS demonstrated health benefits including anabolic, performance enhancing, anti-osteoporotic, anti-diabetic, anti-obesity and wound healing properties [16].

The high nutritional value of quinoa seeds and their high content of bioactive components encouraged planting of quinoa crop in Egypt. Therefore, the objective of this investigation was to characterize the chemical composition and nutritional value of seeds from new quinoa accessions (QA) from Egypt, selected for their high yield and short cultivation period.

EXPERIMENTAL

Materials and methods

All solvents (HPLC grade) and reagents were purchased from Sigma-Aldrich (Steinheim, Germany).

Plant material

Agronomic, preliminary chemical composition and economic evaluation field trial was carried out at Ismailia Research Station, Agriculture Research Center, to evaluate the new selected quinoa accessions [17].

Characterization of chemical composition

The following A.O.A.C. methods were used for the chemical characterisation of QS: Moisture content (method No. 934.01) was determined by drying appropriate amount of the sample in oven (Tit Axon S.R.L via Canova, Italy) at 105 °C until constant weight. Method No. 920.39 was applied for determination of crude fat content using Soxhlet apparatus (FRANK, England). Crude fiber content was measured with method No. 978.10, whereas crude protein content (method No. 990.03) was determined by Kjeldahl apparatus (VELP, Italy). Ash content was measured via method No. 923.03 by heating samples in a muffle furnace at 550 °C until constant weight [18]. Carbohydrate content

was calculated according to Merrill and Kunerth [19]. Sodium, potassium and calcium content was determined by flame photometer (PFP 7, Model Jenway 8515, England) applying method No. 956.01, while magnesium, iron and zinc content was determined by atomic absorption spectroscopy (Perkin-ELMER, 2380, England) according to method No. 968.08 of A.O.A.C. [18].

Amino acids determination

The amino acids profile was carried out on the precipitated protein from defatted quinoa after hydrolysis by 6.0 N HCl for 24 h at 110°C in evacuated ampoules. Quantitative determination of amino acids were carried out by Biochrome 30 instruction manual (Analyzer used), 2005. EZ chrome manual (software for data collection and processing, 2004) according to A.O.A.C. [20].

Determination of fatty acid composition

Extraction procedure: Fatty acids were extracted according to Aldai *et al.* [21]. Approximately 1 g of powdered seeds were accurately weighted into 50 mL conical centrifuge tubes and 1 mg of the internal standard (free heneicosanoic acid, 100 µL of 10 mg mL⁻¹ C21:0 in methanol:toluene (1:1, v/v)) was added before saponification. After that, 6 mL of saponification solution (5 M KOH in methanol:water (50:50, v/v)) were added, tubes were flushed with N₂, shaken for 10 min, and transferred into a 60°C water-bath for 60 min for a direct saponification. Reaction mixtures were diluted with 12 mL 0.5% NaCl and 5 mL of a non-polar solvent (i.e. petroleum spirit). Samples were vortexed for 5 min, few drops of absolute ethanol added and centrifuged at 800 × g for 5 min at 20 °C for layer separation. The top layer, containing the non-saponifiable extract was removed and discarded. Then, 3 mL of glacial acetic acid were added to neutralize KOH fraction. After that 5 mL of a non-polar solvent (petroleum spirit) were added and tubes were vortexed for 10 min. Samples were centrifuged again (800 × g for 5 min at 20 °C) and the top layer transferred to clean screw-cap glass tubes. Once again, 5 mL of a non-polar solvent were added for further clearance. Centrifugation and layer transference steps were repeated again and 100 µL of a water scavenger - 2,2-dimethoxypropane were added to each tube and vortexed for 2 min.

Derivatization procedure: Free fatty acids (FFAs) were methylated according to Aldai *et al.*

[21]. For methylation of free FAs, samples were reduced to dryness under N₂ at 40°C and then re-dissolved in 1mL of methanol: toluene (2:1 vol.) and vortexed for 5 min. Methanol is a catalyst for the (trimethylsilyl) diazomethane (TMS-DM) reaction and drives the reaction in favour of methyl ester formation. At this stage, methylation reagent was added in molar excess of 2 M (trimethylsilyl) diazomethane (TMS-DM) in *n*-hexane (120µL) and the reaction proceeded at 40 °C for 10 min in open tubes. The samples were dried again under gentle stream of N₂ at 40 °C for approximately 20 min. Finally, each sample was reconstituted in 2 ml of *n*-hexane (with 50 ppm of BHT), centrifuged at 20.000 *x g* for 5 min at 7°C then transferred into vials and kept at -20 °C. Before GLC injection, samples were diluted in 1 µl *n*-hexane, then injected into GLC column and run under an optimized temperature program with optimized gas flow rate.

GLC equipment and program: A Varian Star CX3400 GLC (Varian, Spain) equipped with a FID detector, an automatic sample injector (SPI) in one column mode and a Chrompak CP-SIL 88 for FA methyl esters (FAMES) (WCOT FUSED SILICA 100m×0.25mm, 0.2 µm film thickness) with retention gap (FUSED SILICA TUBING 4 m×0.25 mm i.d., Methyl deactivated) was used. Helium was used as the carrier gas with a column head pressure of 355 kPa and a flow rate of approximately 2 ml min⁻¹ measured at 100°C. The GLC conditions were as follows: 100°C, at 2°C min⁻¹ to 170°C, hold for 15 min, at 0.5 °C min⁻¹ to 180 °C, at 10°C min⁻¹ to 200 °C and hold for 10 min, at 2°C min⁻¹ to 230 °C then hold for 10 min; injection temperature was 250 °C; detector temperature was 300 °C. Peaks were identified in comparison to standards and integrated using a conventional integrator program (Saturn GC Workstation Software ver., 5.51).

Statistical analysis

Statistical analysis was carried out using SPSS program (ver. 19) with multi-function utility regarding to the experimental design and multiple comparisons were carried out applying LSD according to Steel *et al.* [22].

RESULTS AND DISCUSSION

Chemical composition of quinoa seeds

Chemical composition of the investigated quinoa seeds from new quinoa accession cultivated in Egypt and their energy values are presented in Table 1. Moisture, ash, crude protein, crude fat, crude fiber and carbohydrate contents of QS were ranged from 10.74 to 11.77%, 3.22 to 3.87%, 11.15 to 17.81%, 4.01 to 6.14%, 6.30 to 8.24 and 56.69 to 66.07%, respectively. These results are very close to those observed in other studies [1, 7-9]. It was observed that ash, crude protein, crude fat and crude fiber contents in seeds of Shams17-2 are significantly ($p<0.05$) lower than those in seeds of Shams16 and Shams14. Energy values indicate that seeds from Shams14 had the highest energy values. In general, some of the analyzed parameters in tested quinoa samples differed significantly ($p<0.05$), which could enlarge their practical uses [5,23,24].

Besides the chemical composition, the content of some minerals in QS was determined, as well. Results presented in Table 2 indicate the high content of the analyzed minerals in the tested QA. From Table 2 it is evident that content of the major minerals Ca, Mg, Na and K varied in the range 1.55, 91.16 and 153.61, 484.26, 338.94 and 200.79, 1.11, 322.97 and 113.21 and 4.11, 3.60 and 3.35 mg.100g⁻¹ in seeds of accessions 17-2, 16 and 14, respectively.

Table 1. Chemical composition and energy value of quinoa seeds cultivated in Egypt.

Accession	Chemical composition, [%]						Energy value [kcal.100 g-1]
	Moisture	Ash	Crude protein	Crude fat	Crude fiber	Carbohydrates	
Shams17-2	11.77 ±0.48 ^b	3.22 ±0.32 ^a	11.15 ±1.69 ^a	4.01 ±0.36 ^a	6.30 ±0.44 ^a	66.07 ±1.98 ^b	440.85 ±13.00 ^a
Shams16	10.74 ±0.14 ^a	3.87 ±0.23 ^a	15.23 ±0.56 ^b	6.14 ±0.63 ^b	8.24 ±0.42 ^b	58.97 ±1.58 ^a	499.30 ±9.16 ^b
Shams14	11.67 ±0.31 ^b	3.30 ±0.69 ^a	17.81 ±0.91 ^c	6.09 ±0.47 ^b	8.18 ±0.42 ^b	56.69 ±0.85 ^a	595.76 ±16.69 ^c

Results are presented as means ± standard deviations (SD) from six independent measurements ($n=6$). Same small letters indicate that values in different accessions are not significantly different ($p>0.05$).

Table 2. Content of chosen minerals in quinoa seeds from new accessions.

Accession	Minerals content*, [mg.100g ⁻¹]					
	Ca	Mg	Na	K	Fe	Zn
Shams17	1.55	484.26	1.11	4.11	12.41	2.12
Shams16	91.16	338.94	322.97	3.60	8.41	3.53
Shams14	153.61	200.79	113.21	3.35	8.10	3.42

* Only one measurement was performed.

Furthermore, Fe and Zn were detected to be 12.41, 8.41 and 8.10, and 2.12, 3.53 and 3.42 mg.100 g⁻¹, for the same sequence, which is in harmony with other studies [1, 3]. It is evident from table 2 that Ca and Na contents in Shams 17-2 are much lower in comparison to the corresponding contents in Shams 14 and 16. It should be noted that Shams 17-2 is a new coloured accession that differs significantly from the non-coloured Shams 14 and 16. It was developed to be rich in anthocyanins rendering a darker colour. It is known that accumulation of minerals and secondary metabolites in plants depends on different factors, such as genetic (cultivar), agro-technique used, climate, etc. The elucidation of this phenomenon will be a subject of our further research on new quinoa cultivars from Egypt.

Amino acid composition of quinoa seeds

The amino acid composition of different QS cultivated in Egypt is given in Table 3. The highest total amino acids were recorded for Shams17-2 followed by Shams14 and Shams16. Interestingly, the highest amount of essential amino acids (EAA) was found in Shams14, while Shams17-2 contains the highest quantities of non-essential amino acids (NEAA). Histidine and Cystine contents were higher in QS in comparison to the referenced egg protein, while among the NEAA Glutamic acid is more than 2-fold higher than in the referenced egg protein. Correspondingly, all essential and non-essential amino acid have been detected in tested quinoa accessions confirming that quinoa protein has balanced amino acid profile, both qualitatively and quantitatively. From the presented results it is evident that total amount of amino acids in the selected quinoa accessions is very close to that in egg (FAO, 1970), which is in agreement with other authors [1,3]. The nutritional evaluation of quinoa protein given in Table 4 indicates its close relativity to the referenced egg protein. In the same context, the essential amino acids index (EAAI%) that is as an indicator for protein quality was in the range 85.21 - 86.92%. As already mentioned, quinoa amino acid profile is considered as better in comparison to wheat protein profile, moreover without Lysine deficiency [1,3,25].

Table 3. Amino acid (AA) composition and content (expressed in g.g⁻¹ N) in seeds of three quinoa accessions compared to hen's egg standard protein (FAO, 1970)

Amino acid	Shams17-2	Shams16	Shams14	Hen's egg (FAO 1970)
Essential amino acids (EAA)				
Threonine	0.253	0.238	0.244	0.320
Valine	0.323	0.363	0.335	0.428
Isoleucine	0.275	0.256	0.267	0.393
Leucine	0.431	0.425	0.432	0.551
Tyrosine	0.259	0.250	0.256	0.260
Phenylalanine	0.307	0.300	0.296	0.358
Histidine	0.226	0.213	0.227	0.152
Lysine	0.338	0.388	0.398	0.436
Methionine	0.156	0.181	0.171	0.210
Cystine	0.124	0.144	0.171	0.110
Non-essential amino acid (NEAA)				
Aspartic acid	0.587	0.594	0.567	0.601
Serine	0.266	0.238	0.267	0.796
Glutamic acid	1.084	1.009	1.040	0.478
Proline	0.254	0.244	0.245	0.260
Glycine	0.339	0.356	0.347	0.207
Alanine	0.318	0.338	0.324	0.370
Arginine	0.641	0.581	0.642	0.381
Total amino acids	6.231	6.118	6.219	6.311
Total EAA	2.742	2.758	2.797	3.218
Total NEAA	3.439	3.360	3.422	3.093

As recommended by FAO and WHO, there are two characteristics determining quality. One of them depends on the ratio between individual and total essential amino acids. Scores for tested protein as well as that of FAO pattern [hen's egg FAO 1970] are presented in Table 5. Calculated results indicate that the score of selected quinoa accessions was slightly lower than the score of each EAA of hen's egg standard protein with the exception of Histidine.

Data in Table 6 illustrates the scores of the protein from the selected quinoa accessions in regards to the limiting essential amino acids,

compared to FAO pattern. From the results, it could be concluded that Leucine is the first limiting amino acid in Shams17-2 and the second in Shams16. Methionine and Cystine are the first limiting AA in Shams17-2. Threonine is the first limiting AA in Shams16 and Shams14. The second limiting AA in Shams14 is Tyrosine while Isoleucine is the third. These results clearly show that variation of amino acid score may be related to each accession and/or cultivation conditions, which is in accordance with other studies [1,3,25].

Table 4. Nutritional evaluation of quinoa protein from new accessions, in comparison to hen's egg protein.

Seeds	TEAA g / 16 N	TNEAA g / 16 N	EAA: NEAA Ratio	EAA: Protein Ratio	NEAA: Total AA Ratio	EAAI %
Shams17-2	43.87	55.81	0.79	0.44	0.44	85.21
Shams16	44.19	53.76	0.82	0.44	0.45	85.27
Shams14	44.75	54.75	0.88	0.45	0.45	86.92
Egg (FAO, 1970)	51.49	49.49	1.04	0.52	0.51	100.00

EAA: NEAA: Ratio of essential amino acids to nonessential amino acid; EAA: Protein Ratio: Ratio of essential amino acids to 100 g protein; NEAA: Total AA Ratio: Ratio of essential amino acids to total amino acid; EAAI %: Essential amino acids index according to FAO

Table 5. Assessment of individual amino acids of quinoa accessions compared to reference essential amino acids in hen's egg protein [mg individual AA.g⁻¹ TEAA].

Amino acids	Shams17-2	Shams16	Shams14	Hen's egg score (FAO 1970)
Threonine	92.27	86.29	87.24	110.42
Valine	117.80	131.62	119.77	147.69
Isoleucine	100.29	92.82	95.46	135.61
Leucine	157.18	154.10	154.45	190.13
Tyrosine	94.46	90.65	91.53	89.72
Phenylalanine	111.96	108.77	105.83	123.53
Histidine	82.42	77.23	81.16	52.45
Lysine	141.50	140.68	142.30	150.45
Methionine + Cystine	102.12	117.84	122.27	151.00

Table 6. Scores of protein from selected quinoa accessions in regards to limiting essential amino acids. Results are expressed in mg.g⁻¹ protein.

Amino acid	Shams17-2	Shams16	Shams14	Suggested amino acid pattern (FAO, 1973)*
Threonine	101.29	85.20	97.73	40
Valine	103.45	104.04	107.27	50
Isoleucine	109.91	91.93	106.82	40
Leucine	98.52	87.12	98.70	70
Tyrosine	118.23	102.50	116.88	35
Phenylalanine	102.37	89.69	98.49	48
Histidine	172.41	145.21	173.16	21
Lysine	112.85	101.10	115.70	55
Methionine+ Cystine	99.96	103.64	121.21	45
First limiting amino acid	Leucine	Threonine	Threonine	-
Second limiting amino acid	Methionine + Cystine	Leucine	Tyrosine	-
Third limiting amino acid	---	Phenylalanine	Isoleucine	-

* According to FAO/WHO AD HOC Committee (FAO, 1973).

$$\text{Amino acid score according to FAO (1973)} = \frac{\text{mg amino acid in 1 g protein}}{\text{mg amino acid suggested by FAO/WHO}} \times 100$$

Fatty acid composition in qs oil of selected accessions

Fatty acid composition of extracted oil from QS cultivated in Egypt are shown in Table 7. All together fourteen fatty acids have been identified. The unsaturated fatty acids (USFA) contents of quinoa seed oils were 86.60, 87.07 and 85.05% while the saturated fatty acids (SFA) recorded 10.90, 9.44 and 10.75% for Shams17-2, Shams16 and Shams14, respectively. Linoleic acid was the predominant USFA with content higher than 50% in all samples. For the best of our knowledge and from parallel comparison of QA oils with some edible oils, the analyzed oil samples demonstrated higher USFA and lower SFA than cottonseed, soybean and olive oils. Therefore it can be considered as one of the richest source of Linoleic acid with considerably high ratio of USFA/SFA. The content of omega-3 fatty acids is 7.44%, 5.25% and 5.14% in Shams17-2, Shams16 and Shams14, respectively. These results are in agreement with previous studies [5, 23, 24, 26-28] and open the possibility of using QS oil as a source of omega-3 FA for enhancing the nutritional value of the diet. Saturated fatty acid content is lower in quinoa oil than presented in common vegetable oils but the difference is minor. Erucic acid, which has been implicated as a pathological factor in cardiovascular disease presents in QA oils at levels below the United States Food and Drug Administration (FDA) limit of 2%. This amount is equivalent to the erucic acid content of canola oil

[26, 28]. Another study reported Erucic content in QS oil of 0.52% [27].

CONCLUSION

Quinoa is a pseudo-cereal with remarkable nutritional and health-promoting values, and results obtained in the current study prove that. The content of essential amino acids and essential fatty acids varied within the different accession. The results for the chemical composition of the selected QA cultivated in Egypt are base for scaling up the production of these promising accessions in the country. Further research on biological properties of quinoa phytochemicals, their bioavailability, mechanisms of action and health promoting benefits is needed for a full integration of this plant in Egyptians' diet.

Acknowledgements: The authors gratefully acknowledge the financial support from the joint research ASRT funded project [Valorization of quinoa (*Chenopodium quinoa*) and its residues after food processing as promising sources of bioactive substances in Egypt] between Faculty of Agriculture, Benha University, Egypt and Institute of Organic Chemistry with Center of Phytochemistry, Bulgarian Academy of Sciences, Bulgaria. Authors also appreciate the valuable cooperation with Agricultural Research Center for providing the samples of newly selected quinoa accessions.

Table 7. Fatty acid profile of three selected quinoa accessions planted in Egypt

Fatty acid	Fatty acid, %			Fatty acids in reference oils*, %		
	Shams 17-2	Shams 16	Shams 14	Cotton seeds oil	Soybean oil	Olive oil
Myristic acid (C14:0)	0.21	0.17	0.17	0.6-1.0	0.05-0.2	0.0-0.05
Palmitic acid (C16:0)	9.29	8.07	9.01	21.4-26.4	8.0-13.5	7.5-20
Palmitoleic acid (C16:1)	0.14	0.10	0.08	0.05-1.2	0.05-0.2	3.0-3.5
Margaric acid (C17:0)	0.05	0.04	0.04	0.05-0.1	0.05-0.1	0.0-0.3
Heptadecenoic acid (C17:1)	0.05	0.04	0.04	0.05-0.1	0.05-0.1	0.0-0.3
Stearic acid (C18:0)	0.52	0.39	0.47	2.1-3.3	2.0-5.4	0.5-5.0
Oleic acid (C18:1)	19.74	19.36	19.59	14.7-21.7	17.0-30.0	55.0-83.0
Linoleic acid (C18:2)	55.75	58.75	56.85	46.7-58.2	48.0-59.0	3.5-21
γ-Linolenic acid (C18:3n6)	0.52	0.39	0.07	0.05-0.4	4.5-11.0	0.0-1.0
α-Linolenic acid (C18:3n3)	7.44	5.25	5.14			
Arachidic acid (C20:0)	0.34	0.30	0.42	0.2-0.5	0.1-0.6	0.0-0.6
Gadoleic acid (C20:1)	1.43	1.50	1.58	0.05-0.1	0.05-0.5	0.0-0.4
Behenic acid (C22:0)	0.49	0.47	0.64	0.05-0.6	0.05-0.7	0.0-0.2
Erucic acid (C22:1)	1.53	1.68	1.67	0.05-0.3	0.05-0.3	--
Unknown	2.49	3.48	4.19	--	--	--
Total SFA	10.90	9.44	10.75	24.4-31.9	10.3-20.5	8.0-26.2
Total USFA	86.60	87.07	85.05	61.7-82.0	69.7-88.7	61.5-92.1
USFA/SFA	7.94	9.22	7.91	2.5-2.6	4.9-6.8	4.2-7.7

* Results according to Egyptian Standard [29], Egyptian Standard [30] and, Egyptian Standard [31].

REFERENCES

1. L.E. Abugoch-James, Chapter 1, Quinoa (*Chenopodium quinoa* Willd.): Composition, Chemistry, Nutritional, and Functional Properties, in *Advances in Food and Nutrition Research*. Academic Press. p. 1. (2009).
2. Vilcacundo, B. Hernández-Ledesma, *Curr. Opin. Food Sci.*, **14**, 1 (2017).
3. A. Bhargava, S. Shukla, D. Ohri, *Ind. Crops Prod.*, **23**, 73 (2006).
4. Matsuo, J. *Japanese Soci. Nutr. Food Sci.*, **56**, 91 (2003).
5. A. Vega-Gálvez, M. Miranda, J. Vergara, E. Uribe, L. Puente, E. A. Martínez, *J. Sci. Food Agric.*, **90**, 2541 (2010).
6. 6. FAO, http://www.fao.org/fileadmin/templates/aiq2013/re/s/en/master_plan.pdf (2012).
7. S. Gebhardt, L. Lemar, D. Haytowitz, P. Pehrsson, M. Nickle, B. Showell, R. Thomas, J. Exler, J. Holden, *United States Department of Agriculture Agricultural Research Service*, (2008).
8. I. Dini, G. C. Tenore, A. Dini, *Food Chem.*, **92**, 125 (2005).
9. S. Navruz-Varli, N. Sanlier, *J. Cereal Sci.*, **69**, 371 (2016).
10. L. Alvarez-Jubete, H. Wijngaard, E. K. Arendt, E. Gallagher, *Food Chem.*, **119**, 770 (2010).
11. R. Repo-Carrasco, C. Espinoza, S. E. Jacobsen, *Food Rev. Int.*, **19**, 179 (2003).
12. B. L. Graf, P. Rojas-Silva, L. E. Rojo, J. Delatorre-Herrera, M. E. Baldeón, I. Raskin, *Compr. Rev. Food Sci. Food Saf.*, **14**, 431 (2015).
13. Y. Tang, X. Li, P. X. Chen, B. Zhang, M. Hernandez, H. Zhang, M. F. Marccone, R. Liu, R. Tsao, *Food Chem.*, **174**, 502 (2015).
14. Y. Tang, B. Zhang, X. Li, P. X. Chen, H. Zhang, R. Liu, R. Tsao, *J. Agric. Food Chem.*, **64**, 1712 (2016).
15. F. Abderrahim, E. Huanatico, R. Segura, S. Arribas, M. C. Gonzalez, L. Condezo-Hoyos, *Food Chem.*, **183**, 83 (2015).
16. B. L. Graf, A. Poulev, P. Kuhn, M. H. Grace, M. A. Lila, I. Raskin, *Food Chem.*, **163**, 178 (2014).
17. A. Shams. Evaluation of New Quinoa Genotypes under Sandy Soil Conditions. in *International Quinoa Conference "Quinoa for Future Food and Nutrition Security in Marginal Environments*. Dubai, UAE, 6-8 December, 38 (2016).
18. A.O.A.C., Official method of analysis. Association official analytical chemists. 17th Ed. Virginia, U.S.A. (2000).
19. A. L. Merrill, B. Kunerth, Energy value of foods: basis and derivation. *Agriculture Handbook*, No.74, in Washington, DC, ARS United States Department of Agriculture (1973).
20. A.O.A.C., Official methods of analysis of the AOAC international. 19th Chapter 4, P. 18-19 ed. (2012).
21. N. Aldai, K. Osoro, L. J. R. Barrón, A. I. Nájera, *J. Chromatogr. A*, **1110**, 133 (2006).
22. R. Steel, J. Torrie, D. Dickey, Principles and procedures of statistics: a biometrical approach. 3rd ed, McGraw-Hill, New York, NY. (1997).
23. N. T. Ahamed, R. S. Singhal, P. R. Kulkarni, M. Pal, *Food Nutr. Bull.*, **19**, 61 (1998).
24. L. E. A. James, *Adv. Food Nutr. Res.*, **58**, 1 (2009).
25. J. Ruales, B. M. Nair, *Plant Foods Hum. Nutr.*, **42**, 1 (1992).
26. S. Wood, L. Lawson, D. J. Fairbanks, L. Robison, W. Andersen, *J. Food Comp. Anal.*, **6**, 41 (1993).
27. F. Jahaniaval, Y. Kakuda, M. Marccone, *J. Am. Oil. Chem. Soc.*, **77**, 847 (2000).
28. J. Ruales, B. M. Nair, *Food Chem.*, **48**, 131 (1993).
29. Egyptian Standards, Vegetable oils as Edible oil (cotton seed oil), in Egyptian organization for standardization and quality control, (2005).
30. Egyptian Standards, Vegetable oils as Edible oil (olive and olive pomace oil), in Egyptian organization for standardization and quality control, (2005).
31. Egyptian Standards, Vegetable oils as Edible oil (soybean oil), in Egyptian organization for standardization and quality control, (2005).

ХИМИЧЕН СЪСТАВ И ХРАНИТЕЛНА СТОЙНОСТ НА СЕМЕНА ОТ НОВИ ГЕНОТИПОВЕ КИНОА, КУЛТИВИРАНИ В ЕГИПЕТ

Х. Баракат¹, И. Халифа¹, Г. А. Газал¹, А. Шамс², П. Н. Денев^{3*}

¹ Катедра по хранителна технология, Земеделски факултет, Университет на Банха, 13736 - Калюбия, Египет.

² Институт по полски култури, Земеделски изследователски център, Гиза, Египет.

³ Институт по органична химия с Център по фитохимия - Българска академия на науките, Лаборатория по биологично активни вещества, бул. „Руски“ 139, 4000 Пловдив, България

Постъпила на 26 април 2017 г.; Коригирана на 13 юни 2017 г.

(Резюме)

Киноата (*Chenopodium quinoa* Willd) е растение, което от скоро се отглежда успешно в Египет, осигурявайки семена, богати на хранителни вещества и биоактивни съединения. Настоящото изследване е насочено към охарактеризиране на химичния състав, хранителната стойност, аминокиселинния и мастнокиселинния състав на избрани генотипове киноа (Shams17-2, Shams16 и Shams14), култивирани в Египет. Съдържанието на влага, пепел, белтък, мазнини, хранителни влакнини и въглехидрати в семената от киноа варира съответно в границите от 10.74 до 11.77%, 3.22 до 3.387%, 11.15 до 17.81%, 4.01 до 6.14%, 6.30 до 8.24 и 56.69 до 66.07%. Shams17-2 е най-богатият генотип на Mg, K и Fe, докато Shams16 е най-богат на Na и Zn. Най-голямо количество общи аминокиселини е отчетено в генотип Shams17-2, докато най-високо съдържание на есенциални аминокиселини е намерено в Shams14. Shams17-2 се отличава с най-голямо количество не-есенциални аминокиселини. Съдържанието на ненаситени мастни киселини в маслата от семена на киноа е 86.60, 87.07 и 85.05%, докато наситените мастни киселини са 10.90, 9.44 и 10.75%, съответно за генотипове Shams17-2, Shams16 и Shams14. От направеното изследване може да се заключи, че семената от киноа от новите Египетски генотипове са добър източник на основни хранителни вещества като минерали, есенциални аминокиселини и есенциални мастни киселини.

Computational and experimental studies of the IR spectra and structure on violuric acid and its anions

Ts. Kolev^{1*}, E. Velcheva², B. Stamboliyska²

¹ Institute of Molecular Biology, Bulgarian Academy of Sciences, 21, G. Bontchev Str., Sofia 1113, Bulgaria

² Institute of Organic Chemistry with Centre of Phytochemistry, Bulgarian Academy of Sciences, Acad. G. Bonchev Str., build. 9, 1113 Sofia, Bulgaria

Received May 01, 2017; Revised June 5, 2017

Dedicated to Acad. Ivan Juchnovski on the occasion of his 80th birthday

The experimental and theoretical IR spectra and structure of violuric acid and its anions have been studied. The triketo tautomer for the molecule and anions are most stable according to the calculations (B3LYP/6-311+G(2df,p). The conversion of molecule into anion causes strong frequency decreases of the three carbonyl stretching bands $\nu(\text{C}=\text{O})$: computed 153 cm^{-1} (B3LYP/6-311+G(2df,p), measured 138 cm^{-1} and other essential IR changes. The formation of violurate dianion has been assumed to take place in DMSO-d₆/CD₃SOCD₂Na solution. The total $\nu(\text{C}=\text{O})$ decrease, caused by the molecule \rightarrow diazanion conversion is: predicted 485 cm^{-1} , measured in DMSO-d₆ 483 cm^{-1} .

Key words: violuric acid; IR; DFT; anions

INTRODUCTION

Bayer was the first to prepare violuric acid (2,4,5,6(1H,3H)-pyrimidinetetrone 5-oxime) as early as 1864 [1]. It is well known the very broad applications of violuric acid in analytical chemistry to detect cations of some metals [2-5] (e.g., used as a reagent for cobalt[2], for determination of copper, cobalt, lead, and iron in table salt [5]). Violuric acid behaves as a weak triprotic acid in aqueous solution ($\text{pK}_{\text{a}1} = 4.35$, $\text{pK}_{\text{a}2} = 9.64$, $\text{pK}_{\text{a}3} = 13.1$) [6,7]. The remarkable ability of its anion to form compounds of differing color with metal ions[8], as well as with organic cations [9] has been underlined in the last 20 years. Violuric acid is used and in biological research. It is active as an antihypoxic agent [10]. It can be used to inhibit and/or prevent the growth of many undesirable forms of algae, bacteria and fungi [11]; as mediator in the laccase-catalyzed pesticide degradation [12], *etc.* Its cobalt complexes are active as antiviral and antibacterial agents [13]. Violuric acid is a reversible monoamine oxidase-B inhibitor and may be useful in the treatment of neurodegenerative diseases such as Parkinson's disease [14]. The complex compounds of violuric acid derivatives with Pt(II) showed a activity to human acute myeloid leukemia HL-60 [15].

Different functional groups in violuric acid, such as the $-\text{C}=\text{O}$, $=\text{N}-\text{OH}$ and $-\text{N}-\text{H}$ groups, provide a large variety of bonding behaviour, so it

is use for the construction of coordination and supramolecular compounds (e.g. the complexes of mononuclear Fe (III), cobalt (III) manganese (II) [16,17 and refs. therein]. In these new crystalline arrangements violurate anion appears as monodentate, chelate or ionic form [16].

The spectral study of violuric acid and their anions attract the attention of the researchers in the last two decades. The subject of these studies is the spectra and structures of mono anion with different counter anions in solid state. Oliveira *et al.* studied vibrational spectra of violuric acid and its Na salt in solid state and in aqueous solution in different pH and propose tentative assignment of observed bands [7]. IR and Raman spectra and tautomerism of violuric acid have been studied on the basis of *ab initio* and DFT calculations [18]. To the best of our knowledge no vibrational spectra in aprotic solvents are published in the literature however it can supply the information about the structure of these species. It is important to know if they exist as solvent separated ions or are kinetically independent ones.

In this study we present and discuss specific comparisons of vibrational and structural data of violuric acid, its anion, dianion, and trianion, based on density functional computations, as well as, on the basis of original and literature experimental data.

* To whom all correspondence should be sent:
E-mail: tskolev@bio21.bas.bg

EXPERIMENTAL AND COMPUTATIONS

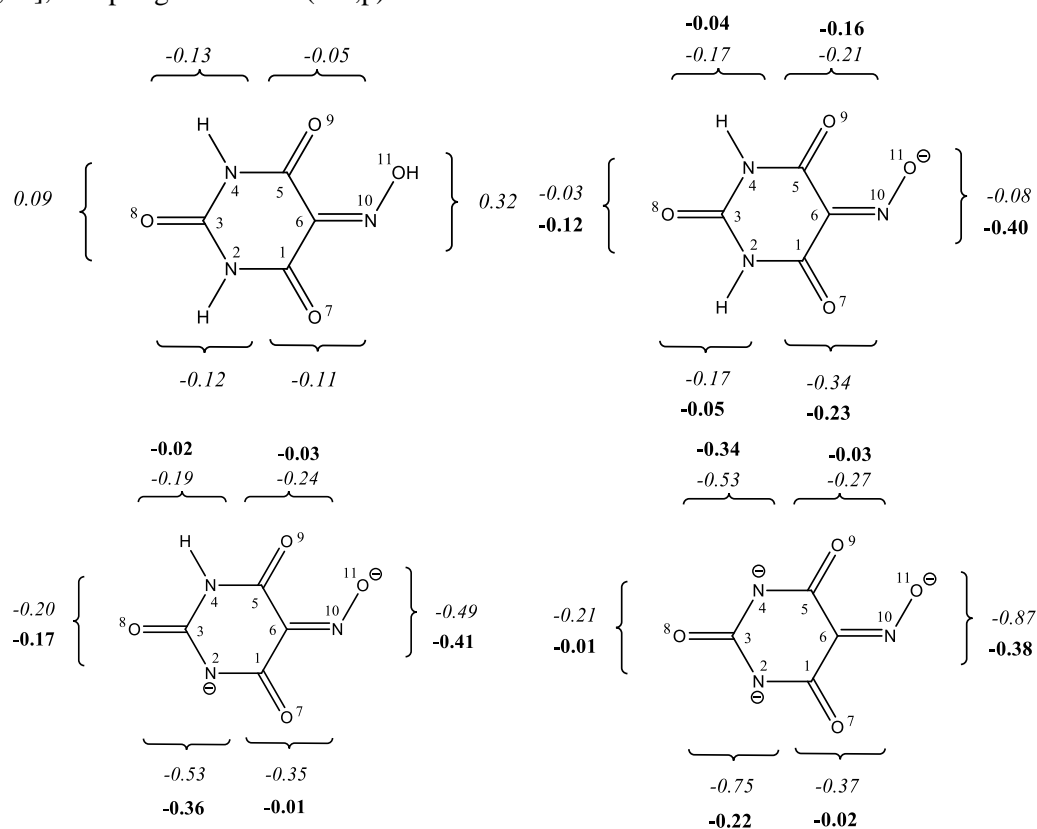
Violuric acid monohydrate (Sigma-Aldrich, 98%) was used without additional purification. We prepared sodium violurate monohydrate from violuric acid and sodium hydroxide [8]. The violurate anion (counter ion Na^+) was prepared by adding dimethyl sulfoxide (0.10 - 0.15 mol l^{-1} DMSO/DMSO- d_6) solutions of violuric acid to excess of dry sodium methoxide- d_0 and - d_3 , and filtration of the reaction mixture by a syringe filter. The violurate dianion (counter ions Na^+) was prepared by adding dimethyl sulfoxide (0.10 - 0.15 mol l^{-1} DMSO/DMSO- d_6) solutions of violuric acid or violurate sodium to DMSO- d_6 /D $_3$ CSOCD $_2$ Na solution. IR spectra were measured on Bruker Tensor 27 Fourier transform infrared (FTIR) spectrophotometer in a CaF_2 cell of 0.13 mm path length and in KBr pellets, at a resolution of 1 cm^{-1} and 64 scans. The quantum chemical calculations were performed using the Gaussian 09 package [19]. The geometry optimizations of the structures investigated were done without symmetry restrictions, using density functional theory (DFT). We employed B3LYP hybrid functional, which combines Becke's three-parameter nonlocal exchange with the correlation functional of Lee *et al.* [20,21], adopting 6-311+G(2df,p) basis sets.

The stationary points found on the molecular potential energy hypersurfaces were characterized using standard harmonic vibrational analysis. The theoretical vibrational spectra were interpreted by means of potential energy distributions (PEDs) using VEDA 4 program [22]. For a better correspondence between experimental and calculated values, we modified the results using the empirical scaling factors.

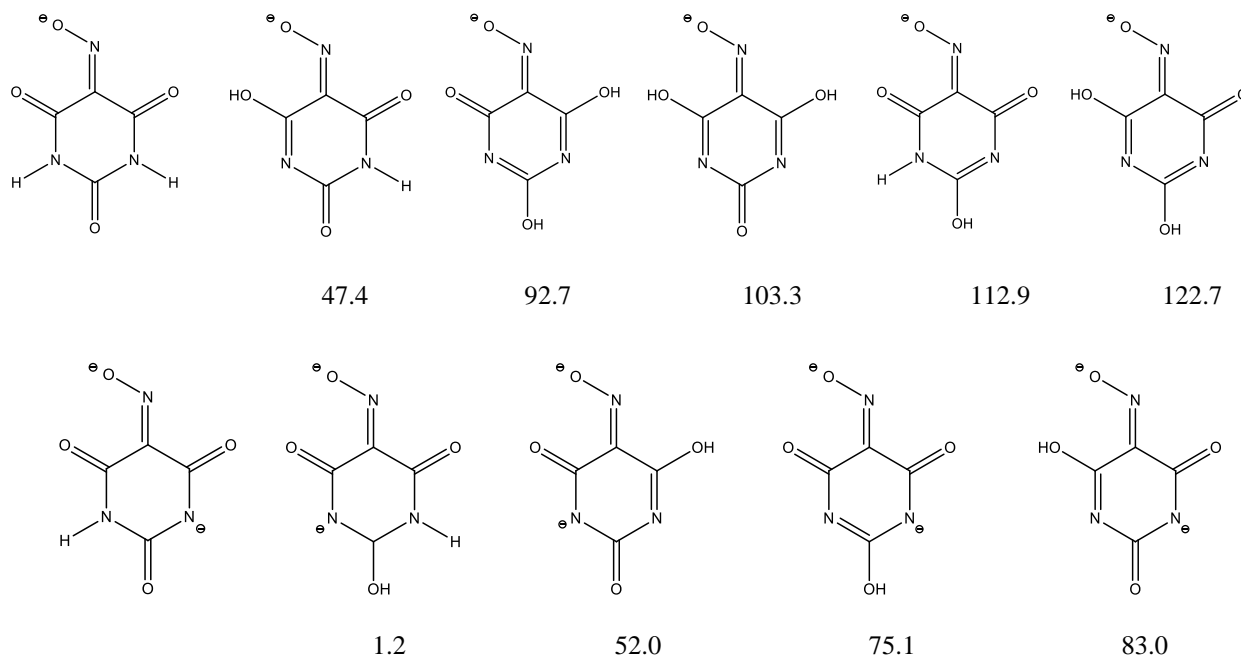
RESULTS AND DISCUSSION

Energy analysis

The violuric acid can exist as 10 different tautomers. The most stable among the molecular tautomers is the triketo form shown in Scheme 1. The same form is supported by single crystal X-ray data [23]. The relative stability of tautomers in the gas phase computed by us is in agreement with the previously computed results at the B3LYP/6-31G* level [18]. The six possible tautomers for anion and five ones for the dianion together with the values of relative energy are shown on Scheme 2. In both anions the triketo form is predicted as the most stable. The largest energy difference between the anionic tautomers studied is 102.7 kJ mol^{-1} ; for the dianionic tautomers it is smaller, 52.0 kJ mol^{-1} .



Scheme 1. B3LYP 6-311+G(2df,p) structure of the most stable tautomers of violuric acid, its anion, dianion, and trianion. The net charges of fragments (in italics) and charge changes (in bold) are given in the formulae.



Scheme 2. The possible tautomers of violuric acid anion and violuric acid dianion and the relative energies with respect to the most stable isomer (ΔE in kJ mol^{-1}).

Infrared analysis

The energy difference $E_1^D = E_{\text{anion}} - E_{\text{molecule}}$ between the most stable forms of anion and molecule can be used as an approximate measure of pKa of a given compound in polar aprotic solvents [24]. The B3LYP value E_1^D of studied species of $1354.3 \text{ kJ mol}^{-1}$ corresponds to a moderately weak acid; its experimental pKa₁ is 4.35 (solvent water). For comparison, the E_1^D energy is lower than E_1^D acetanilide ($1489.06 \text{ kJ mol}^{-1}$ [25]) and a little higher than E_1^D of acesulfame ($1324.31 \text{ kJ mol}^{-1}$ [26]).

The energy difference between the dianion and anion $E_2^D = E_{\text{dianion}} - E_{\text{anion}}$ of 1811.033 is essentially higher, and can be compared with the corresponding energy of paracetamol ($1880.2 \text{ kJ mol}^{-1}$ [27]). The energy difference $E_3^D = E_{\text{trianion}} - E_{\text{dianion}}$ is larger ($2281.16 \text{ kJ mol}^{-1}$). Experimental pKa data in water for the violuric acid dianion and trianion are 9.6 and 13.1, respectively [6,7]. However, we found in the literature neither theoretical, nor experimental data for violuric acid and its anion in DMSO.

The experimental pKa values depend strongly on the solvent, counter ion, nature of both the Brønsted acid and its conjugate base (e.g., carbanion or azanion, with localized or delocalized charge), concentration, temperature [28].

Let us consider consecutively the IR data for the species studied, which will make it possible to specify the spectral changes, caused by the conversion of the violuric acid molecule into corresponding anions.

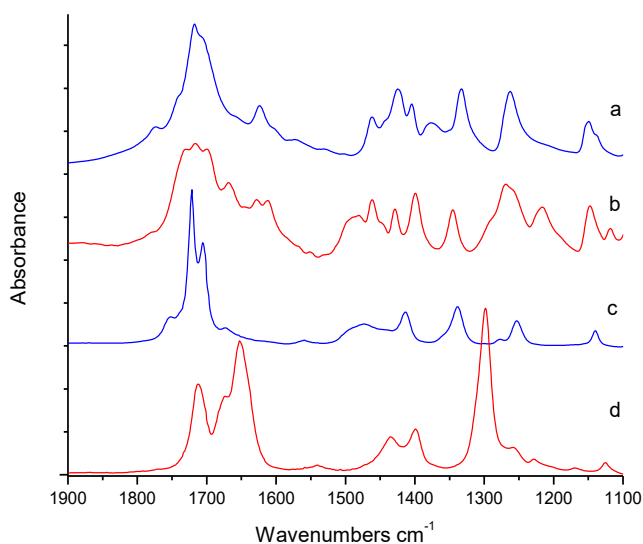


Fig. 2. IR spectra: of violuric acid in KBr (a); sodium salt of violuric acid in KBr (b); violuric acid in DMSO-d₆ (c), anion of violuric acid (counter ion Na⁺) in DMSO-d₆ (d).

The spectrum of violuric acid in solid phase is rather complicated. The conversion of the neutral molecule into anion makes it more difficult. In order to eliminate strong intermolecular interactions in the molecule of violuric acid the experimental spectra were measured in polar aprotic solvent DMSO. It is known that in this solvent the ions exist as free species and there are no anion/counter

ion interactions [29]. The influence of the counterions on the frequencies is neglectful. This makes it possible to compare, in this work, the experimental infrared data for the anions with the theoretical data. The numerical values of the experimental vibrational frequencies in DMSO-d₆ and band intensities are listed with the theoretical ones in Table 1.

Table 1. Theoretical (B3LYP/6-311+G(2df,p) and experimental (solvent DMSO-d₆) vibrational frequencies (cm⁻¹) and IR integrated intensities (A in km.mol⁻¹) of violuric acid and its anion.

No	$\nu_{\text{theor.}}^a$	Theoretical data		Experimental data ^a	
		A ^b	Approximate description ^c	$\nu_{\text{exp.}}$	A ^c
Violuric acid molecule					
1.	3644	186.9	99v(OH)	3500	w
2.	3475	78.5	93 v(NH)	3445	
3.	3471	100.5	94 v(NH)		
4.	1753	65.9	36 v(C ¹² O ²), 31v(C ¹¹ O ¹), 12v(C ¹³ O ³)	1753	m
5.	1737	853.9	37v(C ¹² O ²), 29v(C ¹¹ O ¹)	1722	s
6.	1711	479.2	61v(C ¹³ O ³), 20v(C ¹¹ O ¹)	1706	s
7.	1586	51.6	64 v(C-NO), 16δ(NOH)	1560	vw
8.	1405	188.2	42 v(CN), 20δ(NOH)	1413	m
9.	1378	257.0	42 v(CN), 28 v(CC)	1360	sh
10.	1371	116.0	48 δ(NOH), 12δ(CNH)	1344	sh
11.	1352	36.0	66 δ(CNH), 14δ(OCN)	1339	m
12.	1274	168.6	59 v(CN), 12 v(CC)	1277	w
13.	1185	102.2	37 v(CN), 33 v(CC)		
14.	1105	120.3	25 v(ON), 17 v(CN), 16 δ(NCC)	1140	w
15.	1035	247.8	53 v(ON), 17 v(CN)		
16.	989	1.1	36 v(CN), 16 δ(CNH)		
Violuric acid anion					
1.	3535	40.6	100 v(NH)		
2.	3561	35.4	100 v(NH)		
3.	1713	566.1	69 v(C ⁵ O ¹²)	1716	s
4.	1681	368.7	37 v(C ¹ O ¹¹), 33v(C ⁶ O ¹⁹) s	1676	s
5.	1654	1050.2	37 v(C ¹ O ¹¹), 33v(C ⁶ O ¹⁹) as	1655	vs
6.	1443	34.2	76 v(ON)	1444	sh
7.	1431	139.2	42 v(CN), 20δ(O ¹² CN)	1435	m
8.	1357	53.0	55(CNH), 23 v(C ⁵ O ¹²)	1396	m
9.	1327	20.6	78δ(CNH)	1343	w
10.	1306	961.3	34 v(C-NO), 10 v(N-O)	1299	vs
11.	1236	97.8	59 v(CN)	1255	w
12.	1135	16.2	37 v(CN), 33 v(CC)	1128	w
13.	1050	16.7	25 v(ON), 17 v(CN), 16 δ(NCC)		
14.	1010	11.8	53 v(ON), 17 v(CN)		

^aScaled infrared frequencies by 0.969. ^bVibrational modes: v, stretching; δ, bending; perscripts: s – symmetrical, s – asymmetrical. The numbers before the mode symbols indicate % contribution (10 or more) of a given mode to the corresponding normal vibration, according to the potential energy distribution ^cRelative intensities: vw, very weak; w, weak; m, moderate; s, strong; vs, very strong; sh, shoulder.

The agreement between the calculated frequencies and the experimental data is very good. The mean absolute deviation between experimental and theoretical frequencies is 8 cm^{-1} for the molecule and 11 cm^{-1} for the anion.

According to our calculations the strong band at 3644 cm^{-1} is assigned to $\nu(\text{O-H})$ while the bands at 3475 and 3471 cm^{-1} are attributed to $\nu(\text{N-H})$. The experimental observed bands are lower than calculated ones because of the formation of hydrogen bonds mainly with solvent. Of course, the three carbonyl bands are the strongest and the most interesting in the IR spectra of violuric acid. According to our computations, however, all the $\nu(\text{C=O})$ coordinates are strongly coupled with each other, and the approximate descriptions of the corresponding bands are given in Table 1. The band predicted at 1586 cm^{-1} and measured at 1560 cm^{-1} belongs to $\nu(\text{C=N})$. The bands between 1426 – 1260 cm^{-1} are connected mainly to $\nu_{\text{ring}}(\text{C-N})$ and $\nu_{\text{ring}}(\text{C-C})$. The middle strong band measured at 1140 cm^{-1} is assigned to $\nu(\text{O-N})$ is strongly coupled vibration with $\nu(\text{CN})$ and $\delta(\text{NCC})$.

The strongest IR spectral changes, caused by the molecule \rightarrow anion conversion, take place in the 1800 – 1770 cm^{-1} region (Table 1 and Fig.2). The following bands have been measured in this region of the IR spectrum of violuric acid: 1710 , 1676 and 1655 cm^{-1} . The highly frequency band at 1710 cm^{-1} is attributed to $\nu(\text{C}^3=\text{O}^8)$. The two lower bands are assigned to the asymmetric and symmetric to $\nu(\text{C}^1=\text{O}^7)$ and to $\nu(\text{C}^5=\text{O}^9)$. So, the total $\nu(\text{CO})$ decrease, caused molecule \rightarrow anion conversion is: predicted 153 cm^{-1} , measured 138 cm^{-1} .

The band $\nu(\text{O-N})$ is shifted from 1140 to 1444 cm^{-1} because the bond order increase nearly double. In the spectrum of anion appears very strong band at 1300 cm^{-1} , according the calculations very strong mixed between $\nu(\text{C=N})$, $\nu(\text{O=N})$ and $\nu_{\text{ring}}(\text{C-N})$.

According to our computations, the IR spectrum of the violuric acid dianion should show three bands, corresponding to strongly coupled vibrations of the three carbonyl groups at 1603 cm^{-1} , 1586 cm^{-1} and 1530 cm^{-1} . We tried to prepare dianion (counter ions 2Na^+) by adding dimsil sodium to a DMSO- d_6 solution of violuric acid. The IR spectrum of the solution after metalation showed three bands in the above region: 1600 , 1560 and 1533 cm^{-1} . If we assume that these bands really correspond to $\nu(\text{CO})$ of the dianion, we can calculate the total $\nu(\text{CO})$ decrease, caused by the anion \rightarrow dianion conversion: predicted 332 cm^{-1} , measured 345 cm^{-1} . Respectively, the total $\nu(\text{CO})$ decrease, caused by

the molecule \rightarrow dianion conversion would be: predicted 485 cm^{-1} , measured 483 cm^{-1} .

The IR spectrum of trianion of violuric acid was calculated theoretically by B3LYP/6-311G(2df,p). The $\nu(\text{C=O})$ bands are predicted at 1510 , 1445 and 1410 cm^{-1} , but experimental metalation cannot succeed. Probably in this basic medium violuric acid can undergo some decomposition as cited by [6].

Structural analysis

According to X-ray diffraction the plane of the acetamide group is oriented at 40.4° with respect to the benzene ring, whereas the plane of the carboxylic acid group is essentially coplanar with the benzene ring [21]. According to the calculations in the most stable conformers of the isolated molecule these groups are planar. The same groups in the isolated oxyanion and dianion have been predicted to be again planar. The theoretical and experimental bond lengths and angles in the 4-acetamidobenzoic acid and its oxyanion and dianion are listed in Table 4. The most significant changes caused by the conversion from molecule to anion take place both at the anionic center and next to it, with agrees the data for other anions [25-27,30,31] They are strong shortening of the $\text{N}_{10}\text{-O}_{11}$ with 0.11 \AA and strong lengthening of the $\text{C}_6\text{-N}_{10}$ with 0.09 \AA and shortening of $\text{C}_1\text{-C}_6$ and $\text{C}_5\text{-C}_6$ with 0.05 \AA and 0.04 \AA respectively. The second deprotonation from anion to dianion as can see in Table 2 causes bond shortenings at the azanionic center N_2 and bond lengthenings next to it. The bonds lengths change both at and next to the azanionic center N_4 , caused by the dianion \rightarrow trianion conversion are is qualitatively similar to the azanionic center N_2 . The net electric charges (q_i) of fragments of the species studied are shown in Scheme 1. The charge changes $q_i(\text{anion}) - q_i(\text{molecule})$, $q_i(\text{dianion}) - q_i(\text{anion})$, $q_i(\text{trianion}) - q_i(\text{dianion})$ can also be seen in Scheme 1. The charge changes are usually quite informative to show the distribution of the new charges over the corresponding anions [25-27,30,31]. For the conversions studied the change charges, accompanying the conversion molecule \rightarrow anion \rightarrow dianion \rightarrow trianion are also quite informative, to shown that the first oxanionic charge is delocalized over whole anion. That is in agreement with observed deep color of monoanion in the UV-vis spectra - due of strongly conjugated system. The second and third charges are also delocalized over the dianion and trianion forms.

Table 2. Theoretical (B3LYP/6-311++G**) and experimental bond lengths R (Å) and bond angles A (°) the vialuric acid molecule and its anion, dianion, trianion.

	Molecule		Δ^b	Anion		Δ^c	Dianion		Δ^d	Trianion	
	Exp. ^a	Calc.		Calc.	Calc.		Calc.	Calc.		Calc.	Δ^e
<i>Bond lengths</i>											
R(C ¹ ,N ²)	1.372	1.389	0.017	1.419	0.03	1.378	-0.041	1.353	-0.025		
R(N ² ,C ³)	1.362	1.384	0.022	1.370	-0.014	1.331	-0.039	1.379	0.048		
R(C ³ ,N ⁴)	1.379	1.386	0.007	1.368	-0.018	1.412	0.044	1.376	-0.036		
R(N ⁴ ,C ⁵)	1.361	1.391	0.03	1.425	0.034	1.390	-0.035	1.357	-0.033		
R(C ⁵ ,C ⁶)	1.499	1.491	-0.008	1.450	-0.041	1.456	0.006	1.508	0.052		
R(C ⁶ ,C ¹)	1.506	1.504	-0.002	1.452	-0.052	1.504	0.052	1.511	0.007		
R(C ¹ ,O ⁷)	1.176	1.205	0.029	1.223	0.018	1.242	0.019	1.266	0.024		
R(C ³ ,O ⁸)	1.225	1.207	-0.018	1.226	0.019	1.254	0.028	1.276	0.022		
R(C ⁵ ,O ⁹)	1.212	1.206	-0.006	1.221	0.015	1.239	0.018	1.261	0.022		
R(C ⁶ ,N ¹⁰)	1.275	1.284	0.009	1.374	0.09	1.350	-0.024	1.333	-0.017		
R(N ¹⁰ ,O ¹¹)	1.328	1.348	0.02	1.240	-0.108	1.268	0.028	1.299	0.031		
<i>Bond angles</i>											
A(C ¹ ,N ² ,C ³)	125.9	128.2	2.3	127.9	-0.3	121.5	-6.4	120.8	-0.7		
A(N ² ,C ³ ,N ⁴)	116.1	114.6	-1.5	113.4	-1.2	118.8	5.4	123.9	5.1		
A(C ³ ,N ⁴ ,C ⁵)	128.0	128.5	0.5	128.1	-0.4	127.6	-0.5	121.2	-6.4		
A(N ⁴ ,C ⁵ ,C ⁶)	114.4	114.0	-0.4	114.8	0.8	113.1	-1.7	118.3	5.2		
A(C ⁵ ,C ⁶ ,C ¹)	119.2	120.4	1.2	120.6	0.2	118.9	-1.7	116.9	-2		
A(N ² ,C ¹ ,O ⁷)	119.5	120.9	1.4	116.6	-4.3	119.2	2.6	120.0	0.8		
A(N ² ,C ³ ,O ⁸)	124.0	122.8	-1.2	123.2	0.4	125.7	2.5	118.0	-7.7		
A(N ⁴ ,C ⁵ ,O ⁹)	121.1	120.7	-0.4	116.4	-4.3	117.7	1.3	120.2	2.5		
A(C ⁵ ,C ⁶ ,N ¹⁰)	125.7	126.2	0.5	125.3	-0.9	125.2	-0.1	128.3	3.1		
A(C ⁶ ,N ¹⁰ ,O ¹¹)	117.9	116.5	-1.4	119.0	2.5	120.5	1.5	123.1	2.6		

^aSee Ref. [23]. ^bAlgebraic deviations between experimental and theoretical values. ^cAlgebraic deviations between theoretical values of the anion and molecule ^dAlgebraic deviations between theoretical values of the dianion and anion. ^eAlgebraic deviations between theoretical values of the trianion and dianion. For atom numbering see Scheme 1.

CONCLUSION

We report in this work good theoretical descriptions of the IR and structural changes, caused by the conversion of violuric acid into anion and dianion. We found that B3LYP/6-311+G(2df,p) computation are able to predict well the IR changes, which accompany the violuric acid molecule into anion and dianion conversion. So, we can suppose that the combined experimental/DFT approach applied in this work can be used also in cases of other molecules, anions and dianions, which structures cannot be experimental measured.

Acknowledgements: The financial support of this work by the National Science Fund of Bulgaria (Contracts RNF01/0110), is gratefully acknowledged.

REFERENCES

1. A. Von Bayer, *Ann. Chem.*, **130**, 140 (1864).
2. S. Harasawa, K. Matsusaki, *BUNSEKI KAGAKU*, **18**, 1017(1969).
3. A. K. Singh, M. Katyal, R. P. Singh, *Curr. Sci.*, **45**, 405 (1976).
4. M. Ponikvar, J. F. Liebman, In: The chemistry of hydroxylamines, oximes and hydroxamic acids, Z. Rappoport, J. F. Liebman (eds) 2009, John Wiley & Sons, Ltd. Ch.11, 515.
5. M. Soylak, I. Murat, *Food Anal. Meth.*, **5**, 1003 (2012)
6. J. M. Moratal, A. Prades, M. Julve, J. Faus, *Thermochim. Acta*, **89**, 343 (1985).
7. L. F. C. de Oliveira, P. S. Santos, J. C. Rubim, *J. Raman Spectrosc.*, **22**, 197 (1991).
8. R. M. Awadallah, A. A. M. Belal, R. M. Issa, *Spectrochim. Acta*, **47A**, 154 (1991).
9. T. Kolev, B. B. Koleva, R. W. Seidel, M. Spiteller, W. S. Sheldrick, *Crystal Growth Design*, **9**, 3348 (2009).
10. A. T. Burbello, V. V. Vishvtseva, P. P. Denisenko, A. F. Safonova, E. G. Dobrokhotova, *Eksp Klin Farmakol.*, **58**, 49 (1995).
11. US 3728461A/1975, US 3928017A/1973.
12. X. Jin, X. Yu, G. Zhu, Z. Zheng, F. Feng, Z. Zhang, *Sci. Rep.*, **6**, 35787 (2016).
13. E. L. Chang, C. Simmers, D. A. Knight, *Pharmaceuticals*, **3**, 1711 (2010).
14. N. Z. Shaban, M. S. Masoud, M. A. Mawlawi, D. Awad, O. M. Sadek, *J. Physiol. Biochem.*, **68**, 47 (2012).

15. M. Kavlakova, A. Bakalova, G. Momekov, D. Ivanov, *Arzneimittel-Forschung, Drug Res.*, **62**, 599 (2012)
16. H. C. Garcia, R. Diniz, N.L. Speziali, L.F. C. de Oliveira, *J. Mol. Struct.* **1070** (2014)117.
17. R. Banik, S. Roy, L. Dlhán, J. Titiš, R. Boča, A. M. Kirillov, A. D. Martin, A. Bauza, A. Frontera, A. Rodríguez-Diéguez, J. M. Salas, S. Das, *Dalton Trans.*, **45**, 16166 (2016).
18. J. A. Bonacin, A. L. B. Formiga, V. H. S. de Melo, H. E. Toma, *Vib. Spectrosc.*, **44**, 133 (2007).
19. M. J. Frisch, G. W. Trucks, H. B. Schlegel, G. E. Scuseria, M. A. Robb, J. R. Cheeseman, G. Scalmani, V. Barone, B. Mennucci, G. A. Petersson, H. Nakatsuji, M. Caricato, X. Li, H. P. Hratchian, A. F. Izmaylov, J. Bloino, G. Zheng, J. L. Sonnenberg, M. Hada, M. Ehara, K. Toyota, R. Fukuda, J. Hasegawa, M. Ishida, T. Nakajima, Y. Honda, O. Kitao, H. Nakai, T. Vreven, J.A. Montgomery, Jr., J. E. Peralta, F. Ogliaro, M. Bearpark, J. J. Heyd, E. Brothers, K. N. Kudin, V. N. Staroverov, R. Kobayashi, J. Normand, K. Raghavachari, A. Rendell, J. C. Burant, S. S. Iyengar, J. Tomasi, M. Cossi, N. Rega, J. M. Millam, M. Klene, J. E. Knox, J. B. Cross, V. Bakken, C. Adamo, J. Jaramillo, R. Gomperts, R. E. Stratmann, O. Yazyev, A.J. Austin, R. Cammi, C. Pomelli, J. W. Ochterski, R. L. Martin, K. Morokuma, V. G. Zakrzewski, G. A. Voth, P. Salvador, J. J. Dannenberg, S. Dapprich, A. D. Daniels, Ö. Farkas, J. B. Foresman, J. V. Ortiz, J. Cioslowski, D. J. Fox, Gaussian 09, Revision A1, Gaussian Inc., Wallingford CT, 2009.
20. A. D. Becke, *J. Chem. Phys.* **98**, 5648 (1993).
21. C. Lee, W. Yang, G. R. Parr, *Phys. Rev.*, **B37**, 785 (1998).
22. H. J. Michal, VEDA 4, Warsaw, 2004.
23. B. M. Craven, Y. Mascarenhas, *Acta Cryst.*, **17**, 407 (1964).
24. V. M. Vlasov, L. A. Oshkina, *Org. React.*, **28**, 47 (1993).
25. E. Velcheva, Z. Glavcheva, B. Stamboliyska, *Bulg. Chem. Commun.*, **48**, 514 (2016).
26. A. D. Popova, E. A. Velcheva, B. A. Stamboliyska, *J. Mol. Struct.*, **1009**, 23 (2012).
27. I. G. Binev, P. J. Boyadjieva, Y. I. Binev, *J. Mol. Struct.*, **447**, 235 (1998).
28. O. A. Reutov, K. P. Butin, I. P. Beletskaya, *Usp. Khim. (Russ. Chem. Rev.)*, **43**, 35 (1974).
29. M. Szwarc, *Ions and Ion Pairs in Organic Reactions*, Wiley-Interscience, New York, 1972.
30. J. A. Tsenov, S. S. Stoyanov, *Bulg. Chem. Commun.*, **40**, 320 (2008).
31. D. Yancheva, E. Velcheva, Z. Glavcheva, B. Stamboliyska, A. Smelcerovic *J. Mol. Struct.*, **1108**, 552 (2016).

ТЕОРЕТИЧНО И ЕКСПЕРИМЕНТАЛНО ИЗСЛЕДВАНЕ НА ИЧ СПЕКТРИ И СТРУКТУРАТА НА ВИОЛУРОВАТА КИСЕЛИНА И НЕЙНИТЕ АНИОНИ

Ц. Колев^{1*}, Е. Велчева², Б. Стамболийска²

¹ *Институт на молекулярна биология, Българска академия на науките, ул. „Акад. Г. Бончев“, бл. 21, 1113 София, България*

² *Институт по органична химия с Център по фитохимия, Българска академия на науките, ул. „Акад. Г. Бончев“, бл. 9, 1113 София, България*

Постъпила на 01 май 2017 г.; Коригирана на 05 юни 2017 г.

(Резюме)

Изследвани са експерименталните и теоретичните ИЧ спектри и структурата на виолуровата киселина и нейните аниони. На базата на квантовохимични пресмятания на ниво V3LYP/6-311+G(2df,p) е установено, че трикетто тавтомера е най-стабилен и при молекулата и при изследваните аниони. Превръщането на молекулата в моноанион води до силно честотно понижение и на трите валентни карбонилни трептения: пресметнати 153 cm⁻¹, измерени 138 cm⁻¹ и други значителни промени във вибрационния спектър. Виолуратния дианион е получен в разтвор на ДМСО-d₆ в присъствие на димсил-натрий. Сумарното ν(C=O) понижение причинено от превръщането на молекулата в дианион е пресказано 485 cm⁻¹ и измерено 483 cm⁻¹.

Mono-ring phthalocyanine complexes of large ions Lu³⁺ and Sn⁴⁺: synthesis and comparison of photophysical properties

I. Eneva¹, M. Aliosman^{1,2}, I. Angelov¹, K. Popov¹, V. Mantareva^{1*}

¹*Institute of Organic Chemistry with Centre of Phytochemistry, Bulgarian Academy of Sciences, Acad. G. Bonchev, str., Bld. 9, 1113 Sofia, Bulgaria*

²*Institute of Physical Chemistry, Bulgarian Academy of Sciences, Acad. G. Bonchev, str., Bld. 11, 1113 Sofia, Bulgaria*

Received April 28, 2017; Revised June 14, 2017

Dedicated to Acad. Ivan Juchnovski on the occasion of his 80th birthday

Phthalocyanine complexes have been extensively studied during last years as photosensitizers for photodynamic therapy (PDT). The advantages of metal phthalocyanine complexes (MPcs) of far red absorption and high levels of singlet oxygen generation have been featured some MPcs for clinical PDT. Presently only a few phthalocyanines are approved for clinical PDT. These are ZnPc-liposomes (Italy), differently sulfonated AlPcS₁₋₄, (Photosense, Russia) and a silicon complex (Pc4, USA). The unique absorption properties such as two order higher extinction coefficient at the far red region (670-740 nm) in comparison to the firstly approved porphyrins (~ 630 nm) make MPcs efficiently excitable through disordered tissue. The development of new generation MPcs with favourable physicochemical properties includes complexes of large metal ions such as lutetium and tin, which are actual ions for MPcs within the PDT. The complexes can participate in the intersystem crossing transition to the triplet state which facilitates the further photocatalytic reactions to produce the highly reactive singlet oxygen. The study presents the effective synthesis strategy to prepare large ions phthalocyanines (Sn⁴⁺Pc and Lu³⁺Pc) as mono-ring complexes for advance of PDT efficacy. The effects of the coordinated ions on the photophysical properties of Sn⁴⁺Pc and Lu³⁺Pc were studied in comparison to the metal-free phthalocyanine (H₂Pc).

Key words: phthalocyanine complexes; lutetium, tin; photophysical properties; photodynamic therapy

INTRODUCTION

Phthalocyanines are well known as second generation photosensitizers for biomedical applications, especially the metallated derivatives with ions coordinated in the cavity of the macrocycle [1-5]. The chemical classification of metallophthalocyanines (MPcs) is heterocyclic organic semiconductor molecules with metal ion Mⁿ⁺ of oxidation state $1 \leq n \leq 6$ which can coordinate one or two negatively charged tetraisoindoles ligands yielding in mono - or diphthalocyaninato, i.e. double-decker, complexes [6]. The unique optical and electronic properties of the MPcs besides their high chemical and thermal stability are the key factors for their usage as photosensitizers for photodynamic therapy (PDT) of cancer [1-5] and for optical limiting devices [7, 8]. MPcs have a much higher extinction coefficient ($\epsilon > 10^5 \text{ M}^{-1} \text{ cm}^{-1}$) of the Q band, as approx. in the 650 - 720 nm spectra which makes them efficiently excitable directly through living tissue. MPcs have been widely thought to be ideal photosensitizers for

PDT due to their far-red and high intensity absorption, red shifted fluorescence and high level of singlet oxygen quantum yields [9]. However, as large planar molecules because of strong interactions between the macrocycles, these Pcs readily form stacked aggregates and are poorly soluble which depresses their photoactivity and restrains further studies on their photophysicochemical properties and photodynamic activity [10].

The reducing of the aggregation potential and improving the solubility of the MPcs are currently of an active research interests. The efforts in development of soluble phthalocyanine photosensitizers for PDT applications have been made in order to obtain complexes with favorable photophysical and photochemical characteristics *via* molecular design that facilitates the uptake and selectivity for a high PDT efficiency. Pcs` macrocyclic system is very flexible to modifications of the structure and their photophysical properties can be tuned by altering the substituents on the Pc ring and on the axial position at the coordinated different central metal ions [11, 12]. Phthalocyanines are able to form

* To whom all correspondence should be sent:
E-mail: mantareva@yahoo.com

complexes with a wide range of metals as the role of the central metal is not only to alter their photo-physicochemical properties but most importantly is to prevent the aggregation. The bigger in size encompassed atoms in the central cavity of the Pcs ensures the monomeric state of MPcs molecules in solutions [13,14].

Among the new generation phthalocyanine complexes, lanthanide (III) phthalocyanines are of a high interest, especially the lutetium phthalocyanines (LuPcs) that have been studied due to their rich electrochromic and gas-sensing properties and the ability of the Lu^{3+} for coordination of two or more Pc-molecules per one lutetium ion [15, 16]. The known LuPcs have an optimal singlet oxygen quantum yields (> 0.3) and that property is an indication of the potential of these complexes as photosensitizers for PDT [17, 18]. The first lutetium complex studied for PDT was Lu-texaphyrine which is a porphyrin derivative. Presently this compound is clinically approved for USA as a photosensitizer for PDT in oncology with the commercial name **Lutrin®**. Chemically, Lutrin is a water-soluble compound with high tumor selectivity and it has an intensive absorption maximum at 732 nm but with low efficiency of singlet oxygen quantum yield (~ 0.11) in comparison to other photosensitizers [19-21]. The usage of lutetium ion in phthalocyanine complexes as mono-ring molecule was explored in our recent works suggesting that two newly synthesized methylpyridyloxy- substituted LuPcs have high efficiency for PDT applications [16, 22].

The second metal ion for formation of MPc complex, which is explored in the present study, is tin ($\text{Sn}^{2+/4+}$). Tin characterizes with different oxidation states so that the phthalocyanine Sn^{2+} and Sn^{4+} complexes can be synthesized in dependence on the ratios between the ligand and metal salt. Moreover, the tin ion has a size which is not allowing the coordination within the cavity of the Pc ring. This structure facilitates the existence of molecules in monomeric state due to the steric hindrance which is of importance for the effectiveness of photosensitizers in solution. Similar to Lu, Sn ions tends to form double – decker structures. The monomolecular SnPcs complexes showed relatively long wavelength absorbance (> 690 nm) and high photochemical potential for cancer PDT application [23-25]. Presently Sn^{4+} etiopurpurin (SnET2 , **Purlytin™**) is accepted as a drug for macular degeneration treatment with PDT. The in vitro studies showed stronger influence of the nature of the coordinated

tin ion on the uptake and the photocytotoxicity as compared to the non-coordinated photosensitizers [19, 26].

The macrocyclic molecule of phthalocyanine appears a ligand able to coordinate the most of the metal and semimetal ions in the periodic table. The synthesis of phthalocyanines (Pcs) involves a routine pathway which is based on the reaction of tetracyclomerization starting from the non- or different substituted dinitriles. The addition of metal salts can facilitate the formation of macrocycle and leads to the high yield product of phthalocyanine complex which are further accessible for proper functionalization.

The study presents the synthesis of phthalocyanine complexes coordinated with large ions of Lu^{3+} and Sn^{4+} starting from a metal-free phthalocyanine by using the suitable metal salts and high boiling point solvent. Both complexes were chemically characterized by the means of ^1H NMR, MS, IR and UV-vis spectroscopy. The absorption and fluorescence properties of LuPc and SnPc were investigated in solutions of dimethylformamide in comparison to the metal-free phthalocyanine used as a ligand molecule.

EXPERIMENTAL

General

All reagents and solvents were of reagent-grade quality obtained from commercial suppliers. All solvents used for synthesis such as dimethylformamide (DMF) and quinoline were dried or distilled and stored over molecular sieves (3 Å) before experiments. The used metal salts: $\text{Lu}(\text{OAc})_3$ and SnCl_2 were dried in Glass oven over P_2O_5 . The purity of the products were tested by using thin layer chromatography (TLC). All reactions were carried out under dry nitrogen atmosphere. The spectrophotometric experiments were carried out in diluted solutions ($< 10^{-5}$ M) of dimethylformamide (DMF) of spectroscopic grade.

Instruments and equipment

FT-IR spectra were recorded on a Bruker Tensor 27 apparatus. UV-visible spectra were recorded with a Perkin Elmer Lambda 25 UV/Vis Spectrometer. Fluorescence spectra were recorded with a Perkin Elmer LS 55 Luminescence Spectrometer. ^1H NMR spectra were recorded on Bruker 600 MHz spectrometer in DMSO-d_6 solution. Mass spectrometer (Q-TOF

MS/MS) in ESI mode was used for evidence of both complexes.

Synthesis

The synthesis of metal free phthalocyanine (H_2Pc) was carried out by using the commercially available dilithium phthalocyanine (Sigma-Aldrich). The product was used after extraction on Soxhlet apparatus with methanol and was additionally purified with acetone. The reaction of demetallation of Li_2Pc was carried out according to the well know procedure [15–17]. The phthalocyanine complexes of Lu^{3+} and Sn^{4+} (LuPc and SnPc) were prepared by using the metal – free phthalocyanine, the proper metal salt by using the equal equivalency (1:1) of the molecules of H_2Pc and metal salt was used. The reaction was carried out by using a high boiling point solvent such as quinoline ($> 200\text{ }^\circ\text{C}$) under inert nitrogen atmosphere (Scheme 1). The change of color from dark blue to soft bluish was observed in synthesis of LuPc and the color changes to green for SnPc . The lack of absorption band approx. at 800 nm confirms that both complexes are monomolecular without non-desirable double-decker molecules. As the coordination number of rare-earth metals is above 8, but the obtained Lu^{3+}Pc has 3, we assume that the others are saturated with the solvents molecules.

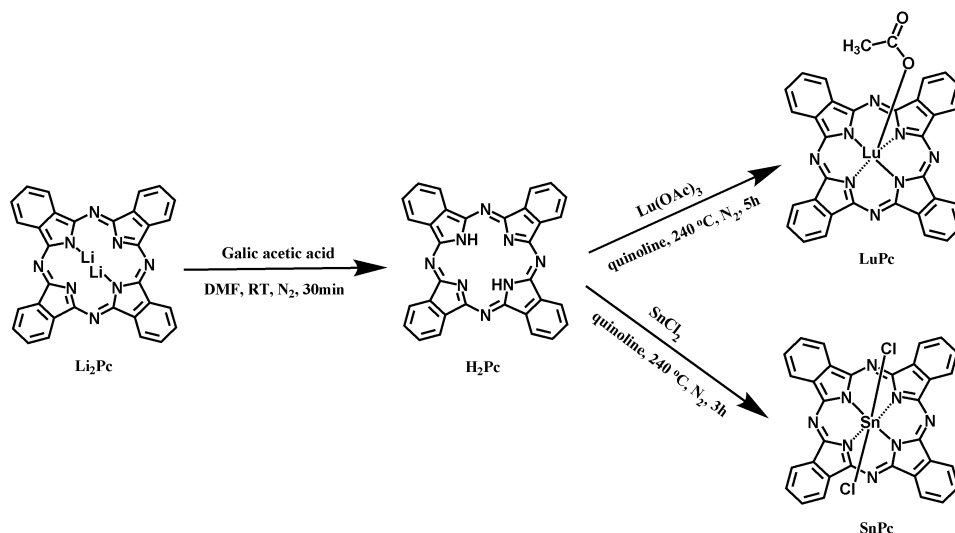
Synthesis of metal free phthalocyanine (H_2Pc)*dy*

The mixture of 0.1 g (0.190 mmol) of dilithium phthalocyanine was dissolved in 10 mL DMF and 10 mL (0.175 mmol) galic acetic acid and stirred under nitrogen atmosphere at room temperature for

30 minutes. After the reaction finished the mixture was precipitated in isopropyl ether and then in water, filtrated out and washed several times with excess of distilled water. Yield: 80 mg (80%). Molecular Formula: $\text{C}_{32}\text{H}_{18}\text{N}_8$, Molecular Weight: 514.54 g/mol. FT-IR [$\nu_{\text{max}}/\text{cm}^{-1}$]: 3272, 1500, 1436, 1333, 1321, 1117, 1093, 1001, 779, 750, 728, 718. UV-Vis (DMF) λ_{max} , nm (log ϵ): 689 (3.82). ^1H NMR (d_6 -DMSO), δ , ppm: 8.47-8.40 (m, 6H, CH Ar), 8.35-8.29 (m, 6H, CH Ar), 7.96-7.90 (m, 4H, CH Ar), 7.73-7.53 (m, 10H, CH arom), 7.33-7.30 (d, 2H, CH arom).

Synthesis of Lu^{3+} - phthalocyanine (LuPc)

A solution of 0.1 g (0.194 mmol) metal free phthalocyanine and 0.082 g (0.195 mmol) $\text{Lu}(\text{OAc})_3$ in dry quinoline was heated while stirring at $240\text{ }^\circ\text{C}$ under nitrogen atmosphere for 5 hours. The reaction was monitored with TLC. Then reaction mixture was cooled to room temperature and precipitated in hexane, filtrated and washed with hexane and an excess of water. Yield: 60 mg (60%). Molecular Formula: $\text{C}_{34}\text{H}_{19}\text{LuN}_8\text{O}_2$, Molecular Weight: 746.53 g/mol. FT-IR [$\nu_{\text{max}}/\text{cm}^{-1}$]: 3049 (Aromatic CH), 2919, 2849 (Aliphatic CH), 1569, 1487, 1454 (ArC=C), 1330, 1283, 1162, 1115, 1078, 887, 805, 779, 733. UV-Vis (DMF) λ_{max} , nm (log ϵ): 669 (4.01). ^1H NMR (d_6 -DMSO), δ , ppm: 9.43-9.42 (m, 4H, CH Ar), 8.92-8.91 (m, 1H, CH Ar), 8.38-8.37 (dd, $J=8.35, 8.29$, 1H, CH Ar), 8.23-8.22 (m, 4H, CH Ar), 8.18-8.16 (m, 1H, CH Ar), 8.04-8.02 (dd, $J=8.55, 8.47$, 1H, CH Ar), 8.00-7.98 (dd, $J=8.08, 8.10$, 1H, CH Ar), 7.79-7.76 (m, 1H, CH Ar), 7.63-7.61 (m, 1H, CH Ar), 7.55-7.53 (m, 1H, CH Ar), 1.66 (s, 3H, CH_3). MS (ESI): m/z 785 [$\text{M} + \text{K}$] $^+$.



Scheme 1. Reaction conditions to obtain phthalocyanine complexes of LuPc and SnPc .

Synthesis of Sn^{4+} -phthalocyanine (**SnPc**)

A solution of 0.1 g (0.194 mmol) metal free phthalocyanine and 0.037 g (0.195 mmol) SnCl_2 in dry quinoline was heated while stirring at 240 °C under nitrogen atmosphere for 3 hours. The reaction was monitored with TLC. Then reaction mixture was cooled to room temperature and precipitated in hexane, filtrated and washed with excess of water. Yield: 38 mg (38%). Molecular Formula: $\text{C}_{32}\text{H}_{16}\text{Cl}_2\text{N}_8\text{Sn}$, Molecular Weight: 702.14 g/mol. FT-IR [$\nu_{\text{max}}/\text{cm}^{-1}$]: 3051 (Aromatic CH), 1487, 1468 (ArC=C), 1335, 1284, 1118, 1075, 1060, 887, 745, 723. UV-Vis (DMF) λ_{max} , nm (log ϵ): 691 (3.87). ^1H NMR (d_6 -DMSO), δ , ppm: 8.92-8.91 (m, 2H, CH Ar), 8.38-8.37 (br, 2H, CH Ar), 8.03-8.02 (d, $J=8.34$, 2H, CH Ar), 8.00-7.99 (d, $J=8.40$, 2h, CH Ar), 7.79-7.76 (m, 3H, CH Ar), 7.64-7.61 (m, 3H, CH Ar), 7.55-7.53 (m, 2H, CH Ar). MS (ESI): m/z 720.5 [$\text{M}+\text{H}_2\text{O}$] $^+$

Absorption and fluorescence study

The obtained complexes of Lu^{3+} and Sn^{4+} phthalocyanines were photophysical studied in DMF solutions. The stock solutions of both complexes and the starting metal-free phthalocyanine were freshly prepared on the basis on the molecular weights with a concentration of 1 mM. The studies were carried out by the several dilutions. The spectra were recorded at room temperature. The dilutions were made in order to prevent the formation of aggregated molecules (dimers or higher associates) in the studied concentration range. Five different concentrations were used for study the absorption characteristics. The fluorescent spectra were recorded in comparison at excitation 610 nm following the same experimental protocol and equipment details for the studied phthalocyanine complexes **LuPc** and **SnPc** versus **H₂Pc**.

RESULTS AND DISCUSSION

Synthesis

Two unsubstituted metal phthalocyanine complexes of Lu^{3+} (**LuPc**) and Sn^{4+} (**SnPc**) were synthesized (Scheme 1) by slight modifications of the known synthetical procedure for preparation of complexes which involves a reaction from metal free phthalocyanine (**H₂Pc**) boiling with the proper metal salt. The high energy is required for formation of these complexes due to the large in

size atoms chosen for coordination with Pc ligand. The synthesis was carried out in 1-pentanol firstly at 140 °C but it was not successful. A high boiling point solvent such as quinoline (> 200 °C) was used for the coordination of both ions and the reactions were performed by preheating of the starting compound to allow the high yielded coordination reactions. The obtained products were precipitated in hexane and washed several times with hexane and excess of distilled water. The formation of the fine sediments was proving the success of reaction with central ions exchange.

The complexes were characterized by various spectroscopic methods. The ^1H NMR spectra (Fig. 1) showed the numbers of protons which are consistent with the predicted structures. Due to low solubility the metal-free **H₂Pc** showed very low intensive ^1H NMR signals. The spectrum appears as inappropriate for presentation vs. the spectra of **LuPc** and **SnPc**.

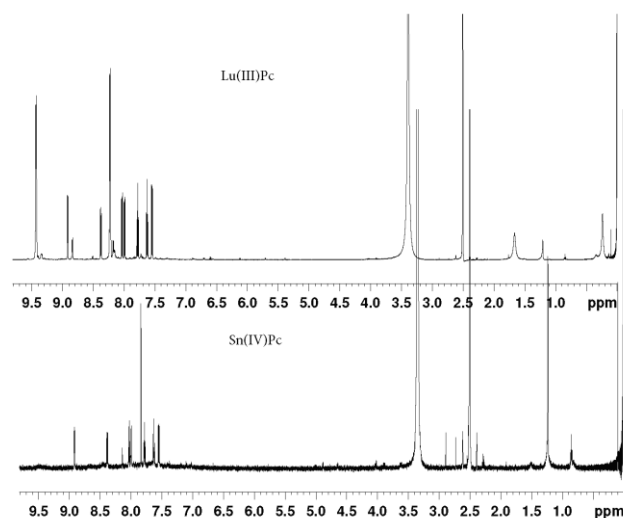


Fig. 1. ^1H NMR spectra

The ESI mass spectra of complexes showed the protonated molecular ion signal as the base peak, of which the isotopic distribution was in good agreement with the simulated pattern as is described in the Experimental part. The main ring structure was proven by the mass of the studied complexes and the basic ligand molecule. FT-IR spectra of the unsubstituted phthalocyanine confirmed the coordination of the ions in the ring molecule of the phthalocyanine (Fig. 2). In order to verify the metallization process the most distinctive feature in the FT-IR spectra for metal-free **H₂Pc** is

a signal for the N–H vibration mode at 3291 cm^{-1} which is not observed for the metallated compounds (**LuPc** and **SnPc**).

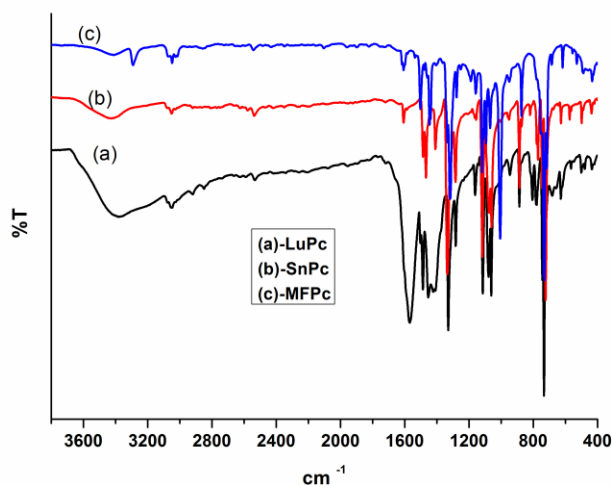


Fig. 2. FT-IR spectra

The electronic absorption spectra of the studied Lu^{3+} and Sn^{4+} phthalocyanines (**LuPc** and **SnPc**) were recorded in organic solution of dimethylformamide (Fig. 3). The spectra showed characteristic absorption bands in the visible red region with absorption maximum of Q-band at 669 nm for **LuPc** and 691 nm for **SnPc**, respectively. In the UV region the characteristic second B bands at 336 nm for **LuPc** and 354 nm for **SnPc** were recorded. The largest atom of Lu contributes to the red absorption of phthalocyanine with 669 nm. The second metal (Sn) allows much more red shifted absorbance for the complex **SnPc** (691 nm) as compare to **H₂Pc** (splitters at 665, 689 nm). The single, narrow Q band was recorded for both metallated phthalocyanine complexes for a wide concentration range of the studied MPCs. The spectra evidenced the photoactive monomeric molecules in organic solutions which are photoactive and can participate in the photosensitization reactions.

Fluorescence emission spectra of **LuPc** and **SnPc** were recorded at excitation 610 nm for the diluted solutions in DMF (Fig. 4). The fluorescence emission maxima are red shifted as compared to the absorption maxima, which are at 688 nm with a shift of 19 nm for **LuPc** and 696 nm (5 nm shift) for **SnPc** as compared to the absorbance band.

The intensity of fluorescence spectra suggested a relatively good fluorescence quantum yield of **SnPc** as its fluorescence intensity is higher than the signal intensity of the starting **H₂Pc**. In case of **LuPc** the intensity of the fluorescence band is twice lower

than the intensity of the fluorescence of **H₂Pc** which is maybe due to the high atomic number of lutetium that facilitates the intersystem crossing (high quantum yields of triplet state) after excitation.

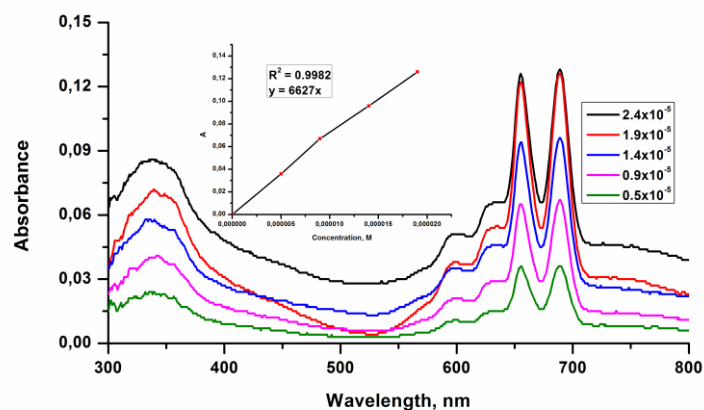
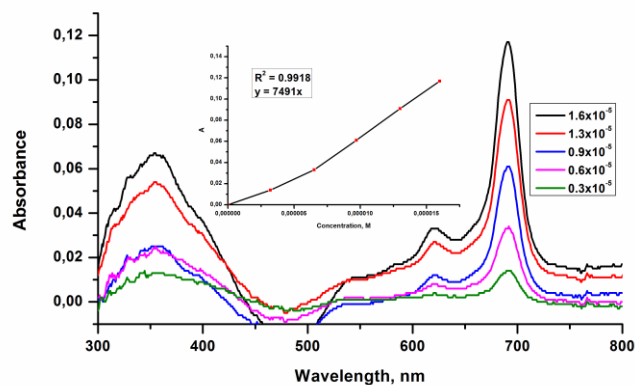
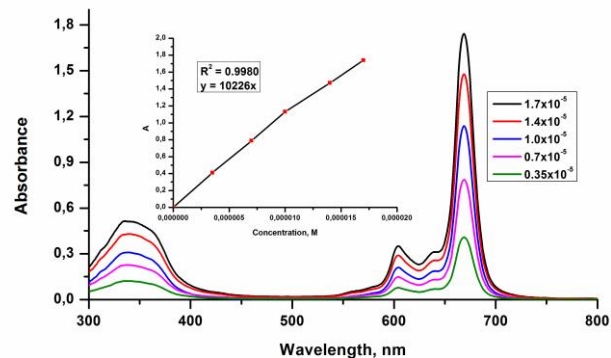


Fig. 3. Absorption spectra of **LuPc** (a), **SnPc** (b) and metal-free **H₂Pc** (c) in DMF for a concentration range.

The both synthesized complexes are more soluble than the H_2Pc which is also an advantage for their further studies as photosensitizers for biomedical applications

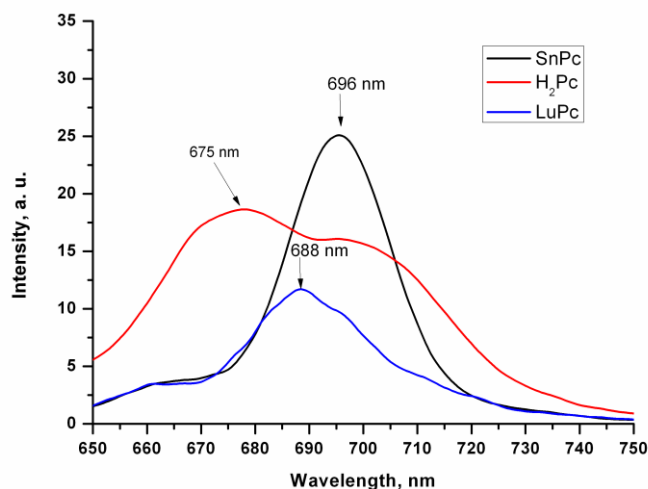


Fig. 4. Fluorescence spectra of **LuPc**, **SnPc** and metal-free **H₂Pc** recorded at excitation 610 nm in DMF.

The model studies of both complexes **LuPc** and **SnPc** and metal-free **H₂Pc** are in progress. The susceptibility of pathogenic bacteria and fungi with antibiotics resistance are under investigation for efficiency of the both complexes.

CONCLUSION

Two unsubstituted complexes of acetated Lu^{3+} and dichloride Sn^{4+} phthalocyanines were synthesized and characterized. The modification of the known synthetic procedure was successful to prepare the large ions phthalocyanine complexes. The pathway involves a reaction between a metal free phthalocyanine and the respective metal salt at high temperature reaction conditions ($> 200^\circ \text{C}$). The obtained compounds were chemically characterized by the means of general spectroscopic techniques such as FT-IR, UV-Vis and ^1H NMR. The absorption spectra of both metal complexes showed monomeric behavior of molecules in solutions, as it was evidenced by a single, narrow Q band in the far red region. The fluorescence spectra suggested a relatively good fluorescence quantum yield of **SnPc** as its fluorescence intensity is higher than the intensity of the fluorescence of the starting **H₂Pc**. Both synthesized metal complexes showed better solubility in organic solutions than the metal-free analogue **H₂Pc** which is an advantage for the further studies of the complexes as photosensitizers for biomedical applications.

Acknowledgements: MA and VM thanks to Bulgarian Academy of Sciences for the project DFNP-150. The authors thank to the National Science Fund (project B02/9/2014) for support.

REFERENCES

1. M. S. Wesley, E. V. Johan, M. A. Cynthia, *Adv. Drug Deliv. Rev.*, **56**, 53 (2004).
2. D. Aydın Tekdaş, U. Kumru, A. G. Gürek, M. Durmuş, V. Ahsen, F. Dumoulin, *Tetrahedron Lett.*, **53**, 5227 (2012).
3. N. Sekkat, H. van den Bergh, T. Nyokong, N. Lange, *Molecules*, **17**, 98 (2012).
4. G. Jori, C. Fabris, S. Soncin, S. Ferro, O. Coppellotti, D. Dei, L. Fantetti, G. Chiti, G. Roncucci, *Lasers Surg. Med.*, **38**, 468 (2006).
5. T. G. S. Denis, T. Dai, A. Izikson, C. Astrakas, R. R. Anderson, M. R. Hamblin, G. P. Tegos, *Virulence*, **2**, 1 (2011).
6. R. Kubiak, J. Janczak, *Cryst. Res. Technol.*, **36**, 1095 (2001).
7. D. Dini, M. J. F. Calvete, M. Hanack, *Chem. Rev.*, **116** (22), 13043 (2016).
8. G. M. Mikheev, I. P. Angelov, V. N. Mantareva, T. N. Mogileva, K. G. Mikheev, *Tech. Phys. Lett.*, **39**, 7, 664 (2013).
9. S. L. Manoto, P. R. Sekhejane, N. N. Houreld, H. Abrahamse, *Photodiagn Photodyn Ther.* **9**, 52 (2012)
10. A. Erdoğan, S. Moenoa, C. Litwinskia, T. Nyokonga, *J. Photochem. Photobiol. A: Chem.*, **210**, 200 (2010).
11. P. Muthukumar, H. S. Kim, J. W. Jeong, Y. A. Son, *J. Molec. Struc.* **1119**, 325 (2016).
12. J. Chen, Q. Gan, S. Li, F. Gong, Q. Wang, Z. Yang, S. Wang, H. Xu, J. S. Ma, G. Yang, *J. Photochem. Photobiol. A: Chem.*, **207**, 58 (2009).
13. V. Mantareva, V. Kussovski, I. Angelov, D. Wöhrle, R. Dimitrov, E. Popova, S. Dimitrov, *Photochem. Photobiol. Sci.*, **10**, 92 (2011).
14. V. Mantareva, V. Kussovski, I. Angelov, E. Borisova, L. Avramov, G. Schnurpfeil, D. Wöhrle, *Bioorg. Med. Chem.*, **15**, 4829 (2007).
15. C. Bozoğlu, M. Arıcı, A. L. Uğur, A. Erdoğan, A. Koca, *Synth. Metals*, **190**, 56 (2014).
16. V. Mantareva, M. Durmuş, M. Aliosman, I. Stoineva, I. Angelov, *Photodiagn Photodyn Ther.*, **14**, 98 (2016).
17. R. Zügler, T. Nyokong, *J. of Molec. Cal. A: Chem.*, **358**, 49 (2012).
18. M. Durmuş, S. Yeşilot, B. Çoşut, A. G. Gürek, A. Klımiç, V. Ahsen, *Synth. Metals*, **160**, 436 (2010).
19. S. Yano, S. Hirohara, M. Obata, Y. Hagiya, S. Ogura, A. Ikeda, H. Kataoka, M. Tanaka, T. Joh, *J. Photochem. Photobiol. C: Photochem. Rew.*, **12**, 46 (2011).
20. S. H. van Rij, P. J. Sadler, *Drug Disc. Today* **Vol. 14**, **23**, 1089 (2009).

21. M. R. Detty, C. L. Gibson, S. J. Wagner, *J. Med. Chem.*, **47**, 3897 (2004).
22. V. Mantareva, V. Kussovski, M. Durmus, E. Borissova, I. Angelov, *Lasers Med Sci.*, **31**, 1591 (2016).
23. S. Khene, A. N. Cammidge, M. J. Cook, T. Nyokong, *J. Porphy. Phthalocy.*, **11**, 761 (2007).
24. M. Idowu, T. Nyokong, *J. Photochem. Photobiol. A: Chem.*, **199**, 282 (2008).
25. J. Alzeer, P. J. C. Roth, N. W. Luedtke, *Chem. Comm.*, **15**, 1970 (2009).
26. Z. Odabas, A. Altindalb, M. Buluta, *Synth. Metals*, **161**, 1742 (2011).

МОНО-ПРЪСТЕННИ ФТАЛОЦИАНИНОВИ КОМПЛЕКСИ С ЙОНИ НА Lu³⁺ и Sn⁴⁺: СИНТЕЗ И СРАВНИТЕЛНИ ИЗСЛЕДВАНИЯ НА ФОТОФИЗИЧНИТЕ СВОЙСТВА

И. Енева, М. Алиосман, И. Ангелов, К. Попов, В. Мантарева*

*Институт по органична химия с Център по фитохимия, Българска академия на науките,
ул. Акад. Г. Бончев, бл. 9, 1113 София, България*

Постъпила на 28 април 2017 г.; Коригирана на 16 юни 2017 г.

(Резюме)

През последните години, фталоцианиновите комплекси се изследват интензивно като фотосенсибилизатори за фотодинамична терапия (ФДТ) поради уникалните им фотофизични свойства. Метал-координираните фталоцианини (МФц) имат свойства, които ги доближават до идеалните за фотосенсибилизатори за ФДТ. Така например висок екстинционен коефициент на ивицата в червената област (680 - 720 nm), която е на 3 порядъка по интензивна в сравнение с тази при порфиринови производни. Фотофизичните свойства на МФц-ни са благоприятни за ефективното им възбуждане директно в тъкани и клетки, като мишена. Понастоящем, ограничен брой МФц-ни с М: Al³⁺, Zn²⁺ и Si⁴⁺ са клинично одобрени за метода ФДТ и се прилагат в терапията на тумори. За нуждите на ФДТ, активно се разработват и изследват ново поколение МФц-ни с различни координиращи метали с висока атомна маса, което ги определя като обемни метални йони. Известно е, че Фц, координирани с подходящ метал, са по - ефективни като фотосенсибилизатори, благодарение на подобрения процес на вътрешносистемен пренос на енергия от синглетно към триплетно възбудено състояние на молекулата. Обещаващ подход с цел подобряване на фотосенсибилизиращата способност на фталоцианините е синтез, включващ комплексобразуване с метали с голям атомен номер като калай (Sn⁴⁺) и лутеций (Lu³⁺). Настоящото изследване представя ефективен синтетичен подход за координиране на фталоцианини с йони с голям атомен номер, като Sn⁴⁺ и Lu³⁺. Бяха изследвани ефектите на използваните метали върху фотофизичните свойства на получените комплекси SnPc и LuPc в сравнение с фталоцианиновия лиганд.

Antioxidant properties of 6-methoxyflavonol glycosides from the aerial parts of *Chenopodium bonus-henricus* L.

Z. Kokanova-Nedialkova, P. Nedialkov

Department of Pharmacognosy, Faculty of Pharmacy, Medical University of Sofia,
2 Dunav str., 1000 Sofia, Bulgaria

Received April 30, 2017; Revised June 13, 2017

Dedicated to Acad. Ivan Juchnovski on the occasion of his 80th birthday

Radical scavenging and antioxidant activities of nine flavonoids previously isolated from the aerial parts of *Chenopodium bonus-henricus* L. were established using DPPH and ABTS free radicals as well as inhibition of lipid peroxidation in a linoleic acid system by the ferric thiocyanate method. Patuletin glycosides, compounds **1**, **2** and **7** showed the highest DPPH (85.78%, 85.59%, 86.07%) and ABTS activity (90.64%, 90.27%, 90.76%) compared to Vitamin C. Spinacetin and 6-methoxykaempferol glycosides compounds **4**, **6** and **3**, **5** respectively possessed a significantly low DPPH activity and demonstrated a high ABTS radical-scavenging activity. Spinacetin and 6-methoxykaempferol glycosides, compounds **8** and **9**, containing esterified ferulic acid in their moiety, demonstrated a moderate DPPH (53.46%, 45.52%) and a high ABTS (83.41%, 74.51%) activity. All flavonoids inhibited significantly the lipid peroxidation of linoleic acid. The results suggest that the aerial parts of *C. bonus-henricus* L. could be a potential source of flavonoids with radical-scavenging and antioxidant activities..

Key words: *Chenopodium bonus-henricus*; flavonoids; DPPH; ABTS; FTC assays

INTRODUCTION

The human body has a complex system of natural enzymatic and non-enzymatic antioxidant defenses which counteract the harmful effects of free radicals and other oxidants. Free radicals are responsible for causing a large number of diseases including cancer [1], cardiovascular disease [2], neural disorders [3], Alzheimer's disease [4], mild cognitive impairment [5], Parkinson's disease, alcohol induced liver disease [6], ulcerative colitis [7] and atherosclerosis [8]. Protection against free radicals can be enhanced by ample intake of dietary antioxidants. Foods containing antioxidants and the antioxidant nutrients may be of major importance in disease prevention. On the other hand the most widely used synthetic antioxidants in food (butylated hydroxytoluene BHT, butylated hydroxyanisole BHA, propyl galate PG and tertiary butylhydroquinone TBHQ) have been suspected to cause or promote negative health effects. For this reason there is a growing interest in utilization of natural sources as antioxidants. *Chenopodium bonus-henricus* L. (Amaranthaceae) is widespread in Europe, western Asia and North America. The leaves and flowering tops of Good King Henry are used as a vegetable in the same manner as spinach in some European traditional cuisines. In Italy,

Spain and England it is used in soups or stews and roughly in salads. In Turkey it is known as "yabanı ispanak" (wild spinach). Canadians have also cultivated the plant as a daily vegetable. The shoots and flower clusters are eaten respectively like asparagus and broccoli [9].

In Bulgarian folk medicine the roots of *C. bonus-henricus* are known as "chuyen" and have been applied externally to treat skin inflammations, wounds and boils. The infusion of the drug has been used as a mild laxative. In Bulgarian food industry the aqueous extract of the roots has been employed in production of halva [10].

Nine flavonol glycosides of patuletin, 6-methoxykaempferol and spinacetin were recently isolated from the aerial part of *C. bonus-henricus*. All flavonoids (100 µM), compared to silybin, significantly reduced the cellular damage caused by CCl₄ in rat hepatocytes, preserved cell viability and GSH level, decreased LDH leakage and reduced lipid damage. High concentrations of compounds showed marginal or no cytotoxicity on HepG2 cell line. The experiment data suggest that the glycosides of 6-methoxykaempferol, spinacetin and patuletin are a promising and safe class of hepatoprotective agents [11]. These results stimulated us also to investigate the radical-scavenging and antioxidant activities of these flavonoids using DPPH and ABTS free radicals and

* To whom all correspondence should be sent:
E-mail: zlatina.kokanova@gmail.com

inhibition of lipid peroxidation in a linoleic acid system by the ferric thiocyanate method (FTC assay).

EXPERIMENTAL

General experimental procedures, chemicals and reagents

2,2-Diphenyl-1-picrylhydrazyl (DPPH) and 2,2'-azino-bis-(3-ethylbenzothiazoline-6-sulfonic acid) diammonium salt (ABTS) were purchased from Sigma-Aldrich (Steinheim, Germany). Linoleic acid (99%) was obtained from Acros organics (Geel, Belgium). Potassium persulphate, Vitamin C (200 mg/2 ml) and ammonium thiocyanate were purchased respectively from Valerus (Sofia, Bulgaria), Sopharma (Sofia, Bulgaria) and Fisher Chemicals (Loughborough, United Kingdom). All chemicals, including the solvents were of analytical grade. UV-VIS, Biochrom Libra S70 (Cambourne, United Kingdom) was used to measure the absorbance.

DPPH radical-scavenging assay

Scavenging activity of flavonoids against DPPH radical was assessed according to the method of Blois with some modifications [12]. Briefly, 0.3 mL of each compound in MeOH (0.1 mM) was mixed with 0.3 mL of DPPH methanol solution (0.1 mM). The reaction mixture was vortexed thoroughly and left in the dark at room temperature for 30 min. The absorbance of the mixture was measured at 517 nm. The ability to scavenge DPPH radical was calculated by the following equation:

$$\% \text{DPPH radical scavenging activity} = \frac{\text{Abs}_{\text{control}} - \text{Abs}_{\text{sample}}}{\text{Abs}_{\text{control}}} \times 100,$$

where $\text{Abs}_{\text{control}}$ is the absorbance of DPPH radical in MeOH, $\text{Abs}_{\text{sample}}$ is the absorbance of DPPH radical solution mixed with a sample. Vitamin C (0.1 mM) was used as a positive control. All determinations were performed in triplicate (n=3).

ABTS radical-scavenging assay

For ABTS assay, the procedure followed the method of Kokanova-Nedialkova *et al.* [13] with some modifications. The stock solutions included 7 mM ABTS solution and 2.4 mM potassium persulphate solution. The working solution was then prepared by mixing the two stock solutions in

equal quantities and allowing them to react for 12-14 h at room temperature in the dark. The solution was then diluted by mixing 1 mL ABTS solution with 60 mL methanol. A fresh ABTS solution was prepared for each assay. 0.2 mL of each compound in MeOH (0.1 mM) was allowed to react with 1 mL of the ABTS solution and the absorbance was taken at 734 nm after 7 min using a spectrophotometer. The ABTS scavenging capacity of the compound was calculated as:

$$\% \text{ABTS radical scavenging activity} = \frac{\text{Abs}_{\text{control}} - \text{Abs}_{\text{sample}}}{\text{Abs}_{\text{control}}} \times 100,$$

where $\text{Abs}_{\text{control}}$ is the absorbance of ABTS radical in methanol; $\text{Abs}_{\text{sample}}$ is the absorbance of an ABTS radical solution mixed with a sample. Vitamin C (0.1 mM) was used as a positive control. All determinations were performed in triplicate (n=3).

Determination of antioxidant activity in linoleic acid system by the FTC method

The antioxidant activity of studied compound (0.1 mM) against lipid peroxidation was measured through ferric thiocyanate assay, as described by Takao *et al.* [14] with some modifications. The reaction solution, containing 0.2 mL of each compound in MeOH (0.1 mM), 0.2 mL of linoleic acid emulsions (25 mg/mL in 99% ethanol), and 0.4 mL of 50 mM phosphate buffer (pH 7.4), was incubated in the dark at 40°C. A 0.05 mL aliquot of the reaction solution was then added to 1.5 mL of 70% (v/v) ethanol and 0.1 mL of 30% (w/v) ammonium thiocyanate. Precisely 3 min after the addition of 0.1 mL of 20 mM ferrous chloride in 3.5% (v/v) hydrochloric acid to the reaction mixture, the absorbance of the resulting red color was measured at 500 nm. Aliquots were assayed every 24 h until the day after the absorbance of the control solution (without compound) reached maximum value. Vitamin C (0.1 mM) was used as a positive control. All determinations were performed in triplicate (n=3).

Statistical analysis

Statistical program "MEDCALC" was used for analysis of the data. The results were expressed as mean (\pm standard deviation, SD) of three independent experiments, each performed in triplicate.

RESULTS AND DISCUSSION

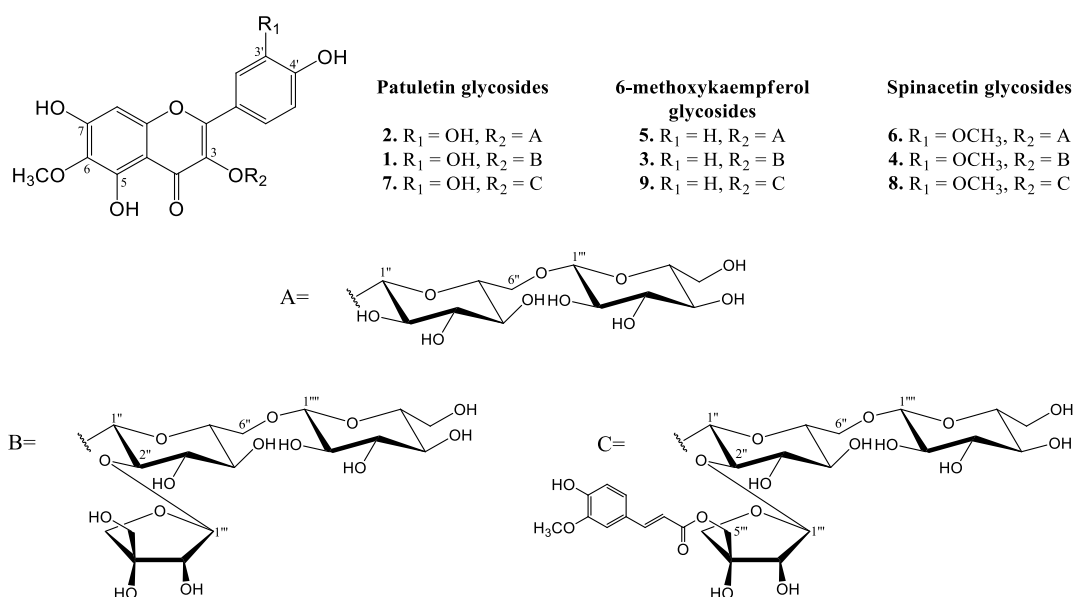
In the present study nine flavonoids, respectively patuletin 3-O- $[\beta$ -apiofuranosyl(1 \rightarrow 2)]- β -glucopyranosyl(1 \rightarrow 6)- β -glucopyranoside **1**, patuletin 3-O-gentiobioside **2**, 6-methoxykaempferol 3-O- $[\beta$ -apiofuranosyl(1 \rightarrow 2)]- β -glucopyranosyl(1 \rightarrow 6)- β -glucopyranoside **3**, spinacetin 3-O- $[\beta$ -apiofuranosyl(1 \rightarrow 2)]- β -glucopyranosyl(1 \rightarrow 6)- β -glucopyranoside **4**, 6-methoxykaempferol 3-O-gentiobioside **5**, spinacetin 3-O-gentiobioside **6**, patuletin-3-O-(5'''-O-E-feruloyl)- β -D-apiofuranosyl(1 \rightarrow 2)[β -D-glucopyranosyl (1 \rightarrow 6)]- β -D-glucopyranoside **7**, spinacetin-3-O-(5'''-O-E-feruloyl)- β -D-apiofuranosyl (1 \rightarrow 2)[β -D-glucopyranosyl(1 \rightarrow 6)]- β -D-glucopyranoside **8** and 6-methoxykaempferol-3-O-(5'''-O-E-feruloyl)- β -D-apiofuranosyl(1 \rightarrow 2)[β -D-glucopyranosyl (1 \rightarrow 6)]- β -D-glucopyranoside **9** (Fig. 1) were tested for their radical-scavenging and antioxidant activities. The radical-scavenging activities of compounds **1-9** (0.1 mM in MeOH) were compared with those of ascorbic acid at the same concentration (0.1 mM in MeOH) and expressed as % of inhibition against DPPH and ABTS (Table 1). There are three criteria for effective radical scavenging activity of flavonoids. The first important criteria is the presence of o-dihydroxy structure in the B ring, which confers higher stability to the radical form and participates in electron delocalization. The 2,3 double bond in conjugation with a 4-oxo function in the C ring is responsible for electron delocalization from the B ring.

Table 1. DPPH and ABTS radical-scavenging activities of flavonoids **1-9**.

Compound	DPPH %	ABTS %
1	85.78 \pm 0.05	90.64 \pm 0.05
2	85.59 \pm 0.36	90.27 \pm 0.09
3	7.16 \pm 0.44	70.18 \pm 0.67
4	13.56 \pm 0.05	71.81 \pm 0.38
5	4.13 \pm 0.54	70.94 \pm 0.47
6	14.62 \pm 0.13	74.41 \pm 0.01
7	86.07 \pm 0.40	90.76 \pm 0.16
8	53.46 \pm 0.53	83.41 \pm 0.65
9	45.52 \pm 0.52	74.51 \pm 0.30
Ascorbic acid	86.46 \pm 0.07	90.79 \pm 0.19

The antioxidant potency is related to structure in terms of electron delocalization of the aromatic nucleus. Where these compounds react with free radicals, the phenoxyl radicals produced are stabilized by the resonance effect of the aromatic nucleus. The third important criteria for a maximum radical scavenging potential is the presence of the 3- and 5-OH groups with 4-oxo function in A and C rings. Rice-Evans *et al.* also reported that the glycosylation of flavonoids reduces their activity when compared to the corresponding aglycones [15].

Patuletin glycosides, compounds **1**, **2** and **7** showed the highest DPPH (85.78, 85.59 and 86.07 %) activity respectively, compared to ascorbic acid (86.46 %) (Table 1). The compounds **1**, **2**, **7** possess 3', 4'-ortho-dihydroxy configuration in B ring, C2-C3 double bond configured with a 4-keto arrangement and a presence of free 5-OH and 7-OH groups, which determine their radical-scavenging activities.

**Fig. 1.** 6-Methoxyflavonol glycosides from the aerial parts of *Chenopodium bonus-henricus* L.

Spinacetin and 6-methoxykaempferol glycosides, respectively compounds **4** (13.56 %), **6** (14.62 %) and **3** (7.16 %), **5** (4.13 %) possessed significantly low DPPH activity and probably it is due to the absence of ortho-dihydroxy configuration. In spinacetin glycosides (compounds **4** and **6**) the 3'-OH group is methylated and the O-methylation of the hydroxyls of the catechol B-ring resulted in a decrease of the antioxidant activity with regard to the patuletin glycosides. In 6-methoxykaempferol glycosides (compounds **3** and **5**) 3'-OH group is missing and these compromise the antioxidant capacity. On the other hand spinacetin and 6-methoxykaempferol glycosides, compounds **8** and **9**, containing esterified ferulic acid in their moiety, demonstrated moderate DPPH (53.46 % and 45.52 %) activity. Ferulic acid possesses three distinctive structural motifs that can possibly contribute to its free radical scavenging capability. The presence of electron donating groups on the benzene ring (3-methoxy and more importantly 4-hydroxyl) of ferulic acid gives the additional property of terminating free radical chain reactions. The next functionality - the carboxylic acid group in ferulic acid with an adjacent unsaturated C-C double bond - can provide additional attack sites for free radicals and thus prevent them from attacking the membrane. In addition, this carboxylic acid group also acts as an anchor of ferulic acid, by which it binds to the lipid bilayer, providing some protection against lipid peroxidation [16].

Patuletin glycosides, compounds **1** (90.64 %), **2** (90.27 %) and **7** (90.76 %) showed the highest ABTS radical-scavenging activity. Activity of these compounds were similar to those of a classical antioxidant, ascorbic acid (90.79 %) (Table 1). Spinacetin and 6-methoxykaempferol glycosides, respectively compounds **4** (71.81 %), **6** (74.41 %), **8** (83.41 %) and **3** (70.18 %), **5** (70.94 %), **9** (74.51 %) also possessed a high ABTS radical-scavenging activity. Their lower activity is probably due to the absence of ortho-dihydroxy configuration in ring B. The results show that compounds **8** and **9** which contain esterified ferulic acid again demonstrate higher activity than the other spinacetin and 6-methoxykaempferol glycosides.

In the present study, the inhibition of lipid peroxidation of flavonoids **1-9** (0.1 mM) was determined in linoleic acid system using the FTC method. During linoleic acid peroxidation, peroxides were formed and these compounds oxidized Fe²⁺ to Fe³⁺. The Fe³⁺ ion formed a complex with SCN⁻, which had a maximum absorbance at 500 nm. Thus, a high absorbance value was an indication of high peroxide formation during the emulsion incubation. The presence of antioxidants in the mixture minimizes the oxidation of linoleic acid and reduce the absorption, respectively.

The absorbance of the control showed a steady increase and reached a maximal value of 1.20 on the 7th day (Fig. 2).

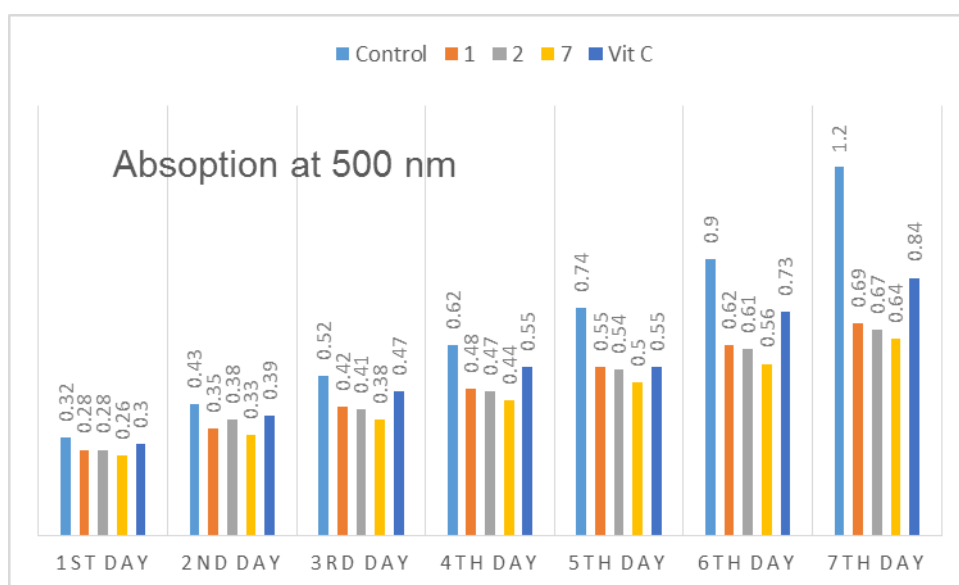


Fig. 2. Antioxidant activity of patuletin glycosides **1**, **2**, **7** in linoleic acid system.

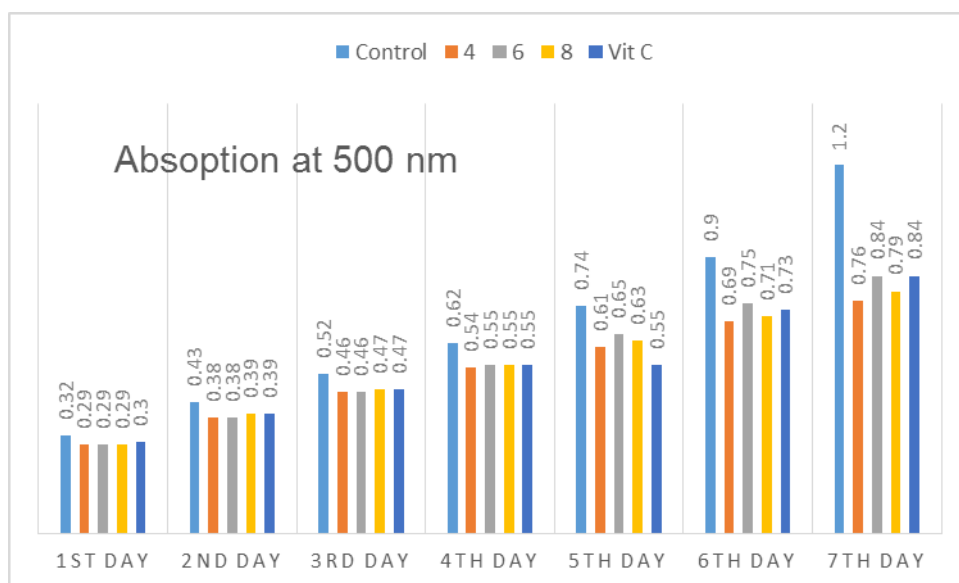


Fig. 3. Antioxidant activity of spinacetin glycosides 4, 6, 8 in linoleic acid system.

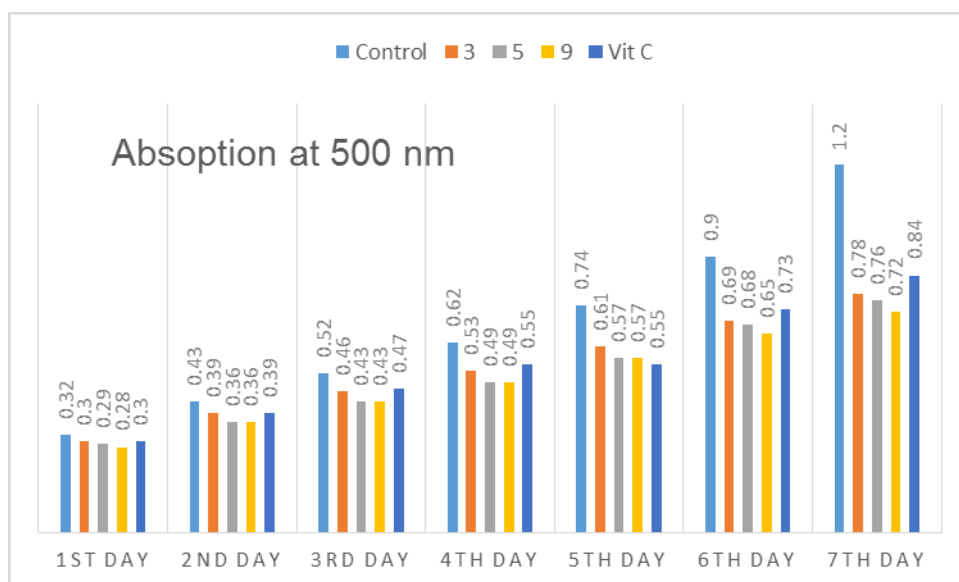


Fig. 4. Antioxidant activity of 6-methoxykaempferol glycosides 3, 5, 9 in linoleic acid system.

The patuletin glycosides compounds 1, 2 and 7 showed the highest capacity to inhibit linoleic acid peroxidation, with absorbance values always under 0.69 during the 7 days of testing (Fig. 2). Their activity was higher than the activity of Vitamin C, a widely used commercial antioxidant and may be it was due to the presence of ortho-dihydroxyl configuration in ring B.

On the other hand spinacetin and 6-methoxykaempferol glycosides, respectively compounds 4, 6, 8 (Fig. 3) and 3, 5, 9 (Fig. 4) also hindered the oxidation of linoleic acid and their activity is similar to that of Vitamin C.

These results indicate that patuletin, spinacetin and 6-methoxykaempferol glycosides, compounds

1-9, can significantly inhibit the peroxidation of linoleic acid and reduce the formation of hydroperoxide, thus implying that these flavonoids are powerful natural antioxidants.

CONCLUSION

Patuletin glycosides (1, 2 and 7) showed the highest DPPH and ABTS radical-scavenging activity. Spinacetin (4 and 6) and 6-methoxykaempferol (3 and 5) glycosides possessed significantly low DPPH activity and demonstrated a high ABTS radical-scavenging activity, compared to Vitamin C. On the other hand spinacetin and 6-methoxykaempferol glycosides (compounds 8 and 9), containing esterified ferulic acid in their moiety,

demonstrated a moderate DPPH and a high ABTS activity. All flavonoids inhibited significantly the lipid peroxidation of linoleic acid. The highest diminution was demonstrated again by patuletin glycosides and they are much more effective than Vitamin C. The results suggests that the wild spinach (*C. bonus-henricus* L.) could be a potential source of flavonoids with radical-scavenging and antioxidant activities.

Acknowledgements: The study was supported by the Council of Medical Science of Medicinal University-Sofia (Contract Nr. 53/2016, Project Nr. 571/21.01.2016).

REFERENCES

1. V. L. Kinnula, J. D. Crapo, *Free Radic. Biol. Med.*, **36**, 718 (2004).
2. U. Singh, I. Jialal, *Pathophysiology*, **13**, 129 (2006).
3. K. Sas, H. Robotka, J. Toldi, L. Vecsei, *J. Neurol. Sci.*, **257**, 221 (2007).
4. M. A. Smith, C. A. Rottkamp, A. Nunomura, A. K. Raina, G. Perry, *Biochim. Biophys. Acta*, **1502**, 139 (2000).
5. I. Guidi, D. Galimberti, S. Lonati, C. Novembrino, F. Bamonti, M. Tiriticco, C. Fenoglio, E. Venturelli, P. Baron, N. Bresolin, E. Scarpini, *Neurobiol. Aging*, **27**, 262 (2006).
6. G. E. Arteel, *Gastroenterol.*, **124**, 778–790 (2003).
7. B. S. Ramakrishna, R. Varghese, S. Jayakumar, M. Mathan, K. A. Balasubramanian, *J. Gastroenterol. Hepatol.*, **12**, 490 (1997).
8. J. M. Upston, L. Kritharides, R. Stocker, *Prog. Lipid Res.*, **42**, 405 (2003).
9. E. Toensmeier, in: Perennial vegetables, B. Watson (ed), Chelsea Green Publ., Vermont, 2007, p. 122.
10. Z. Kokanova-Nedialkova, M. Kondeva-Burdina, D. Zheleva-Dimitrova, V. Tzankova, S. Nikolov, J. Heilmann, P. T. Nedialkov, *Nat. Prod. Comm.*, **10**, 1377 (2015).
11. Z. Kokanova-Nedialkova, P. Nedialkov, M. Kondeva-Burdina, R. Simeonova, V. Tzankova, D. Aluani, *Fitoterapia*, **118**, 13 (2016).
12. M. S. Blois, *Nature*, **181**, 1199 (1958).
13. Z. Kokanova-Nedialkova, P. Nedialkov, S. Nikolov, *Phcog. J.*, **6**, 43 (2014).
14. T. Takao, F. Kitatani, N. Watanabe, A. Yagi, K. Sakata, *Biosci. Biotechnol. Biochem.*, **58**, 1780 (1994).
15. C. Rice-Evans, N. Miller, G. Paganga, *Free Radic. Biol. Med.*, **20**, 7933 (1995).
16. S. Itagaki, T. Kurokawa, C. Nakata, Y. Saito, S. Oikawa, M. Kobayashi, T. Hirano, K. Iseki, *Food Chem.*, **114**, 466 (2009).

АНТИОКСИДАНТНИ СВОЙСТВА НА 6-МЕТОКСИФЛАВОНОЛОВИ ГЛИКОЗИДИ ОТ НАДЗЕМНИТЕ ЧАСТИ НА *Chenopodium bonus-henricus* L.

З. Коканова-Недялкова*, П. Недялков

Катедра “Фармакогнозия”, Фармацевтичен факултет, Медицински университет-София,
ул. Дунав 2, 1000 София, България

Постъпила на 30 април 2017 г.; Коригирана на 13 юни 2017 г.

(Резюме)

Радикал-свързващата и антиоксидантната активност на девет по-рано изолирани от надземната част на *Chenopodium bonus-henricus* L. флавоноиди е установена чрез DPPH и ABTS свободни радикали и чрез инхибиране на липидна пероксидация в система на линоленова киселина чрез фери-тиоцианатен метод. Гликозидите на патuletин, съединения **1**, **2** и **7** показват най-висока DPPH (85.78%, 85.59%, 86.07%) и ABTS активност (90.64%, 90.27%, 90.76%) сравнена с активността на Vitamin C. Гликозидите на спинацетин и 6-метоксикемпферол, съответно съединения **4**, **6** и **3**, **5** притежават значително ниска DPPH активност и проявяват висока ABTS радикал-свързваща активност. Гликозидите на спинацетин и 6-метоксикемпферол, съединения **8** и **9**, съдържащи в молекулата си естерифицирана ферулова киселина проявяват умерена DPPH (53.46%, 45.52%) и висока ABTS (83.41%, 74.51%) активност. Всички флавоноиди значително възпрепятстват окислението на линоленовата киселина. Въз основа на получените резултати надземните части на *C. bonus-henricus* L. могат да бъдат потенциален източник на флавоноиди с радикал-свързваща и антиоксидантна активност.

Enzymatic synthesis of fructo-oligosaccharides by recombinant levansucrase from *Leuconostoc mesenteroides* Lm17

A. S. Salim, V. P. Bivolarski, T. A. Vasileva, Ilia N. Iliev*

Department of Biochemistry and Microbiology, Faculty of Biology, University of Plovdiv "Paisii Hilendarski", 24, Tsar Asen, Str., Plovdiv, Bulgaria

Received May 01, 2017; Revised June 23, 2017

Dedicated to Acad. Ivan Juchnovski on the occasion of his 80th birthday

The levansucrase [EC2.4.1.10] can transfer fructosyl units from sucrose to different acceptors (maltose, lactose) to give a good yields of oligosaccharides that could have prebiotic potential. Selectivity of the reaction of synthesis of fructooligosaccharides (FOSs) using levansucrase was strongly dependent on the enzyme source, type of acceptors and donor/acceptor ratio (D/A). The acceptor specificity studies determined the ability of recombinant levansucrase Lm17 to synthesize different types of (FOSs) using different acceptors. In the present study we first describe that when maltose was the acceptor, the major products was a FOS with degree of polymerization (DP3) (75,5% of total FOS) identified as an erlose. Levansucrase was highly transfructosylating than hydrolytic activity. In carrying out the enzymatic reaction in the presence of 10% sucrose and 5% maltose, K_m of recombinant levansucrase Lm17 was 43.99 ± 7.01 mM sucrose, and V_{max} value was 2.1 ± 7.7 U/ml. This investigation of the properties of recombinant levansucrase Lm17 reveals the potential use of the enzyme as tools for synthesis of short chain FOSs (erlose) with prebiotic potential.

Key words: Levansucrase; *Leuconostoc mesenteroides*; fructooligosaccharides; prebiotics

INTRODUCTION

Lactic acid bacteria (LAB) belonging to the genera *Lactobacillus*, *Streptococcus*, *Leuconostoc* and *Weissella* have been reported as producers of fructosyltransferases (FTFs) [1,2,3,4]. FTFs are classified into a family 68 of glycoside hydrolase enzymes (GH68) (CAZY, <http://cazy.org>) [5]. According to the type of the glycosidic linkages between fructosyl units in the synthesized fructans these enzymes are divided into levansucrases (EC 2.4.1.10) synthesizing levan with β -(2 \rightarrow 6) linkages and inulosucrases (EC 2.4.1.9) synthesizing inulin with β -(2 \rightarrow 1) linkages in the main chain [6]. Microbial levansucrases have a molecular weight in a range of 46-120 kDa [7,8,9,10]. These enzymes catalyze hydrolysis of sucrose in the presence of water as an acceptor (hydrolase activity) and also a transfer of fructosyl residues to different acceptors (transferase activity). When a growing levan chain is used as an acceptor of β -D-fructosyl residues, levan with β -(2 \rightarrow 6) linkages is synthesized. FTF can catalyze fructose transfer from both sucrose and raffinose to variable acceptors. In presence of different monosaccharides, disaccharides and oligosaccharides as acceptors the transferase activity of levansucrase leads to synthesis of fructo-oligosaccharides [11]. The nature of the enzyme,

the sucrose concentration, the type and concentration of acceptors, the temperature and pH of the reaction influence the amount and molecular masses of the synthesized oligosaccharides [8,12,13]. In the case of transfructosylation reaction levansucrases enzyme can use different sugar acceptor molecules such as maltose, lactose, cellobiose, melibiose, isomaltose, D-galactose, D-fructose, and D-xylose, which leads to the synthesis of fructo-oligosaccharides [11]. Currently commercial available FOSs for human consumption are exclusively inulin-type prebiotics with α -(2-1)-linkages. However, the levan-type-FOSs, with α -(2-6)-linked fructose and some α -(2-1)-linked branching, have demonstrated prebiotic effects, in vitro, that surpass inulin-type FOSs [14]. The functional health attributes of prebiotic FOSs are dependent on their chemical structures, in particular the type of hexose moieties, the extent of polymerization and the glycosidic linkages. That's why it is important to characterize new enzymes, for production of fructo-oligosaccharides with different structure and biological activity. The nature of the enzyme, the sucrose concentration, the type and concentration of acceptors, the temperature and pH of the reaction are important characteristic that affect the amount and the structure of the synthesized oligosaccharides [8,12,13].

* To whom all correspondence should be sent:
E-mail: ilievini@abv.bg

In a previous study, we showed that *L. mesenteroides* Lm 17 strain, isolated from fermented cabbage, produces a glucosyltransferase of about 180 kDa and two FTFs with molecular masses about 120 kDa and 86 kDa [15].

The aim of this study was to optimize the transferase reaction of levansucrase from *L. mesenteroides* Lm 17 strain expressed in *E. coli*. The selected enzyme was characterized in terms of the effect of different substrates on its transferase activity, determining the Michaelis constant for different substrates and possible inhibition constant by glucose and fructose. These results will give information for industrial application of levansucrase for the production of novel prebiotic fructo-oligosaccharides.

EXPERIMENTAL

Preparation of a cell free extract and purification of the recombinant levansucrase L17

E. coli BL21(DE3) cells were collected by centrifugation (9,000 rpm, 15 min, 4°C) and washed two times with 20 mM sodium acetate buffer (pH 7.5). The cells were resuspended in a cold sonication buffer containing 20 mM sodium acetate buffer (pH 7.5), 300 mM NaCl, 5 mM imidazole and 5 mM β -mercaptoethanol and then were sonicated (Hielscher Ultrasound Technology UP50H, Germany). The cell debris was separated by centrifugation (9,000 rpm, 15 min, 4°C) and the supernatant was used as a cell free extract. Recombinant enzyme was purified using His Trap FF 5 ml Ni Sepharose Fast Flow column (GE Healthcare). The column was equilibrated with binding buffer (20 mM sodium acetate buffer (pH 7.5), 0.5 M NaCl, 30 mM imidazole) and then the cell free extract was added to the column. To remove the unbound proteins, the column was washed with three volumes of the same buffer. Then the bound His-tagged protein was separated from Ni Sepharose column by elution buffer (binding buffer with 500 mM imidazole). The eluted fraction was concentrated 10-fold using 10,000 MW cut off concentrators (Sartorius) and dialyzed against 20 mM sodium acetate buffer (pH 5.5).

Levansucrase assays and protein determination

One unit of levansucrase activity is defined as the amount of enzyme that catalyzes the formation of 1 μ mol glucose per minute at 30°C in 20 mM sodium acetate buffer (pH 5.5); 0.05 g/l CaCl and

100 g/l of sucrose. Levansucrase activity was determined by measuring the amount of reducing sugars derived from sucrose by the 3,5-dinitrosalicylic acid method (DNS) [16]. For determination of the specific enzyme activity, proteins were assayed by the method of Bradford [17], using bovine serum albumin as a standard. The transferase activity of the purified levansucrase was determined as a difference between the amount of released glucose from sucrose (total activity) and the amount of measured fructose (hydrolytic activity) in the presence of 100 g/l of sucrose. D-glucose and D-fructose were measured enzymatically with hexokinase, glucose-6P dehydrogenase and phospho-glucose isomerase (K-FRUGL kit from Megazyme). All measurements were performed at least in triplicate and average values are given.

Kinetic studies of recombinant levansucrase L17

The kinetics parameters were determined at 35°C in the presence of 20 mM sodium acetate buffer, pH 5.5, 0.05 g/l CaCl₂ and sucrose concentrations ranging from 20 to 1000 mM. All measurements were performed in triplicate and the received data were processed using SigmaPlot 12.0 (Systat Software Inc.). Km and Vmax were determined by nonlinear regression approach according and Lineweaver-Burk equation.

Determination of acceptor specificity of recombinant levansucrase and optimization the reaction conditions for fructooligosaccharides synthesis

To study the acceptor specificity of purified levansucrase various sugar acceptors (fructose, arabinose, maltose, lactose, lactulose, raffinose, fructooligosaccharides and galactooligosaccharides) were tested. The enzymatic synthesis in the presence of sucrose as fructosyl donor and various sugar acceptor molecules was carried out at 35 °C in 20 mM sodium acetate buffer, pH 5.5, containing 0.05 g/l CaCl₂ and 0.5 U/ml purified levansucrase. The reaction volume was 50 ml. Samples were taken at different time points (6 h, 12 h, 24 h, 48 h). In order to optimize the reaction conditions for synthesis of fructooligosaccharides different concentrations of sucrose and acceptors-maltose, lactose, raffinose were tested. To evaluate the influence of enzyme concentration on the reaction conditions and the amount of the synthesized products, synthesis reactions were carried out using 0.5 U/ml, 1 U/ml and 2 U/ml purified levansucrase.

HPLC-analysis of fructooligosaccharides

Separation of oligosaccharides was achieved by using a CarboPac PA1 anion-exchange column (250 mmx64 mm; Dionex) coupled to a CarboPac1 Guard column (Dionex). The following gradient was used: eluent A at 100% (0 min), 70% (10 min), 60% (25 min), 10%.

(80 min), 0% (83 min), 100% (91 min). Eluent A was 0,1 M sodium hydroxide, and eluent B was 0,1 M sodium hydroxide in 0,6 M sodium acetate. Detection was performed with an ED40 electrochemical detector (Dionex), with an Au working electrode, and an Ag.

AgCl reference electrode. The amount of sucrose utilized during the reaction reflected the total enzyme activity. The amount of fructose synthesized reflected the hydrolytic enzyme activity. The total activity minus the hydrolytic activity reflected the transglycosylation enzyme activity (polymer and fructooligosaccharide formation). Based on these data, the hydrolysis versus transglycosylation ratio (end-point conversion) was calculated.

RESULTS AND DISCUSSION

Effect of sucrose/enzyme ratio on the levan and fructooligosaccharides production

In a previous study, we showed that the synthesized polymer from recombinant levansucrase from *L. mesenteroides* Lm 17 is levan [18]. Using different concentrations of levansucrase, 0,5 U/ml, 1 U/ml and 2 U/ml, a study on the influence of enzyme concentration on polysaccharide and oligosaccharide synthesis from 10 % sucrose was carried out at 35°C in 20 mM sodium acetate buffer, pH 5.5, containing 0.05 g/l CaCl₂ (Table 1). The highest amount of the reaction products were established when the enzyme activity in the reaction mixture is 1 U/ml. Interestingly, increasing levansucrase activity to 2 U/ml didn't led to higher concentration of the products. At the 6th hour of the start of the enzyme reaction, maximum sucrose is hydrolyzed using 2U/ml levansucrase (86.2%), which is three times the hydrolysed sucrose using 0.5 U/ml levansucrase. From previous studies is known that glucose has inhibitory effect on hydrolysis and transfructosylation reactions of levansucrase [19]. Table 1 indicates that accumulation of higher amounts of glucose at the early stages of the enzyme reaction inhibits processes for polysaccharide and FOS synthesis. In all reactions

with varying enzyme activities the whole amount of sucrose is hydrolyzed at 12th hour, and hydrolysis of the substrate proceed faster with increasing the levansucrase activity in the reaction mixtures.

Table 1. Profile of the products synthesized by levansucrase L17 at different in presence of 10% sucrose.

Time (h)	Levansucrase activity (U/ml)	Consumed sucrose (%)	F _{POL}	F _{FOS}
3	0.5	2.5	14.9	0.0
	1.0	24.7	60.1	6.2
	2.0	62.4	47.8	1.4
6	0.5	22.7	22.7	0.0
	1.0	61.4	63.1	4.2
	2.0	86.2	54.9	2.0
12	0.5	100	62.3	3.2
	1.0	100	92.8	2.3
	2.0	100	65.8	1.7
24	0.5	100	69.6	3.3
	1.0	100	97.2	2.8
	2.0	100	73.6	2.5

Synthesis of oligosaccharides was observed at the early hours (3th hour) from the beginning of the reaction, when 1 U/ml and 2 U/ml enzyme was used. The results on Table 1 indicate that transfructosylation reaction for production of levan was favored after 6th hour of the beginning, and the hydrolysis reaction was not significant over the same period of the enzyme reaction. These results represent a very important characteristic of the studied recombinant levansucrase with regards to its high transferase to hydrolase ratio. It was reported that production of FOS by FTFs is competitively inhibited by glucose which is formed as a by-product in transfer reaction [20]. We tested the influence of glucose on (277,5 mM) on levansucrase activity. In presence of 277,5 mM and 292 mM sucrose recombinant levansucrase Lm17 shows 23 % of inhibition when 0,5 U/ml enzyme is used and 16 % - when 1 U/ml enzyme is used (Fig. 1). The received results confirmed that the lower amount of levan and FOS formed by levansucrase at 2 U/ml enzyme activity is due to the product inhibition. The higher enzyme activity leads to accumulation of higher amounts of glucose at the earlier stages of the reaction, and cause partial enzyme inhibition. Steinberg et al., 2004 demonstrated inhibitory dose-dependent effect of glucose on FTF activity from *S. mutans* V-1995, as the authors observed 75% inhibition and less fructan production at 160 mM concentration of glucose in the reaction mixture [21]. Product inhibition by fructose has also been reported for glucansucrases synthesizing glucans from sucrose [22, 23].

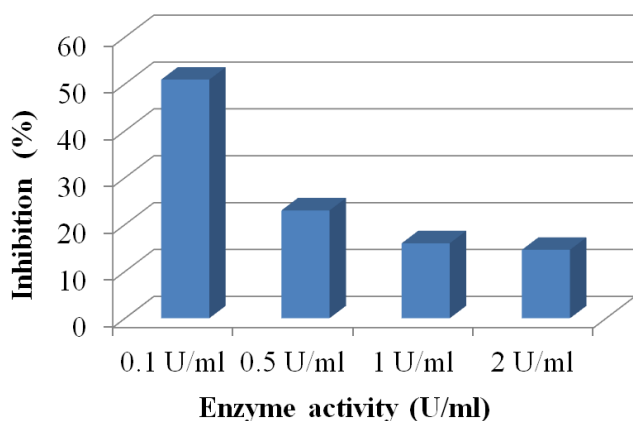


Fig. 1. Inhibition of levansucrase activity (%) by the released glucose.

Acceptor specificity of recombinant levansucrase Lm17

To investigate the donor/acceptor specificity (D/A) of levansucrase from *L. mesenteroides* Lm17 expressed in *E. coli* BL21(DE3), transfructosylation reactions were conducted by using sucrose as a donor of fructose units and fructose, arabinose, maltose, lactose, lactulose, raffinose, fructo-oligosaccharides or galacto-oligosaccharides as acceptors. Synthesis of oligosaccharides was detected only with maltose, lactose, fructo-oligosaccharides and galacto-oligosaccharides as acceptors (Table 2).

Table 2. Acceptor specificity of levansucrase L17.

Sugar acceptors	Synthesis of FOSs
Arabinose	-
Fructose	-
Maltose	+
Lactose	+
Lactulose	-
Raffinose	-
FOSs	+
Galacto-oligosaccharides	+

In the presence of fructose, arabinose, lactulose and raffinose, oligosaccharides were not detected. As a best acceptor for oligosaccharide production from recombinant levansucrase Lm17 was determined to be maltose, which is known to be the best acceptor for the action of dextransucrase enzymes [23]. The highest total amount of synthesized FOS – 20.4% was determined at 12th hour.

Table 2 indicate that the catalytic efficiency of the transfructosylation activity of the studied recombinant levansucrase is dominant after 6 hours of reaction.

Ratio between hydrolysatation and transfructosylation activity of levansucrase Lm17

Equivalent amounts of glucose and fructose from sucrose is released from the hydrolytic activity (Ht) of the levansucrases. The ratio between glucose and fructose, could therefore be used to determine the amount of fructose used for transfructosylation to other sugars, i.e., the transferase activity (Ft). Based on the concentration of released glucose and fructose during the reaction catalyzed by levansucrase L17, was determined the ratio between transferase and hydrolase activity of the enzyme. As is shown on a Fig. 2, during enzyme reaction the transferase activity of of levansucrase L17 was predominant as in the presence only of substrate sucrose (10%), thus in the presence of acceptor maltose (5%). In the presence of 10% sucrose the highest transferase activity was observed at 12th hour, and after that decreases until 48th h.

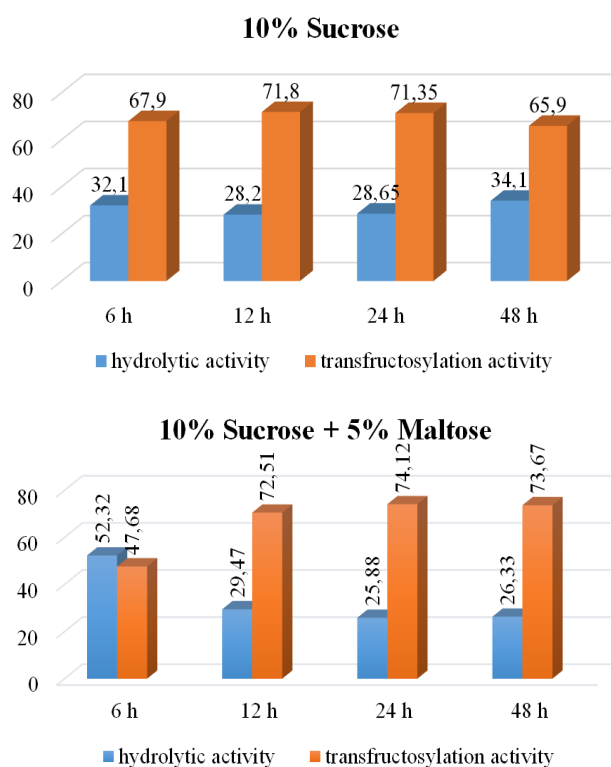


Fig. 2. Profile of hydrolase and transferase activity of levansucrase L17 in the presence of sucrose and maltose.

In the presence of acceptor maltose in the reaction mixture the transferase activity of the enzyme increases. The highest transferase activity in presence of 5 % maltose was observed at 24th hour. Different factors affect the ratio between transferase and hydrolase activity of levansucrase -

sucrose concentration, pH and temperature [10,11]. It is known that the formation of low-molecular-mass fructans at the early stages of the reaction affects the ratio between transferase and hydrolase levansucrase activity by directing the fructose units mostly to elongation of the fructan chains instead to water [24].

Determination of kinetic parameters in presence of 10 % sucrose and 5 % maltose

K_m and V_{max} values were determined at concentrations of sucrose ranging from 20 to 1000mM, and calculated from Lineweaver-Burk plots. K_m of the recombinant levan-sucrase Lm17 was 62.96±6.27mM sucrose, and V_{max} value was 6.34±0.14 U/ml (Fig.3).

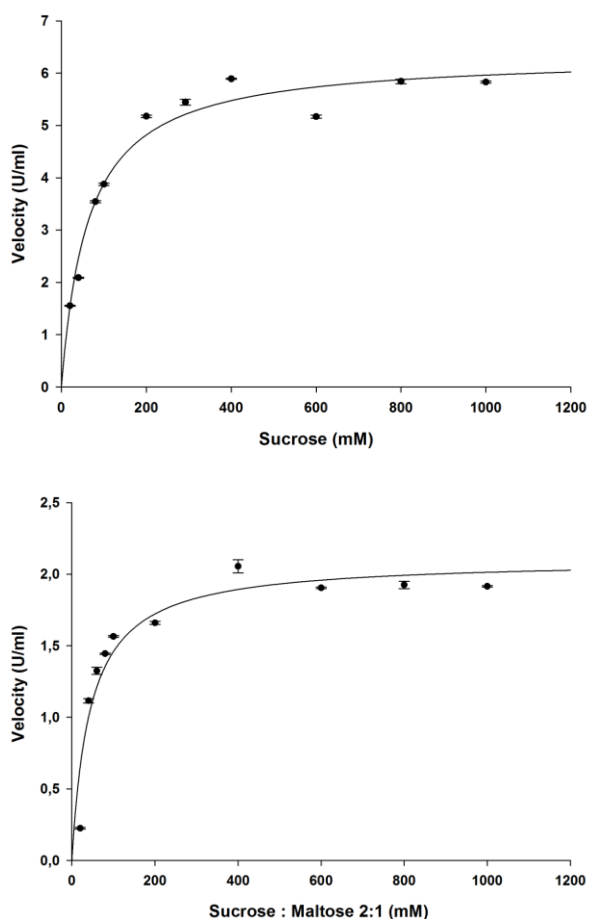


Fig. 3. Kinetics parameters of levansucrase L17 determined in the presence of sucrose and at sucrose/maltose ratio 2:1.

The value of K_m was higher than this one of other recombinant levansucrases: K_m = 36.7±5.4 mM for LevS from *L. mesenteroides* NRRL B-512F [28]; K_m = 27.3 mM for LevC from *L. mesenteroides* ATCC 8293 [25]; K_m = 26.6 mM

for levansucrase M1FT from *L. mesenteroides* B-512FMC [7], and K_m = 14.5±4.2 mM for levansucrase from *Lb. sanfranciscensis* TMW 1.392 [26].

K_m and V_{max} values were determined also in presence of acceptor maltose (D/A = 2 :1). In carrying out the enzymatic reaction in the presence of 10% sucrose and 5% maltose, K_m of recombinant levansucrase Lm17 was 43.99±7.01 mM sucrose, and V_{max} value was 2.1±7.7 U/ml.

CONCLUSION

Selectivity of the reaction of synthesis of FOSs using levansucrase was strongly dependent on the enzyme source, type of acceptors and donor/acceptor ratio. In the present study we first describe that when maltose was the acceptor, the major products was a fructooligosaccharide with DP3 (75,5% of total fructooligosaccharides) identified as an erlose. This investigation of the properties of recombinant levansucrase Lm17 reveals the potential use of the enzyme as tools for synthesis of short chain fructooligosaccharides (erlose) with prebiotic potential.

Acknowledgements: This work was supported by research grant from project no. DM01/7-17.12.2016.

REFERENCES

1. S. K. Malang, N. H. Maina, C. Schwab, M. Tenkanen, Lacroix C, *Food Microbiol.*, **46**, 418 (2015).
2. A. Malik, M. Radji, S. Kralj, L. Dijkhuizen, *FEMS Microbiol. Let.*, **300**, 131 (2009).
3. P. Monsan, S. Bozzonet, C. Albenne, G. Joucla, R. Willemot, M. Remaud-Simeon, *Int Dairy J.*, **11**(9), 675 (2001).
4. M. Tiekling, M. Korakli, M. A. Ehrmann, M. G. Gänzle, R. F. Vogel, *Appl. Environ. Microbiol.*, **69**, 945 (2003).
5. V. Lombard, H. Golaconda Ramulu, E. Drula, P.M. Coutinho, B.Henrissat, *Nucleic Acids. Res.*, **42**, D490 (2014).
6. S. Del Moral, C. Olvera, M.E. Rodriguez, A. Lopez-Munguia, *BMC Biochem.*, **9**, 6 (2008).
7. H.K. Kang, M.Y. Seo, E.S. Seo, D. Kim, S.Y. Chung, A. Kimura, D.F. Day, J.F. Robyt., *Biochim Biophys Acta*, **1727**, 5 (2005).
8. M. Korakli, R. F. Vogel., *Appl. Microbiol. Biotechnol.*, **71**, 790 (2006).

9. S. A. F. T. van Hijum, E. Szalowska, M. J. E. C. van der Maarel, L. Dijkhuizen, *Microbiology*, **150**, 621 (2004).
10. M. L. Velazquez-Hernandez, V. M. Baizabal-Aguirre, A. Bravo-Patino, M. Cajero-Juarez, M. P. Chavez-Moctezuma, J. J. Valdez-Alarcon., *J. Appl. Microbiol.*, **106**, 1763 (2009).
11. S. A. F. T. van Hijum, K. Bonting, M. J. E. C. van der Maarel, L. Dijkhuizen, *FEMS Microbiol. Lett.*, **205**, 323 (2001).
12. S. A. F. T. van Hijum, G. H. van Geel-Schutten, H. Rahaoui, M. J. E. C. van der Maarel, L. Dijkhuizen, *Appl. Environ. Microbiol.*, **68**, 4390 (2002).
13. M. Korakli, M. Pavlovic, M. G. Gänzle, R. F. Vogel, *Appl. Environ. Microbiol.*, **69**, 2073 (2003).
14. S. Bozonnet, M. Dols-Laffargue, E. Fabre, S. Pizzut, M. Remaud-Simeon, P. Monsan, R. M. Willemot., *J. Bacteriology*, **184**, 5753 (2002).
15. T. Vasileva, I. Iliev, M. Amari, V. Bivolarski, M-S. Bounaix, H. Robert, S. Morel, P. Rabier, I. Ivanova, B. Gabriel, C. Fontagné-Faucher, V. Gabriel, *Appl. Biochem. Biotechnol.*, **168**, 718 (2012).
16. G. L. Miller., *Anal. Chem.*, **31**, 426 (1959).
17. M. M. Bradford, *Anal. Biochem.*, **72**, 248 (1976).
18. I. Iliev, T. Vasileva, V. Bivolarski, A. Salim, S. Morel, V. Gabriel, *Biotechnol. Biotech. Equip.*, in press (2017).
19. W. Li, Sh. Yu, T. Zang, B. Jiang, W. Mu, *Appl. Microbiol. Biotechnol.*, **99**, 6959 (2015).
20. J. Y. Jung, S. H. Lee, S. Lee, C. O. Jeon., *J. Bacteriol.*, **194**, 730 (2012).
21. D. Steinberg, M. Feldman, I. Ofek, and E. J. Weiss, *Antimicrob. Chemotherapy*, **54**, 86, (2004).
22. F. Tian, L. Inthanavong, S. Karboune, *Biosci. Biotechnol. Biochem.*, **75**, 1929 (2011).
23. I. Iliev, T. Vasileva, C. Ignatova, I. Ivanova, T. Haertle, P. Monsan, J-M. Chobert, *J. Appl. Microbiol.*, **104**, 243 (2008).
24. S. A. F. T. van Hijum, S. Kralj, L. K. Ozimek, L. Dijkhuizen, G. H. van Geel-Schutten, *Microbiol. Mol. Biol. Rev.*, **70**, 157 (2006).
25. C. Olvera, S. Centeno-Leija, A. Lopez-Munguia, *Antonie van Leeuwenhoek*, **92**, 11 (2007).
26. M. Tiekling, M. A. Ehrmann, R. F. Vogel, M. G. Gänzle, *Appl. Microbiol. Biotechnol.*, **66**, 655 (2005).

ЕНЗИМЕН СИНТЕЗ НА ФРУКТО-ОЛИГОЗАХАРИДИ С ПОМОЩТА НА РЕКОМБИНАНТНА ЛЕВАНЗАХАРАЗА ОТ *LEUCONOSTOC MESENEROIDES* Lm17

А. С. Салим, В. П. Биволарски, Т. А. Василева, И. Н. Илиев*

Катедра „Биохимия и микробиология“, Биологически факултет, ПУ „Паисий Хилендарски“, ул. „Цар Асен, № 24, Пловдив, България

Постъпила на 01 май 2017 г.; Коригирана на 23 юни 2017 г.

(Резюме)

Ензимът леванзахараза [EC2.4.1.10] трансферира фруктозилни остатъци от молекулата на захарозата към различни акцептори (малтоза, лактоза) и се получава добър добив на олигозахариди, които биха имали пребиотичен потенциал. Селективният характер на реакцията за синтез на фруктоолигозахариди (ФОЗ) с помощта на леванзахараза зависи строго от произхода на ензима, вида на акцепторите и съотношението донор/акцептор (Д/А). При изследване специфичността на акцепторите се определи възможността на леванзахараза Lm 17 да синтезира ФОЗ с различни структури при използване на различни акцептори. В настоящото изследване за първи път описахме, че при използване на малтозата като акцептор, основният фруктоолигозахарид, който се получава е със степен на полимеризация 3 (СПЗ) (75,5% от totalното количество синтезирани ФОЗ), идентифициран като ерлоза. Леванзахаразата беше с висока трансфруктозилазна отколкото хидролазна активност. При провеждане на ензимната реакция в присъствие на 10% захароза и 5% малтоза, Km на рекомбинантната леванзахараза Lm17 е 43.99 ± 7.01 mM захароза, и Vmax е 2.1 ± 7.7 U/ml. Това проучване на свойствата на леванзахараза Lm17 разкри потенциала на използване на ензима за синтез на късоверижни ФОЗ (ерлоза) с пребиотичен потенциал.

Influence of ethylene glycol on the hydrolysis-condensation behavior of Ti(IV) butoxide

St. I. Yordanov¹, A. D. Bachvarova-Nedelcheva^{2*}, R. S. Iordanova²

¹ Institute of Metal Science, equipment, and technologies "Acad. A. Balevski" with Center for Hydro- and Aerodynamics at the Bulgarian Academy of Sciences, 67 "Shipchenski prohod" str., 1574 Sofia, Bulgaria

² Institute of General and Inorganic Chemistry, Bulgarian Academy of Sciences, "Acad. G. Bonchev", bl. 11, 1113 Sofia, Bulgaria

Received April 28, 2017; Revised June 06, 2017

Dedicated to Acad. Ivan Juchnovski on the occasion of his 80th birthday

This study is aiming to verify the influence of ethylene glycol (EG) on the degree of hydrolysis – condensation reactions during the sol – gel processing and obtaining of pure titania gels. Two homogeneous gels were obtained using titanium (IV) butoxide with and without addition of EG and presence only of air moisture. By XRD was established that the gel prepared without addition of EG (TBT) is amorphous up to 300 °C while the other one (TBT/EG) is amorphous even at 400 °C. It is found that TiO₂ (anatase) is a dominating crystalline phase during the heating up to 600 °C while at 700 °C, TiO₂ (rutile) appeared. The IR and UV-Vis analyses revealed a completeness of hydrolysis – condensation reactions in the TBT/EG in comparison to pure TBT gel. The UV-Vis spectra of TBT/EG gel exhibited a red shift of the cut-off compared to pure TBT one.

Key words: sol-gel; phase transformations; IR spectra; UV-Vis spectra

INTRODUCTION

The sol–gel derived titanium dioxide nanoparticles are of great interest for many applications. Among different precursors the Ti(IV) n-butoxide is widely used for nanopowders (nanowires, nanotubes, etc.) and films preparation [1, 2]. It is well known that the chemistry of sol–gel process is mainly based on hydrolysis and polycondensation reactions leading to formation of a polymerized oxide network. The systematically studies during the last 20 years aimed to examine the processing parameters that control the degree of hydrolysis – condensation reactions. Some excellent reviews are devoted to this topic [3-6]. The high reactivity of metal alkoxides towards water leads to complex hydrolysis and polymerization reactions. Generally, the hydrolysis reaction is influenced by a number of factors such as nature of the alkyl (R) group, the nature of the solvent, the concentration of the species present in solution, the water to alkoxide molar ratio and the temperature [7,8,9]. Depending on the chemical conditions, very different structures can be obtained ranging from colloidal particles to precipitation or gels. The mechanisms of these reactions have been extensively studied in the case of silicon alkoxides, whereas much less data are available for transition

– metal oxide precursors [10]. It was found that the titania sol–gel process follows essentially a different pathway than the silicon based one [1]. According to Brinker and Sherer [11] the metal alkoxides, especially those of the early transition metals (Ti, Zr) possess lower electronegativity that causes them lower stability toward hydrolysis and condensation. The greater reactivity of these alkoxides requires that they be processed with stricter control of moisture and conditions of hydrolysis in order to prepare homogeneous gels rather than precipitates. The above mentioned is the main reason for the fundamental studies of hydrolysis and condensation of transition metal alkoxides [1,11-13].

Our team has experience on the sol-gel obtaining of powders in different binary and multicomponent systems where Ti(IV) butoxide is used as a main precursor [14-17]. During the structural characterization of these samples some questions arose related to the completeness of the hydrolysis-condensation processes and their dependence on the nature of the dissolvent and temperature. This motivated our research in this direction.

The present paper aiming to verify the influence of ethylene glycol (EG) on the hydrolysis - condensation behavior of Ti(IV) n-butoxide during the sol – gel process and obtaining of pure titania powders. Moreover, the experiments have been

* To whom all correspondence should be sent:
E-mail: albenadb@svr.igic.bas.bg

performed without addition of water in order to prevent the non – equilibrium fast hydrolysis of Ti butoxide. A comparison of the phase formation and short range order of the obtained gels and powders is made as well.

EXPERIMENTAL

Preparation of the gels

Two gels were prepared using Ti(IV) n - butoxide without direct addition of water and the sol-gel hydrolysis reaction was accomplished only in presence of air moisture. One of the gels was obtained without usage of ethylene glycol (EG) as a dissolvent while the other one was prepared by dissolving the Ti butoxide in EG (in 1:1 molar ratio), denoted as TBT and TBT/EG, respectively. According to the literature data [18,19], the using of diols as solvents is preferable due to their ability to modify the metal alkoxides and to act as chelating ligands forming bridges with other alkoxide groups. By this way, the obtained solutions become sufficiently stable. The pH of as-prepared solutions was measured 4-5. The aging of TBT and TBT/EG gels was performed in air for several days in order to allow further hydrolysis. After that they were subjected to the stepwise heating in air up to 700 °C for one hour exposure time for each temperature. In the temperature range 150-200 °C the bulk samples are broken into small pieces during the drying. Further increasing of temperatures (300-700 °C) was important to verify the phase transformations of the gels.

Samples characterization

Powder XRD patterns were registered at room temperature with a Bruker D8 Advance diffractometer using Cu-K α radiation. The infrared spectra were registered in the range 1600-400 cm $^{-1}$ using the KBr pellet technique on a Nicolet-320 FTIR spectrometer with 64 scans and a resolution of ± 1 cm $^{-1}$. The optical absorption spectra of the powdered samples in the wavelength range 200–1000 nm were recorded by a UV–Vis diffused reflectance spectrophotometer "Evolution 300" using a magnesium oxide reflectance standard as the baseline.

RESULTS AND DISCUSSION

Phase transformations

Transparent and monolithic gels were obtained. The XRD patterns of samples heat treated in the temperature range 200-700 °C are shown in Fig. 1.

As it is seen in both samples (TBT and TBT/EG) the amorphous phase is dominant up to 300 °C. At 400 °C in the XRD pattern of TBT first crystals of TiO $_2$ (anatase) (JCPDS 78-2486) are registered, while the TBT/EG sample is still amorphous due to the higher amount of organics as a result of the addition of EG. Thus, the presence of organic groups from the dissolvent led to stabilization of the amorphous state at higher temperatures. In the temperature range 500-600 °C powders containing only crystalline TiO $_2$ (anatase) are observed. The increasing of temperature (700 °C) led to the appearance of TiO $_2$ (rutile) (JCPDS 21-1276). It is worth noting that in the XRD pattern of sample TBT/EG the anatase to rutile phase transformation is more completed (Fig. 1). At 500 °C the average crystallite size (calculated using Sherrer's equation) of TiO $_2$ (anatase) in the TBT and TBT/EG samples is 12 and 5 nm, respectively (Fig. 1). At higher temperature (600 °C) the crystallite size increased and it is about 16 nm in both samples.

UV - Vis spectroscopy

The UV-Vis spectroscopy is applied in order to obtain information for the completeness of the hydrolysis – condensation reactions. The diffuse reflectance absorption spectra of both gels (aged at room temperature) and heated at 200 °C are shown in Fig. 2.

As one can see from the figure, the UV-Vis spectra of TBT and TBT/EG gels are characterized by two bands 240-250 nm and 320-340 nm. It is known, that the main building units in the unhydrolyzed Ti butoxide are isolated TiO $_4$ groups with absorption band in the region 240-260 nm. As a result of the polymerization processes TiO $_4$ groups are transformed into TiO $_6$ units possessing absorption about 320-340 nm [20-22]. Looking at our spectra some differences could be distinguished. It is obvious that in the spectra of TBT/EG gel the band at 320-340 nm is more intensive as compared to 240-250 nm. That is associated with an increase of the polymerization degree of Ti atoms in comparison to pure TBT gel. This experimental fact could be explained by the presence of ethylene glycol. The heating at 200 °C led to the further transformation of TiO $_4$ to TiO $_6$ units and higher degree of polymerization processes, respectively. The other difference is the shifting toward higher wavelengths (340 nm) in the spectra of heated at 200 °C TBT and TBT/EG samples that could be related with the increasing number of reaction intermediates.

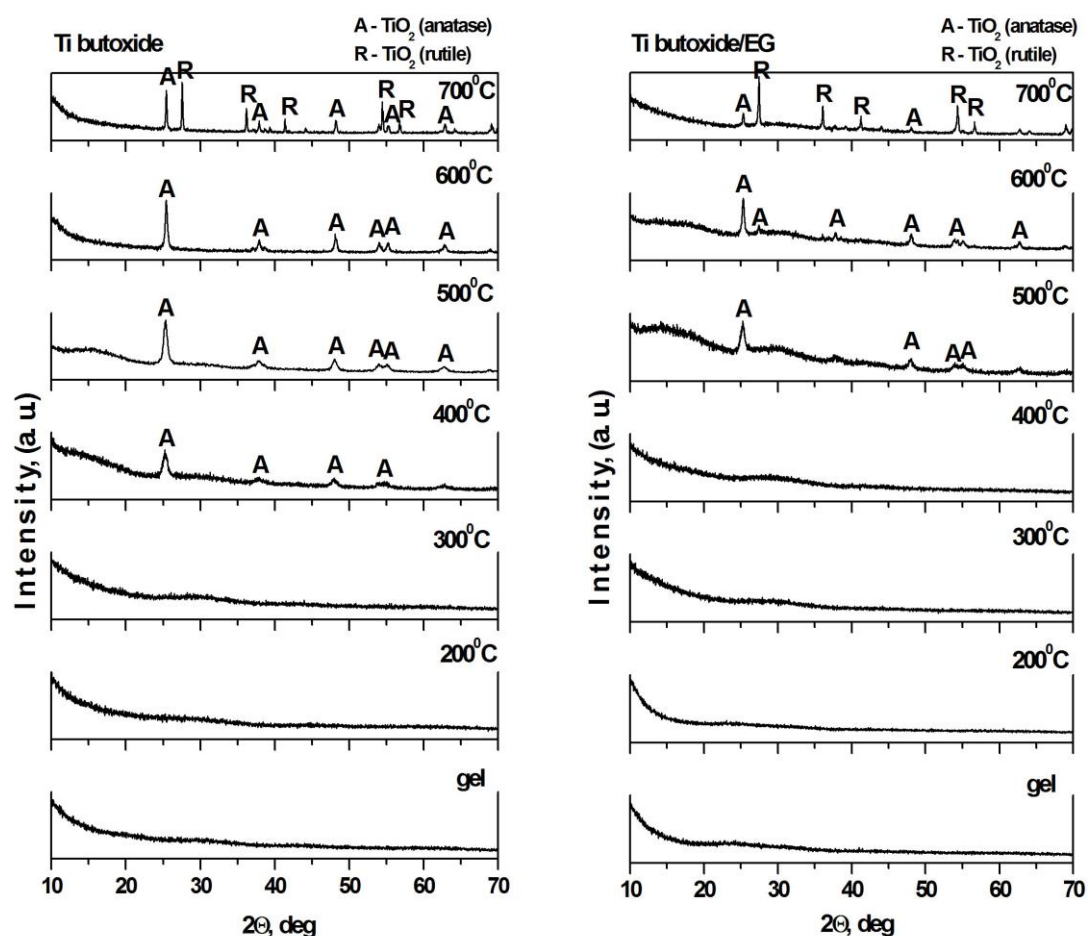


Fig. 1. XRD patterns of Ti (IV) n-butoxide (TBT) and Ti (IV) n-butoxide dissolved in EG (1:1) (TBT/EG) at different temperatures: (A) TiO₂-anatase, (R) TiO₂-rutile).

IR spectroscopy

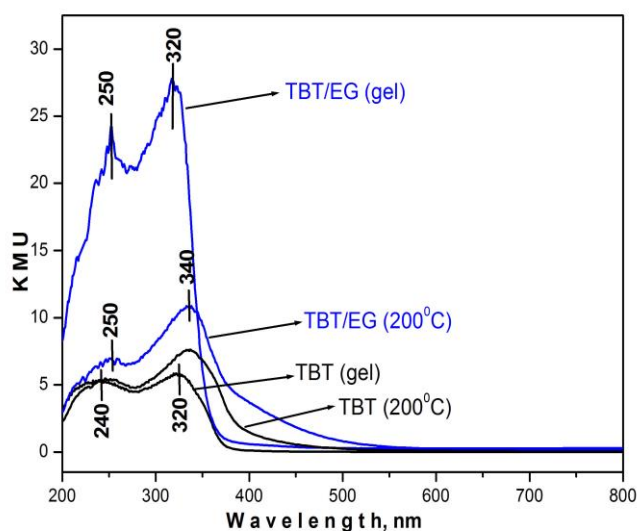


Fig. 2. UV-Vis spectra of TBT and TBT/EG: gels and heat treated at 200 °C.

The IR spectroscopy is used for monitoring the rate and degree of hydrolysis and condensation process as well as the phase transformations in the gels during the heat treatment (in the temperature range 200-500 °C). The obtained by us IR spectra of TBT and TBT/EG are shown in Fig. 3a,b. The assignments of the vibrational bands of separate structural units are made on the basis of well-known spectral data for the precursors (Ti(IV) n-butoxide), ethylene glycol (solvent), n-butanol (product of the hydrolysis-condensation reaction), crystalline TiO₂ (anatase) and TiO₂ (rutile). According to the literature data [23-25] pure Ti(IV) n-butoxide precursor is characterized by bands located between 1500-1300 cm⁻¹ assigned to the bending vibrations of CH₃ and CH₂ groups. The band at 1130 cm⁻¹ is characteristic for the stretching vibrations of Ti-O-C, while those at 1100 and 1040 cm⁻¹ are assigned to the vibrations of terminal and

bridging C-O bonds in butoxy ligands. Broad absorption bands below 1000 cm^{-1} correspond to C-H, C-O and deformation Ti-O-C vibrations [23, 26]. The ethylene glycol possesses asymmetric and symmetric stretching vibrations of C-O bonds in $\text{CH}_2\text{-OH}$ groups at 1090 and 1040 cm^{-1} while in the spectrum of butanol they appeared at 1110 , 1050 cm^{-1} along with a very intensive band at 1070 cm^{-1} [27,28]. The IR spectrum of TiO_2 (anatase) is characterized by bands at $620 - 610$ and $480 - 470\text{ cm}^{-1}$ [29,30] connected with the vibrations of TiO_6 units. As supporting information, the measured by us spectra of ethylene glycol and 1-butanol, are presented in Fig. 4.

Obviously, the absorption region $1100 - 1020\text{ cm}^{-1}$ is very complex due to the overlapping of the vibrations of different structural units from Ti(IV) butoxide, EG and n-butanol. Irrespective of the existing spectral restrictions several authors [23, 24] use these bands for the interpretation of hydrolysis-condensation processes. Looking at the IR spectra of obtained by us TBT and TBT/EG gels (25 °C) (Fig. 3a,b) a difference could be seen regarding the intensity of a band centered at $1130\text{-}1120\text{ cm}^{-1}$. In the TBT spectrum this band is well defined at 1130 cm^{-1} , due to the uncompleted hydrolysis reaction. In the TBT/EG spectrum it is

transformed into a shoulder and shifted to 1120 cm^{-1} may be as a result of breaking of the Ti-O-C linkage. Another important band is that at 1100 cm^{-1} in TBT which is shifted to 1080 cm^{-1} in TBT/EG and its intensity increases as a result of the separation of butanol due to the greater degree of hydrolysis-condensation reactions. Additional confirmation for this suggestion is the decrease of bands intensity in the range $640 - 610\text{ cm}^{-1}$ (Fig. 4) which is a characteristic feature of n-butanol. There is also a broad band in the IR spectrum of TBT at 790 cm^{-1} that could be connected to the vibrations of butoxy groups. But this band is negligible in the spectrum of TBT/EG.

Heating of the gels up to 250 °C (Fig. 3) led to a strong decreasing of the bands in the range $1500 - 1300\text{ cm}^{-1}$ that are typical for the vibrations of CH_2 and CH_3 groups. A decrease in the bands intensity at 1120 , 1080 and 1040 cm^{-1} as a consequence of decreasing of the number of non-hydrolyzed butoxy groups is also observed (Fig. 3). The spectra above 300 °C showed two strong bands near 620 and 480 cm^{-1} that are typical for the vibrations of TiO_6 building units (Fig. 3) [27,28].

It has to be mentioned that at 500 °C the IR spectra of both samples exhibited bands in the

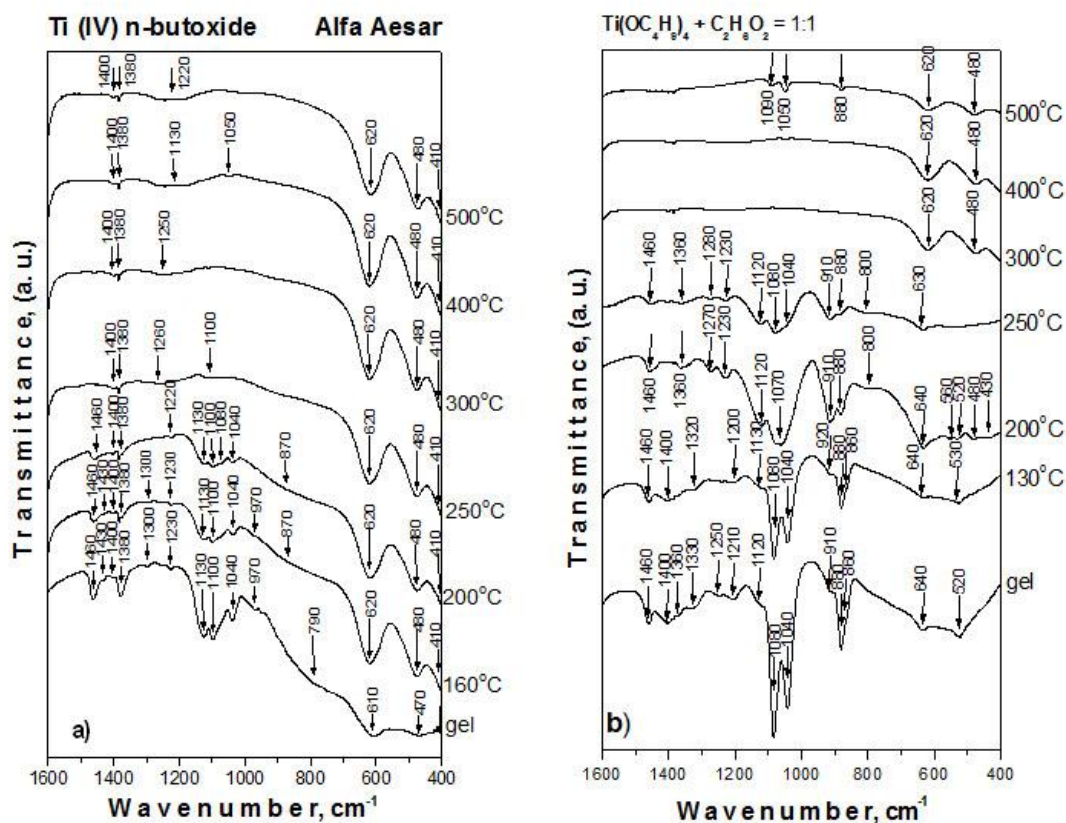


Fig. 3. IR spectra of TBT and TBT/EG: gels and heat treated up to 500 °C .

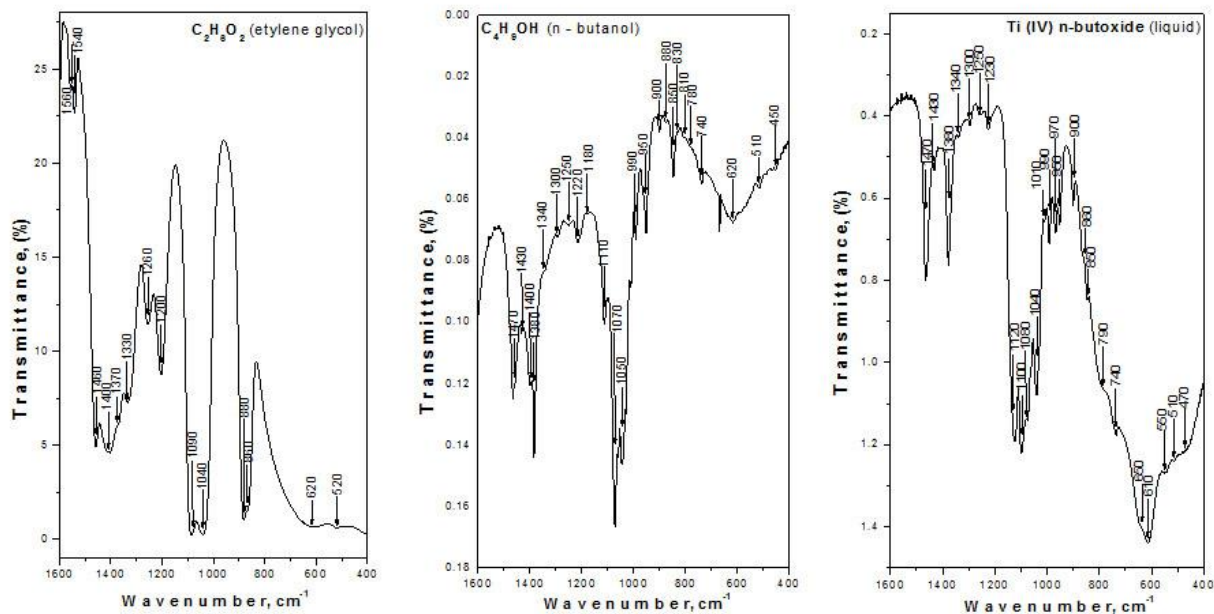


Fig. 4. IR spectra of the used precursors: a) EG, b) n-butanol and c) Ti (IV) n-butoxide.

ranges 1400 - 1220 cm^{-1} and 1090 - 1050 cm^{-1} that could be related to the presence of residual carbon, participating in different organic groups. In our previous investigations [20, 21], by DTA analysis it was established that the carbon exist in the samples even above 500 °C

Analysis of the results

Generally, in our experiments we did not introduce water in order to prevent the non – equilibrium fast hydrolysis of Ti butoxide as well as to avoid obtaining of inhomogeneous gels. Transparent, homogeneous and monolithic TBT and TBT/EG gels have been prepared at presence only of air moisture. From the obtained results is seen that the hydrolysis-condensation processes in both cases are not completed at room temperature and continue in a wide temperature range along with the decomposition of the organic groups. The discussion on the completeness of hydrolysis-condensation processes and transformation of the amorphous gels into nano-crystalline TiO_2 powders is made bearing in mind the changes in the intensity along with shifting of the IR bands (1120, 1080 and 1020 cm^{-1}) as well as the UV-Vis bands (250 and 320 nm). The strong IR band at 1080 cm^{-1} (due to separation of n-butanol) in the TBT/EG indicates fuller hydrolysis. The stronger intensity of UV – Vis band about 320-340 nm as compared to 240-250 nm is a proof for transformation of TiO_4 to TiO_6 units. This is observed in the UV-Vis spectra of TBT/EG gel

and heated at 200 °C sample, which suggest a higher degree of polymerization processes. Obviously, in presence of EG a higher degree of hydrolysis - condensation reactions is achieved.

CONCLUSION

Two homogeneous titania gels obtained with and without addition of EG in presence only of air moisture are prepared. It was established that ethylene glycol preserved the mixed organic-inorganic amorphous structure at higher temperature (400 °C). The spectral analyses revealed a completeness of hydrolysis – condensation reactions in the TBT/EG in comparison to pure TBT gel. A more completed conversion of TiO_2 (anatase) to rutile is registered at 700 °C in the TBT/EG sample.

Acknowledgements: The authors are grateful to the financial support of Bulgarian National Science Fund at the Ministry of Education and Science, Contract No DN07/2 14.12.2016.

REFERENCES

1. M. Gotic, M. Ivanda, A. Sekulic, S. Music, S. Popovic, A. Turkovic, K. Furic, *Mater. Lett.*, **28**, 225 (1996).
2. M. Kumar, S. Badrinarayanan, M. Sastry, *Thin Solid Films*, **358**, 122 (2000).

- X. Chen, S. Mao, *Chem. Rev.*, **107** (7), 2891(2007).
- D. P. Macwan, P. N. Dave, S. Chaturvedi, *J. Mater. Sci.*, **46**, 3669 (2011).
- M. M. Byranvand, A. N. Kharat, L. Fatholahi, Z. M. Beiranvand, *J. Nanostr.*, **3**, 1(2013).
- M. S. Gupta, M. Tripathi, *Chinese Sci. Bull.*, **56** (16) 1639 (2011).
- K. Yu, J. Zhao, Y. Guo, X. Ding, H. Bala, Y. Liu, Z. Wang, *Mater. Lett.*, **59**, 2515 (2005).
- B. Buyuktas, *Trans. Met. Chem.*, **31**, 786 (2006).
- M. E. Simonsen, E. G. Sogaard, *J. Sol-Gel Sci. Technol.*, **53**, 485 (2010).
- S. Cristoni, L. Armelao, S. Gross, E. Tondello, P. Traldi, *Rapid Commun. Mass Spectrom.* **14**, 662 (2000).
- C. J. Brinker, G. W. Sherer, *Sol-Gel Science*, Academic Press (1990).
- S. Sakka, *J. Sol-Gel Sci. Technol.*, **3**, 369 (1994).
- P. Karasinski, *Optica Applicanta*, **XXXV** (1) 1 (2005).
- A. Shalaby, Y. Dimitriev, R. Iordanova, A. Bachvarova-Nedelcheva and Tz. Iliev, *J. Univ. Chem. Technol. Metall.*, **46**, 137 (2011).
- A. Stoyanova, Y. Dimitriev, A. Shalaby, A. Bachvarova-Nedelcheva, R. Iordanova, M. Sredkova, *J. Optoelect. Biomed. Mater.*, **3**, 24 (2011).
- A. Stoyanova, A. Bachvarova-Nedelcheva, R. Iordanova, N. Ivanova, H. Hitkova, M. Sredkova, *Digest J. Nanomater. Biostr.*, **7**, 777 (2012).
- A. Bachvarova-Nedelcheva, R. Gegova, A. Stoyanova, R. Iordanova, V. E. Copcia, N. Ivanova, I. Sandu, *Bulg. Chem. Commun.*, **46**, 585 (2014).
- M. Gonzales, A. Wu, P. Vilarinho, *Chem. Mater.*, **18** 1737 (2006).
- C. Livage, A. Safari, L. Klein, *J. Sol-Gel Sci. Technol.*, **2**, 605 (1994).
- R. Iordanova, R. Gegova, A. Bachvarova-Nedelcheva, Y. Dimitriev, *Phys. Chem. Glasses: Eur. J. Glass Sci. Technol. B*, **56**, 128 (2015)
- R. Iordanova, A. Bachvarova-Nedelcheva, R. Gegova, Y. Dimitriev, *J. Sol-Gel Sci. Technol.*, **79**, 12 (2016).
- V. Barlier, V. Bounor-Legare, G. Boiteux, J. Davenas, *Appl. Surf. Sci.*, **254**, 5408 (2008).
- S. Doeuff, M. Henry, C. Sanchez, J. Livage, *J. Non-Cryst. Sol.*, **89**, 206 (1987).
- M. Henry, J. Leavage, C. Sanchez, *Progr. Sol. State Chem.*, **18**, 259 (1988).
- M. J. Velasco, F. Rubio, J. Rubio, J. Oteo, *Spectr. Lett.*, **32**, 289 (1999).
- S. Barboux-Doeuff, C. Sanchez, *Mater. Res. Bull.*, **29**, 1 (1994).
- O. Zubkova, A. Shabadash, *Zh. Prikl. Spekr.*, **14** (5) 874 (1971).
- K. Kato, A. Tsuge, K. Niihara, *J. Amer. Ceram. Soc.*, **79** (6) 1483 (1996).
- M. Uzunova-Bujnova, D. Dimitrov, D. Radev, A. Bojinova, D. Todorovsky, *Mater. Chem. Phys.*, **110**, 291 (2008).
- I. R. Beattie, T. R. Gilson, *Proc. R. Soc. a*, **307**, 407 (1968).

ВЛИЯНИЕ НА ЕТИЛЕН ГЛИКОЛА ВЪРХУ ХИДРОЛИЗНО – КОНДЕНЗАЦИОННОТО ПОВЕДЕНИЕ НА Ti(IV) БУТОКСИД

Ст. И. Йорданов¹, А. Д. Бъчварова – Неделчева^{2*}, Р. С. Йорданова²

¹ *Институт по металознание, съоръжения и технологии с Център по хидро- и аеродинамика „Акад. Ангел Балеvски“ - БАН, ул. "Шипчеснки проход" 67, 1574 София, България*

² *Институт по Обща и Неорганична Химия - БАН, ул. "Акад. Г. Бончев", бл. 11, 1113 София, България*

Постъпила на 28 април 2017 г.; Коригирана на 06 юни 2017 г.

(Резюме)

Целта на изследването е да се провери влиянието на етилен гликола (ЕГ) върху скоростта на протичане на хидролизно – кондензационните процеси при получаването на гели от титанов бутоксид. Два хомогенни гела са получени със и без добавяне на етилен гликол в присъствие само на атмосферна влага. Чрез РФА бе установено, че гелът (ТБТ), получен от титановият бутоксид без добавяне на ЕГ е аморфен до 300 °С, докато този получен от титановия бутоксид разтворен в етилен гликол (ТБТ/ЕГ) е аморфен до 400 °С. Доказано бе, че доминиращата кристална фаза при нагриване до 600 °С е TiO₂ (анатаз) а при 700 °С е регистриран и TiO₂ (рутил). Спектралните анализи (ИЧ и УВ – Вис) установиха протичането в по-пълна степен на хидролизно – кондензационните реакции при ТБТ/ЕГ в сравнение с чистия ТБТ. УВ - Вис спектрите на гела съдържащ ЕГ показваха едно отместване на абсорбционния ръб към по-високите стойности на дължината на вълната (“red shifting”) в сравнение с чистия ТБТ гелантиоксидантна активност.

Mathematical description of the relation between water and sea organism pollution

K. Peycheva¹, I. Bangov*², M. Stancheva¹

¹Medical University Varna, 86 Tzar Osvoboditel, Varna 9008

²Shumen University, 115 Universitetska str. Shumen, 9712

Received April 18, 2017; Revised May 30, 2017

Dedicated to Acad. Ivan Juchnovski on the occasion of his 80th birthday

Urban and industrial activities introduce large amounts of pollutants into the marine environment, causing significant and permanent disturbances in marine systems and, consequently, environmental and ecological degradation. The present paper explores the heavy metals as contaminants. Our purpose is to develop a mathematical description of the relation between marine water and sediments and sea organism pollution.

Key words: pollutants; heavy metals; sea organisms; sea water

INTRODUCTION

Urban and industrial activities introduce large amounts of pollutants into the marine environment, causing significant and permanent disturbances in marine systems and, consequently, environmental and ecological degradation. This phenomenon is especially significant in coastal zones, as these are the main sinks of almost all anthropogenic pollutants. It has long been recognized that metals in the marine environment are particularly significant in the ecotoxicology, since they are highly persistent and can be toxic in traces. Certain kinds of contaminants, such as heavy metals, occur naturally in the environment and it is important to be able to distinguish between anthropogenic contamination and background or natural levels so as to enable accurate evaluation of the degree of contamination in a particular area [1].

The use of marine organisms as bioindicators for trace metal pollution is currently very common. Algae, molluscs and fishes are among the organisms most used for this purpose [2]. Fishes are able to accumulate trace metals, reaching concentration values that are thousands of times higher than the corresponding concentrations in sea water.

The use of biological species in the monitoring of marine environment quality permits the evaluation of the biologically available levels of contaminants in the ecosystem or the effects of contaminants on living organisms. The analysis of environmental matrices such as water or sediment provides a picture of the total contaminant load

rather than of that fraction of direct ecotoxicological relevance. Thus, the use of biomonitors eliminates the need for complex studies on the chemical speciation of aquatic contaminants.

Because the metal pollution in aquatic environments can be harmful to human health, it is necessary to understand and control the hazard levels of pollution in seafood. Therefore, it is of great importance to determine the levels of As, Cd, Co, Cr, Cu, Fe, Mn, Ni, Pb and Zn in the marine water, sediments and muscles of the different fish species from Black Sea, Bulgaria.

The purpose of this paper is to develop some qualitative measures for an estimate of the transfer of heavy metals from water to some marine species.

NUMERIC ESTIMATIONS

Here, our efforts were directed to create some numeric estimates of the transfer of pollution from the sea water and sediments to fish and other sea organisms. This development will focus further on the development of an engine which will be a part of a warehouse consisting of a database and software attached to it.

First, some correlations between marine pollution with heavy metals and as a result, pollution of the marine organisms, fish, shellfish, etc., (biota) were proposed. As a first step some statistical indicators on the percentage of pollution of the marine biota X_{fw} (from water) and X_{fs} (from sediments) as a percentage of water pollution ($X_{fw}\%$) and as a percentage of contamination of sediments ($X_{fs}\%$) were introduced. They have the following expressions:

* To whom all correspondence should be sent:
E-mail: ivan.bangov@gmail.com

$$X_{fw} = 1.0 - (W_x - F_x) / X_w \quad (1)$$

$$X_{fw}\% = X_w \cdot 100 \quad (1')$$

$$X_{fs} = 1.0 - (S_x - F_x) / X_s \quad (2)$$

$$X_{fs}\% = X_s \cdot 100 \quad (2')$$

W_x and S_x are the amounts of a pollutant (heavy metal element) in water and sediment and F_x is the amount of a contamination (heavy metal element) in fish or mollusc. X_w and X_s are the contaminations from water and sediments respectively from 0 to 1.0, $X_w\%$ and $X_s\%$ are the same values expressed as percentages, from 0% to 100%.

If the entire amount of pollutant passes in fish or mollusks, then the expressions (1) and (2) provide either 1.0 or in percentage 100%. Figure 1 shows some results of these values for 3 fishes in any water and sediments ($X_{fw}\%$, $X_{fs}\%$).

Since fish do not stay in one the same water area we made an average between the numerical values of the waters and sediments of all areas using average values obtained by the following expressions:

$$X_{avfW} = 1.0 - (\text{avrg}W_x - F_x) / \text{avrg}X_w \quad (3)$$

$$X_{avfW}\% = X_{av} \times 100 \quad (3')$$

$$X_{avfS} = 1.0 - (\text{avrg}S_x - F_x) / \text{avrg}X_s \quad (4)$$

$$X_{avfS}\% = X_{avS} \times 100 \quad (4')$$

Here X_{avfW} where the degree of contamination of fish by the average amount of a pollutant in all waters $\text{avrg}X_w$, and X_{avfS} degree of contamination of fish by the average amount of a pollutant in all sediments $\text{avrg}X_s$. It should be noted that we do not know how long the fish stay in either one or another marine area, so we average the waters and sediments. Further, we shall attempt to draw a conclusion about the fish stay. Some results of our calculations are presented in Figure 1 with $X_{avfW}\%$, $X_{avfS}\%$.

But we noticed that the use of separate water and sediments in some cases produce results greater than 100% (see the discussions bellow). This is the case with the element Cu. Clearly, we must use both factors together. So we obtained the following expressions for the pollution:

$$X_{ws} = 1.0 - (W_x + S_x - F_x) / (W_x + S_x) \quad (9)$$

$$X_{ws}\% = X_{ws} \times 100 \quad (10)$$

as well as by using the averaged values for sediments and water we obtain the following expression:

$$X_{avWS} = 1.0 - (\text{av}S_x + \text{av}W_x - F_x) / (\text{av}S_x + \text{av}W_x) \quad (11)$$

$$X_{avWS}\% = X_{avWS} \times 100 \quad (12)$$

Now we attempted to determine the average time that sea organisms stay in both water and

sediments. The expressions for calculation of these values are the following:

$$fSum = \sum_{allelements} X_f \quad (13)$$

Here X_f is the contamination of the fish from all heavy metal elements.

$$wSum = \sum_{allelements} X_w \quad (14)$$

$wSum$ is the pollutions of fish from all waters.

$$wsSum = \sum_{allelements} X_{ws} \quad (15)$$

$wsSum$ is the pollution of the fish from sediments and waters.

So that the accumulation of all the elements for a fish to water W_{all} , for sediment

S_{all} , W_{Sall} , is calculated by following statements:

Accumulation of water:

$$W_{all} = 1 - \frac{(wSum - fSum)}{wSum} \quad (16)$$

Accumulation of sediments:

$$S_{all} = 1 - \frac{(sSum - fSum)}{sSum} \quad (17)$$

Accumulation of water and sediment:

$$W_{Sall} = 1 - \frac{(wsSum - fSum)}{wsSum} \quad (18)$$

Based on these expressions attempt was made to calculate the duration of stay of each fish in water (T_w) and sediment (T_s) in percentages.

This was accomplished with the decision of the two equations:

$$wSum = T_s \cdot sSum + T_w \cdot wSum \quad (19)$$

$$T_w = (1 - T_s) \quad (20)$$

And here we get:

$$T_s = \frac{(wsSum - wSum)}{(sSum - wSum)} \quad (21)$$

$$as \quad T_w = (1 - T_s) \quad (22)$$

Here T_w and T_s are the times which the fish stay in water and in sediments, respectively.

DISCUSSION

The program for calculating the degree of accumulation of toxic metals in fish from sea water and sediments *fish-water.jar* was developed by Prof. Bangov, by using the Java computer platform (Oracle). Data on fish, surface sediment values and sea water from the Black Sea (see the Supporting

data) are given initially in an Excel file format. Then, the file is converted into text (txt) tabbed file format, and the program reads this data and calculates the degree of accumulated based on the expressions 1-22.

These data have been derived from the Varna Medicinal university group respectively for 2011 and are presented in Tables 1S-3S in the Supporting Information. The results from the calculations are illustrated with calculated values for 3 fishes in Figure 1.

After each calculation of the influence of any heavy metal of a fish we have estimates of the percentage of aggregation of all the elements

included and column *All elements to fish* which takes into account the influence of all considered toxic metals and their mutual accumulates in the fish from both the sea water and the surface-sediments. We found that these values from sea water ranged from 30.217% in *horse mackerel* to 40.365% at *sprat*, and values for sediment ranged between 6.188% of *clamshell (wild) (Mytilus edulis)* and *Kefal (M.cephalus) South* 1.785%, and for Combination If water + sediments in the range: 1.641% - 6.686%.

We present in Figure 1 results from two fishes to illustrate the pollution in percentage according the formulas above.

```

WATER "Black sea-Krapets (North)
BG2BS00000MS001 43°36'60.0" / 28°35'60.0"
=====descriptors=====
Elements Cr, [µg/L]=0.4 Mn, [µg/L]=1.0 Ni, [µg/L]=0.6 Cu,
[µg/L]=1.
1 Zn, [µg/L]=18.0 As, [µg/L]=1.5 Cd, [µg/L]=0.06
Hg, [µg/L]=0.05 Pb, [µg/L]=1.5
=====
FISH Капаръоз (A. pontica) North
FISH / ELEMENT RESULTS
Element Cr [µg/g] water-> Xfw = 12.5%-- sediment= Xfs=2.501% -
--avrg water= XavrgW = 7.99%----avrgSediment= XavrgS 0.905%
----water+sediment value= 2.084%
Element Mn [µg/g] water-> Xfw = 22%---- sediment= Xfs =0.043%
---avrg water= XavrgW = 6.986%----avrgSediment= XavrgS 0.024%
----water+sediment value= 0.043%
Element Ni [µg/g] water-> Xfw = 11.667%---- sediment= Xfs
=0.351% -
----avrg water= XavrgW = 7.778%----avrgSediment=XavrgS 0.212%
----water+sediment value= 0.34%
Element Cu [µg/g] water-> Xfw = 75%---- sediment= Xfs =1.801%
---avrg water= XavrgW = 33.906%----avrgSediment= XavrgS 0.826%
----water+sediment value= 1.758%
Element Zn [µg/g] water-> Xfw = 29.033%---- sediment= Xfs
=17.308%
---avrg water= XavrgW = 41.079%----avrgSediment=
XavrgS 10.297%----water+sediment value= 10.844%
Element As [µg/g] water-> Xfw = 34.546%---- sediment= Xfs
=9.269%
---avrg water= XavrgW = 16.866%----avrgSediment= XavrgS 5.957%
----water+sediment value= 7.308%
Element Cd [µg/g] water-> Xfw = 14.001%---- sediment= Xfs
=7.778%
---avrg water= XavrgW = 8.457%----avrgSediment= XavrgS 4.713%
----water+sediment value= 5.001%
Element Hg [µg/g] water-> Xfw 160%---- sediment= Xfs =160%-
--avrg water= XavrgW = 124.445%----avrgSediment= XavrgS
106.706%
----water+sediment value= 80%
Element Pb [µg/g] water-> Xfw = 14.706%---- sediment=
Xs=0.173% -
--avrg water= XavrgW = 5.158%----avrgSediment= XavrgS 0.113%
----water+sediment value= 0.171%
----
All elements from water to fish = 29.438%
All elements from sediments to fish = 2.6%
All elements from water and sediments to fish = 2.389%
Time spent in sediments in % = 1.008%
Time spent in water in % = 98.993%
-----

```

FISH Кая (N. melanostomus) North

Results

```

Element Cr [µg/g] water-> Xfw = 12.5%---- sediment= Xfs =2.501%
---avrg water= XavrgW = 7.99%----avrgSediment= XavrgS 0.905%
----water+sediment value= 2.084%
Element Mn [µg/g] water-> Xfw Xw= 14.001%---- sediment= Xfs
=0.027%
---avrg water= XavrgW = 4.446%----
avrgSediment= XavrgS 0.015%----water+sediment value= 0.027%
Element Ni [µg/g] water-> Xfw = 1.334%---- sediment= Xfs =0.04% -
---avrg water= XavrgW = 0.889%----avrgSediment= XavrgS 0.025%
----water+sediment value= 0.039%
Element Cu [µg/g] water-> Xfw = 126.667%---- sediment= Xfs
=3.041%
---avrg water= XavrgW = 57.262%----
avrgSediment= XavrgS 1.395%----water+sediment value= 2.969%
Element Zn [µg/g] water-> Xfw = 29.033%---- sediment=
Xfs=17.308%
---avrg water= XavrgW = 41.079%
---avrgSediment= XavrgS 10.297%----water+sediment value=
10.844%
Element As [µg/g] water-> Xfw = 60%---- sediment= Xfs=16.098%
----avrg water= XavrgW = 29.293%
---avrgSediment= XavrgS 10.345%----water+sediment value=
12.693%
Element Cd [µg/g] water-> Xfw = 12%---- sediment= Xfs=6.667%
---avrg water= XavrgW = 7.249%
---avrgSediment= XavrgS 4.039%----water+sediment value= 4.286%
Element Hg [µg/g] water-> Xfw = 100%---- sediment= Xfs=100%
---avrg water= XavrgW = 77.778%----avrgSediment= XavrgS 66.691%
----water+sediment value= 50%
Element Pb [µg/g] water-> Xfw = 8.824%---- sediment= Xfs=0.104%
---avrg water= XavrgW = 3.095%----avrgSediment= XavrgS 0.068%
----water+sediment value= 0.103%
----
All elements from water to fish = 30.699%
All elements from sediments to fish = 2.712%
All elements from water and sediments to fish = 2.492%
Time spent in sediments in % = 1.008%
Time spent in water in % = 98.993%
-----

```

Fig. 1. Listing with the results for 2 fishes in Black sea-Krapets water.

In Figure 1 X_w is the percentage of pollution calculated on the local water only, X_s - the percentage of pollution calculated on the local sediments only. The same values are averaged for waters of all locations, X_{avgW} , sediments X_{avgS} , averaged from all locations and the percentage of pollution X_{ws} by using both water and sediment values in the calculations.

One can see from Figure 1 that in the case of Hg for both fish and shell the X_w result is higher than 100%. This indicates that there is another source of pollution, which are obviously sediments. The result X_s show clearly that we have increase pollution of Hg from sediments. When we use the joint pollution of water and sediments we obtain normal value less than 100%. Our calculations show that that the great part of pollution of Hg comes from the sediments.

The data in Figure 1 show that in the case of combined action of the two factors (sea water and surface sediment) data extracting normal appearance. As an example we can cite the estimated value of Hg fish shad caught by region Krapec (North):

Hg [$\mu\text{g} / \text{g}$] value = 0.08 $\rightarrow X_w = 160\%$ ----- $X_s = 160\%$ ----- $X_{avgW} = 124.445\%$ ---- $X_{avgS} = 106.706\%$ ----- $X_{ws} = 80\%$

Here, the value of X_{ws} is equal to 80% (by comparing with $X_{avgW}=124.445\%$ and 106.706% X_{avgS}). Then, a question arises, why a toxic element percentage of the combined influence of

marine water and sediment on fish decreases the contamination of the sea organisms. The explanation is logical. Our data for the contamination of fishes are constant. We haven't got data to form a function that shows how the contamination of marine organism increases with the pollution of the water and when combined we have influence of both factors (sea water and sediment), the percentage that each component introduced into combined value decreases, i.e. it shows that owing to the rich contamination of the sediments a smaller amount of sediment and water pollution is needed in order the same value of the contamination of the fish to be reached.

The time values of the stay in water and sediments show the same trend. Thus, the fish stays very little time in the sediments, but because they are rich of heavy metal pollution the fish absorbs much more contamination. The remaining time the fish is in the waters which are shorter of pollution.

Acknowledgements: The funding from Norwegian fond is acknowledged.

Electronic Supplementary Data available here.

REFERENCES

1. I. Akcali, F. Kucuksezgin, *Marine Pollution Bulletin*, **62**, 637 (2011).
2. P. S Rainbow, *Marine Pollution Bulletin*, **8**, 16 (1995).

МАТЕМАТИЧЕСКО ОПИСАНИЕ НА ЗАВИСИМОСТТА МЕЖДУ ЗАМЪРСЯВАНЕТО НА МОРСКАТА ВОДА И НА МОРСКИТЕ ОРГАНИЗМИ

К. Пенчева¹, И. Бангов^{2*}, М. Станчева¹

¹ Медицински университет, Варна, Цар Освободител, 86, Варна 9008

² Шуменски университет, ул. Университетска, 115. Шумен, 9712

Постъпила на 18 април 2017 г.; Коригирана на 30 май 2017 г.

(Резюме)

Урбанизираните и индустриални активности допринасят за големи количества замърсители в морската среда, причинявайки значителни и постоянни смущения в морските системи и като следствие екологична деградация на околната среда. Настоящата статия изучава тежките метали, като замърсители. Нашата цел е да се развие математическо описание на зависимостта на морските води и седименти и замърсяването на морските организми.

Ab Initio SCF study of the barrier to internal rotation in simple amides

N. G. Vassilev*

Institute of Organic Chemistry with Centre of Phytochemistry, Bulgarian Academy of Sciences, Acad. G. Bonchev Str.,
Block 9, 1113 Sofia, Bulgaria

Received May 03, 2017; Revised July 10, 2017

Dedicated to Acad. Ivan Juchnovski on the occasion of his 80th birthday

The free energies of activation for rotation about the amide C-N bond in R-C(O)NR'₂ (R'=CH₃, R = CN, N₃, C≡C-H, C≡C-CH₃; R'=H, R = C₂H₅, CH(CH₃)₂) were calculated at the MP2(fc)/6-31+G**//6-31G* and at the MP2(fc)/6-311++G**//6-311++G** levels of theory and compared with the NMR liquid and gas-phase data. On the basis of results from this and previous studies we generalize that in case of amides and thioamides the nonbonded interactions in ground state (GS) are mainly responsible for the differences in the rotational barriers and they prevail over the electronic effects of the substituents.

Key words: amides; barrier to internal rotation; ab initio SCF study

INTRODUCTION

The great interest for the amide functional group in chemistry is mainly related to its occurrence as a building block in peptides and proteins. The internal rotation about the amide C-N bond in amides and thioamides has been intensively studied experimentally by NMR spectroscopy in the gas [1-7] and in the liquid phase [8]. The experimental results were used to judge theoretical methods of calculating barrier heights. The origin of the C-N rotational barrier and its relation to amide resonance has also received much attention in the last years [9-14].

Recently the electronic effect of polar substituents on the barrier of internal rotation around the amide carbon-nitrogen bond in p-substituted acetanilides [15, 16] and thioacetanilides [17] were studied at the B3LYP/6-31G(d,p) level. Several linear relationships were established linking the barrier heights with structural and electronic parameters that characterize the amide and thioamide grouping. The results obtained are consistent with the views for a classical amide resonance as being the origin of higher rotational barriers in thioamides than in amides.

Recently we presented *ab initio* calculations [18] of barrier to internal rotation about C-N bond in N,N-dimethylcinnamamides, which were studied by dynamic NMR spectroscopy [19,20]. On the other hand the interest to cinnamamides namely coumaric amides increases in the last years because

of potential antioxidant activity of these compounds [21,22]. The free energy of activation of substituted cinnamamides were reproduced very well using MP2(fc)/6-31+G**//6-31G* energies and PCM/6-31G* energy change from gas phase to chloroform. For all studied compounds the anti transition state (*anti* TS) is more stable and determines the rotational barrier. The remote effect of phenyl substituents in the studied compound has pure electronic origin, which was demonstrated by the relationship between C-N bond order difference and calculated energy barrier [18].

In this paper we continue our investigation of effects of substituents on the height of rotational barriers in amides by *ab initio* studying at the MP2/6-31+G**//6-31G* and at the MP2(fc)/6-311++G**//6-311++G** levels of theory the amides R-C(O)N(CH₃)₂ (R = CN, N₃, C≡C-H, C≡C-CH₃) and in H-C(O)NR₂ (R = C₂H₅, CH(CH₃)₂).

METHODS

The *ab initio* SCF calculations were performed using the package GAMESS [23]. The complete geometry optimization was carried out using the 6-31G* and 6-311++G** basis sets. The molecules were assumed to have C₁ symmetry in the ground state (GS) and C_s symmetry in the transition states (TS). The bond order analysis was done at the HF/6-31G* level of theory as it is implemented in program GAMESS for closed shells by Giambiagi [24] and Mayer [25]. For recent review about bond orders see ref. [26]. The energies were

* To whom all correspondence should be sent:
E-mail: niki@orgchm.bas.bg

then calculated at the MP2(fc)/6-31+G**//6-31G* and at the MP2(fc)/6-311++G**//6-311++G** levels of theory. In calculating the vibrational energies, the vibrational frequencies were scaled by 0.89[27]. In each case 7 (TS) or 8 (GS) scaled frequencies below 500 cm^{-1} were treated as rotations ($E=RT/2$) [27]. The imaginary frequency for the transition states is ignored in all thermodynamics calculations. The effect of solvent on the relative stabilities of the GS and TS was studied using the polarized continuum model (PCM) proposed by Tomasi et al. [28] with the build in parameters for solvents CCl_4 and toluene. In the case of 1,1,2,2-tetrachloroethane (TCE) and diethyl formamide we relied on the experimental data. The static dielectric constant was 8.20 for TCE and 29.02 for diethyl formamide, the dielectric constants at infinite frequency were calculated from the refractive indexes. The solvent radiuses, the solvent densities and the molar volumes were calculated from the tabulated densities and molar masses. In our investigations only the electrostatic contributions were taken into account utilizing single point PCM calculations at HF/6-311++G** level of theory.

RESULTS AND DISCUSSION

Geometry optimization

The heavy-atom framework of the studied molecules in the GS was found to be essentially planar and close to C_s symmetry. The GS structures of H-C(O)NR_2 ($R = \text{C}_2\text{H}_5, \text{CH}(\text{CH}_3)_2$) are an exception (Figure 1 and S1). The two R substituents are not symmetrical [29]. The transition state geometries of studied amides (Figure 1 and 1S) were optimized in C_s symmetry. This approach usually yields transition states, but for some of our structures additional refining of saddle point was necessary in order to locate TS structure with only

one imaginary frequency. Again the TS structures of H-C(O)NR_2 ($R = \text{C}_2\text{H}_5, \text{CH}(\text{CH}_3)_2$) were unsymmetrical (Figure 1S). The calculated energies for GS, *anti* and *syn* TS, are presented in Tables 1 and 1S. The *anti* TS is more stable in all cases. Therefore *anti* TS of studied compounds give the greatest contribution to the rotational barrier.

The most significant structural changes in the process of rotation towards the transition states are that the nitrogen is pyramidalized and the C-N bond lengthens from 1.34-1.35 to 1.40-1.42 Å (Table 2). However, the C=O bond length shortens by 0.01-0.02 Å only. This indicates that the carbonyl group is relatively unaffected by this rotation

Comparison of calculated activation parameters and experimental data

Calculation of the vibrational frequencies confirmed the assignment of the *anti* and *syn* forms as transition states and allowed computation of the enthalpy, entropy and free energy changes at 298K. The thermodynamic results for the isomerisation of the studied amides are presented in Table 3. In present case, ΔH^{298} is obtained from the sum of the changes in the electronic energy, ΔE_e^0 , the zero-point vibrational energy, ΔE_v^0 , and the thermal correction to the zero-point energy, $\Delta \Delta E_v^{298}$. The scaled frequencies were used also for the entropy calculation. In this case the two lowest real frequencies, which correspond to rotations of the methyl groups, need to be treated as hindered rotations. The resultant free energy, $\Delta G^\ddagger(298\text{K})$, for the *anti* TS can be compared with the gas-phase NMR results.

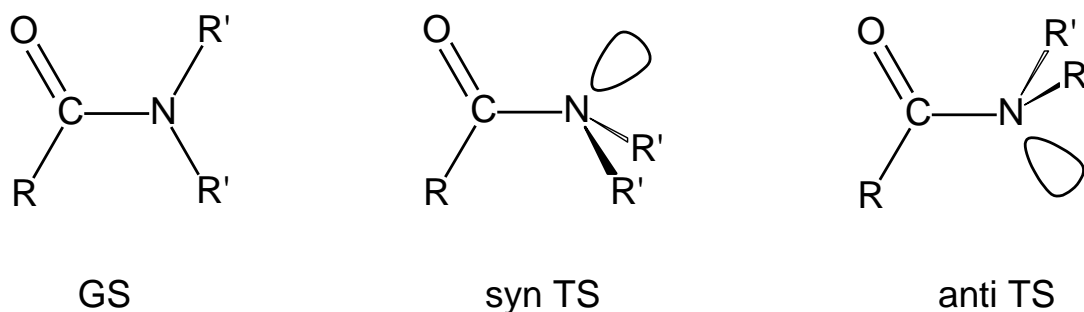


Fig. 1. Ground state (GS) and two transition states (TS) of the studied amides: ($R'=\text{CH}_3, R = \text{CN}, \text{N}_3, \text{C}=\text{C-H}, \text{C}=\text{C-CH}_3$; $R'=\text{H}, R = \text{C}_2\text{H}_5, \text{CH}(\text{CH}_3)_2$).

Table 1. Calculated Electronic energies E_e^0 for the studied amides $R-C(O)NR'_2$ in Hartrees

R	R'	State	ZPE ^b	MP2(fc)/ 6-31+G**// 6-31G*	MP2(fc)/ 6-311++G**// 6-311++G**	PCM/311++G**
CH ₃ C≡C	CH ₃	GS	84.20	-362.822927	-363.035250	-7.2 ^c
CH ₃ C≡C	CH ₃	<i>anti</i> TS	83.98	-362.796311 ^a	-363.009445 ^a	-5.6 ^c
CH ₃ C≡C	CH ₃	<i>syn</i> TS	83.92	-362.795327	-363.009209	-6.6 ^c
HC≡C	CH ₃	GS	67.31	-323.645785	-323.828466	-6.9 ^c
HC≡C	CH ₃	<i>anti</i> TS	67.05	-323.618149 ^a	-323.801902 ^a	-5.3 ^c
HC≡C	CH ₃	<i>syn</i> TS	66.98	-323.617324	-323.801782	-6.1 ^c
N≡C	CH ₃	GS	60.93	-339.732431	-339.915725	-7.2 ^c
N≡C	CH ₃	<i>anti</i> TS	60.60	-339.701189	-339.885634	-5.4 ^c
N≡C	CH ₃	<i>syn</i> TS	60.48	-339.701347 ^a	-339.886375 ^a	-6.0 ^c
N ₃	CH ₃	GS	63.94	-410.926097	-411.140548	-3.4 ^d
N ₃	CH ₃	<i>anti</i> TS	63.70	-410.901043 ^a	-411.116520 ^a	-3.9 ^d
N ₃	CH ₃	<i>syn</i> TS	63.67	-410.900286	-411.116026	-4.0 ^d
H	C ₂ H ₅	GS	107.70	-326.070618	-326.287625	-7.3 ^e
H	C ₂ H ₅	<i>anti</i> TS	106.95	-326.035407 ^a	-326.253552 ^a	-4.4 ^e
H	C ₂ H ₅	<i>syn</i> TS	106.73	-326.033911	-326.252694	-6.4 ^e
H	<i>i</i> -C ₃ H ₇	GS	129.54	-404.411288	-404.688025	-3.7 ^f
H	<i>i</i> -C ₃ H ₇	<i>anti</i> TS	128.60	-404.373029 ^a	-404.650673 ^a	-2.3 ^f
H	<i>i</i> -C ₃ H ₇	<i>syn</i> TS	128.51	-404.371845	-404.650225	-3.3 ^f
CH ₃ C≡C	H	GS	50.16	-284.500681	-284.658790	
CH ₃ C≡C	H	<i>anti</i> TS	50.04	-284.475042 ^a	-284.634549 ^a	
CH ₃ C≡C	H	<i>syn</i> TS	50.03	-284.472365	-284.632523	
HC≡C	H	GS	33.31	-245.323182	-245.451906	
HC≡C	H	<i>anti</i> TS	33.09	-245.296724 ^a	-245.426980 ^a	
HC≡C	H	<i>syn</i> TS	33.06	-245.294253	-245.425100	
N≡C	H	GS	26.98	-261.407503	-261.536917	
N≡C	H	<i>anti</i> TS	26.60	-261.379307 ^a	-261.510356 ^a	
N≡C	H	<i>syn</i> TS	26.52	-261.376991	-261.508455	
N ₃	H	GS	29.92	-332.604377	-332.764778	
N ₃	H	<i>anti</i> TS	29.80	-332.579125 ^a	-332.741088 ^a	
N ₃	H	<i>syn</i> TS	29.76	-332.577935	-332.740094	

^a more stable TS; ^b ZPE is reported in kcal/mol at the HF/6-31G* level scaled by 0.89; ^c Energy change from gas phase to TCE in kcal/mol; ^d Energy change from gas phase to CCl₄ in kcal/mol; ^e Energy change from gas phase to diethyl formamide in kcal/mol; ^f Energy change from gas phase to toluene in kcal/mol.

Table 2. Selected bond lengths, bond orders and imaginary frequencies calculated at HF/6-311++G** level of theory for the studied amides $R-C(O)NR'_2$.

R	R'	State	r _{C-N} (Å)	r _{C=O} (Å)	r _{C-C} (Å)	r _{C-C} (Å)	Bond Order C-N	iv(cm ⁻¹)
CH ₃ C≡C	CH ₃	GS	1.353	1.197	1.185	1.468	0.985	
CH ₃ C≡C	CH ₃	<i>anti</i> TS	1.425	1.182	1.186	1.456	0.849	102.9i
CH ₃ C≡C	CH ₃	<i>syn</i> TS	1.421	1.178	1.186	1.468	1.171	80.3i
HC≡C	CH ₃	GS	1.349	1.195	1.193	1.472	1.018	
HC≡C	CH ₃	<i>anti</i> TS	1.421	1.180	1.184	1.462	0.961	108.6i
HC≡C	CH ₃	<i>syn</i> TS	1.417	1.177	1.184	1.474	1.211	82.1i
N≡C	CH ₃	GS	1.339	1.189		1.490	1.079	
N≡C	CH ₃	<i>anti</i> TS	1.409	1.174		1.484	0.938	114.9i
N≡C	CH ₃	<i>syn</i> TS	1.404	1.171		1.498	1.221	80.5i
N ₃	CH ₃	GS	1.346	1.199		1.410	1.139	
N ₃	CH ₃	<i>anti</i> TS	1.412	1.188		1.393	1.024	105.6i
N ₃	CH ₃	<i>syn</i> TS	1.409	1.182		1.408	1.074	97.3i
H	C ₂ H ₅	GS	1.345	1.195			1.004	
H	C ₂ H ₅	<i>anti</i> TS	1.421	1.180			0.843	252.8i
H	C ₂ H ₅	<i>syn</i> TS	1.416	1.177			0.875	191.5i
H	<i>i</i> -C ₃ H ₇	GS	1.346	1.196			1.019	
H	<i>i</i> -C ₃ H ₇	<i>anti</i> TS	1.416	1.181			0.711	268.0i
H	<i>i</i> -C ₃ H ₇	<i>syn</i> TS	1.413	1.179			0.741	201.2i

Table 3. Calculated barriers of the studied amides R-CONR₂ in the gas phase.

R	R'	Method ^a	TS	$\Delta H^\ddagger(298\text{K})$	$\Delta S^\ddagger(298\text{K})$	$\Delta G^\ddagger(298\text{K})$	$\Delta G_{\text{eff}}^\ddagger(298\text{K})^h$
CH ₃ C≡C	CH ₃	1	<i>anti</i>	15.5	-10.5	18.6	18.1 (18.9)
			<i>syn</i>	16.0	-8.0	18.4	
		2	<i>anti</i>	14.0	-10.5	17.1	16.8 (17.8)
			<i>syn</i>	15.0	-8.0	17.4	
		3	<i>anti</i>	15.0	-10.5	18.1	17.3 (18.0)
			<i>syn</i>	15.1	-8.0	17.5	
exptl(TCE) ^b				19.8 ± 0.4	0.6 ± 1.2		19.6 ± 0.28
HC≡C	CH ₃	1	<i>anti</i>	16.1	-7.7	18.4	18.2 (19.4)
			<i>syn</i>	16.5	-7.5	18.8	
		2	<i>anti</i>	14.2	-7.7	16.5	16.4 (17.8)
			<i>syn</i>	15.2	-7.5	17.5	
		3	<i>anti</i>	15.4	-7.7	17.7	17.3 (18.4)
			<i>syn</i>	15.4	-7.5	17.6	
exptl(TCE) ^b							19.56
CN	CH ₃	1	<i>anti</i>	18.3	-6.8	20.3	19.7 (21.0)
			<i>syn</i>	18.0	-6.5	19.9	
		2	<i>anti</i>	15.5	-6.8	17.6	17.3 (18.8)
			<i>syn</i>	16.0	-6.5	18.0	
		3	<i>anti</i>	17.6	-6.8	19.6	18.7 (20.0)
			<i>syn</i>	16.9	-6.5	18.8	
exptl(gas) ^c							19.0 ± 0.1
exptl(TCE) ^c							21.4
N ₃	CH ₃	1	<i>anti</i>	14.5	-10.3	17.5	17.3 (16.7)
			<i>syn</i>	14.9	-9.9	17.8	
		2	<i>anti</i>	13.7	-10.3	16.7	16.6 (16.1)
			<i>syn</i>	14.7	-9.9	17.7	
		3	<i>anti</i>	13.8	-10.3	16.9	16.6 (16.0)
			<i>syn</i>	14.1	-9.9	17.0	
exptl(gas) ^c							16.5 ± 0.1
exptl(CCl ₄) ^d							17.7
H	C ₂ H ₅	1	<i>anti</i>	20.3	-3.5	19.0	21.1 (22.6)
			<i>syn</i>	20.9	-2.9	18.0	
		2	<i>anti</i>	18.8	-3.5	19.8	19.5 (21.0)
			<i>syn</i>	19.3	-2.9	20.1	
		3	<i>anti</i>	20.0	-3.5	20.1	20.7 (22.0)
			<i>syn</i>	20.3	-2.9	21.2	
exptl(gas) ^e				19.4 ± 0.9	0.8 ± 2.6		19.2 ± 0.1
exptl(neat) ^f							20.4
H	C ₃ H ₇	1	<i>anti</i>	21.9	-1.2	22.2	22.0 (22.9)
			<i>syn</i>	22.4	-1.1	22.8	
		2	<i>anti</i>	19.5	-1.2	19.9	19.6 (20.3)
			<i>syn</i>	19.8	-1.1	20.1	
		3	<i>anti</i>	21.3	-1.2	21.7	21.3 (22.0)
			<i>syn</i>	21.4	-1.1	21.7	
4	<i>anti</i>			19.6			
	<i>syn</i>			21.3			
exptl(gas) ^e				18.8 ± 0.7	-0.6 ± 1.9		19.0 ± 0.1
exptl(toluene) ^g							19.8

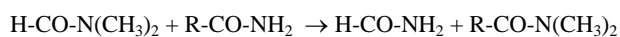
^a 1 - MP2(fc)/6-31+G**//6-31G*, 2 - HF/6-311++G**, 3 - MP2(fc)/6-311++G**//6-311++G**, 4 - QM/MM IMOMM (MP2:MM3) results from reference [29], ^b Reference [33], ^c Reference [34], ^d Reference [35], ^e Reference [36], ^f Reference [37], ^g Reference [38, 39], ^h Values in parenthesis include solvation correction of energy from Table 1.

$\Delta G_{\text{eff}}^\ddagger(298\text{K})$ is calculated by summing the rates through the two possible TS.

When the *syn* TS is slightly higher than *anti* TS, a part of reaction will proceed via the *syn* TS and to take this parallel reaction into account the effective free energy, $\Delta G_{\text{eff}}^{\ddagger}(298\text{K})$, was calculated by summing the rates through the two possible TS. The solvent effect was introduced by adding corrections to GS and both TS from single point PCM calculations given in Table 1. It is seen from Table 3 that the rotational barriers were reproduced very satisfactory. MP2(fc)/6-31+G**//6-31G* level of theory (Method 1) reproduce well $\Delta G_{\text{eff}}^{\ddagger}(298\text{K})$ of studied amides with R = CH₃C≡C and CH₃C≡C, even the solvent effect was reproduced well. In case of R = CN and N₃ Method 1 overestimates $\Delta G_{\text{eff}}^{\ddagger}(298\text{K})$ in gas phase compare to MP2(fc)/6-311++G**//6-311++G** (Method 3). In case of R = H, R' = C₂H₅ or CH(CH₃)₂ HF/6-311++G** (Method 2) reproduce well $\Delta G_{\text{eff}}^{\ddagger}(298\text{K})$ either in gas phase and in solution. Recently reported IMOMM (MP2:MM3) calculation [29] of R = H, R' = CH(CH₃)₂ reproduce also well the barrier in gas phase. In general wider basis sets and addition of electron correlation effects is expecting to improve the calculation rotational barriers. In practice MP2(fc)/6-31+G**//6-31G* results are very often closer to experimental values than MP2(fc)/6-311++G**//6-311++G** results at a much lower computational price. Recently the barriers of rotation around C-N bond in gas phase of simple amides and tioamides were also well reproduced at MP2(fc)/6-31+G**//6-31G* level of theory, as well [30-32].

Effect of the substituents on the rotational barrier

In order to study the effect of substituents we considered two possible transition states and two rotational pathways and examined the following model reaction either in ground state or in the two possible transition states:



This approach was explored before to estimate the difference in repulsion between R and the CH₃ group, the difference in repulsion between R and the amide lone pair and the difference in repulsion between oxygen and amide lone pair [30-32]. The calculated enthalpy of the reaction for the ground state $\Delta\Delta H^{\circ}(\text{GS})$ will be an estimate for the difference in repulsion between R and CH₃ group. The calculated enthalpy of the reaction for the *anti*

transition state $\Delta\Delta H^{\circ}(\text{anti TS})$ will be an estimate for the difference in repulsion between R and amide lone pair, while the calculated enthalpy of the reaction for *syn* transition state $\Delta\Delta H^{\circ}(\text{syn TS})$ will be an estimate for the difference in repulsion between oxygen and amide lone pair. The combined energy differences for both GS and *anti* TS [$\Delta\Delta H^{\circ}(\text{anti TS}) - \Delta\Delta H^{\circ}(\text{GS})$] can be compared with the calculated differences in the calculated enthalpy of activation $\Delta\Delta H^{\ddagger}(0\text{K})$ for the *anti* TS, while the combined energy differences for both GS and *syn* TS [$\Delta\Delta H^{\circ}(\text{syn TS}) - \Delta\Delta H^{\circ}(\text{GS})$] can be compared with the calculated differences in the calculated enthalpy of activation $\Delta\Delta H^{\ddagger}(0\text{K})$ for the *syn* TS. [$\Delta\Delta H^{\circ}(\text{anti TS}) - \Delta\Delta H^{\circ}(\text{GS})$] and [$\Delta\Delta H^{\circ}(\text{syn TS}) - \Delta\Delta H^{\circ}(\text{GS})$] can also be compared with the calculated change in free energy $\Delta\Delta G_{\text{eff}}^{\ddagger}(298\text{K})$ and with the experimental change in free energy of activation $\Delta\Delta G_{\text{exp}}^{\ddagger}(298\text{K})$. All results of calculations for the model reaction are presented in Table 2S. The change in basis set leads to significant changes in $\Delta\Delta G_{\text{eff}}^{\ddagger}(298\text{K})$ moreover in different directions, despite having a small influence on $\Delta\Delta H$. The explanation is hidden in the calculation scheme of $\Delta G_{\text{eff}}^{\ddagger}(298\text{K})$, which is sensitive to the relation of *syn* $\Delta G^{\ddagger}(298\text{K})$ and *anti* $\Delta G^{\ddagger}(298\text{K})$ values. In Table 4 the results of calculation for the model reaction obtained in this and previous papers are summarized. It is seen that the calculated $\Delta\Delta H^{\circ}(\text{anti TS}) - \Delta\Delta H^{\circ}(\text{GS})$ values are a good estimation for the experimental change in free energy $\Delta\Delta G_{\text{exp}}^{\ddagger}(298\text{K})$. With a few exceptions the tendency to increase $\Delta\Delta G_{\text{exp}}^{\ddagger}(298\text{K})$ absolute values from left to right column (decrease of the experimental barriers) is followed by the calculated $\Delta\Delta H^{\circ}(\text{anti TS}) - \Delta\Delta H^{\circ}(\text{GS})$ values. This trend means that the difference in repulsion between R and CH₃ group in GS and difference in repulsion between R and amide lone pair in the preferred *anti* TS are mainly responsible for the decrease in the experimental rotation barriers around amide bond in simple amides. Further improvement in calculation of activation parameters either for rotational barriers or for modelling the effects of substituents require systematic increasing the level of theory (both basis set and method) and such calculations are in progress.

Table 4. Origin of the difference in the rotational barriers (kcal/mol) of the studied amides R-CON(CH₃)₂ in the gas phase.

R	H-CO-N(CH ₃) ₂ + R-CO-NH ₂ → H-CO-NH ₂ + R-CO-N(CH ₃) ₂											
	H	CN	CHF ₂	F	N ₃	CF ₃	Cl	CH ₃	CH ₂ F	CCl ₃	Br	
$\Delta\Delta H^\circ(\text{anti TS})-\Delta\Delta H^\circ(\text{GS})$	0	-1.9	-4.3	-2.5	-3.5	-5.0	-4.8	-3.8	-7.4	-7.5	-5.5	
$\Delta G^\ddagger_{\text{exp}}(298\text{K})$	0	-0.4	-2.0	-2.3	-2.9	-3.3	-4.0	-4.1	-4.2	<-4	-5.3	

$\Delta\Delta H^\circ(\text{GS})$ and $\Delta\Delta H^\circ(\text{anti TS})$ are the energy changes (they include ZPE correction) for the model reaction in the ground and *anti* transition state, respectively. $\Delta\Delta G^\ddagger_{\text{exp}}(298\text{K})$ is the experimental change in free energy. The $\Delta\Delta H^\circ(\text{anti TS})-\Delta\Delta H^\circ(\text{GS})$ values are compilation of data calculated at higher level of theory from this and previous studies

CONCLUSION

The free energy of activation of studied amides were reproduces very well using MP2(fc)/6-31+G**/6-31G* energies and PCM/6-31G* energy change from gas phase to solution. For all studied compounds the *anti* transition state (*anti* TS) is more stable and determines the rotational barrier. The nonbonded interactions in ground state (GS) and *anti* TS are mainly responsible for the differences in the rotational barriers in the studied amides

Acknowledgements: Financial support by the Bulgarian National Science Fund (Grants X-1408 and RNF01/0110) is acknowledged by gratitude.

Electronic Supplementary Data available here.

REFERENCES

- C. B. LeMaster, *Prog. Nucl. Magn. Reson. Spectrosc.*, **31**, 119 (1997).
- A. N. Taha, N. S. True, *J. Phys. Chem. A*, **104**, 2985 (2000).
- A. N. Taha, S. M. Neugebauer-Crawford, N. S. True, *J. Phys. Chem. A*, **104**, 7957 (2000).
- C. L. LeMaster, C. B. LeMaster, N. S. True, *J. Am. Chem. Soc.*, **121**, 4478 (1999).
- A. N. Taha, S. M. Neugebauer Crawford, N. S. True, *J. Am. Chem. Soc.*, **120**, 1934 (1998).
- A. N. Taha, S. M. Neugebauer Crawford, N. S. True, *J. Phys. Chem. A*, **102**, 1425 (1998).
- S. M. Neugebauer Crawford, A. N. Taha, N. S. True, C. B. LeMaster, *J. Phys. Chem. A*, **101**, 4699 (1997).
- W. E. Stewart, T. H. Siddal, III, *Chem. Rev.*, **70**, 517 (1970).
- K. B. Wiberg, K. E. Laidig, *J. Am. Chem. Soc.*, **109**, 5935 (1987).
- M. W. Wong, K. B. Wiberg, *J. Phys. Chem.*, **96**, 668 (1992).
- K. B. Wiberg, P. R. Rablen, *J. Am. Chem. Soc.*, **117**, 2201 (1995).
- K. B. Wiberg, P. R. Rablen, D. J. Rush, T. A. Keith, *J. Am. Chem. Soc.*, **117**, 4261 (1995).
- K. B. Wiberg, D. J. Rush, *J. Am. Chem. Soc.*, **123**, 2038 (2001).
- K. B. Wiberg, D. J. Rush, *J. Org. Chem.*, **67**, 826 (2002).
- S. Ilieva, B. Hadjieva, B. Galabov, *J. Mol. Struct.*, **476**, 151 (1999).
- S. Ilieva, B. Hadjieva, B. Galabov, *J. Org. Chem.*, **67**, 6210 (2002).
- B. Galabov, S. Ilieva, B. Hadjieva, E. Dinchova, *J. Phys. Chem. A*, **107**, 5854 (2003).
- N. G. Vassilev, *Bulg. Chem. Commun.*, **40**, 526 (2008).
- S. L. Spassov, V. S. Dimitrov, M. Agova, I. Kantschowska, R. Todorova, *Org. Magn. Reson.*, **3**, 551 (1971).
- K. Spaargaren, P. K. Korver, P. J. van der Haak, T. J. de Boer, *Org. Magn. Reson.*, **3**, 605 (1971).
- Z. Velkov, Y. Velkov, E. Balabanova, A. Tadjer, *Int. J. Quant. Chem.*, **107**, 1765 (2007).
- Z. Velkov, E. Balabanova, A. Tadjer, *J. Mol. Struct.: THEOCHEM*, **821**, 133 (2007).
- M. W. Schmidt, K. K. Baldridge, J. A. Boatz, S. T. Elbert, M. S. Gordon, J. H. Jensen, S. Koseki, N. Matsunaga, K. A. Nguyen, S. J. Su, T. L. Windus, M. Dupuis, J. A. Montgomery, *J. Comp. Chem.*, **14**, 1347 (1993).
- M. Giambiagi, M. S. D. Giambiagi, D. R. Gempel, C. D. Heymann, *J. Chim. Phys.*, **72**, 15 (1975).
- I. Mayer, *Chem. Phys. Lett.*, **97**, 270 (1983).
- I. Mayer, *J. Comp. Chem.*, **28**, 204 (2007).
- W. J. Hehre, L. Radom, P. V. R. Schleyer, J. A. Pople, *Ab Initio Molecular Orbital Theory*, Wiley, New York, 1986.
- J. Tomasi, M. Persico, *Chem. Rev.*, **94**, 2027 (1994).
- Y. Jean, I. Demachy, A. Lledos, F. Maseras, *J. Mol. Struct.: THEOCHEM*, **632**, 131 (2003).
- N. G. Vassilev, V. S. Dimitrov, *J. Mol. Struct.*, **484**, 39 (1999).
- N. G. Vassilev, V. S. Dimitrov, *J. Mol. Struct.*, **522**, 37 (2000).
- N. G. Vassilev, V. S. Dimitrov, *J. Mol. Struct.*, **654**, 27 (2003).
- S. L. Spassov, V. S. Dimitrov, M. Agova, I. Kantschowska-Dimicoli, R. Todorova-Momcheva, *Org. Magn. Reson.*, **6**, 508 (1974).

34. B. D. Ross, L. T. Wong, N. S. True, *J. Phys. Chem.*, **89**, 836 (1985).
35. L. W. Reeves, K. N. Shaw, *Can. J. Chem.*, **49**, 3671 (1971).
36. C. B. LeMaster, N. S. True, *J. Phys. Chem.*, **93**, 1307 (1989).
37. R. M. Hammaker, B. A. Gugler, *J. Mol. Spectrosc.*, **17**, 356 (1965).
38. U. Berg, Z. Blum, *J. Chem. Res. (S)*, 206 (1983).
39. T. Drakenberg, S. Forsen, *J. Phys. Chem.*, **74**, 1 (1970).

Ab initio SCF ИЗСЛЕДВАНЕ НА БАРИЕРА НА ВЪТРЕШНА РОТАЦИЯ В АМИДИ

Н. Г. Василев

Институт по Органична Химия с Център по Фитохимия, Българска Академия на Науките, ул. „Акад. Г. Бончев” бл. 9, София 1113

Постъпила на 03 МАЙ 2017 г.; Коригирана на 10 юни 2017 г.

(Резюме)

Свободната енергия на активация за ротацията около amidната C-N връзка в R-C(O)NR'₂ (R'=CH₃, R = CN, N₃, C≡C-H, C≡C-CH₃; R'=H, R = C₂H₅, CH(CH₃)₂) е изчислена на MP2(fc)/6-31+G*//6-31G* и на MP2(fc)/6-311++G**//6-311++G** нива на теорията и са сравнени с данните от ЯМР в течна и газова фаза. За всички изследвани съединения *анти* преходното състояние (*anti* TS) е по-стабилно и определя ротационния бариер. На база на резултатите от това и предишни изследвания ние обобщаваме, че в случая на амиди и тиоамиди несвързващите взаимодействия в основно състояние (GS) са основно отговорни за разликите в ротационните бариери и те преобладават над електронните ефекти на заместителите.

Comparison of structure and antioxidant activity of polysaccharides extracted from the leaves of *Plantago major* L., *P. media* L. and *P. lanceolata* L.

P. K. Lukova^{1*}, D. P. Karcheva-Bahchevanska¹, M. M. Nikolova², Ilia N. Iliev², R. D. Mladenov^{1,3}

¹ Department of Pharmacognosy and Pharmaceutical Chemistry, Faculty of Pharmacy, Medical University – Plovdiv, Plovdiv, Bulgaria.

² Department of Biochemistry and Microbiology, Faculty of Biology, University of Plovdiv “Paisii Hilendarski”, Plovdiv, Bulgaria.

³ Department of Botany and Teaching Methods in Biology, Faculty of Biology, University of Plovdiv “Paisii Hilendarski”, Plovdiv, Bulgaria

Received April 14, 2017; Revised June 07, 2017

Dedicated to Acad. Ivan Juchnovski on the occasion of his 80th birthday

In the current study for the first time were investigated the chemical composition and antioxidant activity of polysaccharides isolated from three indigenous for Bulgaria species of *Plantago* genus - *Plantago major* L., *Plantago lanceolata* L. and *Plantago media* L. Crude polysaccharides were extracted from fresh leaves with water and dilute acid and their yield was between 0.64% and 2.79%. The chemical composition of water-extractable polysaccharides (WEPs) and total acid-extractable polysaccharides (TAEPs) of *Plantago* leaves was evaluated by HPLC analysis. The phytochemical data revealed the presence of branched heteropolysaccharides with different neutral/acidic monosaccharide ratio. The predominant monosaccharide unit of WEPs was galacturonic acid (62.64% - 70.58%). Additionally, there were registered small amounts of arabinose and rhamnose. In TAEPs among with galacturonic acid (36.93% - 41.46%), significant amounts of neutral monosaccharides as galactose (22.80% - 46.11%) and rhamnose (16.96% - 35.74%) were determined. Two types of analyses were used to evaluate the antioxidant activity of *Plantago* isolated polysaccharides: DPPH and FRAP assay. Based on DPPH method, WEPs exhibited stronger radical scavenging ability (29.39% - 40.08%) compared to TAEPs (19.44% - 24.15%). In parallel, WEPs showed greater rate of ferric reducing power (103.71 - 137.83 $\mu\text{M TE}/5 \text{ mg Ps}$) compared to TAEPs (34.63 - 117.66 $\mu\text{M TE}/5 \text{ mg Ps}$). Although lower than synthetic BHT, *Plantago* polysaccharides revealed antioxidant potential and could be further explored as promising natural antioxidants for the nutraceutical and pharmaceutical industries.

Key words: *Plantago major* L.; *Plantago media* L.; *Plantago lanceolata* L.; polysaccharides; antioxidant activity

INTRODUCTION

Plantago genus includes herbaceous plant species used worldwide as a remedy for wound healing, inflammations, respiratory disorders and digestive system affections [1-3]. The European Pharmacopoeia has approved for medical uses the leaves from *Plantago lanceolata* and seeds from *P. ovata*, *P. afra* and *P. indica* [4], while *P. major* leaves have been included in World Health Organization Monographs [5]. Fifteen *Plantago* species are native to the Bulgarian flora. Among them *Plantago major* L., *Plantago media* L. and *Plantago lanceolata* L. are widespread in the country and traditionally used by local people [6]. *P. major* and *P. lanceolata* leaves have been known as a rich source of biologically active compounds

like polysaccharides, phenolic acids, flavonoids, iridoid glycosides and vitamins [1-5].

Plant polysaccharides have emerged as an important class of bioactive natural products and widely used in pharmaceuticals, biomaterials, food additives and nutrition [7]. They and their derivatives have been found to possess diverse biological activities, such as immunostimulatory, antiinflammatory, antiviral, antitumor, radioprotective, hepatoprotective and antifatigue effects [7,8]. In addition, many studies elucidate that polysaccharides isolated from plants have antioxidant activity [7,9].

According to European Medicines Agency [10] and Kardošová [3] from *P. lanceolata* leaves have been isolated pectic polysaccharides, rhamnogalacturonan, arabino-galactan and α -D-glucan. Samuelsen *et al.* [2,11] reported in *P. major* leaves the presence of an acidic arabinogalactan and highly esterified pectic polysaccharide,

* To whom all correspondence should be sent:
E-mail: paolina.lukova@gmail.com

composed mainly of arabinose, galactose, rhamnose and galacturonic acid. However, so far no thorough investigation about polysaccharide content of *P. media* leaves has been found in literature. Immunomodulatory and antimicrobial activity of *Plantago* leaves polysaccharides have been reported [2,12], but there is a lack of information about their antioxidant activity.

The aim of this study was to investigate the polysaccharide composition of three widely spread *Plantago* species in Bulgaria (*Plantago major* L., *Plantago media* L. and *Plantago lanceolata* L.) and to determine their antioxidant activity. The phytochemical analysis and antioxidant assessment provide useful information with regard to health promoting and functional quality of the studied medicinal plants.

EXPERIMENTAL

Materials and reagents

Plantago major and *Plantago lanceolata* mature leaves were collected from Thracian valley floristic region, Bulgaria (42°08'N, 24°44'E) and *Plantago media* leaves were collected from Rhodope Mountains floristic region, Bulgaria (41°75'N, 24°16'E), in the vegetative season of 2015. The botanical identification of plant species was carried out according to Tutin *et al.* [13] and Delipavlov and Cheshmedzhiev [6]. Assay kits of monosaccharides, galacturonic acid, bovine serum albumin, 2,2-diphenyl-2-picryl-hydrazyl-hydrate (DPPH), 2,4,6-tris(2-pyridyl)-s-triazine (TPTZ), butylated hydroxytoluene (BHT) were purchased from Sigma Aldrich, US. Arabinogalactan was purchased from Megazyme, Ireland. All other chemicals and solvents used in this study were of analytical grade.

Polysaccharide extraction

Alcohol-insoluble residues (AIR) from *Plantago* leaves were used for isolation of polysaccharides. The procedure was previously reported in our study [14]. Polysaccharides were extracted from AIR with water and dilute hydrochloric acid according to the methodology described by Kratchanova *et al.* [15] with slight modifications.

Determination of the total neutral sugars, uronic acids and protein

The content of total neutral sugars was determined with a colorimetric phenol-sulfuric acid method [16], using glucose (20 - 100 µg/mL) as a

reference standard. Uronic acid analysis followed the method of Blumenkrantz and Asboe-Hansen [17], calibrated against a standard of galacturonic acid (25 - 150 µg/mL). Protein content in the isolated polysaccharides was determined by Bradford method with a bovine serum albumin (0 - 100 µg/mL) as a standard [18].

TFA hydrolysis

The crude water and total acid-extractable polysaccharides (50 mg) were hydrolysed with 2 M trifluoroacetic acid (TFA) at 121°C for 1 h in an autoclave [19].

HPLC analysis

The hydrolysis products composition were determined with HPLC system Konik-Tech, with RI Detector Shodex R1-101 and Tracer Excel ODSB 120/5 µm (150 x 0.4 mm) column, mobile phase water, flow rate 0.1 mL/min and 0.3 mL/min, temperature 30°C. The registered peaks of the samples were evaluated using reference monosaccharide standards.

Determination of antioxidant activity

The 2, 2-diphenyl-2-picryl-hydrazyl-hydrate (DPPH) free radical scavenging activity was determined by using the method reported by Kao and Chen [20] with slight modifications. A 0.5 mM solution of DPPH in methanol was prepared and 0.2 mL of this solution was added to 1 mL of polysaccharide solutions (5 mg/mL). The radical scavenging activity was calculated by the following equation:

$$\% \text{ Inhibition} = \frac{AB - AA}{AB} \times 100$$

where AB was the absorption of the blank sample (t = 0 min) and AA - the absorption of the polysaccharide solution (t = 30 min) [21].

The ferric reducing antioxidant power (FRAP) was determined according to the method of Benzie and Strain [22] with some modifications. FRAP reagent (2.7 mL) was mixed with 0.3 mL of polysaccharide samples (5 mg/mL). The mixture was incubated at 37°C for 30 min in dark, and the absorbance was measured at 593 nm. The results were expressed as micromol Trolox equivalents (0 - 500 µM) per 5 mg polysaccharide (µM TE/5 mg Ps).

BHT (0.1 mg/mL) and arabinogalactan (ArG) (5 mg/mL) were used as controls. All data for antioxidant activity were expressed by triplicate measurements with standard deviation.

RESULTS AND DISCUSSION

Polysaccharide concentration, content of neutral sugars, uronic acids and proteins

The composition of the polysaccharides (Ps) isolated from the three studied *Plantago* species was presented in Table 1. The polysaccharide content after aqueous extraction was between 0.64% and 2.79%, with highest amount established in *P. media* leaves (2.79%). The highest concentration of polysaccharides in *P. major* leaves was detected by total acid extraction (2.47%), whereas the amount of the total-acid extractable polysaccharides in *P. media* and *P. lanceolata* were close-range: 1.46% and 1.22%, respectively. The obtained results correspond to these established by Olennikov *et al.* [23]. They have reported water-soluble polysaccharide content in *P. major* fresh leaves in the range between 1.5% and 3.3%. Kardošová has reported 1.5% concentration of crude water-extractable polysaccharide from *P. lanceolata* leaves per dry mass [3].

The concentration of the neutral sugars in total acid-extractable polysaccharides (TAEPs) in all samples showed twice higher content of neutral sugars (58.05% - 62.54%) compared to water-extractable polysaccharides (WEPs) (29.11% - 37.15%). These results could be attributed to acid hydrolysis of the bond linkages between polysaccharides and cell wall constituents in dilute hydrochloric acid [15, 24]. The water extraction on the other hand is assumed to be non-destructive [15, 24], which can explain the registered lower amount of neutral sugars in water-extractable fractions. The

amount of uronic acids was higher for WEPs (62.29% - 69.82%) compared to TAEPs (36.14% - 41.10%). The ratio between uronic acids and neutral sugars was 2:1 for WEPs and 1:1 for TAEPs. Similar ratio uronic acids to neutral sugars in consequently obtained water and acid-extractable polysaccharides from leek has been reported by Kratchanova *et al.* [15]. They have established 73.6% polyuronic content and 18.4% neutral sugars for WEPs and 27.5% polyuronic content and 71.1% neutral sugars for acid-extractable polysaccharides.

The protein content of all investigated samples was low (0.55% - 2.14%), which indicated a high purity of the extracted polysaccharides. Samuelsen *et al.* have reported protein content in WEPs from *P. major* leaves up to 1.8% [11], while Kardošová has determined significantly higher amount of protein content in *P. lanceolata* leaves WEPs (5.6%) [3].

Monosaccharide composition

HPLC profiles of the polysaccharide hydrolysis products have been shown in Fig. 1. Based on the monosaccharide analysis, WEPs from *P. major* and *P. lanceolata* leaves were found to be mainly composed of galacturonic acid (GalA) - from 62.64% to 70.58% (Table 2). The amount of detected arabinose (Ara) was from 37.36% to 29.42% and rhamnose (Rha) was registered only in traces (Fig. 1A, 1E). Olennikov *et al.* have also determined galacturonic acid as the main monomer in *P. major* water-soluble polysaccharides [23]. Samuelsen *et al.* have reported that in *P. major* leaves was present only galacturonic acid (39.0% - 71.7%) [11], while Kardošová has reported 35.8% galacturonic acid and 21.9% glucuronic acid in WEPs from *P. lanceolata* leaves [3].

Similarly to our results, Kardošová has determined in WEPs from *P. lanceolata* leaves

Table 1. Chemical composition of WEPs and TAEPs from *P. major*, *P. media* and *P. lanceolata* leaves.

Sample	Ps concentration ± SD (g/100 g fresh leaves)	Neutral sugars ± SD (%)	Uronic acid ± SD (%)	Protein ± SD (%)
<i>P. major</i> WEPs	1.84 ± 0.24	37.15 ± 0.28	62.29 ± 1.10	0.56 ± 0.02
<i>P. major</i> TAEPs	2.47 ± 0.26	61.72 ± 3.22	36.14 ± 1.62	2.14 ± 0.31
<i>P. media</i> WEPs	2.79 ± 0.19	34.88 ± 2.10	64.45 ± 2.08	0.67 ± 0.02
<i>P. media</i> TAEPs	1.46 ± 0.32	58.05 ± 1.54	41.10 ± 2.32	0.85 ± 0.05
<i>P. lanceolata</i> WEPs	0.64 ± 0.08	29.11 ± 0.88	69.82 ± 2.46	1.07 ± 0.12
<i>P. lanceolata</i> TAEPs	1.22 ± 0.11	62.54 ± 1.15	36.91 ± 0.77	0.55 ± 0.01

arabinose (26.0%) as main neutral monosaccharide [3], while Samuelsen *et al.* have reported almost equal amounts of arabinose (8.8% - 24%), galactose (8% - 34%) and xylose (11% - 22%) in different fractions of *P. major* WEPs [11].

The presented results suggested that *P. major* and *P. lanceolata* WEPs have been composed of ramified rhamnogalacturonan I (RG I), which main chain was constructed by GalA residues, rarely alternated with Rha units. The registered significant amount of Ara assumed arabinan type side chains, which branch points were the Rha units in RG I. The predominant monosaccharide components in *P. media* WEPs were GalA and Rha, with 1.86 GalA:Rha ratio. The results suggested the presence of more branched heteropolysaccharides, in which main chain every two residues of GalA were alternated with Rha. From HPLC profile of *P. media* WEPs a peak with a retention time of 10.74 min was observed, which probably corresponded to polysaccharide side chains with a degree of polymerization (DP) > 2 (Fig. 1C).

Galactose (Gal), GalA and Rha were the monosaccharide components determined in TAEPs of the three investigated *Plantago* species (Fig. 1B, 1D, 1F). The content of GalA was about 40% for all TAEPs (Table 2). The amount of Rha (35%) in

P. media TAEPs was twice higher compared to *P. major* and *P. lanceolata* TAEPs (17%). The results suggested the presence of RG I polysaccharide with galactan type side chains. *P. media* TAEPs with GalA:Rha ratio 1.16 resulted to be the polysaccharides with the most branched structure among all investigated samples.

Antioxidant activity

The use of more than one method is recommended to give a comprehensive prediction of antioxidant efficacy [25]. Two types of analyses were used to evaluate the antioxidant activity of *Plantago* leaves isolated polysaccharides: DPPH (measures the ability to scavenge free radicals) and FRAP assay (measures the ability to reduce Fe^{3+} to Fe^{2+} by donating an electron). In the present work we study for the first time the antioxidant activity of polysaccharides from *Plantago* leaves. The results from DPPH and FRAP assays were summarized in Table 3. Based on DPPH method, *Plantago* leaves WEPs showed stronger antioxidant activity (29.39% - 40.08%) compared to TAEPs (19.44% - 24.15%). These may be due to the higher content of galacturonic acid in WEPs.

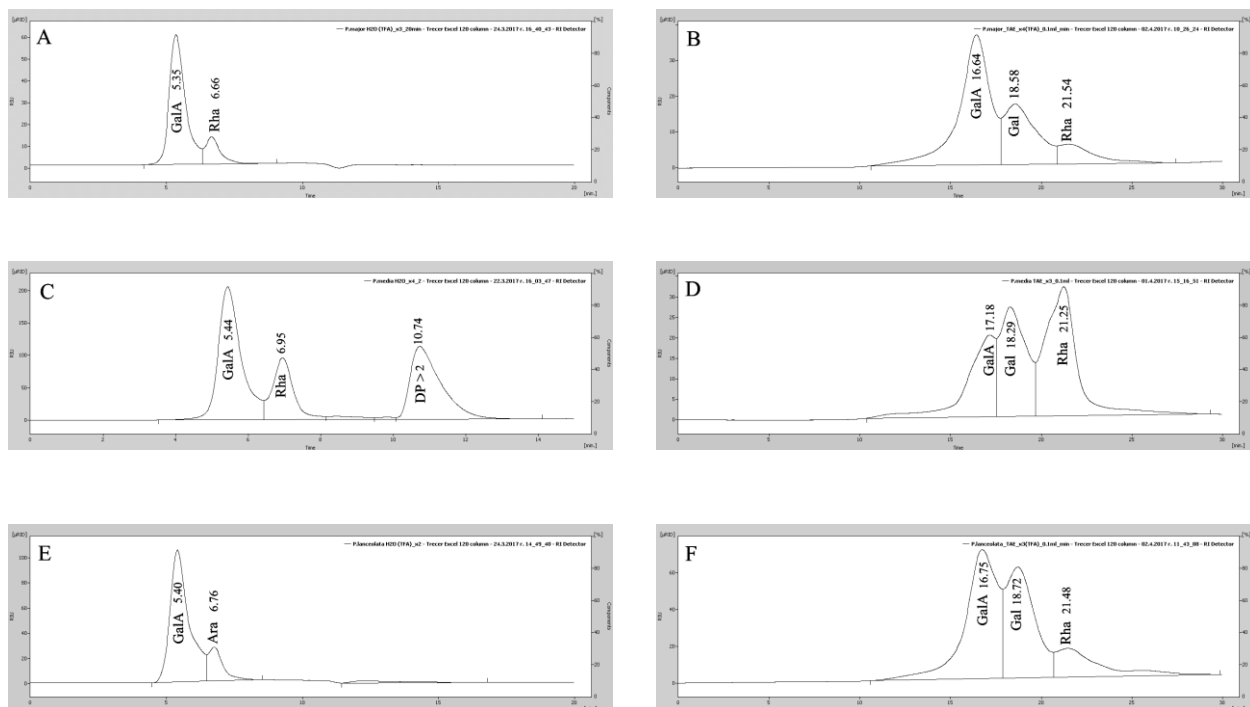


Fig.1. HPLC profiles of polysaccharide hydrolysis products: (A) *P. major* WEPs; (B) *P. major* TAEPs; (C) *P. media* WEPs; (D) *P. media* TAEPs; (E) *P. lanceolata* WEPs; (F) *P. lanceolata* TAEPs.

Table 2. Monosaccharide composition of WEPs and TAEPs from *P. major*, *P. media* and *P. lanceolata* leaves (expressed as % of the total carbohydrates).

Sample	Ara (%)	Rha (%)	Gal (%)	GalA (%)	GalA/Rha
<i>P. major</i> WEPs	37.36	traces	-	62.64	-
<i>P. major</i> TAEPs	-	16.96	46.11	36.93	2.18
<i>P. media</i> WEPs	-	35.12	-	64.88	1.85
<i>P. media</i> TAEPs	-	35.74	22.80	41.46	1.16
<i>P. lanceolata</i> WEPs	29.42	traces	-	70.58	-
<i>P. lanceolata</i> TAEPs	-	17.33	45.55	37.12	2.14

Uronic acids have been considered to be potent antioxidants, which is attributed to the fact that their carbonyl group, similarly to phenolic acids, was attached to a ring molecule [26]. Among the isolated polysaccharides, the most predominant one for its scavenging ability was *P. media* WEPs (40.08%). Arabinogalactan, used as a control, showed close-range scavenging ability (21.19%) to TAEPs (19.44% - 24.15%). The lower antioxidant capacity of TAEPs could be attributed to both the low amount of galacturonic acid and the significant galactose content. According to the investigation of Meng *et al.* [27] the galactose content did not correlated to the polysaccharide antioxidant activity. Our results were in accordance to the investigations of Wang *et al.* [28], who reported a better scavenging ability of different acidic polysaccharide fractions from *Lycium barbarum* L. fruit (52.5% - 84.9%) compared to neutral polysaccharides (38.1%).

In parallel, the same tendency was observed for the FRAP values of the investigated polysaccharides. WEPs exhibited greater rate of ferric reducing power (103.71 - 137.83 $\mu\text{M TE}/5 \text{ mg Ps}$) compared to TAEPs (34.63 - 117.66 $\mu\text{M TE}/5 \text{ mg Ps}$). *P. lanceolata* WEPs had the most pronounced ferric reducing power - 137.83 $\mu\text{M TE}/5 \text{ mg Ps}$, which was in accordance to the highest value of galacturonic acid (70.58%) in *P. lanceolata* WEPs among all isolated polysaccharides. In addition, FRAP values of arabinogalactan (56.28 $\mu\text{M TE}/5 \text{ mg ArG}$) were in close-range to those of TAEPs.

The antioxidant potential of *Plantago* polysaccharides was compared to the synthetic BHT (Table 3). Although the registered values by DPPH and FRAP methods were lower, still *Plantago* polysaccharides showed significant potential as natural antioxidants. In comparison Kardošová and Machová have investigated the effects of rhamnogalacturonan (RG), obtained from

P. lanceolata var. *libor* leaves, on inhibition of lipid peroxidation and reported 45.3% antioxidant activity for 0.227 mM RG [29]. A few data of antioxidant activities of *Plantago* seeds isolated polysaccharides have been reported.

Table 3. Assessment of antioxidant activity of *P. major*, *P. media* and *P. lanceolata* WEPs and TAEPs.

Sample	DPPH \pm SD (%)	FRAP \pm SD ($\mu\text{M TE}/5 \text{ mg Ps}$)
<i>P. major</i> WEPs	35.35 \pm 0.58	103.71 \pm 0.69
<i>P. major</i> TAEPs	19.44 \pm 0.87	34.63 \pm 0.23
<i>P. media</i> WEPs	40.08 \pm 1.75	132.40 \pm 2.11
<i>P. media</i> TAEPs	24.15 \pm 1.03	94.65 \pm 1.10
<i>P. lanceolata</i> WEPs	29.39 \pm 1.50	137.83 \pm 2.57
<i>P. lanceolata</i> TAEPs	24.07 \pm 0.75	117.66 \pm 0.98
<i>Controls:</i>		
Arabinogalactan (ArG)	21.19 \pm 0.13	56.28 \pm 0.15 $\mu\text{M TE}/5 \text{ mg ArG}$
BHT	93.49 \pm 0.06	556.10 \pm 0.09 $\mu\text{M TE}/0.1 \text{ mg BHT}$

Ye *et al.* [30] and Yin *et al.* [31] have investigated the possible antioxidant effect of the polysaccharides obtained from aqueous extracts of dried seeds from *P. asiatica*. According to Ye *et al.* DPPH radical scavenging activity of the investigated polysaccharide increased from 25.6% to 81.4%, when the concentration of the polysaccharides increased from 0.15 to 0.75 mg/mL [30]. On the other hand, Yin *et al.* reported 50.8% DPPH radical scavenging effects of *P. asiatica* seeds WEPs at a concentration of 1 mg/mL, which ability to scavenge free radicals did not increase at higher concentrations [31].

CONCLUSION

In the present study for the first time were investigated and quantified the polysaccharide composition and antioxidant activity of *P. major*,

P. media and *P. lanceolata* leaves from Bulgaria. The phytochemical data revealed the presence of branched heteropolysaccharides with uronic acids:neutral sugars ratio varying from 2:1 for WEPs to 1:1 for TAEPs. The WEPs from *Plantago* leaves were composed mainly from galacturonic acid and minor amounts of arabinose and rhamnose, while in TAEPs galacturonic acid, galactose and rhamnose were detected. Based on DPPH and FRAP methods, *Plantago* isolated polysaccharides showed significant antioxidant activity. Among the investigated polysaccharides *P. media* WEPs exhibited the strongest radical scavenging ability (40.08%) and *P. lanceolata* WEPs showed the greater ferric reducing power (137.83 μ M TE/5 mg Ps). According to the results stated above, it could be concluded that *P. major*, *P. media* and *P. lanceolata* leaves are promising natural sources of biologically active polysaccharides which can be developed as new antioxidants for applications in pharmaceutical and food industries.

Acknowledgements: The authors are grateful to Medical University – Plovdiv for the financial support through Project SDP – 03/2015.

REFERENCES

1. S. Gonçalves, A. Romano. *Ind. Crops Prod.*, **83**, 213 (2016).
2. A. B. Samuelsen, *J. Ethnopharmacol.*, **71**, 1 (2000).
3. A. Kardošová, *Chem. Pap.*, **46**, 127 (1992).
4. European Pharmacopoeia 8th edition, EDQM Council of Europe, Strasbourg, 2014.
5. World Health Organization monographs on medicinal plants commonly used in the Newly Independent States, WHO Press, Geneva, 2010.
6. D. Delipavlov, I. Cheshmedzhiev. Key to the plants in Bulgaria, Academic Publishing House of Agricultural University, Plovdiv, 2003.
7. J. Liu, S. Willför, C. Xu, *Bioact. Carbohydr. Diet. Fibre*, **5**, 31 (2015).
8. M. Jin, Q. Huang, K. Zhao, P. Shang, *Int. J. Biol. Macromol.* **54**, 16 (2013).
9. H.-L. Wang, W.-Y. Chen¹, P.-J. Tsai, C.-Y. Lin, Y.-T. Hsu¹, L.-F. Chen, W.-Z. Wu¹, W.-C. Wang, W.-J. Yang, C.-L. Chang, W.-T. Liao, *Am. J. Plant Sci.*, **7**, 780 (2016).
10. European Medicines Agency, Committee on Herbal Medicinal Products, EMA/HMPC/437858/2010, 2011.
11. A. B. Samuelsen, B. S. Paulsen, J. K. Wold, H. Otsuka, H. Yamada, T. Espevik, *Phytother. Res.*, **9**, 211 (1995).
12. G. Hetland, A. B. Samuelsen, M. Løvik, B. S. Paulsen, I. S. Aaeberge, E. C. Groeng, T. E. Michaelsen, *Scand. J. Immunol.*, **52**, 348 (2000).
13. T. G. Tutin, V. H. Heywood, N. A. Burges, D. H. Valentine (eds.), Flora Europaea. *Plantaginaceae to Compositae* (and *Rubiaceae*), vol. 4, Cambridge University Press, Cambridge, 1976.
14. P. K. Lukova, D. P. Karcheva-Bahchevanska, V. P. Bivolarski, R. D. Mladenov, I. N. Iliev, M. M. Nikolova, *Folia Medica*, **59**, DOI: 10.1515/folmed-2017-0023, (2017).
15. M. Kratchanova, M. Gocheva, E. Pavlova, I. Yanakieva, D. Nedelcheva, V. Kussovski, A. Slavov, *Bulg. Chem. Commun.*, **40**, 561 (2008).
16. M. DuBois, K. Gilles, J. Hamilton, P. Rebers, F. Smith, *Anal. Chem.*, **28**, 350 (1956).
17. N. Blumenkrantz, G. Asboe-Hansen, *Anal. Biochem.*, **54**, 484 (1973).
18. M. M. Bradford, *Anal. Biochem.*, **72**, 248 (1976).
19. X. Li, H. Liao, C. Fan, H. Hu, Y. Li, J. Li, Z. Yi, X. Cai, L. Peng, Y. Tu, *PLoS One*, **11**, e0160026 (2016).
20. T. H. Kao, B. H. Chen, *J. Agric. Food Chem.*, **54**, 7544 (2006).
21. A. Pallag, B. Paşca, T. Jurca, R. Suciuc, S. Nemeth, L. Vicaş, *Farmacia (Bucharest, Rom.)*, **64**, 372 (2016).
22. I. F. Benzie, J. J. Strain, *Anal. Biochem.*, **239**, 70 (1996).
23. D. N. Olennikov, L. M. Tankhaeva, A. B. Samuelsen, *Chem. Nat. Compd.*, **42**, 265 (2006).
24. H.-F. Tan, C.-Y. Gan, *Int. J. Biol. Macromol.*, **85**, 487 (2016).
25. I. D. Dyulgerova, I. Zhelev, D. Mihaylova, *Pharmacogn. Mag.*, **11**, 575 (2015).
26. J. Wang, S. Hu, S. Nie, Q. Yu, M. Xie, *Oxid. Med. Cell. Longevity*, **64**, 1 (2016).
27. L. Meng, S. Sun, R. Li, Z. Shen, P. Wang, X. Jiang, *Carbohydr. Polym.*, **117**, 452 (2015).
28. C. C. Wang, S. C. Chang, B. S. Inbaraj, B. H. Chen, *Food Chem.*, **120**, 184 (2010).
29. A. Kardošová, E. Machová, *Fitoterapia*, **77**, 367, (2006).
30. C.-L. Ye, W.-L. Hu, D.-H. Dai, *Int. J. Biol. Macromol.*, **49**, 466 (2011).
31. J.-Y. Yin, S.-P. Nie, C. Zhou, Y. Wan, M.-Y. Xie, *J. Sci. Food Agric.*, **90**, 210 (2010).

СРАВНЕНИЕ НА СТРУКТУРАТА И АНТИОКСИДАНТНАТА АКТИВНОСТ НА ПОЛИЗАХАРИДИ, ИЗОЛИРАНИ ОТ ЛИСТА НА *Plantago major* L., *P. media* L. И *P. lanceolata* L.

П. К. Лукова^{1*}, Д. П. Карчева-Бахчеванска¹, М. М. Николова², И. Н. Илиев²,
Р. Д. Младенов^{1,3}

¹ Катедра „Фармакогнозия и фармацевтична химия“, Фармацевтичен факултет, Медицински университет – Пловдив, Пловдив, България.

² Катедра „Биохимия и микробиология“, Биологически факултет, ПУ „Паисий Хилендарски“, Пловдив, България.

³ Катедра „Ботаника и методика на обучението по биология“, Биологически факултет, Пловдивски университет „Паисий Хилендарски“, Пловдив, България

Постъпила на 18 април 2017 г.; Коригирана на 2 юни 2017 г.

(Резюме)

В настоящата работа за пръв път са изследвани химичния състав и антиоксидантната активност на полизахариди, получени от *Plantago major* L., *Plantago media* L. и *Plantago lanceolata* L., растящи в България. Полизахаридите са изолирани от свежи листа посредством водна и киселинна екстракция, като получените добиви варират от 0.64% до 2.79%. Химичният състав на водно-екстрахируемите полизахариди (ВЕПЗ) и тотално киселинно-екстрахируемите полизахариди (ТКЕПЗ) е анализиран посредством високоефективна течна хроматография. Фитохимичният анализ показва наличие на разклонени хетерополизахариди с различно съотношение между неутрални и кисели захари. В състава на ВЕПЗ основна монозахаридна единица е галактуроновата киселина (62.64% - 70.58%). Доказани са ниски количества неутрални захари като арабиноза и рамноза. В състава на ТКЕПЗ наред с галактуроновата киселина (36.93% - 41.46%), са установени значителни количества неутрални монозахариди като галактоза (22.80% - 46.11%) и рамноза (16.96% - 35.74%). Антиоксидантната активност на изолираните полизахариди е установена посредством два метода: DPPH и FRAP анализ. Резултатите от DPPH определянето показваха, че ВЕПЗ притежават по-силна радикал-улавяща способност (29.39% - 40.08%) спрямо ТКЕПЗ (19.44% - 24.15%). Аналогични са данните за FRAP анализа: по-силна редуцираща способност при ВЕПЗ (103.71 - 137.83 $\mu\text{M TE}/5 \text{ mg ПЗ}$) в сравнение с ТКЕПЗ (34.63 - 117.66 $\mu\text{M TE}/5 \text{ mg ПЗ}$). Полизахаридите от род *Plantago* показват значителна антиоксидантна активност, въпреки пониските установени стойности спрямо синтетичния антиоксидант ВНТ. Получените данни за изолираните полизахариди биха могли да послужат като бъдеща перспектива за разработване на природни антиоксиданти за хранителната и фармацевтична промишленост.

Multi-analytical study on the wall paintings of Kurilo monastery “St. Ivan Rilski”, Bulgaria

E. Velcheva^{1*}, S. Tapanov², D. Yancheva¹, S. Stoyanov¹, B. Stamboliyska¹

¹ Institute of Organic Chemistry with Centre of Phytochemistry, Bulgarian Academy of Sciences, Acad. G. Bonchev Str., bl. 9, 1113 Sofia, Bulgaria

² National Academy of Art, Faculty of Applied Arts, 73 Tzarigradsko Shose Blvd, 1113 Sofia, Bulgaria

Received May 01, 2017; Revised June 26, 2017

Dedicated to Acad. Ivan Juchnovski on the occasion of his 80th birthday

This contribution describes the results obtained from the characterisation of wall paint materials from Kurilo Monastery “St. Ivan Rilski”, Bulgaria. Fourier Transform Infrared Spectroscopy (FTIR), Raman Spectroscopy (RS), Scanning Electron Microscopy coupled with Energy Dispersive X-ray Spectroscopy (SEM-EDS) and X-Ray Powder Diffraction (XRD) were used for the inorganic content determination. Organic materials in the paint samples were analysed based on Attenuated Total Reflectance (ATR) IR spectra. Via these complementary techniques and by the help of our spectral database, containing local reference materials, we were able to identify the mineral pigments and organic binders in the paint samples.

Key words: Kurilo monastery; pigments; Raman; ATR-IR; SEM-EDX; XRD

INTRODUCTION

Kurilo monastery is situated on the slopes of the Balkan Mountains, 15 km northwest of Sofia. It is one of the monasteries that have remained from the monastic network called “Mala Sveta Gora” (Holy Mount of Sofia) surrounding the city. Founded in the Middle Ages, it was several times destroyed and rebuilt [1,2].

The present monastery church was built in the end of the 16th century and painted in 1596. The restoration and wall painting of the monastery is related to the work of the Bulgarian missionary and enlightener Saint Pimen Zografski [3,4]. Inspired by the idea to awake and strengthen the Bulgarian national consciousness, he has left his solitary confinement at Mount Athos and returned to his homeland to start a broad activity of restoration, building and painting of more than 300 churches and monasteries. Having learnt the icon painting in his youth, Saint Pimen Zografski taught dozens of painters who later became his disciples in the noble work of Bulgarian spirit revival. In this way Saint Pimen Zografski established the first painting school in Bulgarian lands. It accommodated not only painters, but also writers of religious books, teaching the future priests. Regrettably nowadays the enormous contribution of this great Bulgarian cleric is nearly forgotten. Many of the preserved

churches are abandoned in bad condition and need urgent restoration.

There are only limited research on the painting techniques, technology and materials used by the school of Saint Pimen Zografski so far. Therefore a systematic and comprehensive study is necessary in order to identify the color palette – specific pigments, binders and painting techniques in the different churches associated with the school.

The present study is reporting on the pigments and binders used in the wall paintings of Kurilo monastery church (Fig. 1) and will contribute to the characterization of post-Byzantine wall painting in the end of the 16th and the beginning of the 17th century, as well as to acknowledge the great work of St. Pimen Zografski.

Molecular and structural information on the mineral pigments and organic materials is provided by combined Fourier Transform Infrared Spectroscopy (FTIR), Raman Spectroscopy (RS), Scanning Electron Microscopy coupled with Energy Dispersive X-ray Spectroscopy (SEM-EDS) and X-Ray Powder Diffraction (XRD) methods. FTIR and Raman spectroscopies are widely employed in the identification of art and archaeological materials [5-10]. For the complete characterization of the objects, the spectral analysis was complemented with other analytical techniques, such as Scanning Electron Microscopy coupled with Energy Dispersive X-ray

* To whom all correspondence should be sent:
E-mail: ev@orgchm.bas.bg

Spectroscopy (SEM-EDS) and X-Ray Powder Diffraction (XRD).

EXPERIMENTAL

Representative samples were collected from the mural paintings as shown in Figure 2. A brief description of the samples is given in Table 1.

The ATR-FTIR spectra were measured on a Bruker Tensor 27 FT spectrometer by direct deposition on a diamond ATR crystal, by 64 scans at resolution of 2 cm^{-1} in the middle IR region ($600\text{--}4000\text{ cm}^{-1}$).

The Raman spectra were obtained using a LabRAM HR Visible (Horiba Jobin- Yvon) Raman spectrometer. The spectra were collected in the wavenumber range $100 - 4000\text{ cm}^{-1}$ with an integration time of 0.5s and by accumulation of 200 scans for every sample. An objective X50 was used both to focus the incident laser beam onto the sample surface into a spot with a diameter about $2\mu\text{m}$ and to collect the scattered light. The used excitation was He-Ne 633 nm laser line. The laser power on the surface was varied from 0.3 to 10 mW.

Scanning electron microscopy (SEM) of the samples were conducted on JSM 6390 electron microscope (Japan) in conjunction with energy dispersive X-ray spectroscopy (EDS, Oxford INCA Energy 350) in regimes of secondary electron image (SEI) and Backscattered Electron contrast

(BEC). The accelerating voltage was 20 kV, I ~65 mA and the pressure was of the order of 10^{-4} Pa .

Powder X-ray diffraction patterns were collected within the range from 5.3 to $80^\circ 2\theta$ with a constant step $0.02^\circ 2\theta$ on Bruker D8 Advance diffractometer with Cu $K\alpha$ radiation and LynxEye detector. Phase identification was performed with the Diffracplus EVA using ICDD-PDF2 Database.

RESULTS AND DISCUSSION

Pigments identification

The identification of painting materials is considerably facilitated by the use of an appropriate spectral database, especially when spectra from real samples are provided along with the reference materials. For this purpose, we have supported the spectral analysis by comparison with FTIR and Raman spectra from our recently developed spectral database of art and archaeological materials [11]. The database provides information on a number of pigments and dyes, adhesives, oils, resins, gums, bulk components, fillers, mixed materials, as well as archaeological and art work samples [11].

Table 1 shows the identified pigments in the different samples. Selected ATR-FTIR and Raman spectra are illustrated below in Figures 3-6. SEM-EDX and XRD analysis of selected samples are provided in the Supplementary materials.



Fig. 1(a-c). Some of the scenes on the wall paintings in the Kurilo monastery church: Kiss of Judas (a); Saint Malahya (b); and the Last Supper (c).

For references to color in this figure, the reader is referred to the web version of this article.



Fig. 2. . Diagram showing the locations of the samples collected for analysis

Table 1. List of studied samples, elemental analysis and identified pigments

Sample ID	Color	Elemental analysis (EDX)	Pigments
K1	green	Mg, Al, Si, S, K, Ca, Fe	celadonite, goethite, calcite, gypsum
K2	red	Na, Mg, Al, Si, S, K, Ca, Fe, Hg	cinnabar, calcite, gypsum
K3	brown	Mg, Al, Si, S, K, Ca, Fe, Cu, Pb	goethite, plumbojarosite, calcite, dolomite, quartz
K4	red	Mg, Al, Si, S, K, Ca, Fe, Hg	cinnabar, calcite, hematite, gypsum, kaolinite
K5	black	Na, Mg, Al, Si, S, K, Ca, Ti	carbon black, calcite, monohydrocalcite, weddellite, whewellite, quartz
K6	yellow orange	Mg, Al, Si, S, K, Ca, Fe, Zn, Pb	goethite, hematite, massicot, calcite, bassanite
K7	red	Mg, Al, Si, S, K, Ca, Ti, Fe, Pb, Hg	cinnabar, calcite, gypsum, kaolinite, muscovite
K8	brown	Na, Mg, Al, Si, S, Cl, K, Ca, Cr, Fe, Ni	hematite, calcite, gypsum, quartz, talc, halloysite
K9	green	Mg, Al, Si, K, Ca, Ti, Fe	celadonite, calcite, quartz
K10	white	Mg, Al, Si, K, Ca, Fe, Pb	calcite, gypsum, quartz
K11	Gold lead adhesive	Mg, Al, Si, S, K, Ca, Fe, Pb	drying oil mixed with Pb-containing drier and colophony

Red pigments used in the wall paintings are red ochre, cinnabar and red lead. Hg was detected by the EDX analysis in all the red samples. In accordance with this, XRD analysis showed the presence of cinnabar in the three samples, along

with hematite in sample K4 and silicate minerals in samples K4 and K7 (Table 1, Figs 1S and 2S in Supplementary materials). Identification of cinnabar was supported by Raman spectroscopy – the pigment gave characteristic peaks at 346, 288

and 256 cm^{-1} matching with those of the reference cinnabar (Fig. 3). In sample K7 red lead is also present as evidenced by the elemental analysis.

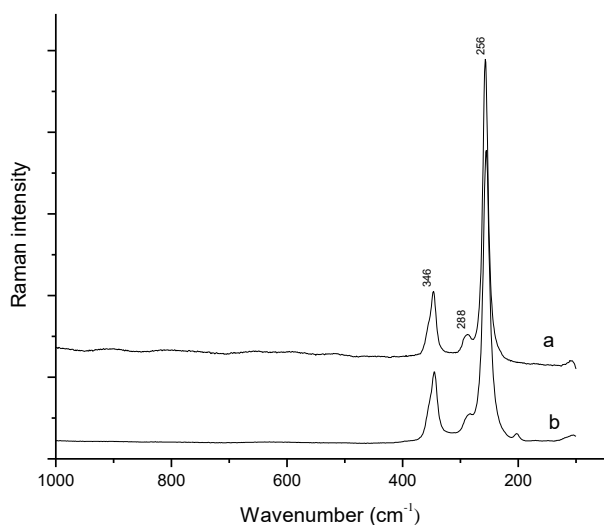


Fig. 3. Raman spectra of sample K2 (a) and reference cinnabar (b); 633 nm excitation, wavenumber range $100\text{--}4000\text{ cm}^{-1}$.

The green colors are achieved by the use of green earth containing the green mineral celadonite, a hydrated silicate of iron and magnesium, as can be seen by the EDX and XRD analysis of samples K1 and K9. In addition, K1 contains goethite. Both samples gave strong fluorescence which did not allow characterization by Raman spectroscopy, but ATR-IR measurements provided good coincidence with reference green earths (Fig. 4).

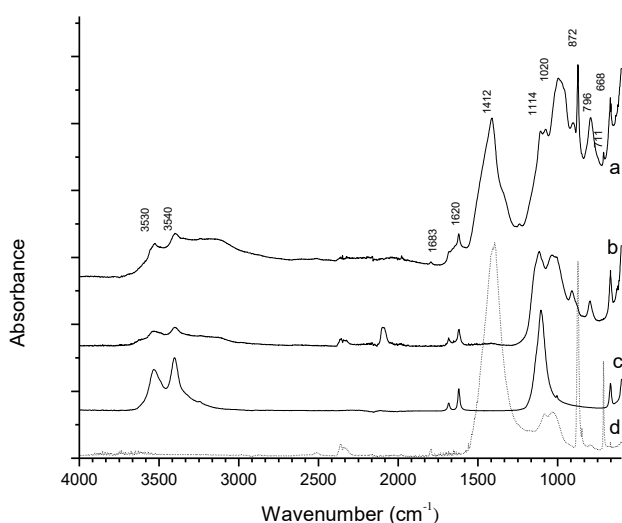


Fig. 4. ATR-IR spectra of sample K1 (a), reference green earth (b), reference gypsum (c), reference calcite (d); wavenumber range $600\text{--}4000\text{ cm}^{-1}$.

Brown color pigments were identified as natural ochres by the simultaneous presence of minerals goethite, plumbojarosite (in sample K3), hematite (in sample K8) and silicate minerals (in both samples) evidenced by the XRD and ATR-IR analysis. The ATR-IR spectra of K3 along with reference goethite and calcite are presented in Fig. 5. Characteristic absorption peaks of goethite are well seen at 896 and 796 cm^{-1} .

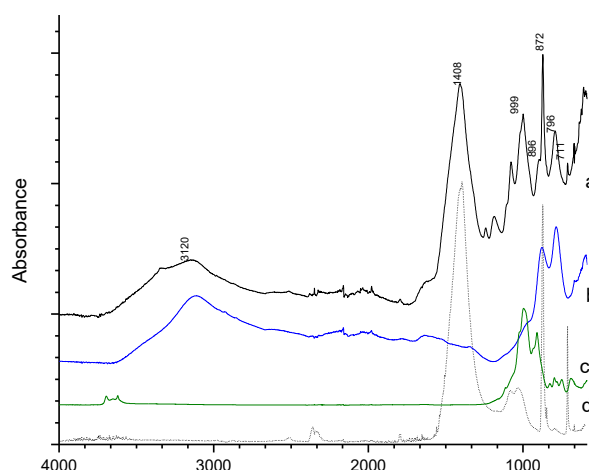


Fig. 5. ATR-IR spectra of sample K3 (a), reference goethite (b), reference kaolinite (c) and reference calcite (d); wavenumber range $600\text{--}4000\text{ cm}^{-1}$.

Yellow color sample showed more complex composition. The presence of yellow ochre was conferred by XRD identification of goethite and hematite and characteristic absorption of silicate minerals revealed by the ATR-IR spectrum. In addition, the elemental analysis showed Pb content, supported by XRD identification of massicot (Fig. 3S in Suppl. material). Evidently the painter has applied a mixture of yellow ochre and massicot in order to achieve the desired color hue.

The black color pigment showed two broad peaks around 1600 and 1360 cm^{-1} in the Raman spectrum as characteristic for carbon based pigments. The XRD analysis showed the presence of calcite, monhydrocalcite, weddellite, whewellite and quartz. The ATR spectrum of the sample gave a good match with those of reference bister pigment, beech wood soot (Fig. 6). This pigment has been made by carbonizing beech wood and it produces a dark greyish brown color rather than true black. However considering the black color of sample K5, it was concluded that the painter has used a mixture of soot pigments.

Calcite and white lead are the pigments used for the white areas. The EDX analysis of sample K10 showed Mg, Al, Si, K, Ca, Fe and Pb content (Fig. 4S in Suppl. material).

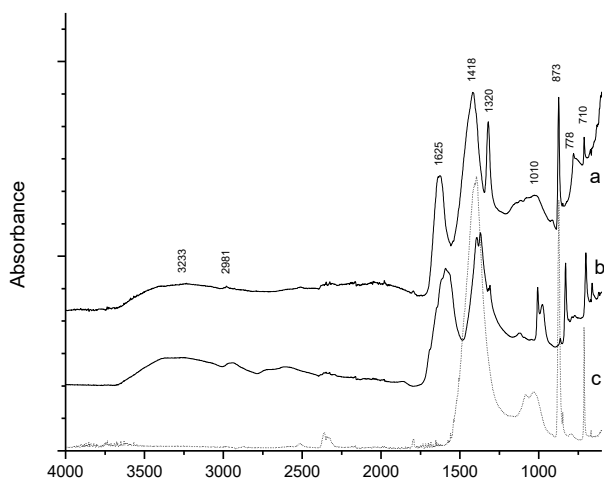


Fig. 6. ATR-IR spectra of sample K5 (a), reference bister (b) and reference calcite (c); wavenumber range 600-4000 cm^{-1} .

Identification of organic materials

Paint binder was identified by the ATR-IR spectra of samples K4 and K6 as egg. In the region 3000-2800 cm^{-1} three bands of weak intensity appeared accompanied by a very weak band around 1740 cm^{-1} (attributed to lipid carbonyl vibrations) and a weak broader band around 1640 cm^{-1} (attributed to protein amide vibrations).

The ATR spectrum of the gold leaf adhesive material (sample K11) provided several strong bands for calcite - at 1412, 873, 711 cm^{-1} , along with less intensive bands in the region 3000-2800 cm^{-1} and around 1730 and 1680 cm^{-1} (Fig. 5). According to the SEM-EDX analysis the elemental composition of the adhesive material consisted of C, O, Mg, Al, Si, S, K, Ca, Fe, Pb.

In order to identify the organic content, the sample was extracted with chloroform solvent. The concentrated extract provided an ATR-FTIR spectrum (Fig. 5b) which shows a close resemblance to a sample of drying oil obtained from the Church "The Nativity of the Virgin" of Rila monastery and reference colophony resin. The absorptions in the region 2950-2830 cm^{-1} are characteristic for C-H stretching vibrations. Several strong bands were found between 1800 and 1700 cm^{-1} . The first of them, at 1727 is assigned to the carbonyl stretching vibration of drying oil, while the other should be attributed to the resin. The position of the shoulder at 1695 is indication that the resin is from the diterpene type, presumably colophony. The presence of Pb in the sample is evidence that the drying of oil was induced by the Pb siccative. Therefore, it was concluded that the

adhesive material was made by a mixture of drying oil and diterpene resin with Pb siccative.

The chemical composition of adhesive material is discussed recently in the other studies on the gilding technique in post-Byzantine wall paintings [12, 13]. The authors have found that the gold leaf was adhered to the paintings by means of a mordant containing linseed oil with a lead-based dryer and an earth pigment or clay.

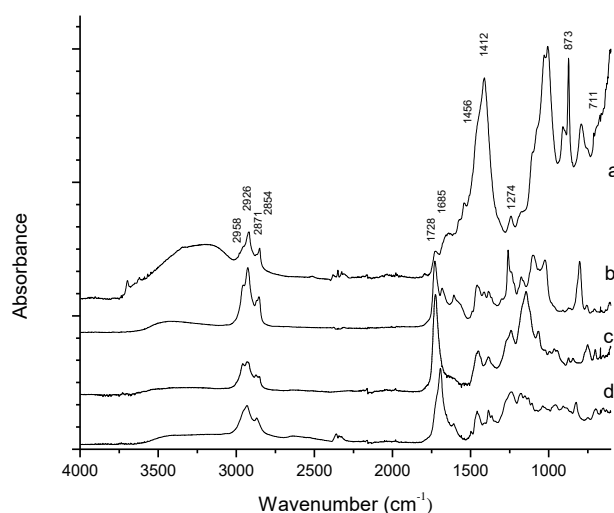


Fig. 7. ATR-IR spectra of sample K11 (a), chloroform extract of sample K11 (b); drying oil from Rila monastery (c), reference colophony (rosin) (d); wavenumber range 600-4000 cm^{-1} .

CONCLUSION

Combined IR, XRF, HR-TEM and XRD analysis showed that the colour palette comprises in natural pigments and synthetic pigments. Green earths containing celadonite and goethite were used as green pigments. Red colored paint samples showed cinnabar, red ochre and red lead content. Yellow and brown colors are based on natural ochre pigments. Calcite and lead white were present in white paint. Extraction by various organic solvents and ATR-IR spectral analysis enabled the identification of adhesive material as made by a mixture of drying oil and diterpene resin with Pb siccative. The desirable color hues were produced by applying mixtures of several pigments. In all cases, egg was used as organic binder. The provided useful information on the pigments, organic binders and fillers indicate that the technique of egg tempera painting was employed.

Acknowledgements: The authors are grateful for financial support by the National Science Fund of Bulgaria (Contract K02-15).

Electronic Supplementary Data available here

REFERENCES

1. V. Pandurski, The Kurilovo Monastery (in Bulg.). Bulgarian Artist Publishing House, Sofia, 1975.
2. L. Prashkov, E. Bakalova, S. Boyadjiev, Monasteries in Bulgaria (in Bulg.), Spectrum Publishing House, Sofia, 1992.
3. P. Dinekov, *Izv. Inst. Bulg. Lit.*, **2**, 233 (1954).
4. Lives of the Saints (in Bulg.), Synodal Publishing House, Sofia, 1991.
5. E. M. A. Ali, H. G. M. Edwards, *Spectrochim. Acta Part A*, **121**, (2014).
6. G. Bitossi, R. Giorgi, M. Mauro, B. Salvadori, L. Dei, *Appl. Spectrosc. Rev.*, **40**, 187, (2005).
7. L. Burgio, R. J. H. Clark, *Spectrochim. Acta Part A*, **57**, 1491 (2001).
8. K. Castro, A. Sarmiento, E. Princi, M. Perez-Alonso, M. D. Rodriguez-Laso, S. Vicini, J. M. Madariaga, E. Pedemonte, *Trends Anal. Chem.*, **26**, 347 (2007).
9. C. Daher, C. Paris, A.-S. Le Ho, L. Bellot-Gurlet, J.-P. Echard, *J. Raman Spectrosc.*, **41**, 1204 (2010).
10. M. R., Derrick, D. C. Stulik, J. M., Landry, *Infrared Spectroscopy in Conservation Science. Scientific Tools for Conservation*. Los Angeles, CA: Getty Conservation Institute, 1999.
11. Z. I. Glavcheva, D. Y. Yancheva, Y. K. Kancheva, E. A. Velcheva, B. A. Stamboliyska, *Bulg. Chem. Commun.*, **46** Special Issue A, **164** (2014).
12. O. Katsibiri, J. J. Boon, *Spectrochim. Acta B*, **59**, 1593 (2004).
13. O. Katsibiri, R. F. Howe, *Microchem. J.*, **94**, 83, 2010.

КОМБИНИРАНО АНАЛИТИЧНО ИЗСЛЕДВАНЕ НА СТЕНОПИСИТЕ ОТ КУРИЛСКИЯ МАНАСТИР "СВ. ИВАН РИЛСКИ"

Е. Велчева^{1*}, С. Тъпанов², Д. Янчева¹, С. Стоянов¹, Б. Стамболийска¹

¹ *Институт по органична химия с център по фитохимия, Българска академия на науките, ул. „Акад. Г. Бончев”, бл.9, 1113 София*

² *Национална художествена академия, ул. „Цариградско шосе” 73, София 1113*

Постъпила на 01 май 2017 г.; Коригирана на 26 юни 2017 г.

(Резюме)

Това изследване представя резултатите, получени при охарактеризирането на художествените материали, използвани за изографисването на Курилския манастир "Св. Иван Рилски", България. За определяне на неорганичните пигменти бяха използвани инфрачервена спектроскопия (FTIR), Раманова спектроскопия, сканираща електронна микроскопия (SEM-EDS) и рентгенова прахова дифракция (XRD). Органичните материали в пробите бяха анализирани въз основа на отражателни инфрачервени спектри (ATR). Чрез тези допълващи се техники и с помощта на нашата спектрална база данни, съдържаща местни референтни материали, ние успяхме да идентифицираме минералните пигменти и органичните свързващи вещества в пробите.

BULGARIAN CHEMICAL COMMUNICATIONS

Instructions about Preparation of Manuscripts

General remarks: Manuscripts are submitted in English by e-mail or by mail (in duplicate). The text must be typed double-spaced, on A4 format paper using Times New Roman font size 12, normal character spacing. The manuscript should not exceed 15 pages (about 3500 words), including photographs, tables, drawings, formulae, etc. Authors are requested to use margins of 3 cm on all sides. For mail submission hard copies, made by a clearly legible duplication process, are requested. Manuscripts should be subdivided into labelled sections, e.g. **Introduction, Experimental, Results and Discussion, etc.**

The title page comprises headline, author's names and affiliations, abstract and key words.

Attention is drawn to the following:

a) **The title** of the manuscript should reflect concisely the purpose and findings of the work. Abbreviations, symbols, chemical formulas, references and footnotes should be avoided. If indispensable, abbreviations and formulas should be given in parentheses immediately after the respective full form.

b) **The author's** first and middle name initials, and family name in full should be given, followed by the address (or addresses) of the contributing laboratory (laboratories). **The affiliation** of the author(s) should be listed in detail (no abbreviations!). The author to whom correspondence and/or inquiries should be sent should be indicated by asterisk (*).

The abstract should be self-explanatory and intelligible without any references to the text and containing not more than 250 words. It should be followed by key words (not more than six).

References should be numbered sequentially in the order, in which they are cited in the text. The numbers in the text should be enclosed in brackets [2], [5, 6], [9–12], etc., set on the text line. References, typed with double spacing, are to be listed in numerical order on a separate sheet. All references are to be given in Latin letters. The names of the authors are given without inversion. Titles of journals must be abbreviated according to Chemical Abstracts and given in italics, the volume is typed in bold, the initial page is given and the year in parentheses. Attention is drawn to the following conventions:

a) The names of all authors of a certain publications should be given. The use of "*et al.*" in the list of references is not acceptable.

b) Only the initials of the first and middle names should be given.

In the manuscripts, the reference to author(s) of cited works should be made without giving initials, e.g. "Bush and Smith [7] pioneered...". If the reference carries the names of three or more authors it should be quoted as "Bush *et al.* [7]", if Bush is the first author, or as "Bush and co-workers [7]", if Bush is the senior author.

Footnotes should be reduced to a minimum. Each footnote should be typed double-spaced at the bottom of the page, on which its subject is first mentioned.

Tables are numbered with Arabic numerals on the left-hand top. Each table should be referred to in the text. Column headings should be as short as possible but they must define units unambiguously. The units are to be separated from the preceding symbols by a comma or brackets.

Note: The following format should be used when figures, equations, *etc.* are referred to the text (followed by the respective numbers): Fig., Eqns., Table, Scheme.

Schemes and figures. Each manuscript (hard copy) should contain or be accompanied by the respective illustrative material as well as by the respective figure captions in a separate file (sheet). As far as presentation of units is concerned, SI units are to be used. However, some non-SI units are also acceptable, such as °C, ml, l, etc.

The author(s) name(s), the title of the manuscript, the number of drawings, photographs, diagrams, etc., should be written in black pencil on the back of the illustrative material (hard copies) in accordance with the list enclosed. Avoid using more than 6 (12 for reviews, respectively) figures in the manuscript. Since most of the illustrative materials are to be presented as 8-cm wide pictures, attention should be paid that all axis titles, numerals, legend(s) and texts are legible.

The authors are asked to submit **the final text** (after the manuscript has been accepted for publication) in electronic form either by e-mail or

mail on a 3.5" diskette (CD) using a PC Word-processor. The main text, list of references, tables and figure captions should be saved in separate files (as *.rtf or *.doc) with clearly identifiable file names. It is essential that the name and version of the word-processing program and the format of the text files is clearly indicated. It is recommended that the pictures are presented in *.tif, *.jpg, *.cdr or *.bmp format, the equations are written using "Equation Editor" and chemical reaction schemes are written using ISIS Draw or ChemDraw programme.

The authors are required to submit the final text with a list of three individuals and their e-mail addresses that can be considered by the Editors as potential reviewers. Please, note that the reviewers should be outside the authors' own institution or organization. The Editorial Board of the journal is not obliged to accept these proposals.

EXAMPLES FOR PRESENTATION OF REFERENCES

REFERENCES

1. D. S. Newsome, *Catal. Rev.–Sci. Eng.*, **21**, 275 (1980).
2. C.-H. Lin, C.-Y. Hsu, *J. Chem. Soc. Chem. Commun.*, 1479 (1992).
3. R. G. Parr, W. Yang, *Density Functional Theory of Atoms and Molecules*, Oxford Univ. Press, New York, 1989.
4. V. Ponec, G. C. Bond, *Catalysis by Metals and Alloys* (Stud. Surf. Sci. Catal., vol. 95), Elsevier, Amsterdam, 1995.
5. G. Kadinov, S. Todorova, A. Palazov, in: *New Frontiers in Catalysis* (Proc. 10th Int. Congr. Catal., Budapest, 1992), L. Guzzi, F. Solymosi, P. Tetenyi (eds.), Akademiai Kiado, Budapest, 1993, Part C, p. 2817.
6. G. L. C. Maire, F. Garin, in: *Catalysis. Science and Technology*, J. R. Anderson, M. Boudart (eds), vol. 6, Springer-Verlag, Berlin, 1984, p. 161.
7. D. Pocknell, *GB Patent 2 207 355* (1949).
8. G. Angelov, PhD Thesis, UCTM, Sofia, 2001.
9. JCPDS International Center for Diffraction Data, *Power Diffraction File*, Swarthmore, PA, 1991.
10. *CA* **127**, 184 762q (1998).
11. P. Hou, H. Wise, *J. Catal.*, in press.
12. M. Sinev, private communication.
13. <http://www.chemweb.com/alchem/articles/1051611477211.html>.

CONTENTS

G. Andreev, Scientific biography of Academician Ivan Juchnovski.....	5
V. Nikolova, D. Cheshmedzhieva, S. Ilieva, B. Galabov, Hydrogen bonding reactivities of atomic sites in the nucleobases	8
S. H. Tsoneva, S. R. Nachkova, G. N. Andreev, P. N. Penchev, Identification of mixture components by multiple linear regression and subtraction of reference spectra: searching infrared and raman libraries	19
A. D. Kosateva, M. Stefanova, S. P. Marinov, L. Gonsalvesh, Organic components in leachates from some Bulgarian lignites	25
K. L. Zaharieva, K. I. Milenova, S. V. Vassilev, S. S. Dimova, I. D. Stambolova, V. N. Blaskov, Preparation and comparative photocatalytic study of NiMnO ₃ /Mn ₂ O ₃ and NiO _{0.8} ZnO _{0.2} /ZnO materials for the removal of Malachite Green dye from aqueous solution.....	30
K. I. Milenova, I. A. Avramova, P. M. Nikolov, Comparison of photocatalytic behaviour under UV-light of PdO-CeO ₂ /Al ₂ O ₃ and PdO-CeO ₂ /ZSM5 for degradation of organic dyes.....	35
T. S. Tsoncheva, G. S. Issa, R. N. Ivanova, M. D. Dimitrov, I. P. Spassova, D. G. Kovatcheva, B. G. Tsyntsarski, N. V. Petrov, Activated carbon from waste biomass as host matrix of binary copper and manganese oxide catalysts for methanol decomposition	41
G. Genova, T. S. Tsoncheva, Silica supported copper and cobalt binary oxides as catalysts for methanol decomposition: Effect of preparation procedure	49
G. S. Issa, T. S. Tsoncheva, A. N. Mileva, M. D. Dimitrov, D. G. Kovacheva, J. Henych, V. Štengl, Copper supported on nanostructured mesoporous ceria-titania composites as catalysts for sustainable environmental protection: Effect of support composition	55
E. Cherneva, Ts. Kolev, Diamides of squaric acid containing methioninamide fragment – synthesis, spectral and theoretical investigation	63
N. Petkova, I. Ivanov, D. Mihaylova, A. Krastanov, Phenolic acids content and antioxidant capacity of commercially available <i>Melissa officinalis</i> L. teas in Bulgaria	69
L. Gonsalvesh, M. Dimov, S. P. Marinov, Production of adsorbents from "End of Life" tyres and characterization of their porous structure	75
M. Guncheva, D. Yancheva, V. Uzunova, P. Ossowicz, K. Idakieva, Y. Raynova, E. Janus, R. Tzoneva, Structural destabilization and enhanced cytotoxicity on murine fibroblasts of <i>Helix pomatia</i> β-hemocyanin in presence of four cholinium amino acids.....	82
Y. Raynova, S. Todinova, K. Idakieva, Modification with sodium periodate increases the structural stability of molluscan hemocyanins	87
R. N. Ivanova, M. D. Dimitrov, D. G. Kovatcheva, T. S. Tsoncheva, Copper and/or cobalt modified nanostructured Ce-Zr mixed oxides as efficient catalysts for ethyl acetate total oxidation	92
B. Stamboliyska, A. Jashari, D. Yancheva, B. Mikhova, D. Batovska, E. Popovski, K. Mladenovska, Structure and radical scavenging activity of isoxazolo- and thiazolohydrazinylidene-chroman-2,4-diones.	99
R. H. Lyapchev, M. G. Dangalov, G. G. Gencheva, N. G. Vassilev, P. Y. Petrov, Atropisomeric phosphorus-decorated 1-phenyl-3,4-dihydroquinazolin-1-ium NHC precursors.....	106
L. Gonsalvesh, A. Popova, S. P. Marinov, M. Stefanova, R. Carleer, J. Yperman, The effect of demineralisation on characteristics and adsorption behaviour of activated carbons prepared from swine manure.....	113
V. Trifonova, K. Vassilev, A. Ahmedova Metallodendrimers for catalytic epoxidation – theoretical insights into structure of Mo (VI) complexes of poly(propylene imine) dendrimers.....	121
A. Yordanova, S. Simova, I. Koseva, R. Nikolova, V. Nikolov, R. Stoyanova, Aluminium-scandium tungstates solid solutions Al _{2-x} Sc _x (WO ₄) ₃ : Al and Sc distribution on a local scale.....	129
E. Velcheva, B. Stamboliyska, S. Stoyanov, Experimental and DFT studies on the IR spectra and structure of 4-acetamidobenzoic acid (acedoben), its oxyanion and dianion.....	137
M. N. Marinov, S. M. Bakalova, R. Y. Prodanova, N. V. Markova, Conformational and spectral properties of newly synthesized compounds obtained by reaction of alrestatin with 3-aminocycloalkanespiro-5-hydantoin.....	146
B. I. Nikolova-Mladenova, L. P. Peikova, M. B. Georgieva, Al. B. Zlatkov, Application of a RP-HPLC method for determination of chemical and physiological stability of two newly synthesized methoxy-benzoylhydrazone derivatives.....	153
B. I. Nikolova-Mladenova, A. G. Bakalova, <i>In silico</i> drug likeness and <i>in vitro</i> cytotoxic activity of some 3,5-disubstituted hydantoin and spirohydantoin.....	159
E. Cherneva, R. T. Buyukliev, N. Burdzhiev, R. Michailova, A. G. Bakalova, Synthesis, physico-chemical investigation, DFT calculations and cytotoxic activity of palladium complexes with 3'-amino-4-thio-1H-tetrahydropyranspiro-5'-hydantoin.....	164
M. Popova, D. Antonova, V. Bankova, Chemical composition of propolis and American foulbrood: Is there any relationship?.....	171

A. Trendafilova, M. Todorova, V. Ivanova, I. Aneva, Phenolic constituents and antioxidant capacity of <i>Inula oculus-christi</i> from Bulgaria.....	176
S. Stoyanov, D. Yancheva, A. Kosateva, IR study on the electrochemical reduction of nimesulide.....	181
V. Nikolova, S. Angelova, T. Dudev, IIA/IIB group metal cations hosted by β -cyclodextrin: a DFT study.....	189
S. M. Bakalova, J. Kaneti, N. Markova, Computational study of exo-selective Diels-Alder cycloadditions, catalyzed by aluminum chloride.....	195
N. V. Georgieva, Z. L. Yaneva ¹ , S. D. Simova, G. D. Nikolova, Synthesis and properties of several Betti bases as potential drugs.....	201
V. Kurteva, A. Trendafilova, S. Simova, Chemical profile of <i>Artemisia annua</i> from the region of Sliven, Bulgaria. A preliminary NMR study	209
D. Gerginova, D. Dimova, S. Simova, Preliminary NMR and chemometric study of pine jams used as medicinal remedies.....	215
N. Markova, A. Georgieva, I. Philipova, I. Angelov, V. Enchev, A. Kril, Cytotoxicity assay and intracellular localization of 2-carbamido-1,3-indandione in Balb/c 3T3 cells.....	221
P. Nikolova, Ch. Georgieva, G. Dimitrov, I. Stoineva, Semisynthesis human insulin: transpeptidation or coupling mechanism?	227
H. Barakat, I. Khalifa, G. A. Ghazal, A. Shams, P. N. Denev, Chemical composition and nutritional value of seeds from new quinoa accessions, cultivated in Egypt.....	231
Ts. Kolev, E. Velcheva, B. Stamboliyska, Computational and experimental studies of the IR spectra and structure on violuric acid and its anions.....	239
I. Eneva, M. Aliosman, I. Angelov, K. Popov, V. Mantareva, Mono-ring phthalocyanine complexes of large ions Lu ³⁺ and Sn ⁴⁺ : synthesis and comparison of photophysical properties.....	246
Z. Kokanova-Nedialkova, P. Nedialkov, Antioxidant properties of 6-methoxyflavonol glycosides from the aerial parts of <i>Chenopodium bonus-henricus</i> L.....	253
A. S. Salim, V. P. Bivolarski, T. A. Vasileva, Iliia N. Iliev, Enzymatic synthesis of fructo-oligosaccharides by recombinant levansucrase from <i>Leuconostoc mesenteroides</i> Lm17.....	259
St. I. Yordanov, A. D. Bachvarova-Nedelcheva, R. S. Iordanova, Influence of ethylene glycol on the hydrolysis-condensation behavior of Ti(IV) butoxide.....	265
K. Peycheva, I. Bangov, M. Stancheva, Mathematical description of the relation between water and sea organism pollution.....	271
N.G. Vassilev, <i>Ab Initio</i> SCF study of the barrier to internal rotation in simple amides.....	275
P. K. Lukova, D. P. Karcheva-Bahchevanska, M. M. Nikolova, I. N. Ilie ² , R. D. Mladeno, Comparison of structure and antioxidant activity of polysaccharides extracted from the leaves of <i>Plantago major</i> L., <i>P. media</i> L. and <i>P. lanceolata</i> L.....	282
E. Velcheva, S. Tapanov, D. Yancheva, S. Soyakov, B. Stamboliyska, Multi-analytical study on the wall paintings of kurilo monastery "St. Ivan Rilski", Bulgaria.....	289
INSTRUCTIONS TO THE AUTHORS	295

СЪДЪРЖАНИЕ

<i>Г. Андреев</i> , Научна биография на Академик Иван Юхновски	5
<i>В. Николова, Д. Чешмеджиева, С. Илиева, Б. Гълъбов</i> , Реактивоспособност към водородно свързване на атомните центрове в азотните бази на нуклеиновите киселини	18
<i>С. Х. Цонева, С. Р. Начкова, Г. Н. Андреев, П. Н. Пенчев</i> , Идентификация на компонентите на смеси с многопроменлива линейна регресия и изваждане на спектри: търсене в инфрачервени и раман спектрални библиотеки.....	24
<i>А. Д. Косатева, М. Стефанова, С. П. Маринов, Л. Гонсалвеш</i> , Органични вещества от излугване на някои български лигнити	29
<i>К. Л. Захариева, К. И. Миленова, С. В. Василев, С. С. Димова, И. Д. Стамболова, В. Н. Блъсков</i> , Получаване и сравнително фотокаталитично изследване на NiMnO ₃ /Mn ₂ O ₃ и NiO _{0.8} ZnO _{0.2} /ZnO материали за премахване на Малахитово зелено багрило от воден разтвор	34
<i>К. И. Миленова, И. А. Аврамова, П. М. Николов</i> , Сравнение на фотокаталитичното поведение под УВ-светлина на PdO-CeO ₂ /Al ₂ O ₃ и PdO-CeO ₂ /ZSM5 за разграждане на органични багрила	40
<i>Т. С. Цончева, Г. С. Исса, Р. Н. Иванова, М. Д. Димитров, И. П. Спасова, Д. Г. Ковачева, Б. Г. Цинцарски, Н. В. Петров</i> , Активен въглен, получен от отпадна биомаса, като носител на смесени мед-манганови оксидни катализатори за разлагане на метанол.....	48
<i>И. Г. Генова, Т. С. Цончева</i> , Би-компонентни катализатори за разпадане на метанол на основата на модифициран с оксиди на медта и кобалта силициев диоксид: влияние на метода на нанасяне.....	54
<i>Г. С. Исса, Т. С. Цончева, А. Н. Милева, М. Д. Димитров, Д. Н. Ковачева, И. Хених, В. Щенгъл</i> , Мед-модифицирани мезопорести наноструктурирани церий-титан оксиди като катализатори за екологосъобразни процеси: Влияние на фазовия състав.....	62
<i>Е. Чернева, Ц. Колев</i> , Диамиди на квадратната киселина, съдържащи метионинамидов остатък – синтез, спектрално и теоретично изследване	68
<i>Н. Петкова, И. Иванов, Д. Михайлова, А. Кръстанов</i> , Съдържание на фенолни киселини и антиоксидантен капацитет на чайове <i>Melissa officinalis</i> L., достъпни в търговската мрежа на България.....	74
<i>Л. Гонсалвеш, М. Димов, С. Маринов</i> , Производство на адсорбенти от отпадни гуми и охарактеризиране на тяхната пориста структура	81
<i>М. Гунчева, Д. Янчева, В. Узунова, П. Осовиц, К. Идакиева, Ю. Райнова, Е. Янус, Р. Цонева</i> , Бета-хемоцианин от <i>Helix rotatia</i> в присъствие на четири органични соли на основата на холин и аминокиселини.....	86
<i>Ю. Райнова, С. Тодинова, К. Идакиева</i> , Модификация с натриев перйодат увеличава структурната стабилност на хемоцианин от моллюсков организми	91
<i>Р. Иванова, М. Димитров, Д. Ковачева, Т. Цончева</i> , Модифицирани с мед и/или кобалт наноструктурирани Се-Zr смесени оксиди като ефективни катализатори за пълно окисление на етилацетат.....	98
<i>Б. Стамболийска, А. Яшари, Д. Янчева, Б. Михова, Д. Бътовска, Е. Поповски, К. Младеновска</i> , Структура и радикал – улавяща активност на триазоло- и изоксазолхидразинилиден-хроман-2,4-диони	105
<i>Р. Хр. Ляпчев, М. Г. Дангалов, Г. Г. Генчева, Н. Г. Василев, П. Й. Петров</i> , Атропизомерни фосфор заместени 1-фенил-3,4-дихидрохиназолин-1-иеви ННС прекурс.....	112
<i>Л. Гонсалвеш, А. Попова, С. Маринов, М. Стефанова, Р. Карлеер, Я. Иперман</i> , Влияние на деминерализацията върху характеристиките и адсорбционното поведение на активни въглени, получени от свински тор.....	120
<i>В. Трифонова, К. Василев, А. Ахмедова</i> , Металодендимери за каталитично епоксидиране - теоретични познания за структурата на Мо (VI) комплекси на поли (пропилен имин) дендримери	128
<i>А. Йорданова, С. Симова, Й. Косева, Р. Николова, В. Николов, Р. Стоянова</i> , Твърди разтвори на алумиево-скандиеви волфраматни Al _{2-x} Sc _x (WO ₄) ₃ : разпределение на Al и Sc на локално ниво.....	136
<i>Е. Велчева, Б. Стамболийска, С. Стоянов</i> , Експериментално и теоретично изследване на ич спектри и структура на 4-ацетамидобензоена киселина (ацедобен), нейните оксианион и дианион.....	145
<i>М. Н. Маринов, С. М. Бакалова, Р. Й. Проданова, Н. В. Маркова</i> , Конформационни и спектрални свойства на новосинтезирани съединения, получени при реакция на алрестатин и 3-аминоциклоалканспиро-5-хидантоини.....	152
<i>Б. И. Николова-Младенова, Л. П. Пейкова, М. Б. Георгиева, Ал. Б. Златков</i> , Приложение на RP-HPLC метод за определяне на химичната и физиологичната стабилност на два новосинтезирани метоксипроизводни бензоилхидразона.....	158

Б. И. Николова-Младенова, А. Г. Бакалова, <i>In silico</i> лекарствено подобие и <i>in vitro</i> цитотоксична активност на някои 3,5-дизаместени хидантоини и спирохидантоини.....	163
Е. Чернева, Р. Т. Буюклиев, Н. Бурджиев, Р. Михайлова, А. Г. Бакалова, Синтез, физико-химично охарактеризиране, теоретично изследване и цитотоксична активност на паладиеви комплекси с 3'-амино-4-тио-1н-тетрахидропиранспиро-5'-хидантоин.....	170
М. Попова, Д. Антонова, В. Банкова, Състав на прополиса и американски гнилец: има ли връзка?.....	175
А. Трендафилова, М. Тодорова, В. Иванова, И. Анева, Фенолни съединения и антиоксидантен капацитет на <i>Inula oculius-christi</i> от България.....	180
С. Стоянов, Д. Янчева, А. Косатева, ИЧ спектрално изследване на електрохимичната редукция на нимезулид.....	188
В. Николова, С. Ангелова, Т. Дудев, Комплексообразуване между метални йони от ПА/ПБ групи и β -циклодекстрин: изследване с теория на функционала на плътността.....	194
С. М. Бакалова, Х. Канети, Н. Маркова, Теоретично изследване на екзо-селективни присъединявания по Дилс – Алдер, катализирани от алуминиев хлорид.....	200
Н. Георгиева, З. Янева, С. Симова, Г. Николова, Синтез и свойства на някои Бети бази като потенциални лекарствени препарати.....	208
В. Куртева, А. Трендафилова, С. Симова, Химичен профил на <i>Artemisia annua</i> от региона на гр. Сливен, България. Предварително ЯМР изследване.....	214
Д. Гергинова, Д. Димова, С. Симова, Изследване на борови сладка използвани в народната медицина посредством ЯМР и хеометрия.....	220
Н. Маркова, А. Георгиева, И. Филипова, И. Ангелов, В. Енчев, А. Крил, Изследване на цитотоксичността и вътреклетъчната локализация на 2-карбамидо-1,3-индандион в Balb/c 3T3 клетки.....	226
П. Николова, Х. Георгиева, Г. Димитров, И. Стойнева, Семисинтез на човешки инсулин: транспептидиране или кондензационен механизъм?.....	230
Х. Баракат, И. Халифа, Г. А. Газал, А. Шамс, П. Н. Денев, Химичен състав и хранителна стойност на семена от нови генотипове киноа, култивирани в Египет.....	238
Ц. Колев, Е. Велчева, Б. Стамболийска, Теоретично и експериментално изследване на ИЧ спектри и структурата на виолуровата киселина и нейните аниони.....	245
И. Енева, М. Алиосман, И. Ангелов, К. Попов, В. Мантарева, Моно-пръстенни фталоцианинови комплекси с йони на Lu^{3+} и Sn^{4+} : синтез и сравнителни изследвания на фотофизичните свойства.....	252
З. Коканова-Недялкова, П. Недялков, Антиоксидантни свойства на 6-метоксифлавонолови гликозиди от надземните части на <i>Cheporodium bonus-henricus</i> L.....	258
А. С. Салим, В. П. Биволарски, Т. А. Василева, И. Н. Илиев, Ензимен синтез на фрукто-олигозахариди с помощта на рекомбинантна леванзахараза от <i>Leuconostoc mesenteroides</i> Lm17.....	264
Ст. И. Йорданов, А. Д. Бъчварова – Неделчева, Р. С. Йорданова, Влияние на етилен гликола върху хидролизно – кондензационното поведение на Ti(IV) бутоксид.....	270
К. Пенчева, И. Бангов, М. Станчева, Математическо описание на зависимостта между замърсяването на морската вода и на морските организми.....	281
П. К. Лукова, Д. П. Карчева-Бахчеванска, М. М. Николова, И. Н. Илиев, Р. Д. Младенов, Сравнение на структурата и антиоксидантната активност на полизахариди, изолирани от листа на <i>Plantago major</i> L., <i>P. media</i> L. и <i>P. lanceolata</i> L.....	294
ИНСТРУКЦИЯ ЗА АВТОРИТЕ	295